COLD-ION POPULATIONS AND COLD-ELECTRON POPULATIONS IN THE EARTH'S MAGNETOSPHERE AND THEIR IMPACT ON THE SYSTEM, 2nd Edition

EDITED BY: Joseph E. Borovsky, Gian Luca Delzanno, Elena Kronberg and Cecilia Norgren

PUBLISHED IN: Frontiers in Astronomy and Space Sciences and Frontiers in Physics

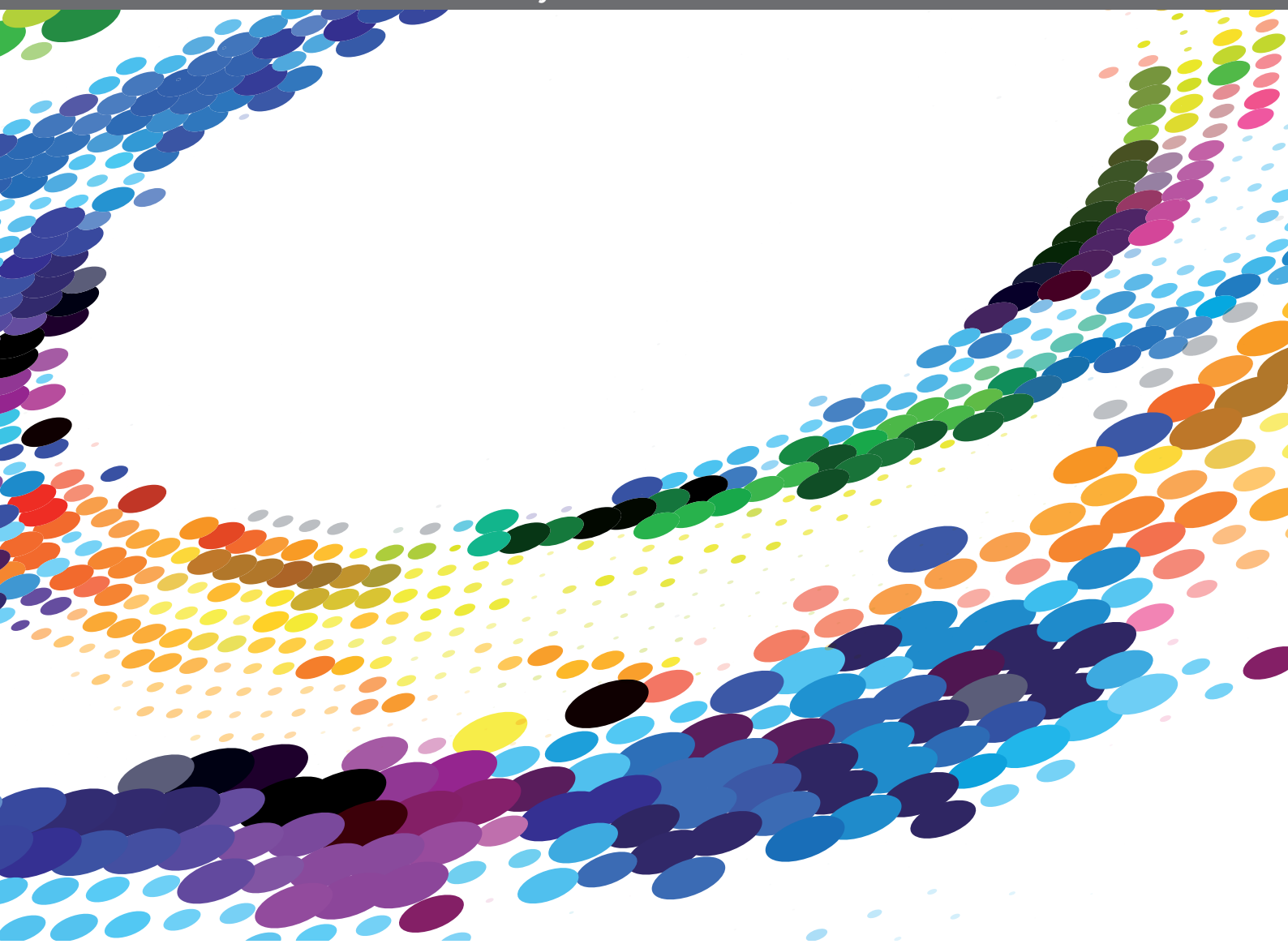

frontiers Research Topics

frontiers

ISSN 1664-8714
ISBN 978-2-8325-2249-3
DOI 10.3389/978-2-8325-2249-3

About Frontiers

Frontiers is more than just an open-access publisher of scholarly articles: it is a pioneering approach to the world of academia, radically improving the way scholarly research is managed. The grand vision of Frontiers is a world where all people have an equal opportunity to seek, share and generate knowledge. Frontiers provides immediate and permanent online open access to all its publications, but this alone is not enough to realize our grand goals.

Frontiers Journal Series

The Frontiers Journal Series is a multi-tier and interdisciplinary set of open-access, online journals, promising a paradigm shift from the current review, selection and dissemination processes in academic publishing. All Frontiers journals are driven by researchers for researchers; therefore, they constitute a service to the scholarly community. At the same time, the Frontiers Journal Series operates on a revolutionary invention, the tiered publishing system, initially addressing specific communities of scholars, and gradually climbing up to broader public understanding, thus serving the interests of the lay society, too.

Dedication to Quality

Each Frontiers article is a landmark of the highest quality, thanks to genuinely collaborative interactions between authors and review editors, who include some of the world's best academicians. Research must be certified by peers before entering a stream of knowledge that may eventually reach the public - and shape society; therefore, Frontiers only applies the most rigorous and unbiased reviews.
Frontiers revolutionizes research publishing by freely delivering the most outstanding research, evaluated with no bias from both the academic and social point of view. By applying the most advanced information technologies, Frontiers is catapulting scholarly publishing into a new generation.

What are Frontiers Research Topics?

Frontiers Research Topics are very popular trademarks of the Frontiers Journals Series: they are collections of at least ten articles, all centered on a particular subject. With their unique mix of varied contributions from Original Research to Review Articles, Frontiers Research Topics unify the most influential researchers, the latest key findings and historical advances in a hot research area! Find out more on how to host your own Frontiers Research Topic or contribute to one as an author by contacting the Frontiers Editorial Office: frontiersin.org/about/contact

COLD-ION POPULATIONS AND COLD-ELECTRON POPULATIONS IN THE EARTH'S MAGNETOSPHERE AND THEIR IMPACT ON THE SYSTEM,
2nd Edition

Topic Editors:
Joseph E. Borovsky, Space Science Institute, United States
Gian Luca Delzanno, Los Alamos National Laboratory (DOE), United States
Elena Kronberg, Ludwig Maximilian University of Munich, Germany
Cecilia Norgren, University of Bergen, Norway

Publisher's note: In this 2nd edition, the following articles have been added: Borovsky JE, Delzanno GL, Kronberg EA and Norgren C (2023) Editorial: Cold-ion populations and cold-electron populations in the Earth's magnetosphere and their impact on the system. Front. Astron. Space Sci. 10:1180235. doi: 10.3389/fspas.2023.1180235; Ripoll J-F, Pierrard V, Cunningham GS, Chu X, Sorathia KA, Hartley DP, Thaller SA, Merkin VG, Delzanno GL, De Pascuale S and Ukhorskiy AY (2023) Modeling of the cold electron plasma density for radiation belt physics. Front. Astron. Space Sci. 10:1096595. doi: 10.3389/fspas.2023.1096595; Maldonado CA, Resendiz Lira PA, Delzanno GL, Larsen BA, Reisenfeld DB and Coffey V (2023) A review of instrument techniques to measure magnetospheric cold electrons and ions. Front. Astron. Space Sci. 9:1005845. doi: 10.3389/fspas.2022.1005845

Citation: Borovsky, J. E., Delzanno, G. L., Kronberg, E., Norgren, C., eds. (2023). Cold-Ion Populations and Cold-Electron Populations in the Earth's Magnetosphere and Their Impact on the System, 2nd Edition. Lausanne: Frontiers Media SA. doi: 10.3389/978-2-8325-2249-3

Table of Contents

05 ***Editorial: Cold-Ion Populations and Cold-Electron Populations in the Earth's Magnetosphere and Their Impact on the System***
Joseph E. Borovsky, Gian Luca Delzanno, Elena A. Kronberg and Cecilia Norgren

08 ***Perspective on Energetic and Thermal Atmospheric Photoelectrons***
W. K. Peterson

15 ***Improving Predictions of the 3D Dynamic Model of the Plasmasphere***
Viviane Pierrard, Edith Botek and Fabien Darrouzet

23 ***The Effect of the Thermosphere on Ionosphere Outflows***
J. Krall and J. D. Huba

30 ***Van Allen Probes Observations of Oxygen Ions at the Geospace Plume***
John C. Foster and Philip J. Erickson

42 ***On the Impacts of Ions of Ionospheric Origin and Their Composition on Magnetospheric EMIC Waves***
Justin H. Lee, Lauren W. Blum and Lunjin Chen

51 ***Magnetospheric Mass Density as Determined by ULF Wave Analysis***
Kazue Takahashi and Richard E. Denton

67 ***Energy Exchange Between Electromagnetic Ion Cyclotron (EMIC) Waves and Thermal Plasma: From Theory to Observations***
M. E. Usanova

73 ***On the Presence and Thermalization of Cold Ions in the Exhaust of Antiparallel Symmetric Reconnection***
Cecilia Norgren, Paul Tenfjord, Michael Hesse, Sergio Toledo-Redondo, Wen-Ya Li, Yin Xu, Norah Kaggwa Kwagala, Susanne Spinnangr, Håkon Kolstø and Therese Moretto

88 ***Dayside Diffuse Aurora and the Cold-Plasma Structuring: A Brief Review***
De-Sheng Han

94 ***High-Latitude Cold Ion Outflow Inferred From the Cluster Wake Observations in the Magnetotail Lobes and the Polar Cap Region***
Kun Li, Mats André, Anders Eriksson, Yong Wei, Jun Cui and Stein Haaland

108 ***The Key Role of Cold Ionospheric Ions As a Source of Hot Magnetospheric Plasma and As a Driver of the Dynamics of Substorms and Storms***
C. R. Chappell, A. Glocer, B. L. Giles, T. E. Moore, M. M. Huddleston and D. L. Gallagher

128 ***Quantification of Cold-Ion Beams in a Magnetic Reconnection Jet***
Yu-Xuan Li, Wen-Ya Li, Bin-Bin Tang, C. Norgren, Jian-Sen He, Chi Wang, Qiu-Gang Zong, S. Toledo-Redondo, M. André, C. Chappell, J. Dargent, S. A. Fuselier, A. Glocer, D. B. Graham, S. Haaland, L. Kistler, B. Lavraud, T. E. Moore, P. Tenfjord, S. K. Vines and J. Burch

139 ***Potential Association Between the Low-Energy Plasma Structure and the Patchy Pulsating Aurora***
Jun Liang, Y. Nishimura, E. Donovan, B. Yang and V. Angelopoulos

158 ***A Review of Observations of Molecular Ions in the Earth's Magnetosphere-Ionosphere System***
Mei-Yun Lin and Raluca Ilie

174 ***Charge-Exchange Byproduct Cold Protons in the Earth's Magnetosphere***
Joseph E. Borovsky, Jianghuai Liu, Raluca Ilie and Michael W. Liemohn

187 ***A Review of Instrument Techniques to Measure Magnetospheric Cold Electrons and Ions***
Carlos A. Maldonado, Pedro A. Resendiz Lira, Gian L. Delzanno, Brian A. Larsen, Daniel B. Reisenfeld and Victoria Coffey

204 ***Modeling of the Cold Electron Plasma Density for Radiation Belt Physics***
J.-F. Ripoll, V. Pierrard, G. S. Cunningham, X. Chu, K. A. Sorathia, D. P. Hartley, S. A. Thaller, V. G. Merkin, G. L. Delzanno, S. De Pascuale and A. Y. Ukhorskiy

frontiers | Frontiers in Astronomy and Space Sciences

TYPE Editorial
PUBLISHED 03 April 2023
DOI 10.3389/fspas.2023.1180235

OPEN ACCESS

EDITED BY
Evgeny V. Mishin,
Air Force Research Laboratory
New Mexico, United States

REVIEWED BY
Colin Forsyth,
University College London,
United Kingdom

*CORRESPONDENCE
Joseph E. Borovsky,
jborovsky@spacescience.org

SPECIALTY SECTION
This article was submitted
to Space Physics,
a section of the journal
Frontiers in Astronomy and
Space Sciences

RECEIVED 05 March 2023
ACCEPTED 24 March 2023
PUBLISHED 03 April 2023

CITATION
Borovsky JE, Delzanno GL, Kronberg EA and Norgren C (2023), Editorial: Cold-ion populations and cold-electron populations in the Earth's magnetosphere and their impact on the system. *Front. Astron. Space Sci.* 10:1180235. doi: 10.3389/fspas.2023.1180235

Editorial: Cold-ion populations and cold-electron populations in the Earth's magnetosphere and their impact on the system

Joseph E. Borovsky[1]*, Gian Luca Delzanno[2], Elena A. Kronberg[3] and Cecilia Norgren[4]

[1]Space Science Institute, Boulder, CO, United States, [2]Los Alamos National Laboratory, Los Alamos, NM, United States, [3]Faculty of Geosciences, Ludwig Maximilian University of Munich, Munich, Germany, [4]Department of Physics and Technology, University of Bergen, Bergen, Norway

KEYWORDS

magnetosphere, ionosphere, space plasma, reconnection, plasma waves, aurora

Editorial on the Research Topic
Cold-ion populations and cold-electron populations in the Earth's magnetosphere and their impact on the system

This Research Topic is the offshoot of an on-line workshop "*The Impact of Cold-Plasma Populations in the Earth's Magnetosphere*" that was held September 28—2 October 2020. The workshop was originally scheduled as an in-person meeting for June 1–4, 2020 in Los Alamos, New Mexico, United States. A growing realization of the importance of cold electrons in the Earth's magnetosphere-ionosphere system led the Research Topic Editors to change "cold plasma" to "cold ions and cold electrons" when creating the title of this Research Topic. The Research Topic highlighting illustration appears in Figure 1.

There are several "cold" populations of ions and electrons in the Earth's magnetosphere, where "cold" indicates low energy. The cold populations have temperatures that are typically less than a few-hundred eV, and often as low as 1 eV and less. Cold-ion populations and cold-electron populations are extremely difficult to measure in the Earth's magnetosphere, and their properties, evolutions, and controlling factors are poorly understood (cf. Delzanno et al., 2021). They are sometimes referred to as the "hidden populations" (Olsen, 1982), but they are known to have multiple impacts on the behavior of the global magnetospheric system. These impacts are extensively reviewed in Delzanno et al. (2021): they include (a) the reduction of the dayside reconnection rate and consequently the reduction of solar-wind/magnetosphere coupling, (b) alteration of the growth rate and saturation amplitudes of plasma waves resulting in alterations of the energization rates of the radiation belts, (c) changes in plasma-wave properties resulting in changes in the loss rates of the ring current and radiation belts, (d) changes in the mass density of the magnetosphere resulting in changes in ULF waves and the radial diffusion of the radiation belts, (e) increases of the mass density in the magnetosphere which increases the growth rate of Kelvin-Helmholtz waves on the magnetopause, (f) spatial and temporal structuring of the aurora, (g) altering magnetotail reconnection, (h) changing spacecraft charging, and (i) acting as sources for warm and hot magnetospheric populations.

This Research Topic contains 17 papers that are a combination of Original Research articles, Review articles, and Perspective articles addressing a wide variety of cold-ion

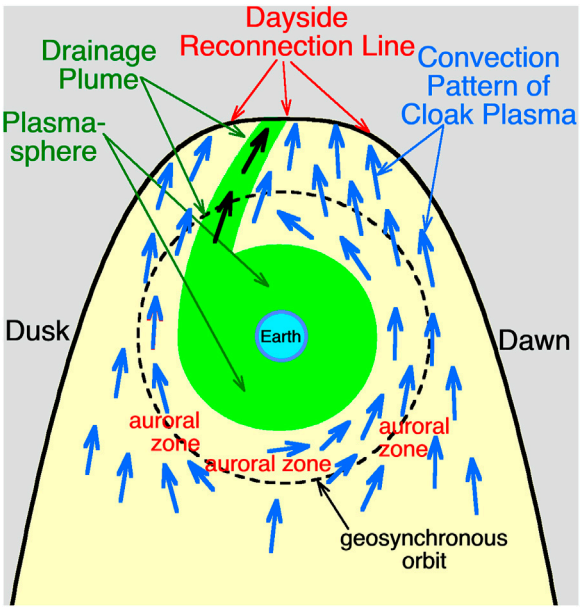

FIGURE 1
A sketch of some of the low-energy populations in the equatorial plane of the magnetosphere during geomagnetically active times. Indicated in green is the plasmaspheric drainage plume flowing into the dayside reconnection line and indicated in blue is the warm plasma cloak flowing into the dayside reconnection line. Geosynchronous orbit is indicated as the dashed black circle.

and cold-electron Research Topic for magnetospheric physics. The 17 papers address the sources of the cold-particle populations, the cold-particle impact on the operation of the magnetosphere-ionosphere system, and measurement techniques for cold electrons and cold ions.

The production of cold-ion populations in the magnetosphere is addressed in a number of papers. Li et al. examine extensive plasma-wake observations of ion outflows from the high-latitude ionosphere into the magnetosphere. Krall and Huba examine the effect of the neutral upper atmosphere's thermal composition and winds on the ion outflow from the ionosphere into the magnetosphere. Borovsky et al. present calculations of the production rates of cold protons in the magnetosphere directly from physical processes ionizing the Earth's cold neutral-hydrogen geocorona.

The properties of cold-particle populations in the Earth's magnetosphere were addressed in several of the Research Topic papers. Lin and Ilie looked at the properties of various molecular-ion populations in the magnetosphere, populations that may be important during times of high geomagnetic activity. Foster and Erickson examined warm and hot oxygen ions in the vicinity of the dayside plasmaspheric drainage plume with implications for localized oxygen outflow from the ionosphere. Takahashi and Denton reviewed critical magnetoseismic observations of the mass densities of ion populations in the magnetosphere; these mass densities impact the properties of ULF waves and can be responsible for mass loading dayside reconnection. Pierrard et al. reviewed improved models of the plasmasphere in the inner magnetosphere: such plasma models are important for the modeling plasma waves in the magnetosphere. Ripoll et al. (2023) reviewed a variety of electron-density models for their usefulness to radiation-belt physics. For cold electrons, Peterson discussed rare measurements of low-energy electrons in the magnetosphere that originated from the ionosphere/atmosphere and elucidated some of the complexities of understanding low-energy-electron dynamics.

Pertaining to the evolution of cold ions in the Earth's magnetospheric system, Usanova reviewed the energy exchange between cold-ion populations and hot-ion and hot-electron populations *via* electromagnetic ion-cyclotron (EMIC) waves and the resulting heating of the cold ions. Chappell et al. reviewed the evolution of cold ions of ionospheric origin becoming critical hot-ion populations in the magnetosphere, in comparison with the more-often-considered solar-wind ion sources of magnetospheric ions.

The physical interactions in the magnetospheric system impacted by cold populations were examined by several papers. Lee et al. reviewed several new results pertaining to EMIC waves and the observed populations of cold ions in the magnetosphere. Norgren et al. investigated the impact of cold ions on magnetic reconnection processes and the properties of cold ions in the outflow jets of reconnection. Li et al. investigate observations of field-aligned beams of cold ions in magnetotail reconnection outflows where the cold ions entered into the outflow jets.

The structuring of the nightside pulsating aurora by structure in the cold plasma of the nightside magnetosphere was reviewed by Liang et al. and the structuring of the dayside diffuse aurora by structure in the cold plasma of the dayside magnetosphere was reviewed by Han.

Finally, Maldonado et al. review measurement techniques for cold ions and cold electrons used in the past and outline innovative methods that could be used in the future.

Author contributions

All authors listed have made a substantial, direct, and intellectual contribution to the work and approved it for publication.

Funding

The work of JB was supported at the Space Science Institute by the NSF GEM Program *via* grant AGS-2027569 and by the NASA Heliophysics LWS program *via* award NNX16AB75G, by the NASA HERMES Interdisciplinary Science Program *via* grant 80NSSC21K1406. The work of EK is supported by German Research Foundation (DFG) under number KR 4375/2-1 within SPP "Dynamic Earth". The work of GD was supported by the Laboratory Directed Research and Development—Exploratory Research (LDRD-ER) Program of Los Alamos National Laboratory under project number 20200276ER. Los Alamos National Laboratory is operated by Triad National Security, LLC, for the National Nuclear Security Administration of U.S. Department of Energy (Contract No. 89233218CNA000001).

Acknowledgments

The authors of this editorial thank Anton Artemyev, John Bonnell, Xuguang Cai, Christopher Cully, Fabien Darrouzet, Mick Denton, Jan Egedal, Dennis Gallagher, Katherine Garcia-Sage, Matina Gkioulidou, Elena Grigorenko, Mike Henderson, Nickolay Ivchenko, Giovanni Lapenta, Jun Linag, Bill Lotko, John Lyon, Binbin Ni, Toshi Nishimura, Vyacheslav Pilipenko, Dimitry Pokhotelov, Scott Thaller, Sergio Toledo-Redondo, Tianran Sun, Roger Varney, Adolfo Vinas, and Tieyan Wang for serving as reviewers for this Research Topic and the authors thank Phil Erickson, Marian Lazar, Larry Lyons, Olga Khabarova, and Chi Wang for their service as editors for this Research Topic.

Conflict of interest

The authors declare that the research was conducted in the absence of any commercial or financial relationships that could be construed as a potential conflict of interest.

Publisher's note

References

Delzanno, G. L., Borovsky, J. E., Henderson, M. G., Resendiz Lira, P. A., Roytershteyn, V., and Welling, D. (2021). The impact of cold electrons and cold ions in magnetospheric physics. *J. Atmos. Sol. Terr. Phys.* 220, 105599. doi:10.1016/j.jastp.2021.105599

Olsen, R. C. (1982). The hidden ion population of the magnetosphere. *J. Geophys. Res.* 87, 3481–3488. doi:10.1029/JA087iA05p03481

Ripoll, J.-F., Pierrard, V., Cunningham, G. S., Chu, X., Sorathia, K., Hartley, D., et al. (2023). Modeling of the ele tron plasma density for radiation belt physics. *Front. Astron. Space Sci.* 2023, 1096595. doi:10.3389/fspas.20XX.744344

frontiers in Astronomy and Space Sciences

PERSPECTIVE
published: 09 April 2021
doi: 10.3389/fspas.2021.655309

Perspective on Energetic and Thermal Atmospheric Photoelectrons

*W. K. Peterson**

Laboratory for Atmospheric and Space Physics, University of Colorado, Boulder, CO, United States

Atmospheric photoelectrons are central to the production of planetary ionospheres. They are created by photoionization of the neutral planetary atmosphere by solar EUV and soft X-ray irradiance. They provide the energy to heat the thermosphere. Thermalized photoelectrons permeate magnetospheres creating polarization electric fields and plasma waves as they interact with ions to maintain charge neutrality. Energetic photoelectrons (>1 eV) have a distinctive energy spectral shape as first revealed in data from the Atmosphere Explorer satellites. Energetic photoelectrons escaping the ionosphere follow local magnetic fields illuminating the planet's magnetic topology. Current models using state-of-the-art EUV observations accurately capture their production and transport. However, in spite of 60 years of space research the electron thermalization processes occurring below 1 eV at low altitudes in planetary thermospheres are not understood quantitatively. Results from event analysis of data from the Mars Atmosphere and Volatile Evolution (MAVEN) mission are not consistent with current models of photoelectron thermalization. The lack of quantitative understanding reflects the complexity of the physics and the lack of a large data base of simultaneous neutral, ion, and electron densities and temperatures in lower planetary thermospheres.

Keywords: photoelectrons, thermalization, ionization, ionosphere, Mars, Earth

OPEN ACCESS

Edited by:
Joseph Eric Borovsky,
Space Science Institute, United States

Reviewed by:
Nickolay Ivchenko,
Royal Institute of Technology, Sweden
Roger Varney,
SRI International, United States

***Correspondence:**
W. K. Peterson
bill.peterson@lasp.colorado.edu

Specialty section:
This article was submitted to Space Physics, a section of the journal Frontiers in Astronomy and Space Sciences

Received: *18 January 2021*
Accepted: *10 March 2021*
Published: *09 April 2021*

Citation:
Peterson WK (2021) Perspective on Energetic and Thermal Atmospheric Photoelectrons. Front. Astron. Space Sci. 8:655309. doi: 10.3389/fspas.2021.655309

INTRODUCTION

Electrons in the atmosphere were investigated by Chapman (1931) and by early radio scientists who inferred the existence of an ionized region surrounding the Earth created by the absorption of radiation from the sun. Early observations of the solar EUV irradiance (e.g., Rense, 1953) and atmospheric photoelectrons (e.g., Hinteregger et al., 1959) demonstrated the need for simultaneous, space based, observations of key ionospheric parameters over all local times and latitudes. NASA addressed this need in the early 1970's with the Atmosphere Explorer (AE) -C, -D, and -E satellites (Dalgarno et al., 1973). The AE satellites provided calibrated measurements of the solar EUV flux, the neutral atmosphere, and ionized components including atmospheric photoelectrons. These data supported the explosion of thermospheric research summarized in Schunk and Nagy (2009).

Current and planned NASA missions investigating planetary thermosheres are focused on understanding energy transport but do not directly address energy transfer associated with electron thermalization. The measurement techniques required to observe energetic (>1 eV) and thermalized (<10,000 °K) photoelectrons have improved since AE. However, there is no systematic investigation of simultaneous *in-situ* electron fluxes spanning the energy range between energetic electrons measured by particle detectors and thermal electrons, measured by Langmuir probes or radars.

I participated in the Atmosphere Explorer mission at the beginning of my career and the Mars Atmosphere and Volatile Evolution (MAVEN) mission to the Martian thermosphere near the end. Here I provide my perspective on observations and models of production, transport, and thermalization of atmospheric photoelectrons. Because of space limitations I'll focus primarily on published observations. The selection of data and models discussed is representative, not complete. Specifically, we do not address the optical observations such as those from NASA's GOLD satellite that use and test models of photoelectron production and transport (e.g., Solomon et al., 2020).

OBSERVATIONS

Figure 1 shows an overview of atmospheric photoelectron observations and selected model outputs from the AE (Dalgarno et al., 1973, inset panel B), Fast Auroral SnapshoT (FAST, Carlson et al., 1998a, inset panel C), and the MAVEN (Jakosky et al., 2015, panel A) satellites. The AE and FAST satellites sampled the Earth's ionosphere; the MAVEN satellite sampled the Martian ionosphere. Each panel shows electron flux in units of $(cm^2\text{-s-sr-eV})^{-1}$ as a function of energy in units of eV. The MAVEN data shown in panel A cover the energy range from 0.01 to 1,000 eV and the flux range from 1 to 10^{25} $(cm^2\text{-s-sr-eV})^{-1}$, spanning both the thermal and energetic ranges. Panels B and C span sub sets of these ranges as indicated by the broad colored lines along the respective axes. In the next few paragraphs the data in **Figure 1** are discussed in the order they were acquired, i.e., AE, FAST, and then MAVEN.

The AE-E data in panel B are reproduced from Doering et al. (1976). The low altitude spectral features in the 20–30 eV range are produced by the ionization of O and N_2 into various energy states by the intense solar irradiance at 30.4 nm. Doering et al.

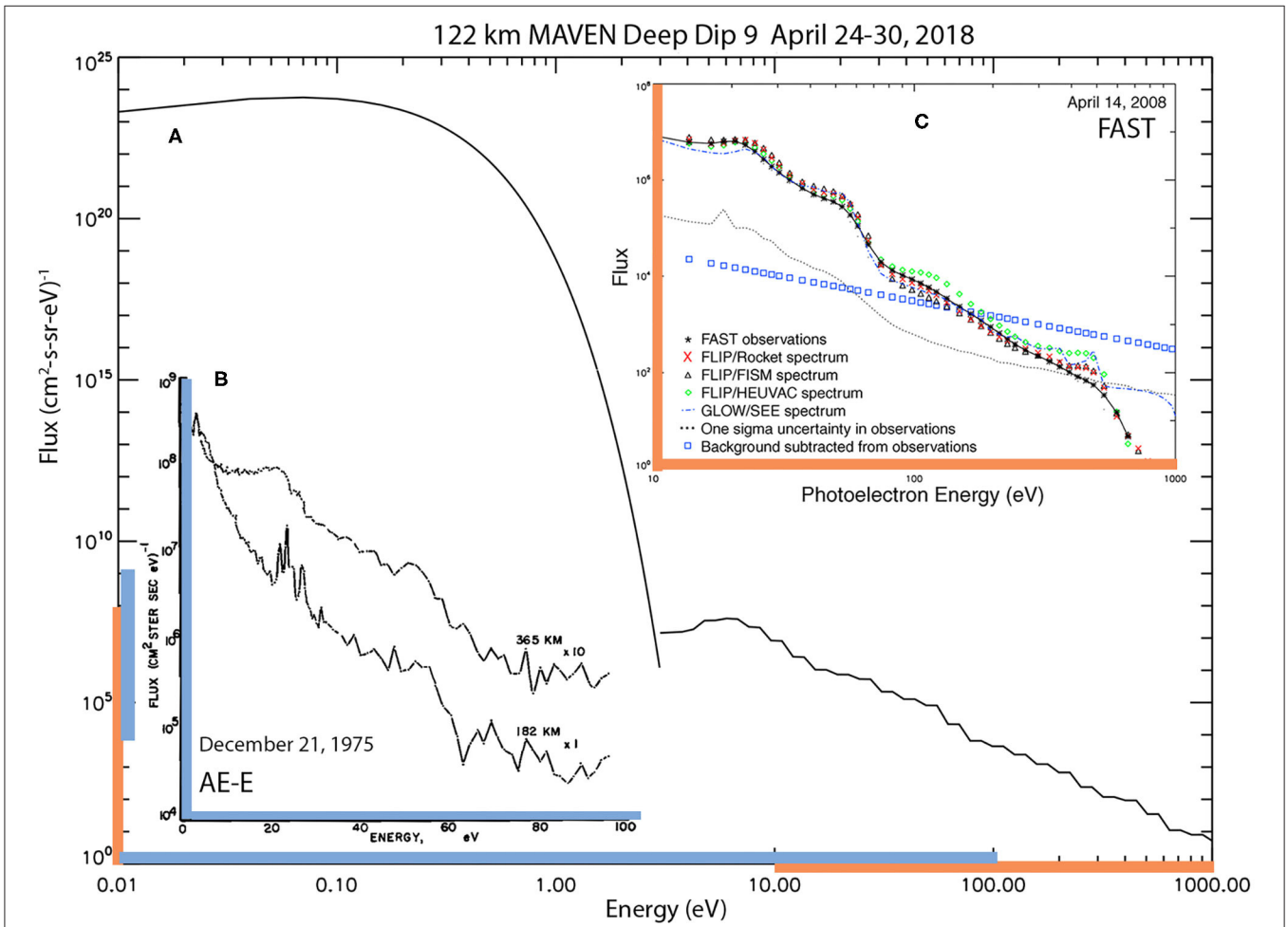

FIGURE 1 | Photoelectron energy spectra in units of number flux $(cm^2\text{-s-sr-eV})^{-1}$ vs. energy from MAVEN **(A)**, AE-E **(B)**, and FAST **(C)**. MAVEN data were acquired at 122 km, below the region of maximum photoelectron production. AE-E data were acquired at 182 and 365 km near and above the region of maximum photoelectron production. FAST data were acquired above 1,000 km in the source cone as described in the text. The number flux ranges for AE-E (blue) and FAST (orange) are sub sets of the MAVEN range as indicated. The AE-E energy scale (blue) is linear; it is logarithmic for FAST (orange) and MAVEN. The solar zenith angles (SZA) for AE-E observations presented are 50° at 182 km and 37° at 365 km. For MAVEN it is 54° at 122 km. For FAST, above 1,000 and for SZA's <90° Peterson et al. (2008) demonstrated that the escaping photoelectron flux is insensitive to the SZA.

show that the strength of the emission features from O and N_2 as a function of altitude follows the changes in both absolute density and composition. Doering noted that the ∼20–30 eV features are smeared out at higher altitudes because the increasing fractional ionization enhances electron-electron collisions. He noted that there is a strong decrease in the spectrum near 60 eV which we now know corresponds to a large decrease in solar irradiance below ∼16 nm (e.g., Woods et al., 2008). Doering et al. were able to determine the absolute spacecraft potential using energy resolved observations of the 20–30 eV emission lines (Lee et al., 1978). A comprehensive summary of the photoelectron data obtained from the AE satellites was published by Lee et al. (1980a,b).

Above 60 eV the signal in panel B is dominated by instrument noise. Winningham et al. (1989) extended the energy range of photoelectron observations to ∼1,000 eV using a more sensitive electron spectrometer with coarser energy resolution. Thousand-eV photoelectrons are produced by the solar soft X-ray flux near 1 nm. Winningham et al. pointed out that the existing observations of the solar flux in the EUV and soft X-ray ranges were inconsistent with their photoelectron observations. This point will be addressed in the section addressing models below.

The data in panel C of **Figure 1** are the daily averaged photoelectron flux measurements acquired above 1,000 km during apogee passes of the FAST satellite equatorward of the auroral zone on April 14, 2008 reproduced from Peterson et al. (2009). These data were acquired in the "source cone." **Figure 2** illustrates the "source cone" concept. It displays data from one of the passes included in the average shown in panel C of **Figure 1**. The FAST electron analyzer has a 360° field of view. The top panel in **Figure 2** shows energy spectra averaged over all angles as a function of time. The bottom panel shows angular spectra averaged over the energy range of 100–12,000 eV. As noted above, the daily average photoelectron spectrum shown in **Figure 1**, Panel C does not include spectra obtained in the polar cap and auroral zone (such as before 19:17 UT in the orbit pass shown in **Figure 2**). The widest band in the lower panel, centered on 180°, is created by energetic photoelectrons produced in the ionosphere below the satellite. The angular width of the band is called the source cone. It is determined by the relative strengths of the magnetic field at the satellite and at the top of the ionosphere, respectively. A weaker band centered on 0° is created by photoelectrons coming from the magnetically conjugate hemisphere (See, for example, Peterson et al., 1977a).

Note that the photoelectron flux in the source cone in units of $(cm^2\text{-s-sr-eV})^{-1}$ above the ionosphere is independent of altitude because of magnetic focusing associated with the source cone formation, as the width of the source cone decreases while the area of the magnetic flux tube increases with increasing altitude. The narrow bands near 90 and 270° come from photoelectrons produced on the spacecraft surface. The vertical bands between 19:20 and 19:25 UT are the noise signal produced by energetic ring current particles that penetrate instrumental shielding.

Peterson et al. (2009) assembled daily averaged photoelectron spectra from within the source cone, corrected individual spectra for spacecraft potential variations and the background from penetrating radiation. The solid black line in panel C of **Figure 1** reports the daily average spectrum for April 14, 2008. The square boxes show the magnitude of the correction for penetrating radiation and the dotted line indicates the estimated one sigma uncertainty of the average spectrum shown. We defer discussion of the model results shown in panel C to the modeling section below.

The data in **Figure 1**, Panel A span 25 orders of magnitude in flux and 5 orders of magnitude in energy. They include thermal electrons with temperatures of <1 eV or $1.16 \cdot 10^4$ °K. The electron data below 3 eV were obtained at Mars from the Langmuir Probe and Waves (LPW) instrument on MAVEN (Andersson et al., 2015). They are presented as a Maxwellian distribution representing the average electron density ($1.2 \cdot 10^5$ cm^{-3}) and average electron temperature (760 °K) observed between 120 and 125 km from April 24 to 30, 2018 during the deep dip #9 interval (Peterson et al., 2020). Above 3 eV the data are from the MAVEN Solar Wind Electron Analyzer (SWEA) instrument (Mitchell et al., 2016) averaged over the same intervals.

GLOBAL INFORMATION OBTAINED FROM LOCALIZED PHOTOELECTRON OBSERVATIONS

The energetic photoelectron energy spectrum is non-thermal and distinct from those found in the solar wind or the magnetosheath. The extremely intense solar He 30.4 nm irradiance produces narrow peaks in the 20–30 eV range that are easily detected by instruments with sufficient energy resolution, as shown in panel B of **Figure 1**. Above ∼60 eV the energy spectrum decreases by almost an order of magnitude corresponding to a decrease in the solar irradiance spectra at ∼15 nm. At higher energies (∼500 eV) emission peaks have been detected in the photoelectron spectra at Mars (Mitchell et al., 2000). These emission features are the result of the production of Auger electrons from atomic oxygen by soft X rays from the sun.

These distinct features in the photoelectron energy spectra allow investigators to use them to trace magnetic field lines, determine global magnetic topology, determine spacecraft potential, infer potential drops along magnetic field lines, and monitor variations in solar extreme ultraviolet (EUV) irradiance. Coates et al. (2011) and others have used instruments with high energy resolution in the 20–30 eV range to identify photoelectrons at large distances from their sources on Venus, Mars, and Titan. Weber et al. (2020), Xu et al. (2019), and others have used instruments with higher sensitivity but coarser energy resolution than those used by Coates et al. to trace and explore the influences and dynamics associated with Martian crustal magnetic fields and their interaction with the solar wind magnetic field. Peterson et al. (1977a,b) used photoelectron energy spectra to identify photoelectrons originating in the magnetically conjugate hemisphere and place limits on the inter-hemispherical potential difference. Peterson et al. (2009, 2012) used photoelectrons to infer solar EUV and XUV energy input

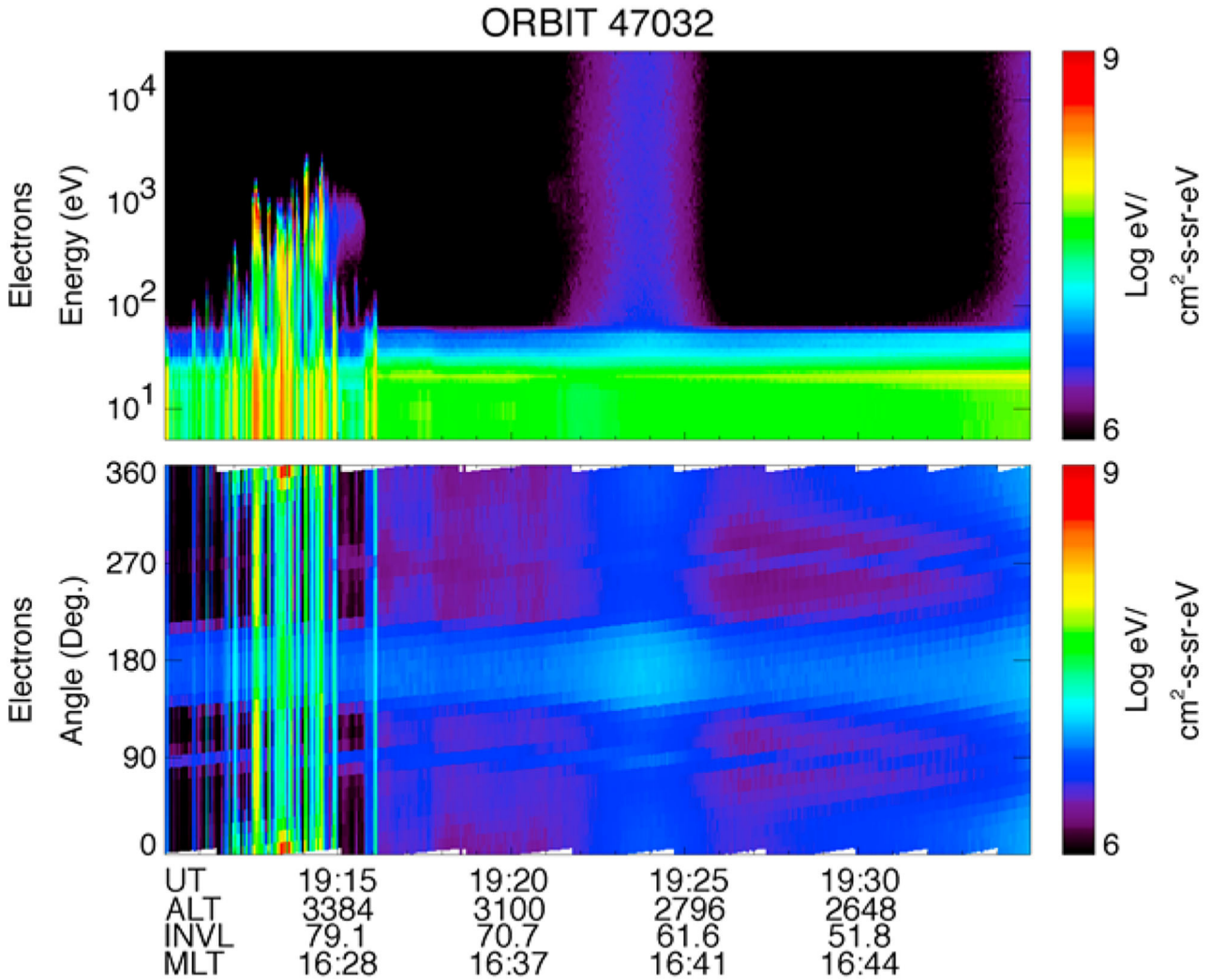

FIGURE 2 | Photoelectron energy flux energy-time (top) and angle-time (bottom) spectrograms from the FAST satellite on April 14, 2008, in units of $(cm^2\text{-s-sr})^{-1}$, are shown by the color bars. Electron pitch angle β in the range 0–180 is related to the angle shown as $\beta = \min(\phi, 360 - \phi)$ where ϕ is the angle shown.

to the thermosphere on both solar flare and solar rotation time scales. Richards and Peterson (2008) directly measured the fraction of conjugate photoelectrons backscattered from the dark hemisphere.

MODELS OF PHOTOELECTRON PRODUCTION, TRANSPORT, AND THERMALIZATION

Initial comparisons of AE photoelectron fluxes and those calculated from AE neutral density and solar EUV measurements were presented by Nagy et al. (1977). Subsequent analysis by Richards and Torr (1984) demonstrated that the generally accepted EUV irradiance spectrum in 1984 (Heroux and Hinteregger, 1978) below 25 nm was inconsistent with observed photoelectron flux above 35 eV. Richards and Torr concluded that the Heroux and Hinteregger solar flux below 25 nm was about a factor of two too low. Modern measurements and models of the solar irradiance confirm the Richards and Torr assertion (e.g., Richards et al., 2006; Woods et al., 2008). The model/data comparisons shown in **Figure 1**, Panel C reproduced from Peterson et al. (2009) illustrate good agreement between observations and current models. The photoelectron models used were the Field Line Interhemispheric Plasma (FLIP) model (Richards et al., 2000) and the Global Airglow (GLOW) model (Solomon et al., 1988). The EUV model/data irradiance sets used as input to the models include a rocket-borne calibration spectrum (Chamberlin et al., 2009), the Solar EUV Experiment (SEE) Version 9 reference spectrum (Woods et al., 2005), the Flare Irradiance Spectral Model (FISM; Chamberlin et al., 2007), and the High-resolution Solar EUV Model for Aeronomic Calculations (HEUVAC; Richards et al., 2006).

The major differences between data and models of energetic photoelectrons now arise from the variability of the solar EUV irradiance, uncertainties in the observed or modeled neutral density from the Mass Spectrometer and Incoherent Scatter (MSIS) model (Hedin et al., 1977) and uncertainties in ionization cross sections, as well as observational uncertainties. McGranaghan et al. (2015) describe a publicly available model that is consistent with the photoelectron data shown in **Figure 1**, with the important caveat that the model has been validated in the low altitude range using electron density, not electron temperature profiles.

THERMALIZATION OF ENERGETIC PHOTOELECTRONS

Thermalized photoelectrons permeate planetary ionospheres and magnetospheres creating polarization electric fields (e.g., Axford, 1968) and plasma waves as they interact with ions to maintain charge neutrality (e.g., Borisov and Nielsen, 2005). They carry field aligned currents (e.g., Carlson et al., 1998b) and transfer energy via a heat flux between the ionosphere and magnetosphere (e.g., Kozyra et al., 1987; Khazanov et al., 2020).

Thermal electrons are created when photoelectron energy is transferred to ions and electrons. There have been too few simultaneous observations of thermal neutral, ion, and electron temperatures in the high-density region of a planetary thermosphere to confirm or refute the assumptions associated with photoelectron thermalization processes included in current models. However, recent results from the MAVEN spacecraft (Hanley et al., 2020; Peterson et al., 2020) have shown that the observed ion, neutral, and electron temperatures on Mars are not consistent with current models. In particular, Hanley et al. have measured ion temperatures using the MAVEN SupraThermal and Thermal Ion Composition (STATIC) instrument (McFadden et al., 2015). They demonstrated that during the MAVEN deep dip interval in October 2015, at the lowest altitudes sampled ($\sim$120 km), the neutral (110 °K), ion (250 °K), and electron (500 °K) temperatures were far from thermal equilibrium and warmer than expected.

DISCUSSION

The production and transport of energetic atmospheric photoelectrons are well-understood and accurately captured by current models using state-of-the-art EUV observations. Techniques have been developed to use the unique energy spectral shape of energetic photoelectrons to tease out details of planetary magnetic topology. However, in spite of 60 years of observations, the processes thermalizing photoelectrons at low altitudes in planetary thermospheres are not quantitatively understood. This lack of progress reflects the complexity of the physics and the lack of a data base of simultaneous neutral, ion, and electron temperatures at low altitudes to guide model development.

Current models of photoelectron thermalization are based on the heat equation which quantifies balance of electron heating and cooling (e.g., Matta et al., 2014). Thermalization occurs where the electron, ion, and neutral temperatures (T_E, T_I, T_N) are equal. It is expected to occur in regions of high density and low fractional ionization. Existing models postulate an altitude (neutral density) where thermalization occurs. MAVEN observations of ion temperatures reported by Hanley et al. (2020) show that thermalization occurs on Mars at higher density ($>10^{11}$ cm^{-3}) and lower fractional ionization ($<2 \times 10^{-6}$) than expected. The analysis of observed electron and neutral temperatures presented in Peterson et al. (2020) suggests thermalization on Mars occurs below 100 km where the Bougher et al. (2015) model gives a density $\sim 10^{12}$ cm^{-3} and a fractional ionization of $\sim 10^{-8}$. Energetic photoelectron production by solar EUV and X-rays occurs well below Earth's mesopause ($\sim$80 km, density $> \sim 10^{14}$ cm^{-3}) where it is strongly modulated by solar activity (e.g., Chamberlin et al., 2007).

Although the data base of incoherent radar ion and electron temperatures is vast, we are unaware of a large-scale data base of simultaneously obtained electron, ion, and neutral temperatures obtained in the Earth's thermosphere at densities $\sim > 10^{12}$ cm^{-3}. Such *in-situ* observations at Earth appear to be possible from satellites at altitudes as low as 100 km (neutral densities $\sim 10^{14}$ cm^{-3} and fractional ionization of $\sim 10^{-9}$) using state-of-the-art- instruments and innovative spacecraft (Sarris et al., 2020; Palmroth et al., 2021). Observations below and above 100 km can be made from rockets.

Maven data and analysis show that current one-dimensional codes which use Maxwellian temperatures, empirical ion and electron temperature profiles, and relatively poorly determined cross sections do not adequately account for energy transfer between ions, neutrals, and electrons at the low temperatures and low altitudes below those that have been sampled on Earth and Mars. Deeper insights into the thermalization will require new observations and models. Relevant observations can be made from satellites and rockets as noted above. They can also be made in laboratory plasma chambers (Koepke, 2008). If sensitive enough diagnostics can be developed, the Enormus Toroidal Plasma Device (ETPD Cooper and Gekelman, 2013) could obtain definitive observations of how electrons, ions, and neutrals thermalize at high densities and low fractional ionization. However, it is more likely that large-scale kinetic codes which do not use assumed electron and ion temperature profiles will provide the needed new insights into the complex physics of electron thermalization.

DATA AVAILABILITY STATEMENT

All datasets presented in this study are included in the article/supplementary material.

AUTHOR'S NOTE

This paper summarizes what I've learned about thermal and energetic atmospheric photoelectrons since I first began investigating them in 1973. This paper examines the source of thermalized photoelectrons, demonstrates that we do not yet

have a quantitative understanding of the thermalization process, and suggests how progress can be made.

AUTHOR CONTRIBUTIONS

The author confirms being the sole contributor of this work and has approved it for publication.

ACKNOWLEDGMENTS

WKP thanks Gwen Hanley for sharing her preliminary ion temperature observations from the MAVEN spacecraft, Phil Richards for re-igniting my interest in atmospheric photoelectrons, and Andrew Yau and Mark Koepke for insightful comments on an early version of this paper.

REFERENCES

Andersson, L., Ergun, R. E., Delory, G. T., Eriksson, A., Westfall, J., Reed, H., et al. (2015). The Langmuir Probe and Waves (LPW) instrument for MAVEN. *Space Sci. Rev*. 195, 173–198. doi: 10.1007/s11214-015-0194-3

Axford, W. I. (1968). The polar wind and the terrestrial helium budget. *J. Geophys. Res. Sp. Phys*. 73, 6855–6859. doi: 10.1029/JA073i021p06855

Borisov, N., and Nielsen, E. (2005). Excitation of plasma waves by unstable photoelectron and thermal electron populations on closed magnetic field lines in the Martian ionosphere. *Ann. Geophys*. 23, 1249–1258. doi: 10.5194/angeo-23-1249-2005

Bougher, S. W., Pawlowski, D., Bell, J. M., Nelli, S., McDunn, T., Murphy, J. R., et al. (2015). Mars global ionosphere-thermosphere model: solar cycle, seasonal, and diurnal variations of the mars upper atmosphere. *J. Geophys. Res. Planets* 120, 311–342. doi: 10.1002/2014JE004715

Carlson, C. W., McFadden, J. P., Ergun, R. E., Temerin, M., Peria, W., Mozer, F. S., et al. (1998b). FAST observations in the downward auroral current region: Energetic upgoing electron beams, parallel potential drops, and ion heating. *Geophys. Res. Lett*. 25, 2017–2020. doi: 10.1029/98GL00851

Carlson, C. W., Pfaff, R. F., and Watzin, J. C. (1998a). The Fast Auroral SnapshoT (FAST) mission. *Geophys. Res. Lett*. 25, 2013–2016. doi: 10.1029/98GL01592

Chamberlin, P. C., Woods, T. N., Crotser, D. A., Eparvier, F. G., Hock, R. A., and Woodraska, D. L. (2009). Solar cycle minimum measurements of the solar extreme ultraviolet (EUV) spectral irradiance on April 14, 2008. *Geophys. Res. Lett*. 36:L05102. doi: 10.1029/2008GL037145

Chamberlin, P. C., Woods, T. N., and Eparvier, G. F. (2007). Flare Irradiance Spectral Model (FISM): daily component algorithms and results. *Space Weather* 5:S07005. doi: 10.1029/2007SW000316

Chapman, S. (1931). The absorption and dissociative or ionizing effect of monochromatic radiation in an atmosphere on a rotating earth. *Proc. Phys. Soc. London* 43, 26–45, 483–501. doi: 10.1088/0959-5309/43/5/302

Coates, A. J., Tsang, S. M. E., Wellbrock, A., Frahm, R. A., Winningham, J. D., Barabash, S., et al. (2011). Atmospheric photoelectrons: comparing Venus, Earth, Mars, and Titan. *Planet. Space Sci.* 59, 1019–1027. doi: 10.1016/j.pss.2010.07.016

Cooper, C. M., and Gekelman, W. (2013). Termination of a magnetized plasma on a neutral gas: the end of the plasma. *Phys. Rev. Lett*. 110:265001. doi: 10.1103/PhysRevLett.110.265001

Dalgarno, A., Hanson, W. B., Spencer, N. W., and Schmerling, E. R. (1973). The atmosphere explorer mission. *Radio Sci.* 8, 263–266. doi: 10.1029/RS008i004p00263

Doering, J. P., Peterson, W. K., Bostrom, C. O., and Potemra, T. A. (1976). High resolution daytime photoelectron energy spectra from AE-E. *Geophys. Res. Lett*. 3, 129–131. doi: 10.1029/GL003i003p00129

Hanley, K. G., Mitchell, D. L., McFadden, J. P., Fowler, C. M., Stone, S. W., Pilinski, M., et. al. (2020). "O_2^+ temperature profiles measured by MAVEN STATIC," in *P049-06 presented at 2020 Fall Meeting, AGU, 1-17 Dec* (San Francisco, CA). doi: 10.5194/epsc2020-349

Hedin, A. E., Salah, E., Evand, J. V., Reber, C. A., Newton, G. P., Spencer, N. W., et al. (1977). A global thermospheric model based on mass spectrometer and incoherent scatter data, MSIS 1. N_2 density and temperature. *J. Geophys. Res*. 82, 2139–2147. doi: 10.1029/JA082i016p02148

Heroux, L., and Hinteregger, H. E. (1978). Aeronomical reference spectrum for solarUV below 2000A°. *J. Geophys. Res*. 8, 5305–5308. doi: 10.1029/JA083iA11p05305

Hinteregger, H. E., Damon, K. R., and Hall, L. A. (1959). Analysis of photoelectrons from solar extreme ultraviolet. *J. Geophys. Res*. 64, 961–969. doi: 10.1029/JZ064i008p00961

Jakosky, B. M., Lin, R. P., and Zurek, R. (2015). The Mars Atmosphere and Volatile Evolution (MAVEN) mission. *Space Sci. Rev*. 195, 3–48. doi: 10.1007/s11214-015-0221-4

Khazanov, G. V., Glocer, A., and Chu, M. (2020). The formation of electron heat flux in the region of diffuse aurora. *J. Geophys. Res.* 125:e2020JA028175. doi: 10.1029/2020JA028175

Koepke, M. E. (2008). Interrelated laboratory and space plasma experiments. *Rev. Geophys*. 46:RG3001. doi: 10.1029/2005RG000168

Kozyra, J. U., Shelley, E. G., Comfort, R. H., Brace, L. H., Cravens, T. E., and Nagy, A. F. (1987). The role of ring current O^+ in the formation of stable auroral red arcs. *J. Geophys. Res*. 92, 7487– 7502. doi: 10.1029/JA092iA07p07487

Lee, J. S., Doering, J. P., Bostrom, C. O., and Potemra, T. A. (1978). Measurement of the daytime photoelectron energy distribution from AE-E with improved energy resolution. *Geophys. Res. Lett*. 5, 581–583. doi: 10.1029/GL005i007p00581

Lee, J. S., Doering, J. P., Potemra, T. A., and Brace, L. H. (1980a). Measurements of the ambient photoelectron spectrum from Atmosphere Explorer: I. AE-E measurements below 300 km during solar minimum conditions. *Planet. Sp. Sci*. 28, 947–971. doi: 10.1016/0032-0633(80)90058-6

Lee, J. S., Doering, J. P., Potemra, T. A., and Brace, L. H. (1980b). Measurements of the ambient photoelectron spectrum from Atmosphere Explorer: II. AE-E measurements from 300 to 1000 km during solar minimum conditions. *Planet. Sp. Sci*. 28, 973–996. doi: 10.1016/0032-0633(80)90059-8

Matta, M., Galand, M., Moore, L., Mendillo, M., and Withers, P. (2014). Numerical simulations of ion and electron temperatures in the ionosphere of Mars: multiple ions and diurnal variations. *Icarus* 227, 78–88. doi: 10.1016/j.icarus.2013.09.006

McFadden, J. P., Kortmann, O., Curtis, D., Dalton, G., Johnson, G., Abiad, R., et al. (2015). MAVEN SupraThermal and Thermal Ion Composition (STATIC) instrument. *Space Sci. Rev*. 195,199–256. doi: 10.1007/s11214-015-0175-6

McGranaghan, R., Knipp, D. J., Solomon, S. C., and Fang, X. (2015). A fast, parameterized model of upper atmospheric ionization rates, chemistry, and conductivity. *J. Geophys. Res. Space Phys*. 120, 4936–4949. doi: 10.1002/2015JA021146

Mitchell, D. L., Lin, R. P., Rème, H., Crider, D. H., Cloutier, P. A., Connerney, J. E. P., et. al. (2000). Oxygen Auger electrons observed in Mars' ionosphere. *Geophys. Res. Lett*. 27, 1871–1874. doi: 10.1029/1999GL010754

Mitchell, D. L., Mazell, C., Sauvaud, J.-A., Thocaven, J.-J., Rouzaud, J., Fedorov, A., et al. (2016). The MAVEN Solar Wind Electron Analyzer (SWEA). *Space Sci. Rev*. 200, 495–528. doi: 10.1007/s11214-015-0232-1

Nagy, A. F., Doering, J. P., Peterson, W. K., Torr, M. R., and Banks, P. M. (1977). Comparison between calculated and measured photoelectron fluxes from Atmosphere Explorer C and E. *J. Geophys. Res*. 82, 5099–5103. doi: 10.1029/JA082i032p05099

Palmroth, M., Grandin, M., Sarris, T., Doornbos, E., Tourgaldis, S., Aikio, A., et al. (2021). Lower-thermsphere-ionosphere (LTI) quantities: current status of measuring techniques and models. *Ann. Geophys*. 49, 189–237. doi: 10.5194/angeo-39-189-2021

Peterson, W. K., Andersson, L., Ergun, R., Thiemann, E., Pilinski, M., Thaller, S., et al. (2020). Subsolar electron temperatures in the lower Martiionosphere. *J. Geophys. Res.* 125:e2019JA027597. doi: 10.1029/2019JA027597

Peterson, W. K., Doering, J. P., Potemra, T. A., Brace, L. H., Heelis, R. A., and Hanson, W. B. (1977b). Measurement of magnetic field aligned potential differences using high resolution conjugate photoelectron energy spectra. *Geophys. Res. Lett*. 4, 373–376. doi: 10.1029/GL004i009p00373

Peterson, W. K., Doering, J. P., Potemra, T. A., McEntire, R. W., and Bostrom, C. O. (1977a). Conjugate photoelectron fluxes observed on Atmosphere Explorer C. Geophys. *Res. Lett*. 4, 109–112. doi: 10.1029/GL004i003p00109

Peterson, W. K., Stavros, E. N., Richards, P. G., Chamberlin, P. C., Woods, T. N., Bailey, S. M., et al. (2009). Photoelectrons as a tool to evaluate spectral variations in solar EUV irradiance over solar cycle timescales. *J. Geophys. Res*. 114:A10304. doi: 10.1029/2009JA014362

Peterson, W. K., Woods, T. N., Chamberlin, P. C., and Richards, G. P. (2008). Photoelectron flux variations observed from the FAST satellite. *Adv. Space Res*. 42, 947–956. doi: 10.1016/j.asr.2007.08.038

Peterson, W. K., Woods, T. N., Fontenla, J. M., Richards, P. G., Chamberlin, P. C., Solomon, S. C., et al. (2012). Solar EUV and XUV energy input to thermosphere on solar rotation time scales derived from photoelectron observations. *J. Geophys. Res*. 117:A05320. doi: 10.1029/2011JA017382

Rense, W. A. (1953). Intensity of Lyman-alpha line in the solar spectrum. *Phys. Rev*. 91,229–302. doi: 10.1103/PhysRev.91.299

Richards, P. G., Buonsanto, M. J., Reinisch, B. W., Holt, J., Fennelly, J. A., Scali, J. L., et al. (2000). On the relative importance of convection and temperature on the behavior of the ionosphere in North America during January 6–12, 1997. *J. Geophys. Res*. 105, 12763–12776. doi: 10.1029/1999JA000253

Richards, P. G., and Peterson, K. W. (2008). Measured and modeled backscatter of ionospheric photoelectron fluxes. *J. Geophys. Res*. 113:A08321. doi: 10.1029/2008JA013092

Richards, P. G., and Torr, D. G. (1984). An investigation of the consistency of ionospheric measurements of the photoelectron flux and solar EUV flux. *J. Geophys. Res*. 89, 5625–5635. doi: 10.1029/JA089iA07p05625

Richards, P. G., Woods, T. N., and Peterson, W. K. (2006). HEUVAC: a new high resolution solar EUV proxy model. *Adv. Sp. Res*. 37, 315–322. doi: 10.1016/j.asr.2005.06.031

Sarris, T. E., Talaat, E. R., Palmroth, M., Dandouras, I., Armandillo, E., Kervalishvili, G., et al. (2020). Daedalus: a low-flying spacecraft for in situ exploration of the lower thermosphere–ionosphere. *Geosci. Instrum. Method. Data. Syst*. 9, 153–191. doi: 10.5194/gi-9-153-2020

Schunk, R., and Nagy, A. (2009). *Ionospheres: Physics, Plasma Physics, and Chemistry (2nd ed., Cambridge Atmospheric and Space Science Series)*. Cambridge: Cambridge University Press. doi: 10.1017/CBO9780511635342

Solomon, S. C., Andersson, L., Burns, A. G., Eastes, R. W., Martinis, C., McClintock, W. E., et al. (2020). Global scale observations and modeling of far ultraviolet airglow during twilight. *J. Geophys. Res*. 125:e2019JA027645. doi: 10.1029/2019JA027645

Solomon, S. C., Hays, P. B., and Abreu, J. V. (1988). The auroral 6300A emission: observations and modeling. *J. Geophys. Res*. 93, 9867–9882. doi: 10.1029/JA093iA09p09867

Weber, T., Brain, D., Xu, S., Mitchell, D., Espley, J., Halekas, J., et al. (2020). The influence of interplanetary magnetic field direction on Martian crustal magnetic field topology. *Geophys. Res. Lett*. 47:e2020GL087757. doi: 10.1029/2020GL087757

Winningham, J. D., Decker, D. T., Kozyra, J. U., and Nagy, A. F., Jasperse, J.R. (1989). Energetic (>60 eV) atmospheric photoelectrons. *J. Geophys. Res*. 94, 15335–15348. doi: 10.1029/JA094iA11p15335

Woods, T. N., Chamberlin, P. C., Peterson, W. K., Meier, R. R., Richards, P. G., Strickland, D. J., et al. (2008). XUV Photometer System (XPS): improved solar irradiance algorithm using CHIANTI spectral models. *Solar Phys*. 250, 235–267. doi: 10.1007/s11207-008-9196-6

Woods, T. N., Eparvier, F. G., Bailey, S. M., Chamberlin, P. C., Lean, J., Rottman, G. J., et al. (2005). The solar EUV Experiment (SEE): mission overview and first results. *J. Geophys. Res*. 110:A01312. doi: 10.1029/2004JA010765

Xu, S., Weber, T., Mitchell, D. L., Brain, D. A., Mazelle, C., DiBraccio,G. A., et al. (2019). A technique to infer magnetic topology at Mars and its application to the terminator region. *J. Geophys. Res*. 124, 1823–1842. doi: 10.1029/2018JA026366

Conflict of Interest: The author declares that the research was conducted in the absence of any commercial or financial relationships that could be construed as a potential conflict of interest.

frontiers in Astronomy and Space Sciences

PERSPECTIVE
published: 07 May 2021
doi: 10.3389/fspas.2021.681401

Improving Predictions of the 3D Dynamic Model of the Plasmasphere

Viviane Pierrard[1,2]*, *Edith Botek*[1] *and Fabien Darrouzet*[1]

[1] Royal Belgian Institute for Space Aeronomy, Solar-Terrestrial Center of Excellence (STCE) and Space Physics, Brussels, Belgium, [2] Center for Space Radiations (CSR) and Georges Lemaître Center for Earth and Climate Research (TECLIM), Earth and Life Institute (ELI), Université catholique de Louvain (UCLouvain), Louvain-la-Neuve, Belgium

In this perspective paper, we review and discuss different ways that can be used to improve the predictions of the models of the plasmaspheric region. The density of the background cold plasma and the plasmapause position are very important to determine the formation and propagation of waves and interactions with the other regions of the magnetosphere. Improvement of predictions includes refinement of the forecast of the geomagnetic indices that influence the density and the temperature of the particles in some models. Progress is also necessary for the understanding of the physical processes that affect the position of the plasmapause and its thickness since this boundary is not always very sharp, especially during low geomagnetic activity. These processes include the refilling after geomagnetic storms and substorms, the links with the ionosphere, and the expanding plasmaspheric wind during prolonged quiet periods. Using observations from *in situ* satellites like Van Allen Probes (EMFISIS and HOPE instruments), empirical relations can be determined to improve the dependence of the density and the temperature as a function of the radial distance, the latitude, and the magnetic local time, inside and outside the plasmasphere. This will be the first step for the improvement of our 3D dynamic SWIFF plasmaspheric model (SPM).

Keywords: plasmasphere, plasmapause, model, improvements, trough, ionosphere

OPEN ACCESS

Edited by:
Joseph Eric Borovsky,
Space Science Institute, United States

Reviewed by:
Michael Denton,
Space Science Institute, United States
Dennis Gallagher,
National Aeronautics and Space Administration (NASA), United States

***Correspondence:**
Viviane Pierrard
viviane.pierrard@aeronomie.be

Specialty section:
This article was submitted to Space Physics, a section of the journal Frontiers in Astronomy and Space Sciences

Received: *16 March 2021*
Accepted: *13 April 2021*
Published: *07 May 2021*

Citation:
Pierrard V, Botek E and Darrouzet F (2021) Improving Predictions of the 3D Dynamic Model of the Plasmasphere. Front. Astron. Space Sci. 8:681401. doi: 10.3389/fspas.2021.681401

INTRODUCTION

The plasmasphere is the extension of the ionosphere at low and mid-latitudes and is filled by low-energy plasma (Lemaire and Gringauz, 1998). Observations of Cluster and IMAGE (Imager for Magnetopause-to-Aurora Global Exploration) spacecraft have provided a new insight into this region (Darrouzet et al., 2009), recently completed by the measurements of Van Allen Probes (Ren et al., 2018). Different empirical and physics-based models have been developed to reproduce the inner region of the magnetosphere and its boundary called the "plasmapause" [see Pierrard et al. (2009) for a review]. It is quite difficult to compare all the existing models, since some are purely empirical (e.g., Sheeley et al., 2001), based on data assimilation; some are an amalgam of different analytical relations (e.g., Gallagher et al., 2000), and others more physics based, e.g., the Dynamic Global Core Plasma Model (DGCPM) of Ober et al. (1997), the fluid model SAMI3 (Huba et al., 2008), or the Ionosphere-Plasmasphere IP model (Maruyama et al., 2016)]. The physical mechanisms can vary in different models, following the theoretical approaches, including the formation of the plasmapause (Lemaire and Pierrard, 2008). Moreover, the results of the models may depend on the magnetic and electric fields used (Pierrard et al., 2008; Reinisch et al., 2009).

Any progress in the understanding of the physical processes and in the magnetic/electric fields is thus relevant to any plasmasphere model advance. Recent developments to model the plasmasphere include monitoring tools based on VLF transmitters (Koronczay et al., 2018). Improvement of any plasmaspheric model means reaching higher precision and sophistication to give the most realistic reproduction of this cold region of the magnetosphere, but the computing time has to be kept sufficiently low to make manageable predictions.

Since each model has advantages and disadvantages, in the present perspective paper, we will not make intercomparisons but focus on the advances that would be useful for any model. These developments are in progress or are planned for the physics-based SWIFF Plasmasphere Model (SPM), a 3D dynamic kinetic model of the plasmasphere first developed by Pierrard and Stegen (2008) and that will be used here to illustrate the results. The SPM model is based on physical mechanisms, including interchange instability for the formation of the plasmapause (Pierrard and Lemaire, 2004), and provides the density and the temperature of the electrons, protons, and other ions, both inside and outside the plasmasphere. Semi-empirical relations derived from previous spacecraft observations are used to determine the electric field from geomagnetic activity indices (Pierrard et al., 2008) and calculate the plasmapause position and the plasmaspheric density. The input of the model is the date that determines the geomagnetic indices Kp and Dst. These indices may be predicted values when forecasting is required, or definitive observed values when past events are simulated. They determine also the convection electric field. The outputs of the model are the plasmapause positions, densities, and temperatures of the different particles in 3D at any position (inside and outside the plasmasphere), defined by the McIlwain (1966) parameter L in Earth radii (Re), the geomagnetic latitude and the magnetic local time (MLT), in geocentric solar magnetospheric (GSM) coordinates, at any required UT time.

The plasmasphere model has been coupled with the ionosphere, using the empirical International Reference Ionosphere, IRI, (Bilitza, 2018) as a boundary condition (Pierrard and Voiculescu, 2011) in the framework of the SWIFF (Space Weather Integrated Forecasting Framework) project that allowed coupling of models for different regions of the magnetosphere (Lapenta et al., 2013). SPM simulations are provided on a near-real-time basis at the ESA SSA (Space Situational Awareness) website (https://swe.ssa.esa.int/space-radiation) since January 2017. Data produced since then are archived and available for visualization from the site. This product enables a continued and quick assessment of electron density plasmasphere conditions, which is critical to monitor the spacecraft's electronic performances when traversing or staying at orbits nearby the Earth. The model will also be made available on the Virtual Space Weather Modeling Center (https://esa-vswmc.eu/) and on the H2020 PITHIA-NRF (Plasmasphere Ionosphere Thermosphere Integrated Research Environment and Access services: a Network of Research Facilities) platform, collecting data and models for the ionosphere and plasmasphere.

Table 1 summarizes the main characteristics of the SPM model, its strengths and weaknesses, as well as the possibilities of improvement that will be explained in more detail in the next sections. These ways to improve the SPM model may be applicable also to other plasmaspheric models. The progress possibilities first explore advances in the relations based on new satellite observations with higher resolution and precision (section Improvement of the Physical Relations by Comparing With New Satellite Data), followed by the refinements of predictions of geomagnetic activity (section Improve Predictions of Kp and Other Geomagnetic Indices), then the evaluation

TABLE 1 | Main characteristics of the SPM model, its present strengths and weaknesses, and the possibilities for improvements.

Model characteristics	Strengths	Weaknesses	Improvement ways
- Input: date (that gives previous Kp)	Simulation for any date, including forecasting	Kp 3-h index, Only a few hours prediction	A longer term for Kp predictions
- PP by interchange instability and convection	MLT propagation, Plume formation	Other possible mechanisms	Other processes can be added
- Kinetic exospheric flux tubes	3D physics-based, latitudinal dependence	Interactions neglected	More empirical to simplify
- Semi-empirical analytic functions	Fast calculations, satellite data average	Not represent exact observations	Use new observations for better relations
- Depend on electric and magnetic fields	Simple Kp dependence, semiempirical models	Not represent exact observations	Models can be adapted
- Coupled to IRI ionosphere (<700 km)	Based on observations	Not a physical model for the ionosphere	Can be coupled to other model(s)
- Refilling between new and vestigial PP	A simple physical mechanism, PP width	Only for individual events	To be automatized, with an L rate
- The trough model based on CA92	Simple analytical relation	Observations much more scattered	Find new relations with recent data
- Output: composition, density, temperature	In 3D, dynamic	Based on statistical averages	Use recent observations for better relations
- Other physical mechanisms	Can be tested	Would increase calculation time	e.g., plasmaspheric mechanisms wind, a magnetosphere link

of the thickness of the plasmapause (PP) boundary related to the refilling and plasmaspheric wind (section Thickness of the Plasmapause Associated to Refilling and Plasmaspheric Wind), and, finally, the coupling with the ionosphere, influencing the composition and the temperature (section Coupling With the Ionosphere, Composition, and Temperature). In addition to the plasmasphere, the consideration of the low density in the region of the plasma trough is important to model because of the development of waves interacting with the other regions of the magnetosphere. We discuss and summarize all these possibilities in the last section—section Discussion and Conclusions.

IMPROVEMENT OF THE PHYSICAL RELATIONS BY COMPARING WITH NEW SATELLITE DATA

The SPM electron density calculations correspond to continuous predictions in a space-time coordinate system. Note that high precision in the coordinate system (and in the eventual changes of coordinates) is important to simulate correctly any space region of the magnetosphere. The model calculates the density every half hour for any L value (in Re), longitude (MLT), and latitude. The main way of validation and improvement of the model consists in the refinement of the semiempirical relations, linking the densities and temperatures with the geomagnetic indices at different positions. The SPM model has been already compared and validated against different spacecraft observations: global views of the plasmasphere obtained from the satellite IMAGE have shown that the model well-reproduced the formation of plumes in the dusk sector during geomagnetic storms (Pierrard and Cabrera, 2005, 2006; Darrouzet et al., 2008); CRRES observations have shown that the plasmasphere density as a function of the geomagnetic activity indices is realistic in the model (Bandic et al., 2016); the MLT propagation of plasmapause structures (Bandic et al., 2017, 2020) was also confirmed by studies based on the observations of the satellites Cluster (Darrouzet et al., 2006, 2013; Verbanac et al., 2015) and THEMIS (Bandic et al., 2017; Verbanac et al., 2018), for instance.

The high-resolution measurements of the Van Allen Probes (VAP), previously called "Radiation Belt Storm Probes" (RBSP), provide new possibilities to validate and improve the empirical relations used in a plasmasphere model, and, especially, in the plasma trough region where the low densities made hard previous observations. VAP was a mission of two spacecraft (A and B) launched in 2012 in tandem along a highly elliptic orbit (perigee of 618 km and apogee of 30,414 km), with 10.2° of inclination and a period of around 9 h (Mauk et al., 2013). The two spacecraft carry identical instruments: the Electric and Magnetic Field Instrument Suite and Integrated Science (EMFISIS) that contains the Waves instrument, a triaxial search coil magnetometer, and sweep frequency receiver. It provides a single electric field component of waves from 10 to 400 kHz in order to measure the spectrum of electron cyclotron harmonic emissions and to measure the frequency of the upper hybrid resonance band, thereby providing an accurate determination of the electron density (Kurth et al., 2015). Data are available at https://emfisis.physics.uiowa.edu/Flight/ from 2012 to 2019. The spacecraft have finished operations in October 2019.

Electron density data obtained by EMFISIS are used for comparison and improvement of the model by filtering out values >2,000 cm^{-3}. This threshold is related to the limited response above 400 kHz of the Waves instrument (Kletzing et al., 2013).

The top left panel of **Figure 1** illustrates the electron densities Ne in cm^{-3}, determined by Van Allen Probe A during a typical month, here chosen to be June 2015, as a function of the corresponding SPM simulations at the same times and positions, using definitive Kp values as input (bottom panel, in green). The color scale corresponds to the McIlwain L values in Re. Due to the upper frequency limit of EMFISIS, comparisons between the model and the data are only made for locations $L > 2$. One can see that the data are located close to the 1:1 diagonal in the range $L \approx 2$–4.5, which principally scans the plasmasphere density, indicating a good global performance of the model in this L range. The clear distinction between low L-high densities and high L-low densities corresponds to a bimodal distribution with a plasmapause separating the plasmasphere and the plasma trough. In this plasma trough region, i.e., beyond the plasmapause limit (typically for $L > 5.5$ during quiet times), the model uses analytical equations deduced by Carpenter and Anderson (1992) (CA92). The density of the trough model is often too low and less scattered in comparison to VAP data, which is not surprising since the simulated trough densities are obtained from averaged statistical results, while the EMFISIS observations concern event intervals that are strongly dependent on the strength of the most recent erosion. The CA92 model represents better the observed trough when Kp is high. This early model and other subsequent models of trough and plasmasphere density can now be revisited, using the new and extensive EMFISIS dataset, taking more into account the MLT and geomagnetic activity dependence, even if during high disturbances the observations can be affected by noise in the low-density plasmatrough [see discussions in Kurth et al. (2015) about the complexity of distinguishing between wavebands]. Other spacecraft, like Arase (Kasahara et al., 2018) for instance, can also be used for comparison and improvement of the models inside and outside the plasmasphere, but measurement errors are also significant in the low-density trough region.

IMPROVE PREDICTIONS OF KP AND OTHER GEOMAGNETIC INDICES

The time variations of the plasmasphere mainly depend on the geomagnetic activity level, determined mainly by activity indices like the planetary Bartels index Kp and Dst (Disturbed Storm Time). High-precision predictions of the plasmasphere model need thus a first realistic forecast of these indices. **Figure 1** (middle panel) illustrates in red the Kp forecast (https://www.swpc.noaa.gov/products/3-day-geomagnetic-forecast), compared with the definitive indexes (ftp://ftp.gfz-potsdam.de/pub/home/obs/kp-ap/tab/) in green (that were used in the model simulations of **Figure 1**, top left panel). Locally huge discordances between forecasted and

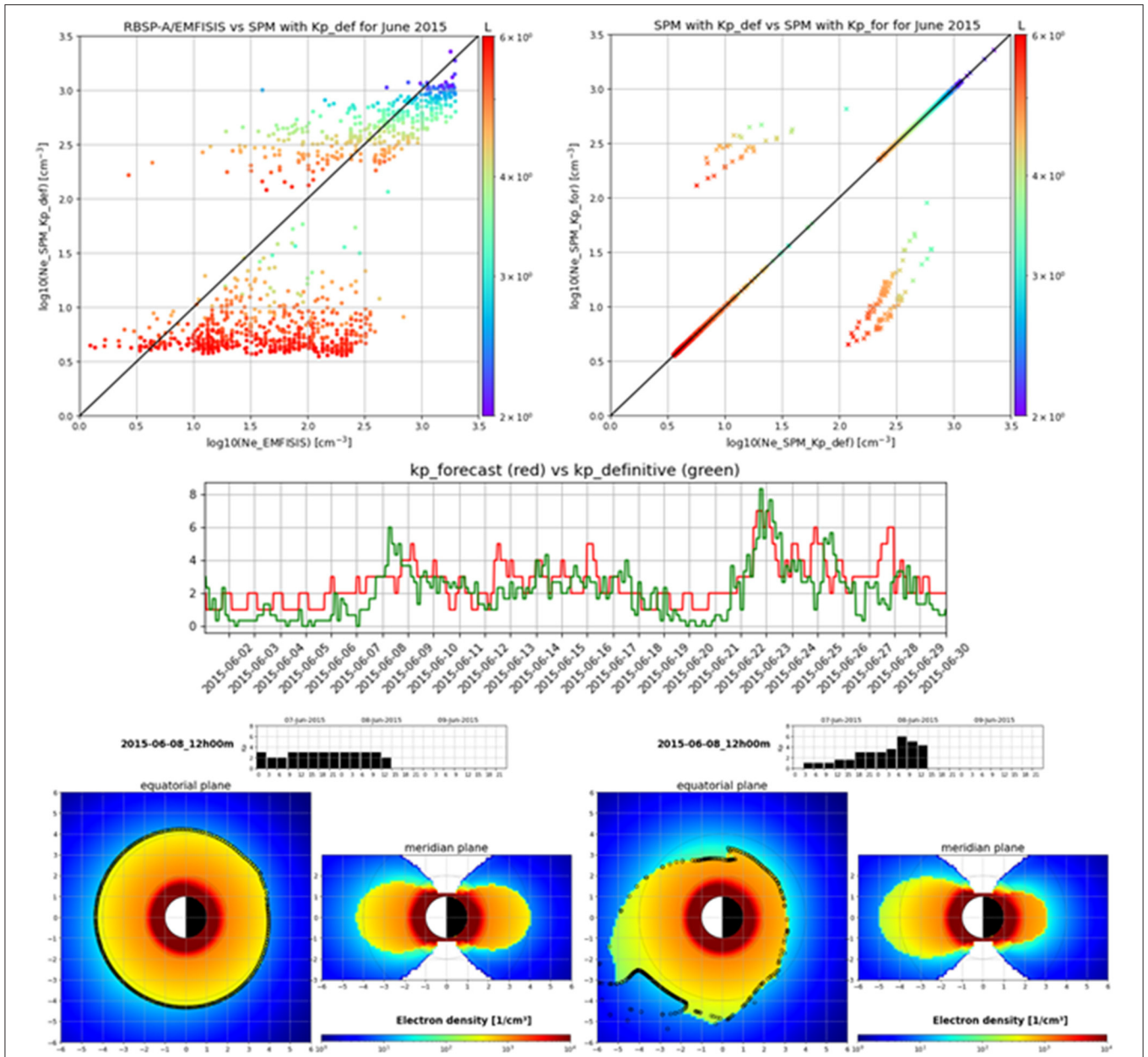

FIGURE 1 | Top left: A scatter plot of the electron densities Ne in cm^{-3} in logarithmic scale observed by VAP-A/EMFISIS satellite for June 2015 (x-axis) as a function of the corresponding simulated data (y-axis), evaluated by the SPM model at the same times and positions and using the definitive Kp indices. The color scale corresponds to the McIlwain L values. Top right: A scatter plot of the electron densities Ne in cm^{-3} in logarithmic scale of the SPM model, using the definitive Kp (x-axis) as a function of those obtained with the predicted Kp (y-axis). Middle panel: Comparison between the Kp forecast from NOAA (red) and the corresponding definitive values from POTSDAM (green) during June 2015. Bottom panels: Density of the electrons (color scale), obtained with the SPM model for 8 June 2015 at 12h00, with the Kp values as predicted (left panels) and with Kp as observed (right panels). The SPM model shows the density in the geomagnetic equatorial plane and in the meridian plane. Kp during the previous 36 h is also illustrated.

definitive Kp can sometimes be observed; for example, around June 8th or 25th, 2015. Despite predictions present strong deviations, the whole forecast of the month represents, in general, a good estimation of the geomagnetic perturbations. The top right panel of **Figure 1** shows the scatter plot of the electron densities obtained with the SPM model, using the definitive Kp (x-axis) as a function of those obtained with the predicted Kp (y-axis). In a period of 1 month, the overall prediction performance of the model is only slightly reduced when the forecasted Kp is used instead of the definitive indices. Only a few points are modified since the Kp of the previous 24 h mainly determines the convection and

thus the plasmapause position as a function of the MLT in the model.

Bottom panels of **Figure 1** show typical results of the model, i.e., the density of the electrons obtained by the model in the geomagnetic equatorial plane and in the meridian plane with the predicted Kp values (two left bottom panels), while the two right panels show the results of the model, using the observed Kp, here for June 8, 2015, at 12h00. The black diamonds show the position of the plasmapause in the equatorial plane. One can see that an increase of Kp (as observed on June 8, 2015, see bottom right panels) leads to the formation of a plume with L $>$ 5 in the afternoon-dusk MLT sector and a low plasmapause in the postmidnight sector. The plasmasphere erosion due to (sub)storms starts at the nightside evolves during the morning, and the associated formation of plumes and their rotation occur at afternoon and evening MLT times. These mechanisms depend strongly on the geomagnetic activity level.

A constant Kp (as obtained from Kp predictions on June 8) gives an almost circular plasmapause in the equatorial plane. When Kp is misestimated, major differences are thus obtained with the model in the region close to the plasmapause, with high overestimation or underestimation if the position is just below or just above the actual plasmapause position, as illustrated in the top right panel of **Figure 1**. For particular events, the differences can be high, as illustrated in the bottom panels. Of course, any model driven by indices such as Kp or Dst, or any other empirically derived average inputs will never be able to reproduce each individual observation, simply because the inputs to the model are purely empirical averages. But realistic simulations can be obtained, especially when initial conditions correspond to observations.

THICKNESS OF THE PLASMAPAUSE ASSOCIATED TO REFILLING AND PLASMASPHERIC WIND

The model provides the radial distance of the plasmapause in the geomagnetic equatorial plane. This is crucial because the density can be very different, depending on if the spacecraft is located below or above the plasmapause. But the plasmapause is not always a sharp frontier. A thin plasmasphere boundary layer (PBL), where the plasma density starts to decrease exponentially with L below the plasmapause limit allows taking into account the width of the PBL, which is observed to linearly depend on the time elapsed since the most recent maximum value of Kp (Kotova et al., 2018). This happens especially during refilling periods after geomagnetic storms, as taken indeed into account by the model (see Pierrard and Stegen, 2008). Refilling is taken into account, using vestigial (during the last 24 h) and new positions of the plasmapause, located further when Kp decreases. Refilling rates can be refined from measurements (Gallagher et al., 2005, 2021; Sandel and Denton, 2007), and dependence on the radial distance can be improved in the model when unsolved problems concerning refilling will be clearer (Gallagher and Comfort, 2016).

Also, often, a sharp plasmapause is not really visible, since the density decreases continuously with the distance, especially during prolonged quiet periods. This can be related to plasmaspheric wind leading to an outward expansion of the plasmasphere perpendicularly to the magnetic field during prolonged quiet periods (Lemaire and Schunk, 1992). Such expansion was confirmed by Cluster observations (Dandouras, 2013) and is planned to be included in the model in the future. This would need Kp variations during several days before the date to be simulated.

COUPLING WITH THE IONOSPHERE, COMPOSITION, AND TEMPERATURE

The model is coupled to the ionosphere using, for the values under 700 km, the IRI model (Bilitza, 2018) based on ionosondes, incoherent scatter radars, topside sounders, and *in situ* spacecraft observations. The ionosphere plays also an important role as boundary conditions. The simulations allow us to choose to consider (or not) a possible sub-corotation lag of the plasmasphere that can sometimes reach 85% of corotation as observed by Burch et al. (2004), caused by a corresponding corotation lag in the upper ionosphere.

Any improvement of the ionosphere model that we use would help to improve plasmaspheric models. A coupling with a physical model of the ionosphere would help to go beyond a statistical representation and include physical mechanisms in this region as well. This influences also the composition of the plasmasphere, where not only electrons are present but also protons, helium, and O^+ ions, which can be very important in the outer plasmasphere during refilling. The helium ions were detected by the EUV (Extreme UltraViolet) instrument onboard the satellite IMAGE and allowed the first global views of the plasmasphere above the North pole between 2000 and 2006 (Burch, 2000; Sandel et al., 2000, 2001). The composition predicted by the model highly depends on the conditions provided by the ionospheric model. Mass density is an important influence on the threshold for wave-particle instabilities and wave propagation. The advancement of measuring and then modeling O^+ in the plasmasphere would be particularly important for understanding the role of the plasmaspheric plasma in the energization and scattering loss of ring current and radiation belt ions, which are especially important space-weather hazards. The density determines the type of waves circulating inside and outside the plasmasphere, and this has a strong influence on the other regions of the magnetosphere like the radiation belts (Pierrard et al., 2020, 2021). The H2020 SafeSpace project (https://www.safespace-h2020.eu/) needs high-precision densities from the SPM model, in view to determine the waves in the magnetosphere. That is why we initiate the improvement of our model in the plasma trough region where high variability is observed.

Even if less is used, the temperature in the plasmasphere is also provided by the SPM model (and by IRI). It is different for the different particle species and slightly increases with the radial distance (Pierrard and Stegen, 2008). The temperature,

ranging typically between 2,000 and 20,000 K, is also measured by the VAP instrument HOPE (Genestreti et al., 2016), and such measurements can be used to improve the temperature in the model as well.

The SPM model also includes high-latitude regions, where the polar wind reduces the ion density [Tam et al. (2007) for a review; Pierrard and Borremans (2012)]. These regions are also subject to improvements since they have been less compared with observations for validation. The latitudinal dependence inside and outside the plasmasphere is assumed to follow the motion of the particles along the magnetic field lines. Latitudinal verifications (Pierrard and Stegen, 2008) were made with data observations of the IMAGE Radio Plasma Imager (RPI) measurements (Reinisch et al., 2001) that provided the first nearly instantaneous electron densities along the magnetic field lines between the satellite and the nearest hemisphere. Moreover, the global meridian views of the KAGUYA satellite have shown that the main mechanism of plasmapause formation takes place first in the equatorial plane during storms, like in the SPM model (Murakami et al., 2016).

DISCUSSION AND CONCLUSIONS

In summary, the SPM simulations globally reproduce the satellite measurements of VAP/EMFISIS electron density in the plasmasphere in general for the regions L = 2–5 for quiet and active times. Inside the plasmasphere, and even more in the plasma trough, some further improvements can be performed, using new relations obtained from VAP. This will be the priority in the improvement of the model, to use these high-resolution observations to refine the relations between the density and L, MLT, latitude, and Kp. Model improvement involves the search of refined analytical equations, parameterized with observations, to obtain a better forecast. In this context, the whole data of EMFISIS (2012–2019) can be used to obtain better statistics, in particular for the plasma trough. Following these changes, an improved version of the SPM model should be available for release into the ESA network in the near future, together with the ionosphere–plasmasphere coupling, already available since its implementation in 2011.

The instrument HOPE onboard VAP can also be used to improve the temperature and composition. Moreover, a comparison study between the observations and the results of the model shows also the interest to consider the plasmapause as a layer with a thickness, especially during the refilling period. The plasmaspheric wind, appearing during very quiet time periods, is also a process that could improve the model in the long term by explaining high densities sometimes observed at large radial distances.

Other improvements depend on the inclusion or refinement of additional physical mechanisms, like coupling the plasmasphere to the energetic plasma of the magnetosphere or include polar wind escape, for instance. Additional investigations for plasmaspheric model improvements can concern the models used for the plasmasphere simulations, like the magnetic field, the electric field, the space coordinates, and the forecast (including indices like Kp, Dst, or even simulations based on direct solar wind predictions).

DATA AVAILABILITY STATEMENT

Publicly available datasets were analyzed in this study. This data can be found at: https://emfisis.physics.uiowa.edu/Flight/.

AUTHOR CONTRIBUTIONS

VP has written this article and has developed the SPM model. EB has made the figures to compare the results of the model with VAP observations. EB and FD have reviewed and improved the paper. All authors contributed to the article and approved the submitted version.

FUNDING

The SafeSpace project has received funding from the European Union's Horizon 2020 research and innovation program under Grant Agreement No. 870437. The PITHIA-NRF project has received funding from the European Union's Horizon 2020 research and innovation programme under grant agreement No. 101007599. The authors thank the project VSWMC and BIRA-IASB for its support.

ACKNOWLEDGMENTS

The authors thank the editors for their invitation to contribute to this special issue about Cold-Ion Populations and Cold-Electron Populations in the Earth's Magnetosphere and Their Impact on the System. The authors acknowledge the providers of the geophysical indices used in the study: Kp forecast (https://www.swpc.noaa.gov/products/3-day-geomagnetic-forecast) and definitive Kp (ftp://ftp.gfz-potsdam.de/pub/home/obs/kp-ap/tab/) and the experimental data VAP/EMFISIS (https://emfisis.physics.uiowa.edu/Flight/). They acknowledge also the team of the HOPE instrument on Van Allen Probes and the team of the ARASE satellite that can provide useful plasmaspheric measurements.

REFERENCES

Bandic, M., Verbanac, G., Moldwin, M., Pierrard, V., and Piredda, G. (2016). MLT dependence in the relationship between plasmapause, solar wind and geomagnetic activity based on CRRES: 1990-1991. *J. Geophys. Res. Space Phys.* 121, 4397–4408. doi: 10.1002/2015JA022278

Bandic, M., Verbanac, G., and Pierrard, V. (2020). Relationship between global plasmapause characteristics and plasmapause structures in the frame of interchange instability mechanism. *J. Geophys. Res. Space Phys.* 125:e2019JA026768. doi: 10.1029/2019JA026768

Bandic, M., Verbanac, G., Pierrard, V., and Cho, J. (2017). Evidence of MLT propagation of the plasmapause inferred from THEMIS data. *J. Atmosph. Solar Terrest. Phys.* 161, 55–63. doi: 10.1016/j.jastp.2017.05.005

Bilitza, D. (2018). IRI the international standard for the ionosphere. *Adv. Radio Sci.* 16, 1–11. doi: 10.5194/ars-16-1-2018

Burch, J. (2000). IMAGE mission overview. *Space Sci. Rev.* 91, 1–14. doi: 10.1023/A:1005245323115

Burch, J. L., Goldstein, J., and Sandel, B. R. (2004). Cause of plasmasphere corotation lag. *Geophys. Res. Lett.* 31:L05802. doi: 10.1029/2003GL019164

Carpenter, D. L., and Anderson, R. R. (1992). An ISEE/whistler model of equatorial electron density in the magnetosphere. *J. Geophys. Res. Space Phys.* 97, 1097–1108. doi: 10.1029/91JA01548

Dandouras, I. (2013). Detection of a plasmaspheric wind in the Earth's magnetosphere by the cluster spacecraft. *Ann. Geophys.* 31, 1143–1153. doi: 10.5194/angeo-31-1143-2013

Darrouzet, F., De Keyser, J., Décréau, P. M. E., El Lemdani-Mazouz, F., and Vallières, X. (2008). Statistical analysis of plasmaspheric plumes with CLUSTER/WHISPER observations. *Ann. Geophys.* 26, 2403–2417. doi: 10.5194/angeo-26-2403-2008

Darrouzet, F., De Keyser, J., Décréau, P. M. E., Gallagher, D. L., Pierrard, V., Lemaire, J. F., et al. (2006). Analysis of plasmaspheric plumes: CLUSTER and IMAGE observations. *Ann. Geophys.* 24, 1737–1758. doi: 10.5194/angeo-24-1737-2006

Darrouzet, F., De Keyser, J., and Pierrard, V. (Eds.). (2009). *The Earth's Plasmasphere: Cluster and IMAGE – A Modern Perspective*. New York, NY: Springer. doi: 10.1007/978-1-4419-1323-4

Darrouzet, F., Pierrard, V., Benck, S., Lointier, G., Cabrera, J., Borremans, K., et al. (2013). Links between the plasmapause and the radiation belt boundaries as observed by the instruments CIS, RAPID and WHISPERonboard cluster. *J. Geophys. Res. Space Phys.* 118, 4176–4188. doi: 10.1002/jgra.50239

Gallagher, D. L., Adrian, M. L., and Liemohn, M. W. (2005). Origin and evolution of deep plasmaspheric notches. *J. Geophys. Res. Space Phys.* 110:A09201. doi: 10.1029/2004JA010906

Gallagher, D. L., and Comfort, R. H. (2016). Unsolved problems in plasmasphere refilling. *J. Geophys. Res. Space Phys.* 121, 1447–1451. doi: 10.1002/2015JA022279

Gallagher, D. L., Comfort, R. H., Katus, R. M., Sandel, B. R., Fung, S. F., and Adrian, M. L. (2021). The breathing plasmasphere: erosion and refilling. *J. Geophys. Res. Space Phys.* 126:e2020JA028727. doi: 10.1029/2020JA028727

Gallagher, D. L., Craven, P. D., and Comfort, R. H. (2000). Global core plasma model. *J. Geophys. Res.* 105, 18819–18833. doi: 10.1029/1999JA000241

Genestreti, K. J., Goldstein, J., Corley, G. D., Farner, W., Kistler, L. M., Larsen, B. A., et al. (2016). Temperature of the plasmasphere from Van Allen Probes HOPE. *J. Geophys. Res. Space Phys.* 122, 310–323. doi: 10.1002/2016JA023047

Huba, J. D., Joyce, G., and Krall, J. (2008). Three-dimensional equatorial spread *F* modeling. *Geophys. Res. Lett.* 35:L10102. doi: 10.1029/2008GL033509

Kasahara, Y., Kasaba, Y., Kojima, H., Yagitani, S., Ishisaka, K., Kumamoto, A., et al. (2018). The plasma wave experiment (PWE) on board the Arase (ERG) satellite. *Earth Planets Space*. 70, 1–28. doi: 10.1186/s40623-018-0842-4

Kletzing, C. A., Kurth, W. S., Acuna, M., MacDowall, R. J., Torbert, R. B., Averkamp, T., et al. (2013). The Electric and Magnetic Field Instrument Suite and Integrated Science (EMFISIS) on RBSP. *Space Sci. Rev.* 179, 127–181. doi: 10.1007/s11214-013-9993-6

Koronczay, D., Lichtenberger, J., Juhasz, L., Steinbach, P., and Hospodarsky, G. (2018). VLF transmitters as tools for monitoring the plasmasphere. *J. Geophys. Res. Space Phys.* 123, 9312–9324. doi: 10.1029/2018JA025802

Kotova, G., Verigin, M., Lemaire, J., Pierrard, V., Bezrukikh, V., and Smilauer, J. (2018). Experimental study of the plasmasphere boundary layer using MAGION 5 data. *J. Geophys. Res. Space Phys.* 123, 1251–1259. doi: 10.1002/2017JA024590

Kurth, W. S., De Pascuale, S., Faden, J. B., Kletzing, C. A., Hospodarsky, G. B., Thaller, S., et al. (2015). Electron densities inferred from plasma wave spectra obtained by the Waves instrument on Van Allen Probes. *J. Geophys. Res. Space Phys.* 120. 904–914. doi: 10.1002/2014JA020857

Lapenta, G., Pierrard, V., Poedts, S., Sebek, O., Travnicek, P. M., Henri, P., et al. (2013). SWIFF: space weather integrated forecasting framework. *J. Space Weather Space Clim.* 3, 1–17. doi: 10.1051/swsc/2013027

Lemaire, J., and Gringauz, K. I. (1998). *The Earth's Plasmasphere*. Cambridge: Cambridge University Press. doi: 10.1017/CBO9780511600098

Lemaire, J., and Pierrard, V. (2008). Comparison between two theoretical mechanisms for the formation of the plasmapause and relevant observations. *Geomagn. Aeronomy* 48, 553–570. doi: 10.1134/S0016793208050010

Lemaire, J., and Schunk, R. W. (1992). Plasmaspheric wind. *J. Atmosph. Solar Terrestrial Phys.* 54, 467–477. doi: 10.1016/0021-9169(92)90026-H

Maruyama, N., Sun, Y.-Y., Richards, P. G., Middlecoff, J., Fang, T.-W., Fuller-Rowell, T. J., et al. (2016). A newsource of the midlatitude ionospheric peak density structure revealed by a new ionosphere-plasmasphere model. *Geophys. Res. Lett.* 43, 2429–2435. doi: 10.1002/2015GL067312

Mauk, B., Fox, N., Kanekal, S., Kessel, R., Sibeck, D., and Ukhorskiy, A. (2013). Science objectives and rationale for the radiation belt storm probes mission. *Space Sci. Rev.* 179, 3–27. doi: 10.1007/s11214-012-9908-y

McIlwain, C. E. (1966). Magnetic coordinates. *Space Sci. Rev.* 5, 585–598. doi: 10.1007/BF00167327

Murakami, G., Yoshioka, K., Yamazaki, A., Nishimura, Y., Yoshikawa, I., and Fujimoto, M. (2016). The plasmause formation seen from meridian perspective by KAGUYA. *J. Geophys. Res. Space Phys.* 121, 11973–11984. doi: 10.1002/2016JA023377

Ober, D. M., Horwitz, J. L., and Gallagher, D. L. (1997). Formation of density troughs embedded in the outer plasmasphere by subauroral ion drift events. *J. Geophys. Res.* 102, 14595–14602. doi: 10.1029/97JA01046

Pierrard, V., and Borremans, K. (2012). "The ionosphere coupled to the plasmasphere and polar wind models," in *Numerical Modeling of Space Plasma Flows: Astronum-2011, ASP Conference series*, eds N. V. Pogorelov, J. A. Font, E. Audit, and G. P. Zank [Orem, UT: Astronomical Society of the Pacific (ASP)].

Pierrard, V., Botek, E., Ripoll, J.-F., and Cunningham, G. S. (2020). Electron dropout events and flux enhancements associated with geomagnetic storms observed by PROBA-V/EPT from 2013 to 2019. *J. Geophys. Res. Space Phys.* 125:e2020JA028487. doi: 10.1029/2020JA028487

Pierrard, V., and Cabrera, J. (2005). Comparisons between EUV/IMAGE observations and numerical simulations of the plasmapause formation. *Ann. Geophys.* 23, 2635–2646. doi: 10.5194/angeo-23-2635-2005

Pierrard, V., and Cabrera, J. (2006). Dynamical simulations of plasmapause deformations. *Space Sci. Rev.* 122, 119–126. doi: 10.1007/s11214-006-5670-3

Pierrard, V., Goldstein, J., André, N., Jordanova, V. K., Kotova, G. A., Lemaire, J. F., et al. (2009). Recent progress in physics-based models of the plasmasphere. *Space Sci. Rev.* 145, 193–229. doi: 10.1007/s11214-008-9480-7

Pierrard, V., Khazanov, G., Cabrera, J., and Lemaire, J. (2008). Influence of the convection electric field models on predicted plasmapause positions during the magnetic storms. *J. Geophys. Res. Space Phys.* 113, 1–21. doi: 10.1029/2007JA012612

Pierrard, V., and Lemaire, J. (2004). Development of shoulders and plumes in the frame of the interchange instability mechanism for plasmapause formation. *Geophys. Res. Lett.* 31, L05809–L05811. doi: 10.1029/2003GL018919

Pierrard, V., Ripoll, J.-F., Cunningham, G., Botek, E., Santolik, O., Thaller, S., et al. (2021). Observations and simulations of dropout events and flux enhancements in October 2013: Comparing MEO equatorial with LEO polar orbit. *J. Geophys. Res. Space Phys.*

Pierrard, V., and Stegen, K. (2008). A three dimensional dynamic kinetic model of the plasmasphere. *J. Geophys. Res. Space Phys.* 113:A10209. doi: 10.1029/2008JA013060

Pierrard, V., and Voiculescu, M. (2011). The 3D model of the plasmasphere coupled to the ionosphere. *Geophys. Res. Lett.* 38:L12104. doi: 10.1029/2011GL047767

Reinisch, B. W., Huang, X., Song, P., Sales, G. S., Fung, S. F., Green, J. L., et al. (2001). Plasma density distribution along the magnetospheric field: RPI observations from IMAGE. *Geophys. Res. Lett.* 28, 4521–4524. doi: 10.1029/2001GL013684

Reinisch, B. W., Moldwin, M. B., Denton, R. E., Gallagher, D. L., Matsui, H., Pierrard, V., et al. (2009). Augmented Empirical models of the plasmaspheric density and electric field using IMAGE and CLUSTER data. *Space Sci. Rev.* 145, 231–261. doi: 10.1007/s11214-008-9481-6

Ren, J., Zong, Q. G., Miyoshi, Y., Rankin, R., Spence, H. E., Funsten, H. O., et al. (2018). A comparative study of ULF waves' role in the dynamics of charged particles in the plasmasphere: Van Allen Probes observation. *J. Geophys. Res. Space Phys.* 123, 5334–5343. doi: 10.1029/2018JA025255

Sandel, B. R., Broadfoot, A. L., Curtis, C. C., King, R. A., Stone, T. C., Hill, R. H., et al. (2000). The extreme ultraviolet imager investigation for the IMAGE mission. *Space Sci. Rev.* 91:197. doi: 10.1023/A:1005263510820

Sandel, B. R., and Denton, M. H. (2007). Global view of refilling of the plasmasphere. *Geophys. Res. Lett.* 34:L17102. doi: 10.1029/2007GL030669

Sandel, B. R., King, R. A., Forrester, W. T., Gallagher, D. L., Broadfoot, A. L., and Curtis, C. C. (2001). Initial results from the IMAGE extreme ultraviolet imager. *Geophys. Res. Lett.* 28:1439. doi: 10.1029/2001GL012885

Sheeley, B. W., Moldwin, M. B., Rassoul, H. K., and Anderson, R. R. (2001). An empirical plasmasphere and trough density model: CRRES observations. *J. Geophys. Res.* 106, 631–641. doi: 10.1029/2000JA000286

Tam, S. W. Y., Chang, T., and Pierrard, V. (2007). Kinetic modeling of the polar wind. *J. Atmosph. Sol. Terr. Phys.* 69, 1984–2027. doi: 10.1016/j.jastp.2007.08.006

Verbanac, G., Bandic, M., and Pierrard, V. (2018). MLT plasmapause characteristics: comparison between THEMIS observations and numerical simulations. *J. Geophys. Res. Space Phys.* 123, 2000–2017. doi: 10.1002/2017JA024573

Verbanac, G., Pierrard, V., Bandic, M., Darrouzet, F., Rauch, J.-L., and Décréau, P. (2015). Relationship between plasmapause, solar wind and geomagnetic activity between 2007 and 2011 using Cluster data. *Ann. Geophys.* 33, 1271–1283. doi: 10.5194/angeo-33-1271-2015

Conflict of Interest: The authors declare that the research was conducted in the absence of any commercial or financial relationships that could be construed as a potential conflict of interest.

frontiers in Astronomy and Space Sciences

MINI REVIEW
published: 16 July 2021
doi: 10.3389/fspas.2021.712616

The Effect of the Thermosphere on Ionosphere Outflows

J. Krall[1]* *and J. D. Huba*[2]

[1]Naval Research Laboratory, Plasma Physics Division, Washington, DC, United States, [2]Syntek Technologies, Fairfax, VA, United States

The Naval Research Laboratory (NRL) Sami2 is Another Model of the Ionosphere (SAMI2) and Sami3 is Also a Model of the Ionosphere (SAMI3) ionosphere/plasmasphere codes have shown that thermosphere composition and winds significantly affect H^+ outflows from the topside ionosphere. In particular, O density inhibits upward diffusion of O^+ from the ionosphere F layer, especially during solar maximum conditions. In addition, winds affect the quiet-time latitudinal extent of the F layer, affecting densities at mid-to-high latitudes that are the source of plasmasphere refilling outflows. Evidence for these effects is reviewed and prospects for forecasting these outflows are explored. Open questions for future research are highlighted.

Keywords: ionosphere, plasmasphere, thermosphere, ionosphere outflow, cold plasma, exosphere

OPEN ACCESS

Edited by:
Elena Kronberg, Ludwig Maximilian University of Munich, Germany

Reviewed by:
Xuguang Cai, National Center for Atmospheric Research (UCAR), United States
Dimitry Pokhotelov, German Aerospace Center (DLR), Germany

***Correspondence:**
J. Krall
jonathan.krall@nrl.navy.mil

Specialty section:
This article was submitted to Space Physics, a section of the journal Frontiers in Astronomy and Space Sciences

Received: *20 May 2021*
Accepted: *23 June 2021*
Published: *16 July 2021*

Citation:
Krall J and Huba J D (2021) The Effect of the Thermosphere on Ionosphere Outflows. Front. Astron. Space Sci. 8:712616. doi: 10.3389/fspas.2021.712616

1 INTRODUCTION

Light ions, H^+ and He^+, commonly flow upward from the topside ionosphere. At high latitudes, these ions constitute the classical polar wind (Bauer and Frihagen, 1966; Dessler and Michel, 1966). At lower latitudes, these outflows fill the plasmasphere (Park, 1970; Gallagher and Comfort, 2016). Because the polar wind and plasmasphere serve as a source and a sink, respectively, for geoeffective energetic ions, thermal (non-energized, Maxwellian) outflows are essential elements of space weather (Bortnik and Thorne, 2007; Millan and Thorne, 2007). Further, observations suggest significant day-to-day variability in thermosphere composition (Krall et al., 2016a; Cai et al., 2020) and winds (McDonald et al., 2015). In this brief review, we consider the effect of thermosphere composition and winds on refilling outflows. Thermosphere dynamics and ionosphere outflows at polar latitudes, a much bigger subject, will not be addressed.

Because the solar cycle so strongly affects thermosphere and exosphere composition, the variation of cold H^+ refilling outflows with the solar cycle, specifically with the $F_{10.7}$ extreme ultraviolet (EUV) index, is quite counter-intuitive. At high $F_{10.7}$, when the ionosphere F layer is relatively strong, observed plasmasphere refilling rates at geosynchronous altitudes are relatively weak (Lawrence et al., 1999; Gallagher et al., 2021). As shown graphically in **Figure 1D**, and described by Richards and Torr (1985), the limiting H^+ outflow flux is proportional to the supply of O^+ ions and H atoms at outflow source height Z_0 (700–1,100 km):

$$\phi\left[\mathrm{cm}^{-2}\mathrm{s}^{-1}\right] = 2.85\times10^{-11}T_n\left[\mathrm{K}\right]^{1/2}n_H\left[\mathrm{cm}^{-3}\right]n_{O^+}\left[\mathrm{cm}^{-3}\right]H_{O^+}\left[\mathrm{cm}\right], \quad (1)$$

where T_n is the thermosphere temperature, H_{O^+} is the O^+ scale height, and the leading coefficient has been updated from 2.50 to 2.85 based on a corresponding update to the H-O^+ charge exchange reaction rate. Previously, the H-O^+ charge exchange reaction rate was based on data for the reverse

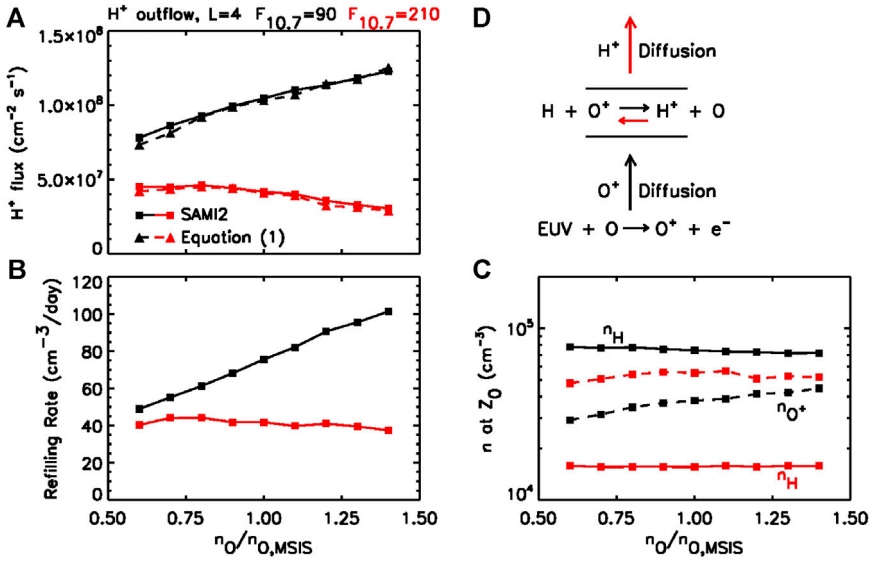

FIGURE 1 | (A) H^+ flux from SAMI2 and from **Eq. 1 (B)** refilling rate, and **(C)** n_H and n_{O^+}, plotted vs. $n_O/n_{O,MSIS}$. Black curves are for low solar activity, $F_{10.7}$ = 90. Red curves are for high solar activity, $F_{10.7}$ = 210. **(D)** Diagram showing the production and upward diffusion of O^+ and H^+ ions. The O density inhibits upward diffusion; this sensitivity to the O density is not explicit in **Eq. 1**. Note: these results (Krall and Huba, 2019a) use 2.50 instead of 2.85 in **Eq. 1** and in the charge-exchange rate.

reaction (Fehsenfeld and Ferguson, 1972) and the finding that the ratio of the forward to reverse reaction rates is 9/8 (Hanson and Ortenburger, 1961). However, recent analysis (Stancil et al., 1999) and measurements (Waldrop et al., 2006; Joshi and Waldrop, 2019) suggest that this ratio is somewhat (≃ 14%) larger, increasing the coefficient in the reaction rate, and in **Eq. 1**, from 2.50 to 2.85.

Let us consider the factors in **Eq. 1**. Relative to densities at solar minimum (low $F_{10.7}$), n_H at solar maximum is much lower (Bishop et al., 2001; Bishop et al., 2004; Nossal et al., 2012; Qian et al., 2018) while n_{O^+} is only somewhat higher (this is at altitude Z_0, which increases with $F_{10.7}$). These densities are shown in **Figure 1C**, where high $F_{10.7}$ is indicated by red curves. This basic understanding of thermal ion outflows, particularly as expressed in **Eq. 1**, compares well to simulations (Richards and Torr, 1985; Krall and Huba, 2019a). However, we are not yet able to forecast these outflows.

In addition, the ionosphere F layer that is the source of these outflows is strongly affected by thermosphere winds (Rishbeth, 1998). Specifically, winds effect the degree to which the ionosphere, which is most strongly generated near the sub-solar point, is transported to the mid-to-high latitudes that are the source of the plasmasphere. While numerical simulations by Krall et al. (2014) demonstrate that plasmasphere morphology and refilling rates are impacted by thermosphere winds, these effects have yet to be directly observed. As it stands, measured post-storm plasmasphere refilling rates at any given height vary by as much as an order of magnitude (Denton et al., 2012), **Figure 1**. These variations are not yet fully explained.

This brief review is based on results from the Sami2 is Another Model of the Ionosphere (SAMI2) and Sami3 is Also a Model of the Ionosphere (SAMI3) ionosphere/plasmasphere codes (Huba et al., 2000; Huba and Krall, 2013). SAMI3 simulates the interaction between ionosphere and plasmasphere ion populations and the thermosphere (Huba and Liu, 2020) and magnetosphere (Huba et al., 2005; Huba and Sazykin, 2014). SAMI2 solves the same equations as SAMI3, but in only a single magnetic longitude. For the results included here, SAMI2 was modified to accommodate counterstreaming H^+ outflows as in Krall and Huba (2019b).

In the next section, the effect of thermosphere composition, particularly the O density, will be demonstrated using SAMI2. This will be followed by SAMI3 results showing the effect of winds. We then discuss the challenge of forecasting these outflows, given observed day-to-day variability in thermosphere composition and winds. We close with a brief list of open questions for future research.

2 SAMI2 RESULTS: THERMOSPHERE COMPOSITION

In a recent simulation (Krall et al., 2016b) of post-storm plasmasphere refilling (Singh and Horwitz, 1992), it was found that model-data agreement was not attainable without careful attention to the thermosphere O density. In particular, O atoms tend to act as a barrier to the upward diffusion of O^+ ions (**Figure 1D**). This effect, which is not explicit in **Eq. 1**, was recently illustrated using the SAMI2 code (Krall and Huba,

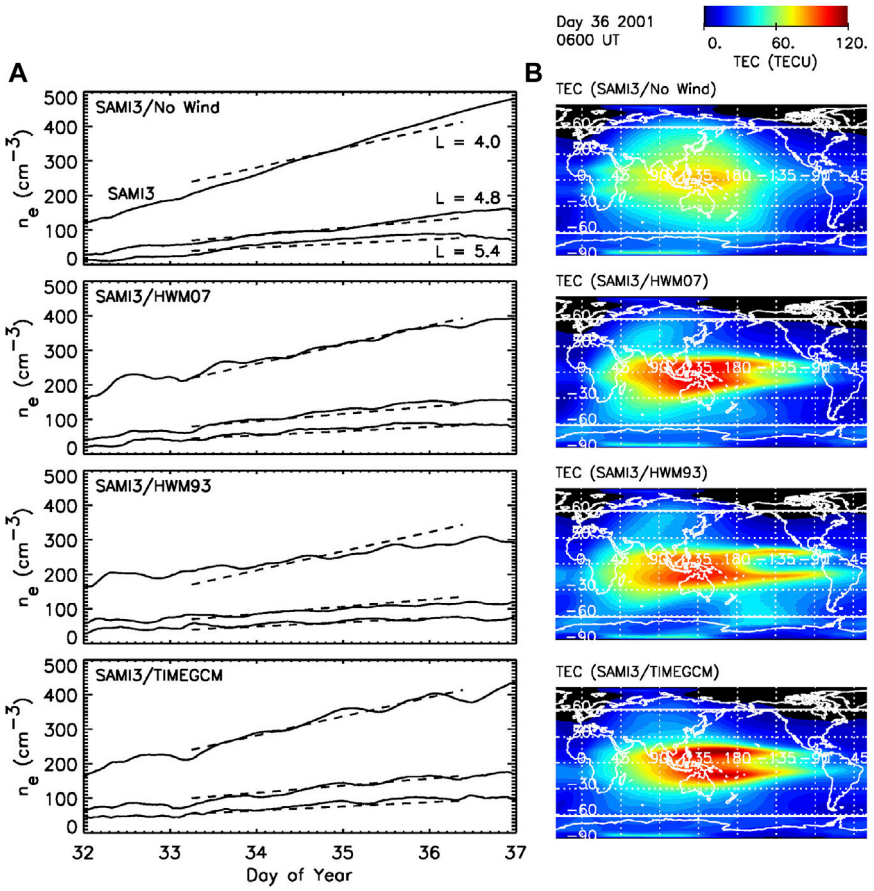

FIGURE 2 | Left column: electron density averaged over longitude in the equatorial plane plotted vs. time for L = 4.0, 4.8 and 5.4 (solid curves) for SAMI3/No Wind, SAMI3/HWM07, SAMI3/HWM93 and SAMI3/TIMEGCM. Dashed lines in each plot indicate observed refilling rates. Right column: total electron content in TEC units is plotted vs. longitude and latitude at 0600 UT on Day 36 for each case. White lines indicate latitude ± 61.5° (L = 4.8).

2019a). The SAMI2 code, which simulates a single magnetic-longitude plane, runs quickly enough to support parameter studies such as described here.

In a series of simulations of outflow and refilling following a model storm, the thermosphere O density was varied relative to values provided by the NRLMSISE-00 (Picone et al., 2002) version of the Magnetic Spectrometer Incoherent Scatter (MSIS) empirical atmosphere model (Hedin, 1987). This was done for solar maximum ($F_{10.7}$ = 210) and minimum ($F_{10.7}$ = 90) conditions. In this study we recorded conditions at outflow source height Z_0, values computed using **Eq. 1**, and the simulated outflow flux above Z_0. At height Z_0, an H^+ ion has an equal chance of being lost to charge exchange or to outflow; these processes are indicated by red arrows in **Figure 1D**.

The results are presented in **Figure 1**. In **Figure 1C**, n_H and n_{O^+} at the outflow source height are plotted vs. $n_O/n_{O,MSIS}$. Note that the much lower value of n_H at $F_{10.7}$ = 210 accounts for the counter-intuitive result that outflow fluxes are smaller at solar maximum, when the ionosphere is strongest.

Increased O levels in the thermosphere affect outflows in two ways, both of which are illustrated in **Figures 1A,B**. First, increased O increases the O supply in the ionosphere. At solar minimum (black curves), this effect dominates; note the increase in O^+ in **Figure 1C**. Second, increased O slows the upward diffusion of O^+. At solar maximum (red curves) the diffusion effect tends to dominate, slowing outflow and refilling. Further results (Krall and Huba, 2019a)], show that the O^+ scale height falls with increasing n_O, but only for solar maximum conditions.

Good agreement between SAMI2 and **Eq. 1**, shown in **Figure 1A**, demonstrates that the effect of the O density is fully consistent with the outflow formulation of Richards and Torr (1985).

3 SAMI3 RESULTS: THERMOSPHERE WINDS

We now consider the effect of thermosphere winds on plasmasphere refilling. As is well known (Rishbeth, 1998; Lühr et al., 2011), the wind-driven dynamo potential drives E × B drifts that affect the buildup of plasma density in the ionosphere. The impact of wind-driven ionosphere variability on plasmasphere refilling was demonstrated in Krall et al. (2014). Here, SAMI3

simulations were shown to compare well to *in situ* measurements of plasmasphere n_e during post-storm refilling, with model-data agreement improving as the thermosphere component of the simulation was improved.

In order to run SAMI3 (or SAMI2), thermosphere densities and winds must be specified. Typically, as in the SAMI2 runs above, we compute densities using MSIS (Hedin, 1987; Picone et al., 2002) and compute winds using the Horizontal Wind Model (Hedin, 1991; Drob et al., 2008; Drob et al., 2015). However, we can instead obtain a thermosphere specification from a first-principles model, such as the Thermosphere Ionosphere Mesosphere Electrodynamics General Circulation Model (TIMEGCM) (Roble and Ridley, 1994). For the results presented here TIMEGCM was driven, at the lower boundary, by climatological tides.

In each of the SAMI3 simulations of Krall et al. (2014), and **Figure 2**, we model five days of refilling following a geomagnetic storm on day 31 of 2001. **Figure 2** (left column) shows refilling as globally averaged n_e at the apex of $L = 4.0$, 4.8, and 5.0 field lines, where L is the McIlwain parameter (McIlwain, 1961). Globally averaged n_e (solid curves) are compared to global refilling rates based on *in situ* measurements (dashed lines) for a variety of thermosphere models: MSIS/No Wind, MSIS/HWM07, MSIS/HWM93 and TIMEGCM. The most realistic model, TIMEGCM, gives the best results; MSIS/HWM07 also works well.

The state of the ionosphere for each case is shown in the right-hand column, where Total Electron Content (vertically integrated n_e) is plotted vs. latitude and longitude at a fixed time. Of interest is the strength of the ionosphere at the mid-to-high latitude source of refilling. In each plot, a horizontal line at latitude $\pm 61.5^\circ$ indicates the source of refilling for $L = 4.8$ (in this version of SAMI3, the geomagnetic field is modeled as an aligned dipole; geographic and geomagnetic coordinates are the same). We see that the case with the strongest refilling (No Wind) has the strongest ionosphere TEC values at this relatively high latitude.

4 DISCUSSION: CAN THESE EFFECTS BE FORECASTED?

Any event that affects thermosphere O densities, exosphere H densities, or thermosphere winds on a global scale, such as a geomagnetic storm or a sudden stratosphere warming (SSW) (Chau et al., 2009; Oberheide et al., 2020), has the potential to affect global refilling rates. For example, Jones et al. (2020) suggests that both SSW events and magnetospheric cooling events affect the density of H atoms in the exobase. In order to understand and predict outflows, it is necessary to understand and predict these episodic events.

In addition, thermosphere observations (McDonald et al., 2015; Cai et al., 2020) suggest significant day-to-day variability. For example, satellite data can be used to estimate the globally averaged O density at altitude 400 km, where O is the dominant atom (Picone et al., 2005). In Krall et al. (2016a), Figure 3, we presented such data with a 4-day resolution, finding that global n_O varies by $\pm$ 16% on time scales of less than 30 days. Lei et al. (2008) analyzed similar data, finding density oscillations with periods of 7 and 9 days. While these data do not demonstrate day-to-day variability, they are suggestive. Further, because tides transport O density (Jones et al., 2014), wind variability could be a source of density variability.

Day-to-day variability of thermosphere winds can be observed in daily measurements of TEC. McDonald et al. (2015) presented such TEC data and showed that, when driven from below by assimilated data, a computer simulation of the thermosphere reproduces about 50% of the observed variability. This forcing from below (McCormack et al., 2017) and resulting impacts (Jones et al., 2014) are increasingly well-understood in terms of tides. Specific mechanisms, such as tidal amplification (Goncharenko et al., 2010; Klimenko et al., 2019) and specific ionosphere signatures (Immel et al., 2006) have been identified. While older simulations (Fang et al., 2013) support the finding that tidal forcing accounts for about one half of observed variability, recent work (Zawdie et al., 2020) comes closer to determining the state of the ionosphere-thermosphere system in enough detail to now-cast the upper-atmospheric source of refilling outflows.

While even less is known about day-to-day variability in the exosphere, recent results are suggestive. For example, climatological analysis of exosphere observations revealed both solar cycle dependence and significant scatter, perhaps indicative of variability (Joshi et al., 2019). Diurnal variability has been quantified (Qian et al., 2018), but does not necessarily imply day-to-day variability. Perhaps more to the point, Forbes et al. (2014) found that signatures of thermosphere tides are detectable in exosphere temperatures. This implies that day-to-day variability in thermosphere tides, which is known to be present for some tidal components, might be a cause of similar variability in exosphere H densities. If present, day-to-day variability in exosphere H densities could contribute to the observed scatter in refilling rates (Krall et al., 2018). Finally, we note that the exosphere could have structure (Hodges, 1994; Cucho-Padin and Waldrop, 2018) not present in these simulations, especially during a storm (Kuwabara et al., 2017; Qin et al., 2017; Zoennchen et al., 2017; Cucho-Padin and Waldrop, 2019).

Simulations suggest that variability in thermosphere winds also affects global E × B drifts in the inner magnetosphere so as to affect the shape of the plasmasphere. Specifically, the Krall et al. (2014) study of **Figure 2**, showed that, when one wind model was exchanged for another, the shape of the model plasmasphere changed. Recent simulations showing model-data agreement for ionosphere/thermosphere interactions on a global scale (Huba and Liu, 2020) suggest that such modeling might soon reproduce ducts, crenelations, and other elements of observed plasmasphere structure (Horwitz et al., 1990). Numerical modeling that self-consistently couples the ionosphere and exosphere (Joshi and Waldrop, 2019) could also bring significant progress. Note that, at the cost of a small time step (about 1 s), SAMI3 does not suffer from the limitations of the diffusive equilibrium approximation (Huba and Joyce, 2014; Ozhogin et al., 2014), and has obtained reasonable model-data agreement (Krall et al., 2014; Krall et al., 2016b) for refilling events. Kinetic treatments (Wang et al., 2015) might prove valuable in validating these results. In addition, a current global

kinetic model, such as Pierrard and Stegen (2008), if coupled to a thermosphere model, might validate the finding (Krall et al., 2014) that the wind-driven dynamo affects the shape of the plasmasphere.

Finally, we should acknowledge that any forecast depends on accurate model inputs. Both satellite (Emmert, 2015) and Arecibo radar data (Joshi et al., 2018) show significant long-term deviations from the MSIS model. New observations of thermosphere winds on a global scale are presently coming from the NASA Ionospheric Connection Explorer (ICON) (Immel et al., 2018). ICON is equipped with a Michelson interferometer, built by the NRL, that measures winds and temperatures in the altitude range 90–300 km (Harding et al., 2021; Makela et al., 2021). We are hopeful that newly accurate thermosphere now-casting data products might be developed.

We close with a list of interesting open questions. What is the magnitude of day-to-day variability, if any, in the thermosphere O density? Does day-to-day variability of thermosphere densities, if any, imply similar variability in the exosphere? Do thermosphere winds truly shape the plasmasphere? How do high-latitude storm-driven winds affect the global wind-driven dynamo and refilling outflows?

AUTHOR CONTRIBUTIONS

Both JK and JH contributed to this work.

FUNDING

This research was supported by NRL Base Funds, NASA Grand Challenge award NNH17AE97I, and NASA Living With a Star award 80NSSC19K0089. The research of JH was also supported by NSF grant AGS 1931415.

ACKNOWLEDGMENTS

We thank Lara Waldrop of University of Illinois at Urbana-Champaign, Susan M. Nossal of University of Wisconsin-Madison, McArthur Jones Jr of NRL, and Alan G. Burns of NCAR for helpful discussions. We thank both reviewers for helpful comments.

REFERENCES

Bauer, S. J. (1966). "The Structure of the Topside Ionosphere," in *Electron Density Profiles in Ionosphere and Exosphere*. Editor J. Frihagen (New York: North-Holland), 387.

Bishop, J., Harlander, J., Nossal, S., and Roesler, F. L. (2001). Analysis of Balmer α Intensity Measurements Near Solar Minimum. *J. Atmos. Solar-Terrestrial Phys.* 63, 341–353. doi:10.1016/S1364-6826(00)00212-1

Bishop, J., Mierkiewicz, E. J., Roesler, F. L., Gómez, J. F., and Morales, C. (2004). Data-model Comparison Search Analysis of Coincident PBO Balmer α, EURD Lyman β Geocoronal Measurements from March 2000. *J. Geophys. Res.* 109, 1–9. doi:10.1029/2003JA010165

Bortnik, J., and Thorne, R. M. (2007). The Dual Role of ELF/VLF Chorus Waves in the Acceleration and Precipitation of Radiation belt Electrons. *J. Atmos. Solar-Terrestrial Phys.* 69, 378–386. doi:10.1016/j.jastp.2006.05.030

Cai, X., Burns, A. G., Wang, W., Qian, L., Solomon, S. C., Eastes, R. W., et al. (2020). The Two-Dimensional Evolution of Thermospheric σO/N Response to Weak Geomagnetic Activity during Solar-Minimum Observed by GOLD. *Geophys. Res. Lett.* 47, e2020GL088838. doi:10.1029/2020GL088838

Chau, J. L., Fejer, B. G., and Goncharenko, L. P. (2009). Quiet Variability of Equatorial E x B Drifts during a Sudden Stratospheric Warming Event. Geophys. Res. Lett. 36, 1–4. doi:10.1029/2008GL036785

Cucho-Padin, G., and Waldrop, L. (2019). Time-dependent Response of the Terrestrial Exosphere to a Geomagnetic Storm. *Geophys. Res. Lett.* 46, 11661–11670. doi:10.1029/2019GL084327

Cucho-Padin, G., and Waldrop, L. (2018). Tomographic Estimation of Exospheric Hydrogen Density Distributions. *J. Geophys. Res. Space Phys.* 123, 5119–5139. doi:10.1029/2018JA025323

Denton, R. E., Wang, Y., Webb, P. A., Tengdin, P. M., Goldstein, J., Redfern, J. A., et al. (2012). Magnetospheric Electron Density Long Term (Day) Refilling Rates Inferred from Passive Radio Emissions Measured by IMAGE RPI during Geomagnetically Quiet Times. *J. Geophys. Res.* 117, A03221. doi:10.1029/2011JA017274

Dessler, A. J., and Michel, F. C. (1966). Plasma in the Geomagnetic Tail. *J. Geophys. Res.* 71, 1421–1426. doi:10.1029/JZ071i005p01421

Drob, D. P., Emmert, J. T., Meriwether, J. W., Makela, J. J., Doornbos, E., Conde, M., et al. (2015). An Update to the Horizontal Wind Model (HWM): The Quiet Time Thermosphere. *Earth Space Sci.* 2, 301–319. doi:10.1002/2014EA000089

Drob, D. P., Emmert, T. J., Crowley, G., Picone, M. J., Shepherd, G. G., Skinner, W., et al. (2008). An Empirical Model of the Earth's Horizontal Wind fields: HWM07. *J. Geophys. Res. Space Phys.* 113, A12304. doi:10.1029/2008JA013668

Emmert, J. T. (2015). Altitude and Solar Activity Dependence of 1967–2005 Thermospheric Density Trends Derived from Orbital Drag. *J. Geophys. Res. Space Phys.* 120, 2940–2950. doi:10.1002/2015JA021047

Fang, T.-W., Akmaev, R., Fuller-Rowell, T., Wu, F., Maruyama, N., and Millward, G. (2013). Longitudinal and Day-To-Day Variability in the Ionosphere from Lower Atmosphere Tidal Forcing. *Geophys. Res. Lett.* 40, 2523–2528. doi:10.1002/grl.50550

Fehsenfeld, F. C., and Ferguson, E. E. (1972). Thermal Energy Reaction Rate Constants for H and CO with O and NO. *J. Chem. Phys.* 56, 3066–3070. doi:10.1063/1.1677642

Forbes, J., Zhang, X., and Bruinsma, S. (2014). New Perspectives on Thermosphere Tides: 2. Penetration to the Upper Thermosphere. *Earth, Planets and Space* 66, 122. doi:10.1186/1880-5981-66-122

Gallagher, D. L., Comfort, R. H., Katus, R. M., Sandel, B. R., Fung, S. F., and Adrian, M. L. (2021). The Breathing Plasmasphere: Erosion and Refilling. *J. Geophys. Res. Space Phys.* 126, e2020JA028727. doi:10.1029/2020JA028727

Gallagher, D. L., and Comfort, R. H. (2016). Unsolved Problems in Plasmasphere Refilling. *J. Geophys. Res. Space Phys.* 121, 1447–1451. doi:10.1002/2015JA022279

Goncharenko, L. P., Chau, J. L., Liu, H.-L., and Coster, A. J. (2010). Unexpected Connections between the Stratosphere and Ionosphere. *Geophys. Res. Lett.* 37, 1-6. doi:10.1029/2010GL043125

Hanson, W. B., and Ortenburger, I. B. (1961). The Coupling between the Protonosphere and the normal F Region. *J. Geophys. Res.* 66, 1425–1435. doi:10.1029/JZ066i005p01425

Harding, B. J., Chau, J. L., He, M., Englert, C. R., Harlander, J. M., Marr, K. D., et al. (2021). Validation of ICON-MIGHTI Thermospheric Wind Observations: 2. Green-line Comparisons to Specular Meteor Radars. *J. Geophys. Res. Space Phys.* 126, e2020JA028947. doi:10.1029/2020JA028947

Hedin, A. E. (1987). MSIS-86 Thermospheric Model. *J. Geophys. Res. Space Phys.* 92, 4649–4662. doi:10.1029/JA092iA05p04649

Hedin, A. E. (1991). Revised Global Model of Thermosphere Winds Using Satellite and Ground-Based Observations. *J. Geophys. Res. Space Phys.* 96, 7657–7688. doi:10.1029/91JA00251

Hodges, R. R. (1994). Monte Carlo Simulation of the Terrestrial Hydrogen Exosphere. *J. Geophys. Res. Space Phys.* 99, 23229–23247. doi:10.1029/94JA02183

Horwitz, J. L., Comfort, R. H., and Chappell, C. R. (1990). A Statistical Characterization of Plasmasphere Density Structure and Boundary Locations. *J. Geophys. Res. Space Phys.* 95, 7937–7947. doi:10.1029/JA095iA06p07937

Huba, J. D., Joyce, G., and Fedder, J. A. (2000). Sami2 Is Another Model of the Ionosphere (Sami2): A New Low-Latitude Ionosphere Model. *J. Geophys. Res.* 105, 23035–23053. doi:10.1029/2000JA000035

Huba, J. D., and Joyce, G. (2014). *Numerical Methods in Modeling the Ionosphere*. Washington, DC: American Geophysical Union, 49–55. chap. 5. doi:10.1002/9781118704417.ch5

Huba, J. D., Joyce, G., Sazykin, S., Wolf, R., and Spiro, R. (2005). Simulation Study of Penetration Electric Field Effects on the Low- to Mid-latitude Ionosphere. *Geophys. Res. Lett.* 32, 1–4. doi:10.1029/2005GL024162

Huba, J. D., and Krall, J. (2013). Modeling the Plasmasphere with Sami3. *Geophys. Res. Lett.* 40, 6–10. doi:10.1029/2012GL054300

Huba, J. D., and Liu, H.-L. (2020). Global Modeling of Equatorial Spread F with Sami3/WACCM-X. *Geophys. Res. Lett.* 47, e2020GL088258. doi:10.1029/2020GL088258

Huba, J. D., and Sazykin, S. (2014). Storm Time Ionosphere and Plasmasphere Structuring: Sami3-RCM Simulation of the 31 March 2001 Geomagnetic Storm. *Geophys. Res. Lett.* 41, 8208–8214. doi:10.1002/2014GL062110

Immel, T. J., England, S. L., Mende, S. B., Heelis, R. A., Englert, C. R., Edelstein, J., et al. (2018). The Ionospheric Connection Explorer Mission: Mission Goals and Design. *Space Sci. Rev.* 214, 1–4. doi:10.1007/s11214-017-0449-2

Immel, T. J., Sagawa, E., England, S. L., Henderson, S. B., Hagan, M. E., Mende, S. B., et al. (2006). Control of Equatorial Ionospheric Morphology by Atmospheric Tides. *Geophys. Res. Lett.* 33. doi:10.1029/2006GL026161

Jones, M., Jr., Forbes, J. M., Hagan, M. E., and Maute, A. (2014). Impacts of Vertically Propagating Tides on the Mean State of the Ionosphere-Thermosphere System. *J. Geophys. Res. Space Phys.* 119, 2197–2213. doi:10.1002/2013JA019744

Jones, M., Jr., Siskind, D. E., Drob, D. P., McCormack, J. P., Emmert, J. T., Dhadly, M. S., et al. (2020). Coupling from the Middle Atmosphere to the Exobase: Dynamical Disturbance Effects on Light Chemical Species. *J. Geophys. Res. Space Phys.* 125, e2020JA028331. doi:10.1029/2020JA028331

Joshi, P. P., Phal, Y. D., and Waldrop, L. S. (2019). Quantification of the Vertical Transport and Escape of Atomic Hydrogen in the Terrestrial Upper Atmosphere. *J. Geophys. Res. Space Phys.* 124, 10468–10481. doi:10.1029/2019JA027057

Joshi, P. P., Waldrop, L. S., and Brum, C. G. M. (2018). Ionospheric O Momentum Balance through Charge Exchange with Thermospheric O Atoms. *J. Geophys. Res. Space Phys.* 123, 9743–9761. doi:10.1029/2018JA025821

Joshi, P., and Waldrop, L. (2019). Parametric Estimation of Neutral Hydrogen Density under Charge Exchange and Quantification of its Effect on Plasmasphere-Ionosphere Coupling. *Earth Space Sci. Open Archive*. doi:10.1002/essoar.10500701.1

Klimenko, M. V., Klimenko, V. V., Bessarab, F. S., Sukhodolov, T. V., Vasilev, P. A., Karpov, I. V., et al. (2019). Identification of the Mechanisms Responsible for Anomalies in the Tropical Lower Thermosphere/ionosphere Caused by the January 2009 Sudden Stratospheric Warming. *J. Space Weather Space Clim.* 9, A39. doi:10.1051/swsc/2019037

Krall, J., Emmert, J. T., Sassi, F., McDonald, S. E., and Huba, J. D. (2016a). Day-to-day Variability in the Thermosphere and its Impact on Plasmasphere Refilling. *J. Geophys. Res. Space Phys.* 121, 6889–6900. doi:10.1002/2015JA022328

Krall, J., Glocer, A., Fok, M.-C., Nossal, S. M., and Huba, J. D. (2018). The Unknown Hydrogen Exosphere: Space Weather Implications. *Space Weather* 16, 205–215. doi:10.1002/2017SW001780

Krall, J., Huba, J. D., Denton, R. E., Crowley, G., and Wu, T.-W. (2014). The Effect of the Thermosphere on Quiet Time Plasmasphere Morphology. *J. Geophys. Res. Space Phys.* 119, 5032–5048. doi:10.1002/2014JA019850

Krall, J., Huba, J. D., Jordanova, V. K., Denton, R. E., Carranza, T., and Moldwin, M. B. (2016b). Measurement and Modeling of the Refilling Plasmasphere during 2001. *J. Geophys. Res. Space Phys.* 121, 2226–2248. doi:10.1002/2015JA022126

Krall, J., and Huba, J. D. (2019b). Simulation of Counterstreaming H+ Outflows during Plasmasphere Refilling. *Geophys. Res. Lett.* 46, 3052–3060. doi:10.1029/2019GL082130

Krall, J., and Huba, J. D. (2019a). The Effect of Oxygen on the Limiting H Flux in the Topside Ionosphere. *J. Geophys. Res. Space Phys.* 124, 4509–4517. doi:10.1029/2018JA026252

Kuwabara, M., Yoshioka, K., Murakami, G., Tsuchiya, F., Kimura, T., Yamazaki, A., et al. (2017). The Geocoronal Responses to the Geomagnetic Disturbances. *J. Geophys. Res. Space Phys.* 122, 1269–1276. doi:10.1002/2016JA023247

Lawrence, D. J., Thomsen, M. F., Borovsky, J. E., and McComas, D. J. (1999). Measurements of Early and Late Time Plasmasphere Refilling as Observed from Geosynchronous Orbit. *J. Geophys. Res. Space Phys.* 104, 14691–14704. doi:10.1029/1998JA900087

Lei, J., Thayer, J. P., Forbes, J. M., Sutton, E. K., Nerem, R. S., Temmer, M., et al. (2008). Global Thermospheric Density Variations Caused by High-Speed Solar Wind Streams during the Declining Phase of Solar Cycle 23. *J. Geophys. Res. Space Phys.* 113, 1–8. doi:10.1029/2008JA013433

Lühr, H., Liu, H., Park, J., and Müller, S. (2011). *New Aspects of the Coupling between Thermosphere and Ionosphere, with Special Regards to CHAMP Mission Results*. Dordrecht: Springer Netherlands, 303–316. doi:10.1007/978-94-007-0326-1_22

Makela, J. J., Baughman, M., Navarro, L. A., Harding, B. J., Englert, C. R., Harlander, J. M., et al. (2021). Validation of ICON-MIGHTI Thermospheric Wind Observations: 1. Nighttime Red-Line Ground-Based Fabry-Perot Interferometers. *J. Geophys. Res. Space Phys.* 126, e2020JA028726. doi:10.1029/2020JA028726

McCormack, J., Hoppel, K., Kuhl, D., de Wit, R., Stober, G., Espy, P., et al. (2017). Comparison of Mesospheric Winds from a High-Altitude Meteorological Analysis System and Meteor Radar Observations during the Boreal winters of 2009–2010 and 2012–2013. *J. Atmos. Solar-Terrestrial Phys.* 154, 132–166. doi:10.1016/j.jastp.2016.12.007

McDonald, S. E., Sassi, F., and Mannucci, A. J. (2015). Sami3/SD-WACCM-X Simulations of Ionospheric Variability during Northern winter 2009. *Space Weather* 13, 568–584. doi:10.1002/2015SW001223

McIlwain, C. E. (1961). Coordinates for Mapping the Distribution of Magnetically Trapped Particles. *J. Geophys. Res.* 66, 3681–3691. doi:10.1029/JZ066i011p03681

Millan, R., and Thorne, R. (2007). Review of Radiation belt Relativistic Electron Losses. *J. Atmos. Solar-Terrestrial Phys.* 69, 362–377. doi:10.1016/j.jastp.2006.06.019

Nossal, S. M., Mierkiewicz, E. J., and Roesler, F. L. (2012). Observed and Modeled Solar Cycle Variation in Geocoronal Hydrogen Using NRLMSISE-00 Thermosphere Conditions and the Bishop Analytic Exosphere Model. *J. Geophys. Res. Space Phys.* 117, 3311. doi:10.1029/2011JA017074

Oberheide, J., Pedatella, N. M., Gan, Q., Kumari, K., Burns, A. G., and Eastes, R. W. (2020). Thermospheric Composition O/N Response to an Altered Meridional Mean Circulation during Sudden Stratospheric Warmings Observed by GOLD. *Geophys. Res. Lett.* 47, e2019GL086313. doi:10.1029/2019GL086313

Ozhogin, P., Song, P., Tu, J., and Reinisch, B. W. (2014). Evaluating the Diffusive Equilibrium Models: Comparison with the IMAGE RPI Field-Aligned Electron Density Measurements. *J. Geophys. Res. Space Phys.* 119, 4400–4411. doi:10.1002/2014JA019982

Park, C. G. (1970). Whistler Observations of the Interchange of Ionization between the Ionosphere and the Protonosphere. *J. Geophys. Res.* 75, 4249–4260. doi:10.1029/JA075i022p04249

Picone, J. M., Emmert, J. T., and Lean, J. L. (2005). Thermospheric Densities Derived from Spacecraft Orbits: Accurate Processing of Two-Line Element Sets. *J. Geophys. Res. Space Phys.* 110, A03301. doi:10.1029/2004JA010585

Picone, J. M., Hedin, A. E., Drob, D. P., and Aikin, A. C. (2002). NRLMSISE-00 Empirical Model of the Atmosphere: Statistical Comparisons and Scientific Issues. *J. Geophys. Res. Space Phys.* 107, 1–16. doi:10.1029/2002JA009430

Pierrard, V., and Stegen, K. (2008). A Three-Dimensional Dynamic Kinetic Model of the Plasmasphere. *J. Geophys. Res. Space Phys.* 113, 1–15. doi:10.1029/2008JA013060

Qian, L., Burns, A. G., Solomon, S. S., Smith, A. K., McInerney, J. M., Hunt, L. A., et al. (2018). Temporal Variability of Atomic Hydrogen from the Mesopause to the Upper Thermosphere. *J. Geophys. Res. Space Phys.* 123, 1006–1017. doi:10.1002/2017JA024998

Qin, J., Waldrop, L., and Makela, J. J. (2017). Redistribution of H Atoms in the Upper Atmosphere during Geomagnetic Storms. *J. Geophys. Res. Space Phys.* 122, 10686–10693. doi:10.1002/2017JA024489

Richards, P. G., and Torr, D. G. (1985). Seasonal, Diurnal, and Solar Cyclical Variations of the Limiting H Flux in the Earth's Topside Ionosphere. *J. Geophys. Res. Space Phys.* 90, 5261–5268. doi:10.1029/JA090iA06p05261

Rishbeth, H. (1998). How the Thermospheric Circulation Affects the Ionospheric F2-Layer. *J. Atmos. Solar-Terrestrial Phys.* 60, 1385–1402. doi:10.1016/S1364-6826(98)00062-5

Roble, R. G., and Ridley, E. C. (1994). A Thermosphere-Ionosphere-Mesosphere-Electrodynamics General Circulation Model (TIME-GCM): Equinox Solar

Cycle Minimum Simulations (30–500 Km). *Geophys. Res. Lett.* 21, 417–420. doi:10.1029/93GL03391

Singh, N., and Horwitz, J. L. (1992). Plasmasphere Refilling: Recent Observations and Modeling. *J. Geophys. Res. Space Phys.* 97, 1049–1079. doi:10.1029/91JA02602

Stancil, P. C., Schultz, D. R., Kimura, M., Gu, J.-P., Hirsch, G., and Buenker, R. J. (1999). Charge Transfer in Collisions of O with H and H with O. *Astron. Astrophys. Suppl. Ser.* 140, 225–234. doi:10.1051/aas:1999419

Waldrop, L. S., Kudeki, E., González, S. A., Sulzer, M. P., Garcia, R., Butala, M., et al. (2006). Derivation of Neutral Oxygen Density under Charge Exchange in the Midlatitude Topside Ionosphere. *J. Geophys. Res. Space Phys.* 111, 1–14. doi:10.1029/2005JA011496

Wang, Y., Tu, J., and Song, P. (2015). A New Dynamic Fluid-Kinetic Model for Plasma Transport within the Plasmasphere. *J. Geophys. Res. Space Phys.* 120, 8486–8502. doi:10.1002/2015JA021345

Zawdie, K. A., Dhadly, M. S., McDonald, S. E., Sassi, F., Coker, C., and Drob, D. P. (2020). Day-to-day Variability of the Bottomside Ionosphere. *J. Atmos. Solar-Terrestrial Phys.* 205, 105299. doi:10.1016/j.jastp.2020.105299

Zoennchen, J. H., Nass, U., Fahr, H. J., and Goldstein, J. (2017). The Response of the H Geocorona between 3 and 8 to Geomagnetic Disturbances Studied Using TWINS Stereo Lyman-α Data. *Ann.* Geophysicae 35, 171–179. doi:10.5194/angeo-35-171-2017

Conflict of Interest: Author JH was employed by Syntek Technologies.

The remaining author declares that the research was conducted in the absence of any commercial or financial relationships that could be construed as a potential conflict of interest.

frontiers in Astronomy and Space Sciences

ORIGINAL RESEARCH
published: 22 July 2021
doi: 10.3389/fspas.2021.705637

Van Allen Probes Observations of Oxygen Ions at the Geospace Plume

John C. Foster and Philip J. Erickson*

Massachusetts Institute of Technology Haystack Observatory, Westford, MA, United States

The geospace plume couples the ionosphere, plasmasphere, and magnetosphere from sub-auroral regions to the magnetopause, on polar field lines, and into the magnetotail. We describe Van Allen Probes observations of ionospheric O+ ions at altitudes of 3–6 R_E in the near vicinity of the geospace plume in the noon and post-noon sector. The temporal variation of warm ion fluxes observed as a function of time on a moving spacecraft is complicated by changing spacecraft position and complex ion drift paths and velocities that are highly sensitive to ion energy, pitch angle and L value. In the "notch" region of lower density plasma outside the morning-side plasmapause, bi-directionally field aligned fluxes of lower energy (<5 keV) ions, following corotation-dominated drift trajectories from the midnight sector, are excluded from geospace plume field lines as they are deflected sunward in the plume flow channel. In general, O+ at ring current energies (~10 keV) is bi-directionally field aligned on plume field lines, while lower energy O^+ (<3 keV) are absent. The observation of ion plumes with energies increasing from ~1 keV–>20 keV in the dusk sector outer plasmasphere is interpreted as evidence for localized ionospheric O+ outflow at the outer edge of the geospace plume with subsequent O+ acceleration to >50 keV in <30 min during the ions' sunward drift.

Keywords: oxygen ions, geospace plume, plasmasphere, ring current, ion acceleration, plasmapause, ion drift, ion outflow

OPEN ACCESS

Edited by:
Elena Kronberg, Ludwig Maximilian University of Munich, Germany

Reviewed by:
Matina Gkioulidou, Johns Hopkins University, United States
Fabien Darrouzet, Belgian Institute for Space Aeronomy, Belgium

****Correspondence:***
John C. Foster
jcfoster@mit.edu

Specialty section:
This article was submitted to Space Physics, a section of the journal Frontiers in Astronomy and Space Sciences

Received: *05 May 2021*
Accepted: *09 July 2021*
Published: *22 July 2021*

Citation:
Foster JC and Erickson PJ (2021) Van Allen Probes Observations of Oxygen Ions at the Geospace Plume. Front. Astron. Space Sci. 8:705637. doi: 10.3389/fspas.2021.705637

INTRODUCTION

Spatially extended, sunward-convecting ionospheric density enhancements are noted in incoherent scatter radar observations immediately equatorward of the dusk-sector ionospheric trough. Regularly seen during disturbed geomagnetic conditions, these were termed storm enhanced density (SED) by Foster (1993). Altitude profiles indicated that SED is characterized by a significant increase in F region scale height and peak altitude (Foster, 1993), and occasionally with strong upward O^+ plasma velocity (>1 km s^{-1}) in the topside F region (Yeh and Foster, 1990; Erickson et al., 2010; Zhang et al., 2017). Combining ground and space-based plasma imaging techniques, Foster et al. (2002) demonstrated that the ionospheric SED plumes were magnetically-connected low-altitude signatures of the drainage plumes (plasmaspheric tails) associated with the stormtime erosion of the outer plasmasphere.

Subsequent studies developed a more comprehensive picture of the redistribution of cold (<1 eV) plasma from the ionosphere and inner magnetosphere to the cusp, magnetopause, polar cap, and into the nightside auroral ionosphere. The nomenclature describing various aspects of these phenomena has varied according to feature identification and scope, and has been largely dependent on the characteristics and location of the separate measurements. Moldwin et al. (2016) synthesized recent plume measurements in different regions and concluded that those structures are involved in a causal chain of plasma redistribution throughout the magnetosphere-ionosphere system. In their recent

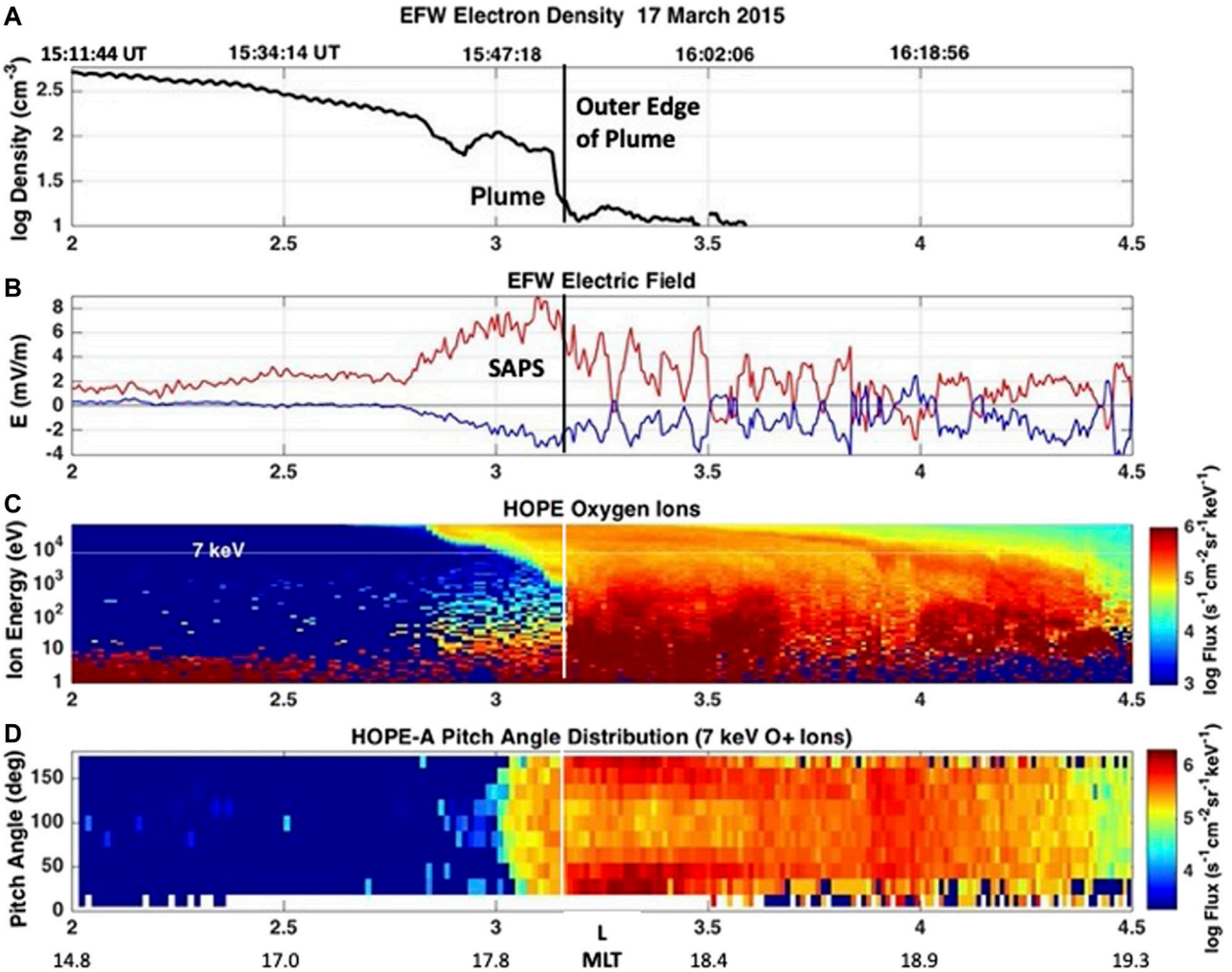

FIGURE 1 | Van Allen Probes A observations crossing the disturbed plasmasphere boundary layer. **(A)** *In situ* cold plasma density observations (EFW boom potential technique). **(B)** Red curve: radially outward EFW electric field (blue curve: azimuthal component). **(C)** HOPE O+ fluxes (10 eV—~60 keV) are shown. O+ with energies <3 keV largely is excluded from plume field lines. A "nose" of hot ring current O^+ ions (>10 keV) extended across the SAPS. **(D)** Bi-directional field aligned O+ fluxes at energies up to ~10 keV (7 keV fluxes shown) were seen immediately adjacent to the outer extent of the geospace plume. [After Foster et al. (2020)].

review, Foster et al. (2020) proposed the recognition of disturbance-related cold plasma redistribution as a unified global phenomenon—the geospace plume.

For cold plasmas of ionospheric origin in the plasmasphere boundary layer (PBL) (Carpenter and Lemaire, 2004), **ExB** redistribution entrains both low altitude ions (O^+ in the ionospheric F region) and high-altitude ions (plasmaspheric and topside H^+, He^+) on the same geomagnetic flux tube. In this way, an active plume advection channel simultaneously drives sunward ion motion at all altitudes from the ionosphere to the apex of the field lines, creating a convection-defined drift shell. A detailed description of the geospace plume at ionospheric heights (the SED plume) has been presented by Foster et al. (2020). A comprehensive statistical analysis of plasmaspheric plumes has been presented by Darrouzet et al. (2008). The appearance and impact of geospace plume plasma at high altitudes in the dayside magnetosphere (Su et al., 2001) and in the reconnection region at the dayside magnetopause (Borovsky, 2014; Walsh et al., 2014) has been described previously.

Van Allen Probes Observations of the Geospace Plume

The instrumentation and orbit of the Van Allen Probes [the Radiation Belt Storm Probes (RBSP); Mauk et al. (2013)] are well designed for *in situ* investigations of geospace plume and outer plasmasphere characteristics and processes in the equatorial region at L ~ 3–6. Wave electric and magnetic field observations made with the Electric and Magnetic Field Instrument and Integrated Science (EMFISIS) instrument (Kletzing et al., 2012) provide plasma density and local magnetic field information. In this study, we concentrate on RBSP observations made with the Helium, Oxygen, Proton, and Electron (HOPE) mass spectrometer (Funsten et al., 2013),

measuring low energy ions and electrons (0.9 eV–56 keV) in the dusk and post-noon sector PBL where energetic ring current ions overlap the outer plasmasphere.

Figure 1 (from Foster et al., 2020) presents a spatially aligned relationship of RBSP Electric Field and Waves [EFW, Wygant et al. (2013)] observations, showing the sub-auroral polarization stream [SAPS; Foster and Burke (2002)] electric field, HOPE ring current ion observations, and the geospace plume observed in cold plasma density at L ~3 by RBSP-A. These observations occurred as the spacecraft's near-equatorial outbound orbit crossed the plasmasphere boundary layer at 18 MLT during a strong disturbance event on March 17, 2015 (Dst was −106 nT at 16 UT and reached −222 nT at 23 UT on 17 March). Our identification of the PBL spans L shells from the inward extent of the SAPS electric fields at L ~ 2.8 to the outer extent of the geospace plume near L ~ 3.15. The close interrelationship of the plasmapause, SAPS, plume, and ion boundaries is clearly seen in this example. Such coordinated multi-instrument observations of the inner magnetosphere and radiation belt environment are a major accomplishment of the Van Allen Probes program, revealing previously undiscovered facets of the system and leading to a clearer understanding of the underlying physical processes and system level effects.

O+ in the Magnetosphere

Earth's ionosphere is the source of singly ionized oxygen ions (O+) in the magnetosphere (e.g. Fuselier et al., 2019). O^+ accelerated to beyond 10 keV populates the main ring current (e.g. Kistler et al., 2016). During disturbed conditions O+ with 10 s keV energy can constitute the dominant ion in the ring current. The source locations and mechanisms associated with the acceleration of the cold (<1 eV) ionospheric O+ ions to multi-keV energies are topics of active investigation. Cusp outflow of ionospheric O^+ ions is believed to be the dominant source of enhanced O^+ in the storm time ring current (Kistler et al., 2016). At ~1 keV final energy, O^+ beams streaming away from a source in the cusp have been seen in the tail lobes and ultimately in the plasma sheet (Kistler et al., 2010; Liao et al., 2010). Ionospheric O^+ outflow reaching nightside field lines can be accelerated along drift trajectories in the magnetotail, reappearing in the inner magnetosphere within the warm plasma cloak (WPC) (Chappell et al., 2008). At energies <~3 keV, ions accelerated earthward from the tail primarily follow eastward corotational drift trajectories, while ions ≥3 keV experience curvature drift westward into the pre-midnight sector. As discussed below, O+ ions following these source/trajectory paths are observed adjacent to the plume and plasmapause in both the noontime and the dusk sectors.

In this study we use *in situ* Van Allen Probes observations to investigate the role played by the geospace plume and processes at the PBL in the source, dynamics, and evolution of O+ in the inner magnetosphere (L < 6). In *O + Pitch Angle Distributions Across the Geospace Plume* we present a schematic equatorial-plane picture of the geospace plume orientation and the configuration of the RBSP orbits for two disturbance events in October 2013. For the lower energy O+ WPC ions we investigate pitch angle distributions and dawn side drift trajectories around the plasmasphere, and their encounter with the geospace plume near noon. In *O+ Outflow at the Geospace Plume and the Plasmapause* we concentrate on O+ ions at the outer boundary of the plasmasphere and plume on the dusk side. Our study finds strong fluxes of <1 keV O+ are present immediately outside the plume, but absent at those energies on plume field lines, while multiple populations of >10 keV ions are observed on plume field lines in the dusk sector. *EMIC Waves* describes our observation of strong helium-band EMIC waves located immediately inside the outer plume boundary for the cases examined in *O+ Outflow at the Geospace Plume and the Plasmapause. The keV O+ Plume: Evidence for Ion Acceleration on Geospace Plume Field Lines* presents evidence for <1 keV O+ outflow at the outer boundary of the geospace plume, with subsequent acceleration to 50 keV energies and the formation of a sunward drifting keV O+ plume. *Acceleration of the keV O+ Plume* addresses potential acceleration mechanisms for the keV O+ plume. Finally, *Conclusion* presents our conclusions.

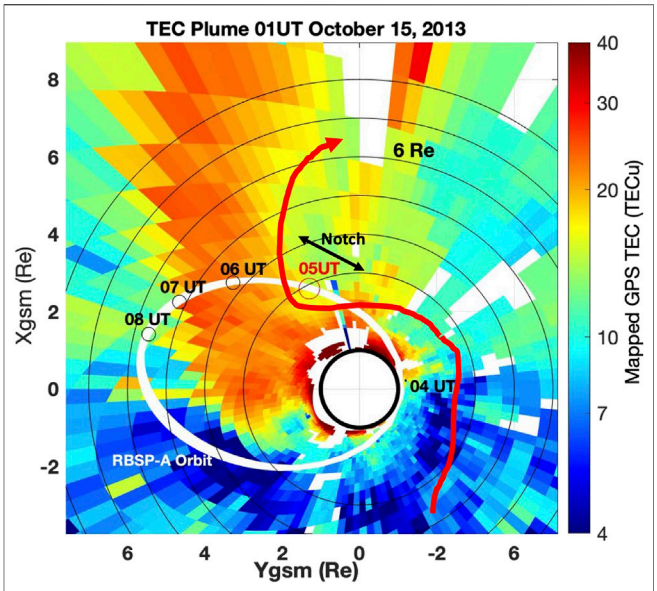

FIGURE 2 | RBSP-A orbit and orbital position at 05 UT on October 15, 2013 are superimposed on an equatorial-plane projection of ground-based GPS TEC observations. These latter are not indicative of absolute plasmaspheric density, but serve to trace boundaries of the geospace plume in the dayside magnetosphere [Foster et al. (2002)]. A schematic drift trajectory for <10 keV ions injected sunward from the magnetotail is shown as a red curve. Crossing the "notch" between the outbound crossing of the dawnside plasmapause and the plume, the spacecraft intersects the injection trajectory of ions of a fixed energy at two separate radial distances leading to the observation of a wedge-shaped ion flux distribution (e.g. Ebihara et al., 2001).

OBSERVATIONS

O+ Pitch Angle Distributions Across the Geospace Plume

Figure 2 presents a schematic introduction to the October 15, 2013 event, using magnetically mapped GPS-derived total electron content measurements as a guide to boundaries of

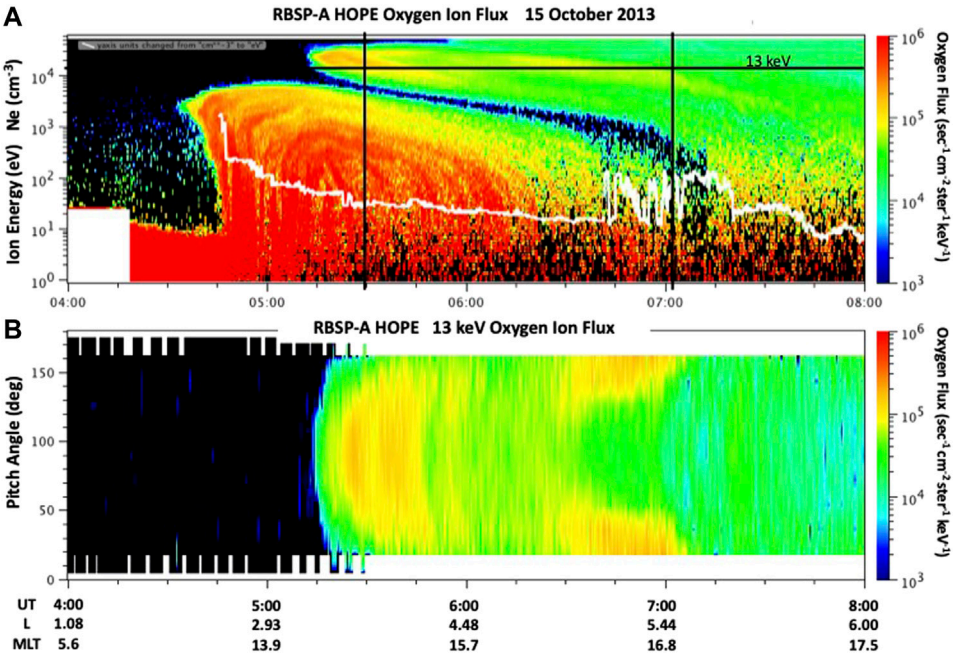

FIGURE 3 | (A) HOPE O+ spectrogram [white curve: EFW electron density (cm^{-3})] for the outbound orbit of RBSP-A shown in **Figure 2**. Probe A exits the plasmasphere at ~04:45 UT, observes a wedge-like spectrogram at energies below the ZEAB as it crosses the morningside notch between the plasmapause and the geospace plume, and encounters the plume at 06:45 UT. For reference with **Figure 4**, two fiducial black vertical lines are shown at 05:30 and 07:02 UT. RBSP-A exited the dusk side of the plume at 07:20 UT. **(B)** Pancake PADs (peaked at 90°) characterize the nose of the ring current O+ ions first observed at 05:15 UT near L ~ 3.5 (13 keV ions are shown). As the morning side of the plume was encountered, the 13 keV O+ ions changed character significantly, becoming bi-directionally field aligned.

plume regions in the magnetospheric equatorial plane. The Van Allen Probe-A orbit crossed the geospace plume at ~07 UT in the dusk sector after sampling (at ~05 UT) a region of lower density cold plasma observed along the spacecraft outbound orbit between the morning-side plasmapause and the inner boundary of the geospace plume. This was a moderate storm event during which the main phase Dst index reached −49 nT at 04 UT on 15 October. Early IMAGE/EUV studies (Gallagher et al., 2005) identified distinct radial structure in imagery of the outer plasmasphere boundary, terming these depressions and crenulations "notches" [see Darrouzet et al. (2009) for a review of plasmasphere structure]. For the orbital configuration shown in **Figure 2**, the outbound Van Allen Probes orbit can exit the morning-side plasmasphere and then intersect the geospace plume as it is extended sunward towards the magnetopause. In this study we refer to this intervening region between the dawn side plasmapause and the plume as "the notch." As shown below, we observe specific characteristics of O+ fluxes in this notch region.

During disturbed conditions, warm ions (H+, O+) injected earthward from the magnetotail with energies (<~10 keV) below the zero-energy Alfvenic boundary, ZEAB (Ejiri, 1978), follow corotation-dominated drift trajectories from the midnight sector that approach the morning side of the geospace plume. As discussed by Ebihara et al. (2001), these ions follow convolved trajectories determined by gradient drift, corotation and convection electric fields. As a result, the temporal variation of warm ion fluxes observed as a function of time on moving spacecraft is complicated by changing spacecraft position and complex ion drift paths that are highly sensitive to ion energy, pitch angle and L value. As the sunward drifting ions encounter convection electric fields carrying the plume toward the dayside magnetopause, their trajectories are deflected sunward. As a result, the spacecraft can intersect the drift path of a given energy ion at multiple times and positions along its orbit. This effect causes the spacecraft to observe a wedge-shaped ion distribution as described by Ebihara et al. (2001) and as seen in the notch in **Figure 3A** during the outbound orbit of RBSP-A (cf. **Figure 2**). During this event, RBSP-A exited the highly eroded plasmasphere at ~04:45 UT (L ~ 2.4; 13 MLT) on its outbound orbital trajectory. A wedge-like notch O+ ion distribution, as described by Ebihara et al. (2001), then was observed between L ~ 3 and L ~ 5 until the inner edge of the plume was encountered at ~06:45 UT (L ~ 5.3; 16.2 MLT). The ZEAB is seen as the narrow, slanting, low ion flux separatrix between the notch ions and the overlying higher energy ring current. EFW cold electron density (cm^{-3}) is overplotted on the ion spectrogram as a white curve. Plume fluxes were encountered between 06:45 and 07:20 UT. A black horizontal line marks the O+ fluxes at 13 keV. Pitch angle distributions (PADs) for the 13 keV ring current O+ ions are presented in **Figure 3B**. The 90° pitch angle ions penetrate most deeply [e.g. Ejiri (1978)] into the inner magnetosphere (05:30 UT, L = 3.8, 14.7 MLT), while O+ at this energy on plume field lines (07:02 UT, L = 5.5, 16.6 MLT) is distinctly bi-directionally field aligned. Black vertical lines on panel A mark these times for reference with **Figure 4**.

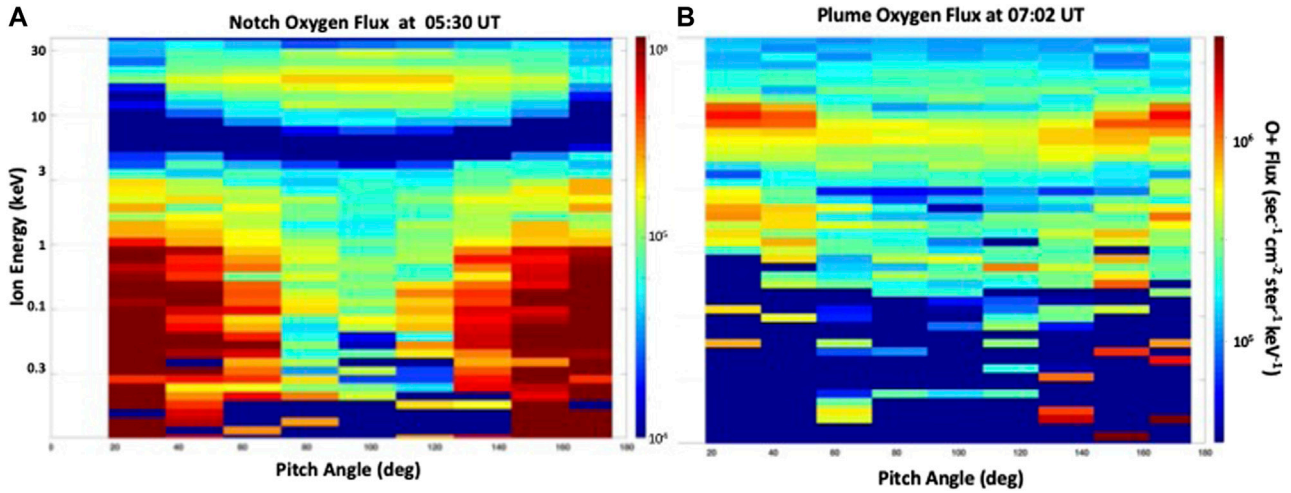

FIGURE 4 | RBSP-A observed O+ pitch angle spectra are shown for the full range of HOPE ion energies on October 15, 2013 for the times indicated in **Figure 3A**. **(A)** In the region between the morning-side plasmapause and the plume (05:30 UT in **Figure 3A**), notch O+ at energies <3 keV tend toward bi-directional field alignement, while ring current O+ (~10 keV) exhibit a pancake PAD. **(B)** On plume field lines (07:02 UT), O+ at ring current energies around 10 keV is bi-directionally field aligned while the lower energy O+ (<5 keV) largely is absent.

In **Figure 4** we present the full HOPE energy range of O+ PADs observed on RBSP-A at the times indicated in **Figure 3A** in the notch (panel A) at 05:30 T, and in the plume (panel B) at 07:02 UT. For the notch pitch angle spectra, those ring current O+ ions above the ZEAB that propagate azimuthally in the anti-corotation direction exhibit pancake distributions peaked at 90°. In sharp contrast, the lower energy (<3 keV) O+ ions in the wedge population below the ZEAB have pronounced bi-directional field alignment consistent with the description of the warm plasma cloak given by Chappell et al. (2008). As also seen in **Figure 3A**, the PADs observed crossing the plume shown in **Figure 4B** indicate that the lower energy O+ ion population seen in the notch largely was absent from plume field lines. In contrast, on this crossing of the geospace plume at L ~ 5 (**Figure 4B**), ring current O+ fluxes at energies 8–15 keV were locally enhanced and bi-directionally field aligned.

O+ Outflow at the Geospace Plume and the Plasmapause

Van Allen Probes observations during a separate, earlier 8–9 October 2013 interplanetary shock event reported by Foster et al. (2015) provided an excellent characterization of the ion populations around dusk sector plume field lines during a moderately disturbed storm. Dst reached -69 nT at 02 UT on 9 October. This event featured an interplanetary shock impacting the magnetosphere at ~20:21 UT on 8 October while RBSP-A was outbound in the dayside plasmasphere at L ~3 and 13 MLT. For the next 5 h, RBSP-A followed an orbital path nearly identical to that shown for the October 15, 2013 event in **Figure 2**, remaining inside the perturbed plasmasphere and developing plume. **Figure 5** presents RBSP-A HOPE O+ and H+ fluxes across this region for the 8–9 October event, with *in situ* cold electron density superimposed on the ion spectra as a white trace. Regularly-decreasing outer plasmasphere density was observed until ~22:00 UT. A density increase at ~ 23:00 UT (L ~ 6; 16 MLT) then marked the entry into the developing geospace plume in the outer regions of the plasmasphere. The spacecraft remained in the plume as it passed apogee and then exited the plume at ~01:30 UT on 9 October (L ~ 5.5; 18.7 MLT). Strong fluxes of 10 eV to >1 keV O+, H+, and He+ (not shown) were observed in the region immediately outside the plume. The final crossing of the structured plume/plasmapause on the inbound orbit was encountered at 02:45 UT (L = 4.1, 19.8 MLT). Subsequently, on the outbound orbit, the contracted plasmapause was crossed at ~ 05:30 UT (L = 3.2, 14.6 MLT). Wedge-like ion distributions were observed in the notch beyond the plasmapause until the plume was encountered at 07:00 UT (L ~ 5; 16 MLT). Similar to 15 October (cf. **Figure 4**), O+ and H+ fluxes with energies 10 eV–>1 keV were absent from dusk sector plume field lines.

Ion PADs observed in the outer portion of the plume on 9 October at ~01:15 UT are shown in **Figure 6**. The strong fluxes of O+ (panel A) with energies <1 keV observed immediately outside the plume (cf. **Figure 5**) were excluded from plume field lines. At higher energies >3 keV, robust fluxes of O+ exhibited an increasing tendency toward bi-directional field alignment as the energy of their observation increased from 3 to 10 keV. Strong 200 eV–3 keV proton fluxes (panel B) also were observed in this region with similar configurations in pitch angle, moving toward bi-directional field alignment with increasing energy. Finally, at higher energies 3–10 keV, H+ exhibited a butterfly PAD symmetrically peaked off 90°.

HOPE oxygen ion fluxes were independently observed by Van Allen Probe B during the October 9, 2013 event as presented in **Figure 7A**. In particular, Probe B preceded Probe A by ~1 h along the same orbital track and also remained in the outer plasmasphere and plume until 01:15 UT (L ~ 4.5; 19.6 MLT).

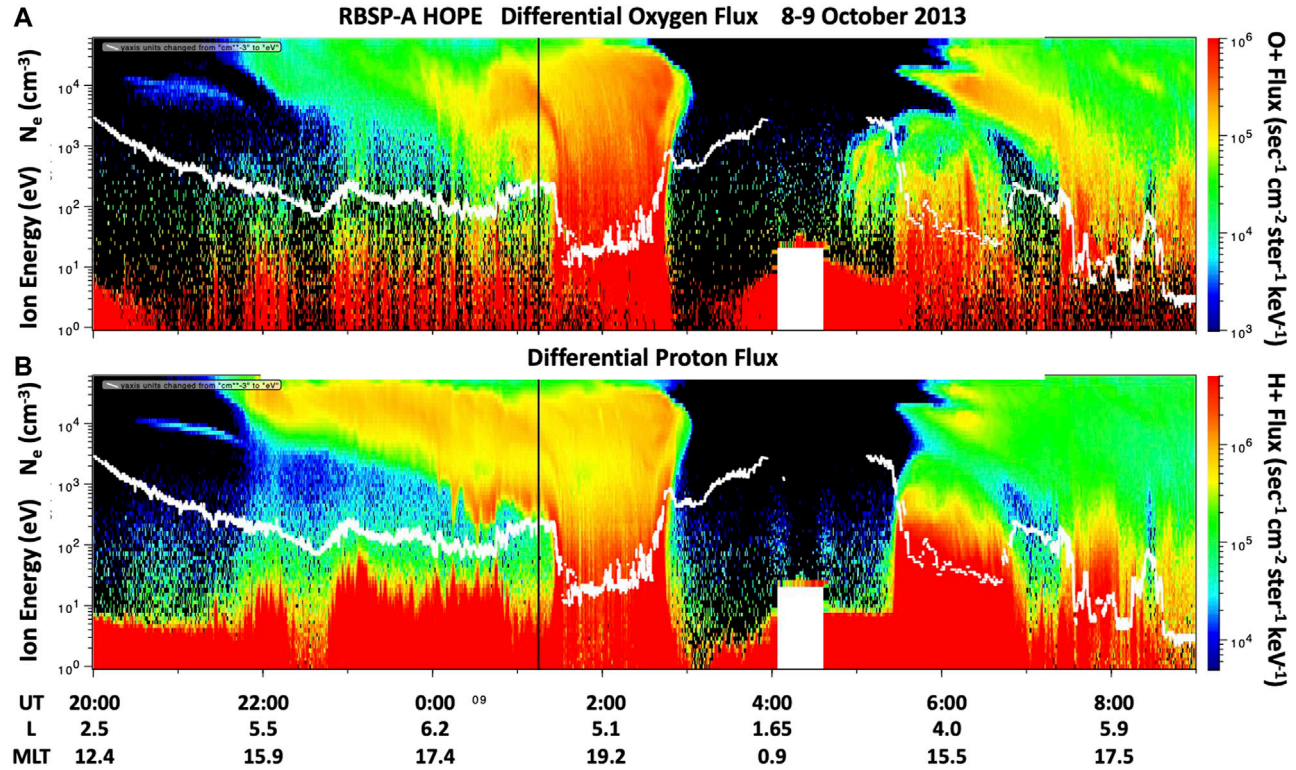

FIGURE 5 | RBSP-A oxygen **(A)** and proton **(B)** ion differential flux spectra are shown for an 8–October 9, 2013 pass following an orbital trajectory (not shown) similar to that shown in **Figure 2**. *In situ* plasma density derived from EMFISIS observations is superimposed as the white curves. RBSP-A traversed the outer region of the evening sector plume from 23:00 to 01:30 UT (apogee at 23:40 UT at 17 MLT). After exiting the plume at ~01:30 UT (L ~ 5.3, 18.5 MLT), the plasmasphere was reentered at ~ 05:30 UT (L = 3.2, 14.6 MLT). Black vertical lines indicate the times of plume O+ and H+ PADs shown in **Figure 6**.

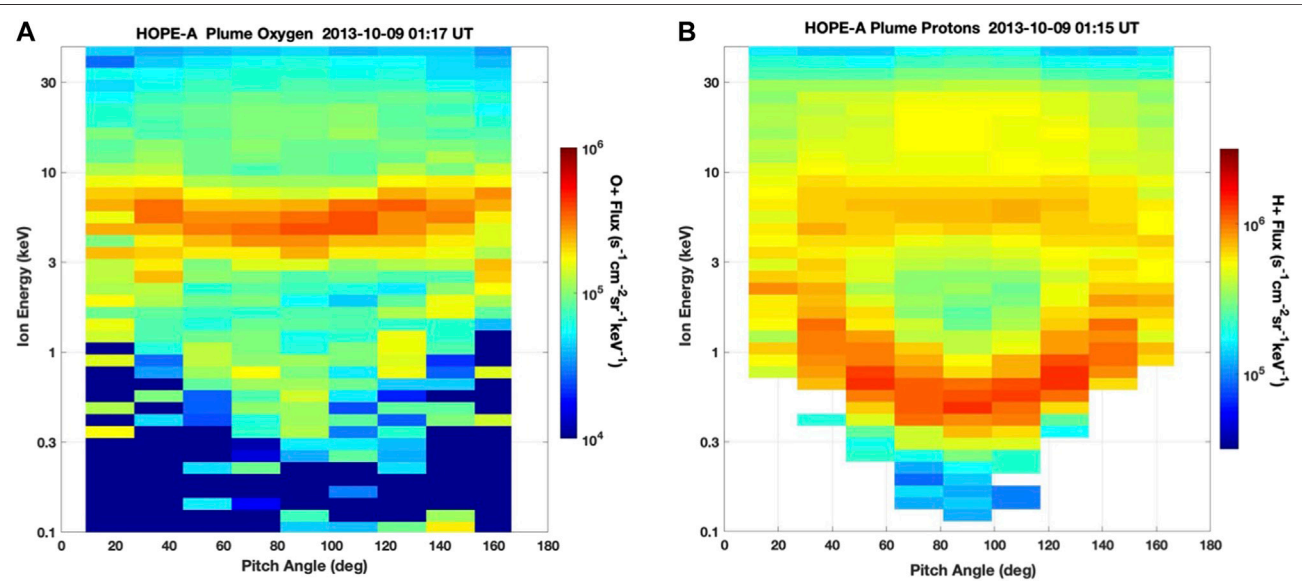

FIGURE 6 | Ion PADs for O+ **(A)** and H+ **(B)** are shown for the RBSP-A plume crossing on October 9, 2013 at the time (at ~01:15 UT) shown by vertical black lines in **Figure 5A,B**. **(A)** O+ with energies <1 keV was not observed on plume field lines, while at higher energies O+ fluxes moved toward a bi-directional field aligned configuration as energy increased from 1 to 10 keV. **(B)** Strong 200 eV–3 keV proton fluxes were also observed in this region with similar configurations in pitch angle, moving to ward bi-directional field alignment with increasing energy. At higher energies 1–10 keV, H+ exhibited a butterfly PAD.

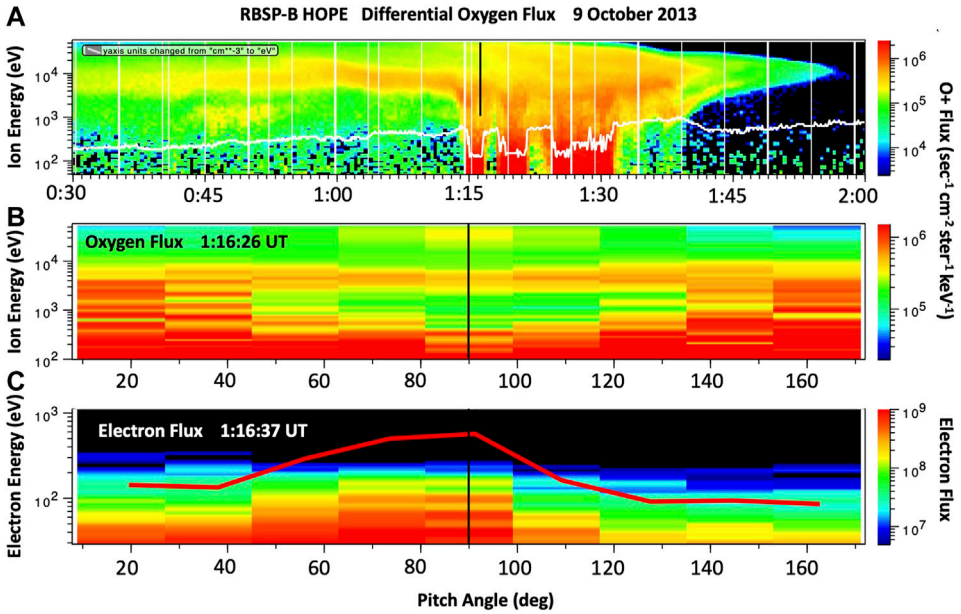

FIGURE 7 | RBSP-B O+ flux observations are plotted from HOPE data for the inbound orbit, showing a crossing of the outer boundary of the plume multiple times beginning at ~01:15 UT on October 9, 2013. **(A)** At each crossing, strong O+ fluxes with energies 10 eV to >5 keV characterized the region immediately beyond the edge of the plume. *In situ* EFW measurements of cold plasma density are shown by the white curve. **(B)** O+ PADs at the edge of the plume are shown for the time indicated by the fiducial black line in **Figure 5A**. **(C)** HOPE electron PADs indicate downflowing electron fluxes at energies up to 300 eV. The PAD for 105 eV electrons is shown as the red curve (black fiducial line indicates 90° pitch angle).

At this point, the spacecraft exited and reentered the geospace plume several times, crossing the outer boundary of the plume six times over a 20 min span. At each plume boundary crossing, consistent ion flux and pitch angle signatures were observed in a configuration similar to those seen by Probe A. Subsequently, as the B spacecraft moved rapidly toward perigee, it reentered the plume for the final time at ~ 01:33 UT (L ~ 4.0; 20.0 MLT) and then smoothly entered the somewhat lower density of the outer plasmasphere at ~01:40 UT (L ~ 3.8; 20.3 MLT).

The O+ PADs at 01:16:26 UT shown in **Figure 7B** [at the fiducial line in (A)] are typical of the observations immediately outside plume field lines made by RBSP-B during its multiple crossings of that region. Whereas **Figure 6A** demonstrated the exclusion of lower energy O+ (100 eV—3 keV) from interior plume field lines, strong bi-directionally field aligned O+ fluxes in that energy range were observed immediately outside the plume (B). There, the higher energy population of ring current O+ at 5–10 keV exhibited a butterfly PAD. The HOPE electron PADs shown in **Figure 7C** indicate downflowing electron fluxes at energies up to 300 eV in this region at the outer edge of the geospace plume. Their potential association with ion acceleration by dispersive Alfven waves (Chaston et al., 2015) will be discussed in *The keV O+ Plume: Evidence for Ion Acceleration on Geospace Plume Field Lines* below.

Figure 8 plots selected individual RBSP-B ion flux profiles as a function of ion energy for the three species (O+, He+, H+) near 01:15 UT on October 9, 2013 (cf. **Figure 7A**) for locations immediately outside (red) and inside (black) the outer edge of the geospace plume. Regardless of species, plume regions are nearly devoid of strong ion fluxes in the 10 eV–1 keV range. By contrast, exterior to the plume, PADs for O+ across the 50 eV–1 keV energy range are bi-directionally field aligned (cf. **Figure 7B**).

DISCUSSION

Electromagnetic Ion Cyclotron (EMIC)

Usanova et al. (2016) outlined the potential importance of the plasmapause for EMIC wave growth and ducting, showing that EMIC wave activity is often observed to be generated in radially narrow regions, just inside the plasmapause. De Soria-Santacruz et al. (2013), using a model reproducing the radial cold plasma density irregularities typical of the storm-time plasmaspheric plume, found that EMIC wave growth was observed only in the helium band, between the oxygen crossover and the helium cyclotron frequency. We have performed a 1,024 point FFT (sliding window, 2/3 overlap) on EMFISIS high resolution magnetic field observations to produce a spectrogram of waves in the EMIC frequency band (~1–10 Hz). As seen in **Figure 9**, He-band EMIC waves were observed immediately inside the plume outer boundary on each successive boundary crossing by RBSP-B. (The white curve shows plasma density (divided by 100) derived from EMFISIS upper hybrid frequency observations. Red curves denote the helium and oxygen cyclotron frequencies.) **Figure 9** shows the absence of EMIC waves in the three regions of strong fluxes of 10 eV–1 keV O+

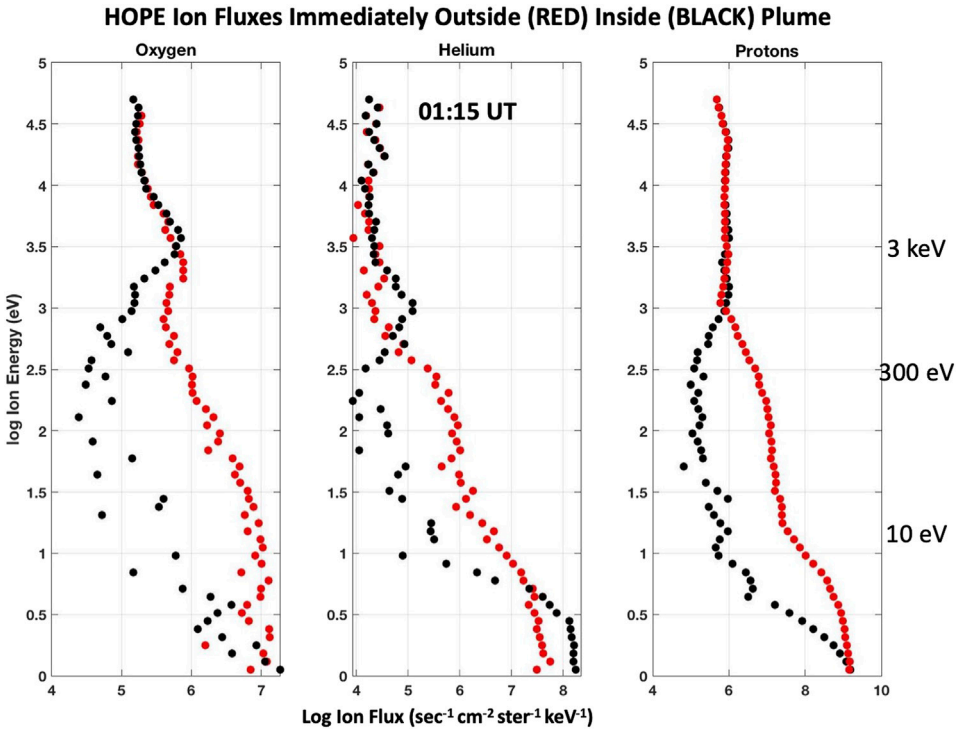

FIGURE 8 | Individual RBSP-B ion fluxes immediately outside (red) and inside (black) the outer edge of the geospace plume are shown versus ion energy for the time indicated by the black vertical line in **Figure 7A**. The strong fluxes of 10 eV–1 keV O+ **(A)**, He+ **(B)**, and H+ **(C)** seen just outside the plume are excluded from adjacent plume field lines. As shown above in **Figure 7B**, the 50 eV–1 keV O+ fluxes immediately exterior to the plume are bi-directionally field aligned.

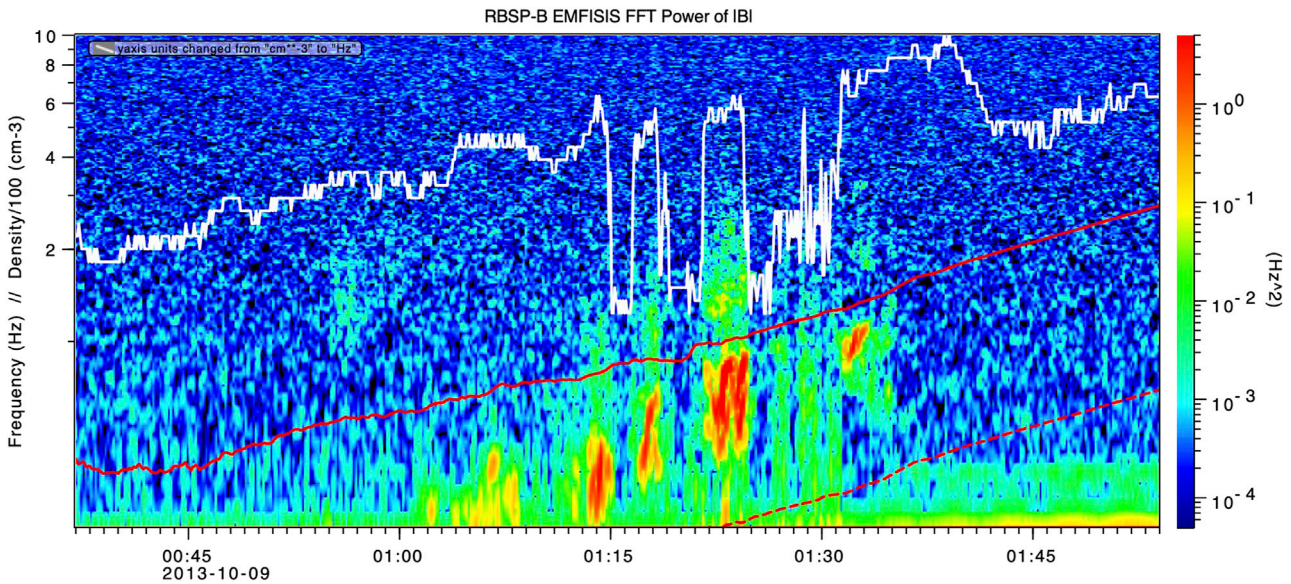

FIGURE 9 | He-band EMIC waves were observed immediately inside the plume outer boundary on each successive boundary crossing by RBSP-B (cf. **Figure 7**). Superimposed are the He+ and O+ ion cyclotron frequencies (red solid and dashed curves) and the EMFISIS plasma density (divided by 100; white) to delineate the plume crossings.

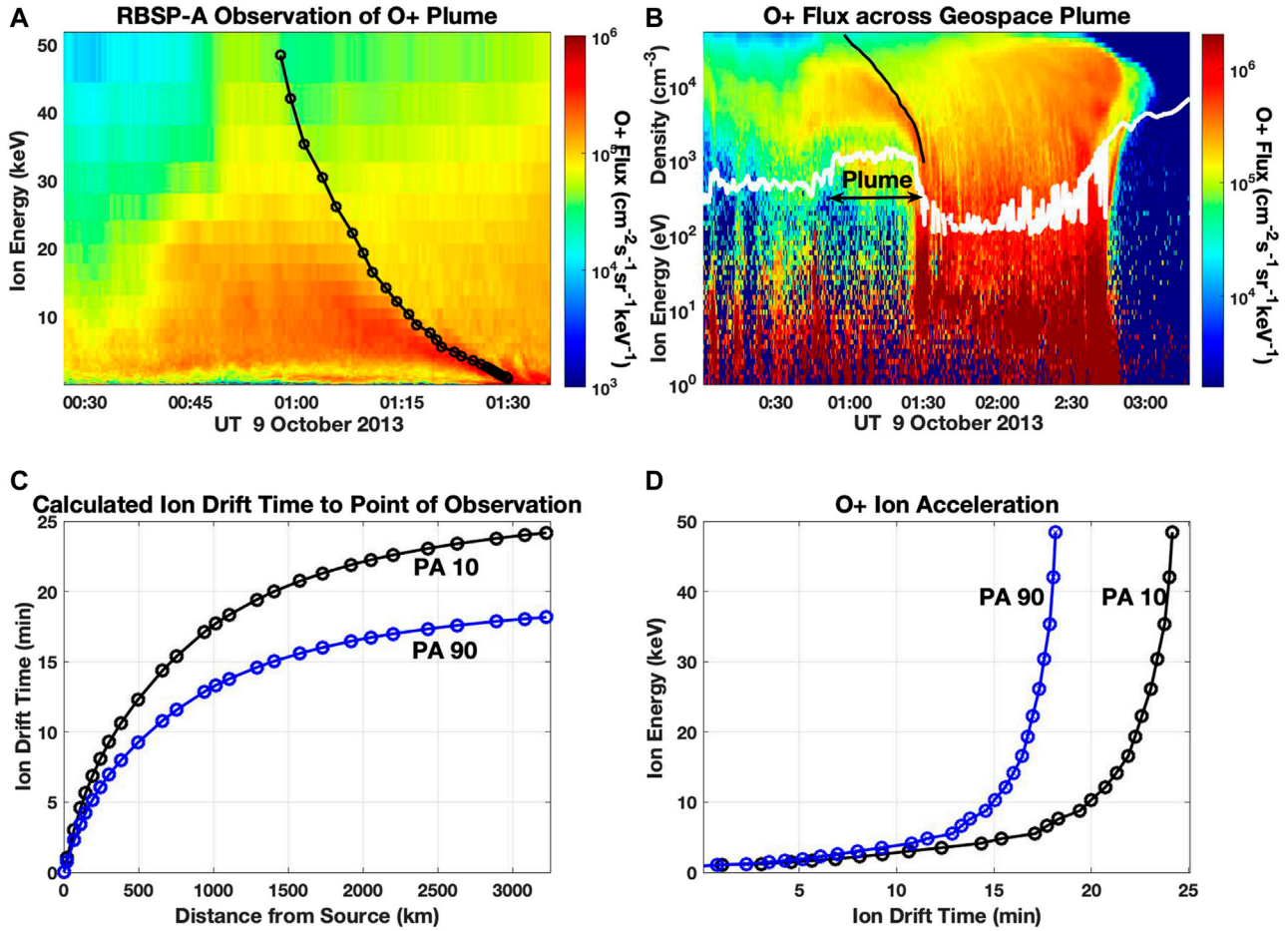

FIGURE 10 | (A) The O+ fluxes on geospace plume field lines shown in **Figure 5A** are replotted on a linear energy scale highlighting a pronounced >1 keV O+ plume with a time-dependent upper energy boundary. The black curve marks the upper energy boundry of the O+ plume fluxes. Circles denote the discrete ion energy channels of the HOPE instrument. **(B)** O+ fluxes and the black boundary line of Panel (A) are replotted versus logarithmic ion energy to emphasize the O+ plume's origin at the outer edge of the geospace plume. EFW cold plasma density is plotted as a white line. **(C)** Calculated O+ drift times to their points of observation (T_N, see text) are plotted versus distance from their source at the plume for ions of a given energy for two values of pitch angle (see text). **(D)** The increase of O+ energy with drift time derived from the observed high energy boundary line shown in **(A)** is shown, indicating the rate of ion acceleration within the O+ plume for two values of ion pitch angle. Comparing the two pitch angle curves for constant drift time away from the ion source it is seen that pitch angles increase with energy during the keV O+ plume acceleration.

just outside the plume, as shown in **Figure 7A**. Strong EMIC waves occurred in a narrow region on adjacent plume field lines where such lower energy O+ was excluded. Denton et al. (2014) have found that a large O+ concentration limits the frequency range of, or even totally quenches, EMIC waves. Our observations are consistent with these theoretical studies of EMIC wave occurrence. A potential role for EMIC waves in the acceleration of ionospheric O+ to ring current energies (>10 keV) is discussed below.

The keV O+ Plume: Evidence for Ion Acceleration on Geospace Plume Field Lines

The presence of strong He-band EMIC waves suggests that ion acceleration processes may be at work in creating the position-dependent energy spectra presented previously, and that we analyze further here. An arched band of O+ at energies >1 keV was observed between 01:00 and 01:30 UT on plume field lines as RBSP-A approached the outer boundary of the geospace plume (cf. **Figure 5A**). As the spacecraft approached the outer edge of the plume, this keV O+ plume appeared to merge smoothly with the narrow region of bi-directionally field aligned 50 eV–1 keV O+ fluxes at the plume outer boundary observed at 01:30 UT. Similar ion plumes were observed for H+ (cf. **Figure 5B**) and He+ (not shown), and associated with the multiple plume boundary crossings by RBSP-B (cf. **Figure 7**, **Figure 8**). In **Figure 10A** we plot the O+ plume fluxes of **Figure 5A** on a linear energy scale between 0.9 and 50 keV as a function of time, along with a solid black curved line marking the upper energy bound of O+ plume fluxes observed as the spacecraft approached the geospace plume outer boundary. At

this position in its orbit (L ~ 5.5; 18 MLT), RBSP-A had a ~100 km/min velocity in the negative X_{GSM} (anti-sunward) direction, while the O+ ions with energies between 1 and 50 keV drifted in the $+X_{GSM}$ direction with velocities varying from 20 to 1,000 km/min depending on energy and pitch angle. We use relativistic computational formulas for ion or electron drift times/velocities as a function of L, particle energy, and pitch angle derived from their description in Schultz and Lanzerotti (1974). For a given energy, ions with more field-aligned equatorial pitch angles have slower sunward (westward) drift velocities and will arrive at a given distance from their source later than 90° pitch angle ions of the same energy. The highest energy ions observed at a given observation time on the moving spacecraft (i.e. distance from their source) as denoted by the black line in **Figure 10A** will have the most field-aligned pitch angles. In the following we will refer to the ions at the upper energy extent of the keV O+ plume as 10° pitch angle ions. For example, the highest O+ plume energy observed at ~01:17 UT was ~8 keV, and we have shown in **Figure 6A** that those 8 keV ions were the most bi-directionally field aligned. RBSP-A crossed the geospace plume outer boundary at ~01:30 UT some 13 min later. Traveling at an assumed constant 100 km/min, the distance from the observation point at 01:17 UT to the apparent source of the plume O+ ions was ~1,300 km.

It is important to note that no reoccurrence of higher energy ions above the black line boundary was observed as time progressed and the distance to the geospace plume outer boundary decreased. This indicates that the ions in the keV O+ plume were being accelerated continually as they propagated away from their source. We replot the O+ fluxes and black plume boundary line in **Figure 10B** on a logarithmic energy scale for a better comparison with earlier figures.

To proceed with analysis, we know both the spacecraft velocity (100 km/min) and the oppositely-directed ion drift velocity as a linear function of ion energy for constant L = 5.5 and 10° pitch angle. (For computational simplicity we assume that L is constant. Near apogee, L at RBSP-A varied from 5.8 to 5.5 between 01:00 and 01:30 UT.) Using **Eq. 1**, we first convert the black curve of observation time (UT_n) vs. ion energy (E_n) to a set of discrete values of drift distance (D_n) versus ion energy at their point of observation (E_n), assuming that the ions originated with 1 keV energy from a source at the outer boundary of the geospace plume crossed by the spacecraft at 01:30 UT (UT_{source}).

$$\boldsymbol{D_n = (UT_{source} - UT_n) * 100\ km/min} \quad (1)$$

The drift velocity of the ions (Vd_n) varies with their energy and pitch angle as they propagate away from their source, so that the propagation time (T_N) to the point of last observation of ions of energy E_n is approximated by the simple piecewise integration of **Eq. 2**.

$$\boldsymbol{T_N = \sum_{n=1}^{N} (2(D_n - D_{n-1}) / (Vd_n + Vd_{n-1}))} \quad (2)$$

The calculated set of ion drift times T_N is presented in **Figure 10C** as a function of distance from the source (D_n) for ions with 10° pitch angle (black curve) and 90° pitch angle (blue curve). Because of their faster drift speed, 90° pitch angle ions arrive at a given distance from the boundary earlier than 10° pitch angle ions of the same energy. We now have discrete arrays of E_n, D_n, and T_N, all derived from the observed black boundary curve (E_n, UT_n) of **Figure 10A**. In **Figure 10D** we plot the calculated values of O+ ion energy (E_n) versus ion drift time (T_N) for 10° (black) and 90° (blue) pitch angle O+ ions, illustrating the time rate of energization for ions in the O+ keV plume. Under this model, for the case observed on October 9, 2013, 10° pitch angle O+ ions with a source population <1 keV were accelerated to 50 keV in ~24 min along their sunward drift trajectory across geospace plume field lines.

The observations presented in **Figure 5** through **Figure 10** indicate O+ ion outflow and rapid (mins) acceleration to multi-keV energies at the outer boundary of the geospace plume in the dusk sector. Strong fluxes of <100 eV ions are observed immediately outside the plume boundary, but are not observed on plume field lines at those energies. Rather, discrete populations of O+, H+, and He+, ion plumes, are observed drifting sunward on geospace plume field lines with energies increasing to 10s keV over <30 min. With increasing drift distance sunward of the geospace plume outer boundary, the ion plume populations are characterized by increasingly bi-directionally field aligned PADs at the highest ion plume energies observed at any given time (cf **Figure 5**, **Figure 6**).

Acceleration of the keV O+ Plume

In this paper we do not attempt to identify or describe an acceleration mechanism for the keV O+ plume. Yue et al. (2019) reported dayside observations during geomagnetically active times of fluxes of H+ at ring current energies of ~30–50 keV that had an additional field-aligned population overlapping the usual pancake population. That study suggested that ions in this energy range with field-aligned PADs probably were accelerated in the post-noon sector, in association with ionospheric disturbances that were triggered by tail injections. Chaston et al. (2015) describe a mechanism that self-consistently drives ionospheric outflow and energization based on storm time measurement of intense broadband low-frequency electromagnetic dispersive Alfvén waves (DAW) on ring current field lines. Hull et al. (2019) found that DAW activity and O^+ outflow/energization is a characteristic feature of the inner magnetosphere during active conditions and that these correlated features are most intense during geomagnetic storms. Waves of this kind accelerate electrons parallel to the geomagnetic field and ions in the perpendicular direction. The ions arrive in the equatorial plane with pitch angles that increase with energy over a range from 10 eV to >50 keV, while the electrons are field aligned at up to ~1 keV. Consistent with the DAW model, **Figure 7C** identified downflowing electron fluxes at energies up to 300 eV along with bi-directional field-aligned ~1 keV ions at the immediate outer edge of the geospace plume. The O+ PADs on geospace plume field lines shown in **Figure 4B**, **Figure 6A** exhibit decreasing pitch angle with energy that appears to be inconsistent with the DAW mechanism. However, those PADs were observed on the spacecraft at a

fixed point in space and time. When the energy—pitch angle spectrum of the accelerated ions is examined for a fixed time after leaving their source (drift time), as can be done by comparing the 10 and 90° pitch angle curves of **Figure 10D**, it is seen that pitch angles increase with energy during the O+ plume acceleration. Thus, these features of our observations are consistent with Alfvénic ion acceleration associated with the presence of dispersive Alfvén waves as discussed by Chaston et al. (2015), Chaston et al. (2016). That study further calculated that this mechanism could accelerate ions to >50 keV as they gradient drift into the noon sector, as we have shown in this study. Such an outflow and ion acceleration mechanism could indeed account for the field-aligned 10–50 keV ion populations observed on the dayside by Yue et al. (2019) and the characteristics of the keV ion plumes we report here.

CONCLUSION

The temporal variation of warm ion fluxes observed as a function of time on a moving spacecraft is complicated by changing spacecraft position and complex ion drift paths and velocities that are highly sensitive to ion energy, pitch angle and L value. The coordinated multi-instrument observations of the inner magnetosphere and radiation belt environment, as shown in this and similar studies, are a major accomplishment of the Van Allen Probes program.

In the dawn to noon sector, the drift paths of lower energy (<5 keV) corotation-dominated O+ ions are deflected sunward as they encounter the geospace plume flow channel and thus, effectively, are excluded from plume field lines. Within the plume on the dayside, O+ ions with ring current energies >10 keV are observed to be locally enhanced and nearly bi-directionally field aligned.

In the dusk sector, at 3–4 R_E altitude, strong fluxes of O+ ions with energies up to ~1 keV energy are observed immediately outside the geospace plume outer boundary. The outflowing ions begin to be accelerated immediately as their sunward drift carries them onto plume field lines, with the result that <1 keV O+ ions appear to be excluded from plume field lines. As these ions continue their sunward drift, they are observed to be accelerated to energies approaching 50 keV. In this way a keV O+ ion plume is formed with a discrete limiting upper energy that increases with increasing distance from the outflowing O+ ions' source at the outer boundary of the geospace plume. Because of the pitch angle dependence of the ions' sunward drift velocities, the highest energy O+ plume ions observed at any distance away from their source are seen to be nearly bi-directionally field aligned. However, when the energy—pitch angle spectrum of the accelerated ions is examined for a fixed time after leaving their source (the ion drift time), we find that pitch angles increase with energy during the keV O+ plume acceleration, consistent with description of (Chaston et al., 2015).

DATA AVAILABILITY STATEMENT

Publicly available datasets were analyzed in this study. This data can be found here: Van Allen Probes observations used in this study can be obtained through instrument websites (EMFISIS wave data: http://emfisis.physics.uiowa.edu; EFW electric field and density data: http://www.space.umn.edu/rbspefw-data/; MagEIS and HOPE particle data: https://rbsp-ect.lanl.gov/rbsp_ect.php.

AUTHOR CONTRIBUTIONS

JF and PE shared in the conception and design of the study and in the analysis of the observations. JF drafted the discussion and conclusions and prepared the manuscript. All authors have reviewed the final manuscript and approve it for publication.

FUNDING

Research at the MIT Haystack Observatory was supported by the NASA Van Allen Probes (RBSP) funding provided under NASA prime contract NAS5-01072, including the EFW investigation (PI: J.R. Wygant, University of Minnesota), and the ECT investigation (PI: H. Spence, University of New Hampshire).

REFERENCES

Borovsky, J. E. (2014). Feedback of the Magnetosphere. *Science* 343, 1086–1087. doi:10.1126/science.1250590

Carpenter, D. L., and Lemaire, J. (2004). The Plasmasphere Boundary Layer. *Ann. Geophys.* 22, 4291–4298. doi:10.5194/angeo-22-4291-2004

Chappell, C. R., Huddleston, M. M., Moore, T. E., Giles, B. L., and Delcourt, D. C. (2008). Observations of the Warm Plasma Cloak and an Explanation of its Formation in the Magnetosphere. *J. Geophys. Res.* 113 (A09206), 1–21. doi:10.1029/2007JA012945

Chaston, C. C., Bonnell, J. W., Reeves, G. D., and Skoug, R. M. (2016). Driving Ionospheric Outflows and Magnetospheric O+ Energy Density with Alfvén Waves. *Geophys. Res. Lett.* 43, 4825–4833. doi:10.1002/2016GL069008

Chaston, C. C., Bonnell, J. W., Wygant, J. R., Kletzing, C. A., Reeves, G. D., Gerrard, A., et al. (2015). Extreme Ionospheric Ion Energization and Electron Heating in Alfvén Waves in the Storm Time Inner Magnetosphere. *Geophys. Res. Lett.* 42 (24), 10531–10540. doi:10.1002/2015GL066674

Darrouzet, F., De Keyser, J., Décréau, P. M. E., El Lemdani-Mazouz, F., and Vallières, X. (2008). Statistical Analysis of Plasmaspheric Plumes with Cluster/WHISPER Observations. *Ann. Geophys.* 26, 2403–2417. doi:10.5194/angeo-26-2403-2008

Darrouzet, F., Gallagher, D. L., André, N., Carpenter, D. L., Dandouras, I., Décréau, P. M. E., et al. (2009). Plasmaspheric Density Structures and Dynamics: Properties Observed by the CLUSTER and IMAGE Missions. *Space Sci. Rev.* 145 (1-2), 55–106. doi:10.1007/s11214-008-9438-910.1007/978-1-4419-1323-4_4

de Soria-Santacruz, M., Spasojevic, M., and Chen, L. (2013). EMIC Waves Growth and Guiding in the Presence of Cold Plasma Density Irregularities. *Geophys. Res. Lett.* 40, 1940–1944. doi:10.1002/grl.50484

Denton, R. E., Jordanova, V. K., and Fraser, B. J. (2014). Effect of Spatial Density Variation and O+ Concentration on the Growth and Evolution of

Electromagnetic Ion Cyclotron Waves. *J. Geophys. Res. Space Phys.* 119, 8372–8395. doi:10.1002/2014JA020384

Ebihara, Y., Yamauchi, M., Nilsson, H., Lundin, R., and Ejiri, M. (2001). Wedge-like Dispersion of Sub-keV Ions in the Dayside Magnetosphere: Particle Simulation and Viking Observation. *J. Geophys. Res.* 106 (A12), 29571–29584. doi:10.1029/2000JA000227

Erickson, P. J., Goncharenko, L. P., Nicolls, M. J., Ruohoniemi, M., and Kelley, M. C. (2010). Dynamics of North American Sector Ionospheric and Thermospheric Response During the November 2004 Superstorm. *J. Atmos. Solar-Terrestrial Phys.* 72 (4), 292–301. doi:10.1016/j.jastp.2009.04.001

Ejiri, M. (1978). Trajectory Traces of Charged Particles in the Magnetosphere. *J. Geophys. Res.* 83 (A10), 4798–4810. doi:10.1029/JA083iA10p04798

Foster, J. C., and Burke, W. J. (2002). SAPS: A New Categorization for Sub-auroral Electric Fields. *Eos Trans. AGU* 83, 393–394. doi:10.1029/2002EO000289

Foster, J. C., Erickson, P. J., Coster, A. J., Goldstein, J., and Rich, F. J. (2002). Ionospheric Signatures of Plasmaspheric Tails. *Geophys. Res. Lett.* 29 (13), 1–1–1–4. doi:10.1029/2002GL015067

Foster, J. C., Erickson, P. J., Walsh, B. M., Wygant, J. R., Coster, A. J., and Zhang, Q. H. (2020). "Multi-Point Observations of the Geospace Plume," in *Dayside Magnetosphere Interactions, Geophysical Monograph Series 248*. Editors Q. Zong, P. Escoubet, D. Sibeck, G. Le, and H. Zhang (New York, NY: John Wiley & Sons), 243–264. doi:10.1002/9781119509592.ch14

Foster, J. C. (1993). Storm Time Plasma Transport at Middle and High Latitudes. *J. Geophys. Res.* 98, 1675–1689. doi:10.1029/92JA02032

Foster, J. C., Wygant, J. R., Hudson, M. K., Boyd, A. J., Baker, D. N., Erickson, P. J., et al. (2015). Shock-Induced Prompt Relativistic Electron Acceleration in the Inner Magnetosphere. *J. Geophys. Res. Space Phys.* 120, 1661–1674. doi:10.1002/2014JA020642

Funsten, H. O., Skoug, R. M., Guthrie, A. A., MacDonald, E. A., Baldonado, J. R., Harper, R. W., et al. (2013). Helium, Oxygen, Proton, and Electron (HOPE) Mass Spectrometer for the Radiation Belt Storm Probes Mission. *Space Sci. Rev.* 179, 423–484. doi:10.1007/s11214-013-9968-7

Fuselier, S. A., Trattner, K. J., Petrinec, S. M., Denton, M. H., Toledo-Redondo, S., André, M., et al. (2019). Mass Loading the Earth's Dayside Magnetopause Boundary Layer and its Effect on Magnetic Reconnection. *Geophys. Res. Lett.* 46, 6204–6213. doi:10.1029/2019GL082384

Gallagher, D. L., Adrian, M. L., and Liemohn, M. W. (2005). Origin and Evolution of Deep Plasmaspheric Notches. *J. Geophys. Res.* 110, A09201. doi:10.1029/2004JA010906

Hull, A. J., Chaston, C. C., Bonnell, J. W., Wygant, J. R., Kletzing, C. A., Reeves, G. D., et al. (2019). Dispersive Alfvén Wave Control of O+ Ion Outflow and Energy Densities in the Inner Magnetosphere. *Geophys. Res. Lett.* 46, 8597–8606. doi:10.1029/2019GL083808

Kistler, L. M., Mouikis, C. G., Klecker, B., and Dandouras, I. (2010). Cusp as a Source for Oxygen in the Plasma Sheet During Geomagnetic Storms. *J. Geophys. Res.* 115 (A03209), 1–14. doi:10.1029/2009JA014838

Kistler, L. M., Mouikis, C. G., Spence, H. E., Menz, A. M., Skoug, R. M., Funsten, H. O., et al. (2016). The Source of O+ in the Storm Time Ring Current. *J. Geophys. Res. Space Phys.* 121, 5333–5349. doi:10.1002/2015JA022204

Kletzing, C. A., Kurth, W. S., Acuna, M., MacDowall, R. J., Torbert, R. B., Averkamp, T., et al. (2013). The Electric and Magnetic Field Instrument Suite and Integrated Science (EMFISIS) on RBSP. *Space Sci. Rev.* 179, 127–181. doi:10.1007/s11214-013-9993-6

Liao, J., Kistler, L. M., Mouikis, C. G., Klecker, B., Dandouras, I., and Zhang, J.-C. (2010). Statistical Study of O+ transport from the Cusp to the Lobes with Cluster CODIF Data. *J. Geophys. Res.* 115 (A00J15), 1–13. doi:10.1029/2010JA015613

Mauk, B. H., Fox, N. J., Kanekal, S. G., Kessel, R. L., Sibeck, D. G., and Ukhorskiy, A. (2013). Science Objectives and Rationale for the Radiation Belt Storm Probes Mission. *Space Sci. Rev.* 179, 3–27. doi:10.1007/s11214-012-9908-y

Moldwin, M. B., Zou, S., and Heine, T. (2016). The story of Plumes: the Development of a New Conceptual Framework for Understanding Magnetosphere and Ionosphere Coupling. *Ann. Geophys.* 34, 1243–1253. doi:10.5194/angeo-34-1243-2016

Schultz, M., and Lanzerotti, L. J. (1974). *Particle Diffusion in the Radiation Belts, Physics and Chemistry in Space*, Vol. 7. New York: Springer-Verlag. 978-3-642-65675-0.

Su, Y.-J., Thomsen, M. F., Borovsky, J. E., and Foster, J. C. (2001). A Linkage Between Polar Patches and Plasmaspheric Drainage Plumes. *Geophys. Res. Lett.* 28, 111–113. doi:10.1029/2000GL012042

Usanova, M. E., Mann, I. R., and Darrouzet, F. (2016). "EMIC Waves in the Inner Magnetosphere," in *Low-Frequency Waves in Space Plasmas, Geophysical Monograph 216*. Editors A. Keiling, D.-H. Lee, and V. Nakariakov. First Edition (New York, NY: John Wiley & Sons), 65–78. doi:10.1002/9781119055006.ch5

Walsh, B. M., Foster, J. C., Erickson, P. J., and Sibeck, D. G. (2014). Simultaneous Ground- and Space-Based Observations of the Plasmaspheric Plume and Reconnection. *Science* 343, 1122–1125. doi:10.1126/science.1247212

Wygant, J. R., Bonnell, J. W., Goetz, K., Ergun, R. E., Mozer, F. S., Bale, S. D., et al. (2013). The Electric Field and Waves Instruments on the Radiation Belt Storm Probes Mission. *Space Sci. Rev.* 179, 183–220. doi:10.1007/s1124-013-0013-710.1007/s11214-013-0013-7

Yeh, H.-C., and Foster, J. C. (1990). Storm Time Heavy Ion Outflow at Mid-latitude. *J. Geophys. Res.* 95, 7881–7891. doi:10.1029/JA095iA06p07881

Yue, C., Bortnik, J., Zou, S., Nishimura, Y., Foster, J. C., Coppeans, T., et al. (2020). Episodic Occurrence of Field-Aligned Energetic Ions on the Dayside. *Geophys. Res. Lett.* 47, e2019GL086384. doi:10.1029/2019GL086384

Zhang, S. R., Erickson, P. J., Zhang, Y., Wang, W., Huang, C., Coster, A. J., et al. (2017). Observations of Ion-Neutral Coupling Associated With strong Electrodynamic Disturbances During the 2015 St. Patrick's Day Storm. *J. Geophys. Res. Space Phys.* 122, 1314–1337. doi:10.1002/2016JA023307

Conflict of Interest: The authors declare that the research was conducted in the absence of any commercial or financial relationships that could be construed as a potential conflict of interest.

frontiers in Astronomy and Space Sciences

MINI REVIEW
published: 28 July 2021
doi: 10.3389/fspas.2021.719715

On the Impacts of Ions of Ionospheric Origin and Their Composition on Magnetospheric EMIC Waves

Justin H. Lee[1]*, *Lauren W. Blum*[2] *and Lunjin Chen*[3]

[1]Space Sciences Department, The Aerospace Corporation, El Segundo, CA, United States, [2]Laboratory for Atmospheric and Space Physics (LASP), Boulder, CO, United States, [3]Department of Physics, The University of Texas at Dallas, Richardson, TX, United States

Large numbers of theory and observation studies have been conducted on electromagnetic ion cyclotron (EMIC) waves occurring in Earth's magnetosphere. Numerous studies have shown that accurately specifying the ions of ionospheric origin and their composition can greatly improve understanding of magnetospheric EMIC waves, specifically their generation, their properties, and their effects on the magnetospheric plasma populations. With the launch and operations of multiple recent missions carrying plasma instrumentation capable of acquiring direct measurements of multiple ion species, we use this opportunity to review recent magnetospheric EMIC wave efforts utilizing these new assets, with particular focus on the role of ions of ionospheric origin in wave generation, propagation, and interaction with particles. The review of progress leads us to a discussion of the unresolved questions to be investigated using future modeling capabilities or when new missions or instrumentation capabilities are developed.

Keywords: EMIC waves, cold plasma, wave-particle interactions, cold ions, energetic particle precipitation

OPEN ACCESS

Edited by:
Cecilia Norgren,
University of Bergen, Norway

Reviewed by:
Sergio Toledo-Redondo,
University of Murcia, Spain
Tieyan Wang,
Rutherford Appleton Laboratory,
United Kingdom

***Correspondence:**
Justin H. Lee
justin.h.lee@aero.org

Specialty section:
This article was submitted to Space Physics, a section of the journal Frontiers in Astronomy and Space Sciences

Received: *02 June 2021*
Accepted: *09 July 2021*
Published: *28 July 2021*

Citation:
Lee JH, Blum LW and Chen L (2021) On the Impacts of Ions of Ionospheric Origin and Their Composition on Magnetospheric EMIC Waves. Front. Astron. Space Sci. 8:719715. doi: 10.3389/fspas.2021.719715

INTRODUCTION

Electromagnetic ion cyclotron (EMIC) waves play a large role in magnetospheric dynamics, from heating of thermal plasma to scattering of radiation belt electrons into Earth's atmosphere (see Thorne et al., 2006, and references therein). **Figure 1A** illustrates some of the main processes involving EMIC waves in Earth's magnetosphere and **Figure 1B** provides an example of complex linear wave dispersion properties introduced when multiple ion species are present in the ambient plasma. Key to determining both wave properties themselves as well as wave impacts on various magnetospheric particle populations is a knowledge of the detailed plasma environment, including the cold ion populations that are often impossible to measure. In particular, ion density, temperature, and ion composition all play important roles in EMIC wave generation, propagation, and subsequent interaction with particles (Anderson et al., 1996; Anderson and Fuselier, 1994; Fuselier and Anderson, 1996; Kozyra et al., 1984, Gomberoff and Neira, 1983; Gomberoff et al., 1996; Gary et al., 2012; Chen et al., 2011; Silin et al., 2011, Lee et al., 2021, and references therein).

In the following sections, we outline recent progress towards understanding the influence of ions of ionospheric origin on EMIC waves both through theoretical, modeling and observational studies. Recent space missions, with improved data quality and data processing tools, have allowed for significant progress characterizing the occurrence and distribution of magnetospheric EMIC waves and the hot proton free energy source that is expected to drive wave generation. However, puzzles remain for developing a more complete understanding of EMIC wave generation and the effects of waves on magnetospheric particles, many centered around measurement challenges and a lack of

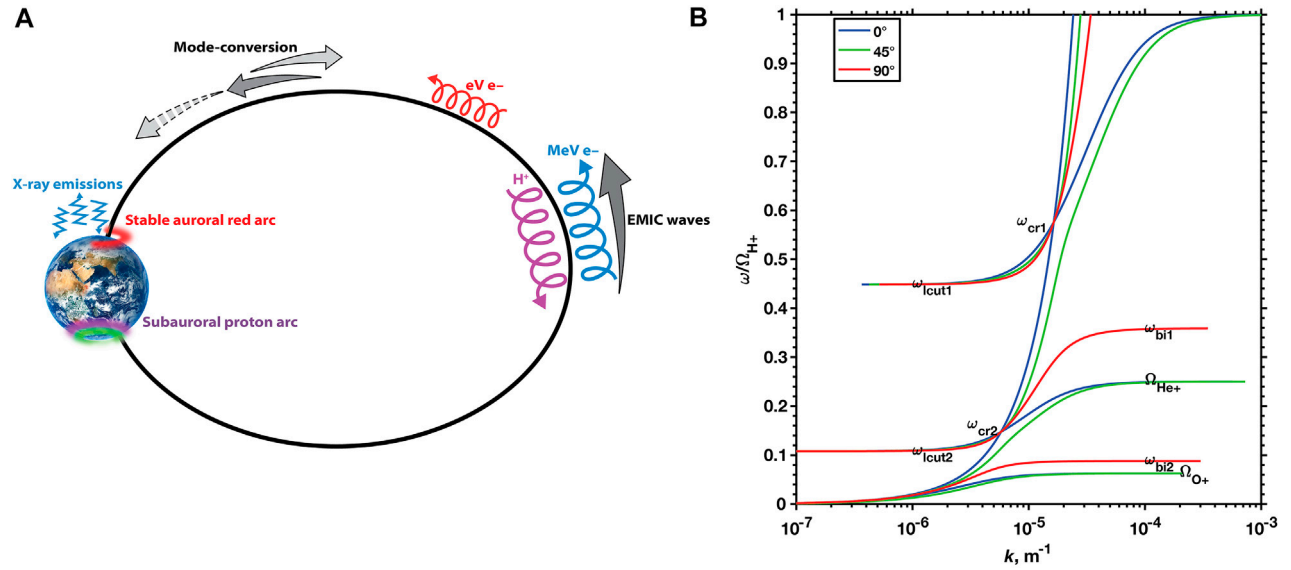

FIGURE 1 | (A) Conceptual overview of processes related to EMIC waves generated in Earth's magnetosphere including wave mode conversion enabled by heavy ion presence, the wave impacts on various particle populations, and manifestation of the wave impacts sometimes observed at low altitudes. **(B)** The dispersion relation (normalized frequency versus wave number) of cold plasma waves below the proton gyrofrequency in a uniform and magnetized plasma with ion composition 70% H^+, 20% He^+, 10% O^+. Background magnetic field is 248 nT (corresponding to the equatorial magnetic field strength at L = 5) and background electron density of 50 cm^{-3} is used. Three values of wave normal angles, 0°, 45°, and 90° are represented by blue, green and red lines respectively. Characteristic frequencies (crossover, cutoff and bi-ion resonant frequencies) are denoted, with subscripts 1 and 2 representing frequencies between H^+ and He^+ gyrofrequencies and between O^+ and He^+ gyro frequencies, respectively. Calculation of those characteristic frequencies can be found elsewhere (e.g., Chen et al., 2014).

routine observations of the cold ion properties including the ion mass composition. These measurements are needed to characterize the variability of abundances of cold and hot ionospheric-originating ions in different magnetospheric regions so that improved understanding can be developed on how they impact wave generation and subsequent wave-particle interactions. Progress as well as remaining questions and challenges on these topics are presented in *Recent Progress and Challenges* Section, and future needs or opportunities discussed in *Discussion and Future Opportunities* Section.

RECENT PROGRESS AND CHALLENGES

Wave Generation and Properties

The large number of satellite missions flying magnetometers are supporting continued studies of EMIC wave properties throughout Earth's magnetosphere. The analysis methods utilized have become somewhat standardized across studies and capable computing systems allow for efficient processing of large spacecraft datasets. Following coordinate transformation routines, most EMIC wave studies rely on Fourier analysis to derive wave power and polarization spectra in the frequency-time domain for interpretation of the wave emissions properties needed to identify the occurrence and properties of EMIC waves. Low wave normal angle coupled with polarization spectra that rotate left-handed with respect to the dominant geomagnetic field component are typically used to identify the presence and generation region of EMIC waves. This is because of linear dispersion theory and solutions that indicate the growth rate of EMIC waves typically maximizes for the left-handed circularly polarized (parallel propagating) mode (Gary et al., 2012 and references therein). When electric field measurements are also available, calculations of the Poynting vector properties in time or frequency domains are applicable to identifying possible wave generation regions and the properties of wave energy (e.g. Vines et al., 2019 and references therein).

Although magnetometer and electric field instrumentation continue to improve in capability, the role of the superposition of multiple wave packets that results in constructive/destructive interference to the detriment of wave analysis methods will continue to complicate analysis of wave properties and applications of the derived properties to investigating theories on wave generation (and propagation, discussed in a later section). For example, recent statistical and case studies showed that experimentally measured EMIC waves do not always have left-hand circular polarization and are often more linear or right-hand polarized, particularly on the morning side of the magnetosphere (Min et al., 2012; Allen et al., 2015; Allen et al., 2016; Saikin et al., 2015; Lee et al., 2019). Although EMIC wave polarization properties can evolve from left-handed to linear and then to right-handed during propagation through a region where wave frequency matches crossover frequencies (as noted by ω_{cr1} and ω_{cr2} in **Figure 1B**), wave superposition can be another reason

for the observed linear polarized wave spectra (Denton et al., 1996; Anderson et al., 1996; Lee and Angelopoulos, 2014a). But EMIC waves may also be generated with linear polarization under specific plasma conditions (Denton et al., 1992), the presence of cold heavy ions can favor the conversion of left-handed waves to linear (Hu et al., 2010), and cold proton presence may enable self-consistent generation of oblique EMIC waves with linear polarization (Toledo-Redondo et al., 2021). Verifying the occurrence of superposed wave packets is needed to futher clarify the conditions when linear EMIC waves can grow preferentially. The importance of this extends to multi-satellite wave analysis methods (e.g. Balikhin et al., 2003; Bellan, 2016; Vines et al., 2021), in which recent studies showed superposed waves limit the effectiveness of multi-satellite wave vector determination (Lee et al., 2019, Lee et al., 2021). The application of wave properties not accounting for superposition can lead to misrepresentation of true wave properties, and this can be propagated when deriving particle pitch angle diffusion coefficients, for example, leading to inaccurate predictions of the effectiveness of EMIC waves in diffusing particles from high to low pitch angles. Future studies should identify and treat time intervals when superposed waves are likely with caution to ensure accurate characterization of EMIC waves.

Improvements to plasma instruments with ion mass discrimination have allowed for a small number of studies to consider and apply multiple ion species measurements to improve understanding of EMIC wave generation. Overall, there continue to be differing methods of utilization of available particle data for investigating EMIC wave generation. Adequate energy range of plasma instrumentation is needed to cover the ions and electrons relevant for EMIC wave studies. As summarized in **Table 1**, this is a broad energy range because EMIC waves can interact with cold and hot ions as well as cold/thermal and relativistic electrons. For hot, energetic (>keV) ions, a sufficiently broad instrument energy range supports accurate specification of the hot ion free energy for wave generation or the hot heavy ions that may damp the waves. Recent studies combining ion measurements from multiple instruments onboard a Van Allen Probes spacecraft have been able to calculate full ion moments (from ~1 eV to 600 keV), for comparison to quasilinear theory for EMIC wave growth (Yue et al., 2019; Noh et al., 2018, Noh et al., 2021). While these studies investigated the relationship of EMIC wave occurrence relative to the hot proton anisotropy, they focused on the role of protons and temperature anisotropy for providing free energy needed for wave instability. This is despite theory showing the importance of heavier ion species in defining the band structure as well as wave growth in each band generally organized by the heavy ion species (e.g. Kozyra et al., 1984; Denton et al., 2014). Provided the cyclotron resonance condition is met, it is possible that heavy ion species with temperature anisotropy could also contribute to wave growth below the corresponding ion gyrofrequency. These contributions of heavy ions to EMIC wave occurrence are pending additional investigation. Investigations of ion composition data with improved availability have shown how the relative flux of inner magnetosphere heavy ions changes with geomagnetic activity (Kistler et al., 2006; Kistler et al., 2016). Similar trends were seen in the outer magnetosphere (Lee et al., 2021). Future efforts will continue to improve understanding how evolution of cold and energetic heavy ions with solar/geomagnetic activity affects EMIC wave growth. The cold ion species, however, are often problematic to characterize.

Measurements of the cold ion species supports the derivation of accurate cold (0–10 s eV) ion moments of solar wind and ionospheric ion species for testing theory of linear wave growth. Routine cold ion measurements are necessary for accurately determining the times or magnetospheric regions where warm plasma effects influence wave growth and subsequent wave-particle interactions, as explored in modeling studies (Chen et al., 2011; Silin et al., 2011). But because of spacecraft positive charging effects, cold ion measurements are often challenging to make and are not available routinely. Active spacecraft potential control (ASPOC) is one method that helps mitigate the positive charging effect (Torkar et al., 2016), decreasing the amount of positive charging but not completely neutralizing it. Few eV ions remain unmeasured most of the time except when plasma bulk flows and ULF waves assist with accelerating these ions above the remnant spacecraft potential energy (André and Cully, 2012; Engwall et al., 2009; Lee et al., 2012, Lee et al., 2019, Lee et al., 2021). Continued efforts (Zurbuchen and Gershman, 2016; Toledo-Redondo et al., 2019; Barrie et al., 2019) to overcome this charging problem can improve understanding of the contribution of cold ions and their mass composition to the generation of EMIC waves and their properties. In the absence of wave measurements themselves, a linear theory proxy based on a proton-electron plasma and the bulk plasma parameters that can be extracted from spacecraft datasets has helped identify when EMIC wave growth is likely (Allen et al., 2016; Blum et al., 2009, Blum et al., 2012); though this proxy method does not always yield agreement, predicting wave growth when no waves were observed (Lin et al., 2014; Zhang et al., 2014). It may be possible that future improvements to this proxy through inclusion of additional measurable ion population parameters can be helpful for interpreting EMIC wave generation.

In addition to EMIC waves characterized in terms of linear theory, triggered (or rising tone) nonlinear EMIC wave emissions are known to evolve out of the linear instability and associated cut-off wave frequencies determined by the ion composition (Omura et al., 2010). The subsequent nonlinear growth of the triggered emissions at their source region is determined by the frequency sweep rate that is proportional to the wave group velocity, which is again influenced by the ion composition. A few studies on observations or simulations of triggered emissions have used estimated or assumed ion composition to investigate the magnetospheric conditions supporting these nonlinear emissions (Pickett et al., 2010; Shoji and Omura, 2013; Grison et al., 2013; Nakamura et al., 2015; Grison et al., 2016, Nakamura et al., 2016). It remains unknown the role of ion composition in nonlinear wave evolution. More frequent and accurate measurements of comprehensive ion composition will support additional studies of nonlinear growth of EMIC waves.

TABLE 1 | Summary of relevant desired particle and field observations for future EMIC wave studies, including instrument challenges for making these measurements.

Observation	Dynamic Range	Measurement details	Measurement challenges	Potentially relevant past instruments
Low-energy/cold ions	0–100 s eV	• Mass discrimination • Charge state • Pitch angle distributions	Remedies for positive spacecraft charging, sufficient sensor geometry factor and collection time	DE 1 IMS, e-POP IRM, Cluster CODIF, RBSP HOPE, MMS HPCA, Arase LEPi
Hot ions	100 s eV—100 keV	• Mass discrimination • Charge state • Pitch angle distributions	Cross-calibration of ion instruments covering broad energy range	RBSP HOPE + RBSPICE, MMS HPCA + EIS, Arase LEPi + MEPi
Low-energy/cold electrons	0–100 s eV	• Differential energies • Pitch angle distributions	Remedies for spacecraft-emitted photoelectrons and secondary electrons	RBSP HOPE, MMS FPI, Arase LEPe, e-POP SEI
Hot/relativistic electrons	100 s keV—several MeV	• Differential energies • Pitch angle distributions	Loss cone resolution	RBSP MagEIS/REPT, MMS FEEPS, Arase XEP
Magnetic and electric fields	DC—200 Hz sampling frequency	• Vector E and B measurement • Simultaneous field measurement capability	3rd (axial) component of E field	RBSP EFW, MMS FIELDS, SWARM ASM, THEMIS FGM/EFI

Finally, recent studies have utilized multipoint measurements and simultaneous wave, hot, and cold plasma measurements to explore the spatio-temporal structure of EMIC wave active regions and their relation to plasma structures (Engebretson et al., 2018; Blum et al., 2017). Coordinated EMIC wave measurements at multiple local times, radial distances, as well as on the ground have revealed that these waves are often radially narrow but extended in time and azimuth (e.g. Mann et al., 2014; Paulson et al., 2014; Blum et al., 2020). Direct associations between EMIC waves and hot ion structures, such as particle injections, have been found across the dusk-side magnetosphere (Remya et al., 2018; Jun et al., 2019; Chen et al., 2020; Blum et al., 2015; Remya et al., 2020), whereas other studies observe EMIC waves well-confined to cold plasma density enhancements and gradients (Usanova et al., 2014; Tetrick et al., 2017; Blum et al., 2020; Yuan et al., 2019). Coordinated multipoint measurements and improved orbital configurations aid in mapping out the spatio-temporal properties of EMIC waves, needed for quantifying their impact on energetic particle populations as discussed more in *Wave Effects* Section , while comprehensive wave and plasma measurements can help reveal the drivers of the wave spatial and temporal properties.

Wave Propagation

EMIC waves of magnetospheric origin have been measured by ground magnetometers and fall into the Pc1-2 (continuous pulsation) frequency range. Magnetically conjugate observations have confirmed that equatorially-generated EMIC waves can propagate all the way to the ground (e.g. Usanova et al., 2008, and references therein). But this is not always the case, particularly during the main phase of geomagnetic storms when a distinct lack of Pc1-2 waves is observed at ground magnetometers compared to *in situ* observations (Engebretson et al., 2008; Posch et al., 2010). Ray tracing of EMIC waves suggests as waves propagate from the equator, the waves should become oblique and eventually reflect at middle magnetic latitude when the wave frequency falls just below the bi-ion hybrid resonant frequency (Rauch and Roux, 1982; Horne and Thorne 1990; Rönnmark and André, 1991; Chen et al., 2014). This bi-ion hybrid resonant frequency (e.g., ω_{bi1} and ω_{bi2} depicted in **Figure 1B**) is also known as the Buchsbaum resonance (Buchsbaum, 1960) and defines a forbidden region of wave propagation. But several potential mechanisms can explain the access of EMIC waves to low altitudes. First, full wave simulations (e.g. Kim and Johnson, 2016) suggest waves can tunnel through the evanescent region via mode conversion at locations where the wave frequency matches the local crossover frequency (e.g. ω_{cr1} and ω_{cr2} depicted in **Figure 1B**). Second, left-handed O^+ band EMIC waves can propagate along the field line toward higher magnetic field regions without being subject to bi-ion hybrid resonance (since O^+ ions are the presumed heaviest ions in the magnetosphere). Third, density irregularities and gradients, such as at the plasmapause (e.g. Chen et al., 2009; de Soria-Santacruz et al., 2013) can keep the EMIC wave normal more or less aligned with the magnetic field, and therefore avoid encountering of the bi-ion hybrid resonance which occurs at perpendicular propagation. Further investigations of the plasma conditions resulting in EMIC wave propagation to the ground, and their dependence on location and geomagnetic activity, will enable us to improve understanding of these phenomena.

Based on known and theorized properties of propagating EMIC waves, satellite wave observations have also been used to infer information about the local plasma environment. The propagation of EMIC waves to and across local crossover frequencies in a multi-ion plasma can allow waves to achieve linear or right-handed polarization. Thus, under certain assumptions on wave generation, wave properties from Fourier spectra and the possibility of crossover frequencies enabling mode-conversion during propagation have been used to infer the ion composition or presence of minor ion species in Earth's magnetosphere (Min et al., 2015; Miyoshi et al., 2019; Engebretson et al., 2018; Bashir and Ilie, 2021). Wave modeling and mode conversion at the bi-ion hybrid resonance has also been presented as a method to derive magnetospheric ion composition (E. H. Kim et al., 2015). While event studies have suggested the presence of He^{++} (Engebretson et al., 2018; Lee et al., 2019), N^+ (Bashir and Ilie, 2021), as well as the more typically assumed O^+ and He^+ species, direct observations of

these ions are often lacking, posing challenges for verification of these techniques to infer ion composition from the properties of propagated EMIC waves. Very few examples exist showing that the ion composition derived using wave spectra in the vicinity of the crossover frequency is consistent with the measured ion composition due to the cold ion populations being partially hidden from detectors because of spacecraft positive charging (Fuselier and Anderson, 1996; Lee and Angelopoulos, 2014b; Lee et al., 2019). Because of various complexities in wave analysis, it would be helpful to future EMIC wave studies to consider particle measurements to support interpretation of wave propagation and mode conversion.

Wave Effects

EMIC waves can interact with a broad range of particle populations in the inner magnetosphere, through cyclotron or Landau resonance as well as non-resonant or nonlinear interactions. Through these interactions, the waves can impact electrons or ions spanning orders of magnitude in energy. We focus on the wave effects on energetic particles in this review and refer the reader to a companion paper dedicated to interactions of EMIC waves with thermal plasmas (M. E. Usanova, submitted to this issue, *Energy exchange between EMIC waves and thermal plasma: from theory to observations*).

It is known that the anomalous resonance condition betweenleft-handed EMIC waves and electrons requires electrons (usually in the relativistic energy range) to overtake the EMIC waves so that in the frame of moving electron gyrocenter the wave polarization is seen as right-handed and the Doppler-shifted wave frequency matches the electron gyrofrequency (conceptualized in **Figure 1A**). For such a condition to be satisfied, EMIC waves with sufficiently large wavenumber ($k_z = \Omega_{ce}/v_z$) are required. In the cold plasma limit with sufficient He^+ ions, He^+ band waves just below the He^+ gyrofrequency attain large wave numbers, and therefore have been proposed as a potential candidate for resonating with relativistic electrons and producing scattering loss (Lyons and Thorne, 1972; Summers and Throne, 2003; Ukhorskiy et al., 2010; Thorne and Kennel, 1971; Shprits et al., 2016). Observational evidence of relativistic electron precipitation in association with EMIC waves has been reported by an increasing number of recent studies (e.g. Rodger et al., 2008; Li et al., 2014; Blum et al., 2015; Blum et al., 2019; Lessard et al., 2019; Qin et al., 2019; Sigsbee et al., 2020; Kim et al., 2021). However, the cold plasma approximation may fail near the He^+ gyrofrequency, and the warm plasma effect of He^+ ions on wave growth should be considered. Spacecraft observations suggest warm plasma effects may be relevant in the inner magnetosphere (Lee et al., 2012) and the inclusion of warm plasma effects in modeling (Chen et al., 2011; Silin et al., 2011; Ni et al., 2018) shows that the excitation of He^+ band waves near the He^+ gyrofrequency tends to require reduced He^+ ion density, and once generated, the warm plasma EMIC waves possess much smaller wavenumber than expected from cold plasma theory. Both points limit the capability of EMIC waves resonating with electrons ≤1 MeV. At the same time, sub-MeV electron precipitation associated with EMIC waves has been reported with statistical lower cut off energy down to 300 keV (e.g. Hendry et al., 2020; Capannolo et al., 2019). Many of the low Earth orbit (LEO) satellite observations used to infer the electron precipitation caused by EMIC waves have not been energy-resolved and future direct measurements will continue to help characterize the spectrum of energetic electrons impacted by EMIC waves (cf. Hendry et al., 2016). Nonetheless, the unexpectedly low (~100 s keV) energy of electrons precipitated by EMIC wave interactions may be explained by a non-resonant scattering mechanism (Chen et al., 2016), when the electrons below the cyclotron resonant energy are also subject to effective scattering due to spatial structure of the EMIC wave packet. Another potential mechanism proposed by Denton et al., 2019 is the resonant interaction of electrons with low amplitude short-wavelength EMIC waves in the H^+ band (with frequency above the He^+ gyrofrequency), though it is unclear how often magnetospheric conditions allow for the generation of such waves. Observations of two components of electric field and three components of magnetic field have been applied to estimate wavenumber of EMIC waves and statistical analysis showed that H^+ band waves carry shorter wavenumber than He^+ band waves, suggesting that H^+ band waves are more likely to resonantly interact with MeV electrons and below (Chen et al., 2019a). Recent magnetospheric studies have observed evidence of EMIC wave scattering within the trapped MeV electron population near the magnetic equator, showing bite-outs at low pitch angles as well as local minima in phase space density profiles concurrent with EMIC wave activity (e.g. Bingley et al., 2019; Usanova et al., 2014; Shprits et al., 2017; Blum et al., 2020). Furthermore, nonlinear electron scattering due to EMIC waves manifested in fine-scale pitch angle distribution variation in association with EMIC waves (Zhu et al., 2020). The electron pitch angle distribution showed a reverse slope with a secondary flux peak near the loss cone at times when intense EMIC waves were present, which may be explained by competition of nonlinear phase bunching that transports electrons from low pitch angle to moderate pitch angle (Albert and Bortnik, 2009), nonlinear loss cone reflection (Su et al., 2012; Chen et al., 2016) that prevent electron scattering into the center of loss cone (e.g., zero pitch angle), and diffusive transport. These collective studies show that the frequency distribution of EMIC waves, as well as cold and warm ion populations, play major roles in determining the effectiveness of these waves in scattering and precipitation loss of energetic electrons to the atmosphere, and pitch-angle and energy-resolved measurements of energetic electrons both near the equator as well as at LEO can help confirm theoretical EMIC wave impacts on radiation belt populations. The future measurements important for characterizing the magnetospheric plasma, EMIC waves, and distribution of trapped electrons impacted by the waves are summarized in **Table 1**.

Although many studies discuss the interactions of EMIC waves with radiation belt electrons, the waves are also believed to have major effects on energetic protons in the ring current or plasma sheet, leading to their precipitation to the ionosphere where the precipitated protons may cause significant impacts to ionospheric electrodynamics. Frey et al., 2004 investigated subauroral morning proton spots (SAMPS) that were thought to be evidence of localized

but intense interactions of EMIC waves with ring current protons in association with plasmaspheric refilling after geomagnetic storms. Fuselier et al., 2004 and Spasojevic and Fuselier (2009) also explored sub-auroral proton precipitation through use of IMAGE FUV images and their association with plasmaspheric plumes in the afternoon sector. Yahnin et al., 2007 showed conjugate ground-based observations with low altitude proton measurements to confirm the role of EMIC waves as the mechanism leading to these subauroral proton spots. Such precipitation images can help map out spatial and temporal evolution of EMIC wave active regions. In addition to localized interactions, modeling studies investigated cyclotron resonant interactions of EMIC waves with central plasma sheet protons (Cao et al., 2016) to indicate protons in this magnetosphere region can be efficiently scattered by EMIC waves. Model-data investigations of proton field-line curvature (FLC) scattering were unable to reproduce measurements of enhanced proton precipitating flux at low altitude and suggested that proton scattering by EMIC waves should be considered (Chen et al., 2019b). Additional modeling work investigating the combined effects of FLC and EMIC wave scattering showed that protons scattered by EMIC waves significantly impact ionospheric electrodynamics at afternoon to dusk MLTs comparable to the electron precipitation dominant between pre-midnight to morning MLTs (Zhu et al., 2021). The LEO satellites that provided the measurements of proton precipitating flux for the above studies could be improved by expanding the energy range and spectral resolution of instrumentation. In addition, orbital coverage and networking with existing missions could enable continued studies of the asymmetric input of energetic particle flux into the ionosphere that requires resolving temporospatial processes. These future efforts will enable us to understand the quantitative effects of magnetospheric EMIC waves on the coupled magnetosphere-ionosphere system and how those effects change as functions of solar or geomagnetic activity and magnetosphere-ionosphere regions.

DISCUSSION AND FUTURE OPPORTUNITIES

A variety of recent missions have provided opportunities to launch scientific instrumentation and apply them to investigations of EMIC waves throughout Earth's magnetosphere. An ideal measurement suite for investigating EMIC waves has been summarized in **Table 1**, along with challenges for future instrumentation. In addition to developments to necessary instrumentation, future space science missions could investigate various questions remaining related to the generation and effects of EMIC waves on magnetospheric plasma populations and potential subsequent effects on the ionosphere. To make significant progress on this topic, constellation-class missions are required. The waves should ideally be observed in their source regions in the magnetosphere and distributed members of the satellite constellation could then be able to observe how the generated waves:

1. Propagate from magnetospheric source regions to higher latitudes and often to the ground.
2. Impact trapped particle populations so that an improved quantitative understanding of EMIC wave effectiveness on particle scattering (and heating) can be developed.
3. May result in time-dependent impacts on the ionosphere and its electrodynamics.

AUTHOR'S NOTE

JL was employed by the company The Aerospace Corporation, a nonprofit corporation incorporated under the General Non-Profit Corporation Laws of the State of California.

AUTHOR CONTRIBUTIONS

JL coordinated the overall preparation of the manuscript. JL and LB focused on the review of recent observations and LC focused on the review of recent developments in theory and modeling. All authors contributed to manuscript revision, read, and approved the submitted version.

FUNDING

JL acknowledges support from NASA Grant No. 80NSSC18K1378. LC acknowledges support of NASA Grants No's. 80NSSC18K1224 and 80NSSC19K0283. LB's contributions were supported by the NASA Grant No. 80NSSC21K0087. While preparing this review, the authors learned of the passing of S. Peter Gary (1939–2021). We will remember Peter for his many pioneering efforts in space plasma physics, with particular distinction in theory of plasma waves including electromagnetic ion cyclotron waves, as well as for his enthusiasm and mentorship.

REFERENCES

Albert, J. M., and Bortnik, J. (2009). Nonlinear Interaction of Radiation belt Electrons with Electromagnetic Ion Cyclotron Waves. *Geophys. Res. Lett.* 36, L12110. doi:10.1029/2009GL038904

Allen, R. C., Zhang, J.-C., Kistler, L. M., Spence, H. E., Lin, R.-L., Klecker, B., et al. (2016). A Statistical Study of EMIC Waves Observed by Cluster: 2. Associated Plasma Conditions. *J. Geophys. Res. Space Phys.* 121, 6458–6479. doi:10.1002/2016JA022541

Allen, R. C., Zhang, J. C., Kistler, L. M., Spence, H. E., Lin, R. L., Klecker, B., et al. (2015). A Statistical Study of EMIC Waves Observed by Cluster: 1. Wave Properties. *J. Geophys. Res. Space Phys.* 120, 5574–5592. doi:10.1002/2015JA021333

Anderson, B. J., Denton, R. E., and Fuselier, S. A. (1996). On Determining Polarization Characteristics of Ion Cyclotron Wave Magnetic Field Fluctuations. *J. Geophys. Res.* 101 (A6), 13195–13213. doi:10.1029/96JA00633

Anderson, B. J., and Fuselier, S. A. (1994). Response of thermal Ions to Electromagnetic Ion Cyclotron Waves. *J. Geophys. Res.* 99 (A10), 19413–19425. doi:10.1029/94JA01235

André, M., and Cully, C. M. (2012). Low-energy Ions: A Previously Hidden Solar System Particle Population. *Geophys. Res. Lett.* 39, a–n. doi:10.1029/2011GL050242

Balikhin, M. A., Pokhotelov, O. A., Walker, S. N., Amata, E., Andre, M., Dunlop, M., et al. (2003). Minimum Variance Free Wave Identification: Application to Cluster Electric Field Data in the Magnetosheath. *Geophys. Res. Lett.* 30 (10), 1508. doi:10.1029/2003GL016918

Barrie, A. C., Cipriani, F., Escoubet, C. P., Toledo-Redondo, S., Nakamura, R., Torkar, K., et al. (2019). Characterizing Spacecraft Potential Effects on Measured Particle Trajectories. *Phys. Plasmas* 26, 103504. doi:10.1063/1.5119344

Bashir, M. F., and Ilie, R. (2021). The First Observation of N + Electromagnetic Ion Cyclotron Waves. *J. Geophys. Res. Space Phys.* 126, e2020JA028716. doi:10.1029/2020JA028716

Bellan, P. M. (2016). Revised Single-spacecraft Method for Determining Wave Vector K and Resolving Space-time Ambiguity. *J. Geophys. Res. Space Phys.* 121, 8589–8599. doi:10.1002/2016JA022827

Bingley, L., Angelopoulos, V., Sibeck, D., Zhang, X., and Halford, A. (2019). The Evolution of a Pitch-Angle "Bite-Out" Scattering Signature Caused by EMIC Wave Activity: A Case Study. *J. Geophys. Res. Space Phys.* 124, 5042–5055. doi:10.1029/2018ja026292

Blum, L. W., Artemyev, A., Agapitov, O., Mourenas, D., Boardsen, S., and Schiller, Q. (2019). EMIC Wave-Driven Bounce Resonance Scattering of Energetic Electrons in the Inner Magnetosphere. *J. Geophys. Res. Space Phys.* 124, 2484–2496. doi:10.1029/2018JA026427

Blum, L. W., Bonnell, J. W., Agapitov, O., Paulson, K., and Kletzing, C. (2017). EMIC Wave Scale Size in the Inner Magnetosphere: Observations from the Dual Van Allen Probes. *Geophys. Res. Lett.* 44, 1227–1233. doi:10.1002/2016GL072316

Blum, L. W., Halford, A., Millan, R., Bonnell, J. W., Goldstein, J., Usanova, M., et al. (2015). Observations of Coincident EMIC Wave Activity and Duskside Energetic Electron Precipitation on 18-19 January 2013. *Geophys. Res. Lett.* 42, 5727–5735. doi:10.1002/2015GL065245

Blum, L. W., MacDonald, E. A., Clausen, L. B. N., and Li, X. (2012). A Comparison of Magnetic Field Measurements and a Plasma-Based Proxy to Infer EMIC Wave Distributions at Geosynchronous Orbit. *J. Geophys. Res.* 117, 5220. doi:10.1029/2011JA017474

Blum, L. W., MacDonald, E. A., Gary, S. P., Thomsen, M. F., and Spence, H. E. (2009). Ion Observations from Geosynchronous Orbit as a Proxy for Ion Cyclotron Wave Growth during Storm Times. *J. Geophys. Res.* 114, a–n. doi:10.1029/2009JA014396

Blum, L. W., Remya, B., Denton, M. H., and Schiller, Q. (2020). Persistent EMIC Wave Activity across the Nightside Inner Magnetosphere. *Geophys. Res. Lett.* 47, e2020GL087009. doi:10.1029/2020gl087009

Buchsbaum, S. J. (1960). Ion Resonance in a Multicomponent Plasma. *Phys. Rev. Lett.* 5, 495–497. doi:10.1103/PhysRevLett.5.495

Cao, X., Ni, B., Liang, J., Xiang, Z., Wang, Q., Shi, R., et al. (2016). Resonant Scattering of central Plasma Sheet Protons by Multiband EMIC Waves and Resultant Proton Loss Timescales. *J. Geophys. Res. Space Phys.* 121, 1219–1232. doi:10.1002/2015JA021933

Capannolo, L., Li, W., Ma, Q., Chen, L., Shen, X. C., Spence, H. E., et al. (2019). Direct Observation of Subrelativistic Electron Precipitation Potentially Driven by EMIC Waves. *Geophys. Res. Lett.* 46, 12711–12721. doi:10.1029/2019GL084202

Chen, H., Gao, X., Lu, Q., Tsurutani, B. T., and Wang, S. (2020). Statistical Evidence for EMIC Wave Excitation Driven by Substorm Injection and Enhanced Solar Wind Pressure in the Earth's Magnetosphere: Two Different EMIC Wave Sources. *Geophys. Res. Lett.* 47, e2020GL090275. doi:10.1029/2020GL090275

Chen, L., Jordanova, V. K., Spasojević, M., Thorne, R. M., and Horne, R. B. (2014). Electromagnetic Ion Cyclotron Wave Modeling during the Geospace Environment Modeling challenge Event. *J. Geophys. Res. Space Phys.* 119, 2963–2977. doi:10.1002/2013JA019595

Chen, L., Thorne, R. M., and Bortnik, J. (2011). The Controlling Effect of Ion Temperature on EMIC Wave Excitation and Scattering. *Geophys. Res. Lett.* 38, a–n. doi:10.1029/2011GL048653

Chen, L., Thorne, R. M., Bortnik, J., and Zhang, X. J. (2016). Nonresonant Interactions of Electromagnetic Ion Cyclotron Waves with Relativistic Electrons. *J. Geophys. Res. Space Phys.* 121, 9913–9925. doi:10.1002/2016JA022813

Chen, L., Thorne, R. M., and Horne, R. B. (2009). Simulation of EMIC Wave Excitation in a Model Magnetosphere Including Structured High-Density Plumes. *J. Geophys. Res.* 114, a–n. doi:10.1029/2009JA014204

Chen, L., Zhu, H., and Zhang, X. (2019a). Wavenumber Analysis of EMIC Waves. *Geophys. Res. Lett.* 46, 5689–5697. doi:10.1029/2019GL082686

Chen, M. W., Lemon, C. L., Hecht, J., Sazykin, S., Wolf, R. A., Boyd, A., et al. (2019b). Diffuse Auroral Electron and Ion Precipitation Effects on RCM-E Comparisons with Satellite Data during the 17 March 2013 Storm. *J. Geophys. Res. Space Phys.* 124, 4194–4216. doi:10.1029/2019JA026545

de Soria-Santacruz, M., Spasojevic, M., and Chen, L. (2013). EMIC Waves Growth and Guiding in the Presence of Cold Plasma Density Irregularities. *Geophys. Res. Lett.* 40, 1940–1944. doi:10.1002/grl.50484

Denton, R. E., Anderson, B. J., Ho, G., and Hamilton, D. C. (1996). Effects of Wave Superposition on the Polarization of Electromagnetic Ion Cyclotron Waves. *J. Geophys. Res.* 101 (A11), 24869–24885. doi:10.1029/96JA02251

Denton, R. E., Hudson, M. K., and Roth, I. (1992). Loss-cone-driven Ion Cyclotron Waves in the Magnetosphere. *J. Geophys. Res.* 97 (A8), 12093–12103. doi:10.1029/92JA00954

Denton, R. E., Jordanova, V. K., and Fraser, B. J. (2014). Effect of Spatial Density Variation and O+ Concentration on the Growth and Evolution of Electromagnetic Ion Cyclotron Waves. *J. Geophys. Res. Space Phys.* 119, 8372–8395. doi:10.1002/2014JA020384

Denton, R. E., Ofman, L., Shprits, Y. Y., Bortnik, J., Millan, R. M., Rodger, C. J., et al. (2019). Pitch Angle Scattering of Sub-MeV Relativistic Electrons by Electromagnetic Ion Cyclotron Waves. *J. Geophys. Res. Space Phys.* 124, 5610–5626. doi:10.1029/2018JA026384

Engebretson, M. J., Lessard, M. R., Bortnik, J., Green, J. C., Horne, R. B., Detrick, D. L., et al. (2008). Pc1-Pc2 Waves and Energetic Particle Precipitation during and after Magnetic Storms: Superposed Epoch Anal- Ysis and Case Studies. *J. Geophys. Res.* 113, A01211. doi:10.1029/2007ja012362

Engebretson, M. J., Posch, J. L., Capman, N. S. S., Campuzano, N. G., Bělik, P., Allen, R. C., et al. (2018). MMS, Van Allen Probes, GOES 13, and Ground-Based Magnetometer Observations of EMIC Wave Events before, during, and after a Modest Interplanetary Shock. *J. Geophys. Res. Space Phys.* 123, 8331–8357. doi:10.1029/2018JA025984

Engwall, E., Eriksson, A. I., Cully, C. M., André, M., Puhl-Quinn, P. A., Vaith, H., et al. (2009). Survey of Cold Ionospheric Outflows in the Magnetotail. *Ann. Geophys.* 27, 3185–3201. doi:10.5194/angeo-27-3185-2009

Frey, H. U., Haerendel, G., Mende, S. B., Forrester, W. T., Immel, T. J., and Østgaard, N. (2004). Subauroral Morning Proton Spots (SAMPS) as a Result of Plasmapause-Ring-Current Interaction. *J. Geophys. Res.* 109, A10305. doi:10.1029/2004JA010516

Fuselier, S. A., and Anderson, B. J. (1996). Low-energy He+and H+distributions and Proton Cyclotron Waves in the Afternoon Equatorial Magnetosphere. *J. Geophys. Res.* 101 (A6), 13255–13265. doi:10.1029/96JA00292

Fuselier, S. A., Gary, S. P., Thomsen, M. F., Claflin, E. S., Hubert, B., Sandel, B. R., et al. (2004). Generation of Transient Dayside Subauroral Proton Precipitation. *J. Geophys. Res.* 109, A12227. doi:10.1029/2004JA010393

Gary, S. P., Liu, K., and Chen, L. (2012). Alfvén-cyclotron Instability with Singly Ionized Helium: Linear Theory. *J. Geophys. Res.* 117, a–n. doi:10.1029/2012JA017740

Gomberoff, L., Gratton, F. T., and Gnavi, G. (1996). Acceleration and Heating of Heavy Ions by Circularly Polarized Alfvén Waves. *J. Geophys. Res.* 101 (A7), 15661–15665. doi:10.1029/96JA00684

Gomberoff, L., and Neira, R. (1983). Convective Growth Rate of Ion Cyclotron Waves in a H+−He+and H+−He+−O+plasma. *J. Geophys. Res.* 88 (A3), 2170–2174. doi:10.1029/JA088iA03p02170

Grison, B., Darrouzet, F., Santolík, O., Cornilleau-Wehrlin, N., and Masson, A. (2016). Cluster Observations of Reflected EMIC-Triggered Emission. *Geophys. Res. Lett.* 43, 4164–4171. doi:10.1002/2016GL069096

Grison, B., Santolík, O., Cornilleau-Wehrlin, N., Masson, A., Engebretson, M. J., Pickett, J. S., et al. (2013). EMIC Triggered Chorus Emissions in Cluster Data. *J. Geophys. Res. Space Phys.* 118, 1159–1169. doi:10.1002/jgra.50178

Hendry, A. T., Rodger, C. J., Clilverd, M. A., Engebretson, M. J., Mann, I. R., Lessard, M. R., et al. (2016). Confirmation of EMIC Wave-Driven Relativistic Electron Precipitation. *J. Geophys. Res. Space Phys.* 121, 5366–5383. doi:10.1002/2015JA022224

Hendry, A. T., Santolik, O., Miyoshi, Y., Matsuoka, A., Rodger, C. J., Clilverd, M. A., et al. (2020). A Multi-Instrument Approach to Determining the Source-Region Extent of EEP-Driving EMIC Waves. *Geophys. Res. Lett.* 47, e2019GL086599. doi:10.1029/2019GL086599

Horne, R. B., and Thorne, R. M. (1990). Ion Cyclotron Absorption at the Second Harmonic of the Oxygen Gyrofrequency. *Geophys. Res. Lett.* 17, 2225–2228. doi:10.1029/gl017i012p02225

Hu, Y., Denton, R. E., and Johnson, J. R. (2010). Two-dimensional Hybrid Code Simulation of Electromagnetic Ion Cyclotron Waves of Multi-Ion Plasmas in a Dipole Magnetic Field. *J. Geophys. Res.* 115, a–n. doi:10.1029/2009JA015158

Jun, C. W., Yue, C., Bortnik, J., Lyons, L. R., Nishimura, Y., Kletzing, C., et al. (2019). A Statistical Study of EMIC Waves Associated with and without Energetic Particle Injection from the Magnetotail. *J. Geophys. Res. Space Phys.* 124, 433–450. doi:10.1029/2018JA025886

Kim, E. H., and Johnson, J. R. (2016). Full-wave Modeling of EMIC Waves Near the He + Gyrofrequency. *Geophys. Res. Lett.* 43, 13–21. doi:10.1002/2015GL066978

Kim, E. H., Johnson, J. R., Kim, H., and Lee, D. H. (2015). Inferring Magnetospheric Heavy Ion Density Using EMIC Waves. *J. Geophys. Res. Space Phys.* 120, 6464–6473. doi:10.1002/2015JA021092

Kim, H., Schiller, Q., Engebretson, M. J., Noh, S., Kuzichev, I., Lanzerotti, L. J., et al. (2021). Observations of Particle Loss Due to Injection-Associated Electromagnetic Ion Cyclotron Waves. *J. Geophys. Res. Space Phys.* 126, e2020JA028503. doi:10.1029/2020JA028503

Kistler, L. M., Mouikis, C. G., Cao, X., Frey, H., Klecker, B., Dandouras, I., et al. (2006). Ion Composition and Pressure Changes in Storm Time and Nonstorm Substorms in the Vicinity of the Near-Earth Neutral Line. *J. Geophys. Res.* 111 (A11). doi:10.1029/2006ja011939

Kistler, L. M., Mouikis, C. G., Spence, H. E., Menz, A. M., Skoug, R. M., Funsten, H. O., et al. (2016). The Source of O+ in the Storm Time Ring Current. *J. Geophys. Res. Space Phys.* 121 (6), 5333–5349. doi:10.1002/2015ja022204

Kozyra, J. U., Cravens, T. E., Nagy, A. F., Fontheim, E. G., and Ong, R. S. B. (1984). Effects of Energetic Heavy Ions on Electromagnetic Ion Cyclotron Wave Generation in the Plasmapause Region. *J. Geophys. Res.* 89 (A4), 2217–2233. doi:10.1029/JA089iA04p02217

Lee, J. H., and Angelopoulos, V. (2014a). Observations and Modeling of EMIC Wave Properties in the Presence of Multiple Ion Species as Function of Magnetic Local Time. *J. Geophys. Res. Space Phys.* 119, 8942–8970. doi:10.1002/2014JA020469

Lee, J. H., and Angelopoulos, V. (2014b). On the Presence and Properties of Cold Ions Near Earth's Equatorial Magnetosphere. *J. Geophys. Res. Space Phys.* 119, 1749–1770. doi:10.1002/2013JA019305

Lee, J. H., Chen, L., Angelopoulos, V., and Thorne, R. M. (2012). THEMIS Observations and Modeling of Multiple Ion Species and EMIC Waves: Implications for a Vanishing He+stop Band. *J. Geophys. Res.* 117, a–n. doi:10.1029/2012JA017539

Lee, J. H., Turner, D. L., Toledo-Redondo, S., Vines, S. K., Allen, R. C., Fuselier, S. A., et al. (2019). MMS Measurements and Modeling of peculiar Electromagnetic Ion Cyclotron Waves. *Geophys. Res. Lett.* 46, 11622–11631. doi:10.1029/2019GL085182

Lee, J. H., Turner, D. L., Vines, S. K., Allen, R. C., Toledo-Redondo, S., Bingham, S. T., et al. (2021). Application of Cold and Hot Plasma Composition Measurements to Investigate Impacts on Dusk-Side Electromagnetic Ion Cyclotron Waves. *J. Geophys. Res. Space Phys.* 126, e2020JA028650. doi:10.1029/2020JA028650

Lessard, M. R., Paulson, K., Spence, H. E., Weaver, C., Engebretson, M. J., Millan, R., et al. (2019). Generation of EMIC Waves and Effects on Particle Precipitation during a Solar Wind Pressure Intensification with B Z >0. *J. Geophys. Res. Space Phys.* 124, 4492–4508. doi:10.1029/2019JA026477

Li, Z., Millan, R. M., Hudson, M. K., Woodger, L. A., Smith, D. M., Chen, Y., et al. (2014). Investigation of EMIC Wave Scattering as the Cause for the BARREL 17 January 2013 Relativistic Electron Precipitation Event: A Quantitative Comparison of Simulation with Observations. *Geophys. Res. Lett.* 41, 8722–8729. doi:10.1002/2014GL062273

Lin, R.-L., Zhang, J.-C., Allen, R. C., Kistler, L. M., Mouikis, C. G., Gong, J.-C., et al. (2014). Testing Linear Theory of EMIC Waves in the Inner Magnetosphere: Cluster Observations. *J. Geophys. Res. Space Phys.* 119 (2), 1004–1027. doi:10.1002/2013JA019541

Lyons, L. R., and Thorne, R. M. (1972). Parasitic Pitch Angle Diffusion of Radiation belt Particles by Ion Cyclotron Waves. *J. Geophys. Res.* 77, 5608–5616. doi:10.1029/ja077i028p05608

Mann, I. R., Usanova, M. E., Murphy, K., Robertson, M. T., Milling, D. K., Kale, A., et al. (2014). Spatial Localization and Ducting of EMIC Waves: Van Allen Probes and Ground-Based Observations. *Geophys. Res. Lett.* 41, 785–792. doi:10.1002/2013GL058581

Min, K., Lee, J., Keika, K., and Li, W. (2012). Global Distribution of EMIC Waves Derived from THEMIS Observations. *J. Geophys. Res.* 117, a–n. doi:10.1029/2012JA017515

Min, K., Liu, K., Bonnell, J. W., Breneman, A. W., Denton, R. E., Funsten, H. O., et al. (2015). Study of EMIC Wave Excitation Using Direct Ion Measurements. *J. Geophys. Res. Space Phys.* 120, 2702–2719. doi:10.1002/2014JA020717

Miyoshi, Y., Matsuda, S., Kurita, S., Nomura, K., Keika, K., Shoji, M., et al. (2019). EMIC Waves Converted from Equatorial Noise Due to M/Q = 2 Ions in the Plasmasphere: Observations from Van Allen Probes and Arase. *Geophys. Res. Lett.* 46, 5662–5669. doi:10.1029/2019GL083024

Nakamura, S., Omura, Y., and Angelopoulos, V. (2016). A Statistical Study of EMIC Rising and Falling Tone Emissions Observed by THEMIS. *J. Geophys. Res. Space Phys.* 121, 8374–8391. doi:10.1002/2016JA022353

Nakamura, S., Omura, Y., Shoji, M., Nosé, M., Summers, D., and Angelopoulos, V. (2015). Subpacket Structures in EMIC Rising Tone Emissions Observed by the THEMIS Probes. *J. Geophys. Res. Space Phys.* 120, 7318–7330. doi:10.1002/2014JA020764

Ni, B., Cao, X., Shprits, Y. Y., Summers, D., Gu, X., Fu, S., et al. (2018). Hot Plasma Effects on the Cyclotron-Resonant Pitch-Angle Scattering Rates of Radiation Belt Electrons Due to EMIC Waves. *Geophys. Res. Lett.* 45, 21–30. doi:10.1002/2017GL076028

Noh, S.-J., Lee, D.-Y., Choi, C.-R., Kim, H., and Skoug, R. (2018). Test of Ion Cyclotron Resonance Instability Using Proton Distributions Obtained from Van Allen Probe-A Observations. *J. Geophys. Res. Space Phys.* 123, 6591–6610. doi:10.1029/2018JA025385

Noh, S. J., Lee, D. Y., Kim, H., Lanzerotti, L. J., Gerrard, A., and Skoug, R. M. (2021). Upper Limit of Proton Anisotropy and its Relation to Electromagnetic Ion Cyclotron Waves in the Inner Magnetosphere. *J. Geophys. Res. Space Phys.* 126, e2020JA028614. doi:10.1029/2020JA028614

Omura, Y., Pickett, J., Grison, B., Santolik, O., Dandouras, I., Engebretson, M., et al. (2010). Theory and Observation of Electromagnetic Ion Cyclotron Triggered Emissions in the Magnetosphere. *J. Geophys. Res.* 115, A07234. doi:10.1029/2010JA015300

Paulson, K. W., Smith, C. W., Lessard, M. R., Engebretson, M. J., Torbert, R. B., and Kletzing, C. A. (2014). *In Situ* observations of Pc1 Pearl Pulsations by the Van Allen Probes. *Geophys. Res. Lett.* 41, 1823–1829. doi:10.1002/2013GL059187

Pickett, J. S., Grison, B., Omura, Y., Engebretson, M. J., Dandouras, I., Masson, A., et al. (2010). Cluster Observations of EMIC Triggered Emissions in Association with Pc1 Waves Near Earth's Plasmapause. *Geophys. Res. Lett.* 37, a–n. doi:10.1029/2010GL042648

Posch, J. L., Engebretson, M. J., Murphy, M. T., Denton, M. H., Lessard, M. R., and Horne, R. B. (2010). Probing the Relationship between Electromagnetic Ion Cyclotron Waves and Plasmaspheric Plumes Near Geosynchronous Orbit. *J. Geophys. Res.* 115, A11205. doi:10.1029/2010ja015446

Qin, M., Hudson, M., Li, Z., Millan, R., Shen, X., Shprits, Y., et al. (2019). Investigating Loss of Relativistic Electrons Associated with EMIC Waves at Low L Values on 22 June 2015. *J. Geophys. Res. Space Phys.* 124, 4022–4036. doi:10.1029/2018JA025726

Rauch, J. L., and Roux, A. (1982). Ray Tracing of ULF Waves in a Multicomponent Magnetospheric Plasma: Consequences for the Generation Mechanism of Ion Cyclotron Waves. *J. Geophys. Res.* 87, 8191–8198. doi:10.1029/ja087ia10p08191

Remya, B., Sibeck, D. G., Halford, A. J., Murphy, K. R., Reeves, G. D., Singer, H. J., et al. (2018). Ion Injection Triggered EMIC Waves in the Earth's Magnetosphere. *J. Geophys. Res. Space Phys.* 123, 4921–4938. doi:10.1029/2018JA025354

Remya, B., Sibeck, D. G., Ruohoniemi, J. M., Kunduri, B., Halford, A. J., Reeves, G. D., et al. (2020). Association between EMIC Wave Occurrence and Enhanced Convection Periods during Ion Injections. *Geophys. Res. Lett.* 47, e2019GL085676. doi:10.1029/2019GL085676

Rodger, C. J., Raita, T., Clilverd, M. A., Seppälä, A., Dietrich, S., Thomson, N. R., et al. (2008). Observations of Relativistic Electron Precipitation from the

Radiation Belts Driven by EMIC Waves. *Geophys. Res. Lett.* 35, L16106. doi:10.1029/2008GL034804

Rönnmark, K., and André, M. (1991). Convection of Ion Cyclotron Waves to Ion-Heating Regions. *J. Geophys. Res.* 96, 17573–17579. doi:10.1029/91JA01793

Saikin, A. A., Zhang, J. C., Allen, R. C., Smith, C. W., Kistler, L. M., Spence, H. E., et al. (2015). The Occurrence and Wave Properties of H + -, He + -, and O + -band EMIC Waves Observed by the Van Allen Probes. *J. Geophys. Res. Space Phys.* 120, 7477–7492. doi:10.1002/2015JA021358

Shoji, M., and Omura, Y. (2013). Triggering Process of Electromagnetic Ion Cyclotron Rising Tone Emissions in the Inner Magnetosphere. *J. Geophys. Res. Space Phys.* 118, 5553–5561. doi:10.1002/jgra.50523

Shprits, Y. Y., Drozdov, A. Y., Spasojevic, M., Kellerman, A. C., Usanova, M. E., Engebretson, M. J., et al. (2016). Wave-induced Loss of Ultra-relativistic Electrons in the Van Allen Radiation Belts. *Nat. Commun.* 7 (1), 1–7. doi:10.1038/ncomms12883

Shprits, Y. Y., Kellerman, A., Aseev, N., Drozdov, A. Y., and Michaelis, I. (2017). Multi-MeV Electron Loss in the Heart of the Radiation Belts. *Geophys. Res. Lett.* 44, 1204–1209. doi:10.1002/2016GL072258

Sigsbee, K., Kletzing, C. A., Faden, J. B., Jaynes, A. N., Reeves, G. D., and Jahn, J. M. (2020). Simultaneous Observations of Electromagnetic Ion Cyclotron (EMIC) Waves and Pitch Angle Scattering during a Van Allen Probes Conjunction. *J. Geophys. Res. Space Phys.* 125, e2019JA027424. doi:10.1029/2019JA027424

Silin, I., Mann, I. R., Sydora, R. D., Summers, D., and Mace, R. L. (2011). Warm Plasma Effects on Electromagnetic Ion Cyclotron Wave MeV Electron Interactions in the Magnetosphere. *J. Geophys. Res.* 116, A05215. doi:10.1029/2010JA016398

Spasojevic, M., and Fuselier, S. A. (2009). Temporal Evolution of Proton Precipitation Associated with the Plasmaspheric Plume. *J. Geophys. Res.* 114, a–n. doi:10.1029/2009JA014530

Su, Z., Zhu, H., Xiao, F., Zheng, H., Shen, C., Wang, Y., et al. (2012). Bounce-averaged Advection and Diffusion Coefficients for Monochromatic Electromagnetic Ion Cyclotron Wave: Comparison between Test-Particle and Quasi-Linear Models. *J. Geophys. Res.* 117, a–n. doi:10.1029/2012JA017917

Summers, D., and Thorne, R. M. (2003). Relativistic Electron Pitch-Angle Scattering by Electromagnetic Ion Cyclotron Waves during Geomagnetic Storms. *J. Geophys. Res.* 108, 1143. doi:10.1029/2002JA009489

Tetrick, S. S., Engebretson, M. J., Posch, J. L., Olson, C. N., Smith, C. W., Denton, R. E., et al. (2017). Location of Intense Electromagnetic Ion Cyclotron (EMIC) Wave Events Relative to the Plasmapause: Van Allen Probes Observations. *J. Geophys. Res. Space Phys.* 122 (4), 4064–4088. doi:10.1002/2016ja023392

Thorne, R. M., Horne, R. B., Jordanova, V. K., Bortnik, J., and Glauert, S. (2006). "Interaction of Emic Waves with thermal Plasma and Radiation belt Particles," in *Magnetospheric ULF Waves: Synthesis and New Directions*. Editors K. Takahashi, P. J. Chi, R. E. Denton, and R. L. Lysak (Washington, DC, USA: American Geophysical Union), 213–223. doi:10.1029/169GM14

Thorne, R. M., and Kennel, C. F. (1971). Relativistic Electron Precipitation during Magnetic Storm Main Phase. *J. Geophys. Res.* 76 (1), 4446–4453. doi:10.1029/JA076i019p04446

Toledo-Redondo, S., Lavraud, B., Fuselier, S. A., André, M., Khotyaintsev, Y. V., Nakamura, R., et al. (2019). Electrostatic Spacecraft Potential Structure and Wake Formation Effects for Characterization of Cold Ion Beams in the Earth's Magnetosphere. *J. Geophys. Res. Space Phys.* 124, 10048–10062. doi:10.1029/2019JA027145

Toledo-Redondo, S., Lee, J. H., Vines, S. K., Turner, D. L., Allen, R. C., André, M., et al. (2021). Kinetic Interaction of Cold and Hot Protons with an Oblique EMIC Wave Near the Dayside Reconnecting Magnetopause. *Geophys. Res. Lett.* 48, e2021GL092376. doi:10.1029/2021GL092376

Torkar, K., Nakamura, R., Tajmar, M., Scharlemann, C., Jeszenszky, H., Laky, G., et al. (2016), Active Spacecraft Potential Control Investigation. *Space Sci. Rev.* 199 (1-4), 515–544. doi:10.1007/s11214-014-0049-3

Ukhorskiy, A. Y., Shprits, Y. Y., Anderson, B. J., Takahashi, K., and Thorne, R. M. (2010). Rapid Scattering of Radiation belt Electrons by Storm-Time EMIC Waves. *Geophys. Res. Lett.* 37, a–n. doi:10.1029/2010GL042906

Usanova, M. E., Drozdov, A., Orlova, K., Mann, I. R., Shprits, Y., Robertson, M. T., et al. (2014). Effect of EMIC Waves on Relativistic and Ultrarelativistic Electron Populations: Ground-Based and Van Allen Probes Observations. *Geophys. Res. Lett.* 41, 1375–1381. doi:10.1002/2013GL059024

Usanova, M. E., Mann, I. R., Rae, I. J., Kale, Z. C., Angelopoulos, V., Bonnell, J. W., et al. (2008). Multipoint Observations of Magnetospheric Compression-Related EMIC Pc1 Waves by THEMIS and CARISMA. *Geophys. Res. Lett.* 35, L17S25. doi:10.1029/2008GL034458

Vines, S. K., Anderson, B. J., Allen, R. C., Denton, R. E., Engebretson, M. J., Johnson, J. R., et al. (2021). Determining EMIC Wave Vector Properties through Multi-point Measurements: The Wave Curl Analysis. *J. Geophys. Res. Space Phys.* 126, e2020JA028922. doi:10.1029/2020JA028922

Vines, S. K., Allen, R. C., Anderson, B. J., Engebretson, M. J., Fuselier, S. A., Russell, C. T., et al. (2019). EMIC Waves in the Outer Magnetosphere: Observations of an Off-Equator Source Region. *Geophys. Res. Lett.* 46, 5707–5716. doi:10.1029/2019GL082152

Yahnin, A. G., Yahnina, T. A., and Frey, H. U. (2007). Subauroral Proton Spots Visualize the Pc1 Source. *J. Geophys. Res.* 112, a–n. doi:10.1029/2007JA012501

Yuan, Z., Yu, X., Ouyang, Z., Yao, F., Huang, S., and Funsten, H. O. (2019). Simultaneous Trapping of Electromagnetic Ion Cyclotron and Magnetosonic Waves by Background Plasmas. *J. Geophys. Res. Space Phys.* 124, 1635–1643. doi:10.1029/2018JA026149

Yue, C., Jun, C. W., Bortnik, J., An, X., Ma, Q., Reeves, G. D., et al. (2019). The Relationship between EMIC Wave Properties and Proton Distributions Based on Van Allen Probes Observations. *Geophys. Res. Lett.* 46, 4070–4078. doi:10.1029/2019GL082633

Zhang, J.-C., Saikin, A. A., Kistler, L. M., Smith, C. W., Spence, H. E., Mouikis, C. G., et al. (2014). Excitation of EMIC Waves Detected by the Van Allen Probes on 28 April 2013. *Geophys. Res. Lett.* 41, 4101–4108. doi:10.1002/2014GL060621

Zhu, H., Chen, L., Claudepierre, S. G., and Zheng, L. (2020). Direct Evidence of the Pitch Angle Scattering of Relativistic Electrons Induced by EMIC Waves. *Geophys. Res. Lett.* 47, e2019GL085637. doi:10.1029/2019GL085637

Zhu, M., Yu, Y., Tian, X., Shreedevi, P. R., and Jordanova, V. K. (2021). On the Ion Precipitation Due to Field Line Curvature (FLC) and EMIC Wave Scattering and Their Subsequent Impact on Ionospheric Electrodynamics. *J. Geophys. Res. Space Phys.* 126, e2020JA028812. doi:10.1029/2020JA028812

Zurbuchen, T. H., and Gershman, D. J. (2016). Innovations in Plasma Sensors. *J. Geophys. Res. Space Phys.* 121, 2891–2901. doi:10.1002/2016JA022493

Conflict of Interest: The authors declare that the research was conducted in the absence of any commercial or financial relationships that could be construed as a potential conflict of interest.

Publisher's Note: All claims expressed in this article are solely those of the authors and do not necessarily represent those of their affiliated organizations, or those of the publisher, the editors and the reviewers. Any product that may be evaluated in this article, or claim that may be made by its manufacturer, is not guaranteed or endorsed by the publisher.

frontiers in Astronomy and Space Sciences

REVIEW
published: 24 August 2021
doi: 10.3389/fspas.2021.708940

Magnetospheric Mass Density as Determined by ULF Wave Analysis

Kazue Takahashi[1]* *and Richard E. Denton*[2]

[1]Applied Physics Laboratory, The Johns Hopkins University, Laurel, MD, United States, [2]Department of Physics and Astronomy, Dartmouth College, Hanover, NH, United States

The technique to estimate the mass density in the magnetosphere using the physical properties of observed magnetohydrodynamic waves is known as magnetoseismology. This technique is important in magnetospheric research given the difficulty of determining the density using particle experiments. This paper presents a review of magnetoseismic studies based on satellite observations of standing Alfvén waves. The data sources for the studies include AMPTE/CCE, CRRES, GOES, Geotail, THEMIS, Van Allen Probes, and Arase. We describe data analysis and density modeling techniques, major results, and remaining issues in magnetoseismic research.

Keywords: magnetosphere, mass denisty, toroidal Alfvén waves, spacecraft observations, data analysis techniques, modeling techniques

OPEN ACCESS

Edited by:
Gian Luca Delzanno, Los Alamos National Laboratory (DOE), United States

Reviewed by:
Vyacheslav Pilipenko, Institute of Physics of the Earth (RAS), Russia
Nickolay Ivchenko, Royal Institute of Technology, Sweden

***Correspondence:**
Kazue Takahashi
kazue.takahashi@jhuapl.edu

Specialty section:
This article was submitted to Space Physics, a section of the journal Frontiers in Astronomy and Space Sciences

Received: *12 May 2021*
Accepted: *30 July 2021*
Published: *24 August 2021*

Citation:
Takahashi K and Denton RE (2021) Magnetospheric Mass Density as Determined by ULF Wave Analysis. Front. Astron. Space Sci. 8:708940. doi: 10.3389/fspas.2021.708940

1 INTRODUCTION

Mass density (denoted ρ) is a fundamental quantity of the magnetospheric plasma. The density controls the properties of various ion-scale plasma waves and the time scale of global magnetospheric processes. The density is also a key quantity in studying the ionospheric response to the solar activity and the coupling between the magnetosphere and the ionosphere. Despite the importance of ρ, its determination from particle data is difficult because no particle detector is capable of covering the full range of energies, pitch angles, and ion composition, which is necessary to obtain the density through moment calculation. This makes indirect techniques very valuable.

The idea of using ultralow-frequency (ULF) waves as a tool to estimate ρ, now known as magnetoseismology, was presented as early as the late 1950s (Obayashi and Jacobs, 1958) based on the magnetohydrodynamic (MHD) theory of magnetospheric ULF waves (Dungey, 1954). Both the shear mode (Alfvén waves) and compressional mode (fast magnetosonic waves) have been used in magnetoseismology. This paper describes Alfvén wave techniques, termed normal mode magnetoseismology (Chi and Russell, 2005). The publication of the cross-phase technique to determine the frequency of standing Alfvén waves (field line resonances, FLRs) (Waters et al., 1991) led to numerous magnetoseismic studies using ground magnetometer data. We will focus on data analysis and modeling techniques for spacecraft data. Readers are referred to Menk and Waters (2013) and Del Corpo et al. (2020) for results based on ground observations and to Denton (2006) for early results based on spacecraft observations.

The remainder of this paper is as follows. **Section 2** presents the theoretical background and modeling approach. **Section 3** presents data analysis results. **Section 4** presents discussion, and **section 5** presents the conclusions.

2 BASIC TECHNIQUES

2.1 The Concept

Techniques to infer mass density structures are well established in terrestrial and solar seismology. Our idea is to use similar techniques to infer the mass distribution in the terrestrial magnetosphere. The basic

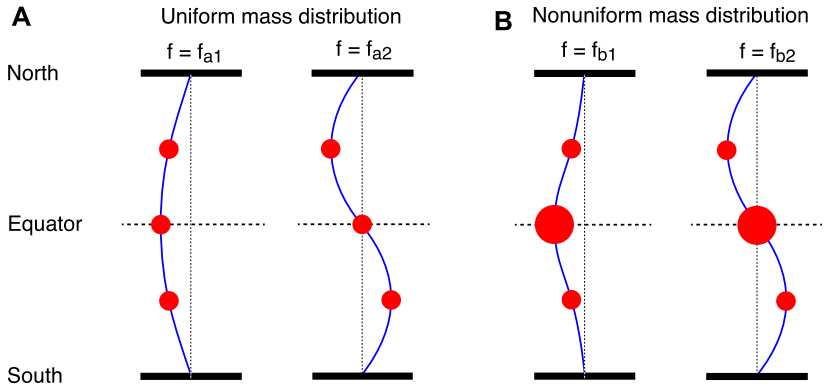

FIGURE 1 | String analogy of standing Alfvén waves. The blue curves represent the field line, and the size of the filled red circles represents the mass density value. The string is tied at the northern and southern ends corresponding to the ionospheric footpoints of the field line. **(A)** Structure of the fundamental **(left)** and second harmonic **(right)** modes for the case of a uniform mass density distribution along the field line. The node or antinode is located at the equator (horizontal dashed line). The mode frequencies are denoted f_{a1} and f_{a2}. **(B)** Same as **(A)** but for a mass density distribution that is peaked at the equator. The mode frequencies are denoted f_{b1} and f_{b2}.

principle of magnetoseismology is that ρ is related to the frequency and mode structure of standing Alfvén waves. **Figure 1** illustrates this relationship using a string model of magnetic field lines. The frequency of vibrations of the string (blue curves) is determined by the tension (restoring force) of the string and the mass (filled red circles) attached to the string. The discrete mass distribution is only for illustrative purposes. In reality, the mass is distributed continuously.

Figure 1A illustrates the fundamental and second harmonic modes for the case of a uniform mass distribution along the field line. The mode structure is a sine function for either harmonic, and the frequencies are related as $f_{a2} = 2f_{a1}$. The time-of-flight calculation described below gives exact solutions of the mode frequency and structure for all harmonics.

Figure 1B illustrates the case of a nonuniform mass density distribution with a peak at the equator. In this case, the mode structure of the fundamental mode is not a sine function, and the frequency of the fundamental mode (f_{b1}) is lower than f_{a1}. However, the equatorial mass density does not affect the mode structure or the frequency of the second harmonic because the string displacement is zero (node) at the equator. As a consequence, the mode of the second harmonic is a sine function, the same as in **Figure 1A**. The mass density effects on the wave properties occur for higher harmonics also. This means that we can infer the mass density distribution from the frequencies and mode structures determined using spacecraft data.

2.2 Wave Equation

To advance the concept illustrated in **Figure 1** to magnetoseismology of the real magnetosphere, we obtain the relationship between the waves and ρ using the cold plasma MHD wave equation (e.g., Radoski and Carovillano, 1966)

$$\frac{\partial^2 \delta \mathbf{E}}{\partial t^2} = \mathbf{V}_A \times \mathbf{V}_A \times (\nabla \times \nabla \times \delta \mathbf{E}), \quad (1)$$

where $\delta\mathbf{E}$ is the wave electric field and $\mathbf{V}_A$ is the Alfvén velocity, which depends on the magnetic field $\mathbf{B}$ and ρ as $\mathbf{V}_A = \mathbf{B}(\mu_0\rho)^{-1}$; μ_0 is the permeability of free space. A justification for using the cold plasma equation is found in the appendix of Singer et al. (1981). When perfect wave reflection is imposed at the ionosphere, the equation for a dipole magnetosphere yields two purely transverse standing Alfvén wave solutions, which are known as the axisymmetric toroidal mode (Radoski and Carovillano, 1966) and the guided poloidal mode (Radoski, 1967). Magnetic field perturbation and fluid motion are in the azimuthal direction for the toroidal mode and in the meridional plane for the poloidal mode. The toroidal (poloidal) mode corresponds to the limit of $m = 0$ ($|m| = \infty$), where m is the azimuthal wave number (<0 for westward propagation). The polarization state is relevant to magnetoseismology because the wave frequency depends on it. In the dipole field, the fundamental toroidal frequency (f_{T1}) is 1.4 times the fundamental poloidal frequency (f_{P1}) if ρ is constant along the field line (Cummings et al., 1969). This translates to a factor of ~2 difference in ρ (see **Eq. 4**). The idealized wave modes explain many observable features of standing Alfvén waves in the magnetosphere, both waves with toroidally (azimuthally) oscillating magnetic perturbations excited by large-scale solar wind disturbances and waves with poloidally (radially) oscillating magnetic perturbations excited by internal instabilities. Spacecraft detect toroidal waves routinely, and magnetoseismic studies usually rely on these waves.

Poloidal waves are detected also, but these waves have not been used much in magnetoseismology. Considering the fact that poloidal waves are not detected by ground magnetometers because of the ionospheric screening of high-m waves (Hughes and Southwood, 1976) and also the fact that the waves exhibit a different local time occurrence distribution than toroidal waves (Arthur and McPherron, 1981), poloidal waves could be a valuable resource in future magnetoseismic studies. Poloidal waves have the advantage of being excited nearly exclusively at the second harmonic (Cummings et al., 1969; Takahashi and McPherron, 1984; Anderson et al., 1990; Liu et al., 2013), reducing the uncertainty in harmonic mode identification. But a disadvantage to using poloidal waves is that the wave frequency

depends on the radial pressure gradient, which is not always well determined (Denton, 2003, and references therein).

The magnetospheric magnetic field significantly differs from the dipole field at large distances or during geomagnetically disturbed periods, making it difficult to exactly solve **Eq. 1**. Fortunately, MHD-scale disturbances quickly settle to toroidal eigenmode oscillations (Allan et al., 1986; Lee and Lysak, 1989) through the FLR process (e.g., Chen and Hasegawa, 1974), and we can treat each field line to be an independent oscillator in the context of magnetoseismology. For example, we can use the time-of-flight approximation for the fundamental frequency f_1 on a field line (Warner and Orr, 1979; Wild et al., 2005)

$$f_1 = \left(2\int_S^N \frac{ds}{V_A}\right)^{-1}, \tag{2}$$

where s is distance along the field line and the integral is taken between the southern (S) and northern (N) ionospheric footpoints. In this approximation, there is no distinction between toroidal and poloidal frequencies, the frequency of the nth harmonic (f_n) is equal to nf_1, and the f_n value is higher than that obtained by more accurate methods (Takahashi and McPherron, 1984). More accurate eigenmode solutions are obtained by numerically solving the equation

$$\mu_0\rho\frac{\partial^2(\xi_i/h_i)}{\partial t^2} = \frac{1}{h_i^2}\mathbf{B}\cdot\nabla\{h_i^2[\mathbf{B}\cdot\nabla(\xi_i/h_i)]\}, \tag{3}$$

where ξ_i is the field line displacement associated with the wave and h_i is the scale factor vector of the background magnetic field **B**, with the suffix i indicating the direction within the plane perpendicular to **B** (Singer et al., 1981). To solve this equation for a general magnetic field geometry, one selects two adjacent model magnetic field lines to specify the direction (polarization axis) of magnetic field perturbation. This flexibility is valuable in consideration of theoretical studies (Lee et al., 2000; Wright and Elsden, 2016) indicating that the polarization axis of toroidal waves is not tangential to the magnetic field L shells when the ρ distribution is not axisymmetric. The two field lines are best chosen at the magnetic equator, where the properties have the strongest effect on the wave frequency. A somewhat more self-consistent approach would be to use the equations of Rankin et al. (2006), who solve for the coupled toroidal and poloidal waves.

A practical procedure to estimate the mass density (denoted ρ_{est}) from the observed wave frequency f_{obs} is as follows. In the first step, we obtain the reference eigenfrequency f_{ref} by solving the wave equation for a reference mass density ρ_{ref} (e.g., 1 amu cm^{-3}) at a reference point (e.g., magnetic equator) after choosing models for the magnetic field and mass density variation along the field line. In the second step, we obtain ρ_{est} using the relationship

$$\rho_{est} = \rho_{ref}(f_{ref}/f_{obs})^2. \tag{4}$$

The mass density values at other locations along the field line are obtained using the model field line mass distribution function.

2.3 Magnetic Field and Mass Density Field Line Distribution Models

The quality of the models for the magnetic field and field line mass density distribution determines the accuracy of ρ_{est}. For the magnetic field, several models are available (e.g., Tsyganenko, 1989; Tsyganenko and Sitnov, 2005; Sitnov et al., 2008), and it is even possible to use magnetic fields obtained by global MHD simulation (e.g., Claudepierre et al., 2010). We can choose the best field model by comparing model fields with the field that is observed by the same satellite used for wave observation. This is an advantage of using spacecraft data instead of ground magnetometer data. An even greater advantage relates to determination of the equatorial location of the field line, and hence the L shell and magnetic local time (MLT). That is much less of a problem for spacecraft data, especially for spacecraft with near-equatorial orbits. For field lines mapping from the ground to geostationary orbit ($L \sim 7$) or beyond, inaccuracies in mapping can be severe, where L is the magnetic shell parameter.

As for the mass density field line distribution model, we cannot impose many constraining conditions because we have a small number of observable eigenmodes, unlike in terrestrial or solar magnetoseismology. Therefore, we adopt models with a small number of free parameters. The most frequently used mass density model has only two free parameters (ρ_{eq} and α)

$$\rho = \rho_{eq}(LR_E/r)^\alpha, \tag{5}$$

where ρ_{eq} is the equatorial mass density, R_E is the Earth's radius, r is geocentric distance to the field line, and the power law index α specifies how ρ varies along the field line (Radoski and Carovillano, 1966; Cummings et al., 1969). We can add more flexibility to the model density by using polynomial expansion in terms of a parameter related to s (Denton et al., 2001, 2004; Takahashi and Denton, 2007). In the Takahashi and Denton (2007) study, the parameter is defined to be

$$\tau = \int ds/B, \tag{6}$$

where B is the magnitude of the magnetic field. The mass density model is expressed as

$$\log_{10}\rho = c_2\tau^2 + c_4\tau^4 + c_6\tau^6. \tag{7}$$

Only even terms appear in this equation because of the assumption that the mass density distribution is symmetric about the equator. Although this model has only three free parameters, it is capable of modeling an equatorial enhancement of mass density in a way that the power-law model (**Eq. 5**) cannot.

3 DATA ANALYSIS RESULTS

3.1 Spacecraft and Data

Any magnetospheric spacecraft carrying science experiments is a good data source for magnetoseismology. Three types of spacecraft data have been used. They are **E** and **B** fields and

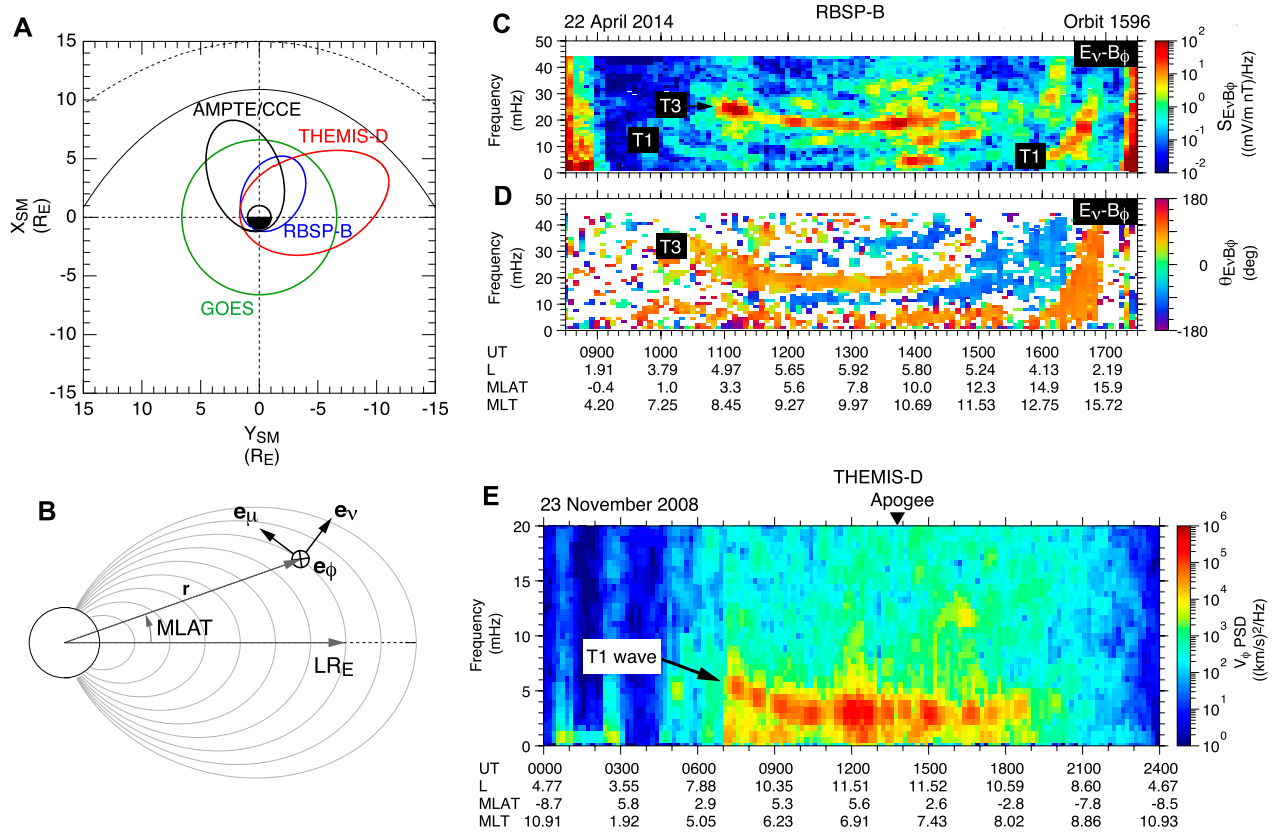

FIGURE 2 | Examples of orbital dynamic spectra showing toroidal waves. **(A)** Selected THEMIS-D and RBSP-B orbits. Orbits of GOES and AMPTE/CCE are included as a reference. **(B)** Coordinate systems for spacecraft positions and the observable vector quantities used in data analysis **(C,D)** Cross-power spectra and cross-phase spectra of the E_ν and B_ϕ components measured by RBSP-B (after Takahashi and Denton, 2021). **(E)** Dynamic spectra of the V_ϕ component measured by THEMIS-D (after Takahashi et al., 2016).

the plasma bulk velocity (**V**). Convective anisotropy of energetic particles can be used as a proxy to **V** (Takahashi et al., 2002). **Figure 2** shows examples of toroidal waves detected by two representative magnetospheric spacecraft with low orbital inclination: Van Allen Probes (Radiation Belt Storm Probes, RBSP)-B and Time History of Events and Macroscale Interactions during Substorms (THEMIS)-D. **Figure 2A** shows the equatorial projection of the selected orbits of these spacecraft in solar magnetic (SM) coordinates. RBSP-B, with apogee at ~6 R_E, covers the inner magnetosphere. THEMIS-D, with apogee at ~12 R_E, covers the outer magnetosphere. **Figure 2B** shows the coordinate systems used for spacecraft position and measured vector quantities.

Figures 2C,D were generated from the toroidal components, δE_ν and δB_ϕ, measured by RBSP-B on the orbit shown in **Figure 2A**. The cross-power spectra (**Figure 2C**) show several toroidal harmonics, the most obvious being the fundamental (T1), second (T2), and third (T3) harmonics. The cross-phase spectra (**Figure 2D**), displayed only when the δE_ν-δB_ϕ coherence is higher than 0.5, also show several bands corresponding to the band structure in the cross-power spectra. The cross-phase spectra are the key to identifying the harmonic modes when many harmonics coexist or when the spectral intensity changes with time (Takahashi and Denton, 2021).

Figure 2E was generated from the δV_ϕ component measured by THEMIS-D on the orbit shown in **Figure 2A**. For an equatorially orbiting spacecraft, the velocity is a sensitive indicator of odd mode waves, which have antinodes at or near the equator. The velocity often is the best quantity for toroidal wave analysis when the electric fields measured on the same spacecraft are contaminated by spacecraft wake or charging. In this example, a strong T1 spectral line is visible. A caveat with the velocity data is that the δ**V** spectral intensity diminishes at $L < 7$, where the δ**V** is weak because of strong background B.

Included in **Figure 2A** are the orbit of geostationary satellites (e.g., Geostationary Operational Environmental Satellite, GOES) and an orbit of Active Magnetospheric Particle Tracer Explorers (AMPTE)/Charge Composition Explorer (CCE). The GOES satellites provide continuous **B** field data (not shown) at $L \sim 7$. Harmonic mode identification is relatively easy with the GOES data because the magnetic latitude (MLAT) of the spacecraft does not change. Denton et al. (2016) used 12 years of data from multiple GOES satellites to develop a number of models of varying complexity for ρ at geostationary orbit. The most complicated models could determine ρ within a factor of 1.6, accounting for about two-thirds of the variance. Some GOES spacecraft carry detectors for energetic (>80 keV) protons

(Rodriguez, 2014), and data from the detectors can be used to determine the frequency of oscillatory convective anisotropy induced by standing Alfvén waves (e.g., Takahashi et al., 2002). This capability remains to be utilized.

CCE had an orbital configuration intermediate between THEMIS and RBSP and was operational between 1984 and 1989. Min et al. (2013) used magnetometer data from this spacecraft to construct mass density models covering L = 4–9 and MLT = 0300–1900. The study also determined toroidal wave frequencies using GOES magnetometer data and found the frequencies to be consistent with those at CCE for $L \sim 7$.

Magnetoseismology works when the driver fast mode waves for exciting toroidal waves have a wide spectral band to excite multiharmonic toroidal waves over a wide range of L. If the fast mode waves have a narrow spectrum, toroidal waves will be excited in a narrow L range and we will not be able to determine the L profile of ρ. Monochromatic fast mode waves such as wave guide modes could be excited in the magnetosphere and could produce ground magnetic pulsations with L-independent frequencies (Marin et al., 2014) while exciting magnetospheric toroidal waves on an isolated L shell. However, as **Figure 2** indicates, toroidal waves (especially in the dayside magnetosphere) are usually excited over a wide frequency range in response to broadband fast mode waves generated either by dynamic pressure variations intrinsic to the solar wind (Sarris et al., 2010) or by compressional ULF waves generated in the ion foreshock (Takahashi et al., 1984). We believe that broadband fast mode waves are always present in the magnetosphere in addition to possible waveguide modes.

3.2 Field Line Mass Density Distribution

A number of studies used toroidal wave frequencies (f_{Tn}, n being the harmonic mode number) to find an optimal value of the α parameter appearing in **Eq. 5**. These studies found α values in the range 0–2, which is closer to α = 0–1 for the electron diffusive equilibrium expected in the plasmasphere rather than a collisionless distribution (α = 3–4) expected in the plasmatrough (Angerami and Carpenter, 1966; Takahashi et al., 2004). For example, Takahashi et al. (2004) obtained $\alpha \sim 0.5$ by a statistical analysis of the f_{Tn}/f_{T1} ratio of toroidal waves detected by the Combined Release and Radiation Effects Satellite (CRRES) spacecraft at L = 4–6 in the postnoon sector. Takahashi et al. (2015a) obtained $\alpha \sim 0$ from a detailed analysis of multiharmonic toroidal waves (n = 1–11) detected by the RBSP spacecraft during a plasmaspheric pass in the dawn sector. A statistical analysis of the f_{Tn}/f_{T3} ratios at RBSP in the noon sector (Takahashi and Denton, 2021) found $\alpha \sim 2$ at L = 4–6 in both the plasmasphere and the plasmatrough. Note that the α value does not need be the same between the electron density (n_e) and ρ because multiple ion species with different masses and charge states, which in general have different pitch angle distributions, contribute to the latter.

In magnetoseismology, multiharmonic toroidal waves are interpreted to be superposition of independent linear waves. If the waveform is nonlinearly distorted, it will lead to regularly spaced spectral peaks and will affect α estimation. It is known that nonlinearly distorted poloidal waves produce regularly spaced spectral peaks (Higuchi et al., 1986; Takahashi et al., 2011). It is not clear whether similar distortion occurs during toroidal wave events. However, statistically determined frequency spacing between toroidal harmonics is not even, and we believe that the distortion is rare. Note that the theoretical frequencies of linear toroidal waves are evenly spaced in a dipole magnetosphere if we set α = 6 in **Eq. 5** (Cummings et al., 1969; Schulz, 1996). The statistical results favoring $\alpha < 2$ are an indication that nonlinear distortion is negligible.

A statistical analysis of GOES magnetometer data (Takahashi and Denton, 2007) determined the f_{Tn}/f_{T3} ratios at geostationary orbit ($L \sim 7$) for n = 1–5 as shown in **Figures 3A,B**. This analysis indicated that the power-law model is only a rough approximation and that the ratios change with MLT. This finding led the authors to adopt the model given by **Eq. 7**. The results (**Figure 3C**) indicate that the mass density is peaked at the equator with the peak more pronounced at the later local times. The cause of the peak remains to be determined.

A follow-up study (Denton et al., 2015) using the same data as those of Denton et al. (2016) developed a model for the α index at geostationary orbit,

$$\begin{aligned}\alpha_{3\mathrm{Dmodel}} &= 2.2 + 1.3 \cdot \cos(\mathrm{MLT} \cdot 15^{\circ}) + 0.0026 \cdot \mathrm{AE} \\ &\quad \cdot \cos((\mathrm{MLT} - 0.8) \cdot 15^{\circ}) + 2.1 \cdot 10^{-5} \cdot \mathrm{AE} \cdot \mathrm{F}_{10.7} \\ &\quad - 0.010 \cdot \mathrm{F}_{10.7}, \end{aligned} \tag{8}$$

where $F_{10.7}$ is the solar extreme ultraviolet (EUV) flux index, AE is the auroral electrojet index, and MLT is in hours. **Eq. 8** modeled binned values of α within a standard deviation of 0.3.

A recent study used observationally determined MLAT of the nodes of toroidal waves to select α values (Takahashi and Denton, 2021). The results shown in **Figure 4** were obtained by a statistical analysis of the MLAT dependence of the amplitude and the phase of the δE_v and δB_ϕ components measured by RBSP over a 6-month period during which the spacecraft were located on the dayside. The panels in the top and middle rows show the results for T3–T5 waves. The panels at the bottom indicate the relationship between α and the node latitudes assuming a dipole field, and the intersects of the vertical dashed lines (observed node latitudes) and the theoretical curves give the α values. This analysis indicated $\alpha \sim 1.7$ (horizontal dashed line), not far from $\alpha \sim 2$ derived in the same study using the frequencies.

3.3 Average Ion Mass

A useful variable in magnetoseismology is the average ion mass M given by

$$M = \rho / n_e, \tag{9}$$

where ρ is derived from toroidal wave frequencies and n_e is sometimes available from examination of plasma wave spectra observed at spacecraft such as CRRES (Anderson et al., 1992) and RBSP (Kurth et al., 2015). The magnetospheric plasma is mostly composed of H^+, He^+, and O^+, which means that the mass density is expressed as

$$\rho \sim n_{H^+} m_{H^+} + n_{He^+} m_{He^+} + n_{O^+} m_{O^+}, \tag{10}$$

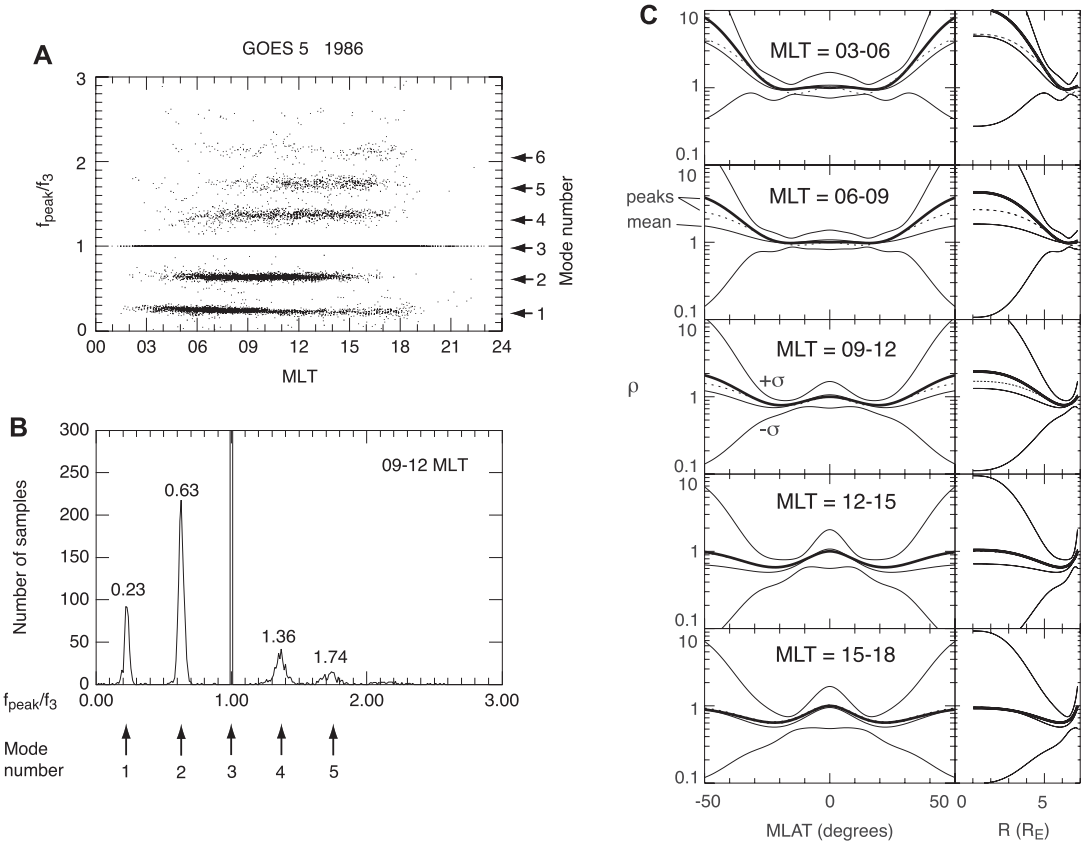

FIGURE 3 | Results of GOES magnetic field data analysis (after Takahashi and Denton, 2007). **(A)** Frequencies at the peak of B_ϕ power spectra normalized to the frequency of the third harmonic (f_3). **(B)** Histogram of the normalized frequencies for 0900–1200 MLT. **(C)** Field line mass density distribution models in different MLT sectors. The mass density on the GOES magnetic field line is plotted as a function of both MLAT **(left column)** and geocentric distance, R, to the field line **(right column)**.

with the constraint of charge neutrality

$$n_e \sim n_{H^+} + n_{He^+} + n_{O^+}, \tag{11}$$

where n_i and m_i ($i = H^+$, He^+, or O^+) are the number density and the mass of the ion species, respectively. Although we cannot determine all of the three ion number densities from the two variables ρ and n_e, we can use M to infer the ion composition. The value of M should be between 1 amu (all-H^+ plasma) and 16 amu (all-O^+ plasma). The n_{He^+}/n_{H^+} ratio being relatively stable (Craven et al., 1997; Krall et al., 2008), M is a good indicator of the variability of n_{O^+}.

Figure 5 shows the statistical properties of M samples derived using CRRES data for 1991 (solar maximum) and setting $\alpha = 0.5$ (Takahashi et al., 2006). The occurrence distribution (**Figure 5A**) is mostly confined within 1–16 amu as expected with a median value of 3 amu. Because He^+ cannot raise M to >4 amu and H^+ carries the highest number density in general, it is concluded that there were substantial amounts of O^+. In addition, M differs between the plasmasphere and the plasmatrough. **Figure 5B** shows that $M \sim 1.5$ in the plasmasphere ($n_e > 100\ cm^{-3}$) and $M \sim 3$ amu in the plasmatrough ($n_e < 20\ cm^{-3}$). Geomagnetic activity also controls M, as shown in **Figure 5C**, with higher values occurring when the ring current index Dst has larger magnitudes. O^+ ions originate from the ionosphere, and the solar EUV intensity ($F_{10.7}$) controls the density, temperature, and scale height of the O^+ ions that are transported to the magnetosphere. A study that combined ρ determined using toroidal wave frequencies and ions detected by particle experiments at geosynchronous orbit (Denton et al., 2011) showed that while ρ has maximum value at solar maximum, the electron density has minimum value, so that the n_{O^+}/n_e ratio varied between ~0.2 at solar maximum and $\sim 2 \times 10^{-3}$ at solar minimum.

This n_{O^+} variability leads to a solar cycle variation of ρ, as demonstrated in the statistical result (Takahashi et al., 2010) shown in **Figure 6**. There is a high degree of anticorrelation between $F_{10.7}$ and the T3 wave frequency (f_{T3}) at GOES, which means a positive correlation between $F_{10.7}$ (solar flux units, $10^{-22}\ m^{-2}\ Hz^{-1}$) and ρ (amu cm^{-3}) expressed as,

$$\log \rho = 0.421 + 0.00390 F_{10.7}. \tag{12}$$

This equation indicates a factor of ~4 variation of ρ over a solar cycle. Note that the GOES measurements were made at $L \sim 7$ and the ρ samples were taken from the 0600–1200 MLT sector, which means that the spacecraft was mostly in the plasmatrough. A

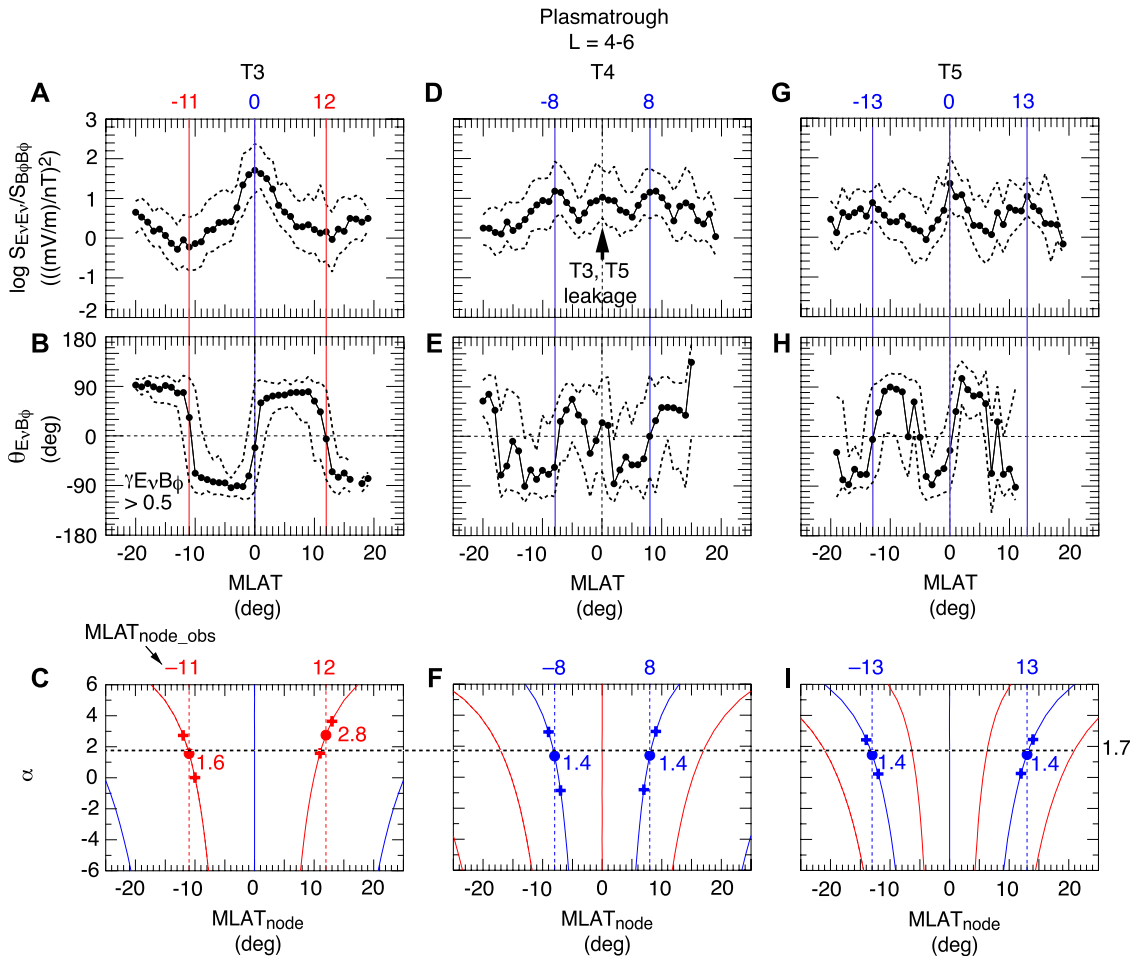

FIGURE 4 | Determination of the mass density model parameter α using the node latitudes of toroidal waves observed by RBSP (after Takahashi and Denton, 2021). **(A)** E_y to B_ϕ power ratio in the band occupied by T3 waves. The black dots are the medians, and the dashed lines indicate the upper and lower quartiles. The colored vertical lines indicate the nodes of E_y (red) and B_ϕ (blue). **(B)** E_y-B_ϕ cross phase in the T3 wave band. **(C)** Mass density model parameter α corresponding to the node latitudes of T3 waves **(D–F)** Same as **(A–C)** but for T4 waves B Same as **(A–C)** but for T5 waves.

similar study using Geotail data (Takahashi et al., 2014) found that ρ at $L \sim 11$ in the 0400–0800 MLT sector varied by a smaller factor of ~2 over a solar cycle. This difference could be accounted for by the L localization of an O^+-rich region, as described next.

3.4 *L* Dependence of Ion Composition

Spatial localization of heavy ion concentration is one of the important magnetospheric phenomena that magnetoseismology can uniquely address. We show two examples. The first example (**Figure 7**) is taken from Takahashi et al. (2008) and shows the L profile of magnetoseismic variables for a drainage plume crossing by the CRRES spacecraft. Although the n_e profile (**Figure 7B**) clearly indicates the distinction between the plasmatrough and the drainage plume, there is no change in f_{T1} (**Figure 7A**) at the trough-plume boundary. This difference is explained by a higher heavy ion concentration in the plasmatrough, which is evident in the L profiles of M (**Figure 7C**) and n_{O^+}/n_e (**Figure 7D**). **Figure 7E** shows that O^+ ions account for the majority of the mass density in the plasmatrough.

The second example (Nosé et al., 2015) is shown in **Figure 8**. **Figure 8A** shows that M is elevated as high as 8 amu over an L distance ~1 just outside the electron plasmapause located at $L \sim 3$. Another study, which combined observations of Arase and RBSP (Nosé et al., 2020), demonstrated that O^+ enhancement is limited in local time as well.

The lower two panels of **Figure 8** are included to show the difficulty in determining ρ using particle data. **Figure 8B** shows ion number densities calculated using data from the RBSP Helium, Oxygen, Proton, and Electron (HOPE) mass spectrometer (Funsten et al., 2013) in the energy range 30 eV—1 keV. Although HOPE has a lower energy limit at 1 eV, energies lower than 30 eV were excluded to avoid spacecraft charging effects. The HOPE-derived densities ($<1\ cm^{-3}$) are well below n_e ($>50\ cm^{-3}$) determined from the plasma wave spectra, meaning that the bulk of the mass density is carried by ions with energies lower than 30 eV. **Figure 8C** shows

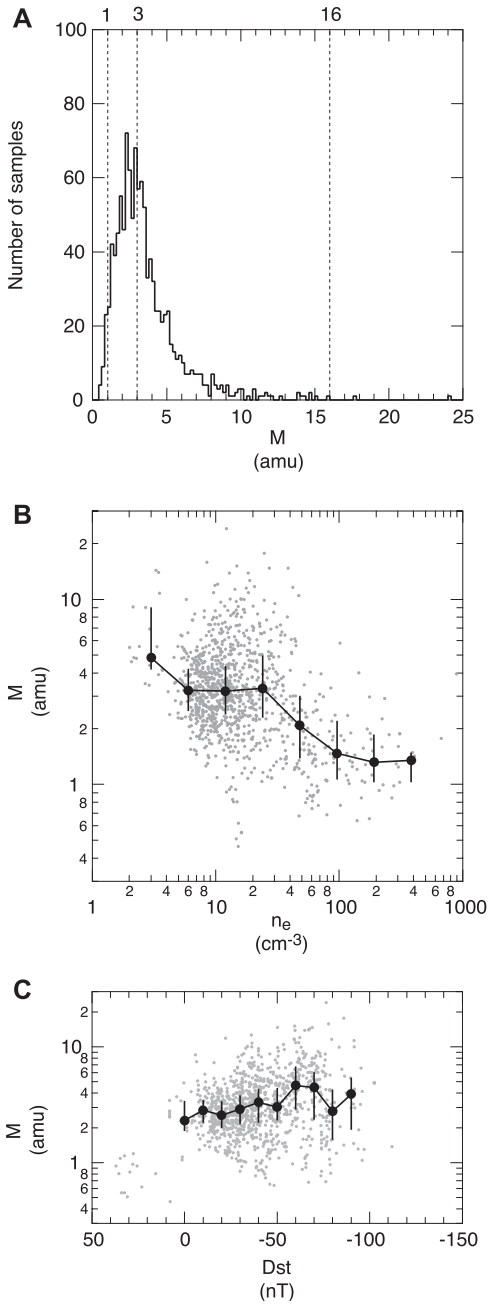

FIGURE 5 | Statistical properties of the average ion mass (*M*) obtained using CRRES data and assuming α = 0.5 (after Takahashi et al., 2006). **(A)** Occurrence distribution. **(B)**. Dependence on electron density n_e. The gray dots are individual samples, the filled black circles are medians, and the vertical bars connect the upper and lower quartiles. **(C)** Dependence on Dst.

that there is no indication of heavy ion enhancement in the HOPE data at the location where *M* is elevated. This example demonstrates that magnetoseismology captures low-energy ions that contribute to the mass density but are not measured by particle instruments.

3.5 Ion Measurements During Flow Events

An exception to the limitation of particle experiments occurs when the cold ion population is embedded in a fast bulk flow so that the population can be detected by particle instruments with the lower energy cutoff well above the thermal energy of the cold ions. Such flow events occur during Pc5 wave events in the outer magnetosphere (Chen, 2004; Hirahara et al., 2004; Lee and Angelopoulos, 2014) and provide opportunities to validate results from magnetoseismology.

Figure 9 shows a comparison of the ion mass density derived from ion flux measurements during a Pc5 wave event reported by Hirahara et al. (2004) and the ρ value estimated from the frequency of the wave (Takahashi et al., 2014). A 12-s snapshot of the ion phase space density (**Figure 9B**) exhibits three peaks at negative velocities. These peaks are attributed to the cold O^+, He^+, and, H^+ ions that are convected at the same $\delta\mathbf{E} \times \mathbf{B}$ velocity. The velocity (>100 km/s peak to peak, **Figure 9A**) is higher than the background plasma convection velocity. The peaks are separated because the ion instrument (an electrostatic analyzer) does not distinguish ion species and the velocity is calculated assuming all detected ions are protons. By assigning a correct mass value to the ions contributing to each peak, it is possible to obtain the number density and mass density for each ion at each instrument duty cycle, as shown in **Figure 9C**. The mass density summed over the three ion species is 3.9 amu cm^{-3} when averaged over the time interval shown in **Figure 9C**. This is close to the value 3.1 amu cm^{-3} that is obtained from the toroidal Pc5 wave frequency. This comparison could be extended to a statistical study using many flow events detected by Geotail (e.g., Hirahara et al., 2004) and THEMIS (e.g., Lee and Angelopoulos, 2014).

3.6 Global Models

A major goal of magnetoseismology is to develop a global model of ρ. Ideally, the model will reach a degree of maturity similar to that of existing models of the magnetic field (e.g., Sitnov et al., 2008), the electron density (e.g., Carpenter and Anderson, 1992; O'Brien and Moldwin, 2003; Archer et al., 2015; Liu et al., 2015), the He^+ density (e.g., Gallagher et al., 2021), and the density of low energy (but excluding cold) ions (e.g., Kistler and Mouikis, 2016). Magnetoseismic studies using ground magnetometer data have made significant progress in this regard. For example, Del Corpo et al. (2020) generated a global equatorial ρ model covering L = 2.3–8 and MLT = 0600–1800 using measurements by ~20 pairs of stations included in the European quasi-Meridional Magnetometer Array (EMMA) magnetometer network.

By contrast, there is much room for improvement in spacecraft data analysis. Spacecraft studies are invaluable because they provide information on the configuration of the background magnetic field and on n_e (for derivation of *M*), as we stated in **sections 2.3** and **3.3**. Although multiyear spacecraft observations cover the entire dayside magnetosphere (see **Figure 2**) as well as a large portion of the magnetotail, statistical analysis of the data has been limited. Notable exceptions are GOES (e.g., Takahashi et al., 2010) and Geotail

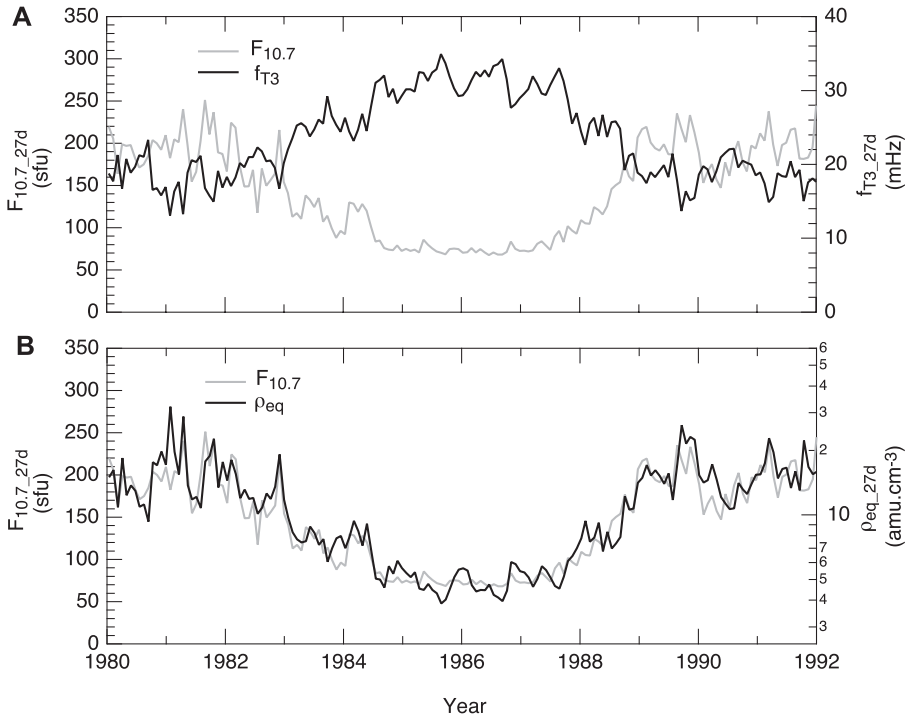

FIGURE 6 | Results of a magnetoseismic study using GOES magnetometer data (after Takahashi et al., 2010). **(A)** Comparison of the $F_{10.7}$ index and the frequency of third harmonic toroidal waves at GOES over a solar cycle. The data are 27-day averages. **(B)** Comparison of the $F_{10.7}$ index and the mass density estimated from the wave frequency.

(Takahashi et al., 2014) studies covering a solar cycle and an AMPTE/CCE study covering ~4 years (Takahashi et al., 2002; Min et al., 2013).

Figure 10 illustrates the potential of spacecraft data for the global model. **Figure 10A** shows the rate of detection of fundamental toroidal waves obtained in a study (Takahashi et al., 2015b) that used ion bulk velocity but did not convert the wave frequency to ρ. The waves are detected at a high rate on the dayside from $L = 6$ to $L = 12$ (spacecraft apogee). The rate becomes low on the nightside, but toroidal waves are still detected there along with Pi2 pulsations, most often after substorm onsets (Takahashi et al., 1988; Takahashi et al., 2018) and when ULF waves generated in the ion foreshock penetrate deep into the magnetosphere (Takahashi et al., 2020). The presence of substorm-related toroidal waves is evident in **Figure 10B** as a region of large δV_ϕ amplitudes in the premidnight sector.

Figure 11 shows a magnetoseismic study using toroidal waves detected by the Arase spacecraft in the midnight sector away from the magnetic equator. The waves were detected after Pi2 onsets on the ground. An RBSP spacecraft located near the magnetic equator detected compressional oscillations, which can be cavity mode oscillations. Because the AE index had moderate values (<200 nT) during the wave event in this example, we expect that nightside Pi2 waves and toroidal waves are commonly excited and can be easily detected off the magnetic equator in association with small substorms or other minor disturbances in the magnetotail. Because it appears difficult to determine nightside toroidal wave frequencies with ground magnetometers (Takahashi et al., 2020), we expect that a model derived using spacecraft data will perform better on the nightside than models derived using only ground data.

4 DISCUSSION

We discuss limitations, unresolved issues, and areas in need of improvements in magnetoseismic studies.

4.1 Ionospheric Boundary Condition

To relate observed f_{Tn} to ρ, standing wave equations (e.g., **Eq. 3**) are solved usually assuming perfect reflection, corresponding to infinitely high height-integrated Pedersen conductivity Σ_P, at a fixed ionospheric altitude. In reality, the ionosphere has a finite thickness and the conductivity is finite. We discuss whether the assumption is appropriate.

The assumption of a thin ionosphere is justified because the thickness of the ionosphere (~300 km) is much shorter than the hemispheric length (>15,000 km) of magnetic field lines at $L >$ 2.5, where reliable measurements of wave frequency can be made by spacecraft on low-inclination elliptical orbits (Takahashi and Denton, 2021). On these field lines, the Alfvén wave velocity at the ionospheric altitude is usually higher than near the equator, making the Alfvén wave travel time through the ionosphere much smaller than that through the region above the ionosphere. This means that the details of wave propagation through the ionosphere do not affect f_{Tn} in any significant way.

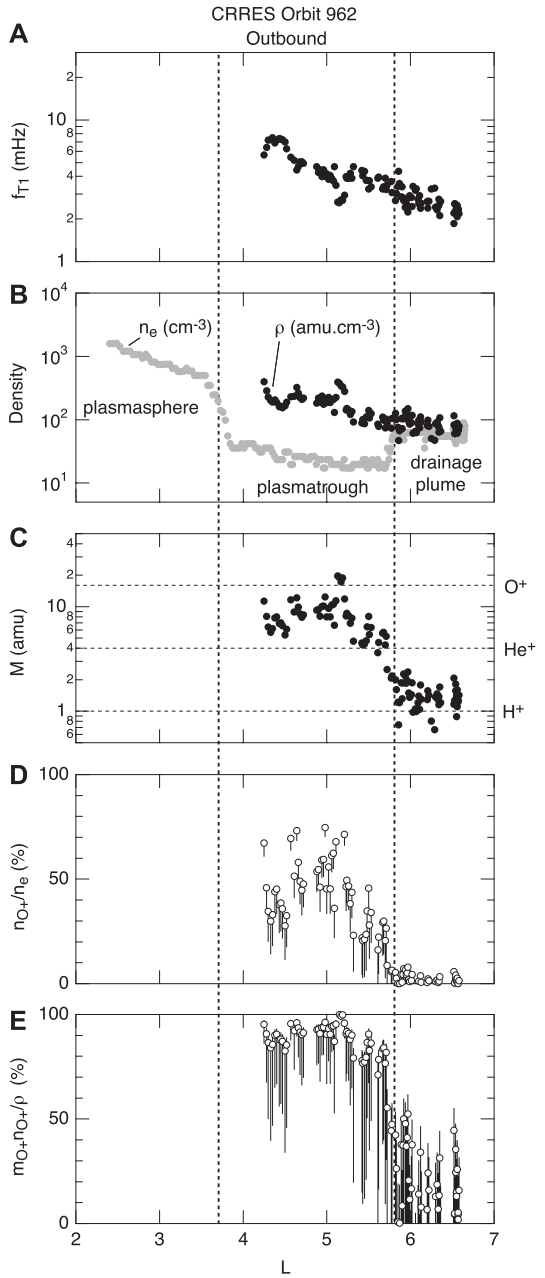

FIGURE 7 | Magnetoseismic variables plotted versus L for a drainage plume crossing by CRRES (after Takahashi et al., 2008). **(A)** Fundamental toroidal wave frequency. **(B)** Mass density and electron density. **(C)** Average ion mass. **(D)** Oxygen number density normalized to the electron density. The vertical bars indicate the possible range assuming (H^+-O^+) plasma and (He^+-O^+) plasma, and the open circles indicate the assumption of a fixed n_{He^+}/n_e ratio 0.07. **(E)** Mass density carried by O^+ normalized to ρ.

There are questions about the Σ_P. This conductivity, which controls the damping rate of toroidal waves, depends on solar illumination and particle precipitation from the magnetosphere, both of which are a function of latitude and local time as well. According to numerical studies of the Σ_P dependence of f_{Tn} (e.g., Newton et al., 1978), the frequency is very close to that of perfectly reflected waves when Σ_P is higher than a critical value (denoted Σ_{P0}) corresponding to impedance matching between the ionosphere and the waves. At locations where solar illumination is low or zero, the conductivity may become lower than Σ_{P0}, leading to strong damping of the waves or transition of the waves to free-end modes with lower f_{Tn} values (Newton et al., 1978). If one end of a field line is anchored to the sunlit part of the ionosphere and the other is anchored to the dark part, theory predicts that the usual half-wave T1 modes turn to quarter-wave modes (Allan and Knox, 1979). Quarter-wave modes at $L \sim 3$ have been detected at the dawn terminator by ground magnetometers (Obana et al., 2008). If the quarter-wave and half-wave modes are not distinguished, it will lead to a serious error in ρ. Investigation of the quarter-wave modes in space remains to be done.

Yet nightside multiharmonic toroidal waves are readily detected by spacecraft and exhibit properties consistent with high ionospheric reflection even when observed within the plasmasphere (Takahashi et al., 2020), where precipitation is not expected to be high enough to maintain high Σ_P according to empirical ionospheric density models (e.g., Wallis and Budzinski, 1981). This poses an interesting question of what elevates the ionospheric conductivity and whether high

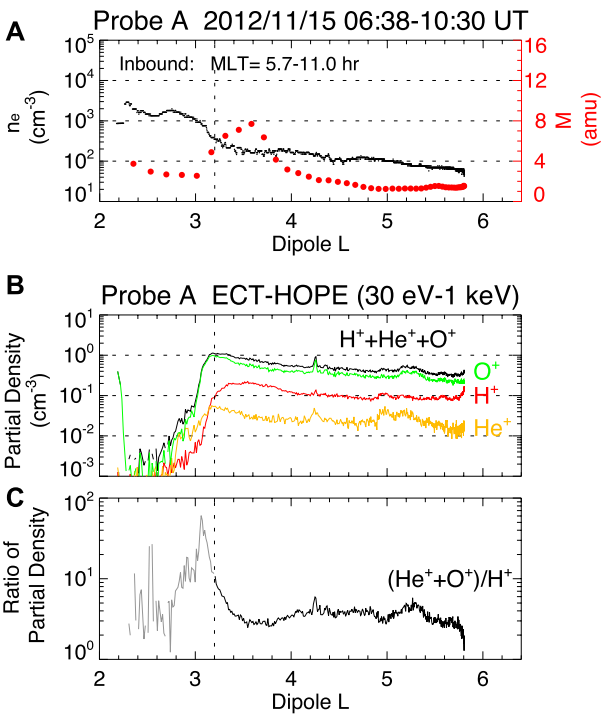

FIGURE 8 | Localized heavy ion density enhancement reported in an RBSP study (after Nosé et al., 2015). **(A)** L profile of the electron density (black curve) and the average ion mass (red dots). **(B)** Number density of the H^+, He^+, and O^+ ions obtained by taking the moment of ion fluxes measured by the HOPE instrument in the energy range 30 eV–1 keV. **(C)** Number density ratio between the heavy ions (He^+ and O^+) and H^+, calculated using the data shown in panel **(B)**.

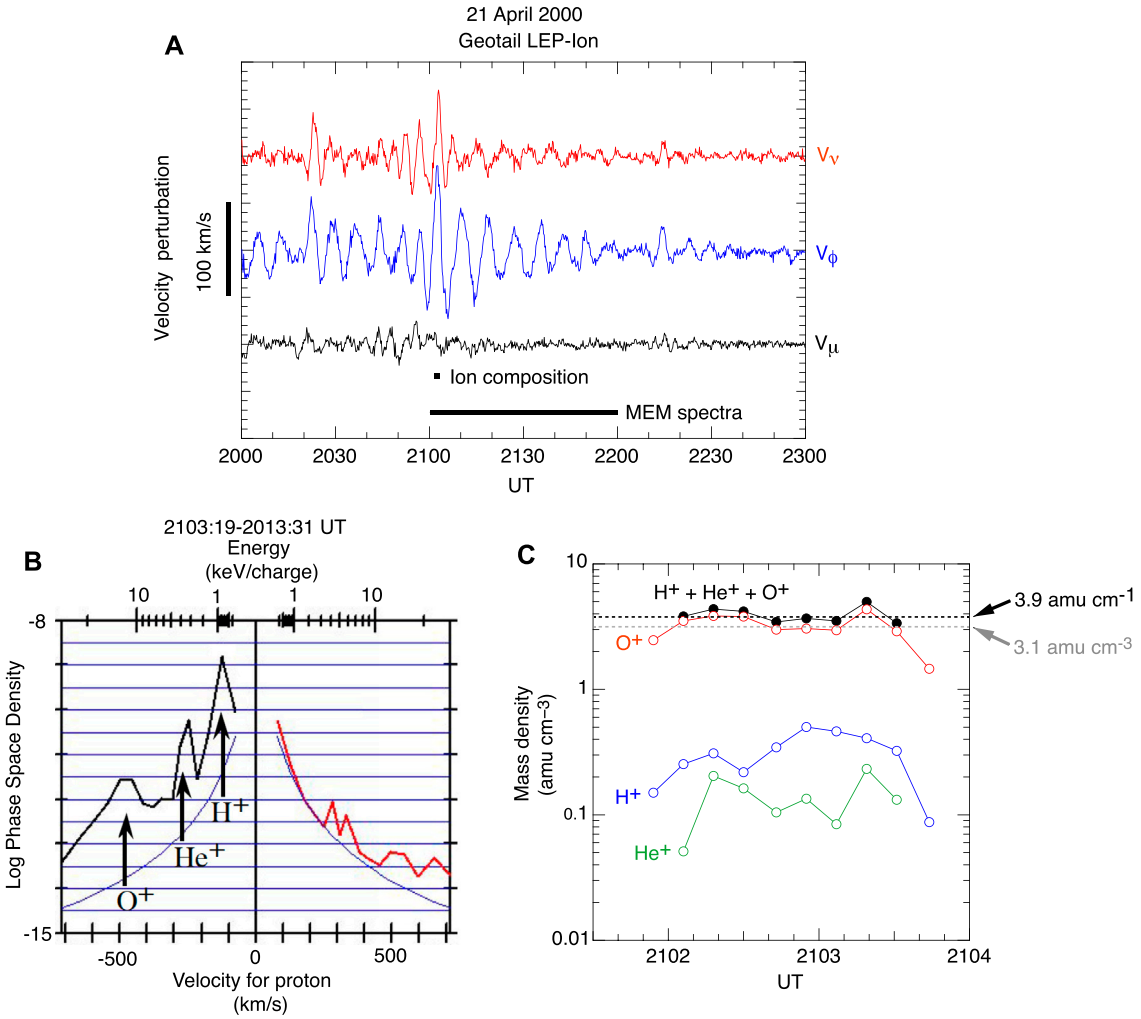

FIGURE 9 | Mass density analysis using Geotail data. **(A)** Ion bulk velocity data indicating a Pc5 fundamental toroidal wave event (after Takahashi et al., 2014). The frequency of the V_ϕ oscillation is 2.2 mHz according to the V_ϕ power spectrum computed from the 1-h data segment labeled "MEM spectra." **(B)** Ion phase space density snapshot obtained using ion fluxes measured in a 12-s interval during the wave event (after Hirahara et al., 2004). **(C)** Partial and total mass densities obtained using the phase space density for the 2.5-min interval labeled "Ion composition" in panel **(A)** (after Takahashi et al., 2014). The black and gray horizontal dashed lines indicate the mass densities derived from the ion data and from the Pc5 wave frequency, respectively.

conductivity occurs commonly to make nightside magnetoseismology possible. One interesting possibility is that ULF waves themselves enhance ionospheric conductivity through modulation of electron precipitation (Jaynes et al., 2015). Wang et al. (2020) reported strong modulation of the conductivity by storm-time compressional Pc5 waves. Whether similar precipitation modulations occur during less geomagnetically active periods remains to be understood.

4.2 Challenges in Spacecraft Data Analysis

Magnetoseismology based on spacecraft data poses challenges that are not encountered with ground magnetometer data. First, wave frequency and amplitude seen from a moving spacecraft change continuously even if the waves do not have intrinsic temporal variations. The L dependence is particularly important. For example, f_{T1} within the plasmasphere decreases from ~20 mHz at $L \sim 2.5$ to ~ 5 mHz at $L \sim 4$ (Takahashi and Anderson, 1992; Takahashi and Denton, 2021). As spacecraft such as THEMIS and RBSP move rapidly in the radial direction in the $L < 4$ region, it is necessary to choose a proper time window for spectral analysis so that the spatial variation of the frequency is resolved. The studies cited in this paper used data windows of a fixed length, although Min et al. (2013) introduced a variable data sampling rate to handle the spatial variation of f_{Tn} at $L > 4$.

The inferred ρ is proportional to the inverse square of the observed Alfvén frequency (**Eq. 4**), and we usually consider that frequency to be the largest source of error. The uncertainty of the frequency can be determined from the frequency spectrum (Denton et al., 2001). Other sources of error are the magnetic field at the spacecraft location and the field line dependence of the magnetic field and mass density. In most cases, the magnetic field at the spacecraft location is known. In the best case, the

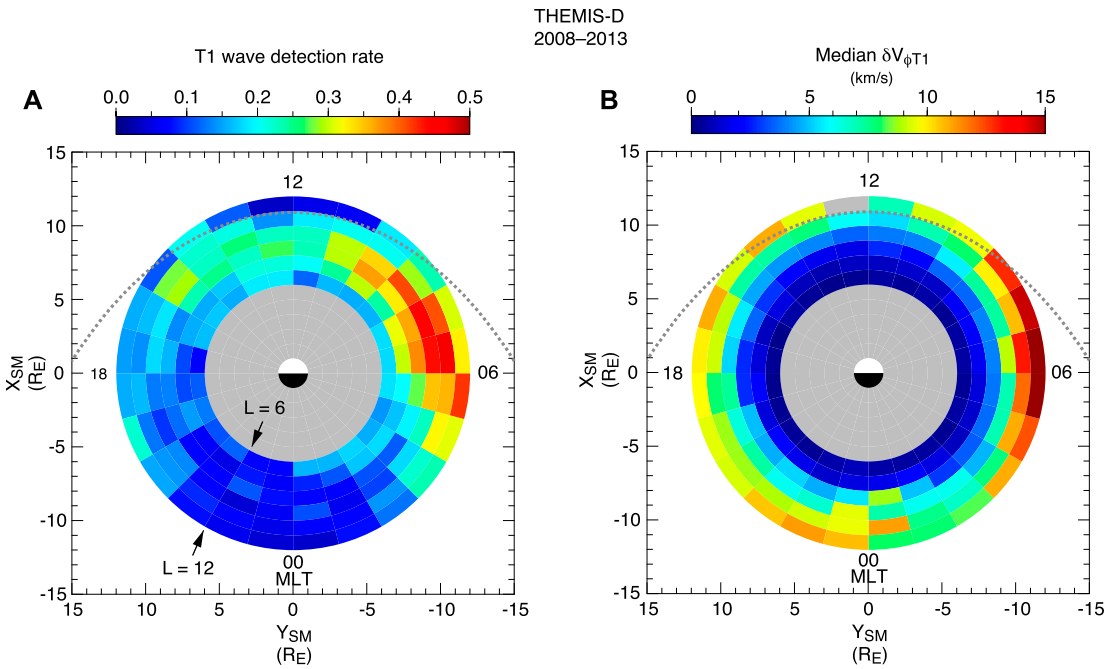

FIGURE 10 | *L*-MLT maps of fundamental toroidal waves detected in the ion bulk velocity measured by THEMIS-D (after Takahashi et al., 2015b). The dotted line is a model magnetopause. **(A)** Rate of detection. **(B)** Median amplitude.

measurement is near the magnetic equator, which is the region that most greatly affects the Alfvén frequency. The field line dependence of the magnetic field and mass density does have some effect on the inferred value of the mass density, but that effect is usually smaller than the uncertainty associated with the frequency. If, on the other hand, the field line is mapped from low-Earth orbit or the ground, or if the spacecraft is in the outer magnetosphere (particularly at L greater than 8), there can be significant uncertainties for the magnetic field and/or field line mapping (Takahashi et al., 2006; Takahashi et al., 2010).

Another issue related to spacecraft motion is frequency shift. The shift occurs because toroidal waves have a finite L width (FLR width) within which the wave phase changes by 180°. In regions where the wave frequency decreases with L (e.g., the plasmasphere), the wave phase is delayed from lower L to higher L. This spatial phase structure leads to frequency downshift (upshift) at spacecraft moving to higher (lower) L by an amount given by

$$\Delta f = \frac{v_L}{2\pi\varepsilon}, \tag{13}$$

where v_L is the equatorial L-crossing speed and ε is the equatorial semiwidth of FLR (Vellante et al., 2004; Heilig et al., 2013). The frequency shift is found to be significant (20–25 mHz for T1 waves at $L < 2.4$) when observations are compared between the polar-orbiting Challenging Minisatellite Payload (CHAMP) spacecraft and ground magnetometers (Heilig et al., 2013).

At equatorial-orbiting spacecraft, Δf is smaller but may not be negligible. As an example, we evaluate Δf at RBSP. For the spacecraft, v_L has a peak value of ~ 5 km/s at L = 1.5, decreases to ~3 km/s at L = 3, and becomes zero at $L \sim 6$ (apogee). If we assume ε = 200 km, which was the case for a 14 mHz toroidal wave at $L \sim 5$ (Takahashi et al., 2015a), we get $\Delta f \sim 2$ mHz at L = 3. This frequency shift is ~ 10% of f_{T1} (~20 mHz) at L = 3 (Takahashi and Anderson, 1992) and translates to a ρ error of ~ 20% (see **Eq. 4**). This error can explain why M derived from f_{Tn} observed on outbound RBSP passes is higher at $L < 3$ (large v_L) than at $L > 3$ (small v_L) (Vellante et al., 2021). Evaluation of ε at various radial distances and local times is necessary to improve our understanding of Δf.

Finally, fully automated methods are lacking to determine f_{Tn} in space. As a result, only a small fraction of satellite data that are potentially useful has been used in magnetoseismic studies. The procedure is the easiest for T1 waves detected in the outer magnetosphere using plasma bulk flow data (Takahashi et al., 2014; Takahashi et al.,2016). Regular oscillations in the azimuthal component of the velocity are almost always associated with T1 waves, and not much manual work is required to distinguish them from other waves. Processing magnetic field data from geostationary orbits is also relatively easy with the spacecraft staying at a fixed L leading to a stable appearance of the spectral intensity of each harmonic. Processing data from elliptically orbiting spacecraft is the most difficult because of the rapid change of spacecraft radial distance, crossing of the nodes, and the presence of waves other than toroidal waves.

It appears that at some stage we need to introduce a technique such as neural network analysis to automate the interpretation of the wave spectra. The main required capability of the technique is to reject spectral peaks that do not result from toroidal waves. In this regard, we note that the quality of **E** and **B** data from

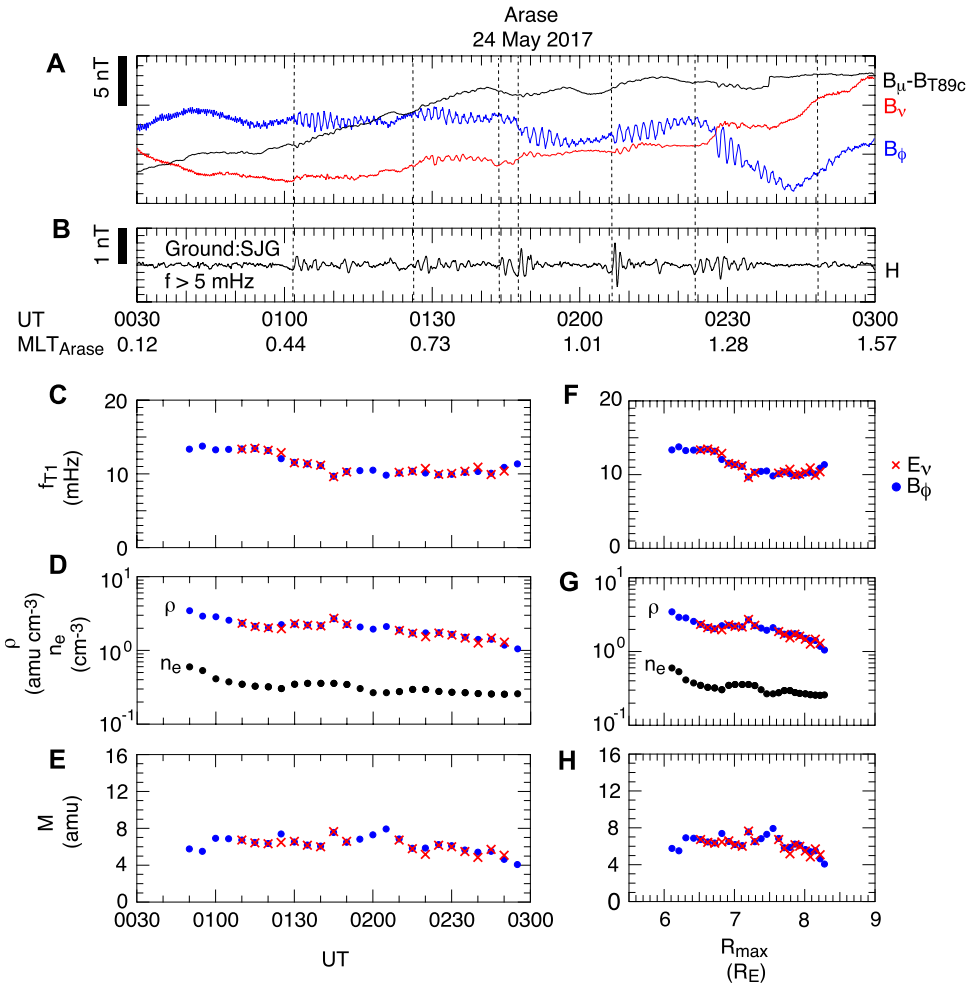

FIGURE 11 | Magnetoseismic analysis of toroidal waves detected by the Arase spacecraft in the midnight sector (after Takahashi et al., 2018). **(A)** Magnetic field components in a magnetic-field-aligned coordinate system based on the T89c magnetic field model (Tsyganenko, 1989). Fundamental toroidal waves are visible in the B_ϕ component. **(B)** High-pass-filtered ground magnetic field *H* component at San Juan. The dashed vertical lines indicate Pi2 onsets. **(C)** Frequency of the fundamental toroidal waves. The color indicates the source field component. **(D)** Mass density derived from the wave frequency and the electron density determined from plasma wave spectra. **(E)** Average ion mass. **(F–H)** Same quantities as in **(C–E)** but plotted as a function of the maximum geocentric distance to the model field line.

spacecraft depends on the mode of sensor operation, location and attitude of the spacecraft, and the plasma environment (for **E**). In addition, spacecraft spin and nutation of sensor booms introduce noise lines at fixed frequencies but with varying amplitudes. Some of the spectral peaks caused by these artifacts are predictable, but they can overlap f_{Tn} as spacecraft move in *L*. Also, there are unpredictable peaks that originate from ULF waves that are not toroidal waves. An automated method to determine electron density has been developed by applying a neural-network algorithm to plasma wave spectrograms (Zhelavskaya et al., 2016), and we may design a similar algorithm for f_{Tn}.

4.3 Modeling

Although significant progress has been made modeling the mass density and field line dependence at geostationary orbit (e.g., Denton et al., 2015; Denton et al.,2016), further work needs to be done to develop an accurate radially dependent model. Neural network analysis might also be helpful here, as it has been for modeling electron density (Chu et al., 2017).

Another need is for event-specific mass density field line dependence. With the possible exception of the event studied by Denton et al. (2009), which had a particularly accurate set of frequencies, significant uncertainty in the observed Alfvén frequencies has precluded an accurate determination of event-specific field line dependence. So, most studies have been statistical (e.g., Denton et al., 2006, Denton et al., 2015; Takahashi and Denton, 2007). Perhaps the mode structure technique described in subsection 3.2 will enable event-specific determination of the field line dependence, but that is yet to be shown.

Finally, we note that magnetoseismology belongs to a family of techniques to probe the magnetospheric plasma structure without using *in situ* particle measurements. Other techniques include EUV imaging of the plasmasphere (Sandel et al., 2003), energetic

neutral atom remote (ENA) sensing of energetic ions (Roelof et al., 1985; Brandt et al., 2005), estimation of n_e using whistler waves (Carpenter and Smith, 1964; Park, 1974), spacecraft potential (Pedersen et al., 1984; Archer et al., 2015), or plasma wave spectra (upper hybrid resonance) (Mosier et al., 1973; Moldwin et al., 2002; Thomas et al., 2021). These indirect techniques are complementary to each other. For example, the global imaging techniques are capable of taking snapshots of plasma structures, which cannot be obtained using the magnetoseismic or n_e techniques unless we have a large number of measurement points. The magnetoseismic and n_e techniques provide the total densities, whereas ENA images provide information on the density of energetic ions (>10 keV). Improvement of magnetoseismic techniques and associated datasets is much desired to enhance the synergy of different density-related techniques.

5 CONCLUSION

Toroidal waves detected by spacecraft are a valuable resource from which the magnetospheric mass density (ρ) is estimated. Some spacecraft also provide electron density (n_e) data, and from the average ion mass M ($= \rho/n_e$), we can infer the ion composition and the presence of heavy ions (i.e., O^+). We reviewed progress made mainly in the past decade. The basic techniques to identify wave frequencies and convert them to the mass density are well established. The challenge is to apply the techniques to data from various spacecraft in an efficient way to develop global ρ and M models that have dependencies on position, solar activity, and solar wind and geomagnetic conditions.

AUTHOR CONTRIBUTIONS

KT and RD jointly prepared this review paper, based mostly on their own research published in scientific journals.

FUNDING

National Science Foundation, Award Number 1840970. National Aeronautics and Space Administration, Award Number 80NSSC20K1446 and Award Number 80NSSC21K0453.

ACKNOWLEDGMENTS

This paper is an expanded version of a presentation made at the 2020 meeting entitled "The Impact of the Cold Plasma Populations in the Earth's Magnetosphere." The authors thank Gian Luca Delzanno and Joseph E. Borovsky for organizing the meeting and encouraging preparation of this manuscript.

REFERENCES

Allan, W., and Knox, F. B. (1979). The Effect of Finite Ionosphere Conductivities on Axisymmetric Toroidal Alfvén Wave Resonances. *Planet. Space Sci.* 27, 939–950. doi:10.1016/0032-0633(79)90024-2

Allan, W., White, S. P., and Poulter, E. M. (1986). Impulse-excited Hydromagnetic Cavity and Field-Line Resonances in the Magnetosphere. *Planet. Space Sci.* 34, 371–385. doi:10.1016/0032-0633(86)90144-3

Anderson, B. J., Engebretson, M. J., Rounds, S. P., Zanetti, L. J., and Potemra, T. A. (1990). A Statistical Study of Pc 3–5 Pulsations Observed by the AMPTE/CCE Magnetic fields experiment, 1. Occurrence Distributions. *J. Geophys. Res.* 95, 10495–10523. doi:10.1029/JA095iA07p10495

Anderson, R. R., Gurnett, D. A., and Odem, D. L. (1992). The CRRES Plasma Wave experiment. *J. Spacecraft Rockets* 29, 570–574. doi:10.2514/3.25501

Angerami, J. J., and Carpenter, D. L. (1966). Whistler Studies of the Plasmapause in the Magnetosphere: 2. Electron Density and Total Tube Electron Content Near the Knee in Magnetospheric Ionization. *J. Geophys. Res.* 71, 711–725. doi:10.1029/JZ071i003p00711

Archer, M. O., Hartinger, M. D., Walsh, B. M., Plaschke, F., and Angelopoulos, V. (2015). Frequency Variability of Standing Alfvén Waves Excited by Fast Mode Resonances in the Outer Magnetosphere. *Geophys. Res. Lett.* 42, 10150–10159. doi:10.1002/2015gl066683

Arthur, C. W., and McPherron, R. L. (1981). The Statistical Character of Pc 4 Magnetic Pulsations at Synchronous Orbit. *J. Geophys. Res.* 86, 1325. doi:10.1029/JA086iA03p01325

Brandt, P. C., Mitchell, D. G., Roelof, E. C., Krimigis, S. M., Paranicas, C. P., Mauk, B. H., et al. (2005). ENA Imaging: Seeing the Invisible. *Johns Hopkins APL Tech. Dig.* 26, 143–155.

Carpenter, D. L., and Anderson, R. R. (1992). An ISEE/whistler Model of Equatorial Electron Density in the Magnetosphere. *J. Geophys. Res. Space Phys.* 97, 1097–1108. doi:10.1029/91ja01548

Carpenter, D. L., and Smith, R. L. (1964). Whistler Measurements of Electron Density in the Magnetosphere. *Rev. Geophys.* 2. doi:10.1029/RG002i003p00415

Chen, L., and Hasegawa, A. (1974). A Theory of Long-Period Magnetic Pulsations: 1. Steady State Excitation of Field Line Resonance. *J. Geophys. Res.* 79, 1024–1032. doi:10.1029/JA079i007p01024

Chen, S. H. (2004). Dayside Flow Bursts in the Earth's Outer Magnetosphere. *J. Geophys. Res.* 109. doi:10.1029/2003ja010007

Chi, P. J., and Russell, C. T. (2005). Travel-time Magnetoseismology: Magnetospheric Sounding by Timing the Tremors in Space. *Geophys. Res. Lett.* 32, L18108. doi:10.1029/2005gl023441

Chu, X., Bortnik, J., Li, W., Ma, Q., Denton, R., Yue, C., et al. (2017). A Neural Network Model of Three-Dimensional Dynamic Electron Density in the Inner Magnetosphere. *J. Geophys. Res. Space Phys.* 122, 9183–9197. doi:10.1002/2017ja024464

Claudepierre, S. G., Hudson, M. K., Lotko, W., Lyon, J. G., and Denton, R. E. (2010). Solar Wind Driving of Magnetospheric ULF Waves: Field Line Resonances Driven by Dynamic Pressure Fluctuations. *J. Geophys. Res. Space Phys.* 115. doi:10.1029/2010ja015399

Craven, P. D., Gallagher, D. L., and Comfort, R. H. (1997). Relative Concentration of He^+ in the Inner Magnetosphere as Observed by the DE 1 Retarding Ion Mass Spectrometer. *J. Geophys. Res. Space Phys.* 102, 2279–2289. doi:10.1029/96ja02176

Cummings, W. D., O'Sullivan, R. J., and Coleman, P. J. (1969). Standing Alfvén Waves in the Magnetosphere. *J. Geophys. Res.* 74, 778–793. doi:10.1029/JA074i003p00778

Del Corpo, A., Vellante, M., Heilig, B., Pietropaolo, E., Reda, J., and Lichtenberger, J. (2020). An Empirical Model for the Dayside Magnetospheric Plasma Mass Density Derived from EMMA Magnetometer Network Observations. *J. Geophys. Res. Space Phys.* 125. doi:10.1029/2019ja027381

Denton, R. E., Décréau, P., Engebretson, M. J., Darrouzet, F., Posch, J. L., Mouikis, C., et al. (2009). Field Line Distribution of Density at L = 4.8 Inferred from Observations by CLUSTER. *Ann. Geophysicae* 27, 705–724. doi:10.5194/angeo-27-705-2009

Denton, R. E., Lessard, M. R., Anderson, R., Miftakhova, E. G., and Hughes, J. W. (2001). Determining the Mass Density along Magnetic Field Lines from

Toroidal Eigenfrequencies: Polynomial Expansion Applied to CRRES Data. *J. Geophys. Res. Space Phys.* 106, 29915–29924. doi:10.1029/2001ja000204

Denton, R. E. (2006). "Magneto-seismology Using Spacecraft Observations," in *Magnetospheric ULF Waves: Synthesis and New Directions*. Editors K. Takahashi, P. J. Chi, R. E. Denton, and R. L. Lysak (Washington DC: AGU). 307–317.

Denton, R. E. (2003). Radial Localization of Magnetospheric Guided Poloidal Pc 4–5 Waves. *J. Geophys. Res.* 108, 1105. doi:10.1029/2002ja009679

Denton, R. E., Takahashi, K., Amoh, J., and Singer, H. J. (2016). Mass Density at Geostationary Orbit and Apparent Mass Refilling. *J. Geophys. Res. Space Phys.* 121, 2962–2975. doi:10.1002/2015ja022167

Denton, R. E., Takahashi, K., Anderson, R. R., and Wuest, M. P. (2004). Magnetospheric Toroidal Alfvén Wave Harmonics and the Field Line Distribution of Mass Density. *J. Geophys. Res.* 109, A06202. doi:10.1029/2003ja010201

Denton, R. E., Takahashi, K., Galkin, I. A., Nsumei, P. A., Huang, X., Reinisch, B. W., et al. (2006). Distribution of Density along Magnetospheric Field Lines. *J. Geophys. Res.* 111, A04213. doi:10.1029/2005ja011414

Denton, R. E., Takahashi, K., Lee, J., Zeitler, C. K., Wimer, N. T., Litscher, L. E., et al. (2015). Field Line Distribution of Mass Density at Geostationary Orbit. *J. Geophys. Res. Space Phys.* 120, 4409–4422. doi:10.1002/2014ja020810

Denton, R. E., Thomsen, M. F., Takahashi, K., Anderson, R. R., and Singer, H. J. (2011). Solar Cycle Dependence of Bulk Ion Composition at Geosynchronous Orbit. *J. Geophys. Res. Space Phys.* 116, A03212. doi:10.1029/2010ja016027

Dungey, D. W. (1954). *Electrodynamics of the Outer Atmosphere*. PA: Scientific Report, Ionosphere Research Laboratory, Pennsylvania State University, University Park, 69.

Funsten, H. O., Skoug, R. M., Guthrie, A. A., MacDonald, E. A., Baldonado, J. R., Harper, R. W., et al. (2013). Helium, Oxygen, Proton, and Electron (HOPE) Mass Spectrometer for the Radiation Belt Storm Probes mission. *Space Sci. Rev.* 179, 423–484. doi:10.1007/s11214-013-9968-7

Gallagher, D. L., Comfort, R. H., Katus, R. M., Sandel, B. R., Fung, S. F., and Adrian, M. L. (2021). The Breathing Plasmasphere: Erosion and Refilling. *J. Geophys. Res. Space Phys.* 126. doi:10.1029/2020ja028727

Heilig, B., Sutcliffe, P. R., Ndiitwani, D. C., and Collier, A. B. (2013). Statistical Study of Geomagnetic Field Line Resonances Observed by CHAMP and on the Ground. *J. Geophys. Res. Space Phys.* 118, 1934–1947. doi:10.1002/jgra.50215

Higuchi, T., Kokubun, S., and Ohtani, S. (1986). Harmonic Structure of Compressional Pc5 Pulsations at Synchronous Orbit. *Geophys. Res. Lett.* 13, 1101–1104. doi:10.1029/GL013i011p01101

Hirahara, M., Seki, K., Saito, Y., and Mukai, T. (2004). Periodic Emergence of Multicomposition Cold Ions Modulated by Geomagnetic Field Line Oscillations in the Near-Earth Magnetosphere. *J. Geophys. Res. Space Phys.* 109, A0321. doi:10.1029/2003ja010141

Hughes, W. J., and Southwood, D. J. (1976). The Screening of Micropulsation Signals by the Atmosphere and Ionosphere. *J. Geophys. Res.* 81, 3234–3240. doi:10.1029/JA081i019p03234

Jaynes, A. N., Lessard, M. R., Takahashi, K., Ali, A. F., Malaspina, D. M., Michell, R. G., et al. (2015). Correlated Pc4–5 ULF Waves, Whistler-Mode Chorus, and Pulsating aurora Observed by the Van Allen Probes and Ground-Based Systems. *J. Geophys. Res. Space Phys.* 120, 8749–8761. doi:10.1002/2015ja021380

Kistler, L. M., and Mouikis, C. G. (2016). The Inner Magnetosphere Ion Composition and Local Time Distribution over a Solar Cycle. *J. Geophys. Res. Space Phys.* 121, 2009–2032. doi:10.1002/2015ja021883

Krall, J., Huba, J. D., and Fedder, J. A. (2008). Simulation of Field-Aligned H^+ and He^+ Dynamics during Late-Stage Plasmasphere Refilling. *Ann. Geophysicae* 26, 1507–1516. doi:10.5194/angeo-26-1507-2008

Kurth, W. S., De Pascuale, S., Faden, J. B., Kletzing, C. A., Hospodarsky, G. B., Thaller, S., et al. (2015). Electron Densities Inferred from Plasma Wave Spectra Obtained by the Waves Instrument on Van Allen Probes. *J. Geophys. Res. Space Phys.* 120, 904–914. doi:10.1002/2014JA020857

Lee, D.-H., and Lysak, R. L. (1989). Magnetospheric ULF Wave Coupling in the Dipole Model: The Impulsive Excitation. *J. Geophys. Res.* 94, 17097–17103. doi:10.1029/JA094iA12p17097

Lee, D. H., Lysak, R. L., and Song, Y. (2000). Field Line Resonances in a Nonaxisymmetric Magnetic Field. *J. Geophys. Res. Space Phys.* 105, 10703–10711. doi:10.1029/1999ja000295

Lee, J. H., and Angelopoulos, V. (2014). On the Presence and Properties of Cold Ions Near Earth's Equatorial Magnetosphere. *J. Geophys. Res. Space Phys.* 119, 1749–1770. doi:10.1002/2013ja019305

Liu, W., Cao, J. B., Li, X., Sarris, T. E., Zong, Q. G., Hartinger, M., et al. (2013). Poloidal ULF Wave Observed in the Plasmasphere Boundary Layer. *J. Geophys. Res. Space Phys.* 118, 4298–4307. doi:10.1002/jgra.50427

Liu, X., Liu, W., Cao, J. B., Fu, H. S., Yu, J., and Li, X. (2015). Dynamic Plasmapause Model Based on THEMIS Measurements. *J. Geophys. Res. Space Phys.* 120, 10543–10556. doi:10.1002/2015ja021801

Marin, J., Pilipenko, V., Kozyreva, O., Stepanova, M., Engebretson, M., Vega, P., et al. (2014). Global Pc5 Pulsations during strong Magnetic Storms: Excitation Mechanisms and Equatorward Expansion. *Ann. Geophysicae* 32, 319–331. doi:10.5194/angeo-32-319-2014

Menk, F. W., and Waters, C. L. (2013). *Magnetoseismology*. Weinheim: Wiley VCH. doi:10.1002/9783527652051

Min, K., Bortnik, J., Denton, R. E., Takahashi, K., Lee, J., and Singer, H. J. (2013). Quiet Time Equatorial Mass Density Distribution Derived from AMPTE/CCE and GOES Using the Magnetoseismology Technique. *J. Geophys. Res. Space Phys.* 118, 6090–6105. doi:10.1002/jgra.50563

Moldwin, M. B., Downward, L., Rassoul, H. K., Amin, R., and Anderson, R. R. (2002). A New Model of the Location of the Plasmapause: CRRES Results. *J. Geophys. Res.* 107, 1339. doi:10.1029/2001ja009211

Mosier, S. R., Kaiser, M. L., and Brown, L. W. (1973). Observations of Noise Bands Associated with the Upper Hybrid Resonance by the Imp 6 Radio Astronomy Experiment. *J. Geophys. Res.* 78, 1673–1679. doi:10.1029/JA078i010p01673

Newton, R. S., Southwood, D. J., and Hughes, W. J. (1978). Damping of Geomagnetic Pulsations by the Ionosphere. *Planet. Space Sci.* 26, 201–209. doi:10.1016/0032-0633(78)90085-5

Nosé, M., Matsuoka, A., Kumamoto, A., Kasahara, Y., Teramoto, M., Kurita, S., et al. (2020). Oxygen Torus and its Coincidence with EMIC Wave in the Deep Inner Magnetosphere: Van Allen Probe B and Arase Observations. *Earth Planets Space* 72, 111. doi:10.1186/s40623-020-01235-w

Nosé, M., Oimatsu, S., Keika, K., Kletzing, C. A., Kurth, W. S., Pascuale, S. D., et al. (2015). Formation of the Oxygen Torus in the Inner Magnetosphere: Van Allen Probes Observations. *J. Geophys. Res. Space Phys.* 120, 1182–1196. doi:10.1002/2014ja020593

Obana, Y., Menk, F. W., Sciffer, M. D., and Waters, C. L. (2008). Quarter-wave Modes of Standing Alfvén Waves Detected by Cross-phase Analysis. *J. Geophys. Res. Space Phys.* 113. doi:10.1029/2007ja012917

Obayashi, T., and Jacobs, J. A. (1958). Geomagnetic Pulsations and the Earth's Outer Atmosphere. *Geophys. J. Int.* 1, 53–63. doi:10.1111/j.1365-246X.1958.tb00034.x

O'Brien, T. P., and Moldwin, M. B. (2003). Empirical Plasmapause Models from Magnetic Indices. *Geophys. Res. Lett.* 30, 1152. doi:10.1029/2002gl016007

Park, C. G. (1974). Some Features of Plasma Distribution in the Plasmasphere Deduced from Antarctic Whistlers. *J. Geophys. Res.* 79, 169–173. doi:10.1029/JA079i001p00169

Pedersen, A., Cattell, C. A., Mozer, F., Falthammar, C.-G., Lindqvist, P.-A., Formisano, V., et al. (1984). Quasistatic Electric Field Measurements with Spherical Double Probes on the GEOS and ISEE Satellites. *Space Sci. Rev.* 37, 269–312. doi:10.1007/BF00226365

Radoski, H. R., and Carovillano, R. L. (1966). Axisymmetric Plasmasphere resonances:Toroidal Mode. *Phys. Fluids* 9, 285–291. doi:10.1063/1.1761671

Radoski, H. R. (1967). Highly Asymmetric MHD Resonances: The Guided Poloidal Mode. *J. Geophys. Res.* 72, 4026–4027. doi:10.1029/JZ072i015p04026

Rankin, R., Kabin, K., and Marchand, R. (2006). Alfvénic Field Line Resonances in Arbitrary Magnetic Field Topology. *Adv. Space Res.* 38, 1720–1729. doi:10.1016/j.asr.2005.09.034

Rodriguez, J. V. (2014). *GOES 13–15 MAGE/PD Pitch Angle Algorithm Theoretical Basis Document*. Version 1.0. Silver Spring, MD: Report, National Oceanic and Atmospheric Administration/National Environmental Satellite, Data, and Information Service/National Geophysical Data Center.

Roelof, E. C., Mitchell, D. G., and Williams, D. J. (1985). Energetic Neutral Atoms (E ~50 Kev) from the Ring Current: IMP 7/8 and ISEE 1. *J. Geophys. Res.* 90. doi:10.1029/JA090iA11p10991

Sandel, B. R., Goldstein, J., Gallagher, D. L., and Spasojevic, M. (2003). Extreme Ultraviolet Imager Observations of the Structure and Dynamics of the Plasmasphere. *Space Sci. Rev.* 109, 25–46. doi:10.1023/B:SPAC.0000007511.47727.5b

Sarris, T. E., Liu, W., Li, X., Kabin, K., Talaat, E. R., Rankin, R., et al. (2010). THEMIS Observations of the Spatial Extent and Pressure-Pulse Excitation of Field Line Resonances. *Geophys. Res. Lett.* 37, L15104. doi:10.1029/2010gl044125

Schulz, M. (1996). Eigenfrequencies of Geomagnetic Field Lines and Implications for Plasma-Density Modeling. *J. Geophys. Res. Space Phys.* 101, 17385–17397. doi:10.1029/95ja03727

Singer, H. J., Southwood, D. J., Walker, R. J., and Kivelson, M. G. (1981). Alfven Wave Resonances in a Realistic Magnetospheric Magnetic Field Geometry. *J. Geophys. Res. Space Phys.* 86, 4589–4596. doi:10.1029/JA086iA06p04589

Sitnov, M. I., Tsyganenko, N. A., Ukhorskiy, A. Y., and Brandt, P. C. (2008). Dynamical Data-Based Modeling of the Storm-Time Geomagnetic Field with Enhanced Spatial Resolution. *J. Geophys. Res.* 113, A07218. doi:10.1029/2007JA013003

Takahashi, K., and Anderson, B. J. (1992). Distribution of ULF Energy ($F <$ 80 mHz) in the Inner Magnetosphere: A Statistical Analysis of AMPTE CCE Magnetic Field Data. *J. Geophys. Res.* 97, 10751. doi:10.1029/92ja00328

Takahashi, K., Denton, R. E., Anderson, R. R., and Hughes, W. J. (2004). Frequencies of Standing Alfvén Wave Harmonics and Their Implication for Plasma Mass Distribution along Geomagnetic Field Lines: Statistical Analysis of CRRES Data. *J. Geophys. Res. Space Phys.* 109, A08202. doi:10.1029/2003ja010345

Takahashi, K., Denton, R. E., Anderson, R. R., and Hughes, W. J. (2006). Mass Density Inferred from Toroidal Wave Frequencies and its Comparison to Electron Density. *J. Geophys. Res. Space Phys.* 111, A01201. doi:10.1029/2005ja011286

Takahashi, K., Denton, R. E., and Gallagher, D. (2002). Toroidal Wave Frequency at L = 6–10: Active Magnetospheric Particle Tracer Explorers/CCE Observations and Comparison with Theoretical Model. *J. Geophys. Res. Space Phys.* 107. , 2002 SMP 2–1–SMP 2–14. doi:10.1029/2001ja000197

Takahashi, K., Denton, R. E., Hirahara, M., Min, K., Ohtani, S.-i., and Sanchez, E. (2014). Solar Cycle Variation of Plasma Mass Density in the Outer Magnetosphere: Magnetoseismic Analysis of Toroidal Standing Alfvén Waves Detected by Geotail. *J. Geophys. Res. Space Phys.* 119, 8338–8356. doi:10.1002/2014ja020274

Takahashi, K., Denton, R. E., Kurth, W., Kletzing, C., Wygant, J., Bonnell, J., et al. (2015a). Externally Driven Plasmaspheric ULF Waves Observed by the Van Allen Probes. *J. Geophys. Res. Space Phys.* 120, 526–552. doi:10.1002/2014ja020373

Takahashi, K., and Denton, R. E. (2007). Magnetospheric Seismology Using Multiharmonic Toroidal Waves Observed at Geosynchronous Orbit. *J. Geophys. Res.* 112. doi:10.1029/2006ja011709

Takahashi, K., Denton, R. E., Motoba, T., Matsuoka, A., Kasaba, Y., Kasahara, Y., et al. (2018). Impulsively Excited Nightside Ultralow Frequency Waves Simultaneously Observed on and off the Magnetic Equator. *Geophys. Res. Lett.* 45, 7918–7926. doi:10.1029/2018gl078731

Takahashi, K., and Denton, R. E. (2021). Nodal Structure of Toroidal Standing Alfvén Waves and its Implication for Field Line Mass Density Distribution. *J. Geophys. Res. Space Phys.* 126. doi:10.1029/2020ja028981

Takahashi, K., Denton, R. E., and Singer, H. J. (2010). Solar Cycle Variation of Geosynchronous Plasma Mass Density Derived from the Frequency of Standing Alfvén Waves. *J. Geophys. Res. Space Phys.* 115, A07207. doi:10.1029/2009ja015243

Takahashi, K., Glassmeier, K. H., Angelopoulos, V., Bonnell, J., Nishimura, Y., Singer, H. J., et al. (2011). Multisatellite Observations of a Giant Pulsation Event. *J. Geophys. Research-Space Phys.* 116. doi:10.1029/2011ja016955

Takahashi, K., Hartinger, M. D., Angelopoulos, V., and Glassmeier, K.-H. (2015b). A Statistical Study of Fundamental Toroidal Mode Standing Alfvén Waves Using THEMIS Ion Bulk Velocity Data. *J. Geophys. Res. Space Phys.* 120, 6474–6495. doi:10.1002/2015ja021207

Takahashi, K., Kokubun, S., Sakurai, T., McEntire, R. W., Potemra, T. A., and Lopez, R. E. (1988). AMPTE/CCE Observations of Substorm-Associated Standing Alfvén Waves in the Midnight Sector. *Geophys. Res. Lett.* 15, 1287–1290. doi:10.1029/GL015i011p01287

Takahashi, K., Lee, D.-H., Merkin, V. G., Lyon, J. G., and Hartinger, M. D. (2016). On the Origin of the Dawn-Dusk Asymmetry of Toroidal Pc5 Waves. *J. Geophys. Res. Space Phys.* 121, 9632–9650. doi:10.1002/2016ja023009

Takahashi, K., McPherron, R. L., and Hughes, W. J. (1984). Multispacecraft Observations of the Harmonic Structure of Pc 3-4 Magnetic Pulsations. *J. Geophys. Res.* 89, 6758–6774. doi:10.1029/JA089iA08p06758

Takahashi, K., and McPherron, R. L. (1984). Standing Hydromagnetic Oscillations in the Magnetosphere. *Planet. Space Sci.* 32, 1343–1359. doi:10.1016/0032-0633(84)90078-3

Takahashi, K., Ohtani, S.-i., Denton, R. E., Hughes, W. J., and Anderson, R. R. (2008). Ion Composition in the Plasma Trough and Plasma Plume Derived from a Combined Release and Radiation Effects Satellite Magnetoseismic Study. *J. Geophys. Res. Space Phys.* 113. doi:10.1029/2008ja013248

Takahashi, K., Vellante, M., Del Corpo, A., Claudepierre, S. G., Kletzing, C., Wygant, J., et al. (2020). Multiharmonic Toroidal Standing Alfvén Waves in the Midnight Sector Observed during a Geomagnetically Quiet Period. *J. Geophys. Res. Space Phys.* 125. doi:10.1029/2019ja027370

Thomas, N., Shiokawa, K., Miyoshi, Y., Kasahara, Y., Shinohara, I., Kumamoto, A., et al. (2021). Investigation of Small-Scale Electron Density Irregularities Observed by the Arase and Van Allen Probes Satellites inside and outside the Plasmasphere. *J. Geophys. Res. Space Phys.* 126. doi:10.1029/2020ja027917

Tsyganenko, N. A. (1989). A Magnetospheric Magnetic Field Model with a Warped Tail Current Sheet. *Planet. Space Sci.* 37, 5–20. doi:10.1016/0032-0633(89)90066-4

Tsyganenko, N. A., and Sitnov, M. I. (2005). Modeling the Dynamics of the Inner Magnetosphere during strong Geomagnetic Storms. *J. Geophys. Res. Space Phys.* 110, A03208. doi:10.1029/2004ja010798

Vellante, M., Takahashi, K., Corpo, A., Zhelavskaya, I. S., Goldstein, J., Mann, I. R., et al. (2021). Multi-instrument Characterisation of Magnetospheric Cold Plasma Dynamics in the 22 June 2015 Geomagnetic Storm. *J. Geophys. Res. Space Phys.* 126. doi:10.1029/2021ja029292

Vellante, M., Vellante, M., Lühr, H., Zhang, T. L., Wesztergom, V., Villante, U., et al. (2004). Ground/satellite Signatures of Field Line Resonance: A Test of Theoretical Predictions. *J. Geophys. Res.* 109, A06210. doi:10.1029/2004ja010392

Wallis, D. D., and Budzinski, E. E. (1981). Empirical-models of Height Integrated Conductivities. *J. Geophys. Res. Space Phys.* 86, 125–137. doi:10.1029/JA086iA01p00125

Wang, B., Nishimura, Y., Hartinger, M., Sivadas, N., Lyons, L. L., Varney, R. H., et al. (2020). Ionospheric Modulation by Storm Time Pc5 ULF Pulsations and the Structure Detected by PFISR-THEMIS Conjunction. *Geophys. Res. Lett.* 47. doi:10.1029/2020gl089060

Warner, M. R., and Orr, D. (1979). Time of Flight Calculations for High Latitude Geomagnetic Pulsations. *Planet. Space Sci.* 27, 679–689. doi:10.1016/0032-0633(79)90165-x

Waters, C. L., Menk, F. W., and Fraser, B. J. (1991). The Resonance Structure of Low Latitude Pc3 Geomagnetic-Pulsations. *Geophys. Res. Lett.* 18, 2293–2296. doi:10.1029/91gl02550

Wild, J. A., Yeoman, T. K., and Waters, C. L. (2005). Revised Time-Of-Flight Calculations for High-Latitude Geomagnetic Pulsations Using a Realistic Magnetospheric Magnetic Field Model. *J. Geophys. Res.* 110. doi:10.1029/2004ja010964

Wright, A. N., and Elsden, T. (2016). The Theoretical Foundation of 3D Alfvén Resonances: Normal Modes. *Astrophysical J.* 833, 230. doi:10.3847/1538-4357/833/2/230

Zhelavskaya, I. S., Spasojevic, M., Shprits, Y. Y., and Kurth, W. S. (2016). Automated Determination of Electron Density from Electric Field Measurements on the Van Allen Probes Spacecraft. *J. Geophys. Res. Space Phys.* 121, 4611–4625. doi:10.1002/2015ja022132

Conflict of Interest: The authors declare that the research was conducted in the absence of any commercial or financial relationships that could be construed as a potential conflict of interest.

Publisher's Note: All claims expressed in this article are solely those of the authors and do not necessarily represent those of their affiliated organizations, or those of the publisher, the editors and the reviewers. Any product that may be evaluated in this article, or claim that may be made by its manufacturer, is not guaranteed or endorsed by the publisher.

frontiers in Astronomy and Space Sciences

MINI REVIEW
published: 17 September 2021
doi: 10.3389/fspas.2021.744344

Energy Exchange Between Electromagnetic Ion Cyclotron (EMIC) Waves and Thermal Plasma: From Theory to Observations

M. E. Usanova *

Laboratory for Atmospheric and Space Physics, University of Colorado at Boulder, Boulder, CO, United States

The cold plasmaspheric plasma, the ring current and the radiation belts constitute three important populations of the inner magnetosphere. The overlap region between these populations gives rise to wave-particle interactions between different plasma species and wave modes observed in the magnetosphere, in particular, electromagnetic ion cyclotron (EMIC) waves. These waves can resonantly interact with multiple particle species, being an important loss process for both ring current ions and radiation belt electrons, as well as a cold plasma heating mechanism. This mini-review will focus on the interaction between EMIC waves and cold and thermal plasma, specifically the role of EMIC waves in cold and thermal electron and ion heating. It will discuss early theoretical results in conjunction with numerical modelling and recent satellite observations, and address outstanding problems and controversies in this field.

Keywords: EMIC waves, cold plasma, energy exchange, Landau heating, plasmasphere

OPEN ACCESS

Edited by:
Cecilia Norgren,
University of Bergen, Norway

Reviewed by:
Binbin Ni,
Wuhan University, China
Anton Artemyev,
Space Research Institute (RAS), Russia

****Correspondence:***
M. E. Usanova
maria.usanova@lasp.colorado.edu

Specialty section:
This article was submitted to Space Physics, a section of the journal Frontiers in Astronomy and Space Sciences

Received: *20 July 2021*
Accepted: *30 August 2021*
Published: *17 September 2021*

Citation:
Usanova ME (2021) Energy Exchange Between Electromagnetic Ion Cyclotron (EMIC) Waves and Thermal Plasma: From Theory to Observations. Front. Astron. Space Sci. 8:744344. doi: 10.3389/fspas.2021.744344

INTRODUCTION

Electromagnetic ion cyclotron (EMIC) waves are transverse plasma waves generated in the equatorial magnetosphere by ~10–100 keV ion distributions with temperature anisotropy ($T_{perp} > T_{para}$, where perpendicular and parallel are defined with respect to the background magnetic field) (Cornwall, 1965). They are typically observed in space and on the ground in the Pc1-2 frequency range between 0.1–5 Hz, though can be observed even at higher frequencies deep in the inner magnetosphere (Sakaguchi et al., 2013). Minor ion species, helium and oxygen, also present in a magnetospheric plasma, produce forbidden band gaps for EMIC wave generation and propagation that split the wave spectrum into multiple branches below the H^+, He^+, and O^+ gyrofrequencies (e.g., Fraser, 1985). For each branch, the wave growth rate and cut-off frequencies are determined by a proton temperature anisotropy, ion composition, and cold plasma density (e.g., Kozyra et al., 1984). Statistical surveys from various satellite missions, covering the whole magnetosphere have reported EMIC wave observations throughout all magnetic local times (MLTs) and L-shells and examined their properties and occurrence distributions depending on geomagnetic conditions and solar wind drivers (Anderson et al., 1992; Denton et al., 2002; Fraser and Nguyen, 2001; Halford et al., 2010; Usanova et al., 2012; Keika et al., 2013; Meredith et al., 2014; Allen et al., 2015; Saikin et al., 2015; Wang et al., 2015; Jun et al., 2019; Grison et al., 2021).

Ions and electrons can resonantly interact with EMIC waves if the Doppler-shifted wave frequency (in the frame of reference of the particle) is equal to an integral multiple of the particle gyrofrequency: $\omega - k_{\|}v_{\|} = n\Omega/\gamma$, $n = 0, \pm 1, \ldots$where ω is the wave frequency, $k_{\|}$ is the

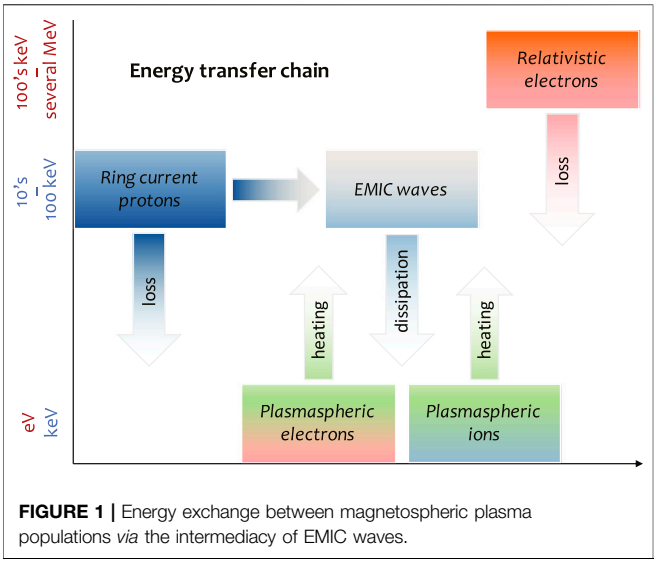

FIGURE 1 | Energy exchange between magnetospheric plasma populations *via* the intermediacy of EMIC waves.

parallel (to the background magnetic field, $\boldsymbol{B}$) wave number, $v_{||}$ is the electron parallel velocity, $\Omega = qB/m$ is the particle cyclotron frequency, and $\gamma = 1/\sqrt{1-(v/c)^2}$ is the relativistic correction. Both the theory and the observations have shown that EMIC wave growth leads to the isotropization of the initially unstable proton distribution and consequent pitch-angle scattering and loss of protons into the atmosphere (see, e.g., Cornwall, 1965; Usanova et al., 2010; Søraas, et al., 2013; Yahnin et al., 2021). The condition for this resonance is satisfied if protons move along the field in the opposite direction to the waves. Interaction with EMIC waves is also believed to be an important loss mechanism for ~ hundreds keV–several MeV radiation belt electrons, which can undergo cyclotron resonance with EMIC waves and consequent pitch-angle scattering into the atmosphere through the anomalous Doppler-shifted cyclotron resonance (Horne and Thorne, 1998; Summers et al., 2007; Blum et al., 2015; Capannolo et al., 2021). Since EMIC waves are predominantly left-hand polarized, electrons must overtake the wave with a velocity sufficient to Doppler shift the wave frequency to the relativistic electron cyclotron, frequency reversing the relevant sense of polarization from left-to right-handed. Cyclotron resonance with energetic electrons and ions does not change particle energy, only resulting in scattering (momentum exchange) without energy coupling. EMIC waves can also experience Landau resonance, $\omega = k_{||}v_{||}$, which is most significant for highly-oblique EMIC waves due to the presence of a parallel component of the wave electric field (Thorne and Horne, 1992). Landau interactions usually lead to wave attenuation and energy transfer to ~ eV-ten's eV cold/thermal electrons (Cornwall et al., 1971; Horne and Thorne, 1998; Wang et al., 2019) and ~keV ions (e.g., Omura et al., 1985; Kitamura et al., 2018) and also contribute to scattering of relativistic electrons (Wang et al., 2016; Fu et al., 2018). Finally, EMIC waves can undergo bounce resonance interactions with energetic electrons causing particle scattering (Cao et al., 2017; Blum et al., 2019). These resonant interactions take place when the electron bounce period (or integer number of such periods) matches the wave period (Schulz and Lanzerotti, 1974; Shprits, 2009). As a result, EMIC waves act as an intermediary that couples energy and momentum between the cold/thermal, the hot and the relativistic plasma, as schematically shown in **Figure 1**.

The focus of this mini-review is the energy transfer between EMIC waves and cold and warm plasma populations and the role of EMIC waves in electron and ion heating. For other aspects of EMIC wave generation and the role of cold plasma in EMIC wave-particle interactions please refer to the following recently published relevant reviews. The effects of cold plasma density on EMIC wave growth and its role in energetic particle precipitation is highlighted in Usanova and Mann (2016) and Blum and Breneman (2020). The role of the plasmapause and cold plasma gradients for wave growth and ducting is discussed in Usanova et al. (2016); the review also examined wave characteristics in the source region, and considers the effect of plasma composition on the wave spectrum and propagation to the ground. The contribution of ionospheric ions in wave generation, propagation, and interaction with particles and the importance of cold ion composition measurements for new satellite missions to improve understanding of EMIC waves is addressed in Lee et al. (2021). The general questions of energy coupling between EMIC waves and cold plasma are outlined in Delzanno et al. (2021).

STABLE AURORAL ARCS AND LANDAU RESONANT HEATING OF THERMAL ELECTRONS

Stable auroral red (SAR) arcs are optical emission at predominately 630 nm observed in the mid-latitude ionosphere during periods of increased magnetic activity (Roach and Roach, 1963; Cornwall et al., 1971; Inaba et al., 2020). The red line corresponds to the excitation of atomic oxygen at ~400 km altitudes. Despite more than 50 years of research, the generation mechanism for SARs is still controversial and may be caused by the three possible processes: Coulomb collisions of plasmaspheric electrons with ring current ions (Cole, 1965; Kozyra et al., 1987; Fok et al., 1993; Inaba et al., 2020); heating the plasmaspheric electrons *via* Landau resonance with EMIC waves (Cornwall et al., 1971; Thorne and Horne, 1992; Zhou et al., 2013) and acceleration of plasmaspheric electrons into the ionosphere by kinetic Alfvén waves (Hasegawa and Mima, 1978).

Investigation of the role of EMIC waves in SAR arcs generation stared with an early theoretical work by Cornwall et al. (1971) who proposed the following model. It involves energy transport between anisotropic ring current protons that serve as a source of free energy and excite EMIC waves inside the plasmapause and precipitate while the cyclotron waves are absorbed by plasmaspheric (1–10 eV) electrons. This increases the electron temperature in the direction parallel to the ambient field and leads directly to heat conduction into the ionosphere and drives SARs. The associated proton Coulomb dissipation warms plasmaspheric electrons to temperatures at which electron Landau damping becomes efficient and more prominent than

Coulomb scattering. The model predicts that SAR arcs are generated in a narrow region just inside the plasmapause (at L-shells from 2 to 4) that corresponds to their observed latitudinal extent in the ionosphere of several hundred kilometers. However, a later observational study by Kozyra et al. (1987) showed that the energetic, <20 keV O^+ ring current species can play a more important role than H^+ in the Coulomb scattering and can be responsible for heating of plasmaspheric electrons and SAR formation. Motivated by Kozyra et al. (1987), Thorne and Horne (1992) performed a wave ray tracing in a multicomponent plasma and confirmed that EMIC waves can play an important role in both the energy transfer to plasmaspheric electrons and the subsequent downward heat conduction to SAR arc altitudes. They demonstrated that EMIC waves can experience enhanced path integrated amplification along the steep plasmapause density gradient. Subsequently, when the wave propagation vector becomes highly oblique, absorption occurs during Landau resonance with thermal plasmaspheric electrons which requires an electron temperature above 1 eV. Coulomb scattering by energetic O^+ was suggested to act as the primer to heat plasmaspheric electrons for efficient ion-cyclotron wave absorption.

Further, Erlandson et al. (1993) presented simultaneous observations of EMIC waves and subauroral electron temperature enhancements on the polar orbiting DE-2 satellite and confirmed that EMIC waves were responsible for Landau heating the low energy electrons which precipitate to the ionosphere and produce ionospheric temperature enhancements. However, their observations could not pinpoint the heating region location and whether the electrons were heated at the ionospheric altitudes or near the equator. Zhou et al. (2013) observed EMIC waves generated by anisotropic 10–25 keV protons together with electron heating in the equatorial magnetosphere on THEMIS satellites. The observations were combined with calculations of the wave Landau damping rates due to the cold electron gyroresonance with EMIC waves. This work corroborated the original idea of Cornwall et al. (1971) as well as supported the possibility of equatorial electron heating by obliquely propagating EMIC waves.

Recently, Inaba et al. (2020) reported conjugate measurements of a SAR arc observed by an all-sky imager in Finland and the Arase satellite. The Arase observation shows that the SAR arc appeared in the overlap region between a plasmaspheric plume and the ring-current ions and that electromagnetic ion cyclotron waves and kinetic Alfven waves were not observed above the SAR arc. These observations suggest that the heating of plasmaspheric electrons *via* Coulomb collision with ring-current ions is the most plausible mechanism for the SAR-arc generation. There was still a possibility that due to the measurements at ~30 degrees off the equator the waves might have reflected above the satellite location along the magnetic field line and therefore were not observed. However, this work strongly implies that the SAR generation mechanism is controversial and warrants further investigation.

The relationship between EMIC waves and electron heating in plasmaspheric plumes was investigated by Yuan et al. (2014). Using *in situ* Cluster observations, they found that the electron heating was much stronger for field-aligned electrons, consistent with Landau damping predictions. Further, using theoretical calculations of the Landau resonant interaction between electrons and observed EMIC waves, they demonstrated that Landau damping of oblique EMIC waves is a reasonable candidate to heat cold electrons in plasmaspheric plumes.

Note that the studies based on the quasi-linear theory assume that EMIC waves are small in amplitude (in relation to the amplitude of the background magnetic field), experiencing multiple random-phase interactions with electrons which makes this process stochastic or diffusive. Since EMIC waves can exhibit nonlinear features, e.g., consisting of discrete elements that may have rising and falling tones, as well as high amplitudes, non-linear interactions are also necessary to consider (e.g., Nakamura et al., 2016; Shoji et al., 2021). The role of non-linear processes in energy exchange between EMIC waves and cold electrons was addresses by Wang et al. (2019) who conducted test-particle simulations and investigated the role of non-linear Landau resonance. They concluded that the nonlinear wave-particle interactions can occur at typical EMIC wave amplitudes (a few nT in magnetic and a few mV/m in electric field) and may play an important role in EMIC wave damping in the equatorial region, being more prominent than linear Landau damping, especially for obliquely propagating waves.

LANDAU HEATING OF THERMAL IONS (H^+, HE^+ AND O^+)

Satellite measurements from different missions have shown that thermal (~10s to 100s eV) He^+ ions can be resonantly heated by EMIC waves in the direction perpendicular to the background magnetic field (e.g., Mauk et al., 1981; Roux et al., 1982; Mouikis et al., 2002). The role of EMIC waves in cold ion heating has been investigated using both quasi-linear theory and electromagnetic hybrid simulations, where ions are treated kinetically and electrons are treated as conducting fluid. The simulations focused on the self-consistent nonlinear evolution of EMIC waves in plasma consisting of electrons, protons, and He^+ and showed that the decrease of initial energetic proton temperature anisotropy results in EMIC wave growth and helium ion heating (Omura et al., 1985; Denton et al., 1993; Gary et al., 1994). Ma et al. (2019) presented Van Allen Probes observations of EMIC waves and He^+ and O^+ ions and explained the nature of EMIC wave interactions with thermal and energetic ions using a quasi-linear analysis. Their diffusion coefficient calculations indicate that H^+-band EMIC waves can heat He^+ ions, while He^+-band waves can energize O^+ ions at thermal energies and pitch angles up to ~80° through multiple harmonic cyclotron resonances. While thermal ions are heated in the transverse direction, the more energetic ring current ions are precipitated into the upper atmosphere through pitch angle scattering.

Anderson and Fuselier (1994) and Fuselier and Anderson (1996) examined H^+ and He^+ ion measurements in the 1–160 eV range on AMPTE/CCE to investigate the thermal ion response to the waves. They showed that for protons the perpendicular heating was modest, consistent with a non-resonant

interaction near the equator. By contrast, He^+ energization was ~20 times stronger and peaked at pitch angles intermediate between field-aligned and perpendicular directions, consistent with a gyroresonant interaction off the equator. Omidi et al. (2010) and Bortnik et al. (2010) further examined the nonlinear evolution of EMIC waves using 2.5D hybrid simulations along with detailed test particle calculations. They found that the nonlinear evolution of EMIC waves involves generation of electrostatic waves with a wavelength half of that of the ion cyclotron waves and also results in parallel heating of cold He^+ and H^+ ions for substantially long periods.

The non-linear wave interactions with ions were recently investigated using high-resolution ion measurements on MMS spacecraft. Kitamura et al. (2018) presented the first observational evidence of energy transfer from energetic ring current protons to cold helium ions *via* EMIC wave-particle interactions confirming earlier simulation results. The wave-ion phase relations demonstrated that a cyclotron resonance transferred energy from 14–30 keV protons to waves, which in turn non-resonantly accelerated cold He^+ to energies up to ~2 keV. Further, utilizing the same instrumentation and technique as in Kitamura et al. (2018), Abid et al. (2021) showed that 1–100 eV protons can also be non-linearly energized by EMIC waves through phase bunching.

CONCLUSION

Over the recent several decades of space exploration, significant progress has been made in understanding of energy transfer processes in the magnetosphere and the coupling between different plasma populations within this complex system. EMIC waves have been shown to act as an intermediary that couples energy and momentum between different energy magnetospheric plasma populations via various resonance mechanisms. High-resolution satellite observations, theory and self-consistent simulations have answered a lot of questions regarding the role of EMIC waves in Landau heating of plasmaspheric electrons and heavy ions. Despite the long history of research in this area, there are still open questions, for example, the role of EMIC waves in red auroral arc generation and the location of regions where the energy transfer predominately takes place. Recent studies have also underlined the significance of nonlinear processes in EMIC wave-particle interactions and placed emphasis on the potential to include those in global magnetospheric models which will be a next critical step towards predictive modeling.

AUTHOR CONTRIBUTIONS

MU is the only contributing author for this review.

FUNDING

The work on this review was supported by NASA Awards 80 NSSC19K0265 and NAS5-01072.

REFERENCES

Abid, A. A., Lu, Q., Gao, X. L., Alotaibi, B. M., Ali, S., Qureshi, M. N. S., et al. (2021). Energization of Cold Ions by Electromagnetic Ion Cyclotron Waves: Magnetospheric Multiscale (MMS) Observations. *Phys. Plasmas* 28, 072901. doi:10.1063/5.0046764

Allen, R. C., Zhang, J. C., Kistler, L. M., Spence, H. E., Lin, R. L., Klecker, B., et al. (2015). A Statistical Study of EMIC Waves Observed by Cluster: 1. Wave Properties. *J. Geophys. Res. Space Phys.* 120, 5574–5592. doi:10.1002/2015JA021333

Anderson, B. J., and Fuselier, S. A. (1994). Response of thermal Ions to Electromagnetic Ion Cyclotron Waves. *J. Geophys. Res.* 99 (A10), 19,413–19,425. doi:10.1029/94JA01235

Anderson, B. J., Erlandson, R. E., and Zanetti, L. J. (1992). A Statistical Study of Pc 1-2 Magnetic Pulsations in the Equatorial Magnetosphere: 1. Equatorial Occurrence Distributions. *J. Geophys. Res.* 97 (A3), 3075–3088. doi:10.1029/91JA02706

Blum, L. W., and Breneman, A. W. (2020). "Observations of Radiation belt Losses Due to Cyclotron Wave-Particle Interactions," in *The Dynamic Loss of Earth's Radiation Belts*. Editors A.N. Jaynes and M.E. Usanova (Elsevier) chap. 3, 49–98. doi:10.1016/B978-0-12-813371-2.00003-2 Available at: https://www.sciencedirect.com/science/article/pii/B9780128133712000032

Blum, L. W., Halford, A., Millan, R., Bonnell, J. W., Goldstein, J., Usanova, M., et al. (2015). Observations of Coincident EMIC Wave Activity and Duskside Energetic Electron Precipitation on 18-19 January 2013. *Geophys. Res. Lett.* 42, 5727–5735. doi:10.1002/2015GL065245

Blum, L. W., Artemyev, A., Agapitov, O., Mourenas, D., Boardsen, S., and Schiller, Q. (2019). EMIC Wave-Driven Bounce Resonance Scattering of Energetic Electrons in the Inner Magnetosphere. *J. Geophys. Res. Space Phys.* 124, 2484–2496. doi:10.1029/2018JA026427

Bortnik, J., Thorne, R. M., and Omidi, N. (2010). Nonlinear Evolution of EMIC Waves in a Uniform Magnetic Field: 2. Test-Particle Scattering. *J. Geophys. Res.* 115, 741–744. doi:10.1029/2010JA015603

Cao, X., Ni, B., Summers, D., Bortnik, J., Tao, X., Shprits, Y. Y., et al. (2017). Bounce Resonance Scattering of Radiation belt Electrons by H^+ Band EMIC Waves. *J. Geophys. Res. Space Phys.* 122, 1702–1713. doi:10.1002/2016JA023607

Capannolo, L., Li, W., Spence, H., Johnson, A. T., Shumko, M., Sample, J., et al. (2021). Energetic Electron Precipitation Observed by FIREBIRD-II Potentially Driven by EMIC Waves: Location, Extent, and Energy Range from a Multievent Analysis. *Geophys. Res. Lett.* 48, e2020GL091564. doi:10.1029/2020GL091564

Cole, K. D. (1965). Stable Auroral Red Arcs, Sinks for Energy of Dst main Phase. *J. Geophys. Res.* 70 (7), 1689–1706. doi:10.1029/JZ070i007p01689

Cornwall, J. M., Coroniti, F. V., and Thorne, R. M. (1971). Unified Theory of SAR Arc Formation at the Plasmapause. *J. Geophys. Res.* 76 (19), 4428–4445. doi:10.1029/JA076i019p04428

Cornwall, J. M. (1965). Cyclotron Instabilities and Electromagnetic Emission in the Ultra Low Frequency and Very Low Frequency Ranges. *J. Geophys. Res.* 70 (1), 61–69. doi:10.1029/JZ070i001p00061

Delzanno, G. L., Borovsky, J. E., Henderson, M. G., Resendiz Lira, P. A., Roytershteyn, V., and Welling, D. T. (2021). The Impact of Cold Electrons and Cold Ions in Magnetospheric Physics. *J. Atmos. Solar-Terr. Phys.* 220, 105599. doi:10.1016/j.jastp.2021.105599

Denton, R. E., Hudson, M. K., Fuselier, S. A., and Anderson, B. J. (1993). Electromagnetic Ion Cyclotron Waves in the Plasma Depletion Layer. *J. Geophys. Res.* 98, 13,477–13,490. doi:10.1029/93JA00796

Denton, R. E., LaBelle, J., and Zhu, X. (2002). Location of Pc 1-2 Waves Relative to the Magnetopause. *Ann. Geophys.* 20, 1763–1767. doi:10.5194/angeo-20-1763-2002

Erlandson, R. E., Aggson, T. L., Hogey, W. R., and Slavin, J. A. (1993). Simultaneous Observations of Subauroral Electron Temperature Enhancements and

Electromagnetic Ion Cyclotron Waves. *Geophys. Res. Lett.* 20, 1723–1726. doi:10.1029/93gl01975

Fok, M.-C., Kozyra, J. U., Nagy, A. F., Rasmussen, C. E., and Khazanov, G. V. (1993). Decay of Equatorial Ring Current Ions and Associated Aeronomical Consequences. *J. Geophys. Res.* 98 (A11), 19381–19393. doi:10.1029/93JA01848

Fraser, B. J., and Nguyen, T. S. (2001). Is the Plasmapause a Preferred Source Region of Electromagnetic Ion Cyclotron Waves in the Magnetosphere? *J. Atmos. Solar-Terr. Phys.* 63, 1225–1247. doi:10.1016/S1364-6826(00)00225-X

Fraser, B. J. (1985). Observations of Ion Cyclotron Waves Near Synchronous Orbit and on the Ground. *Space Sci. Rev.* 42, 357–374. doi:10.1007/BF0021499310

Fu, S., Ni, B., Lou, Y., Bortnik, J., Ge, Y., Tao, X., et al. (2018). Resonant Scattering of Near-Equatorially Mirroring Electrons by Landau Resonance with H^+ Band EMIC Waves. *Geophys. Res. Lett.* 45, 10,866–10,873. doi:10.1029/2018GL079718

Fuselier, S. A., and Anderson, B. J. (1996). Low-energy He+and H+distributions and Proton Cyclotron Waves in the Afternoon Equatorial Magnetosphere. *J. Geophys. Res.* 101 (A6), 13255–13265. doi:10.1029/96JA00292

Gary, S. P., McKean, M. E., Winske, D., Anderson, B. J., Denton, R. E., and Fuselier, S. A. (1994). The Proton Cyclotron Instability and the Anisotropy/β Inverse Correlation. *J. Geophys. Res.* 99 (A4), 5903–5914. doi:10.1029/93JA03583

Grison, B., Santolík, O., Lukačevič, J., and Usanova, M. E. (2021). Occurrence of EMIC Waves in the Magnetosphere According to Their Distance to the Magnetopause. *Geophys. Res. Lett.* 48, e2020GL090921. doi:10.1029/2020gl090921

Halford, A. J., Fraser, B. J., and Morley, S. K. (2010). EMIC Wave Activity during Geomagnetic Storm and Nonstorm Periods: CRRES Results. *J. Geophys. Res.* 115, a–n. doi:10.1029/2010JA015716

Hasegawa, A., and Mima, K. (1978). Anomalous Transport Produced by Kinetic Alfvén Wave Turbulence. *J. Geophys. Res.* 83 (A3), 1117–1123. doi:10.1029/JA083iA03p01117

Horne, R. B., and Thorne, R. M. (1998). Potential Waves for Relativistic Electron Scattering and Stochastic Acceleration during Magnetic Storms. *Geophys. Res. Lett.* 25, 3011–3014. doi:10.1029/98GL01002

Inaba, Y., Shiokawa, K., Oyama, S. i., Otsuka, Y., Oksanen, A., Shinbori, A., et al. (2020). Plasma and Field Observations in the Magnetospheric Source Region of a Stable Auroral Red (SAR) Arc by the Arase Satellite on 28 March 2017. *J. Geophys. Res. Space Phys.* 125, e2020JA028068. doi:10.1029/2020JA028068

Jun, C. W., Yue, C., Bortnik, J., Lyons, L. R., Nishimura, Y., Kletzing, C., et al. (2019). A Statistical Study of EMIC Waves Associated with and without Energetic Particle Injection from the Magnetotail. *J. Geophys. Res. Space Phys.* 124, 433–450. doi:10.1029/2018JA025886

Keika, K., Takahashi, K., Ukhorskiy, A. Y., and Miyoshi, Y. (2013). Global Characteristics of Electromagnetic Ion Cyclotron Waves: Occurrence Rate and its Storm Dependence. *J. Geophys. Res. Space Phys.* 118, 4135–4150. doi:10.1002/jgra.50385

Kitamura, N., Kitahara, M., Shoji, M., Miyoshi, Y., Hasegawa, H., Nakamura, S., et al. (2018). Direct Measurements of Two-Way Wave-Particle Energy Transfer in a Collisionless Space Plasma. *Science* 361, 1000–1003. doi:10.1126/science.aap8730

Kozyra, J. U., Cravens, T. E., Nagy, A. F., Fontheim, E. G., and Ong, R. S. B. (1984). Effects of Energetic Heavy Ions on Electromagnetic Ion Cyclotron Wave Generation in the Plasmapause Region. *J. Geophys. Res.* 89 (A4), 2217–2233. doi:10.1029/JA089iA04p02217

Kozyra, J. U., Shelley, E. G., Comfort, R. H., Brace, L. H., Cravens, T. E., and Nagy, A. F. (1987). The Role of Ring Current O^+ in the Formation of Stable Auroral Red Arcs. *J. Geophys. Res.* 92, 7487. doi:10.1029/JA092iA07p07487

Lee, J. H., Blum, L. W., and Chen, L. (2021). On the Impacts of Cold Plasma and Ion Composition on Magnetospheric EMIC Waves. *Front. Astron. Space Sci.* 28 July 2021. doi:10.3389/fspas.2021.719715

Ma, Q., Li, W., Yue, C., Thorne, R. M., Bortnik, J., Kletzing, C. A., et al. (2019). Ion Heating by Electromagnetic Ion Cyclotron Waves and Magnetosonic Waves in the Earth's Inner Magnetosphere. *Geophys. Res. Lett.* 46, 6258–6267. doi:10.1029/2019GL083513

Mauk, B. H., McIlwain, C. E., and McPherron, R. L. (1981). Helium Cyclotron Resonance within the Earth's Magnetosphere. *Geophys. Res. Lett.* 8 (1), 103–106. doi:10.1029/GL008i001p00103

Meredith, N. P., Horne, R. B., Kersten, T., Fraser, B. J., and Grew, R. S. (2014). Global Morphology and Spectral Properties of EMIC Waves Derived from CRRES Observations. *J. Geophys. Res. Space Phys.* 119, 5328–5342. doi:10.1002/2014JA020064

Mouikis, C. G., Kistler, L. M., Baumjohann, W., Lund, E. J., Korth, A., Klecker, B., et al. (2002). Equator-S Observations of He^+ energization by EMIC Waves in the Dawnside Equatorial Magnetosphere. *Geophys. Res. Lett.* 29 (10), 74–81. doi:10.1029/2001GL013899

Nakamura, S., Omura, Y., and Angelopoulos, V. (2016). A Statistical Study of EMIC Rising and Falling Tone Emissions Observed by THEMIS. *J. Geophys. Res. Space Phys.* 121, 8374–8391. doi:10.1002/2016JA022353

Omidi, N., Thorne, R. M., and Bortnik, J. (2010). Nonlinear Evolution of EMIC Waves in a Uniform Magnetic Field: 1. Hybrid Simulations. *J. Geophys. Res.* 115, 1–11. doi:10.1029/2010JA015607

Omura, Y., Ashour-Abdalla, M., Gendrin, R., and Quest, K. (1985). Heating of thermal Helium in the Equatorial Magnetosphere: A Simulation Study. *J. Geophys. Res.* 90, 8281–8292. doi:10.1029/JA090iA09p08281

Roach, F. E., and Roach, J. R. (1963). Stable 6300 Å Auroral Arcs in Mid-latitudes. *Planet. Space Sci.* 11, 523–540. doi:10.1016/0032-0633(63)90076-X

Roux, A., Perraut, S., Rauch, J. L., de Villedary, C., Kremser, G., Korth, A., et al. (1982). Wave-particle Interactions Near Ω_{He^+} observed on Board GEOS 1 and 2: 2. Generation of Ion Cyclotron Waves and Heating of He^+ ions. *J. Geophys. Res.* 87 (A10), 8174–8190. doi:10.1029/JA087iA10p08174

Saikin, A. A., Zhang, J. C., Allen, R. C., Smith, C. W., Kistler, L. M., Spence, H. E., et al. (2015). The Occurrence and Wave Properties of H^+ -, He^+ -, and O^+ -band EMIC Waves Observed by the Van Allen Probes. *J. Geophys. Res. Space Phys.* 120, 7477–7492. doi:10.1002/2015JA021358

Sakaguchi, K., Kasahara, Y., Shoji, M., Omura, Y., Miyoshi, Y., Nagatsuma, T., et al. (2013). Akebono Observations of EMIC Waves in the Slot Region of the Radiation Belts. *Geophys. Res. Lett.* 40, 5587–5591. doi:10.1002/2013GL058258

Schulz, M., and Lanzerotti, L. J. (1974). *Particle Diffusion in the Radiation Belts*. New York: Springer. doi:10.1007/978-3-642-65675-0

Shoji, M., Miyoshi, Y., Kistler, L. M., Asamura, K., Matsuoka, A., Kasaba, Y., et al. (2021). Discovery of Proton hill in the Phase Space during Interactions between Ions and Electromagnetic Ion Cyclotron Waves. *Sci. Rep.* 11, 13480. doi:10.1038/s41598-021-92541-0

Shprits, Y. Y. (2009). Potential Waves for Pitch-Angle Scattering of Near-Equatorially Mirroring Energetic Electrons Due to the Violation of the Second Adiabatic Invariant. *Geophys. Res. Lett.* 36, L12106. doi:10.1029/2009GL038322

Søraas, F., Laundal, K. M., and Usanova, M. (2013). Coincident Particle and Optical Observations of Nightside Subauroral Proton Precipitation. *J. Geophys. Res. Space Phys.* 118, 1112–1122. doi:10.1002/jgra.50172

Summers, D., Ni, B., and Meredith, N. P. (2007). Timescales for Radiation belt Electron Acceleration and Loss Due to Resonant Wave-Particle Interactions: 2. Evaluation for VLF Chorus, ELF Hiss, and Electromagnetic Ion Cyclotron Waves. *J. Geophys. Res.* 112, a–n. doi:10.1029/2006JA011993

Thorne, R. M., and Horne, R. B. (1992). The Contribution of Ion-Cyclotron Waves to Electron Heating and SAR-Arc Excitation Near the Storm-Time Plasmapause. *Geophys. Res. Lett.* 19, 417–420. doi:10.1029/92GL00089

Usanova, M. E., and Mann, I. R. (2016). "Understanding the Role of EMIC Waves in Radiation Belt and Ring Current Dynamics: Recent Advances," in *Waves, Particles, and Storms in Geospace: A Complex Interplay*. Editors G. Balasis, I. A. Daglis, and I. R. Mann (Oxford University Press) chap. 10, 1–13. doi:10.1093/acprof:oso/9780198705246.001.0001

Usanova, M. E., Mann, I. R., Kale, Z. C., Rae, I. J., Sydora, R. D., Sandanger, M., et al. (2010). Conjugate Ground and Multisatellite Observations of Compression-Related EMIC Pc1 Waves and Associated Proton Precipitation. *J. Geophys. Res.* 115, A07208. doi:10.1029/2009JA014935

Usanova, M. E., Mann, I. R., Bortnik, J., Shao, L., and Angelopoulos, V. (2012). THEMIS Observations of Electromagnetic Ion Cyclotron Wave Occurrence: Dependence on AE, SYMH, and Solar Wind Dynamic Pressure. *J. Geophys. Res.* 117. doi:10.1029/2012JA018049

Usanova, M. E., Mann, I. R., and Darrouzet, F. (2016). "EMIC Waves in the Inner Magnetosphere," in *Low-Frequency Waves in Space Plasmas*. Editors A. Keiling, D.-H. Lee, and V. Nakariakov (Hoboken, NJ: John Wiley & Sons), 65–78. doi:10.1002/9781119055006.ch5

Wang, D., Yuan, Z., Yu, X., Deng, X., Zhou, M., Huang, S., et al. (2015). Statistical Characteristics of EMIC Waves: Van Allen Probe Observations. *J. Geophys. Res. Space Phys.* 120, 4400–4408. doi:10.1002/2015JA021089

Wang, B., Su, Z., Zhang, Y., Shi, S., and Wang, G. (2016). Nonlinear Landau Resonant Scattering of Near Equatorially Mirroring Radiation belt Electrons by Oblique EMIC Waves. *Geophys. Res. Lett.* 43, 3628–3636. doi:10.1002/2016GL068467

Wang, B., Li, P., Huang, J., and Zhang, B. (2019). Nonlinear Landau Resonance between EMIC Waves and Cold Electrons in the Inner Magnetosphere. *Phys. Plasmas* 26, 042903. doi:10.1063/1.5088374

Yahnin, A. G., Popova, T. A., Demekhov, A. G., Lubchich, A. A., Matsuoka, A., Asamura, K., et al. (2021). Evening Side EMIC Waves and Related Proton Precipitation Induced by a Substorm. *J. Geophys. Res. Space Phys.* 126, e2020JA029091. doi:10.1029/2020JA029091

Yuan, Z., Xiong, Y., Huang, S., Deng, X., Pang, Y., Zhou, M., et al. (2014). Cold Electron Heating by EMIC Waves in the Plasmaspheric Plume with Observations of the Cluster Satellite. *Geophys. Res. Lett.* 41, 1830–1837. doi:10.1002/2014GL059241

Zhou, Q., Xiao, F., Yang, C., He, Y., and Tang, L. (2013). Observation and Modeling of Magnetospheric Cold Electron Heating by Electromagnetic Ion Cyclotron Waves. *J. Geophys. Res. Space Phys.* 118, 6907–6914. doi:10.1002/2013JA019263

Conflict of Interest: The author declares that the research was conducted in the absence of any commercial or financial relationships that could be construed as a potential conflict of interest.

frontiers in Astronomy and Space Sciences

ORIGINAL RESEARCH
published: 17 September 2021
doi: 10.3389/fspas.2021.730061

On the Presence and Thermalization of Cold Ions in the Exhaust of Antiparallel Symmetric Reconnection

Cecilia Norgren [1], Paul Tenfjord [1], Michael Hesse [2], Sergio Toledo-Redondo [3], Wen-Ya Li [4], Yin Xu [5], Norah Kaggwa Kwagala [1], Susanne Spinnangr [1], Håkon Kolstø [1] and Therese Moretto [2]*

[1]Space Plasma Physics Group, Department of Physics and Technology, University of Bergen, Bergen, Norway, [2]NASA Ames Research Center, Moffet Field, CA, United States, [3]Department of Electromagnetism and Electronics, University of Murcia, Murcia, Spain, [4]State Key Laboratory of Space Weather, National Space Science Center, Chinese Academy of Sciences, Beijing, China, [5]School of Space and Environment, Beihang University, Beijing, China

Using fully kinetic 2.5 dimensional particle-in-cell simulations of anti-parallel symmetric magnetic reconnection, we investigate how initially cold ions are captured by the reconnection process, and how they evolve and behave in the exhaust. We find that initially cold ions can remain cold deep inside the exhaust. Cold ions that enter the exhaust downstream of active separatrices, closer to the dipolarization front, appear as cold counter-streaming beams behind the front. In the off-equatorial region, these cold ions generate ion-acoustic waves that aid in the thermalization both of the incoming and outgoing populations. Closest to the front, due to the stronger magnetization, the ions can remain relatively cold during the neutral plane crossing. In the intermediate exhaust, the weaker magnetization leads to enhanced pitch angle scattering and reflection. Cold ions that enter the exhaust closer to the X line, at active separatrices, evolve into a thermalized exhaust. Here, the cold populations are heated through a combination of thermalization at the separatrices and pitch angle scattering in the curved magnetic field around the neutral plane. Depending on where the ions enter the exhaust, and how long time they have spent there, they are accelerated to different energies. The superposition of separately thermalized ion populations that have been accelerated to different energies form the hot exhaust population.

Keywords: magnetic reconnection, particle-in-cell (PIC), space physics, cold plasma, cold ion heating, plasma waves

OPEN ACCESS

Edited by:
Marian Lazar,
Ruhr-Universität Bochum, Germany

Reviewed by:
Giovanni Lapenta,
KU Leuven, Belgium
Jan Egedal,
UW Madison International Division,
United States

****Correspondence:***
Cecilia Norgren
cecilia.norgren@uib.no

Specialty section:
This article was submitted to Space Physics, a section of the journal Frontiers in Astronomy and Space Sciences

Received: *24 June 2021*
Accepted: *30 August 2021*
Published: *17 September 2021*

Citation:
Norgren C, Tenfjord P, Hesse M, Toledo-Redondo S, Li W-Y, Xu Y, Kwagala NK, Spinnangr S, Kolstø H and Moretto T (2021) On the Presence and Thermalization of Cold Ions in the Exhaust of Antiparallel Symmetric Reconnection. Front. Astron. Space Sci. 8:730061. doi: 10.3389/fspas.2021.730061

1 INTRODUCTION

Magnetic reconnection is a fundamental plasma process that converts energy stored in the magnetic fields to plasma energy by enabling the reconfiguration of the magnetic field topology. Cold plasma can be abundant in regions of magnetic reconnection, and impact the reconnection process in several ways (for a recent review, see Toledo-Redondo et al., 2021). Examples include, but are not limited to, mass loading (Fuselier et al., 2017; Dargent et al., 2020; Tenfjord et al., 2020), introduction of an extra *cold ion* diffusion region (Toledo-Redondo et al., 2016a; Divin et al., 2016), modifications to the Hall physics (Toledo-Redondo et al., 2015; André et al., 2016; Toledo-Redondo et al., 2018), and plasma heating (Toledo-Redondo et al., 2016b; Toledo-Redondo et al., 2017). In the magnetotail, cold lobe plasma below a few hundreds of eV (e.g., Engwall et al., 2009) can be heated to several keV

(e.g., Ergun et al., 2018), and at the dayside cold magnetospheric plasma of a few tens of eV (e.g., Borovsky and Denton, 2008) can be heated to hundreds of eV (e.g., Toledo-Redondo et al., 2016b) as a consequence of the reconnection process. However, where, how, and to what extent cold plasma is heated (or not) by reconnection is still not fully understood.

Cold ions have been observed deep within the exhaust, both at the dayside and nightside. In the nightside magnetotail, in the vicinity of dipolarization fronts, both Nagai et al. (2002) and Xu et al. (2019) found, in addition to a hot component, two cold beams counter-streaming parallel to the magnetic field. They proposed that the cold ions moved along the reconnected field lines directly from the lobes due to the topological change enabled by reconnection. The counter-streaming beams are attributed to Fermi acceleration of ions initially dwelling on flux tubes downstream of the front that are being swept up as the front expands past them. This process is also described by Eastwood et al. (2015), although the authors attributed the source population to pre-existing plasma sheet, not the lobes. Closer to the X line, Alm et al. (2018) also found that cold ions could dominate the density well inside the separatrices, and account for a significant fraction even when the magnetic field amplitude approached zero. Counter-streaming beams observed during nightside reconnection has also been attributed to acceleration by the Hall electric field (Wygant et al., 2005). This is also shown in numerical simulations (e.g., Divin et al., 2016). While some studies suggest that the Fermi and Hall mechanisms may be dominant in the far and near exhaust, respectively, their relation and effectiveness are not fully understood. For example, Drake et al. (2009) noted that the energization by the Hall electric field arose from a potential, and that the oscillatory motion along the normal direction of the current sheet did not lead to a significant net energization. Drake et al. (2009) also presented a model of the ion heating based on a scenario of counter-streaming ion populations, originating from opposite sides of the current sheet and being subject to Fermi acceleration in the exhaust. Haggerty et al. (2015) developed the model further by taking into account a parallel electric field supported by the heated electrons moving downstream, away from the X line. The corresponding electric field potential slows down ions in the frame of the outflow field lines, reducing the acceleration, and thereby the ion heating.

At the dayside magnetopause, Li et al. (2017) observed parallel jets, carried by cold magnetospheric ions, on the magnetosheath boundary of the exhaust, showing that initially cold ions could remain cold while traversing the exhaust. Toledo-Redondo et al. (2016b) showed that cold ions could be found inside the reconnection exhaust far away from the X line. Closer to the X line, they found that the cold ions were heated by waves and large electric field gradients inside the separatrix region. Graham et al. (2017) also found that cold magnetospheric ions could interact with magnetosheath ions that enter the magnetosphere through the finite gyroradius effect. The resulting ion-ion streaming instability lead to the formation of lower-hybrid waves that can heat the cold ions. Schriver and Ashour-Abdalla (1990) also suggested that cold inflow plasma in the plasma sheet boundary layer could be heated through an ion-ion streaming instability due to the cold inbound plasma and the hotter parallel ion beams commonly observed there (e.g., Eastman et al., 1986; Nagai et al., 1998). These findings suggest that the separatrices, and the proximity to the X line, may play a role in how cold ions are heated. Dayside observations have also indicated that cold ions may become more efficiently heated if their relative density is lower (Toledo-Redondo et al., 2016b; Toledo-Redondo et al., 2017). These findings are also consistent with those by Xu et al. (2019), who presented one case where the density of the cold populations were large enough such that the density across the front remained approximately constant, in contrast to the more commonly observed density decrease (e.g., Runov et al., 2011).

The thermal population inside the exhaust of reconnection has been studied by several authors. Using hybrid simulations, Nakamura et al. (1998) showed that ion orbit characteristics vary as a function of the distance from the reconnection line due to the change in magnetic field curvature. Based on the magnetic field curvature parameter $\kappa^2 = r_B/\rho_i$ (Büchner and Zelenyi, 1989), where r_B is the radius of magnetic field curvature, and ρ_i is the ion gyroradius, they defined three classes of orbits. Closer to the jet front, in the magnetic pile-up region, the radius of magnetic field curvature typically exceeded the ion gyroradii, and the inflow population could remain magnetized and formed the cold counter-streaming beams mentioned above. In an intermediate region, where the radius of curvature was comparable to the ion gyroradii, the motion became stochastic. Closer to the X line, where the ion gyroradii greatly exceeded the curvature radius, the ions followed typical Speiser orbits (Speiser, 1965), meandering in the field reversal and slowly turning towards the outflow direction over the course of several bounces. The Speiser orbits typically form distributions in the shape of half circles (e.g., Nakamura et al., 1998; Zenitani et al., 2013; Vines et al., 2017) that rotates around the current sheet normal direction with distance from the X line (Arzner and Scholer, 2001; Drake et al., 2015; Nagai et al., 2015). The relative location in the circle is related to the amount of gyroturning around the normal magnetic field, which in turn is related to the number of bounces around the neutral plane the corresponding particles has performed (e.g., Zenitani et al., 2013).

In this work, we take a new integrated look at the acceleration and formation of a thermalized exhaust from initially cold inflow ions. We focus on the distinction between the cold ions being swept up by the exhaust as it expands (e.g., Eastwood et al., 2015) and the cold ions entering the exhaust closer to the X line (e.g., Zenitani et al., 2013). Using a fully kinetic 2.5D particle-in-cell simulation, where a cold inflow is captured by the reconnection process, we address the following questions:

1) When can cold ions potentially appear deep within the exhaust?
2) When do the initially cold ions remain cold, and when are they heated?
3) How are the cold ions heated?

2 SIMULATION SET-UP

To investigate how the cold ions are accelerated and thermalized, we perform a fully kinetic 2.5D particle-in-cell simulation (Hesse et al., 1999) with symmetric inflow conditions and no guide field.

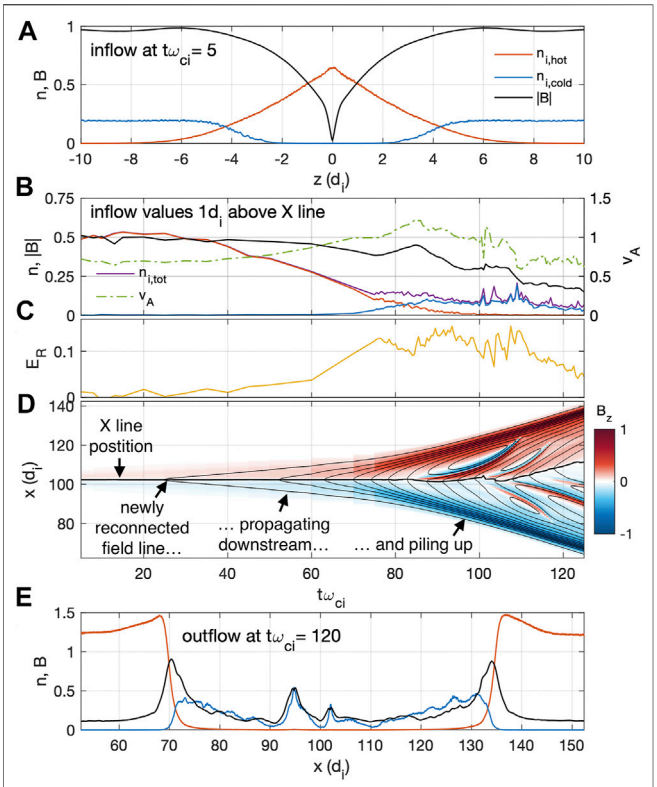

FIGURE 1 | (A) Magnetic field $|\mathbf{B}|$ and densities $n_{i,hot}$, and $n_{i,cold}$ in the inflow along a vertical cut through the X line at $t\omega_{ci} = 5$. **(B)** $|\boldsymbol{B}|$, $n_{i,hot}$, $n_{i,cold}$, n_{tot}, and v_A in the inflow $1d_i$ above the X line. **(C)** Reconnection rate, here defined as the out-of-plane electric field E_y at the X line. **(D)** Magnetic field B_z around the equatorial plane as function of time and x. The thicker black line shows the location of the X line, while the thinner black lines show equipotential contours of A_y. Newly reconnected field lines appear at the X line and propagate outwards. **(E)** Magnetic field $|\mathbf{B}|$ and densities $n_{i,hot}$, and $n_{i,cold}$ in the outflow along a horizontal cut through the X line at $t\omega_{ci} = 120$. Note that the colors of the lines are consistent throughout the figure, and we therefore only define the legend the first time a quantity appear.

The simulation is initialized with a Harris sheet equilibrium of hot ions and electrons. In addition, we add cold ions and electrons to the inflow regions:

$$B_x = B_0 \tanh(z/L)$$
$$n = n_0 \cosh^{-2}(z/L) + n_c\left[\frac{1}{2} + \frac{1}{2}\tanh\left(\frac{|z| - 2L}{0.5L}\right)\right].$$

Densities are normalized to n_0, times to the inverse ion cyclotron frequency ω_{ci}^{-1}, lengths to the ion inertial length $d_i = c/\omega_{pi}$, velocities to the Alfvén speed v_A, and energies to $m_i v_A^2$. These quantities are based on either or both of n_0 and B_0: $\omega_{pi} = (n_0 e^2/m_i \epsilon_0)^{1/2}$, $v_A = B_0^2/(\mu_0 m_i n_0)$, and $\omega_{ci} = B_0/e m_i$. The ion-to-electron mass ratio is $m_i/m_e = 100$, the ion-to-electron temperature ratio of the hot species is $T_i/T_e = 5$, with $n_0(T_i + T_e) = 0.5B_0^2$, and the electron plasma-to-cyclotron frequency ratio is $\omega_{pe}/\omega_{ce} = 2$, giving $c/v_A = (m_i/m_e)^{1/2}\omega_{pe}/\omega_{ce} = 20$. The half width of the Harris current sheet is $L = 2d_i$. The cold ion density is $n_c = 0.2n_0$, and the temperatures of the cold protons and electrons are initially $T_{ic} = T_{ec} = 0$, where the subscript 'c' refers to the cold populations. We choose to set the initial temperature to zero to be better able to follow the evolution of the initially cold populations in phase space. The particles are initialized as three ion and three electron populations: the hot Harris sheet populations, the cold plasma originating from the north ($z > 0$), and the cold plasma originating from the south ($z < 0$). As such, we are able to trace the origin of the particles at later times when they are mixed within the exhaust. The simulation box size is $200 \times 25d_i$ divided into a grid of 6400×1600 cells. The boundary conditions are periodic in x and reflective in z. The out-of-plane electric field at the reflective boundary ($z = \pm 12.5d_i$) is $E_y = 0$, which implies the conservation of magnetic flux. To initiate reconnection, a localized perturbation is added to the center of the box.

3 FORMATION OF DIPOLARIZATION FRONT DUE TO DECREASE IN INFLOW DENSITY

The formation of dipolarization fronts have been attributed to three main mechanisms: jet braking (Birn et al., 2011), transient reconnection (Sitnov et al., 2009; Birn et al., 2011; Fu et al., 2013), and spontaneous formation (Sitnov et al., 2013). In this section, we show that the dipolarization fronts in our simulation form due to transient reconnection associated with the transition from (hot) dense to (cold) tenuous inflow plasma.

Figure 1A shows the magnetic field and density profiles along a vertical cut (z) through the X line, at $t\omega_{ci} = 5$. We note that the deviation of the originally hot plasma $n_{i,hot}$ in **Figure 1A** from a Harris sheet density profile is due to the initial perturbation. **Figure 1B** shows the temporal evolution of the density and magnetic field in the inflow, 1 d_i above the X line. As the denser Harris sheet plasma is processed by the reconnection process, and moved downstream of the separatrices and X line, the inflow adjacent to the X line is gradually replaced by the more tenuous and cold population, resulting in a density decrease. The magnetic field also decreases, albeit slower than $\sqrt{n}$, and the combined effect leads to an increase in the inflow Alfvén speed v_A. We note that a significant portion of the decrease of $|\mathbf{B}|$ at later times is due to flux exhaustion caused by the finite simulation domain. However, the main sequence of interest is the increase in v_A, which is not dominated by this effect. At the same time that v_A increases, we observe an increase in the reconnection rate, defined as the out-of-plane electric field E_y at the X line (normalized to $v_A B_0$) (**Figure 1C**), closely related to the changes in v_A. We therefore conclude that, consistent with mass-loading scaling, the increase in reconnection rate is due to the transition from a dense to a tenuous inflow plasma.

The increase in reconnection rate leads to the formation of two flux pile-up regions propagating away from the X line. This is seen in **Figure 1D** where we plot $B_z(x, t)$ at $z = 0$. The thicker black line shows the location of the main X line. The thinner black lines are equipotential contours of the magnetic vector potential A_y, defined by the in-plane magnetic field (B_x, B_z) through $\mathbf{B} = \nabla \times \mathbf{A}$, and show the motion of field lines in the outflow.

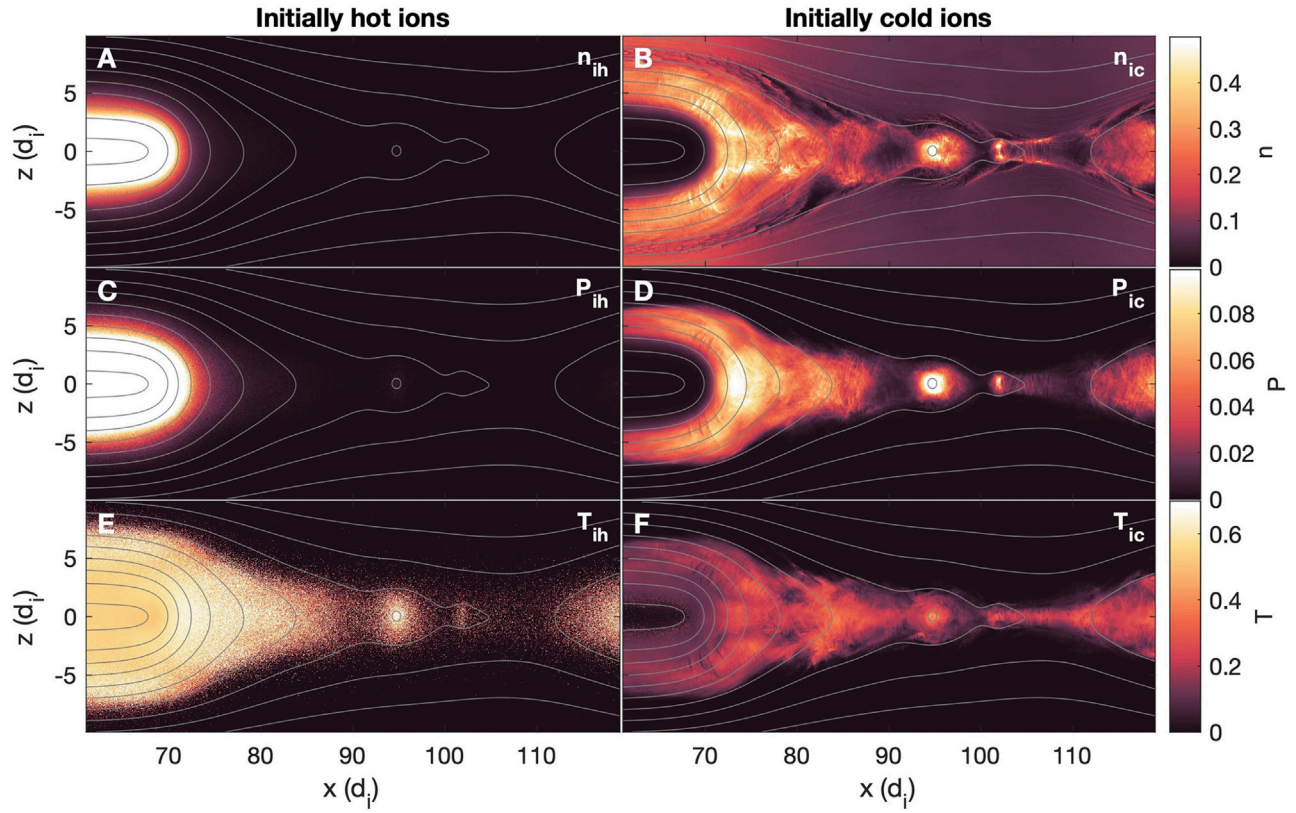

FIGURE 2 | Density, pressure, and temperature of initially hot and cold ions at $t\omega_{ci}$ = 120: **(A)** n_{ih}, **(B)** n_{ic}, **(C)** P_{ih}, **(D)** P_{ic} **(E)** T_{ih}, **(F)** T_{ic}. The initially cold plasma dominate the density and pressure at $x \gtrsim 71$ and $x \gtrsim 71$, respectively. While the hot temperature exceeds the cold temperature in large parts of the exhaust, their effect on the dynamics inside the exhaust is negligible due to their low density. The initially cold ions are heated to temperatures comparable to the initial temperature of the Harris sheet ions.

Newly reconnected field lines appear at the main X line and adjacent to islands, and propagate outwards. The islands are seen as localized regions of B_z reversals, numbering five in total, with the first one appearing at $t\omega_{ci} \sim 85$. The slopes of the lines indicate the propagation speeds of the field lines. When the reconnection rate increases, we can see how newly reconnected field lines appear at a greater rate and propagate outwards at a higher speed, such that they stack up and form two regions of stronger magnetic field B_z. In magnetotail nomenclature, these flux pile-up regions are commonly referred to as dipolarizing flux bundles (DFB), and the leading edges of the two DFBs as dipolarization fronts (DFs) (e.g., Liu et al., 2013). In the magnetotail, the tailward propagating front is also referred to as an anti-dipolarization front (e.g., Li et al., 2014). At $t\omega_{ci}$ = 120, these fronts have reached $x \approx 70$ and $x \approx 135$. In **Figure 1E**, we can see how the fronts roughly separate the initially hot and cold plasmas. From this, we conclude that the dipolarization fronts can be considered as compressed versions of the initial current sheet edge. The field lines that reconnected faster, and went on to form these flux pile-up regions, were also the ones that separated the hot from the cold plasma. This is why the initially cold plasma end up deep within the exhaust, all the way to the dipolarization fronts. Whether or not this initially cold plasma can remain cold depends on the heating mechanisms.

In the following, we will mainly focus on the time $t\omega_{ci}$ = 120, where the two flux pile-up regions have expanded to x = 70 and x = 135. In **Figure 2**, we show the density, pressure, and temperature of the initially hot and cold ions, respectively. The gray contour lines show the in-plane magnetic field. The main X line is located at x = 109, with a second and third X line at x = 100, and x = 91. These three X lines straddle two magnetic islands that are centered at x = 95, and x = 102. In order to more easily compare the hot and cold ion contributions to density and pressure in the exhaust, we have saturated the color scales. In the equatorial plane, the cold ion density exceeds the hot ion density for $x \gtrsim 71$, while the cold ion pressure exceeds the hot ion pressure for $x \gtrsim 72$ in the left exhaust. While the hot temperature exceeds the cold temperature in large parts of the exhaust, their effect on the dynamics inside the exhaust is negligible due to their low density. The initially cold ions are heated to temperatures comparable to the initial temperature of the hot Harris sheet ions, where the initial Harris sheet temperature is given by $T_i = 0.5B_0^2/n_0(1 + T_e/T_i) \approx 0.42$. These values are also comparable to the levels of ion heating predicted by Drake et al. (2009), $T_i = m_i v_0^2/3 \approx 0.16 - 0.33$, where $v_0 \approx 0.7$–1.0 is the speed of the exhaust magnetic field lines that varies slightly throughout the

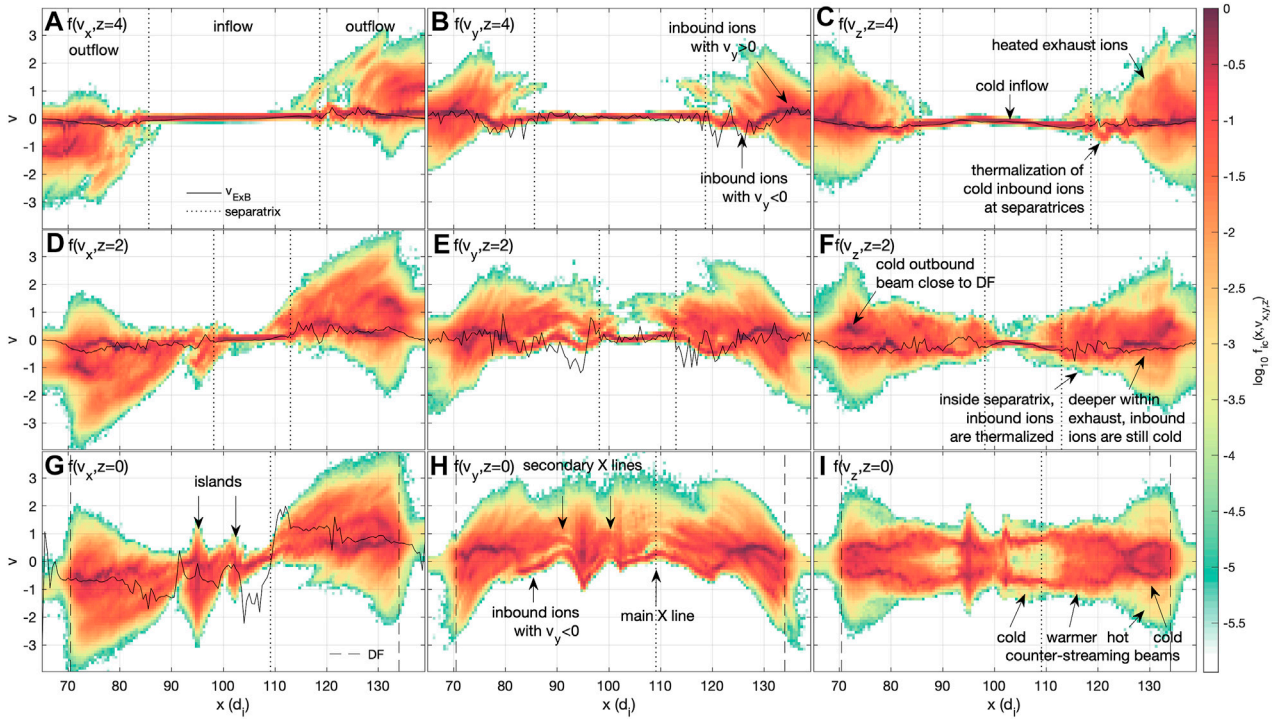

FIGURE 3 | Reduced distributions of initially cold ions at $t\omega_{ci} = 120$, at **(A–C)** $z = 4$, **(D–F)** $z = 2$, and **(G–I)** $z = 0$. The vertical dashed lines show the location of the separatrix, which at $z = 0$ maps to the X line. The solid line shows $\mathbf{v}_{E\times B}$. We do not show these in panels **(H)** and **(I)** because they contain B_x, which is small there. While the cold ions are most apparent in the inflow, they are also present in the outflow. In an intermediate region, just inside the separatrices, the cold incoming population is affected by the dynamics at the separatrices, and becomes partly thermalized. This is perhaps most prominently seen in $f(x, v_z)$.

exhaust (as shown by the slope of the black lines in **Figure 1D**). At the same time, the hot ions are heated to slightly higher values. Overall, the density, pressure, and temperature of initially cold ions are fairly structured. Concentrations of cold ions are found inside the islands, and adjacent to the front (extending along the magnetic field toward the north and the south, as well as along the equatorial plane towards the X line). The density cavities located at the separatrices are associated with high speed electron flows toward the X line (not shown). To investigate the kinetic structure responsible for the density, pressure, and temperature profiles, we will in the next section study the ion distributions within the exhaust.

4 KINETIC STRUCTURE OF ION DISTRIBUTIONS WITHIN THE EXHAUST

In this section we investigate the structure of the ion distributions within the exhaust. **Figure 3** shows the reduced distributions of initially cold ions $f_{ic}(x, v_x)$, $f_{ic}(x, v_y)$, $f_{ic}(x, v_z)$ at $z = [0, 2, 4]$ between the two dipolarization fronts at time $t\omega_{ci} = 120$. The reduced distributions are integrated over the remaining velocity dimensions, e.g. $f(v_x) = \int f(v_x, v_y, v_z)dv_y dv_z$. At this time, the initially cold ions dominate the density and pressure within the exhaust (see **Figure 1E** and **Figure 2**), which is why we do not include the initially hot population in the further analysis. The distributions are sampled over boxes spanning a spatial domain of $\Delta x \times \Delta z = 0.5 \times 0.5$, i.e. $x = 75 \rightarrow x = 75 \pm 0.25$, and $z = 4 \rightarrow z = 4 \pm 0.25$. The dotted vertical lines show the location of the separatrices, the dashed vertical lines at $z = 0$ show the locations of the DFs, and the black solid lines show the corresponding components of $\mathbf{v}_{E\times B}$. The still cold populations are identified by higher phase space densities that occupy a relatively small velocity interval. The initially cold ions that have become heated are seen as (relatively) lower phase space densities that occupy larger velocity intervals.

Heated ions are observed throughout the exhaust. Cold ions are most prominent in the inflow region at $z = 2$ and $z = 4$, but are also found throughout the exhaust, at all z. In an intermediate region, inside the separatrices, the inbound ions ($v_z < 0$) are affected by the convergent electric field associated with the separatrix density cavities. At $z = 4$, this region is clearly seen between $x = 118$ and $x = 127$ for the right exhaust (**Figure 3C**). At $z = 2$, this region has extended over a larger range along x ($x = 113–124$), and the inbound ions have become more thermalized (**Figure 3F**). At $z = 0$, this region maps to the intermediate exhaust (**Figure 3I**). In $f(v_z, z = 0)$, we see counter-streaming populations throughout the exhaust. The coldest populations are found in the vicinity of the X lines and the DFs (where they are superposed on a hot population). Outbound cold ions ($v_z > 0$) in $f(v_z, z = 2)$ are only observed in the immediate vicinity of the DFs ($70 < x < 75$ in left exhaust). This means that only a portion of the cold beams observed at $z = 0$ are actually leaving the equatorial

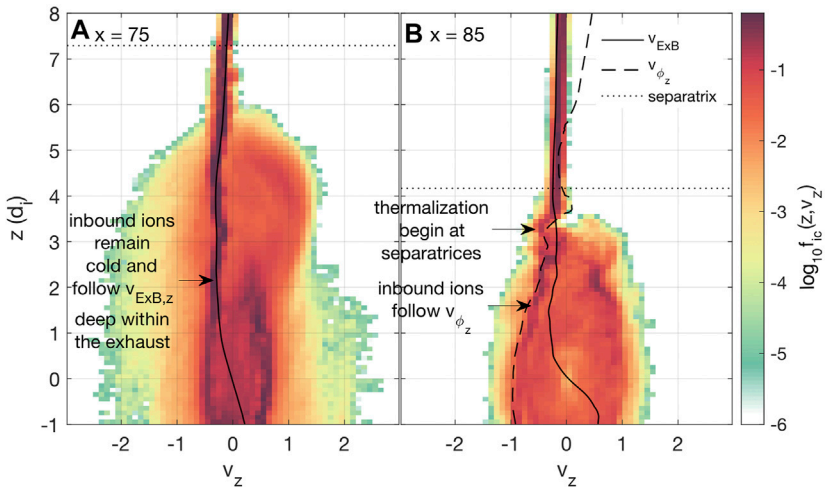

FIGURE 4 | Reduced ion distributions $f(z, v_z)$ at **(A)** $x = 75$ and **(B)** 85 at $t\omega_{ci} = 120$. The solid, dashed, and dotted lines show $v_{E\times B,z}$, $v_{\phi_z} = \sqrt{2e\phi_z/m_i}$, where $\phi_z = -\int E_z dz$, and the location of the separatrix, respectively. Further away from the X line, at $x = 75$, the cold inbound ions remain cold and follow $v_{E\times B,z}$ deep within the exhaust. Closer to the X line, at $x = 85$, the cold inbound ions begin to thermalize and deviate from $v_{E\times B,z}$ shortly after crossing the separatrix. Although the phase space density of the inbound beam decreases away from the separatrix, the remnants of it follow v_{ϕ_z}. The thermal population consists largely of ions that have already crossed $z = 0$ one or multiple times.

region with their temperature relatively intact. In the rest of the exhaust (closer to the separatrices and X lines), the outbound plasma at $z \geq 2$ is strictly thermal.

In $f(v_y, z = 0)$, we see a distinct transition in the speed of the cold ion population at around $x = 82$ in the left exhaust (with a corresponding transition in the right exhaust). At $x < 82$, the cold ions are observed at $v_y > 0$, while at $x > 82$ the cold ions are observed at $v_y < 0$ (with gradually increasing v_y towards the X line). As explained by Divin et al. (2016), the initially $v_y < 0$ is acquired through a process where the inbound ions are first accelerated by the Hall electric field E_z leading to an enhanced flow v_z towards the equatorial plane. This v_z is turned towards $-\hat{y}$ by the Lorentz force $v_z B_x < 0$. They defined the discrete transition in v_y as the edge of the ion diffusion region. We note that similar behaviour is also observed inside the separatrices in the off-equatorial regions. However, the transition is continuous here as $v_y < 0$ is gradually turned towards $v_y > 0$ by the out-of-plane electric field E_y deeper within the exhaust. Closest to the DF, the cold beam seen at $v_y > 0$ approaches $v_y = 0$. In the following sections, we will investigate the role of separatrices and magnetic field curvature in shaping the kinetic structure of cold ions inside the exhaust.

4.1 The Role of Separatrices in Ion Thermalization

Depending on where the ions cross into the exhaust the inbound ion motion v_z, mentioned in the previous section, can either be on average magnetized ($v_\perp \approx v_{E\times B}$) or demagnetized ($v_\perp \neq v_{E\times B}$). This is illustrated in **Figure 4**, where we plot the reduced distributions $f_{ic}(v_z)$ as a function of z at $x = 75$ and 85. The dotted line (now horizontal) again shows the separatrix location, while the solid lines show $v_{E\times B,z}$. As expected, the ion edge (e.g., Gosling et al., 1990; Lindstedt et al., 2009), i.e. the location at where the first reconnected ions appear (here represented by the thermal population centered on $v_z > 0$) inside of the separatrix, is further inside the separatrix deeper within the exhaust. At $x = 75$ and $x = 85$, B_x dominates the magnetic field in the range $|z| > 1.5$ and $|z| > 0.5$, respectively. Where B_x dominates, v_z constitutes a perpendicular component of the ion flow, and a deviation of the cold ions from $v_{E\times B,z}$ signifies demagnetization. At $x = 75$, the cold ion population follows $v_{E\times B,z}$ until $z \approx 2$ (see also Toledo-Redondo et al., 2018), while at $x = 85$, they deviate shortly after crossing the separatrix. At $x = 85$, the Hall electric field E_z is quasi-stationary over the time it takes for an ion to cross from the separatrix to the neutral plane. For this location, we have also plotted the speed $v_{\phi_z} = \sqrt{2e\phi_z/m_i}$ corresponding to the Hall electric field potential $\phi_z = -\int E_z dz$. We have grounded the potential to a region just outside the separatrix. The increase in v_{ϕ_z} seen outside the separatrices is due to wave effects formed due to the finite box size, and have no effect on the dynamics within the exhaust. Although the inbound beam is gradually thermalized between the separatrix and the neutral plane, it roughly follows v_{ϕ_z} all the way to $z = 0$. This indicates that these ions are demagnetized, and accelerated across the magnetic field by E_z as explained by Divin et al. (2016). This initial speed, governed by the potential, roughly forms the outer boundary of the thermal ion population within the separatrices at this location. This thermal population consists mainly of ions that have crossed the neutral plane at least once. We note that although the other components can also lead to demagnetization, here we chose to focus on v_z to illustrate the clear difference between v_{ϕ_z} and $v_{E\times B,z}$ at $x = 85$.

To further illustrate, and to better understand the differences between the populations that remain cold deep within the exhaust, and the population inside the separatrices that are slightly more thermalized, we make use of test particles

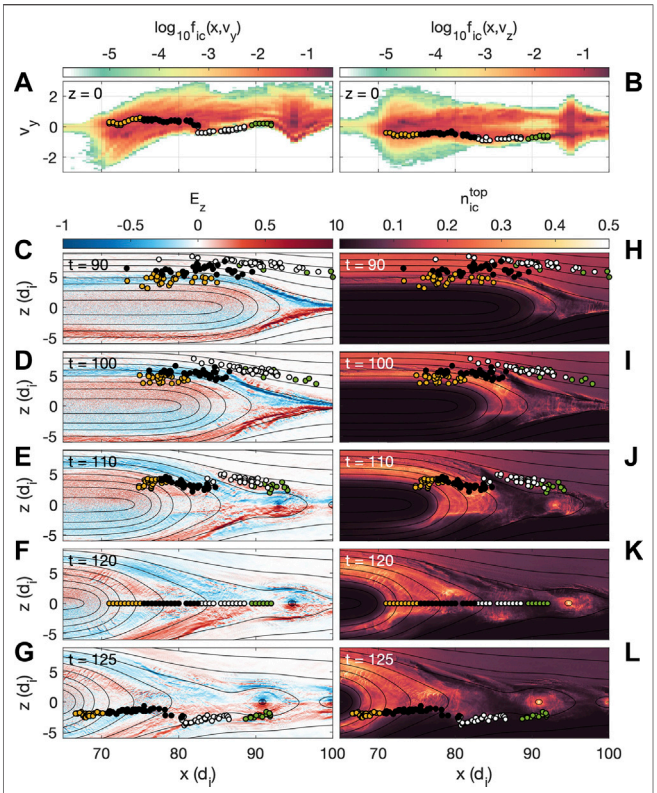

FIGURE 5 | Test particle positions at five different times. The initial conditions for each particle are taken at t = 120, from the locations in phase space shown in **(A, B)**. **(C–G)**, and **(H–L)** shows the particle position for five different times, overlaid E_z and n_{ic}^{top}, respectively. The subdivision into yellow/black/white/green populations are partly based on the initial conditions, and further explained in the text.

integrated in the dynamically changing electric and magnetic fields. The initial velocities of the test ions are chosen from the cold component of $f_{ic}^{top}(x, z = 0, t = 120)$, see **Figures 5A,B**. They are integrated forward in time until t = 125, and backward until t = 90. The location of the ions are shown overlaid E_z (**Figures 5C–G**) and n_{ic}^{top} (**Figures 5H–L**) for t = [90, 100, 110, 120]. We have divided the ions into four groups, based on the ions speed v_y, and postition x at t = 120; yellow ($v_y > 0$, $x \leq 75$), black ($v_y > 0$, $75 < x \leq 85$), white ($v_y < 0$), and green ($v_y > 0$, $75 < x < 90$). We note that the out-of-plane displacement of the ions during the integrated time interval is about $4 - 8d_i$. This corresponds to 0.3–0.5R_E (n = 0.3 cm^{-3}, $1d_i \approx 415$ km, $1R_E \sim 15d_i$), which is less than estimates of the dawn-dusk scale of plasma sheet flows derived from observations (Nakamura et al. (2004) finds a dawn-dusk extent of about $2 - 3R_E$). The 3D structure of the reconnection exhaust in the magnetotail should therefore be large enough to accommodate the level of acceleration seen in our simulations.

The main difference between the yellow/black and the white/green ions is where they cross the separatrices, or rather, what sort of separatrices they cross. While the separatrices, by definition, span the entire range of x in the simulation, they are highly active closer to the X line, and comparatively inactive, further away. Here, we define active separatrices as characterized by large amplitude parallel electron flows toward the X line, associated density cavities, and electric fields, electrostatic waves propagating along the magnetic field in the direction of the electron flow, and in general stronger Hall fields. While a Hall electric field can still be observed inside the inactive separatrices, it is typically weaker, and is generally characterized by the absence of deeper density cavities, small to none parallel electron flow, and less wave activity. The white/green ions enter the exhaust at active separatrices, are slightly thermalized at the separatrices, substantially accelerated by E_z, and eventually form the hot thermal population. The green ones first enter an island, while the white ones directly enter the open exhaust. The yellow/black populations enter the exhaust at inactive separatrices, or rather, the separatrices expand to encompass them. When they are caught up by the expanding exhaust region, they are picked up by the motional electric field E_y, and are accelerated while remaining relatively magnetized.

In addition, the black and white ions also show distinct differences in their z distribution. In **Figure 5B**, we can see that the white ions overall have larger $|v_z|$ at $z = 0$. The white ions, affected by the Hall electric field, gain higher v_z, and are able to penetrate deeper into the southern side of the exhaust. This is reflected in the density n_{ic}^{top}.

The subdivision into the yellow and black populations is mainly based on their behaviour around, and after having crossed, the neutral plane. While the time period of the test particles is not large enough to properly display their different behaviours, the density structure is. At all times, there is a clear cutoff in n_{ic}^{top} at about $z = -2$ in the intermediate exhaust. Closer to the dipolarization front, the density extends below $z = -2$. At t = 125, the black ions are situated at the edge of the density cutoff and are just about to reflect. In contrast, the yellow ions, located approximately at the same z, continue downward. In the next section, we will show that whether ions are reflected or not is largely due to the level of magnetization.

4.2 The Role of Magnetic Field Curvature in Ion Thermalization

To illustrate how the ion magnetization changes from directly adjacent the front, to a distance away, we take a closer look at the magnetic curvature $\mathbf{k}_B = \hat{b} \cdot \nabla \hat{b}$, where $\hat{b} = \mathbf{B}/|\mathbf{B}|$ is the magnetic field unit vector. Büchner and Zelenyi (Büchner and Zelenyi, 1989) defined the curvature parameter $\kappa^2 = r_B/\rho_i$, where $r_B = |\mathbf{k}_B|^{-1}$ is the curvature radius and $\rho_i = v_{i,\perp}/\omega_{ci}$ is the ion gyroradius. For $\kappa \gg 1$, the particle motion is adiabatic and the magnetic moment is conserved. This implies that the change in pitch angle as the ion approaches the neutral plane is reversed when the ion leaves the neutral plane on the other side. Hence, the shape of an ensemble is relatively well preserved after transmission. For $\kappa \to 1$, the motion becomes stochastic, which enables non-reversible pitch-angle scattering during the neutral sheet crossing. **Figure 6B** shows the 2D map of $\log_{10} r_B$, while **Figure 6C** shows the value at $z = 0$. For reference, in **Figure 6A** we also show the 2D density map of initially cold ions originating from the top. In the equatorial plane, closer to the front, due to the flux-pile up and more dipolarized magnetic

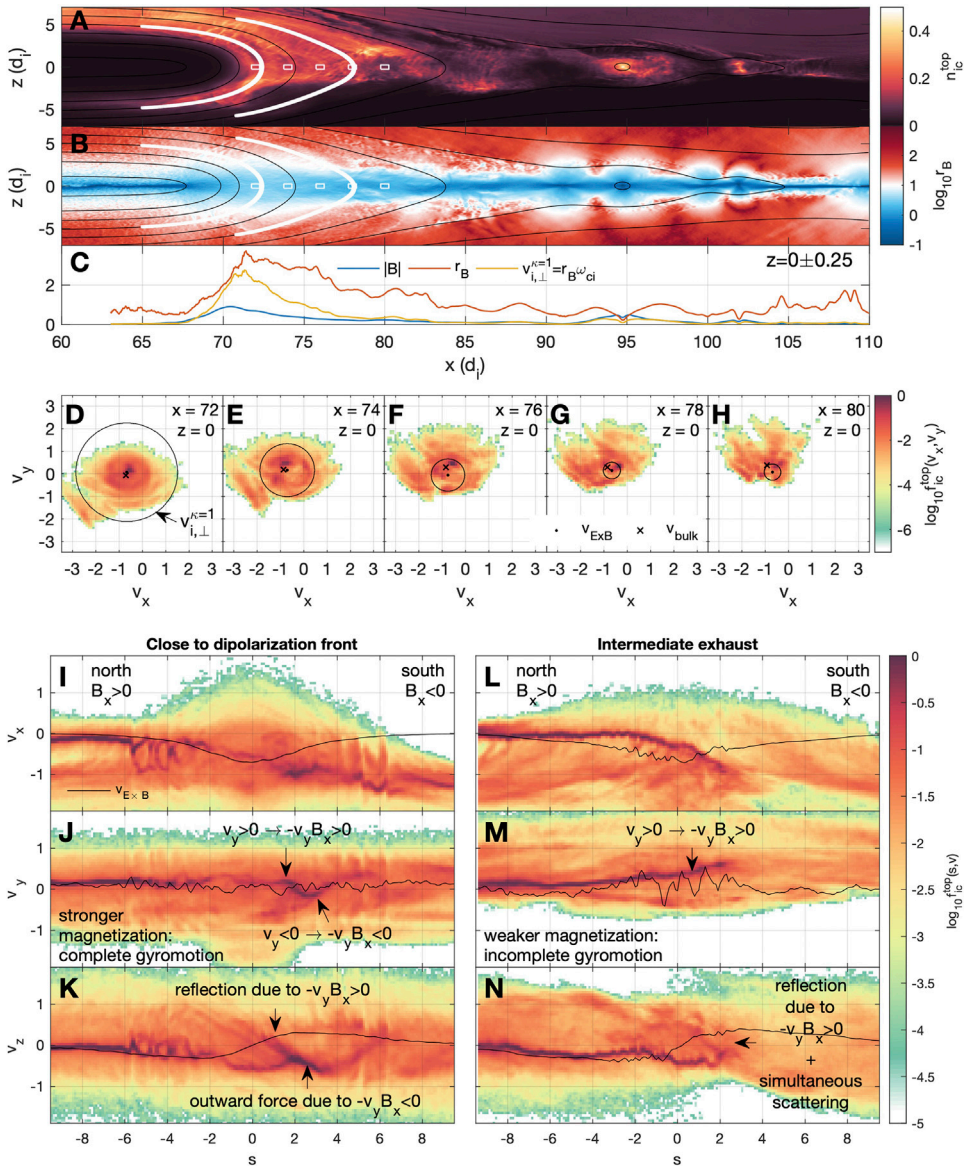

FIGURE 6 | (A) Density of initially cold ions originating from the north, n_{ic}^{top}. **(B)** Magnetic field curvature radius $\log_{10} r_B$. **(C)** Magnetic field magnitude $|\mathbf{B}|$, r_B, and $v_{i,\perp}^{\kappa=1} = r_B\omega_{ci}$. **(D–H)** Reduced distributions $f_{ic}^{top}(v_x, v_z)$ at $z = 0$, and six different x, marked by white squares in **(A, B)**. The cross '×' shows the bulk velocity, the dot '·' shows $\mathbf{v}_{E\times B}$, and the larger circle shows $v_{i,\perp}^{\kappa=1}$, centered on $\mathbf{v}_{E\times B}$. **(I–N)** Reduced distributions $f(s, v)$ along the two different field lines marked as white lines in **(A, B)**. Panels **(I–K)** corresponds to the field lines located furthest downstream. The black line shows $\mathbf{v}_{E\times B}$. The s is the length along the field line, where $s = 0$ corresponds to $z = 0$, and $s > 0$ ($s < 0$) corresponds to $z < 0$ ($z > 0$).

field, the magnetic field is stronger, the magnetic curvature is smaller, and consequently the radius of curvature is larger. Since the gyroradii vary significantly over our ensemble of ions due to differences in particle speed, so will κ. In **Figure 6C**, we have plotted the speed $v_{i,\perp} = \kappa^{-2} r_B \omega_{ci}$, for $\kappa = 1$. The speed corresponding to $\kappa = 1$ (yellow line) peaks at $r_B\omega_{ci} \approx 2.5$ at about $x = 72$. At about $x = 75$, $r_B\omega_{ci} \approx 1$.

Figures 6D–H show 2D reduced distributions $f(v_x, v_y)$ at $z = 0$, and $x = [72, 74, 76, 78, 80]$ (white squares in **Figures 6A,B**). At $z = 0$, the magnetic field is dominated by B_z, and $f(v_x, v_y)$ is therefore the distribution in the plane perpendicular to $\mathbf{B}$, such that $v_{i,\perp} = \sqrt{v_x^2 + v_y^2}$. The circles overlaid the distributions show $v_{i,\perp} = \kappa^{-2} r_B \omega_{ci}$, with $\kappa = 1$, based on the local magnetic field, and centered on $v_{E\times B}$ (marked by the dot '·'). The bulk velocity is shown with the cross ('×'). The radii of the circles are given by the local value of $v_{i,\perp}^{\kappa=1}$ (yellow line in **Figure 6C**). Ions outside (inside) the circle correspond to $\kappa < 1$ ($\kappa > 1$), or equivalently $\rho_i > r_B$ ($\rho_i < r_B$). Hence, we expect ions that are well within the circles to follow adiabatic motion and to experience only limited pitch-angle scattering. In contrast, ions that are located close to, and

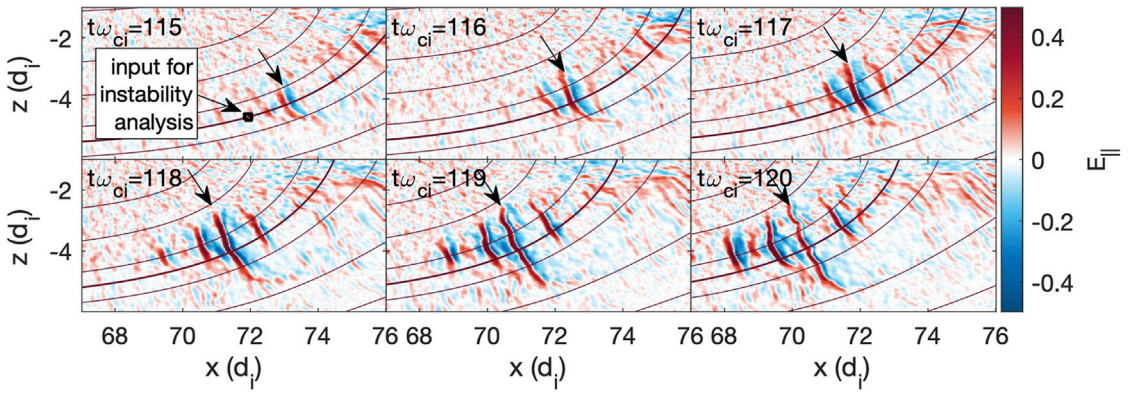

FIGURE 7 | Electrostatic solitary waves inside the southern exhaust. The arrow recurring in every panel identifies one given structure.

outside, the circles are expected to experience significant pitch angle scattering. Closest to the front (x = 72), $v_{i,\perp}^{\kappa=1}$ is relatively large, and even encompass the majority of the thermal population. At x = 74, the cold population is still well inside $v_{i,\perp}^{\kappa=1}$, but a large part of the thermal population is outside. At x = 76, 78, 80, the drift of the cold populations, and even their thermal spread becomes comparable to, and eventually exceeds, $v_{i,\perp}^{\kappa=1}$. Based on this, we expect ions crossing the neutral plane closer to the DF to experience less pitch-angle scattering, and to be able to remain relatively cold while traversing to the other side of the current sheet.

To investigate the evolution of the ion distributions around the neutral plane, we plot the 1D reduced distributions f_{ic}^{top} along two select field lines (marked as white lines in **Figures 6A,B**). In **Figures 6I–K**, we show the highlighted field line closest to the front, in the region where n_{ic}^{top} extends below $z = -2$ and $v_{i,\perp}^{\kappa=1} \gtrsim 2$ at $z = 0$. In **Figures 6L–N**, we show the highlighted field line in the intermediate exhaust, where n_{ic}^{top} has a cut-off at $z = -2$ and $v_{i,\perp}^{\kappa=1} \approx 0.5$ at $z = 0$. The distributions are plotted as a function of distance along the field line s, where $s = 0$ corresponds to $z = 0$, and, because the direction of the field line runs from north to south, $s > 0$ ($s < 0$) corresponds to $z < 0$ ($z > 0$). The corresponding components of $\mathbf{v}_{E\times B}$ are shown as black lines.

We start by looking at the field line located closer to the front (**Figures 6I–K**). At about $s = -10$, the cold populations slowly drift with the magnetic field. In $f_{ic}^{top}(v_x)$ a hotter outbound (leaving the neutral plane) beam is also observed at about $v_x = -1$. At around $s = -5$, we see clear evidence of ion trapping in $f_{ic}^{top}(v_x)$ and $f_{ic}^{top}(v_z)$. These structures in phase space correspond to the small density enhancements seen at around $x = 70$ and $z = 5$ in **Figure 6A**. We will discuss the corresponding waves further in **Section 4.3**. Here we merely note that these structures contribute to the cold ion thermalization already before they enter the central current sheet. The cold inbound ions roughly follow $\mathbf{v}_{E\times B}$ until $s \approx -2$. Here the rapid rotation of the magnetic field from $\hat{x}$ to $\hat{z}$ leads to the deviation of v_z from $v_{E\times B,z}$, such that the perpendicular motion becomes parallel as part of the Fermi acceleration (slingshot) process (Northrop, 1963). In $f_{ic}^{top}(v_y)$, the cold population is seen to oscillate a few times close to $v_y = 0$. This is due to the gyration around the magnetic field of the relatively well magnetized ions. The level of magnetization is also seen in $f_{ic}^{top}(v_x)$ at $z = 0$, which in this location represents a perpendicular component. Close to $z = 0$, the cold component has a speed $v_x \approx v_\perp \approx v_{E\times B,x}$. After the neutral plane crossing ($z < 0$, $s > 0$), some of the cold ions are reflected at $s \approx -2$, while some manage to continue outward. While both E_z and $v_x B_y$ play minor roles in the acceleration along $\hat{z}$, the main responsible force is $-v_y B_x$. The ions that are reflected have a speed $v_y > 0$ and therefore experience an upward force $-v_y B_x > 0$, since $B_x < 0$ in the south. The ions that manage to continue outward are the ones that have crossed into $v_y < 0$ during the gyromotion and experience a downward force $-v_y B_x < 0$. We also note that we can still identify the cold component in $f_{ic}^{top}(v_x)$ at $s = 10$. In the other two components, the beam is thermalized at about $s = 7$.

We now look at the field line located further away from the front, in the intermediate exhaust (**Figures 6L–N**). With exception for the ion trapping seen closer to the front, the behaviour is approximately similar until $s = -3$. One important difference between the two field lines is the behaviour in $f_{ic}^{top}(v_y)$ inside $s \approx -3$. Closer to the front, the cold population was seen to oscillate close to v_y as part of their gyromotion. Further from the front, the cold population is instead experiencing a continual increase in v_y until $s \approx 2$, whereafter it no longer is identifiable in any of the components. The positive v_y leads to a reflective (upward) force $-v_y B_x > 0$. As a result, the entire cold population is reflected, explaining the density cutoff seen at $z \approx -2$ in **Figure 6A**. The absence of v_y-oscillations in this location is related to the level of magnetization. The bounce distance ($\sim 4d_i$) becomes comparable to the gyroradius such that complete gyromotion is not possible. During the reflection, the beam is also thermalized due to the enhanced pitch-angle scattering.

4.3 The Role of Streaming Instabilities Deep Within the Exhaust

Inside the exhaust, we observe two off-equatorial regions (one in the north and one in the south) where electrostatic solitary waves (ESW) form (**Figure 7**). The ESWs form at around $z = \pm 4$ and

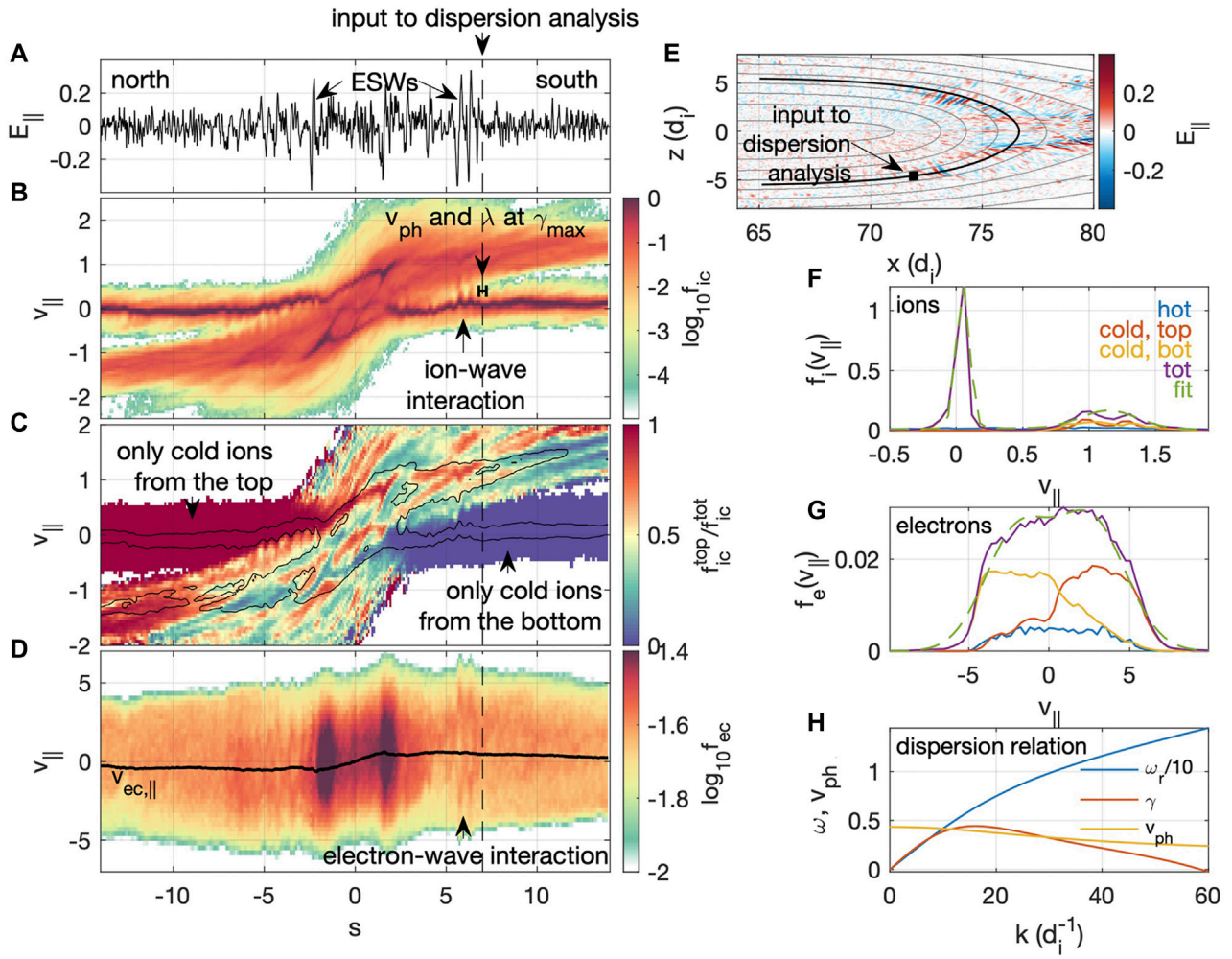

FIGURE 8 | Thermalization due to ion-acoustic waves within the exhaust. Panels **(A–E)** show quantities sampled along a magnetic field line marked by the black line in panel **(E)**. They are plotted as a function of the distance along the field line s, where $s = 0$ is the equatorial plane and $s > 0$ is in the region $z < 0$ (since the magnetic field direction is from north to south). **(A)** Parallel electric field $E_{||}$. **(B)** Reduced ion distribution of initially cold ions, $\log_{10} f_{ic}$. **(C)** Mixing level of ions originating from the north and south, respectively, $f_{mix} = f_{ic}^{top}/f_{ic}$. For $f_{mix} = 1$ (red) and 0 (purple), all the ions are originating from the top and bottom, respectively. For $f_{mix} = 0.5$ (yellow), half of the ions are originating from the top, and half from bottom. For reference we show $\log_{10} f_{ic} = -1$ as black contours. **(D)** Reduced distribution of originally cold electrons, $\log_{10} f_{ec}$. We have saturated the color scale to highlight the features in the region of the waves. **(E)** Parallel electric field $E_{||}$. **(F)** Ion, and **(G)** electron distributions at the location marked by a black square in panel **(E)**, and the vertical dashed lines in **(A–D)**. The dashed green line marks a fit to the data using three Maxwellians. **(H)** Dispersion relation obtained based on the Maxwellian fits in **(F–G)**. The positive growth rate is due to an ion-acoustic instability. The phase speed v_{ph} and wavelength λ at max growth γ_{max} is shown as a black bar in **(B)**.

grow both in amplitude and perpendicular (to **B**) extent as they propagate downstream with the magnetic field at low parallel speeds. To investigate how they form we examine a timestep ($t\omega_{ci}$ = 115) before they have grown to their full strength. **Figures 8A–D** shows a few quantities plotted as a function of the distance s along a magnetic field line marked in **Figure 8E** (the same field line is also marked by the thicker black line in **Figure 7**). $s = 0$ marks the neutral plane $z = 0$, $s > 0$ is in the region $z < 0$ (since the magnetic field direction is from north to south), and $s < 0$ is in the region $z > 0$. **Figure 8A** shows the parallel electric field $E_{||}$ in which the ESWs are seen as bipolar spikes. **Figure 8B** shows the reduced distribution function of the initially cold ions as a function of $v_{||}$. The inbound ions move at low parallel speeds further out, and are gradually accelerated as they approach and cross the neutral plane. This acceleration is due to Fermi acceleration, where the initial v_y gained by E_y is first turned towards z by the magnetic force $-v_y B_x$, and thereafter towards $-x$ by $v_y B_z$. We note that the final speed gain is consistent with what we expect due to Fermi acceleration: $v_{after} = -v_{before} + 2v_{DF}$, where the speed of the front $v_{DF} \approx 0.5$. Oscillations in the cold component indicate that they are affected by the parallel electric field. The results of the wave-ion interaction, for a closely located field line, are also seen in **Figures 6I,K** where we only plot the ions originating from the north.

The level of plasma mixing, defined by the phase space density ratio of cold ions originating from the top to all cold ions: f_{mix} =

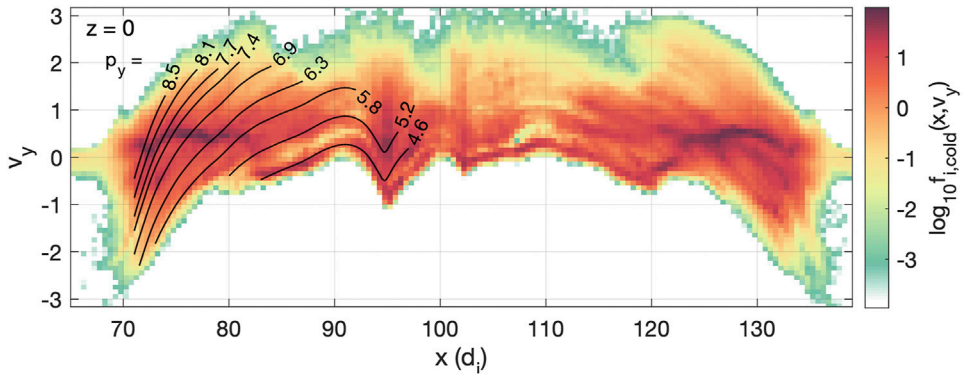

FIGURE 9 | Reduced ion distribution $f(x, v_y)$ at $z = 0$, and $t = 120$. The lines show contours of constant canonical momentum $p_y = m_i v_y + qA_y$, which well explains the overall phase space structure (x, v_y) of the thermalized exhaust. Since $v_y(t = 0) = 0$, ions with the same p_y originated from the same flux tube, defined by a given A_y. Ions with $v_y > 0$ (< 0) are currently downstream (upstream) of their original flux tube.

f_{ic}^{top}/f_{ic} is shown in **Figure 8C**. Red (purple) indicates that all ions originate from the top (bottom) while yellow indicates mixed origin. The thin black lines in this panel are added as reference and shows the contour levels $\log_{10} f_{ic} = -1$. While most of the mixing seem to occur close to the equatorial plane, there is also clear evidence of mixing associated with the ESWs. While the inbound ions can remain cold deep within the exhaust, we see in the electron distribution that the electrons are heated (**Figure 8D**). We note that this color scale is saturated to highlight the region of phase space affected by the waves. In the location of the waves, electrons form clear hole-like structures (e.g. immediately to the left of the vertical dashed line). The black line show the electron bulk speed, with a finite antiparallel (parallel) drift to the north (south) side of the equatorial plane.

In **Figure 7**, we can see that the ESWs convect downstream with the magnetic field. In the frame of the magnetic field, their motion is approximately field-aligned. To investigate what kind of instability may generate the waves that grow into ESWs we therefore solve the one-dimensional electrostatic plasma dispersion equation:

$$0 = \sum_s \frac{\omega_{ps}^2}{k^2 v_{ts}^2} Z'\left(\frac{\omega - k v_{ds}}{k v_{ts}}\right)$$

where Z is the plasma dispersion function (Fried and Conte, 1961), ω_{ps} again is the plasma frequency, v_{ds} is the bulk drift speed, $v_{ts} = \sqrt{2T_s/m_s}$ is the parallel thermal speed, of population s, $\omega = \omega_r + i\gamma$ is the complex frequency with real frequency ω, and imaginary frequency γ as the growth rate. The input is taken from the location marked by black squares in **Figure 7A** and **Figure 8E**, and a dashed vertical line in **Figures 8A–D**. In the dispersion relation solver, we include six populations seen in **Figure 8F** (ions) and **Figure 8G** (electrons): the initially hot ions and electrons (Harris sheet populations), the initially cold ions and electrons from the top and bottom, respectively. The parameters are: n_i = [0.05, 0.08, 0.15], n_e = [0.11, 0.13, 0.04], v_{di} = [0.5, 1.15, 0.05] v_{de} = [−2.1, 2.7, 0.5], v_{ti} = [1.5, 0.3, 0.07], v_{te} = [2.8, 3.0, 4.0]. The initially hot plasma does not change the results, but we include them for completeness. Effectively, there are one electron and two ion distributions: (1) a mix of all electrons combined, (2) the cold inbound ion population at $v_\parallel \approx 0$ consisting of ions originating from the southern inflow, and (3) the outbound ion beam at $v_\parallel > 0$ consisting of a mixture of ions originating from the top and bottom. The resulting dispersion relation is shown in **Figure 8H**. Positive growth rates are found for $0 < kd_i \lesssim 60$, with a peak growth rate $\gamma_{max} \lesssim 0.5$ at $k_{max}d_i \approx 16$. This wave number corresponds to a wavelength $\lambda \approx 0.4$. At k_{max}, $\omega \approx 6$, with the corresponding phase speed $v_{ph} \sim 0.4$. The wavelength (width of bar) and phase speed (vertical location of bar) at max growth rate are plotted in **Figure 8B**, and correspond well to the observed wave parameters. The wave growth is attributed to an ion-acoustic instability due to the cold population at $v_\parallel \sim 0$, and the heated drifting electrons. We note that in the absence of the electrons, an ion-ion drift instability would also grow. However, due to the presence of the electrons, it is stabilized. In the next section, we will investigate how the ions that were demagnetized at the separatrices subsequently form the hot thermal exhaust.

5 FORMATION OF THE THERMALIZED EXHAUST

In this section we investigate the formation of the thermal population within the exhaust. The distribution $f_{ic}(x, v_y)$ in **Figure 9** (see also **Figure 3**) exhibits discrete structures in phase space. One of the most distinct structures is a cold beam ranging between $v_y \approx -0.5$ at $x \approx 82$ and $v_y \approx 0.5$ at $x \approx 92$ (with corresponding structures in the right exhaust). As explained in **Section 4**, this beam is formed by a combination of forces $E_y > 0$ and $v_z B_x < 0$ acting on the ions during their first inbound leg towards the neutral plane from the inflow regions. Where $v_y < 0$, $v_z B_x$ is dominating, while where $v_y > 0$, E_y has been dominating. Divin et al. (2016) showed that this striation in phase space followed contours of constant canonical momentum $p_y = m_i v_y + qA_y$. Echoes of this initial striation are seen in both exhausts. While the first echo is towards higher v_y, the striations successively rotate counter-clockwise (clockwise) in

the left (right) exhaust, such that the range of v_y eventually covers a large range of positive and negative values. The first echo is comprised of ions that have crossed the neutral plane once, have been turned around by B_x, and returned to $z = 0$ again. During this motion, they have been accelerated to slightly higher v_y, by the reconnection electric field E_y. Once they have acquired a $v_y > 0$, they will start to become turned downstream by $v_yB_z < 0$. These two forces will jointly move the initial striation to higher v_y and lower x. By plotting contours of constant p_y in **Figure 9**, we show that also the higher order (in terms of bounces) striations approximately follow contours of constant p_y. This kind of trajectory was first described by Speiser (1965). That is, the thermal exhaust is formed by a superposition of Speiser orbits with varying initial conditions, related to where they enter the exhaust. As explained by Divin et al. (2016), the change in v_y of the zero order striation is due to spatially different acceleration by the Hall electric field E_z. Closest to the X line, the integrated electric field is smaller than further downstream, and therefore the initial v_z leading to v_y through v_zB_x is larger further away from the X line. We also note that each time the ions cross the neutral sheet, they are scattered in the highly curved magnetic field, smearing out and further blending the superposed structures.

By integrating test particles in the dynamically changing fields, we find that p_y is constant to a good approximation. Initially at $t = 0$, all of these ions had $v_y = 0$, such that $p_y = qA_y^{t=0}$. Since a given value of A_y defines an in-plane field line (B_x, B_z), the value of p_y informs us of what flux tube the ion were originally located on. For the values of p_y shown in **Figure 9**, the corresponding flux tubes were initially located at $z = \pm$[4.3, 4.7, 5.1, 5.4, 5.9, 6.5, 7.0, 7.6, 8.2]. Correspondingly, as the simulation progresses, the deviation of A_y from its initial value $A_y^{t=0}$, $\Delta A_y = A_y(t) - A_y^{t=0}$, tells us how much the ion is currently deviating from its original flux tube. We can not measure ΔA_y in nature, however, the argument can be extended to v_y

$$\Delta v_y = -\frac{q}{m_i}\Delta A_y,$$

where $\Delta v_y = v_y(t) - v_y^{t=0}$. In our simulation $\Delta v_y = v_y(t)$, since $v_y^{t=0} = 0$. In nature, comparing, for example, the thermal and bulk speeds of lobe ions to those of exhaust ions, we also typically expect $v_y(t) \gg v_y^{t=0}$, such that $\Delta v_y \approx v_y(t)$. Therefore, ions with $v_y > 0$ ($\Delta A_y < 0$) are currently located downstream of their original flux tube, while ions with $v_y < 0$ ($\Delta A_y > 0$) are currently located upstream of their original flux tube. To intuitively understand this, it is perhaps easiest to consider an ion impinging upon the X line from the top or the bottom inflow regions, with small velocity v_x. Such an ion would first be accelerated by the Hall electric field E_z, across the magnetic field, leading to $\Delta A_y > 0$. The finite v_z would be turned toward $-\hat{y}$ by the force v_zB_x. The increase in ΔA_y is offset by the decrease in v_y ($\Delta v_y < 0$), such that the change in canonical momentum $\Delta p_y = m\Delta v_y + q\Delta A_y \approx 0$. The ion will thereafter dwell for some time in the X line region, performing meandering motion in the B_x field reversal, and being accelerated by E_y, increasing v_y. During this time, when the ion remains close to the X line, the magnetic field will convect past it, such that it is successively moved to more upstream field lines ($\Delta A_y < 0$). The decrease in ΔA_y is offset by the change in v_y ($\Delta v_y > 0$), again keeping p_y constant. The obtained v_y will be turned toward $\pm x$ by the force v_yB_z. The larger v_y, the larger the force, and resulting v_x. An ion that were significantly delayed, instead gained a larger v_y, and will be better able to catch up to its original field line $A_y^{t=0}$ (Drake et al., 2009). We also recall that A_y is defined by both $B_x = -\partial_z A_y$ and $B_z = \partial_x A_y$. The information of both magnetic field components in the force terms v_zB_x and v_yB_z are thus contained within A_y, which also helps us understand the connection between the described forces, and why the structure of the phase space is so well described by p_y.

We can also think of ΔA_y and Δv_y in terms of diffusion. As described above, an ensemble of ions that dwells in the vicinity of the X line, being accelerated by E_y, sees the magnetic field lines move past them. Or, in other words, the magnetic field diffuses across the ensemble of ions. Further downstream, when v_y is turned to v_x, the ions are catching up to their original field lines, and the diffusion is reversed. The primary diffusion is done by the electric field, which performs work on the ions. Since the reversed diffusion is done by magnetic forces, no work is done, and a net energy transfer between magnetic field and plasma is realized.

6 DISCUSSION AND SUMMARY

In this study, we have investigated the occurrence and heating of initially cold ions during symmetric magnetic reconnection. We showed that ions that enter the exhaust at active separatrices with large gradients and electric fields become heated and thermalized more efficiently than ions that enter the exhaust at inactive separatrices lacking large gradients and electric fields. These findings are consistent with observations at the dayside magnetopause (Toledo-Redondo et al., 2016b). The ions that enter the exhaust at inactive separatrices are typically picked up as the exhaust expands into them, both in the outflow (x) and normal (z) directions. While Eastwood et al. (2015) suggested that ion beams observed close to the dipolarization front originated from the pre-existing plasma sheet, Birn et al. (2017) concluded that they originated from the lobes. We find that the cold beams can originate from an extended range of z's that may include, but also extends well outside, the pre-existing hot current sheet population. The cold ion beams closer to the front originate on lower z's, while those further away originate at higher z's. This is illustrated both in **Figure 5** (c.f. original locations of yellow and black ions) and **Figure 9** where the cold beam (here seen in $f_{ic}(v_y)$) extend over a range of p_y. Recall that p_y indicated the original z location of the field line/particle, and that lower p_y corresponded to a field line initially located further out in the inflow. How far this range of z's extends likely depend on the stage of reconnection. The further the front has propagated, the larger range of z's can be picked up without being significantly thermalized at the separatrices. In addition, while cold counter-streaming beams could be observed close to the equatorial plane throughout the exhaust, the beams that entered the exhaust at inactive separatrices could remain colder in all three components. Also, closer to the X line, the v_z was gained mainly through acceleration by E_z, while further downstream, the v_z gain was through Fermi acceleration (mediated by E_y).

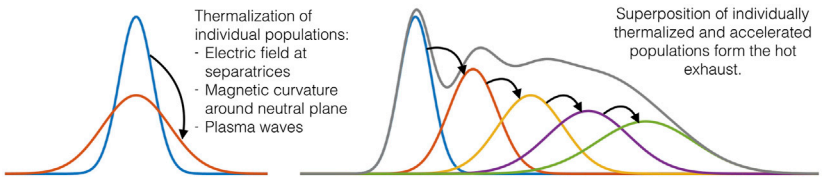

FIGURE 10 | Illustration of thermalization process of cold ions. Individual populations are thermalized by one or several processes, for example separatrix activity, magnetic field curvature scattering, or plasma waves. The hot exhaust is formed by a superposition of these individually thermalized populations that are accelerated to different energies.

The separatrix environment, and therefore also the ion thermalization at the separatrices may be sensitive to the reduced mass ratio we employ in this simulation (e.g., Lapenta et al., 2010). However, we note that observations also show divergent electric field at the separatrix electron flow channels. The integrated potential associated with these fields in observations could be comparable or higher than the inflow energy of the cold ions (Norgren et al., 2020). We also note that out-of-plane instabilities active at the separatrices, such as the lower-hybrid-drift instability, or ion-ion cross-field drift instabilities do not develop in our 2D simulation. Based on previous observations at the magnetopause, such instabilities would also act to enhance the ion thermalization at the separatrices (e.g., Toledo-Redondo et al., 2017; Graham et al., 2017).

In our simulation, electrostatic field-aligned waves were also found to impact the ion thermalization in the off-equatorial region deep within the exhaust. The waves were produced by an ion-acoustic instability due to the cold inbound ion population and the drifting electrons. Field-aligned electrostatic waves has also been found in observations in the vicinity of dipolarization fronts relatively close to the neutral plane (Liu et al., 2019). These waves were likely generated by cold proton, and potentially oxygen, beams. Field-aligned electrostatic waves have also been identified in regions closer to the separatrix in the magnetopause boundary layer at the dayside (Steinvall et al., 2021). Similar to our results, they found the waves to be driven by an ion acoustic instability. Altogether, these results shows that waves may play a role in the thermalization of cold ion populations in many different subregions during reconnection.

We showed that the cold ions that entered the exhaust downstream of active separatrices could remain cold all the way to the neutral plane, and beyond. After having crossed the neutral plane, ions in the intermediate exhaust, reflected back at about a distance of $2d_i$ from the neutral plane after having crossed it. Closer to the dipolarization fronts, due to the higher level of magnetization, the cold ions could also continue outward beyond $z = \pm 2d_i$. At the neutral plane, the incoming cold populations also experienced pitch angle scattering due to magnetic field curvature. As such, at a given location, the inbound beam (approaching the neutral plane) is colder than its outgoing counterpart. This is consistent with observations from the vicinity of dipolarization fronts in the magnetotail where Xu et al. (2019) observed cold beams propagating along the magnetic field. The beam approaching the neutral plane was colder than the beam leaving it. Overall, the region along $\hat{z}$ in which we expect to observe counter-streaming cold ion beams is more limited in the intermediate exhaust than closer to the front.

Since the majority of the outflow is dominated by the species that were initially cold, the division into a hot and cold ion diffusion region such as explored by Divin et al. (2016), and typically invoked at the magnetopause (Toledo-Redondo et al., 2015), is not applicable here. At the dayside, the multiple ion diffusion regions are typically a result of the multiple inflow populations, e.g. cold magnetospheric plasma and warm magnetosheath plasma (Toledo-Redondo et al., 2015). Although the heated ions seen inside the separatrix in **Figure 3** do not follow $\mathbf{v}_{E\times B}$, this is not an indication of multiple ion diffusion regions, it is merely a superposition of inbound and outbound populations of the same origin. However, multiple ion diffusion regions could exist in the tail if there are multiple species in the inflow (e.g., oxygen ions (Wygant et al., 2005; Tenfjord et al., 2018), if there is an extended region of overlap of hot and cold plasma in the transition from the plasma sheet to the lobes, if there are overlapping regions with ions of different origins (for example the ionosphere and solar wind), or if there are significant north-south plasma asymmetries, for example due to mantle plasma (e.g., Artemyev et al., 2017) or asymmetric ionospheric outflow (e.g., Glocer et al., 2020).

In this study, we have investigated the acceleration, thermalization, and occurrence of cold ions in the exhaust of symmetric antiparallel magnetic reconnection. The overall temperature increase was comparable to the predictions based on the counter-streaming ion model by Drake et al. (2009). However, we found that several processes conspire to form the eventually hot thermalized exhaust (**Figure 10**). The initially cold populations are thermalized due to interactions at the separatrices, around the neutral plane, and due to waves inside the exhaust. At the same time, the individual populations are accelerated (mainly) by the out-of-plane electric field E_y. At a given position, we can find populations that have been accelerated to different energies, depending on where they entered the exhaust. Together, the thermalization and superposition of ions that have been accelerated to different energies form the hot exhaust population. The acceleration by E_y lead to super-Alfvénic speeds. If we assume an inflow magnetic field of 20 nT, and a plasma sheet density of 0.3 cm^{-3} (recall that the Alfvén speed in our simulation is based on the inflow magnetic field and central Harris sheet density), the Alfvén speed is $v_A \approx 800$ km/s. An ion accelerated to $1v_A$ and $2v_A$ thus has an energy of about 3300 eV and 13400 eV, respectively. As for the overall

temperature seen in **Figure 2F**, T_i = 0.3 corresponds to about 2000 eV. These energies are comparable to average ion temperatures in the central plasma sheet (e.g., Baumjohann et al., 1989). This suggests that magnetic reconnection can heat cold lobe plasma to large enough energies to replenish the hot plasma sheet.

DATA AVAILABILITY STATEMENT

The dataset used in this study can be found at UiB Open Research data: https://doi.org/10.18710/0257WR.

AUTHOR CONTRIBUTIONS

CN planned the study and executed the simulation, performed the data analysis, scientific interpretation and lead the manuscript writing. PT, MH, YX shared in the conception of the study. PT, MH shared in the simulation execution and data analysis. PT, MH, ST, WL, YX, NK, SS, HK shared in the scientific interpretation and discussion of the simulation results. All authors shared in the writing of the manuscript.

FUNDING

This study was supported by NOTUR/NORSTOR under project NN9496K. CN and PT received support from the Research Council of Norway under contract 300865. MH's work prior to moving to NASA ARC was supported by NASA contract NNG04EB99C at SwRI. STR, WL, and PT acknowledges support from the International Space Science Institute (ISSI) international team 'Cold plasma of ionospheric origin in the Earth's magnetosphere'. The open access publishing fee is funded by the University of Bergen.

REFERENCES

Alm, L., André, M., Vaivads, A., Khotyaintsev, Y. V., Torbert, R. B., Burch, J. L., et al. (2018). Magnetotail Hall Physics in the Presence of Cold Ions. *Geophys. Res. Lett.* 45, 10941–10950. doi:10.1029/2018GL079857

André, M., Li, W., Toledo-Redondo, S., Khotyaintsev, Y. V., Vaivads, A., Graham, D. B., et al. (2016). Magnetic Reconnection and Modification of the Hall Physics Due to Cold Ions at the Magnetopause. *Geophys. Res. Lett.* 43, 6705–6712. doi:10.1002/2016GL069665

Artemyev, H., Angelopoulos, A. V., and au, V. (2017). Ion Dynamics in Magnetotail Reconnection in the Presence of Density Asymmetry. *J. Geophys. Res. Space Phys.* 122, 2010–2023. doi:10.1002/2016JA023651

Arzner, K., and Scholer, M. (2001). Kinetic Structure of the post Plasmoid Plasma Sheet during Magnetotail Reconnection. *J. Geophys. Res.* 106, 3827–3844. doi:10.1029/2000JA000179

Baumjohann, W., Paschmann, G., and Cattell, C. A. (1989). Average Plasma Properties in the central Plasma Sheet. *J. Geophys. Res.* 94, 6597–6606. doi:10.1029/ja094ia06p06597

Birn, J., Nakamura, R., Panov, E. V., and Hesse, M. (2011). Bursty Bulk Flows and Dipolarization in MHD Simulations of Magnetotail Reconnection. *J. Geophys. Res.* 116, A01210. doi:10.1029/2010JA016083

Birn, J., Runov, A., and Zhou, X. Z. (2017). Ion Velocity Distributions in Dipolarization Events: Distributions in the central Plasma Sheet. *J. Geophys. Res. Space Phys.* 122, 8014–8025. doi:10.1002/2017JA024230

Borovsky, J. E., and Denton, M. H. (2008). A Statistical Look at Plasmaspheric Drainage Plumes. *J. Geophys. Res. (Space Physics)* 113, A09221. doi:10.1029/2007ja012994

Büchner, J., and Zelenyi, L. M. (1989). Regular and Chaotic Charged Particle Motion in Magnetotaillike Field Reversals: 1. Basic Theory of Trapped Motion. *J. Geophys. Res.* 94, 11821–11842. doi:10.1029/JA094iA09p11821

Dargent, J., Aunai, N., Lavraud, B., Toledo-Redondo, S., and Califano, F. (2020). Simulation of Plasmaspheric Plume Impact on Dayside Magnetic Reconnection. *Geophys. Res. Lett.* 47, e86546. doi:10.1029/2019GL086546

Divin, A., Khotyaintsev, Y. V., Vaivads, A., André, M., Toledo-Redondo, S., Markidis, S., et al. (2016). Three-scale Structure of Diffusion Region in the Presence of Cold Ions. *J. Geophys. Res. Space Phys.* 121, 001–012. doi:10.1002/2016JA023606

Drake, J. F., Swisdak, M., Phan, T. D., Cassak, P. A., Shay, M. A., Lepri, S. T., et al. (2009). Ion Heating Resulting from Pickup in Magnetic Reconnection Exhausts. *J. Geophys. Res. (Space Physics)* 114, A05111. doi:10.1029/2008ja013701

Drake, H., Phan, J. F., Eastwood, T. D., McFadden, J. P., and au, J. P. (2015). Ion Temperature Anisotropy across a Magnetotail Reconnection Jet. *Geophys. Res. Lett.* 42, 7239–7247. doi:10.1002/2015GL065168

Eastman, T. E., DeCoster, R. J., and Frank, L. A. (1986). Velocity Distributions of Ion Beams in the Plasma Sheet Boundary Layer. *Wash. DC Am. Geophys. Union Geophys. Monogr. Ser.* 38, 117–126. doi:10.1029/GM038p0117

Eastwood, J. P., Goldman, M. V., Newman, H., Mistry, D. L., Lapenta, R., and au, G. (2015). Ion Reflection and Acceleration Near Magnetotail Dipolarization Fronts Associated with Magnetic Reconnection. *J. Geophys. Res. Space Phys.* 120, 511–525. doi:10.1002/2014JA020516

Engwall, E., Eriksson, A. I., Cully, C. M., André, M., Torbert, R., and Vaith, H. (2009). Earth's Ionospheric Outflow Dominated by Hidden Cold Plasma. *Nat. Geosci* 2, 24–27. doi:10.1038/ngeo387

Ergun, R. E., Goodrich, K. A., Wilder, F. D., Ahmadi, N., Holmes, J. C., Eriksson, S., et al. (2018). Magnetic Reconnection, Turbulence, and Particle Acceleration: Observations in the Earth's Magnetotail. *Geophys. Res. Lett.* 45, 3338–3347. doi:10.1002/2018GL076993

Fried, B. D., and Conte, S. D. (1961). *The Plasma Dispersion Function*. New York, NY: Academic Press.

Fu, H. S., Cao, J. B., Khotyaintsev, Y. V., Sitnov, M. I., Runov, A., Fu, S. Y., et al. (2013). Dipolarization Fronts as a Consequence of Transient Reconnection: *In Situ* Evidence. *Geophys. Res. Lett.* 40, 6023–6027. doi:10.1002/2013GL058620

Fuselier, S. A., Burch, J. L., Mukherjee, J., Genestreti, K. J., Vines, S. K., Gomez, R., et al. (2017). Magnetospheric Ion Influence at the Dayside Magnetopause. *J. Geophys. Res. Space Phys.* 122, 8617–8631. doi:10.1002/2017ja024515

Glocer, A., Welling, D., Chappell, C. R., Toth, G., Fok, M. C., Komar, C., et al. (2020). A Case Study on the Origin of Near-Earth Plasma. *J. Geophys. Res. Space Phys.* 125, e28205. doi:10.1029/2020JA028205

Gosling, J. T., Thomsen, M. F., Bame, S. J., Onsager, T. G., and Russell, C. T. (1990). The Electron Edge of Low Latitude Boundary Layer during Accelerated Flow Events. *Geophys. Res. Lett.* 17, 1833–1836. doi:10.1029/GL017i011p01833

Graham, D. B., Khotyaintsev, Y. V., Norgren, C., Vaivads, A., André, M., Toledo-Redondo, S., et al. (2017). Lower Hybrid Waves in the Ion Diffusion and Magnetospheric Inflow Regions. *J. Geophys. Res. Space Phys.* 122, 517–533. doi:10.1002/2016JA023572

Haggerty, C. C., Shay, M. A., Drake, J. F., Phan, T. D., and McHugh, C. T. (2015). The Competition of Electron and Ion Heating during Magnetic Reconnection. *Geophys. Res. Lett.* 42, 9657–9665. doi:10.1002/2015GL065961

Hesse, M., Schindler, K., Birn, J., and Kuznetsova, M. (1999). The Diffusion Region in Collisionless Magnetic Reconnection. *Phys. Plasmas* 6, 1781–1795. doi:10.1063/1.873436

Lapenta, G., Markidis, S., Divin, A., Goldman, M., and Newman, D. (2010). Scales of Guide Field Reconnection at the Hydrogen Mass Ratio. *Phys. Plasmas* 17, 082106. doi:10.1063/1.3467503

Li, S.-S., Liu, J., Angelopoulos, V., Runov, A., Zhou, X.-Z., and Kiehas, S. A. (2014). Antidipolarization Fronts Observed by Artemis. *J. Geophys. Res. Space Phys.* 119, 7181–7198. doi:10.1002/2014JA020062

Li, W. Y., André, M., Khotyaintsev, Y. V., Vaivads, A., Fuselier, S. A., Graham, D. B., et al. (2017). Cold Ionospheric Ions in the Magnetic Reconnection Outflow Region. *J. Geophys. Res. Space Phys.* 122, 10,194–10,202. doi:10.1002/2017JA024287

Lindstedt, T., Khotyaintsev, Y. V., Vaivads, A., André, M., Fear, R. C., Lavraud, B., et al. (2009). Separatrix Regions of Magnetic Reconnection at the Magnetopause. *Ann. Geophys.* 27, 4039–4056. doi:10.5194/angeo-27-4039-2009

Liu, J., Angelopoulos, V., Runov, A., and Zhou, X. Z. (2013). On the Current Sheets Surrounding Dipolarizing Flux Bundles in the Magnetotail: The Case for Wedgelets. *J. Geophys. Res. (Space Physics)* 118, 2000–2020. doi:10.1002/jgra.50092

Liu, C. M., Vaivads, A., Graham, D. B., Khotyaintsev, Y. V., Fu, H. S., Johlander, A., et al. (2019). Ion-Beam-Driven Intense Electrostatic Solitary Waves in Reconnection Jet. *Geophys. Res. Lett.* 46, 12702–12710. doi:10.1029/2019gl085419

Nagai, T., Fujimoto, M., Saito, Y., Machida, S., Terasawa, T., Nakamura, R., et al. (1998). Structure and Dynamics of Magnetic Reconnection for Substorm Onsets with Geotail Observations. *J. Geophys. Res.* 103, 4419–4440. doi:10.1029/97JA02190

Nagai, T., Nakamura, M., Shinohara, I., Fujimoto, M., Saito, Y., and Mukai, T. (2002). Counterstreaming Ions as Evidence of Magnetic Reconnection in the Recovery Phase of Substorms at the Kinetic Level. *Phys. Plasmas* 9, 3705–3711. doi:10.1063/1.1499117

Nagai, T., Shinohara, I., and Zenitani, S. (2015). Ion Acceleration Processes in Magnetic Reconnection: Geotail Observations in the Magnetotail. *J. Geophys. Res. Space Phys.* 120, 1766–1783. doi:10.1002/2014JA020737

Nakamura, M. S., Fujimoto, M., and Maezawa, K. (1998). Ion Dynamics and Resultant Velocity Space Distributions in the Course of Magnetotail Reconnection. *J. Geophys. Res.* 103, 4531–4546. doi:10.1029/97JA01843

Nakamura, R., Baumjohann, W., Mouikis, C., Kistler, L. M., Runov, A., Volwerk, M., et al. (2004). Spatial Scale of High-Speed Flows in the Plasma Sheet Observed by Cluster. *Geophys. Res. Lett.* 31, L09804. doi:10.1029/2004gl019558

Norgren, C., Hesse, M., Graham, D. B., Khotyaintsev, Y. V., Tenfjord, P., Vaivads, A., et al. (2020). Electron Acceleration and Thermalization at Magnetotail Separatrices. *J. Geophys. Res. (Space Physics)* 125, e27440. doi:10.1029/2019ja027440

Northrop, T. G. (1963). Adiabatic Charged-Particle Motion. *Rev. Geophys.* 1, 283–304. doi:10.1029/RG001i003p00283

Runov, A., Angelopoulos, V., Zhou, X.-Z., Zhang, X.-J., Li, S., Plaschke, F., et al. (2011). A THEMIS Multicase Study of Dipolarization Fronts in the Magnetotail Plasma Sheet. *J. Geophys. Res.* 116, A05216. doi:10.1029/2010JA016316

Schriver, D., and Ashour-Abdalla, M. (1990). Cold Plasma Heating in the Plasma Sheet Boundary Layer: Theory and Simulations. *J. Geophys. Res.* 95, 3987–4005. doi:10.1029/JA095iA04p03987

Sitnov, M. I., Swisdak, M., and Divin, A. V. (2009). Dipolarization Fronts as a Signature of Transient Reconnection in the Magnetotail. *J. Geophys. Res.* 114, A04202. doi:10.1029/2008JA013980

Sitnov, M. I., Buzulukova, N., Swisdak, M., Merkin, V. G., and Moore, T. E. (2013). Spontaneous Formation of Dipolarization Fronts and Reconnection Onset in the Magnetotail. *Geophys. Res. Lett.* 40, 22–27. doi:10.1029/2012GL054701

Speiser, T. W. (1965). Particle Trajectories in Model Current Sheets: 1. Analytical Solutions. *J. Geophys. Res.* 70, 4219–4226. doi:10.1029/jz070i017p04219

Steinvall, K., Khotyaintsev, Y. V., Graham, D. B., Vaivads, A., André, M., and Russell, C. T. (2021). Large Amplitude Electrostatic Proton Plasma Frequency Waves in the Magnetospheric Separatrix and Outflow Regions during Magnetic Reconnection. *Geophys. Res. Lett.* 48, e2020GL090286. doi:10.1029/2020gl090286

Tenfjord, P., Hesse, M., and Norgren, C. (2018). The Formation of an Oxygen Wave by Magnetic Reconnection. *J. Geophys. Res. Space Phys.* 123, 9370–9380. doi:10.1029/2018JA026026

Tenfjord, P., Hesse, M., Norgren, C., Spinnangr, S. F., Kolstø, H., and Kwagala, N. (2020). Interaction of Cold Streaming Protons with the Reconnection Process. *J. Geophys. Res. Space Phys.* 125, e27619. doi:10.1029/2019JA027619

Toledo-Redondo, S., Vaivads, A., André, M., and Khotyaintsev, Y. V. (2015). Modification of the Hall Physics in Magnetic Reconnection Due to Cold Ions at the Earth's Magnetopause. *Geophys. Res. Lett.* 42, 6146–6154. doi:10.1002/2015gl065129

Toledo-Redondo, S., André, M., Khotyaintsev, Y. V., Vaivads, A., Walsh, A., Li, W., et al. (2016a). Cold Ion Demagnetization Near the X-Line of Magnetic Reconnection. *Geophys. Res. Lett.* 43, 6759–6767. doi:10.1002/2016GL069877

Toledo-Redondo, S., André, M., Vaivads, A., Khotyaintsev, Y. V., Lavraud, B., Graham, D. B., et al. (2016b). Cold Ion Heating at the Dayside Magnetopause during Magnetic Reconnection. *Geophys. Res. Lett.* 43, 58–66. doi:10.1002/2016gl069877

Toledo-Redondo, S., André, M., Khotyaintsev, Y. V., Lavraud, B., Vaivads, A., Graham, D. B., et al. (2017). Energy Budget and Mechanisms of Cold Ion Heating in Asymmetric Magnetic Reconnection. *J. Geophys. Res. Space Phys.* 122, 9396–9413. doi:10.1002/2017JA024553

Toledo-Redondo, S., Dargent, J., Aunai, N., Lavraud, B., André, M., Li, W., et al. (2018). Perpendicular Current Reduction Caused by Cold Ions of Ionospheric Origin in Magnetic Reconnection at the Magnetopause: Particle-in-Cell Simulations and Spacecraft Observations. *Geophys. Res. Lett.* 45, 10,033–10,042. doi:10.1029/2018GL079051

Toledo-Redondo, S., André, M., Aunai, N., Chappell, C. R., Dargent, J., Fuselier, S. A., et al. (2021). Impacts of Ionospheric Ions on Magnetic Reconnection and Earth's Magnetosphere Dynamics. *Rev. Geophys.* 59, e2020RG000707. doi:10.1029/2020RG000707

Vines, S. K., Fuselier, S. A., Trattner, K. J., Burch, J. L., Allen, R. C., Petrinec, S. M., et al. (2017). Magnetospheric Ion Evolution across the Low-Latitude Boundary Layer Separatrix. *J. Geophys. Res. Space Phys.* 122, 10,247–10,262. doi:10.1002/2017JA024061

Wygant, J. R., Cattell, C. A., Lysak, R., Song, Y., Dombeck, J., McFadden, J., et al. (2005). Cluster Observations of an Intense normal Component of the Electric Field at a Thin Reconnecting Current Sheet in the Tail and its Role in the Shock-like Acceleration of the Ion Fluid into the Separatrix Region. *J. Geophys. Res.* 110, A09206. doi:10.1029/2004JA010708

Xu, Y., Fu, H. S., Norgren, C., Toledo-Redondo, S., Liu, C. M., and Dong, X. C. (2019). Ionospheric Cold Ions Detected by MMS behind Dipolarization Fronts. *Geophys. Res. Lett.* 46, 7883–7892. doi:10.1029/2019GL083885

Zenitani, S., Shinohara, I., Nagai, T., and Wada, T. (2013). Kinetic Aspects of the Ion Current Layer in a Reconnection Outflow Exhaust. *Phys. Plasmas* 20, 092120. doi:10.1063/1.4821963

Conflict of Interest: The authors declare that the research was conducted in the absence of any commercial or financial relationships that could be construed as a potential conflict of interest.

Publisher's Note: All claims expressed in this article are solely those of the authors and do not necessarily represent those of their affiliated organizations, or those of the publisher, the editors and the reviewers. Any product that may be evaluated in this article, or claim that may be made by its manufacturer, is not guaranteed or endorsed by the publisher.

frontiers in Astronomy and Space Sciences

MINI REVIEW
published: 22 September 2021
doi: 10.3389/fspas.2021.725677

Dayside Diffuse Aurora and the Cold-Plasma Structuring: A Brief Review

De-Sheng Han *

State Key Laboratory of Marine Geology, School of Ocean and Earth Science, Tongji University, Shanghai, China

Diffuse aurora is generated by the precipitation of hot electrons from the central plasma sheet due to wave-particle interaction. Near magnetic local noon (MLN), the diffuse aurora was often observed in structured forms, such as in stripy or patchy. In the magnetosphere, when the hot electrons meet with a cold plasma structure, the threshold of resonance energy for the electrons in the cold plasma region can be lowered, leading to more electrons being involved in the wave-particle interaction and being scattered into the loss cone. As a result, stronger diffuse aurora can be produced in the correspondent region. Based on this mechanism, the structured dayside diffuse auroras have been suggested to correspond to the cold plasma structures in the dayside outer magnetosphere. This brief review focuses on showing that 1) the stripy diffuse auroras observed near MLN are specifically informative, 2) there are two types of diffuse aurora near MLN, which may correspond to cold plasmas originating from inside and outside the magnetosphere, respectively, and 3) we can study the inside-outside coupling by using the interaction between diffuse and discrete auroras observed near MLN.

Keywords: diffuse aurora, dayside aurora, cusp aurora, cold plasma, throat aurora

OPEN ACCESS

Edited by:
Gian Luca Delzanno,
Los Alamos National Laboratory (DOE), United States

Reviewed by:
Toshi Nishimura,
Boston University, United States
Michael Henderson,
Los Alamos National Laboratory (DOE), United States

***Correspondence:**
De-Sheng Han
handesheng@tongji.edu.cn

Specialty section:
This article was submitted to Space Physics, a section of the journal Frontiers in Astronomy and Space Sciences

Received: *15 June 2021*
Accepted: *10 September 2021*
Published: *22 September 2021*

Citation:
Han D-S (2021) Dayside Diffuse Aurora and the Cold-Plasma Structuring: A Brief Review. Front. Astron. Space Sci. 8:725677. doi: 10.3389/fspas.2021.725677

INTRODUCTION

Background About Diffuse Aurora

The auroras observed on the ground can be classified into two broad categories, i.e., discrete and diffuse auroras, which are different in appearance and generation mechanisms. Discrete auroras are generally characterized by intense auroral emission in both green (wavelength of 557.7 nm) and red (wavelength of 630.0 nm) lines and often appear as auroral arcs, bands, curls, and rays. It is believed that the discrete auroras are produced by electrons accelerated by quasi-static electric field or Alfven waves and are associated with the field-aligned current. Diffuse auroras generally appear at the equatorward edge of the auroral oval (Lui et al., 1973) with relatively homogenous emission in the green line observations. Initially, diffuse aurora studies mainly focused on where the source particles are from, whether these particles have been accelerated, or how these particles are scattered into the loss cone. In the 1970s, thanks to the rapid development of satellites, it was revealed that the electrons for producing the diffuse aurora originated from the central plasma sheet (CPS) (Meng et al., 1979), and their energy did not significantly change from the source region to the topside ionosphere. Therefore, the research on diffuse aurora after the 1980s mainly focused on the scattering mechanism of particles. Now, it has been widely accepted that the electron diffuse aurora are generated by precipitation of hot electrons (> 1.0 Kev) from the CPS through wave-particle interaction by the whistler-mode chorus (Ni et al., 2011b; Nishimura et al., 2010; Thorne et al., 2010) or electron cyclotron harmonic (ECH) (Horne and Thorne, 2000; Liang et al., 2011; Ni et al., 2011a; Zhang et al., 2014) waves.

The source particle of diffuse aurora is the earthward particle injection during substorms. Because the injected electrons drift from midnight toward dawn and noon sectors, the diffuse aurora is the strongest on the post-midnight sector (Newell et al., 2009) and is gradually weakening toward the dawn and noon sectors. Dayside diffuse aurora has been early noticed (Newell and Meng, 1992; Sandholt et al., 1998). Sandholt et al. (1998) classified the dayside optical auroras into seven types, in which the type 3 aurora was the diffuse aurora. For the electron scattering mechanisms, a few studies suggested that dayside diffuse auroras are associated with the chorus waves (Ebihara et al., 2007; Ni et al., 2014; Nishimura et al., 2013). At the same time, it has been noticed that ECH waves play a role in producing the diffuse auroras on the dayside (Han et al., 2017; Lou et al., 2021). Frey et al., 2019 summarized that dayside diffuse auroras show various structures and suggested that the diffuse auroral structure may correspond to low-energy plasma density structures in the dayside outer magnetosphere.

This paper will not discuss the electron scattering mechanism for producing the diffuse aurora but will focus on the implications of structured dayside diffuse aurora on the cold plasma structuring in the dayside outer magnetosphere.

Distribution of Structured and Unstructured Diffuse Auroras in the Dayside

Although satellites have advantages in providing global coverage in auroral observation, they generally have limitations on spatial and temporal resolutions. In contrast, ground-based instruments can easily overcome these disadvantageous factors. On making dayside optical auroral observations on the ground, the observation site is required to be under the aurora oval and, at the same time, be dark on the dayside. Only a few places can meet these requirements on Earth. Svalbard Island in the north of Europe is one of such places in the Northern Hemisphere. Chinese Yellow River Station (YRS) is situated at Ny-Alesund in Svalbard, where is just fit for making dayside optical auroral observations from the beginning of November to the middle of February for each year. YRS has three individual all-sky imagers equipped with narrowband filters centered at 427.8, 557.5, and 630.0 nm, respectively (Hu et al., 2009). YRS has carried out auroral observations in the same mode, i.e., with 10-s time resolution, since November 2003 up to the present. The long-lasting and high-quality data accumulation provides an unprecedented opportunity for the dayside auroral study. The observational results discussed here are mainly obtained from the YRS station.

Using observations from Svalbard, Sandholt et al. (1998) suggested that the dayside diffuse auroras are caused by precipitation of CPS electrons drifted from the nightside. However, they did not do further studies on it. Using 7-years observations from YRS, Han et al. (2015) carried out a statistical survey on the dayside diffuse aurora. They found that the dayside diffuse auroras can be classified into two broad categories: structured and unstructured diffuse auroras. The structured diffuse auroras are predominantly observed near magnetic local noon (MLN), and the unstructured ones are in the morning. The main results and the implications are illustrated in **Figure 1**. The observational results were explained as follows by considering the source particle properties of diffuse aurora and the cold plasma structuring in the dayside magnetosphere (Han et al., 2015; Han et al., 2017).

The source particles for diffuse auroras are hot electrons from CPS (Horne et al., 2003). These particles originate from the earthward particle injection during substorms on the nightside (Newell et al., 2009) and drift around the Earth toward dawn and local noon sectors. As drifting, a portion of the electrons can be scattered into the loss cone and produce diffuse aurora. This leads to the diffuse aurora being the most intense near midnight and gradually weakening toward dawn and noon sectors (Newell et al., 2004). At the same time, the electron density gradually decreases from midnight toward the local noon.

The essential differences for the structured and unstructured diffuse auroras lie in the size of the diffuse auroral region. If the auroral region is large enough, it will be full of the field of view and thus be observed as 'unstructured'. Otherwise, if the diffuse auroral region is not so large and its shape can be identified in the field of view, it will be observed as "structured". In the morning, the diffuse auroras are predominantly observed as "unstructured". This can be understood as that the source particle for diffuse aurora still has a high density in the morning, so it can produce diffuse aurora in a large area, which is often observed as "unstructured".

Han et al. (2015) suggested that the reasons for the diffuse auroras observed near MLN become much structured should be related to cold-plasma structuring in the dayside outer magnetosphere. In previous, both theoretical (Demekhov and Yu., 1994; Ni et al., 2014) and observational (Nishimura et al., 2013) works have shown that a structured diffuse aurora corresponds to a cold plasma structure in the magnetosphere. The cold plasma structure plays a crucial role in the generation of the structured diffuse aurora by decreasing the energy threshold and increasing the growth rate of whistler cyclotron instability (Brice and Lucas, 2012; Li et al., 2011). This means that the existence of the cold plasma structure will enable more particles to be scattered into the loss cone and thus lead to a stronger aurora. Based on this theory, because the density of the source particle decreases toward local noon, even though some of them still can be scattered into loss cone and produce diffuse aurora, the auroral intensity may be too weak to be detected by a camera in general. Under such a condition, if there is a cold plasma structure in the magnetosphere, more electrons passing through this structure will be scattered into the loss cone. Thus, the auroral intensity conjugate to the cold plasma structure will be increased and thus be observed as structured diffuse aurora. This well explained why the structured diffuse auroras are predominantly observed near local noon.

Stripy Diffuse Auroras Observed Near Magnetic Local Noon

Satellite observations frequently detected cold plasma structures in the dayside outer magnetosphere (Chen and Moore, 2006; Lee et al., 2015). However, it is not easy to determine the three-

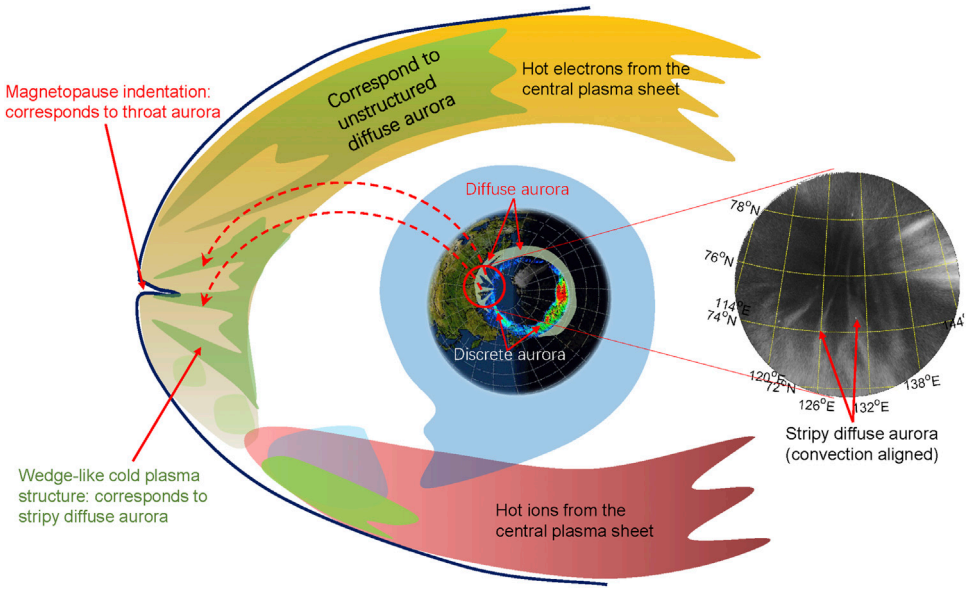

FIGURE 1 | The implications of the statistical results about dayside diffuse aurora. The convection-aligned stripy diffuse aurora observed near magnetic local noon is very informative (revised from Figure 15 in Han et al., 2015).

dimensional (3-D) shape of the cold plasma even with simultaneous observations from multiple satellites. Han et al. (2015) noticed that the structured diffuse auroras observed near MLN mainly show stripy and patchy forms. Importantly, they found that the stripy diffuse auroras are convection-aligned and show tapered at the end. Based on these properties, Han et al., 2015 suggested that these stripy diffuse auroras should correspond to wedge-like cold plasma structures radially aligned from low to high L shells in the dayside outer magnetosphere. **Figure 1** shows a stripy diffuse aurora example and schematically illustrates the projection of the wedge-like structure on the equatorial plane.

The possible origin for the cold plasmas observed in the dayside outer magnetosphere include ionospheric outflow, plasma aspherical drainage plume, and solar wind penetration (Delzanno et al., 2021). The 3-D shape of the cold plasma structure is useful in inferring its generation mechanism. Based on the convection-aligned orientation of the stripy diffuse aurora, Han et al. (2015) suggested that the wedge-like cold plasma structure in the magnetosphere should also be convection-aligned, as indicated in **Figure 1**. This information led Han et al. (2017) to suggest that the cold plasmas forming the wedge-like structure are most likely from the ionospheric outflow. It is well known that solar EUV ionization can produce dense plasma in the midlatitude ionosphere. When these plasmas were conveyed toward high latitudes by ionospheric convection, stripy high-density plasma structures may be formed in the ionosphere. These structures have been observed as the tongue of ionization (Foster et al., 2005) or poleward moving plasma concentration enhancement (PMPCE) (Zhang et al., 2013). Further, Zhang et al. (2016) indicated that the PMPCE might be associated with ionospheric outflows. Thus, from the convection-aligned property of the stripy diffuse aurora, we infer that 1) the correspondent cold plasma structure in the dayside outer magnetosphere should be in a wedge-like form and be convection-aligned, 2) these cold plasmas are originated from the ionospheric outflow, and 3) it is the ionosphere that determines the convection-aligned features for the wedge-like cold plasma structure. We expect future observations to verify these inferences.

Two Types of Diffuse Auroras Observed Near Magnetic Local Noon

By examining the observations at Yellow River Station, Han et al. (2017) revealed that there exist two types of structured diffuse auroras near MLN, which are with obviously different dynamical properties and are called Type 1 and Type 2 diffuse auroras. The auroral movies provided in Supporting Information (SI) in Han et al. (2017) showed the differences in the dynamic properties for the two types of diffuse auroras in detail. Han et al. (2017) showed that Type 1 diffuse auroras are generally in stripy or patchy forms and show fast drifting or pulsating. Actually, Type 1 diffuse auroras are the same as the structured patchy diffuse auroras defined in Han et al. (2015). Thus, they may reflect the cold plasma structuring in the dayside outer magnetosphere, as discussed above.

On the other hand, Type 2 diffuse auroras are always adjacent to the discrete aurora oval and drift together with the nearby discrete aurora much slower than the drifting speed of Type 1. This result naturally reminds us to consider the possible linkage between the Type 2 diffuse aurora and the nearby discrete aurora. Han et al. (2017) confirmed this linkage by coordinated observations from Magnetospheric Multiscale (MMS) satellites

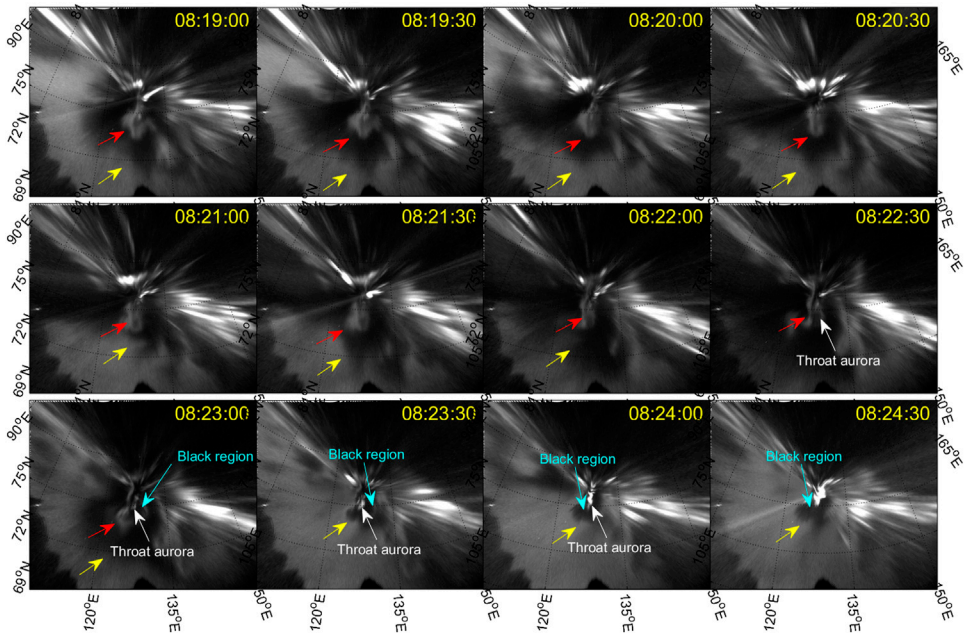

FIGURE 2 | A typical case observed on Nov. 27, 2008 for showing how the diffuse auroras can be used to analyze the dayside magnetospheric processes. Yellow and red arrows indicate Type 1 and Type 2 diffuse auroras, respectively. Type 2 diffuse aurora is believed to be related to the penetrated magnetosheath particles. A throat aurora is developed from the Type2 diffuse aurora from 08:22:30UT. At the same time, a black region is appeared. From 08:23:30, the Type 1 diffuse aurora drift poleward but cannot come into the black region, which means the field lines threading the black region is opened.

near the magnetopause and ground-based all-sky imager at Yellow River Station. Han et al. (2017) found that Type1 and Type 2 diffuse auroras correlate with the number density increase of O+ and He2+ ions, respectively. It is generally accepted that O+ ions are originated from the ionosphere. In contrast, highly charged ion species, such as He2+ ions, are originated from the solar wind. Therefore, Han et al. (2017) suggested that Type 2 diffuse auroras are related to cold plasmas originating from the solar wind.

The possible mechanisms for the solar wind particles entering the magnetosphere include the dayside reconnection (Fuselier and Lewis, 2011), high-latitude reconnection (Song et al., 1994), and impulsive plasma penetration (Lemaire, 1977). The solar wind consists primarily of electrons and protons with the temperature of the order of 10 eV flowing at around 400 km/s. For ions, the flow kinetic energy is ~ 1.0 keV and dominates over the thermal energy. The total energy of the magnetosheath ions is ~ 1.0 keV, while that of the electrons is even lower. Although solar wind particles are traditionally not regarded as cold plasmas, their temperature is about one order lower than that of the electrons in the CPS. Therefore, once entering the magnetosphere, they can also act as a cold plasma structure in producing the diffuse aurora by decreasing the threshold energy of the electrons participating in the wave-particle resonances.

In summary, Han et al., 2017 showed two types of diffuse aurora near MLN, which may correspond to cold plasmas originating from inside and outside the magnetosphere, respectively. It provides a feasible method for inferring the two-dimensional information of magnetosheath particles penetrating into the magnetosphere near the dayside magnetopause.

Using Diffuse Aurora to Analyze the Magnetospheric Processes

The diffuse auroras are all on the closed field lines (inside the magnetosphere). Near MLN, the discrete auroras are believed to be on the open field lines (outside the magnetosphere) (Lockwood, 1997). The diffuse and discrete auroras observed near MLN often show close interaction (Han et al., 2015). Therefore, we suggest that we can study the inside-outside coupling by using the interaction between the diffuse and discrete auroras observed near MLN. Han (2019) analyzed such an event observed on November 27, 2008, as shown in **Figure 2**.

In **Figure 2**, a yellow arrow on each image approximately indicates the poleward edge of Type 1 diffuse aurora, and a red arrow indicates the Type 2 diffuse aurora. From 08:22:30UT, the Type 2 diffuse aurora split, and a black region appeared, as indicated by the blue arrow. At the same time, a discrete aurora started to appear in the center of the diffuse aurora, as indicated by the white arrow. This discrete aurora is called throat aurora (Han et al., 2015) and has been suggested to be associated with magnetopause reconnection (Han et al., 2019; Feng et al., 2020). With the throat aurora gradually brightened, a large area of Type 1 diffuse aurora (indicated by yellow arrow) just drifted poleward and surrounded the throat aurora from 08:23:30UT to 08:24:30UT. Most interestingly, the black region surrounding the

throat aurora kept dark all the time, i.e., the large area of Type 1 diffuse drifting poleward but cannot enter into the black region. Because diffuse auroras are caused by particles on the closed field lines, this observational fact means that the electrons on the closed field lines cannot reach the black region anyway. This can be explained by that the black region was on opened field lines at that time. Because the black region was initially covered by diffuse aurora, i.e., on the closed field lines, *Han* [2019] suggested that the black region's field lines are newly opened by magnetopause reconnection. Further, because the appearance of the black region is closely related to the throat aurora, this indicates that the generation of throat aurora is associated with the magnetopause reconnection. This example well demonstrates the inside-outside magnetospheric coupling by taking advantage of the two-dimensional continuous observations of aurora. The auroral observations may also be used to study how the cold plasmas affect the magnetopause reconnection (Borovsky and Denton, 2008; Borovsky et al., 2008).

CONCLUSION

Based on theoretical works of inferring cold plasma structuring from the structured diffuse auroras, observational results about the dayside diffuse aurora are well explained. Among the dayside diffuse aurora structures, the north-south aligned stripy diffuse auroras are the most informative. The convection-aligned feature reminds us to consider that the related cold plasma structure should be wedge-like in the magnetosphere and these cold plasmas are most likely from the ionospheric outflow. These outflowed cold plasmas may involve the dayside magnetopause reconnection, although the details need further study. Near magnetic local noon, two types of structured diffuse auroras were resolved. Type 1 is suggested to be related to ionospheric outflow, while Type 2 is believed to be involved in particles penetrated from the magnetosheath. Based on these understandings and combined with the advantages of two-dimensional continuous auroral observation, we can infer some physical processes near the dayside magnetopause.

AUTHOR CONTRIBUTIONS

The author confirms being the sole contributor of this work and has approved it for publication.

FUNDING

This work is supported by the National Natural Science Foundation of China (No. 42030101) and Shanghai Science and Technology Innovation Action Plan (No.21DZ1206102). D-SH is the PI of these fundings.

REFERENCES

Borovsky, J. E., and Denton, M. H. (2008). A Statistical Look at Plasmaspheric Drainage Plumes. *J. Geophys. Res.* 113 (A9). doi:10.1029/2007ja012994

Borovsky, J. E., Hesse, M., Birn, J., and Kuznetsova, M. M. (2008). What Determines the Reconnection Rate at the Dayside Magnetosphere? *J. Geophys. Res.* 113 (A7). doi:10.1029/2007ja012645

Brice, N., and Lucas, C. (2012). Influence of Magnetospheric Convection and Polar Wind on Loss of Electrons from the Outer Radiation belt. *J. Geophys. Res.* 76 (4), 900–908. doi:10.1029/ja076i004p00900

Chen, S. H., and Moore, T. E. (2006). Magnetospheric Convection and thermal Ions in the Dayside Outer Magnetosphere. *J. Geophys. Res.* 111 (A3). doi:10.1029/2005ja011084

Delzanno, G. L., Borovsky, J. E., Henderson, M. G., Resendiz Lira, P. A., Roytershteyn, V., and Welling, D. T. (2021). The Impact of Cold Electrons and Cold Ions in Magnetospheric Physics. *J. Atmos. Solar-Terrestrial Phys.* 220, 105599. doi:10.1016/j.jastp.2021.105599

Demekhov, A. G., and Yu, T. V. (1994). A Mechanism of Formation of Pulsating Aurorae. *J. Geophys. Res.* 99 (99), 5831–5841. doi:10.1029/93ja01804

Ebihara, Y., Tanaka, Y. M., Takasaki, S., Weatherwax, A. T., and Taguchi, M. (2007). Quasi-stationary Auroral Patches Observed at the South Pole Station. *J. Geophys. Res.* 112 (A1), A01201. doi:10.1029/2006ja012087

Feng, H.-T., Han, D.-S., Chen, X.-C., Liu, J.-J., and Xu, Z.-H. (2020). Interhemispheric Conjugacy of Concurrent Onset and Poleward Traveling Geomagnetic Responses for Throat aurora Observed under Quiet Solar Wind Conditions. *J. Geophys. Res. Space Phys.* 125, e2020JA027995. doi:10.1029/2020JA027995

Foster, J. C., Coster, A. J., Erickson, P. J., Holt, J. M., Lind, F. D., Rideout, W., et al. (2005). Multiradar Observations of the Polar Tongue of Ionization. *J. Geophys. Res. Space Phys.* 110 (A9), A09S31-01–A09S31-12. doi:10.1029/2004ja010928

Frey, H. U., Han, D., Kataoka, R., Lessard, M. R., Milan, S. E., Nishimura, Y., et al. (2019). Dayside Aurora. *Space Sci. Rev.* 215 (8), 51. doi:10.1007/s11214-019-0617-7

Fuselier, S. A., and Lewis, W. S. (2011). Properties of Near-Earth Magnetic Reconnection from *In-Situ* Observations. *Space Sci. Rev.* 160 (1-4), 95–121. doi:10.1007/978-1-4614-3046-9_6

Han, D.-S., Xu, T., Jin, Y., Oksavik, K., Cai Chen, X., Liu, J-J., et al. (2019). Observational Evidence for Throat aurora Being Associated with Magnetopause Reconnection. *Geophys. Res. Lett.* 46, 7. doi:10.1029/2019GL083593

Han, D., Chen, X.-C., Liu, J.-J., Qiu, Q., Keika, K., Hu, Z.-J., et al. (2015). An Extensive Survey of Dayside Diffuse aurora Based on Optical Observations at Yellow River Station. *J. Geophys. Res. Space Phys.* 120 (9), 7447–7465. doi:10.1002/2015ja021699

Han, D. (2019). Ionospheric Polarization Electric Field Guiding Magnetopause Reconnection: A Conceptual Model of Throat aurora. *Sci. China Earth Sci.* 62 (12), 2099–2105. doi:10.1007/s11430-019-9358-8

Han, D. S., Li, J.-X., Nishimura, Y., Lyons, L. R., Bortnik, J., Zhou, M., et al. (2017). Coordinated Observations of Two Types of Diffuse Auroras Near Magnetic Local Noon by Magnetospheric Multiscale mission and Ground All-Sky Camera. *Geophys. Res. Lett.* 44 (16), 8130–8139. doi:10.1002/2017gl074447

Horne, R. B., and Thorne, R. M. (2000). Electron Pitch Angle Diffusion by Electrostatic Electron Cyclotron Harmonic Waves: The Origin of Pancake Distributions. *J. Geophys. Res. Atmospheres* 105 (A3), 5391–5402. doi:10.1029/1999ja900447

Horne, R. B., Thorne, R. M., Meredith, N. P., and Anderson, R. R. (2003). Diffuse Auroral Electron Scattering by Electron Cyclotron Harmonic and Whistler Mode Waves during an Isolated Substorm. *J. Geophys. Res. Space Phys.* 108 (A7). doi:10.1029/2002ja009736

Hu, Z. J., Yang, H., Huang, D., Araki, T., Sato, N., Taguchi, M., et al. (2009). Synoptic Distribution of Dayside aurora: Multiple-Wavelength All-Sky Observation at Yellow River Station in Ny-Ålesund, Svalbard. *J. Atmos. Solar-Terrestrial Phys.* 71 (8), 794–804. doi:10.1016/j.jastp.2009.02.010

Lee, S. H., Zhang, H., Zong, Q. G., Wang, Y., Otto, A., Rème, H., et al. (2015). Asymmetric Ionospheric Outflow Observed at the Dayside Magnetopause. *J. Geophys. Res. Space Phys.* 120 (5), 3564–3573. doi:10.1002/2014ja020943

Lemaire, J. (1977). Impulsive Penetration of Filamentary Plasma Elements into the Magnetospheres of the Earth and Jupiter. *Planet. Space Sci.* 25 (9), 887–890. doi:10.1016/0032-0633(77)90042-3

Li, W., Bortnik, J., Thorne, R. M., Nishimura, Y., Angelopoulos, V., and Chen, L. (2011). Modulation of Whistler Mode Chorus Waves: 2. Role of Density Variations. *J. Geophys. Res. Atmospheres* 116 (A6), 2235–2239. doi:10.1029/2010ja016313

Liang, J., Ni, B., Spanswick, E., Kubyshkina, M., Donovan, E. F., Uritsky, V. M., et al. (2011). Fast Earthward Flows, Electron Cyclotron Harmonic Waves, and Diffuse Auroras: Conjunctive Observations and a Synthesized Scenario. *J. Geophys. Res.* 116 (A12), A12220. doi:10.1029/2011ja017094

Lockwood, M. (1997). Relationship of Dayside Auroral Precipitations to the Open-Closed Separatrix and the Pattern of Convective Flow. *J. Geophys. Res.* 102 (A8), 17475–17487.

Lou, Y., Cao, X., Ni, B., Tu, W., Gu, X., Fu, S., et al. (2021). Diffuse Auroral Electron Scattering by Electrostatic Electron Cyclotron Harmonic Waves in the Dayside Magnetosphere. *Geophys. Res. Lett.* 48 (5), e2020GL092208. doi:10.1029/2020GL092208

Lui, A. T. Y., Perreault, P., Akasofu, S. I., and Anger, C. D. (1973). The Diffuse aurora. *Planet. Space Sci.* 21 (5), 857. doi:10.1016/0032-0633(73)90102-5

Meng, C. I., Mauk, B., and Mcilwain, C. E. (1979). Electron Precipitation of Evening Diffuse aurora and its Conjugate Electron Fluxes Near the Magnetospheric Equator. *J. Geophys. Res. Space Phys.* 84 (A6), 2545–2558. doi:10.1029/ja084ia06p02545

Newell, P. T., and Meng, C. I. (1992). Mapping the Dayside Ionosphere to the Magnetosphere According to Particle Precipitation Characteristics. *Geophys. Res. Lett.* 19 (6), 609–612. doi:10.1029/92gl00404

Newell, P. T., Ruohoniemi, J. M., and Meng, C.-I. (2004). Maps of Precipitation by Source Region, Binned by IMF, with Inertial Convection Streamlines. *J. Geophys. Res.* 109 (A10). doi:10.1029/2004ja010499

Newell, P. T., Sotirelis, T., and Wing, S. (2009). Diffuse, Monoenergetic, and Broadband aurora: The Global Precipitation Budget. *J. Geophys. Res.* 114 (A9). doi:10.1029/2009ja014326

Ni, B., Bortnik, J., Nishimura, Y., Thorne, R. M., Li, W., Angelopoulos, V., et al. (2014). Chorus Wave Scattering Responsible for the Earth's Dayside Diffuse Auroral Precipitation: A Detailed Case Study. *J. Geophys. Res. Space Phys.* 119 (2), 897–908. doi:10.1002/2013ja019507

Ni, B., Thorne, R. M., Horne, R. B., Meredith, N. P., Shprits, Y. Y., Chen, L., et al. (2011a). Resonant Scattering of Plasma Sheet Electrons Leading to Diffuse Auroral Precipitation: 1. Evaluation for Electrostatic Electron Cyclotron Harmonic Waves. *J. Geophys. Res.* 116 (A4). doi:10.1029/2010ja016232

Ni, B., Thorne, R. M., Meredith, N. P., Horne, R. B., and Shprits, Y. Y. (2011b). Resonant Scattering of Plasma Sheet Electrons Leading to Diffuse Auroral Precipitation: 2. Evaluation for Whistler Mode Chorus Waves. *J. Geophys. Res.* 116 (A4), A04219. doi:10.1029/2010ja016233

Nishimura, Y., Bortnik, J., Li, W., Thorne, R. M., Lyons, L. R., Angelopoulos, V., et al. (2010). Identifying the Driver of Pulsating aurora. *Science* 330 (6000), 81–84. doi:10.1126/science.1193186

Nishimura, Y., Bortnik, J., Li, W., Thorne, R. M., Ni, B., Lyons, L. R., et al. (2013). Structures of Dayside Whistler-Mode Waves Deduced from Conjugate Diffuse aurora. *J. Geophys. Res. Space Phys.* 118 (2), 664–673. doi:10.1029/2012ja018242

Sandholt, P. E., Farrugia, C. J., and Cowley, S. W. H. (1998). Pulsating Cusp aurora for Northward Interplanetary Magnetic Field. *J. Geophys. Res.* 103 (A11), 26507. doi:10.1029/98ja02433

Song, P., Holzer, T. E., Russell, C. T., and Wang, Z. (1994). Modelling the Low-Latitude Boundary Layer with Reconnection Entry. *Geophys. Res. Lett.* 21 (7), 625–628. doi:10.1029/94GL00374

Thorne, R. M., Ni, B., Tao, X., Horne, R. B., and Meredith, N. P. (2010). Scattering by Chorus Waves as the Dominant Cause of Diffuse Auroral Precipitation. *Nature* 467 (7318), 943–946. doi:10.1038/nature09467

Zhang, Q.-H., Zong, Q-G., Lockwood, M., Heelis, R. A., Hairston, M., Liang, J., et al. (2016). Earth's Ion Upflow Associated with Polar Cap Patches: Global and *In Situ* Observations. *Geophys. Res. Lett.* 43 (5), 1845–1853. doi:10.1002/2016gl067897

Zhang, Q. H., Zhang, B. C., Moen, J., Lockwood, M., McCrea, I. W., Yang, H. G., et al. (2013). Polar Cap Patch Segmentation of the Tongue of Ionization in the Morning Convection Cell. *Geophys. Res. Lett.* 40 (12), 2918–2922. doi:10.1002/grl.50616

Zhang, X.-J., Angelopoulos, V., Ni, B., Thorne, R. M., and Horne, a. R. B. (2014). Extent of ECH Wave Emissions in the Earth's Magnetotail. *J. Geophys. Res. Space Phys. Plasmas* 119, 5561–5574. doi:10.1002/2014JA019931

Conflict of Interest: The author declares that the research was conducted in the absence of any commercial or financial relationships that could be construed as a potential conflict of interest.

Publisher's Note: All claims expressed in this article are solely those of the authors and do not necessarily represent those of their affiliated organizations, or those of the publisher, the editors, and the reviewers. Any product that may be evaluated in this article, or claim that may be made by its manufacturer, is not guaranteed or endorsed by the publisher.

frontiers in Physics

REVIEW
published: 20 October 2021
doi: 10.3389/fphy.2021.743316

High-Latitude Cold Ion Outflow Inferred From the Cluster Wake Observations in the Magnetotail Lobes and the Polar Cap Region

Kun Li[1], Mats André[2], Anders Eriksson[2], Yong Wei[3], Jun Cui[1] and Stein Haaland[4,5]*

[1]Planetary Environmental and Astrobiological Research Laboratory (PEARL), School of Atmospheric Sciences, Sun Yat-sen University, Zhuhai, China, [2]Swedish Institute of Space Physics, Uppsala, Sweden, [3]Institute of Geology and Geophysics, Chinese Academy of Sciences, Beijing, China, [4]Max Planck Institute for Solar System Research, Göttingen, Germany, [5]Birkeland Centre for Space Science, University of Bergen, Bergen, Norway

Cold ions with low (a few eV) thermal energies and also often low bulk drift energies, dominate the ion population in the Earth's magnetosphere. These ions mainly originate from the ionosphere. Here we concentrate on cold ions in the high latitude polar regions, where magnetic field lines are open and connected to the magnetotail. Outflow from the ionosphere can modify the dynamics of the magnetosphere. *In-situ* observations of low energy ions are challenging. In the low-density polar regions the equivalent spacecraft potential is often large compared to cold ion energies and the ions cannot reach the spacecraft. Rather, a supersonic ion flow creates an enhanced wake. The local electric field associated with this wake can be used to detect the drifting cold ions, and this wake technique can be used for statistical studies. In this paper, we review some of the key results obtained from this technique. These results help us to understand how cold ionospheric outflow varies with various conditions of solar activities and the Earth's intrinsic magnetic field.

Keywords: cold ion, ionospheric outflow, polar wind, solar wind, geomagnetic field

OPEN ACCESS

Edited by:
Gian Luca Delzanno, Los Alamos National Laboratory (DOE), United States

Reviewed by:
William Lotko, National Center for Atmospheric Research (UCAR), United States
Christopher Cully, University of Calgary, Canada

****Correspondence:***
Kun Li
likun37@mail.sysu.edu.cn

Specialty section:
This article was submitted to Space Physics, a section of the journal Frontiers in Physics

Received: *18 July 2021*
Accepted: *30 September 2021*
Published: *20 October 2021*

Citation:
Li K, André M, Eriksson A, Wei Y, Cui J and Haaland S (2021) High-Latitude Cold Ion Outflow Inferred From the Cluster Wake Observations in the Magnetotail Lobes and the Polar Cap Region. Front. Phys. 9:743316. doi: 10.3389/fphy.2021.743316

INTRODUCTION

Ions of ionospheric origin have for decades been suggested to be a very important part of the magnetospheric plasma population [1–5]. The outflow comes from both high and low latitudes, both providing significant contributions of similar order of magnitude (e.g. 106). Recent review papers summarize several studies of ionospheric outflow (107; [6–9]). Here we concentrate on the outflow from high latitudes. In terms of source region, there are broadly three regions in the high latitude ionosphere relevant for outflow and supply of ionospheric plasma to the magnetosphere. They are the dayside cusp region, the polar cap and the auroral zone.

The auroral region constitutes the boundary between open and close field lines, and is home to multiple energization mechanisms, including particle precipitation, Joule heating, quasi-static electric fields, and wave-particle interactions (see, e.g. [10,11]). Ion escaping from the auroral region can have energies ranging from a few eV to a few tens of keV. During the geomagnetic storm times, ion outflow from the auroral region contains a significant fraction of oxygen ions. A similar outflow of oxygen ions also takes place at the cusp region, where the magnetosheath has direct access to the small region of the polar ionosphere. Energization processes are similar to those in the

nightside auroral region. Due to plasma transport, outflow from the dayside cusp can also be observed over the polar cap, the high-latitude mantle, and the distant tail regions [12–16].

Poleward of the auroral region, in the polar cap, magnetic field lines are "open" (connected to the interplanetary magnetic field). Upflow in this region is initially driven by an ambipolar electric field set up by the difference in scale height between electrons and ions. Simulations (e.g. [17]) and observations (e.g. [18]) suggest a total potential drop of a few volts due to this ambipolar electric field. Energization is thus only a few eV, but this is enough to energize light ions sufficiently to escape Earth's gravitational field. Low-energy ionospheric outflow set up by this ambipolar electric field was firstly predicted by Axford [19] and Banks and Holzer [20], and is often referred to as the polar wind. Additional acceleration mechanisms such as the mirror force and the centrifugal force [21,22], provide some additional energy, but these ions typically remain "cold" for a long time as they move through the magnetosphere.

On short time scales, ouflow of these cold ions plays an important role for dynamics of the magnetosphere (e.g. [23]). Due to the combination of parallel motion along the magnetic field lines, and perpendicular motion through convection of magnetic flux tubes, a large fraction of ions emanating from the ionosphere end up in the Earth's tail plasma sheet after having been transported through the magnetospheric tail lobes. The nightside plasma sheet is of key importance for magnetospheric dynamics and space weather effects like geomagnetic storms and substorms. In particular, magnetic reconnection taking place in the thin current sheet, converts magnetic energy to kinetic energy and results in the deposition of large amounts of energy into the inner magnetosphere, the ring current and the auroral ionosphere.

On a microscopic scale, magnetic reconnection implies a decoupling between particles and the magnetic field in a localized region. This leads to the creation of an electron diffusion region and an ion diffusion region, which scale sizes are governed by the respective inertial lengths and gyroradii of the ions and electrons. Due to their low energy and temperature compared to the pre-existing ions in the plasma sheet, cold ions effectively introduce an intermediate diffusion region into this picture [24,25]. The kinetic physics of reconnection can be drastically changed when cold ions are introduced, e.g., by locally reducing the Hall currents and by introducing new instabilities [26–28]. The large-scale reconnection rate does not seem to change much, at least not for magnetospheric conditions [29].

On geological time scales, ionospheric outflow can also influence the evolution of the atmosphere [30–33]. A frequently recurring question here is the role of a planet's intrinsic magnetic field. On one side, it is claimed that a magnetic field provides some protection against direct solar wind interaction (e.g. [34]), but on the other side, and as noted above, a magnetic field also facilitates some of the escape mechanisms responsible for long term atmospheric evolution (e.g., [35,36]) [37]).

Measuring low energy ions in the terrestrial magnetosphere is notoriously difficult. In the Earth's low density magnetotail lobes, spacecraft are usually positively charged due to photoelectron emission. This positive electric potential effectively shields the spacecraft and its instruments from any ions with energies lower than the equivalent electric potential energy of the spacecraft. Consequently, direct measurements of cold ions with particle detectors in this part of the magnetosphere are not possible unless the spacecraft charge can be neutralized [1,3,4,9,38]. Cold ions in the magnetosphere have therefore been considered "invisible" for a long time. However, an indirect method, based on observations of an enhanced electrostatic wake by the Cluster satellites made it possible to determine the bulk flow velocity of cold ions [39–41]. In this paper, we briefly review this wake method and some of the key results obtained from this technique.

This paper is organized as follows: In *Detecting Cold Ion Outflow*, we first outline the methodology to infer flow velocity and density of cold ions from Cluster mission data, and then briefly introduce the observations of ionospheric outflow prior to the Cluster mission. In *Transport of Cold Ions in the Magnetosphere*, we present results based on a large data set of wake measurement from the Cluster satellites. In particular, we use these observations to infer the ionospheric source region, transport paths and fate of the outflowing ions. In *The Role of the Earth's Intrinsic Magnetic Field* and *Energy Sources for the Outflow*, we present studies on the role of the Earth's magnetic field and the energy sources of cold ion outflow, respectively. In Discussion, we discuss possible comparison using results from the wake technique on Earth with observational studies for other terrestrial planets. Finally, *Summary* summarizes the paper.

DETECTING COLD ION OUTFLOW

Characterization of cold ion outflow requires knowledge about number density and flow velocity of the cold ions. A major challenge with *in-situ* spacecraft observations of low energy plasma is spacecraft charging. One primary source region, the polar cap, is magnetically connected to the magnetospheric lobes—large regions of space characterized by very low plasma densities, typically less than 0.1 cm^{-3} (e.g. [42]). A sunlit spacecraft in such environments will rapidly be charged up to several tens of volt due to photoemission of electrons (e.g. [43,44]). This spacecraft charging acts as a barrier to ions with energies below energy associated with the electric potential of the spacecraft. Consequently, cold ions will be invisible for particle detectors onboard the spacecraft, so alternative methods to determine density and flow velocity have to be used.

Cold Ion Density Determination

In addition to particle instruments and calculation of plasma moments, two alternative methods to determine cold plasma density are possible with Cluster observations. The Wave of HIgh frequency and Sounder for probing Electron density by Relaxation (WHISPER—see e.g. [45]) relies on the identification of the plasma frequency in a wave spectrum and can provide very accurate measurements of electron densities. However, it is not always possible to automatically determine a

single unique resonance line, so densities from WHISPER are not always available. Furthermore, in active mode, WHISPER operation involves excitation over a wide frequency range to determine the resonance line. The lowest possible excitation frequency of WHISPER is around 4 kHz, corresponding to approximately 0.2 cm^{-3} as the lowest detectable electron density value. In addition, contamination from the locally produced photoelectrons can also influence WHISPER measurements.

A second, and frequently used method is based on utilization of the spacecraft charging [44,46]. As shown in e.g. Pedersen et al. [46], a functional relationship between spacecraft charge and the ambient electron density of the form, $N_e = A \exp(-\frac{V_{sp}}{B})$, exists. Here, N_e is the electron density and V_{sp} is the spacecraft potential relative to the ambient plasma. On Cluster, the spacecraft potential is routinely measured by the Electric Field and Wave instrument (EFW- see [47]). A and B are empirical constants, and can be determined from cross-calibration with other instruments including the CIS [48], PEACE [49] and WHISPER [50] when densities obtained from these instruments were available (e.g., [44,46]). Assuming quasi-neutrality, the cold ion density is identical to electron density. This technique has been used by e.g. Svenes et al. [42], and Haaland et al. [51,52] to study cold ion density in the polar cap and lobe regions and their response to changes in the solar irradiation and solar wind—magnetosphere coupling.

Cold Ion Bulk Velocity Inferred From Electrostatic Wake Measurements

Spacecraft in the low-density lobes are often positively charged to tens of volts. The outflowing positive ionospheric ions are typically supersonic with bulk velocity corresponding to an energy of only a few eV and an even lower thermal velocity. These ions are not deflected by the spacecraft body but by the much larger electrostatic structure due to the spacecraft voltage, causing an enhanced ion wake. Since the flow is subsonic with respect to the thermal speed of the electrons, the wake charges negatively. Both ions and electrons can here be treated as essentially unmagnetized (e.g. [39–41,53]). Consequently, a local electrostatic electric field arises due to the wake caused by the charged spacecraft. By measuring this electric field of the wake region, as well as the unperturbed electric field outside the wake, the velocity and direction of the bulk cold ion flow can be determined [53]. Cluster, with its two complementary electric field instruments, is able to measure both the wake field and the unperturbed electric field.

Each wire boom pair of the EFW instrument has two probes 88 m apart. Given a length scale of the wake on the order of 100 m [41,54], the electric field measured by EFW, E^{EFW}, is a superposition of the wake field and large-scale background electric field.

The unperturbed electric field can be measured by the Electron Drift Instrument (EDI) [55,56]. EDI emits electron beams with an energy of 0.5 or 1 keV in the direction perpendicular to the ambient magnetic field, B. The emitted electrons gyrate and return to the instrument, where their gyro center displacement ("drift step") and thus convection are determined. In the magnetotail lobes, the gyro-radius of the emitted electron beams is usually on the order of kilometers and thus much larger than the wake dimensions. The electric field measured by EDI, E^{EDI}, is thus largely unaffected by the wake field.

The wake field can be calculated by subtracting the two measurements, $E^W = E^{EFW} - E^{EDI}$, and since the ions are essentially unmagnetized this gives the direction of the bulk flow velocity, u. In the magnetotail lobes, the perpendicular bulk velocity of cold ion flow is equal to the magnetospheric convection velocity, $u_\perp$, which can be inferred from $u_\perp = E^{EDI} \times B/B^2$. With knowledge about the direction of the total bulk flow velocity and the perpendicular convection, the parallel bulk flow velocity, $u_\vee$, of cold ions can be determined. Combined with cold ion density estimated from the spacecraft potential as described above, it is possible to calculate the flux of cold ions. Details concerning the data analysis and error estimates are given by [40] and in Appendix A of André et al. [5]. A comparison between the enhanced wakes in the polar lobes and narrow wakes in the solar wind and in low Earth orbit is given by André et al. [8].

Data Set of Cold Ions

Many studies have investigated ion outflow at high latitudes. Early observations with particle detectors on satellites include hydrogen polar wind outflow by [57] and the discovery of precipitating keV oxygen ions in the magnetosphere by [58], showing the existence of an ionospheric ion population at higher altitude. Observations have then been obtained by several satellites including S3-3, Dynamics Explorer 1, Viking, Akebono, Freja, Polar, FAST, DMSP and Cluster, by several sounding rockets, and by the European Incoherent Scatter (EISCAT) radar and the EISCAT Svalbard (ESR) radar. A schematic summary of observations is given in **Figure 2** in Yau et al. [59] and recent reviews are given by [7,60]), André et al. [8] and Toledo-Redondo et al. [9].

In the ionosphere a spacecraft can be negatively charged due to the high density and high flux of electrons. At higher altitudes in a low-density plasma, the photoelectrons emitted by a spacecraft in sunlight can dominate, causing positive charging. At altitudes of several R_E (Earth radii) in the polar lobes, spacecraft charging of tens of volts positive is common. This will obviously prohibit positive ions of ionospheric origin with energies of a few eV to reach the spacecraft.

Comparing observations of low-energy ions by different particle detectors using different techniques with different nominal lowest energy channels on different spacecraft, is not trivial. For statistical studies this must include different phases of a solar cycle in different regions, with gradually increasing spacecraft charging as altitude is increasing and density is decreasing. Nevertheless, it is clear that in the energy range where particle detectors and the wake method overlap (order 10 eV) results from low altitudes (ionosphere to a few thousand kilometers) where spacecraft charging is less of a problem and from high altitudes (several Re), both techniques give an average total outflow rate of the order 10^{26} ions s^{-1}, see Table 2 in Peterson et al. [61], Table 1, André et al. [8] and Table 2, Toledo-Redondo et al. [9].

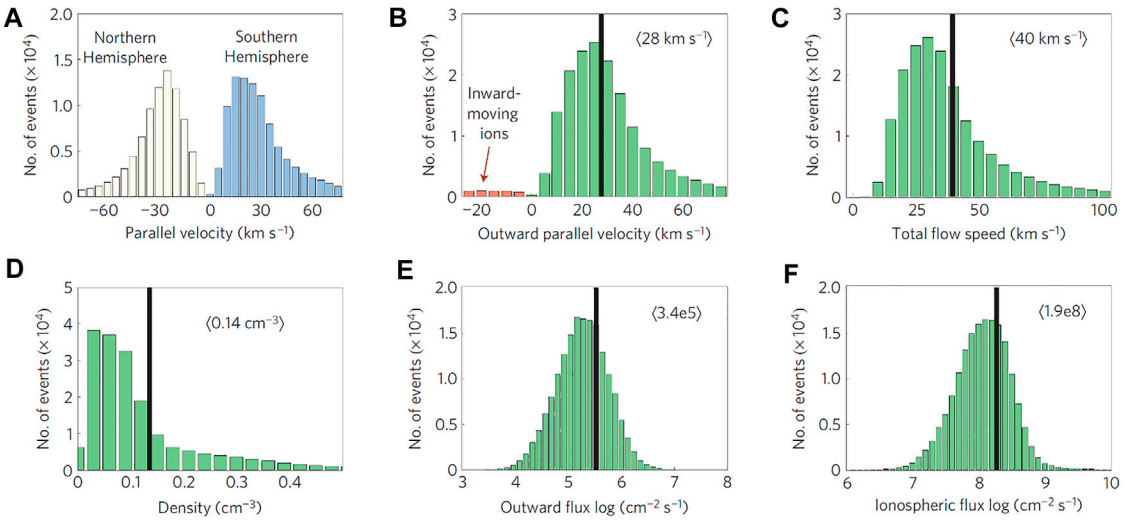

FIGURE 1 | Properties of cold ion outflow. **(A)** Parallel velocity. **(B)** Outward velocity aligned with the magnetic field lines. **(C)** Total speed of cold ions. **(D)** Cold ion density derived from measurements of spacecraft potential. **(E)** Outflow flux calculated from outflow parallel velocity times density with a fact of 0.8 for proton, assuming the outflow consists of 80% of protons. **(F)** Flux in the topside ionosphere mapped from the locations of Cluster to the altitude of 1000 km, where the strength of the magnetic field is assumed to be 37 μT. Adopted from [53].

The spacecraft potential at high altitude can during some periods be artificially reduced by emitting a plasma cloud (the Polar satellite [3]) or a beam of positive ions (Cluster and MMS, [62,63]). Typically a satellite potential of a few volts positive remains. Observations by the Polar satellite at altitudes of 5,000 and 50,000 km using active spacecraft potential control and particle detectors are roughly consistent with the Cluster observations we discuss in detail, although a significant fraction of the low-energy ions may still not reach Polar ([3,40,53,61,64,65]. *In situ* comparison of two Cluster spacecraft in the same polar lobe region at an altitude of about 100,000 km give similar results for both satellites, with one spacecraft using the wake method and the other using particle detectors and artificial reduction of the spacecraft potential [39]. Again direct detection of ions with an onboard instrument, and the Cluster wake technique, give consistent results. The techniques have different advantages. For example, a mass spectrometer can identify different ion species, while the wake technique can detect ions down to the lowest thermal energies and can routinely be used for statistical studies covering many years.

Detailed comparison is further complicated by the fact that ions typically are gradually energized as they move upward. Particle tracing over altitude ranges of several R_E using different observations to initiate the particles still give reasonably consistent results. Tracing based on observations by Polar [66], Akebono [67,68] and on the Cluster wake method [69,70] all show that low-energy ions are common in the magnetotail lobes and often are a significant supply to the tail magnetosheet.

The Cluster wake technique can detect low energy (eV) positive ions also using instruments on a spacecraft charged to tens of volts positive, and can be used for statistical studies during many years. As described above, this technique is based on supersonic flowing ions causing an enhanced wake. Using this technique, and 5 years of observations from one of the four Cluster satellites, ([39,53] presented the first survey of cold ion measurements in the polar cap and lobe regions. Their results demonstrated that the ionospheric outflow during most of the time is dominated by very cold ions—a population that until then had been invisible. By combining outflow velocity and density [40], also estimated the total outflow rate to be the order of 10^{26} ions s^{-1}. As noted above, this value is consistent with observations at much lower altitude where spacecraft charging is less of a problem, but is higher than that in previous studies at high altitudes based on measurements of ions with higher energies (Table 1), [53].

The outflow velocities derived from the wake method, the simultaneously obtained outflow density from spacecraft potential measurements, and outflow fluxes are summarized in **Figure 1**. **Figure 1A** is the histogram of the parallel velocities of cold ions. The mean parallel velocity of outward moving cold ions is 28 km s^{-1}. There are also a few cases of inward moving cold ions as seen in **Figure 1B**.

A follow-up study using the wake technique was presented by André et al. [5]. They used measurements from two of the four Cluster satellites over a 10-year period (2001–2010, nearly a full solar cycle). During this time EDI was operational on the two spacecraft, so velocity estimates could be obtained, needed to estimate the flux. For each year data from 3 July to 3 November were used, centered on 3 September when the polar orbit apogee of about 20 R_E was at local midnight and thus close to the center of the geomagnetic tail behind the Earth, although this time period may introduce a hemispherical seasonal bias because it is closer to the northern summer solstice than to the southern summer solstice. All parts of orbits on the nightside ($X_{GSM} < 0$)

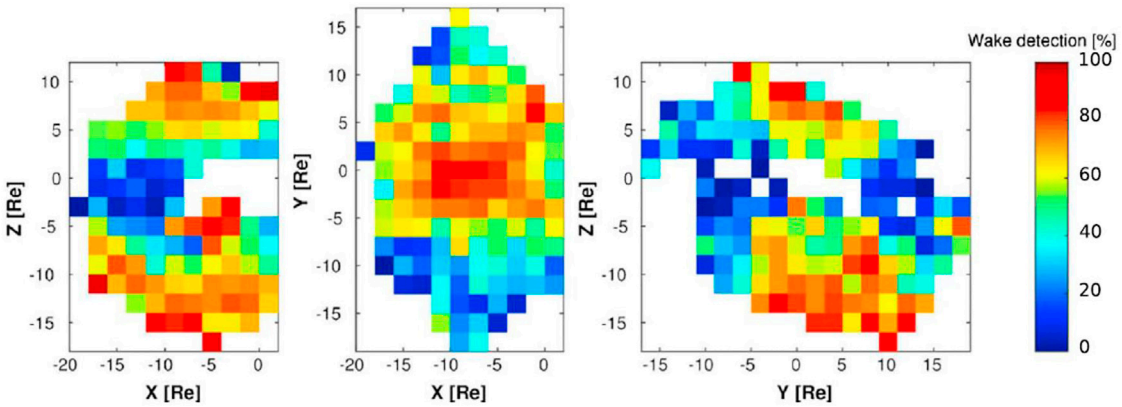

FIGURE 2 | The occurrence rate of cold ions defined by wake detection. A total of about 1,680,000 data are obtained from Cluster 1 and 3 during the years from 2001 to 2010. Adopted from [5].

and geocentric distances beyond 5 R_E were used. In this study, approximately 1,680,000 data points (4 s spacecraft spins) were used to search for enhanced wakes. The presence of a wake was detected in approximately 1,070,000 data points, corresponding to 64% of the total observation time. Cold ions are therefore present in the lobes and polar cap regions most of the time. **Figure 2** shows the occurrence rate of cold ions inferred from wake detections as color-coded maps. The occurrence rate is defined as the ratio of number of wake detections to the total number of measurements in the spatial ranges of the grids in **Figure 2**. In many regions, the occurrence rates of wake detection were above 50%.

After selection of data points with low enough error to be used for estimates of density, velocity, and flux, the number of data points is reduced to 320,000. These data show that the outflow of cold ions is of the order of 10^{26} ions/s and often dominates over the outflow at higher energies.

In addition to the pioneering studies by [39,40] and André et al. [5], a number of other studies (e.g. [69–76]) have made use of this data set to investigate the role of cold ions in the magnetosphere. *Transport of Cold Ions in the Magnetosphere* and *The Role of the Earth's Intrinsic Magnetic Field* of our paper discuss some of the key results from these studies.

TRANSPORT OF COLD IONS IN THE MAGNETOSPHERE

Transport of cold ions from their source in the high latitude polar ionosphere is facilitated by a combination of parallel motion of the ions along the magnetic field, and the convection of magnetic flux tubes due to the solar wind-magnetosphere interaction.

Since the Cluster observations are obtained from point measurements of E-fields, mainly in the high-altitude polar cap and lobe regions, they do not provide much information about the transport paths of ions. Neither the source region nor the fate of the outflowing ions can be directly determined from local measurements alone. One possibility to assess details about the transport of cold ions through the magnetosphere is to use particle tracing. Using a model of the Earth's magnetic field, and the observed convection at Cluster [69,70], used first order guiding center approximations [77] to trace the motion of individual ions from the location of Cluster, either backward to the source region of the ions in the ionosphere, or downtail to the Earth's plasma sheet where many cold ions end up.

Mapping the Ionospheric Source of Cold Ions

One of the objectives of the Li et al. [69] study was to assess the role of solar wind-magnetopshere interaction and geomagnetic activity on ion outflow. **Figure 3**, adapted from their paper, shows color coded maps of source regions of the cold ions for various geomagnetic disturbance activities as reflected by the Dst index. The fluxes shown in the figure are mapped to the altitude of 1000 km. The upper row shows maps for the northern hemisphere and the lower row shows maps for the southern hemisphere. From **Figure 3**, one notes that geomagnetic activity influences cold ion outflow and the source regions in two ways. The outflow flux varies, and the source area changes with geomagnetic activity.

During quiet conditions (Dst>0 nT, shown in panels 1) and 4)), the outflow fluxes are fairly low, on the order of 10^8 ions s^{-1} cm^{-2}, and mostly emanating from a rather small area at high latitudes in the polar cap. Conversely, during high activity (Dst < -20nT, panels 3) and 6)), outflow fluxes are higher by almost an order of magnitude, and the outflow now occurs from a larger area. This is consistent with and expanding/contracting polar cap during disturbed/quiet conditions (e.g. [78]).

The increased flux during disturbed conditions can probably be attributed to a combination of enhanced ionization (e.g. [5]) and enhanced upward/outward forces such as the mirror force or centrifugal force [21,22,79].

From **Figure 3**, it is also seen that there are regions of enhanced outflow near the dayside cusp and the nightside auroral region during disturbed conditions. This may suggest

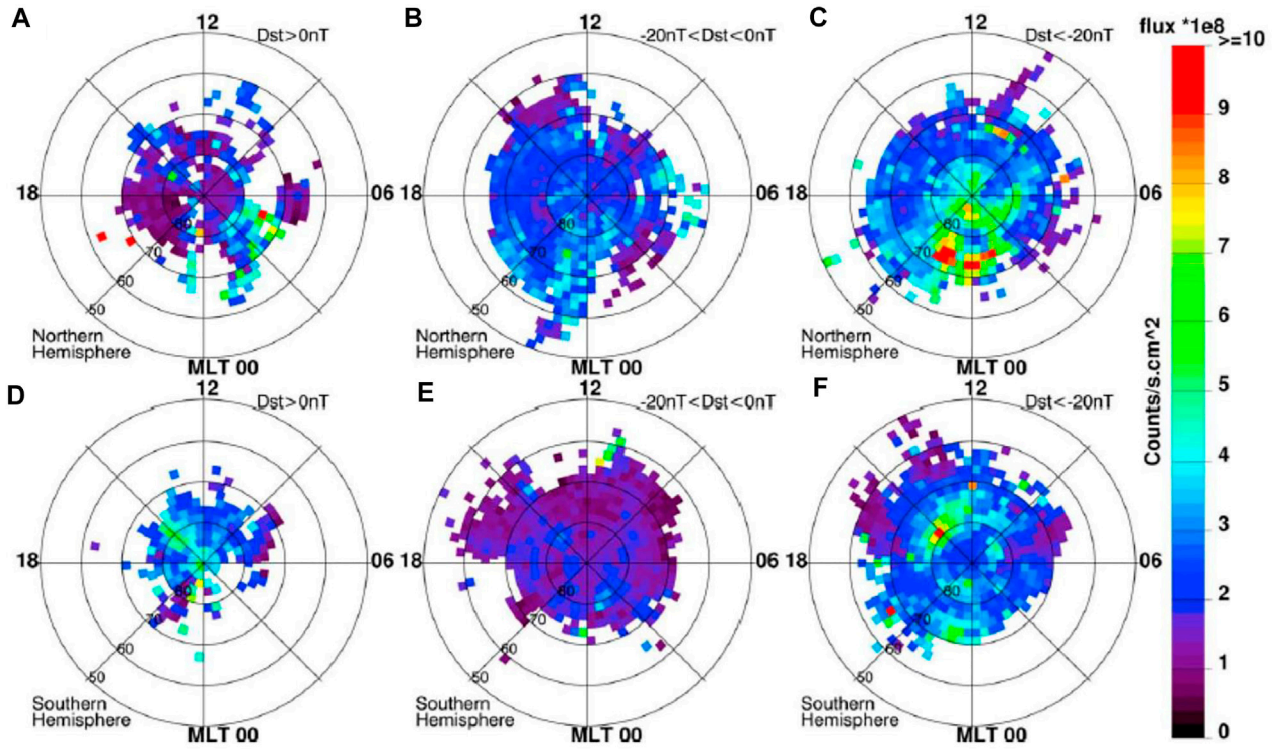

FIGURE 3 | Cold ion outflow flux in the northern **(A–C)** and the southern **(D–F)** hemispheres. For each hemisphere, the three panels from left to right show the fluxes under quiet, moderate, and disturbed geomagnetic conditions, respectively. Each colored pixel indicates the mean flux. From Li et al., (2012).

that particle precipitation or energy flux in the form of waves from the solar wind or the magnetosphere drives some of the outflow. The apparent north-south asymmetry in outflow flux was caused by the Cluster's orbit. Due to the tailward magnetospheric convection, ions escaping from the dayside are likely to travel to higher altitudes than that from the nightside. During the time when cold ions were measured, the Cluster satellites were at higher altitudes in the southern hemisphere than in the northern hemisphere. Therefore, we see more ions from the dayside of the southern polar cap and also from the nightside of the northern polar cap.

To study changes in the cold ion outflow during different phases of geomagnetic storms, Haaland et al. [72] have divided the data from André et al. [5] into subsets according to different phases in various storm events. They have calculated the total outflow rates from the measured outflow fluxes and simultaneously estimated areas of the outflow region, which are modulated by the upstream solar wind conditions and the intensity of the ring current [78]. It is found that the outflow rates and the size of outflow regions are moderate before the main phase of a geomagnetic storm. During the storm main phase, both the cold ion density and velocity increase, and the polar cap regions expand. The average outflow rate increases by almost an order of magnitude during the peak phase of a generic storm compared with the quiet time. The increased outflow velocity may be attributed to larger centrifugal forces during the main phase with enhanced magnetospheric convection.

Determining the Fate of Cold Ions

As noted above, transport of cold ions in the magnetosphere is controlled by the combination of motion along the magnetic field and magnetospheric convection. In the stretched magnetic field of the magnetotail lobes, convection is mainly towards the central plasma sheet, and the same for all species and energies. The parallel velocity, on the other hand, is generally different for different energies of the ions. This leads to a velocity filter effect that separates ions by energy and origin.

Ions with a high parallel velocity can escape the magnetotail and be lost into the solar wind without reaching the plasma sheet, while ions with lower parallel velocities can reach the plasma sheet where they eventually get heated. Likewise, ions starting at high latitudes, or the dayside ionosphere, will have longer transport paths than ions from lower latitudes in the nightside, and are more likely to be lost (e.g., [12,14,32]).

Haaland et al. [71] used the convection velocities obtained from the Cluster/EDI measurements and parallel velocities and flux of cold ions to estimate the fate of cold ion outflow. Their results, summarized in **Figure 4**, show that the fate of outflowing ions is highly affected by the interplanetary magnetic field (IMF) and consequently the level of the geomagnetic activity. A northward IMF leads to nearly stagnant magnetospheric convection, but there is still cold ion outflow. Under such conditions, most of the outflowing cold ions are lost downtail into the solar wind. The fraction of cold ions directly lost in this way varies from about 4% during storm periods to about 96%

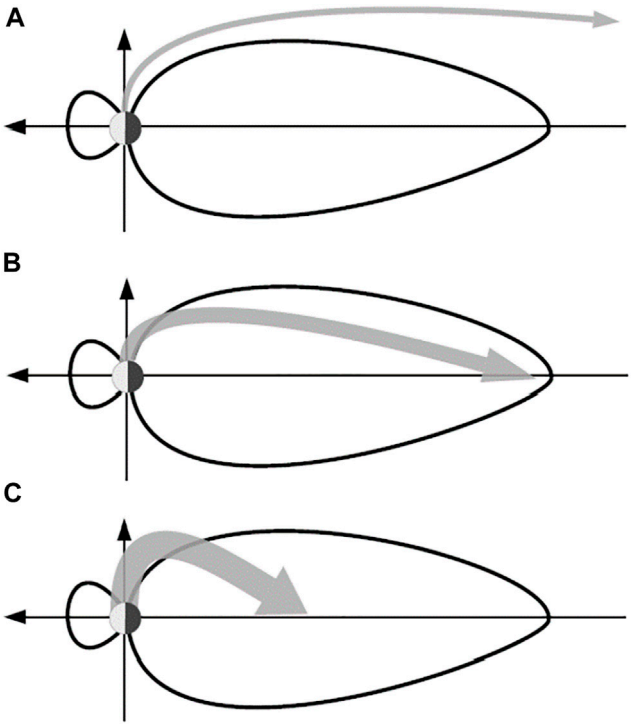

FIGURE 4 | Schematic plots of the trajectories of cold ions during **(A)** quiet, **(B)** moderate, and **(C)** storm periods. The width of the grey arrow in each panel indicates the flux of cold ions. The geomagnetic quiet conditions correspond to near stagnant magnetospheric convection, with relatively small outflow fluxes from the ionosphere. Strong magnetospheric convection happens during the geomagnetic storm periods. Although the outflow fluxes are large compared to that during the quiet periods, most of the cold ions reach the plasma sheet before moving far down-tail. From Haaland et al. [71].

during quiet periods. This is consistent with the recent results that the plasma sheet is primarily supplied by ions of ionosphere origin during storm periods [80].

Cold ions are mainly accelerated by the centrifugal force during the transport through the magnetosphere [53,81,82]. The centrifugal force is small, so that cold ions typically remain cold. Li et al. [70] used particle tracing to study the transport of cold ions in more detail. Their results showed that it takes about 2–4 h for a cold ion to travel from the ionosphere to the plasma sheet. Due to enhanced convection, and to some degree increased parallel velocity, the travel time decreases with increasing geomagnetic activity. During the geomagnetic storm periods, cold ions therefore land on the plasma sheet closer to the Earth than during the quiet periods. Furthermore, the results show a persistent dawn-dusk asymmetry with more cold ions ending up near dusk, even though there is no such asymmetry in the source region. This is consistent with simulations by Cully et al. [67] for low-energy ions and by [83] for O^+ ions. This phenomenon can be explained by the fact that the movements of outflowing ions are largely constrained by the convection electric field. The averaged convection equipotentials are skewed 2–3 h clockwise under most conditions, as simulated by Weimer [84] and observed by Haaland et al. [85]. Therefore, ions from the dayside traveling tailward typically have a velocity component in the duskward direction and end up in the dusk sector of the plasma sheet.

THE ROLE OF THE EARTH'S INTRINSIC MAGNETIC FIELD

Throughout Earth's geological history, both orientation and strength of the geomagnetic field have changed dramatically, often within short geological time scales (e.g., [33,86–88]). Changes in the magnetic field will affect the shape, size and location of the polar cap—the source region for cold ion outflow—and consequently the total outflow. Ion outflow is also affected by the strength of the geomagnetic field, since this will influence the interaction between the solar wind and the atmosphere.

In the following, we show how changes in orientation of the geomagnetic field due to the rotation of Earth impact cold ion outflow. We also show how cold ion outflow is affected by changes in strength of the geomagnetic field based on comparison studies of outflow from ionospheric source regions with different geomagnetic field strength, but with similar solar zenith angles and levels of geomagnetic activities. The results of these studies help us to understand the importance of magnetic field strength for quenching planetary mass loss.

The Impact of Geomagnetic Field Orientation

Due to the rotation of the Earth and the offset between the geomagnetic dipole axis and the rotation axis, the geomagnetic dipole tilt angle varies on a seasonal and diurnal basis. This results in corresponding variations in the illuminated area of the polar cap. Studies based on simulations (e.g. [89]) and observations (e.g. [90]) show that variations in the plasma density and temperature in the ionosphere are significantly influenced by the Solar Zenith Angle (SZA). Using the above described cold ion data derived from the plasma wake, Maes et al. [76] showed that both cold ion density and cold ion outflow velocity decrease with increasing SZA, with substantially lower plasma density and outflow velocity for SZA values larger than about 100°.

Figure 5 shows various cold ion outflow parameters in the topside ionosphere [73] as a function of solar wind energy input rate under different conditions of solar EUV and hemispheric dipole tilt angle (μ) using the cold ion data base obtained with Cluster [5]. Here, the μ is defined as the tilt angle of the projection of the outward directed dipole axis on the GSE XZ plane, it is positive or negative as the axis in the hemisphere tilts toward the Sun or the tail. The solar wind energy input rate is estimated from the ε parameter as a measure of the electromagnetic Poynting flux that enters the magnetosphere [91].

As we can see in **Figure 5**, changes in μ controls the outflow density (**Figure 5A**), and the outflow density also increases with increasing solar wind energy. In contrast, turning of μ from negative to positive seems to result in a small increase in the parallel velocity (**Figure 5B**). Comparing the values in **Figure 5C**

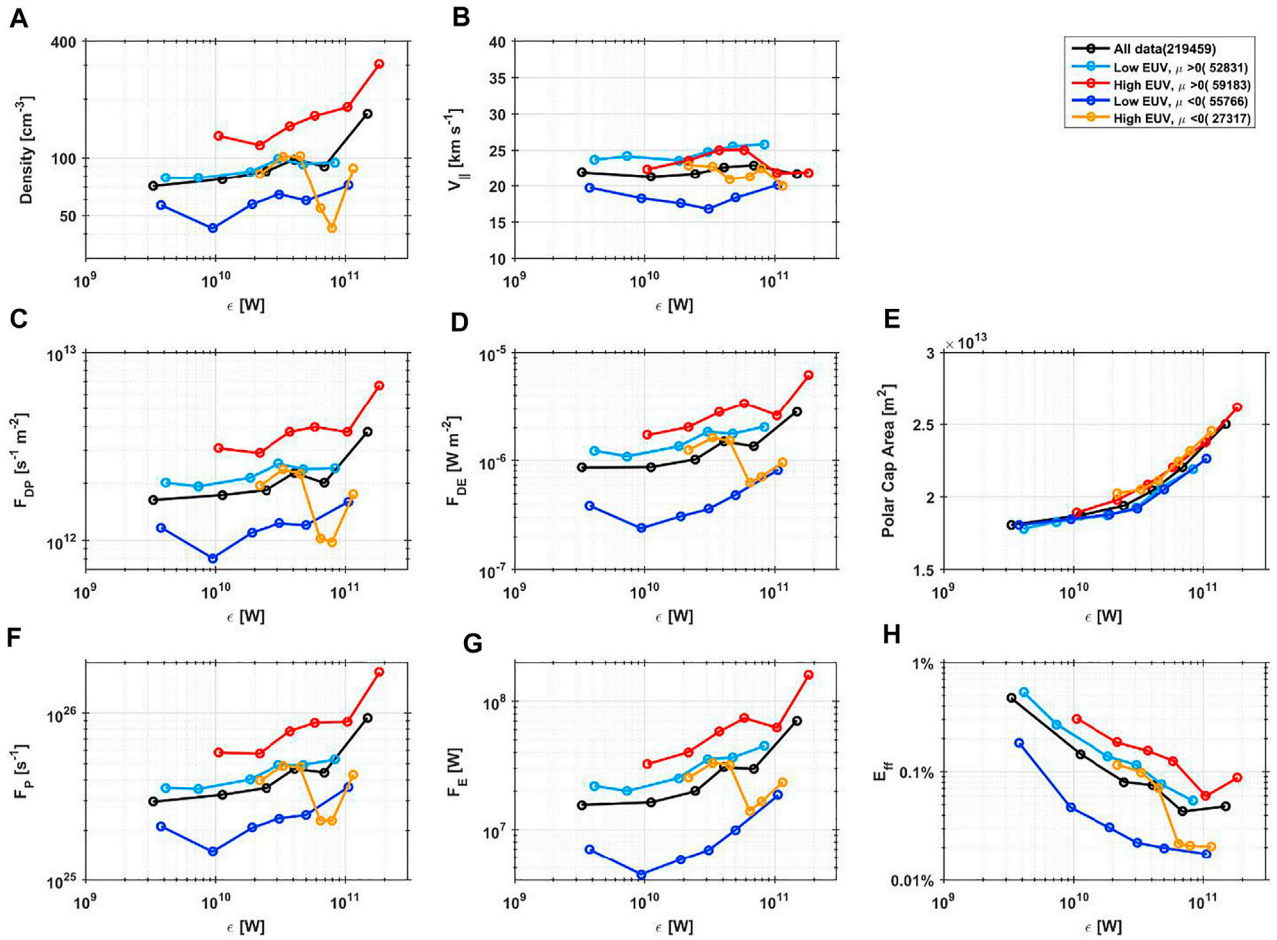

FIGURE 5 | Cold ion outflow parameters in the topside ionosphere as a function of the ε parameter under different conditions of solar EUV and geomagnetic dipole tilt angle (μ). Each panel shows median values calculated from the 10-years data set described in *Data Set of Cold Ions*. High and low solar EUV are defined as $F_{10.7}$ being higher and lower than 155, respectively. F_{DP} and F_P stand for outflow particle flux and outflow rate, respectively. F_{DE} and F_E are outflow energy flux and outflow power, respectively. E_{ff} is the energy coupling coefficient calculated from $E_{ff} = F_E/\varepsilon$. From Li et al., (2017).

with different signs of μ but with the same ε parameter under the condition of high solar EUV, the increases in the density and the velocity result in an increase in the outflow particle flux (F_{DP}) and the outflow energy flux (F_{DE}) by a factor of 2 as μ turns from negative to positive. The condition of high solar EUV and negative μ cannot be used for comparison because the number of data points under this condition is not comparable to that under other conditions. The turning of the dipole axis does not change the polar cap area. So, the total hemispheric outflow rate of particle (F_P, shown in **Figure 5F**) and total hemispheric outflow rate of energy (F_E, shown in **Figure 5G**), respectively calculated from F_{DP} and F_{DE} times the outflow area (**Figure 5E**, see details of calculation in [73]), also increase by a factor of 2 as μ turns from negative to positive.

Therefore, the geomagnetic orientation can control the F_P and the F_E by changing the outflow density. The changes in the parallel velocity due to changes in the geomagnetic orientation is considerably small and can be statistically negligible in estimating the F_P and the F_E.

The Impact of Geomagnetic Field Strength

In addition to variations over time, the geomagnetic field also possess strong spatial inhomogeneities (e.g., [92]; 109). In particular, and perhaps best known, the region of reduced field strength known as the South Atlantic Anomaly (e.g., [93]; 108 [94]) allows particles to penetrate deeper into the atmosphere due to the lower mirror altitude, and can locally modify the ionosphere (e.g., [93,95,96]). More relevant for ionospheric outflow is the magnetic field strength in the polar cap regions [97].

Li et al [75] investigated the role of geomagnetic field strength in ion outflow. They analyzed the outflow from different regions of the polar cap ionosphere in the southern hemisphere where there are significant spatial inhomogeneities in magnetic field strength. The northern polar cap has a relatively uniform spatial distribution of magnetic field [97] and thus the data from the northern hemisphere are not used for the analysis. Once again using the above described Cluster wake data set and particle tracing, they determined the outflow density (*n*) and the outflow

particle flux (*Fp*) at the locations of the source region. The magnetic field strength in the source region of the outflow, $|B|$, is obtained from the international geomagnetic reference field (IGRF) model. They sorted the observations into subsets according to levels of geomagnetic activity (AE index), solar activity ($F_{10.7}$), and SZA.

The results shown in **Figures 1–3** of Li et al. [75] suggest that there is an anti-correlation between $|B|$ and n (and F_P as well). Their results suggest that the anti-correlation mostly happen during periods with the $F_{10.7}$ index between 150 sfu and 200 sfu. When $F_{10.7}$ was either smaller than 150 sfu or larger than 200 sfu, the anti-correlation became less prominent. This can be explained by the contraction and inflation of the atmosphere during low and extremely high solar activities. Let us assume that electrons precipitate from the lobes or solar wind with the same properties (such as pitch angle, energy, density, and strength of magnetic field at their source region) for outflow events in similar levels of geomagnetic activity with similar SZAs. In the case of low solar activities, the precipitating electron cannot reach the atmosphere. In the lcase of extremely high solar activity, all energies of the precipitating electrons will be lost in the atmosphere. This leads to the fact that the occurrence rate of anti-correlation is low when the level of solar activity is low or extremely high. Therefore, within the range of the magnetic field strength in the polar region of the southern hemisphere at present time, the intrinsic magnetic field is anti-correlated with ionospheric outflow during the periods of high levels of solar activity (150 sfu < $F_{10.7}$ < 200 sfu).

Energy Sources for the Outflow

To estimate how efficiently the Sun transfers energies to ion outflow, the power of ion outflow (defined in *The Role of the Earth's Intrinsic Magnetic Field*, as the hemispheric outflow rate of kinetic energy carried by escaping cold ions) stemming from solar wind and solar illumination are quantified. These quantities are important to answer the question (though this question is highly debated and remains open): whether the intrinsic magnetic field of a planet is necessary to prevent loss of its atmosphere into space?

Li et al. [73,74] investigated how efficiently solar energy in the form of illumination and Poynting flux, is converted to energy driving ionospheric outflow at Earth. A proxy for solar energy input rate was derived from measurements of the solar wind (the ε parameter—see e.g. [91]), and solar illumination (calculated from the total solar irradiance (TSI) of 1,361 W m^{-2} [98], which is the solar electromagnetic irradiation power per unit area integrated over all wavelength, times the cross-sectional area of the ionosphere looking from the Sun). The above-described cold ion data set based on Cluster wake measurements, combined with a total outflow area as based on an expanding/contracting polar cap as described in [78] were used to estimate the total power of ion outflow.

Figure 6 shows how the total hemispheric power of the outflowing ions, F_E, varies as a function of the solar wind energy input rate. **Figure 6A** shows the results for an illuminated polar cap source region, and **Figure 6B** shows the corresponding results for a dark polar cap region. These results indicate that solar wind energy is the main energy source for the cold ion outflow when the ε parameter is larger than 10^{10} W.

When more than 95% of the polar cap is illuminated (**Figure 6A**), the total hemispheric power associated with the outflow of cold ions increases from 10^7 W to 10^8 W with increasing solar wind energy input. However, when the ε parameter is smaller than 10^{10} W, the outflow power, F_E, is almost a constant around 10^7 W when the polar cap is illuminated, suggesting that solar illumination rather than solar wind energy input in the form of Poynting flux, is the primary energy source for the outflow.

For dark conditions (**Figure 6B**), F_E is almost an order of magnitude smaller. From this, Li et al [73,74] inferred that solar illumination alone provides energy sufficient to sustain outflow power of the order of 10^7 W, indicating that the main energy source for cold ion outflow is the solar illumination when the ε parameter is smaller than 10^{10} W.

We note that F_E is not zero when the combined solar wind Poynting flux and solar illumination are extremely small. This may be explained by transport of energy from the illuminated area outside the polar cap due to the circulation in the atmosphere. Polar rain precipitation or more energetic precipitation inside nightside polar cap region may also contribute to energization.

From **Figure 5H**, we also infer that only about 0.1% of the solar wind Poynting flux is converted into ion outflow power when the ε parameter is around 10^{10} W. This value decreases to about 0.01% with increasing ε values. Contributions to ion outflow energization from solar illumination are about 6–7 orders of magnitude smaller than that of the solar wind electromagnetic energy input.

DISCUSSION

A recurring question concerning the escape of matter from planetary atmospheres is the role of an intrinsic planetary magnetic field [35,37]. For example, at Mars and Venus, the loss through atmospheric outflow has sometimes been attributed to the lack of an intrinsic magnetic field [99]. It has therefore somewhat naively been assumed that a strong planetary magnetic field and the presence of a magnetosphere prevent erosion of the atmosphere. However, this assumption was challenged when the cold ions were taken into account in estimations of total outflow rates. For example, the study by [40] concluded that previous estimates of ion outflow from Earth were underestimated. Updated values on outflow rates, where cold ions are included, suggests total outflow rates from Earth of the same order of magnitude as ion outflow rates from Mars reported in, e.g., Fränz et al. [100]; Persson et al. [101]; Ramstad and Barabash, (2021).

Different planets possess different atmospheres and have different energy transfer processes. In this context it is interesting to understand how the energy sources (solar EUV and solar wind energy) control the ion supply in the ionospheric source region and the energy needed to reach escape velocity and determine whether the outflow is limited by available ion sources or by energy available for the ions to reach escape velocity.

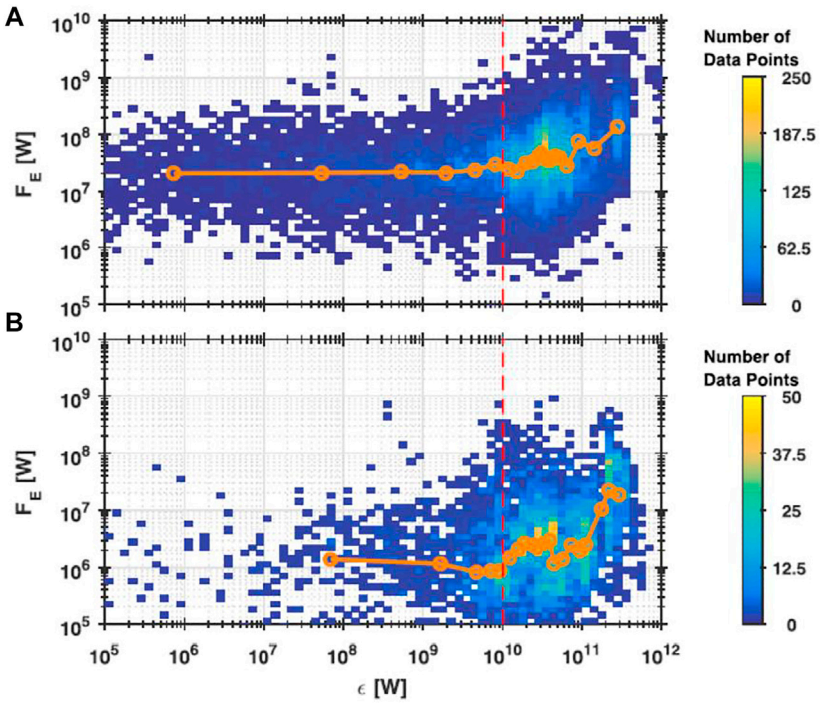

FIGURE 6 | Total hemispheric power, F_E, as a function of the ε parameter for the conditions where more than 95% of the polar cap is sunlit (**Figure 6A**) and dark (**Figure 6B**), respectively. Colored pixels show the numbers of data points in corresponding ranges of F_E and ε parameter. Values indicated by open circles are median values of F_E. Under conditions where ε is less than 10^{10} W, indicated by the red dash line, solar illumination is considered the main energy source of the cold ion outflow. From Li et al., (2018).

A simple model would include an ionospheric source of ions (ionization provided by solar EUV radiation; other ionization processes such as particle precipitation and cosmic ray absorption are ignored in this simple model) and energy for the ions to obtain escape velocity (energy carried by the solar wind, converted to suitable electromagnetic form to energize the ions). Reality is more complex, with both sources (solar EUV, solar wind) contributing to both the ionospheric source and the energy to reach escape velocity. As one can see in **Figure 5**, more solar EUV gives more ions (per unit area in the ionosphere). More solar EUV also gives higher ambipolar electric field and maybe slightly higher outflow velocity [76]. More solar wind energy gives higher ion density (higher scale height) in the ionosphere since some energy can be dissipated in the ionosphere and consequently higher ion outflow density (**Figure 5A**). More solar wind energy also gives larger polar cap area (**Figure 5E**). In **Figure 5B**, the ion outflow velocity does not really increase. The outflow flux increases since the density of the outflow increases, as comparing **Figure 5C** with **Figure 5A**. During geomagnetic storms also the velocity can increase but density is still more important for outflow per unit area [72]. The total outflow also increases with increased solar wind energy since the polar cap area increases (**Figure 5E**), which is the more important effect.

From the above analysis, the outflow mechanism can be said to be source-limited in the sense that increased outflow flux depends on higher density in the outflow than higher outflow speed. The cause may be increased solar EUV or solar wind energy through low-altitude energy deposition illustrated for another region for one geomagnetic storm in **Figure 1** of Strangeway et al. [11]). The outflow mechanism can also be said to be energy-limited in the sense that more solar wind energy will increase the outflow by increasing its density. The total outflow is energy-dependent also since the polar cap area is enlarged during periods of high solar wind energy input. Therefore, it is not simple to distinguish between source-limited or energy-limited in the case of ionospheric outflow from Earth, as that has been analyzed for Martian ionospheric outflow [37].

Other studies of ion outflow from Earth consider other regions and other ion species. One example is an investigation of the dayside high latitude region during a geomagnetic storm, dominated by O^+ ions [11,102]. In that study, two primary energy sources are considered; Poynting flux and soft electron precipitation, as observed by the FAST satellite at 4,000 km. The best controlling parameter is the density of precipitating electrons, but the energy sources are strongly correlated. The scenario is that the precipitating energy (originating in the solar wind) dissipated in the ionosphere increases the scale height and increases the number of upwelling ions. Note that not all of the precipitating energies could be traced back to the solar wind, one exception is the wave-induced electron precipitation (defined as the broadband precipitation by 110) originating from the ionosphere, although this type of precipitation mainly happens in the premidnight sector of aurora region. Wave energization is then needed to provide transverse (to the magnetic field) heating which, together with the magnetic mirror force in a converging/diverging geomagnetic field can cause ion outflow ([11], **Figure 1**). Here it is believed that increased (solar wind) energy input results in a higher ionospheric scale height (more ions in the source), while solar wind energy is needed for wave heating for the O^+ ions to reach escape

velocity. Since the [11] study is limited to a selected geomagnetic storm, seasonal and solar cycle effects such as varying solar EUV are not considered. They also point out that the results "should be used in conjunction with classical polar wind models".

It is also useful to compare the energy transfer efficiencies from our studies with investigations of ion outflow from other planets. Care must be taken when trying to reach general conclusions since the studies are obtained with different instruments, and cover different energies, ion masses and parts of the solar cycle. Recent estimates of the coupling coefficient by several researchers are based on different definitions, making it difficult to directly compare the energy transfer efficiencies [37,101]. Nevertheless, one interesting aspect is that an intrinsic planetary magnetic field has been considered as a "shield" needed for planets and exoplanets to protect the atmosphere and ionosphere. Recent simulations and estimates show that this assumption is not necessarily correct, an intrinsic field might well increase the outflow [35–37].

SUMMARY

Ionospheric outflow from the Earth mainly consists of cold ions with both kinetic and thermal energies smaller than 100 eV during geomagnetically quiet times. Cold ions are important to understand the ionospheric outflow, but measuring cold ions with regular ion detectors in space often suffers from spacecraft charging issue for a spacecraft operating in a sunlit and tenuous plasma environment. Statistical studies of cold ions in the polar lobes has not been available until the wake technique utilizing the electric field measurements from two complementary electric field instruments on Cluster satellites. The main conclusions from the wake method are summarized as below:

- The wake method has revealed and allowed characterization of cold ions previously invisible.
- Cold ions dominate the ion population in the magnetotail lobes and polar cap region, especially during geomagnetically quiet times.
- Average outflow rates are of the order of 10^{26} ions s^{-1}. One main source region of cold ions in the magnetosphere is the polar cap ionosphere with open magnetic field. During periods of geomagnetic storm, both the outflow flux and the size of polar cap increase.
- The fate of cold ions is controlled by the magnetospheric convection and the parallel velocities of cold ions. There are high fluxes of cold ions in the topside ionosphere during the geomagnetic storm periods. But because of high magnetospheric convection velocity, most of them could reach the plasma sheet before they are transported far in the magnetotail.
- Cold ion outflow is modulated by solar wind energy input and solar irradiation. About 0.01–0.1% of solar wind energy input is transferred to the cold ion outflow. While the efficiencies for solar irradiation transferring energy to cold ion outflow are 6–7 orders of magnitude smaller.
- Cold ion outflow is also affected by the orientation of the geomagnetic dipole axis. The orientation of the geomagnetic dipole axis controls the illuminated area of the polar cap and thus the outflow.
- Within the range of the magnetic field strength in the polar region of the southern hemisphere at present time, the strength of intrinsic magnetic field is anti-correlated with ionospheric outflow during the periods of high levels of solar activity.

For the outflow of cold ions in the polar cap and magnetotail lobes we investigate, solar EUV illumination and solar wind energy both contribute to the ionospheric source of ions and the energy needed to reach escape velocity. Usually, the increase of density rather than the increase of velocity is more important for the outflow per unit area when solar EUV illumination or solar wind energy is increased. In addition, the increase of the polar cap, the outflow area, with solar wind energy input, is an important factor for the total outflow.

Nevertheless, some fundamental question about the electric field enabling cold ions to escape remains to answer: how do the electrons from the polar rain and the photo-emission play a role in affecting the ambipolar electric field ? How is the ambipolar electric field affected by the solar wind and the geomagnetic condition? To answer these questions with observations, a special instrument proposed by Li et al. [103] should be built to measure the extremely small electric field.

It is still difficult to estimate from observations how much of the ionospheric ions in the plasma sheet will end up in various parts of the magnetosphere although some simulations have been conducted [104]. Many ions do not escape directly down the geomagnetic tail into the solar wind but return back to the magnetosphere [71] and some may be lost into the ionosphere [105], but most ions are likely to eventually leave the magnetosphere into the solar wind (e,g, André at al. 2015). Unlike O^+ ions, protons are heated and mixed up with ions of the solar wind. These protons of ionospheric origin become un-distinguishable from the solar wind, leading to a further complication to study the fate of the ionospheric ions.

AUTHOR CONTRIBUTIONS

KL, MA, SH, YW, and JC contributed to conception and design of the study. AE and MA organized the database. KL performed the statistical analysis. KL wrote the first draft of the manuscript. MA and SH wrote sections of the manuscript. All authors contributed to manuscript revision, read, and approved the submitted version.

FUNDING

This work was supported by the pre-research project on Civil Aerospace Technologies No. D020104 funded by China's National Space Administration, and the National Natural Science Foundation of China under Grant 41704164. MA is supported by the Swedish National Space Agency contract 2020-00058.

ACKNOWLEDGMENTS

MA and SH acknowledge support from the ISSI international team cold plasma of ionospheric origin at the Earth's

magnetosphere. We acknowledge the essential studies to measure cold ions with the wake method by E. Engwall. We also thank the tremendous help and contributions to the studies utilizing the cold ion data by L. Chai, P. W. Daly, M. Förster, M. Fränz, E. Grigorenko, E. Kronberg, L. Maes, R. Maggiolo, H. Nilsson, Q. Y. Ren, Z. J. Rong, W. X. Wan, and H. Zhao.

REFERENCES

1. Chappell CR, Baugher CR, and Horwitz JL. New Advances in thermal Plasma Research. *Rev Geophys* (1980) 18(4):853–61. doi:10.1029/RG018i004p00853
2. Chappell CR, Moore TE, and Waite JH. The Ionosphere as a Fully Adequate Source of Plasma for the Earth's Magnetosphere. *J Geophys Res* (1987) 92(A6):5896. doi:10.1029/JA092iA06p05896
3. Moore TE, Chappell CR, Chandler MO, Craven PD, Giles BL, Pollock CJ, et al. High-Altitude Observations of the Polar Wind *Science* (1997) 277(5324):349–51. doi:10.1126/science.277.5324.349
4. Olsen RC, Chappell CR, Gallagher DL, Green JL, and Gurnett DA. The Hidden Ion Population: Revisited. *J Geophys Res* (1985) 90(A12):12121–32. doi:10.1029/JA090iA12p12121
5. André M, Li K, and Eriksson AI. Outflow of Low-Energy Ions and the Solar Cycle. *J Geophys Res Space Phys* (2015) 120(2):1072–85. doi:10.1002/2014ja020714
6. Yamauchi M. Terrestrial Ion Escape and Relevant Circulation in Space. *Ann Geophys* (2019) 37:1197–222. doi:10.5194/angeo-37-1197-2019
7. Yau AW, Abe T, André M, Howarth AD, and Peterson WK. Ionospheric Ion Acceleration and Transport. In: R Maggiolo, N André, H Hasegawa, and DT Welling, editors. *Magnetospheres in the Solar System, Geophysical Monograph*. John Wiley & Sons (2021). doi:10.1002/9781119507512
8. André M, Eriksson AI, Khotyaintsev YV, and Toledo-Redondo S. The Spacecraft Wake: Interference with Electric Field Observations and a Possibility to Detect Cold Ions. *J Geophys Res Space Phys* (2021) 126:e2021JA029493. doi:10.1029/2021JA029493
9. Toledo-Redondo S, André M, Aunai N, Chappell CR, Dargent J, Fuselier SA, et al. Impacts of Ionospheric Ions on Magnetic Reconnection and Earth's Magnetosphere Dynamics. *Rev Geophys* (2021) 59:e2020RG000707. doi:10.1029/2020RG000707
10. André M, and Yau A. Theories and Observations of Ion Energization and Outflow in the High Latitude Magnetosphere. *Space Sci Rev* (1997) 80(1/2):27–48. doi:10.1023/A:100492161988510.1007/978-94-009-0045-5_2
11. Strangeway RJ, Ergun RE, Su Y, Carlson CW, and Elphic RC. Factors Controlling Ionospheric Outflows as Observed at Intermediate Altitudes. *J Geophys Res* (2005) 110(A3). doi:10.1029/2004ja010829
12. Krcelic P, Haaland S, Maes L, Slapak R, and Schillings A. Estimating the Fate of Oxygen Ion Outflow from the High-Altitude Cusp. *Ann Geophys* (2020) 38(2):491–505. doi:10.5194/angeo-38-491-2020
13. Liao J, Kistler LM, Mouikis CG, Klecker B, Dandouras I, and Zhang J-C. Statistical Study of O+transport from the Cusp to the Lobes with Cluster CODIF Data. *J Geophys Res* (2010) 115(A12):a–n. doi:10.1029/2010ja015613
14. Schillings A, Slapak R, Nilsson H, Yamauchi M, Dandouras I, and Westerberg L-G. Earth Atmospheric Loss through the Plasma Mantle and its Dependence on Solar Wind Parameters. *Earth Planets Space* (2019) 71(1). doi:10.1186/s40623-019-1048-0
15. Seki K, Hirahara M, Terasawa T, Mukai T, Saito Y, Machida S, et al. Statistical Properties and Possible Supply Mechanisms of Tailward Cold O+beams in the Lobe/mantle Regions. *J Geophys Res* (1998) 103:4477–89. doi:10.1029/97ja02137
16. Slapak R, Nilsson H, and Westerberg LG. A Statistical Study on O+ Flux in the Dayside Magnetosheath. *Ann Geophys* (2013) 31:1005–10. doi:10.5194/angeo-31-1005-2013
17. Khazanov GV, Krivorutsky EN, and Sibeck DG. Formation of the Potential Jump over the Geomagnetically Quiet Sunlit Polar Cap Region. *J Geophys Res Space Phys* (2019) 124(6):4384–401. doi:10.1029/2019ja026576
18. Kitamura N, Seki K, Nishimura Y, Terada N, Ono T, Hori T, et al. Photoelectron Flows in the Polar Wind during Geomagnetically Quiet Periods. *J Geophys Res* (2012) 117(A7):a–n. doi:10.1029/2011ja017459
19. Axford WI. The Polar Wind and the Terrestrial Helium Budget. *J Geophys Res* (1968) 73:6855–9. doi:10.1029/JA073i021p06855
20. Banks PM, and Holzer TE. The Polar Wind. *J Geophys Res* (1968) 73(21):6846–54. doi:10.1029/JA073i021p06846
21. Cladis JB, Collin HL, Lennartsson OW, Moore TE, Peterson WK, and Russell CT. Observations of Centrifugal Acceleration during Compression of Magnetosphere. *Geophys Res Lett* (2000) 27:915–8. doi:10.1029/1999GL010737
22. Comfort RH. The Magnetic Mirror Force in Plasma Fluid Models. In: TE Moore, JH Waite, TW Moorehead, and WB Hanson, editors. *Modeling Magnetospheric Plasma* (1988). p. 51–3. doi:10.1029/GM044p0051
23. Winglee RM, Chua D, Brittnacher M, Parks GK, and Lu G. Global Impact of Ionospheric Outflows on the Dynamics of the Magnetosphere and Cross-Polar Cap Potential. *J Geophys Res* (2002) 107(A9):1237. doi:10.1029/2001JA000214
24. Divin A, Khotyaintsev YV, Vaivads A, André M, Toledo-Redondo S, Markidis S, et al. Three-scale Structure of Diffusion Region in the Presence of Cold Ions. *J Geophys Res Space Phys* (2016) 121:001–12. doi:10.1002/2016JA023606
25. Toledo-Redondo S, André M, Khotyaintsev YV, Vaivads A, Walsh A, Li W, et al. Cold Ion Demagnetization Near the X-Line of Magnetic Reconnection. *Geophys Res Lett* (2016) 43(13):6759–67. doi:10.1002/2016gl069877
26. André M, Li W, Toledo-Redondo S, Khotyaintsev YV, Vaivads A, Graham DB, et al. Magnetic Reconnection and Modification of the Hall Physics Due to Cold Ions at the Magnetopause. *Geophys Res Lett* (2016) 43(13):6705–12. doi:10.1002/2016GL069665
27. Graham DB, Khotyaintsev YV, Norgren C, Vaivads A, André M, Toledo-Redondo S, et al. Lower Hybrid Waves in the Ion Diffusion and Magnetospheric Inflow Regions. *J Geophys Res Space Phys* (2017) 122:517–33. doi:10.1002/2016JA023572
28. Steinvall K, Khotyaintsev YV, Graham DB, Vaivads A, André M, and Russell CT. Large Amplitude Electrostatic Proton Plasma Frequency Waves in the Magnetospheric Separatrix and Outflow Regions during Magnetic Reconnection. *Geophys Res Lett* (2021) 48:e2020GL090286. doi:10.1029/2020GL090286
29. Dargent J, Aunai N, Lavraud B, Toledo-Redondo S, and Califano F. Simulation of Plasmaspheric Plume Impact on Dayside Magnetic Reconnection. *Geophys Res Lett* (2020) 47:e2019GL086546. doi:10.1029/2019GL086546
30. Kulikov YN, Lammer H, Lichtenegger HIM, Penz T, Breuer D, Spohn T, et al. A Comparative Study of the Influence of the Active Young Sun on the Early Atmospheres of Earth, Venus, and Mars. *Space Sci Rev* (2007) 129(1-3):207–43. doi:10.1007/s11214-007-9192-4
31. Lammer H, Zerkle AL, Gebauer S, Tosi N, Noack L, Scherf M, et al. Origin and Evolution of the Atmospheres of Early Venus, Earth and Mars. *Astron Astrophys Rev* (2018) 26(1):2. doi:10.1007/s00159-018-0108-y
32. Slapak R, Schillings A, Nilsson H, Yamauchi M, Westerberg L-G, and Dandouras I. Atmospheric Loss from the Dayside Open Polar Region and its Dependence on Geomagnetic Activity: Implications for Atmospheric Escape on Evolutionary Timescales. *Ann Geophys* (2017) 35:721–31. doi:10.5194/angeo-35-721-2017
33. Wei Y, Pu Z, Zong Q, Wan W, Ren Z, Fraenz M, et al. Oxygen Escape from the Earth during Geomagnetic Reversals: Implications to Mass Extinction. *Earth Planet Sci Lett* (2014) 394:94–8. doi:10.1016/j.epsl.2014.03.018
34. Wei Y, Fraenz M, Dubinin E, Woch J, Lühr H, Wan W, et al. Enhanced Atmospheric Oxygen Outflow on Earth and Mars Driven by a Corotating Interaction Region. *J Geophys Res* (2012) 117:a–n. doi:10.1029/2011JA017340
35. Gunell H, Maggiolo R, Nilsson H, Stenberg Wieser G, Slapak R, Lindkvist J, et al. Why an Intrinsic Magnetic Field Does Not Protect a Planet against Atmospheric Escape. *A&A* (2018) 614:L3. doi:10.1051/0004-6361/201832934
36. Gronoff G, Arras P, Baraka S, Bell JM, Cessateur G, Cohen O, et al. Atmospheric Escape Processes and Planetary Atmospheric Evolution. *J Geophys Res Space Phys* (2020) 125:e2019JA027639. doi:10.1029/2019JA027639

37. Ramstad R, and Barabash S. Do Intrinsic Magnetic Fields Protect Planetary Atmospheres from Stellar Winds?. *Space Sci Rev* (2021) 217. doi:10.1007/s11214-021-00791-1
38. Delzanno GL, Borovsky JE, Henderson MG, Resendiz Lira PA, Roytershteyn V, and Welling DT. The Impact of Cold Electrons and Cold Ions in Magnetospheric Physics. *J Atmos Solar-Terrestrial Phys* (2021) 220: 105599. doi:10.1016/j.jastp.2021.105599
39. Engwall E, Eriksson AI, and Forest J. Wake Formation behind Positively Charged Spacecraft in Flowing Tenuous Plasmas. *Phys Plasmas* (2006) 13(6): 062904. doi:10.1063/1.2199207
40. Engwall E, Eriksson AI, Cully CM, André M, Puhl-Quinn PA, Vaith H, et al. Survey of Cold Ionospheric Outflows in the Magnetotail. *Ann Geophys* (2009) 27:3185–201. doi:10.5194/angeo-27-3185-2009
41. Eriksson AI, André M, Klecker B, Laakso H, Lindqvist P-A, Mozer F, et al. Electric Field Measurements on Cluster: Comparing the Double-Probe and Electron Drift Techniques. *Ann Geophys* (2006) 24:275–89. doi:10.5194/angeo-24-275-2006
42. Svenes KR, Lybekk B, Pedersen A, and Haaland S. Cluster Observations of Near-Earth Magnetospheric Lobe Plasma Densities - a Statistical Study. *Ann Geophys* (2008) 26:2845–52. doi:10.5194/angeo-26-2845-2008
43. Grard RJL, and Jones D. An Evaluation of Experimental Errors in Electromagnetic Wave Measurements Aboard Satellites. *J Geophys Res* (1973) 78(25):5507–14. doi:10.1029/JA078i025p05507
44. Lybekk B, Pedersen A, Haaland S, Svenes K, Fazakerley AN, Masson A, et al. Solar Cycle Variations of the Cluster Spacecraft Potential and its Use for Electron Density Estimations. *J Geophys Res* (2012) 117(A1). doi:10.1029/2011ja016969
45. Trotignon JG, Décréau PME, Rauch JL, Randriamboarison O, Krasnoselskikh V, Canu P, et al. How to Determine the thermal Electron Density and the Magnetic Field Strength from the Cluster/Whisper Observations Around the Earth. *Ann Geophys* (2001) 19: 1711–20. doi:10.5194/angeo-19-1711-2001
46. Pedersen A, Lybekk B, André M, Eriksson A, Masson A, Mozer FS, et al. Electron Density Estimations Derived from Spacecraft Potential Measurements on Cluster in Tenuous Plasma Regions. *J Geophys Res* (2008) 113:a–n. doi:10.1029/2007JA012636
47. Gustafsson G, Boström R, Holback B, Holmgren G, Lundgren A, Stasiewicz K, et al. The Electric Field and Wave experiment for the Cluster mission. *Space Sci Rev* (1997) 79:137–56. doi:10.1023/A:1004975108657
48. Rème H, Aoustin C, Bosqued JM, Dandouras I, Lavraud B, Sauvaud JA, et al. First Multispacecraft Ion Measurements in and Near the Earth's Magnetosphere with Identical Cluster Ion Spectrometry (CIS) Experiments. *Ann Geophysicae* (2001) 19:1303–54. doi:10.5194/angeo-19-1303-2001
49. Johnstone AD, Alsop C, Burge S, Carter PJ, Coates AJ, Coker AJ, et al. Peace: A Plasma Electron and Current Experiment. *Space Sci Rev* (1997) 79:351–98. doi:10.1023/A:1004938001388
50. Décréau PME, Fergeau P, Fergeau P, Krannosels'Kikh V, Lévêque M, Martin P, et al. WHISPER, A Resonance Sounder and Wave Analyser: Performances and Perspectives for the Cluster Mission. *Space Sci Rev* (1997) 79:157–93. doi:10.1023/A:100493132640410.1007/978-94-011-5666-0_7
51. Haaland S, Svenes K, Lybekk B, and Pedersen A. A Survey of the Polar Cap Density Based on Cluster EFW Probe Measurements: Solar Wind and Solar Irradiation Dependence. *J Geophys Res* (2012) 117:A01216. doi:10.1029/2011JA017250
52. Haaland S, Lybekk B, Maes L, Laundal K, Pedersen A, Tenfjord P, et al. North-south Asymmetries in Cold Plasma Density in the Magnetotail Lobes: Cluster Observations. *J Geophys Res Space Phys* (2017) 122(1):136–49. doi:10.1002/2016ja023404
53. Engwall E, Eriksson AI, Cully CM, André M, Torbert R, and Vaith H. Earth's Ionospheric Outflow Dominated by Hidden Cold Plasma. *Nat Geosci* (2009) 2:24–7. doi:10.1038/ngeo387
54. Cully CM, Ergun RE, and Eriksson AI. Electrostatic Structure Around Spacecraft in Tenuous Plasmas. *J Geophys Res* (2007) 112:a–n. doi:10.1029/2007JA012269
55. Paschmann G, Quinn JM, Torbert RB, Vaith H, McIlwain CE, Haerendel G, et al. The Electron Drift Instrument on Cluster: Overview of First Results. *Ann Geophys* (2001) 19(10/12):1273–88. doi:10.5194/angeo-19-1273-2001
56. Paschmann G, Quinn JM, Torbert RB, McIlwain CE, Vaith H, Haaland S, et al. Results of the Electron Drift Instrument on Cluster. *J Geophys Res Space Phys* (2021) 126:e2021JA029313. doi:10.1029/2021JA029313
57. Hoffman JH, Dodson WH, Lippincott CR, and Hammack HD. Initial Ion Composition Results from the Isis 2 Satellite. *J Geophys Res* (1974) 79: 4246–51. doi:10.1029/JA079i028p04246
58. Shelley EG, Johnson RG, and Sharp RD. Satellite Observations of Energetic Heavy Ions during a Geomagnetic Storm. *J Geophys Res* (1972) 77:6104–10. doi:10.1029/JA077i031p06104
59. Yau AW, Peterson WK, and Abe T. Measurements of Ion Outflows from the Earth's Ionosphere. In: CR Chappell, RW Schunk, PM Banks, JL Burch, and RM Thorne, editors. 1st ed.. John Wiley & Sons (2017). p. 19–31. doi:10.1002/9781119066880.ch2*Geophys Monogr*
60. Yau AW, Abe T, and Peterson WK. The Polar Wind: Recent Observations. *J Atmos Solar-Terrestrial Phys* (2007) 69(16):1936–83. doi:10.1016/j.jastp.2007.08.010
61. Peterson WK, Andersson L, Callahan BC, Collin HL, Scudder JD, and Yau AW. Solar-minimum Quiet Time Ion Energization and Outflow in Dynamic Boundary Related Coordinates. *J Geophys Res* (2008) 113:a–n. doi:10.1029/2008JA013059
62. Torkar K, Riedler W, Escoubet CP, Fehringer M, Schmidt R, Grard RJL, et al. Active Spacecraft Potential Control for Cluster - Implementation and First Results. *Ann Geophys* (2001) 19:1289–302. doi:10.5194/angeo-19-1289-2001
63. Torkar K, Nakamura R, Tajmar M, Scharlemann C, Jeszenszky H, Laky G, et al. Active Spacecraft Potential Control Investigation. *Space Sci Rev* (2016) 199(1-4):515–44. doi:10.1007/s11214-014-0049-3
64. Su Y-J, Horwitz JL, Moore TE, Giles BL, Chandler MO, Craven PD, et al. Polar Wind Survey with the Thermal Ion Dynamics Experiment/Plasma Source Instrument Suite Aboard POLAR. *J Geophys Res* (1998) 103(A12): 29305–37. doi:10.1029/98JA02662
65. Peterson WK, Collin HL, Lennartsson OW, and Yau AW. Quiet Time Solar Illumination Effects on the Fluxes and Characteristic Energies of Ionospheric Outflow. *J Geophys Res* (2006) 111:A11S05. doi:10.1029/2005JA011596
66. Huddleston MM, Chappell CR, Delcourt DC, Moore TE, Giles BL, and Chandler MO. An Examination of the Process and Magnitude of Ionospheric Plasma Supply to the Magnetosphere. *J Geophys Res* (2005) 110:A12202. doi:10.1029/2004JA010401
67. Cully CM, Donovan EF, Yau AW, and Opgenoorth HJ. Supply of thermal Ionospheric Ions to the central Plasma Sheet. *J Geophys Res* (2003) 108(A2): 1092. doi:10.1029/2002JA009457
68. Yau AW, Howarth A, Peterson WK, and Abe T. Transport of thermal-energy Ionospheric Oxygen (O+) Ions between the Ionosphere and the Plasma Sheet and Ring Current at Quiet Times Preceding Magnetic Storms. *J Geophys Res* (2012) 117:a–n. doi:10.1029/2012JA017803
69. Li K, Haaland S, Eriksson A, André M, Engwall E, Wei Y, et al. On the Ionospheric Source Region of Cold Ion Outflow. *Geophys Res Lett* (2012) 39(18). doi:10.1029/2012gl053297
70. Li K, Haaland S, Eriksson A, André M, Engwall E, Wei Y, et al. Transport of Cold Ions from the Polar Ionosphere to the Plasma Sheet. *J Geophys Res Space Phys* (2013) 118(9):5467–77. doi:10.1002/jgra.50518
71. Haaland S, Eriksson A, Engwall E, Lybekk B, Nilsson H, Pedersen A, et al. Estimating the Capture and Loss of Cold Plasma from Ionospheric Outflow. *J Geophys Res* (2012) 117:a–n. doi:10.1029/2012JA017679
72. Haaland S, Eriksson A, André M, Maes L, Baddeley L, Barakat A, et al. Estimation of Cold Plasma Outflow during Geomagnetic Storms. *J Geophys Res Space Phys* (2015) 120(12). doi:10.1002/2015ja021810
73. Li K, Wei Y, André M, Eriksson A, Haaland S, Kronberg EA, et al. Cold Ion Outflow Modulated by the Solar Wind Energy Input and Tilt of the Geomagnetic Dipole. *J Geophys Res Space Phys* (2017) 122(10):658–10. doi:10.1002/2017ja024642
74. Li K, Wei Y, Haaland S, Kronberg EA, Rong ZJ, Maes L, et al. Estimating the Kinetic Energy Budget of the Polar Wind Outflow. *J Geophys Res Space Phys* (2018) 123(9):7917–29. doi:10.1029/2018ja025819
75. Li K, Förster M, Rong Z, Haaland S, Kronberg E, Cui J, et al. The Polar Wind Modulated by the Spatial Inhomogeneity of the Strength of the Earth's Magnetic Field. *J Geophys Res Space Phys* (2020) 125(4). doi:10.1029/2020ja027802

76. Maes L, Maggiolo R, De Keyser J, André M, Eriksson AI, Haaland S, et al. Solar Illumination Control of the Polar Wind. *J Geophys Res Space Phys* (2017) 122(11):11468–411480. doi:10.1002/2017ja024615
77. Northrop TG. *The Adiabatic Motion of Charged Particles*. New York: Interscience Publishers (1963).
78. Milan SE. Both solar Wind-Magnetosphere Coupling and Ring Current Intensity Control of the Size of the Auroral Oval. *Geophys Res Lett* (2009) 36(18). doi:10.1029/2009gl039997
79. Nilsson H, Waara M, Marghitu O, Yamauchi M, Lundin R, Rème H, et al. An Assessment of the Role of the Centrifugal Acceleration Mechanism in High Altitude Polar Cap Oxygen Ion Outflow. *Ann Geophys* (2008) 26:145–57. doi:10.5194/angeo-26-145-2008
80. Kistler LM. Ionospheric and Solar Wind Contributions to the Storm-Time Near-Earth Plasma Sheet. *Geophys Res Lett* (2020) 47:e2020GL090235. doi:10.1029/2020GL090235
81. Nilsson H, Engwall E, Eriksson A, Puhl-Quinn PA, and Arvelius S. Centrifugal Acceleration in the Magnetotail Lobes. *Ann Geophys* (2010) 28:569–76. doi:10.5194/angeo-28-569-2010
82. Nilsson H, Barghouthi IA, Slapak R, Eriksson AI, and André M. Hot and Cold Ion Outflow: Observations and Implications for Numerical Models. *J Geophys Res Space Phys* (2013) 118(1):105–17. doi:10.1029/2012ja017975
83. Pham KH, Lotko W, Varney RH, Zhang B, and Liu J. Thermospheric Impact on the Magnetosphere through Ionospheric Outflow. *J Geophys Res Space Phys* (2021) 126:e2020JA028656. doi:10.1029/2020JA028656
84. Weimer DR. Models of High-Latitude Electric Potentials Derived with a Least Error Fit of Spherical Harmonic Coefficients. *J Geophys Res* (1995) 100(A10): 19595–607. doi:10.1029/95JA01755
85. Haaland SE, Paschmann G, Förster M, Quinn JM, Torbert RB, McIlwain CE, et al. High-latitude Plasma Convection from Cluster EDI Measurements: Method and IMF-Dependence. *Ann Geophys* (2007) 25:239–53. doi:10.5194/angeo-25-239-2007
86. Glassmeier K-H, and Vogt J. Magnetic Polarity Transitions and Biospheric Effects. *Space Sci Rev* (2010) 155:387–410. doi:10.1007/s11214-010-9659-6
87. Cnossen I, and Richmond AD. How Changes in the Tilt Angle of the Geomagnetic Dipole Affect the Coupled Magnetosphere-Ionosphere-Thermosphere System. *J Geophys Res* (2012) 117:a–n. doi:10.1029/2012ja018056
88. Reshetnyak MY, and Pavlov VE. Evolution of the Dipole Geomagnetic Field. Observations and Models. *Geomagn Aeron* (2016) 56:110–24. doi:10.1134/S0016793215060122
89. Glocer A, Kitamura N, Toth G, and Gombosi T. Modeling Solar Zenith Angle Effects on the Polar Wind. *J Geophys Res* (2012) 117:a–n. doi:10.1029/2011ja017136
90. Kitamura N, Ogawa Y, Nishimura Y, Terada N, Ono T, Shinbori A, et al. Solar Zenith Angle Dependence of Plasma Density and Temperature in the Polar Cap Ionosphere and Low-Altitude Magnetosphere during Geomagnetically Quiet Periods at Solar Maximum. *J Geophys Res* (2011) 116(A8):a–n. doi:10.1029/2011ja016631
91. Perreault P, and Akasofu S-I. A Study of Geomagnetic Storms. *Geophys J Int* (1978) 54(3):547–73. doi:10.1111/j.1365-246X.1978.tb05494.x
92. Juárez MT, Tauxe L, Gee JS, and Pick T. The Intensity of the Earth's Magnetic Field over the Past 160 Million Years. *Nature* (1998) 394:878–81. doi:10.1038/29746
93. Cole KD. Airglow and the South Atlantic Geomagnetic Anomaly. *J Geophys Res* (1961) 66(9):3064. doi:10.1029/JZ066i009p03064
94. Finlay CC, Kloss C, Olsen N, Hammer MD, Tøffner-Clausen L, Grayver A, et al. The CHAOS-7 Geomagnetic Field Model and Observed Changes in the South Atlantic Anomaly. *Earth Planets Space* (2020) 72:156. doi:10.1186/s40623-020-01252-9
95. Abdu MA, Batista IS, Carrasco AJ, and Brum CGM. South atlantic Magnetic Anomaly Ionization: A Review and a New Focus on Electrodynamic Effects in the Equatorial Ionosphere. *J Atmos Solar-Terrestrial Phys* (2005) 67(17-18): 1643–57. doi:10.1016/j.jastp.2005.01.014
96. Koch S, and Kuvshinov A. Does the South Atlantic Anomaly Influence the Ionospheric Sq Current System? Inferences from Analysis of Ground-Based Magnetic Data. *Earth, Planets and Space* (2015) 67:10. doi:10.1186/s40623-014-0172-0
97. Laundal KM, Cnossen I, Milan SE, Haaland SE, Coxon J, Pedatella NM, et al. North-south Asymmetries in Earth's Magnetic Field. *Space Sci Rev* (2017) 206:225–57. doi:10.1007/s11214-016-0273-0
98. Kopp G, and Lean JL. A New, Lower Value of Total Solar Irradiance: Evidence and Climate Significance. *Geophys Res Lett* (2011) 38:a–n. doi:10.1029/2010GL045777
99. Jakosky BM, Slipski M, Benna M, Mahaffy P, Elrod M, Yelle R, et al. Mars' Atmospheric History Derived from Upper-Atmosphere Measurements of38Ar/36Ar. *Science* (2017) 355(6332):1408–10. doi:10.1126/science.aai7721
100. Fränz M, Dubinin E, Nielsen E, Woch J, Barabash S, Lundin R, et al. Transterminator Ion Flow in the Martian Ionosphere. *Planet Space Sci* (2010) 58(11):1442–54. doi:10.1016/j.pss.2010.06.009
101. Persson M, Futaana Y, Ramstad R, Schillings A, Masunaga K, Nilsson H, et al. Global Venus-Solar Wind Coupling and Oxygen Ion Escape. *Geophys Res Lett* (2021) 48(3). doi:10.1029/2020gl091213
102. Tsyganenko NA. Modeling the Dynamics of the Inner Magnetosphere during strong Geomagnetic Storms. *J Geophys Res* (2005) 110(A3). doi:10.1029/2004ja010798
103. Li K, Haaland S, and Wei Y. A New Concept to Measure the Ambipolar Electric Field Driving Ionospheric Outflow. *J Geophys Res Space Phys* (2021) 126(2). doi:10.1029/2020ja028409
104. Moore TE, Fok M-C, and Garcia-Sage K. The Ionospheric Outflow Feedback Loop. *J Atmos Solar-Terrestrial Phys* (2014) 115-116:59–66. doi:10.1016/j.jastp.2014.02.002
105. Seki K, Elphic RC, Hirahara M, Terasawa T, and Mukai T. On Atmospheric Loss of Oxygen Ions from Earth through Magnetospheric Processes. *Science* (2001) 291(5510):1939–41. doi:10.1126/science.1058913
106. André M., and Cully C. M. (2012). Low-Energy ions: A Previously Hidden Solar System Particle Population. *Geophys Res Lett* 39:L03101. doi:10.1029/2011GL050242
107. Welling D. T., André M., Dandouras I., Delcourt D., Fazakerley A., Fontaine D., et al. (2015) The Earth: Plasma Sources, Losses, and Transport Process *Space Sci Rev* 192:145–208. doi:10.1007/s11214-015-0187-2
108. Vernov S. N., Gorchakov E. V., Shavin P. I., and Sharvina K. N.Radiation Belts in the Region of the South-Atlantic Magnetic Anomaly. *Space Sci Rev* (1967) 7:490–533. doi:10.1007/BF00182684
109. Jacobs J. A.Variations in the Intensity of the Earth's Magnetic Field. *Surveys Geophys* (1998) 19:139–187. doi:10.1023/A:1006579708430
110. Newell P. T., Liou K., and Wilson G. R.Polar Cap Particle Precipitation and Aurora: Review and Commentary. *J Atmos Solar-Terr Phys* (2009) 71: 199–215. doi:10.1016/j.jastp.2008.11.004

Conflict of Interest: The authors declare that the research was conducted in the absence of any commercial or financial relationships that could be construed as a potential conflict of interest.

frontiers in Astronomy and Space Sciences

REVIEW
published: 21 October 2021
doi: 10.3389/fspas.2021.746283

The Key Role of Cold Ionospheric Ions As a Source of Hot Magnetospheric Plasma and As a Driver of the Dynamics of Substorms and Storms

C. R. Chappell[1]*, *A. Glocer*[2], *B. L. Giles*[2], *T. E. Moore*[3], *M. M. Huddleston*[4] and *D. L. Gallagher*[5]

[1]Department of Physics and Astronomy, Vanderbilt University, Nashville, TN, United States, [2]NASA/Goddard Space Flight Center, Greenbelt, MD, United States, [3]NASA/Goddard Space Flight Center (Emeritus), Greenbelt, MD, United States, [4]Department of Physics, Trevecca University, Nashville, TN, United States, [5]NASA/Marshall Space Flight Center, Huntsville, AL, United States

OPEN ACCESS

Edited by:
Joseph Eric Borovsky,
Space Science Institute, United States

Reviewed by:
Binbin Ni,
Wuhan University, China
Scott Alan Thaller,
University of Colorado Boulder, United States
John Lyon,
Dartmouth College, United States

***Correspondence:**
C. R. Chappell
rick.chappell@vanderbilt.edu

Specialty section:
This article was submitted to Space Physics, a section of the journal Frontiers in Astronomy and Space Sciences

Received: 23 July 2021
Accepted: 28 September 2021
Published: 21 October 2021

Citation:
Chappell CR, Glocer A, Giles BL, Moore TE, Huddleston MM and Gallagher DL (2021) The Key Role of Cold Ionospheric Ions As a Source of Hot Magnetospheric Plasma and As a Driver of the Dynamics of Substorms and Storms. Front. Astron. Space Sci. 8:746283. doi: 10.3389/fspas.2021.746283

The solar wind has been seen as the major source of hot magnetospheric plasma since the early 1960's. More recent theoretical and observational studies have shown that the cold (few eV) polar wind and warmer polar cusp plasma that flow continuously upward from the ionosphere can be a very significant source of ions in the magnetosphere and can become accelerated to the energies characteristic of the plasma sheet, ring current, and warm plasma cloak. Previous studies have also shown the presence of solar wind ions in these magnetospheric regions. These studies are based principally on proxy measurements of the ratios of He^{++}/H^{+} and the high charge states of O^{+}/H^{+}. The resultant admixture of ionospheric ions and solar wind ions that results has been difficult to quantify, since the dominant H^{+} ions originating in the ionosphere and solar wind are indistinguishable. The ionospheric ions are already inside the magnetosphere and are filling it from the inside out with direct access from the ionosphere to the center of the magnetotail. The solar wind ions on the other hand must gain access through the outer boundaries of the magnetosphere, filling the magnetosphere from the outside in. These solar wind particles must then diffuse or drift from the flanks of the magnetosphere to the near-midnight reconnection region of the tail which takes more time to reach (hours) than the continuously large outflowing ionospheric polar wind (10's of min). In this paper we examine the magnetospheric filling using the trajectories of the different ion sources to unravel the intermixing process rather than trying to interpret only the proxy ratios. We compare the timing of the access of the ionospheric and solar wind sources and we use new merged ionosphere-magnetosphere multi-fluid MHD modeling to separate and compare the ionospheric and solar wind H^{+} source strengths. The rapid access of the initially cold polar wind and warm polar cusp ions flowing down-tail in the lobes into the mid-plane of the magnetotail, suggests that, coupled with a southward turning of the IMF Bz, these ions can play a key triggering role in the onset of substorms and subsequent large storms.

Keywords: ionospheric source, magnetospheric plasma, magnetospheric dynamics, magnetospheric substorms and storms, cold ionospheric ions becoming energized in the magnetosphere

INTRODUCTION

In this paper we will review how the Earth's ionosphere populates the different regions of more energetic particles in the magnetosphere and combined with the changing solar wind Bz can drive the dynamics of the magnetosphere. We will begin with a review of the ionospheric role as a source and end with a focus on more recent results which continue to build the case for the ionosphere's role as a driver of magnetospheric processes.

The magnetospheric community has always thought about the ionosphere as playing a very important role in storms and substorms as a recipient of energy from the magnetosphere and setting up the current systems that are an integral part of storm dynamics. In this paper we will look differently at that understanding and ask the question, not just how does the ionosphere respond to magnetospheric storms, but how does the ionosphere participate as a driver that causes magnetospheric substorms and storms to happen.

In terms of specific objectives of this paper we will talk about the influence of the ionospheric plasma throughout the magnetosphere, that is in regions like the plasmasphere, plasma trough, polar cap, magnetotail lobes, plasma sheet, warm plasma cloak, ring current, and radiation belts—all of the major areas in which the ionosphere is playing a role.

Initially, we want to show how the ionospheric plasma that has energies of only a few eV can become energized in the magnetosphere to the energies of the different regions in which it ends up and can actually create these regions. We want to look at individual ion trajectories that show how the cold ions are energized in the different regions into which they move. Then in combination with the solar wind Bz, we show how the ionospheric particles can become a major driving mechanism for substorms and storms.

It is also important to call attention to the role of ionospheric plasma in magnetic reconnection and the continuing challenge of measuring low energy plasma. Both the dayside solar wind-magnetosphere and nightside magnetotail reconnection regions become populated with ionospheric plasma. The ionospheric ions, both from the duskside plumes and detached regions that come off the plasmasphere and the warm plasma cloak bring particles to the nose of the magnetosphere and affect the reconnection process there (Fuselier et al., 2019), while high latitude outflow of the polar wind and polar cusp affects magnetotail reconnection (Toledo-Redondo et al., 2021). These initially polar wind ions are very difficult to measure in the lobes because of their low energies and densities and the effects of positive spacecraft potential, which means that they are often unseen. Most of our early measurements of the magnetosphere had no observations of any particles in the lobes of the tail. In addition, the ambient low energy electrons were almost impossible to measure amidst the spacecraft charging and the photoelectrons that are created by the action of the sunlight on the different materials on the spacecraft surfaces.

HISTORICAL OVERVIEW

Figure 1 is a decades old sketch of the magnetosphere that was originally created to show the solar wind entry (pink regions at the sunward boundary) into the magnetosphere and formation of the distinctive regions of the magnetosphere. This figure originally was missing two very important things. We did not know about the polar wind at that time, the very low-energy few eV outflowing H^+ and He^+ ions, and we could not tell the difference between H^+ ions that came from the solar wind and H^+ ions that came from the ionosphere. To the measurements that we are able to make, these two sources of H^+ look exactly the same. To distinguish between the two, we will have to model that difference with multi-fluid merged ionosphere/magnetosphere MHD models which will be discussed later in this paper.

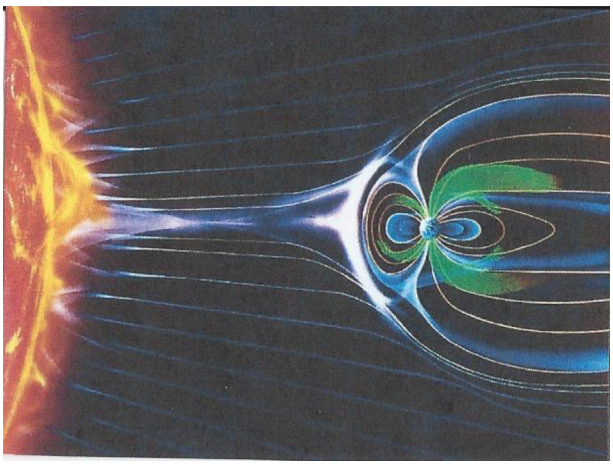

FIGURE 1 | A sketch of the solar-terrestrial connection that includes the contribution of the Earth's ionosphere to the magnetosphere.

Those two things, the inability to see the outflowing polar wind, which had not been even theoretically predicted until 1968 (Banks and Holzer, 1968, Banks et al., 1971) and the inability to tell the difference between solar wind and ionospheric H^+, gave us the misimpression that all of the magnetospheric plasmas with the exception of the plasmasphere (the blue region close to the Earth in **Figure 1**) came from the solar wind. After the theory and measurements of the 1970's, 80's, and 90's (Hoffman, 1970; Nagai et al., 1984; Chandler et al., 1991; Abe et al., 1996; Moore et al., 1997; Yau and Andre, 1997), the green outflowing ions were added to this conceptual image of the magnetosphere.

Our early measurements in the late 50's and early 60's also led us to the same inaccurate "solar wind only" conclusion because early on in space missions, we could only measure the very high energy particles but not the low energy ones. Geiger counters were flown on the early explorer satellites and measured the radiation belts (MeV). Then with the development of channel electron multipliers, experimenters were able to measure ion and electron energies down to ~100 eV in particle detectors and we started seeing the plasma sheet and the ring current. Some of the early spaceborne ion traps and ground-based whistler observations could measure the higher densities (>10 ions/cm^3) of the plasmasphere down to a few eV (Carpenter, 1963; Gringauz, 1963), but the spacecraft, particularly those which went farther out into the magnetosphere that had no spacecraft

potential control, could not see the low energy particles with energies less than 10's of eV.

This combination of factors led researchers to think that the solar wind was delivering most of the particle populations to the magnetosphere, a conclusion which is now being challenged by more recent data. Research at the Lockheed Palo Alto Research Laboratory in the early 1970's using the Light Ion Mass Spectrometer on the OGO-5 satellite (Harris and Sharp, 1969) gave new information on the low energy, few eV ions in the magnetosphere with a particular emphasis on the dynamics of the plasmasphere. The filling and draining of the plasmasphere and its changes in size and shape were intriguing (Chappell et al., 1970; Chappell, 1972). It was realized that measurements of the low-energy (0–50 eV) ions were needed using instruments that had higher sensitivities and a spinning spacecraft so that pitch angle distributions as well as composition and energy could be determined. These measurements would give an understanding of how the ions were moving and, in particular, how they were flowing upward out of the ionosphere to fill the plasmasphere. In this same time period, satellite measurements had shown the presence of energetic O^+ at high altitudes indicating both an ionospheric source and the ability to energize the originally cold ionospheric ions (Shelley et al., 1972).

NASA created the Dynamics Explorer mission and a new group, now at the NASA/Marshall Space Flight Center proposed an instrument, the Retarding Ion Mass Spectrometer, for the mission and was selected (Chappell et al., 1981). Dynamics Explorer was a two polar, co-planar spacecraft mission, one in a low Earth orbit to measure the atmosphere and ionosphere and one with a 4 Re apogee that could see the outflowing ions as they left the ionosphere and entered the magnetosphere. The RIMS instrument was on the higher altitude spacecraft. It was an interesting time in which the members of the science working group for the mission were trying to decide when in the orbit the different instruments would be operated because there wasn't enough telemetry to run all of them all the time. This led to spirited discussions between the RIMS group, whose interest was to measure at lower to middle latitudes so that the plasmasphere could be studied, and the investigators who wanted to measure the polar cap region to study the aurora.

The investigator group compromise led to RIMS low energy ion measurements in both the low latitudes and the high latitude polar regions. That turned out to be an important decision, because what was observed, when the Dynamics Explorer 1 spacecraft was up over the polar regions, was that there were very large fluxes of ion outflow. It came from the polar wind (Nagai et al., 1984), the polar cusp (Gurgiolo and Burch, 1982), the nightside auroral zone (Yau et al., 1985) and was all seen at high latitudes; this changed our perspective significantly

At this time in the mid-80's it was realized that there was a lot of ion outflow that was seen from RIMS (Lockwood et al., 1985; Giles et al., 1994) and also from the Lockheed instrument at higher energies, the Energetic Ion Composition Spectrometer, (Shelley et al., 1982; Yau et al., 1985) and a mass spectrometer on the Akebono spacecraft (Yau and Andre, 1997). These large amounts of ions were flowing upward out of the polar cap, the polar cusp and nightside auroral regions. This led to the thought about whether there was enough outflow so that if one estimated where the ions could go back in the magnetotail, it would give the observed densities in these higher altitude regions of the magnetosphere that had already been measured at higher energy (See **Figure 2**). This was confirmed; there was enough ion outflow from the polar regions that could move up through the lobes of the tail to the mid-plane to make the plasma sheet and the ring current, although back then the low energy lobe ions were invisible to spacecraft flying in the lobes because of the positive spacecraft potentials.

Although the low energy outflow could not be seen in the lobes, it could be seen by the RIMS instrument down at a few Re altitude (Nagai et al., 1984). RIMS also had an aperture plane around the entrance to the instrument that could be negatively biased to help offset the positive spacecraft potential. But still, all of the spacecraft that operated at higher altitudes in the lobes measured no low energy ions. In the (Chappell et al., 1987) paper it was speculated that the low energy polar wind ions must be invisible in the lobes of the tail because of positive spacecraft potential, but the low altitude data and calculations showed that there was enough of it to create the observed densities of the plasma sheet and the ring current. The DE RIMS measurements started the thinking about the ionosphere as a source of magnetospheric particles.

Subsequent to the Chappell et al., 1987 paper, Dominique Delcourt did ion trajectory modeling (Delcourt et al., 1993) which showed that not only did the outflowing ionospheric ions flow through the lobes into the mid-plane of the magnetospheric tail with enough flux to create the densities that had been measured in the plasma sheet and ring current, but that in addition, these initiatively low energy polar wind and polar cusp outflowing ions would become energized in their trajectories to create the energies that are found in these regions of the tail—enough density and enough energy!

A Changing Perspective

Given that low energy ions can move up out of the ionosphere, across the polar cap into the lobes of the tail and then into the mid-plane of the tail, it is important to think about the magnetosphere in a different way. We tend to think about it in terms of the distinctive plasma populations observed in differing regions with distinguishing energies and behaviors. We think about the lobes, the plasma sheet, the ring current, the warm plasma cloak, the plasmasphere, and the radiation belts. Our thinking about regions of plasma tends to conceptualize the magnetosphere as a superposition of these regions, but there is a growing realization that they are an interconnected continuum, a tapestry, of plasma transport and physical processes. The pictures (regions) on tapestries are made by a series of threads of different colors that are woven into this tapestry to create the images that you see.

As in the tapestry's threads, the observed regions of the magnetospheric system are created by the motion of ions and electrons flowing through the magnetosphere, while being energized by the cross-tail potential, parallel potentials, wave-particle interactions and reconnection. A single ion can start in the ionosphere as a polar wind ion with an energy of few eV and

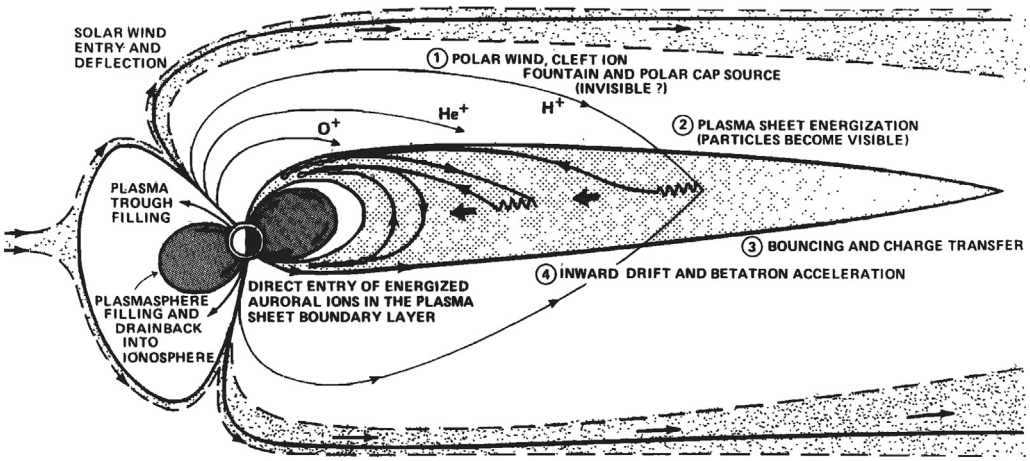

FIGURE 2 | A schematic look at the process by which the Earth's ionosphere might supply plasma to the different regions of the magnetosphere (Chappell et al., 1987).

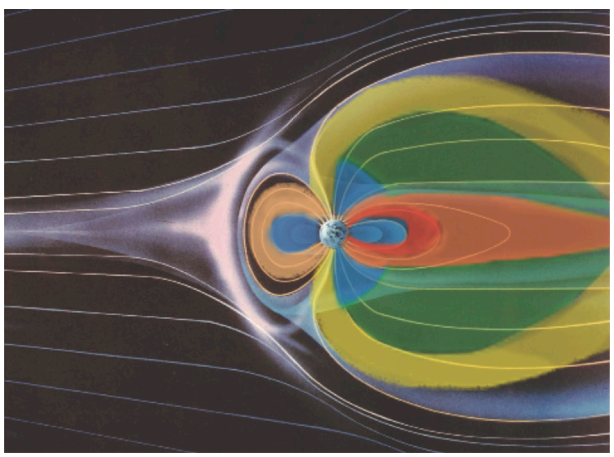

FIGURE 3 | A schematic look at the flow of ionospheric plasma from the Earth upward into the magnetosphere to form the different regions of hot plasma.

flow into the polar cap, where it can pick up additional energy and then move into the lobes, making 10–100 eV ions. (**Figure 3**).

After it has been a 1 eV and then tens of eV in the polar cap and lobe it can convect into the plasma sheet, by a process that will be discussed later, and can be energized by curvature drift in the cross-tail potential and reconnection to the keV energies that are observed in the plasma sheet. As it drifts back earthward, it can be energized further by the cross-tail potential and betatron acceleration to make the ring current energies (10's of KeV) in the midnight to dusk sector, which we observe (Huddleston et al., 2005). Some of the outflow that enters the tail closer to the Earth and on the dawnside of the magnetosphere acquires less energy and makes the warm plasma cloak in the midnight to noon dawnside sector (Chappell et al., 2008).

This is the tapestry and the challenge will be to try to measure the motion of all the ions and electrons which create it. Their presence contributes substantially to the environment of the plasma sheet in which reconnection subsequently takes place. It is important, but it is difficult to understand the magnetosphere just from the point of view of moments and composition ratios. Those are valuable; the ratio of H^+ to He^{++} is valuable as a rough indicator of the solar wind source, just as H^+, He^+ and O^+ are indicators of the ionospheric source, but they can be difficult to explain without knowing their trajectory time history.

A corollary perspective emphasized by the tapestry concept and that should be mentioned is that while the level of magnetic activity is an important indicator of what's going on in the magnetosphere. But the magnetosphere, this magnetic activity from the currents in the ionosphere and the ring current are more a result of what the solar wind and magnetosphere have done than a cause, although we correlate with these indices because they tell us that the magnetosphere is in different states of dynamic change. It is important to keep in mind that these magnetic indices show the results of the magnetospheric dynamics that began earlier in time and are not the cause!

As we think about the role of the ionospheric source in the magnetosphere, there are two types of particles that flow out of the ionosphere and we have named them after the people who largely discovered them. One group is called Strangeway particles. Strangeway particles are based on the papers that Bob Strangeway has written using FAST data (Strangeway et al., 2005). These are particles that require energy input, such as precipitating particles and waves from the magnetosphere, in order to heat the ions and electrons enough that they can escape the gravitational confinement and flow upward out of the ionosphere. That happens typically in the polar cusp and the nightside auroral zone and they can escape into the magnetosphere. These particles do certainly vary with the solar wind conditions and particularly the Bz component of the solar wind interplanetary magnetic field.

The other particles are Banks and Holzer particles that are named after Peter Banks and Tom Holzer whose theoretical work together with Ian Axford (Banks and Holzer, 1968) showed that the top of the ionosphere should be sending off a flow of plasma,

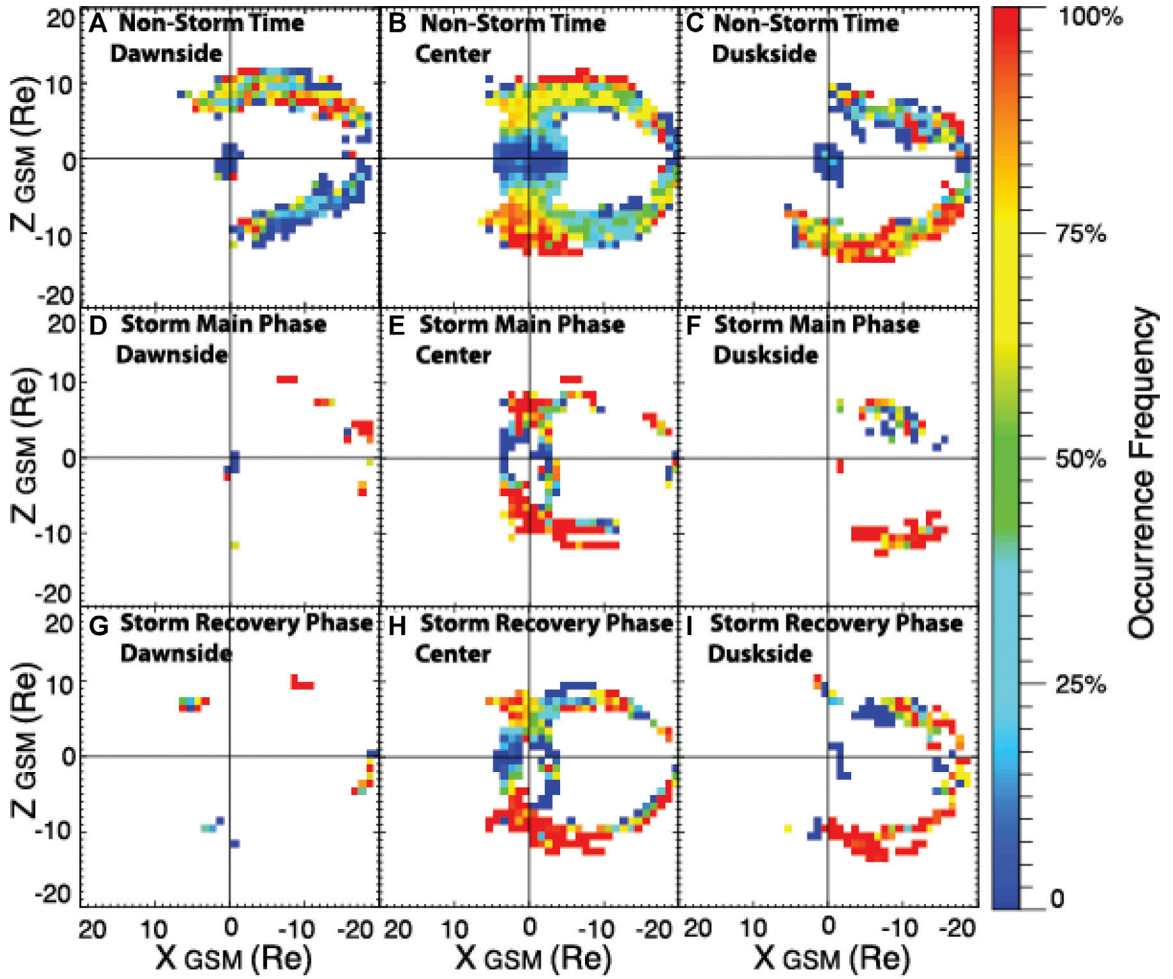

FIGURE 4 | Observations from the Cluster satellite of outflowing O^+ ions from the polar cusp seen in the lobes of the magnetotail.

referred to as the polar wind, all the time, even with no external energy input, beyond that provided by the sunlight, which creates the F- region of the ionosphere. On the topside of the F-region, there is a charge separation electric field that forms between the dominant O^+ ions and the electrons, that can accelerate the minor ions off the top of the ionosphere, H^+ and He^+ principally. These supersonic light ions can fill up the plasmasphere at low to mid-latitudes, and at higher latitudes, can flow across the polar cap and out into the lobes.

The polar wind ions can be further energized as they flow through the polar cusp, across the polar cap and auroral zones by both waves and precipitating particles as well as centrifugal acceleration becoming a more "generalized" polar wind (Schunk and Sojka, 1997; Barakat and Schunk, 2006). At lower L shells, the upward polar wind fills up the plasmasphere, and at L-shells above, approximately eight on the dayside, the polar wind will flow poleward through the polar cusp and the convection field will carry it across the polar cap and out into the lobes of the magnetotail.

Of these two types of particles, the Strangeway particles which require energy input from above to escape the ionosphere, such as precipitating particle energy and wave energy, can also be accelerated to higher even higher energies. The Banks and Holzer polar wind, which flows off the top of the ionosphere all the time, from any location in which the ionosphere is in the Sun, gives very large upward fluxes and requires no extra energy from external sources. The Banks and Holzer polar wind flux of 90% H^+ and 10% He^+ which is of the order of 3×10^8 ions/cm^2 sec or 10^{25}–10^{26} ions/sec flowing out of the ionosphere into the lobes and into the magnetosphere, is a substantial contributor of ions and electrons (Andre and Yau, 1997). The Strangeway particles are also substantial contributors, mostly O^+, H^+, He^+, with fluxes as high as 10^9 ions/cm^{2}sec, but from the auroral oval dominantly. Their total upward flux is more limited because the total ionospheric area from which they flow out is more limited than the large area of sunlit ionosphere from which the polar wind originates.

Figure 4 shows measurements of Strangeway particles in the lobe of the tail. These measurements are from Liao et al. (2010) using mass spectrometer data from the Cluster spacecraft. This is outflowing O^+ (Liao et al., 2010; Mouikis et al., 2010; Kistler et al.,

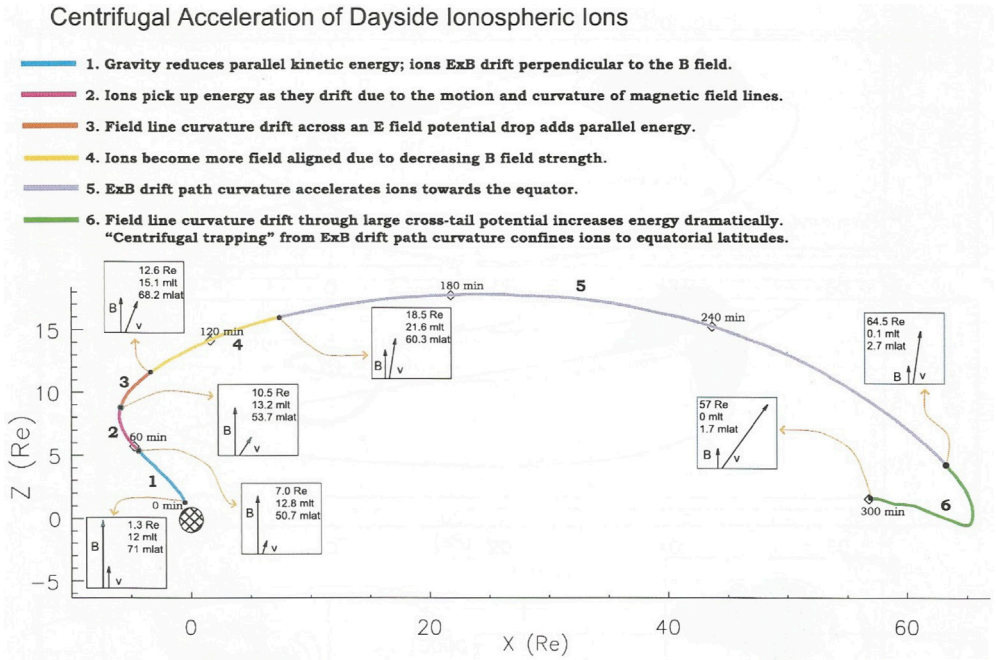

FIGURE 5 | The trajectory of a polar wind ion moving from the dayside ionosphere out through the polar cap and tail lobes to the plasma sheet and its energization.

2010). The Sun is off to the left in each one of these pictures. This is basically when the Cluster spacecraft was in the lobes out to about 20 Re, sampling ions that were coming out of the polar cusp. The three vertical panels show the dawn-side, center and dusk-side of the tail, and then non-storm time, storm main phase and recovery in the three rows. The colors on the right show the occurrence frequency. One can see that red is 100%, yellow 75%, down to blue around 25% or less. In the center of the tail, there is a very high probability of seeing cusp outflowing particles in the lobes of the tail. Those are the Strangeway particles and they can come out of the night side auroral zone as well. The nightside auroral zone would typically feed upflowing particles directly into the earthward part of the plasma sheet or the conjugate hemisphere rather than through the lobes as is the case with the upflowing ions from the polar cusp.

Some of those outflowing particles can go through regions like the polar cusp or the night side auroral zone where they get further energized. There is also a basic process that energizes the polar wind continuously (**Figure 5**). This is an ion trajectory that is from Huddleston et al., 2005 using the modeling developed by Delcourt et al., 1993, and Delcourt et al., 1994, and looking at Polar satellite data from the Thermal Ion Dynamics Experiment, TIDE (Moore et al., 1995) and modeling the ion trajectories. Work on this topic was also done by Horwitz, 1994, and John Cladis (1986, 2000). The figure shows an ion leaving the ionosphere with the Sun to the left.

On the dayside, the upflowing particle is the polar wind moving upward at a few eV. It follows the magnetic field lines, and as it moves up into the magnetosphere, it goes through an area where the field line is curved. When it's curved, it causes a curvature drift on the particle which in this case is out of the page. That drift moves the particle across the cross-tail potential and energizes it. Few eV ions can become 10 eV, and then they flow out through the lobes.

A river of ions continuously flows outward through the magnetospheric lobes as shown by the trajectory. Along the ion trajectory are times; 2 hours, out to about 6 hours by the time it gets to the plasma sheet in the mid-plane of the tail at 60 Re. When it is in the lobes; it is very low energy, 10s of eV, until it reaches the mid-plane of the magnetotail. At that point there can be very distended or stretched magnetic field lines and this creates a very large curvature drift again, out of the page of the figure, and the ion drifts in the direction of the cross-tail potential and gets further energized to keV.

This process will be examined in more detail later in the paper. This figure shows that a few eV polar wind particle can become more energized in the lobe and then further substantially energized as it moves into the mid-plane region. This illustrates that prior to missions like Polar which had high sensitivity low energy ion instruments and spacecraft potential control, we could not see what was happening in the lobes and our ideas about how the magnetosphere fills were shaped without this information. The fact that there was H^+ in the solar wind and H^+ in the plasma sheet with about the same energies, made it seem natural that the solar wind was the source of the plasma sheet. As it turned out there are large fluxes of low energy plasma continuously flowing through the lobes into the plasma sheet region, as subsequent missions would clearly show (Liemohn et al., 2005).

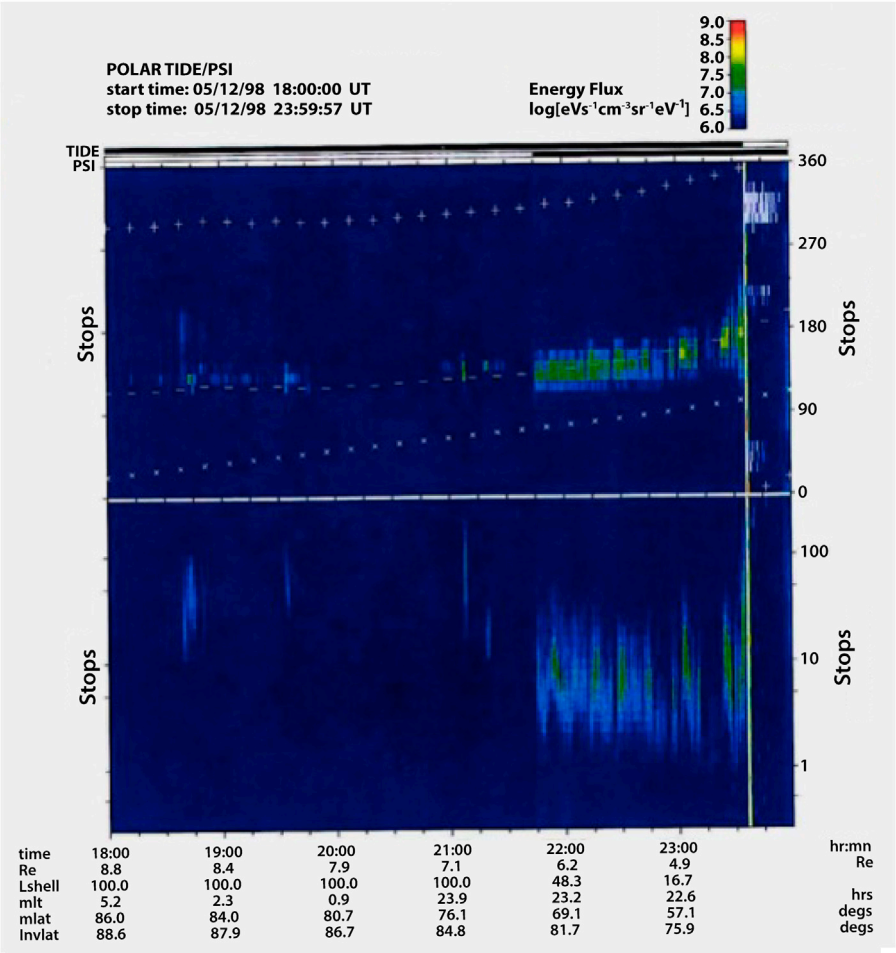

FIGURE 6 | A segment of data on the polar wind measured by the TIDE instrument on Polar taken in the lobe of the magnetotail showing the important effect of the plasma neutralizing device.

The Ion Source in the Magnetosphere is Revealed

Figure 6 shows a segment of one orbit of measurements from the POLAR spacecraft TIDE instrument, looking at the low energy ions. The lower panel shows an energy-time spectrogram for 1–400 eV, ions and the upper panel is a spin angle-time spectrogram showing the two magnetic field directions (+ and–symbols) and the ram velocity direction. (x symbol). Knowing that the polar wind ions could not be seen in the lobes unless the spacecraft potential could be controlled, the TIDE investigator group added a plasma source instrument, which sends out an ion-electron xenon plasma so that the spacecraft could draw back the charge that it needed to hold itself at the plasma potential of about one volt (Moore et al., 1995). The photoelectrons leaving the surface of the spacecraft typically charge it positively, so a cloud of electrons and ions can be ejected from the spacecraft enabling the spacecraft to draw back the electrons it needs to neutralize the positive charge.

The solid lines across the top of **Figure 6** show when the TIDE instrument (top line) and the PSI spacecraft potential device (second line down) are operating. At the beginning of this panel, the PSI is turned off and we see no ions at low energies in the lower panel. At 2145 UT, the PSI neutralizer is turned on and the low energy polar wind ions appear in the lower panel which is an energy-time spectrogram. The polar wind is seen flowing along that magnetic field line out of the northern hemisphere. We're looking at polar wind energies here now of 1–10 eV, whereas before the neutralizer turned on, there was nothing to see except a few particles that were up in the 100 eV range. The polar wind is out in the lobes which contain outflowing polar wind as long as the ionosphere location that feeds that flux tube was in the sunlight. This is a very important result! The TIDE instrument on Polar was able to measure the outflowing polar wind at altitudes from just above the ionosphere to its apogee at 9 R_E and give the characteristics of the outflowing polar wind (Su et al., 1998). Using these polar wind outflow measurements, the strength of the ionospheric source was also measured, Chappell et al., 2000.

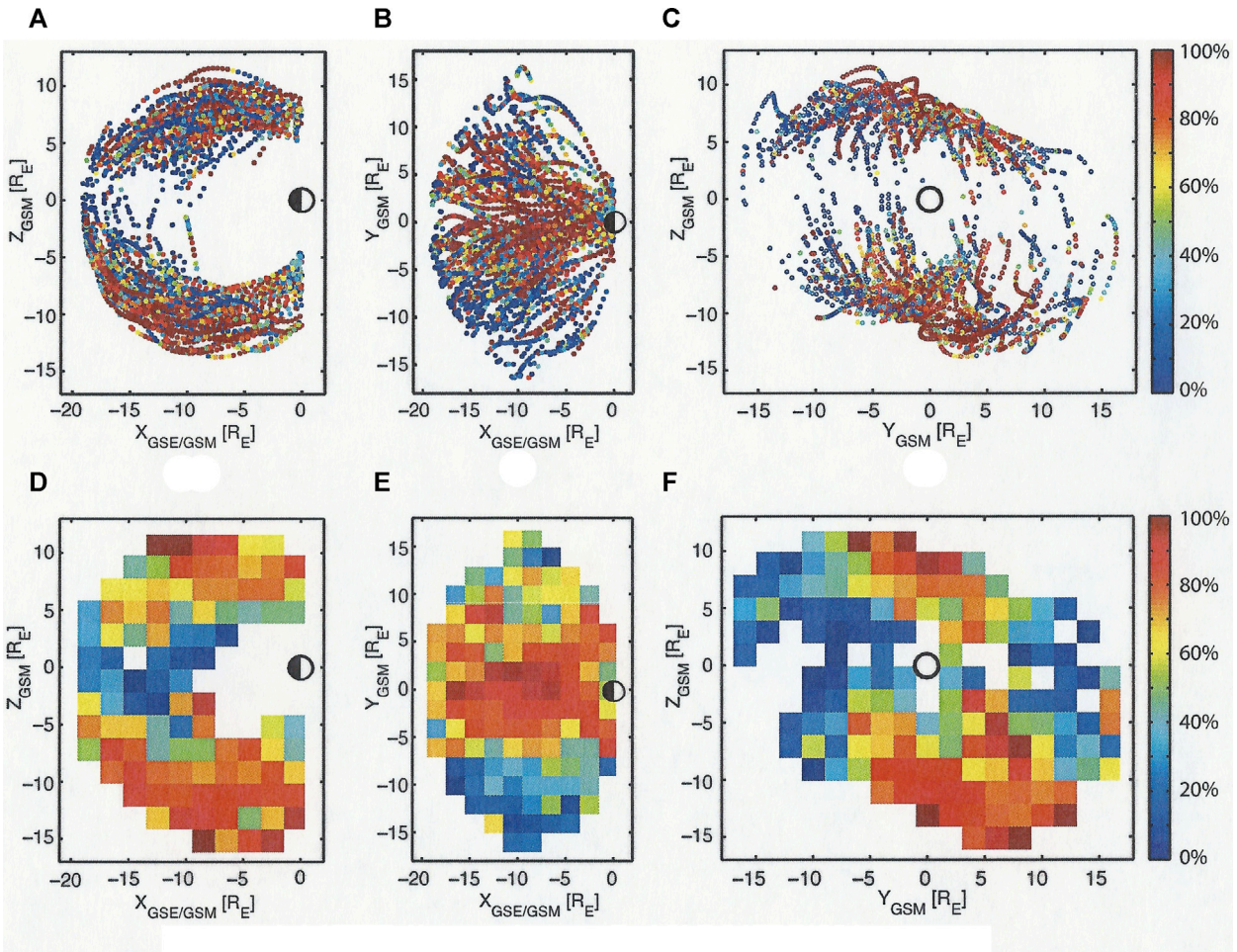

FIGURE 7 | Measurements of the polar wind in the lobes of the magnetotail using the spacecraft wake from a group of plasma and field instruments on Cluster.

On the Cluster mission there was an ion emitter device to help control spacecraft potential. There was also a very clever complement of instruments that could measure the wake direction of the plasma that was flowing past the spacecraft when the satellite was in the lobe (Engwall et al., 2006; 2009a; 2009b). The investigators could measure the characteristics of the wake, the direction that the ions were flowing, and what their energies and fluxes were. They found out that the lobe contained polar wind ions and electrons (Banks and Holzer particles) as shown in **Figure 7** in addition to the polar cusp particles (Strangeway particles) shown in **Figure 5**.

For the few eV polar wind particles, the fluxes that were measured in the lobe by the Cluster experiment were equal to what had been predicted by the theory almost 20 years before! **Figure 7** shows orbital segments of the Cluster spacecraft location in the tail lobes. The scale on the right-hand side is the occurrence frequency of polar wind observations varying from 100% in red all the way down to 0% in blue. The Cluster spacecraft is going through the lobe, then the plasma sheet, then the other lobe. The substantial red, and red-yellow shading shows that along those orbits, the lobe has polar wind flowing out. The left-hand figure is looking from the dawnside of the magnetosphere with the Sun to the right. The middle figure is looking down from above the North Pole and one can see the red part of the orbits are in the center of the tail as expected. The right-hand figure is looking from behind the Earth toward the Sun. The polar wind is seen in the lobes both north and south of the plasma sheet. A suggestion here is that one does not expect to see the polar wind outflows in the plasma sheet region because the polar wind will become energized and have its distribution changed which will not permit this wake technique to work. This also supports the idea that the polar wind/lobal wind flows into the plasma sheet where it is transformed to become an important part of the plasma sheet with different energy and pitch angle characteristics!

The Cluster wake measurements (Engwall et al., 2009b; Andre and Cully, 2012) as well as the direct polar TIDE measurements using the plasma neutralizer show the omnipresence of the polar wind in the lobes (Liemohn et al., 2005). **Figure 8** is from Haaland et al., 2012 using data from the Cluster mission looking at where the outflowing polar wind goes, as a function of the southward component of the IMF Bz in the solar wind. When the Bz is southward, the magnetic merging of the solar wind magnetic field with the magnetosphere increases the strength of convection

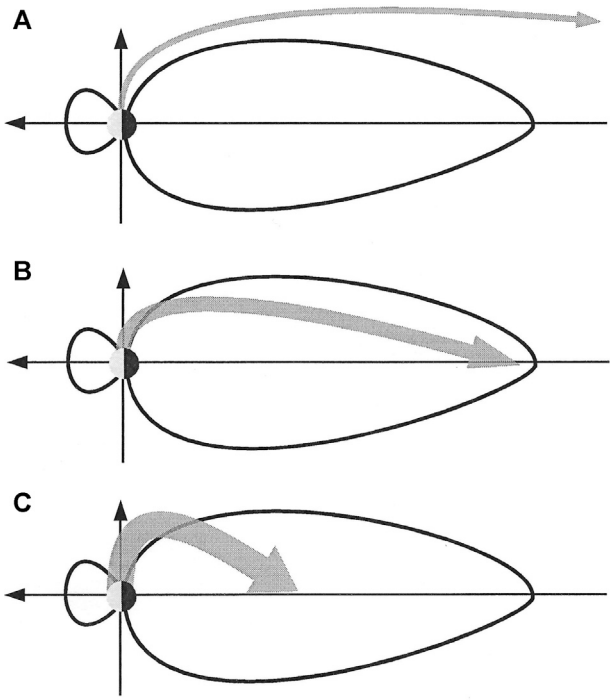

FIGURE 8 | The paths of the outflowing polar wind as measured on the Cluster spacecraft showing the influence of the solar wind Bz.

electric field and the cross-tail potential and that causes the outflowing polar wind in the lobes to be pushed into the center part of the tail and energized.

Panel a shows a northward Bz, where there is no convection electric field in the magnetotail. The polar wind comes out of the polar cap and vents out of the tail. Haaland et al., 2012 shows that 90% of the polar wind exhausts out of the back of the tail during northward Bz. A small amount of the exhausting polar wind may get caught up far back down the tail, but during northward positive Bz, it mostly vents out. In panel b, as soon as the solar wind turns Bz southward, there is an increasing cross-tail potential and convection field that starts to drive the polar wind into the plasma sheet region. The higher the southward Bz is, as shown in panel c, the closer to the Earth these ions are convected into the plasma sheet region. Haaland was able to estimate that 90% of the ions that were flowing down the tail and flowing out the back of the tail, in northward Bz conditions, are driven into the plasma sheet during southward Bz conditions and are then able to have a significant influence in creating the plasma sheet environment in which reconnection subsequently takes place. Earlier work by Cully et al., 2003a and Cully et al., 2003b also showed the linkage between outward flowing ions from the ionosphere and their access into the plasma sheet region.

Timing of the Ionosphere and Solar Wind Sources

The length of time involved in supplying ionospheric and solar wind plasma to the magnetosphere is a very important element in assessing their relative strength and their impact on the dynamic processes that they drive. The purpose of this section is to develop an idea of how the solar wind plasma versus the ionospheric plasma contributes to the plasma sheet, ring current and warm plasma cloak.

It is possible to do the proxy measurements of He^{++}/H^{+} and O^{6+}/H^{+} for the solar wind and O^{+}/H^{+} or He^{+}/H^{+} for the ionosphere, but it must be remembered that for the H^{+} part of these ratios, it is not known where the H^{+} came from because solar wind H^{+} looks exactly like ionospheric H^{+}, from a measurement point of view.

Figure 9 shows an ion trajectory starting in the dayside ionosphere as a polar wind ion and moving through the polar cap and lobe into the plasma sheet and subsequently the ring current. This ion trajectory code was developed by Delcourt et al. (1993) and was used by Huddleston et al. (2005) as a way of interpreting the ion characteristics that were being measured by the TIDE instrument on the POLAR spacecraft. The trajectory calculations show how the ion moves from the ionosphere through the magnetosphere, how it changes energy and how long it takes to make this journey. This trajectory model uses a Tsyganenko magnetic field model (Tsyganenko, 1989) and a Weimer convection field model. This case is set up for a Kp of 2. The ion is started on the dayside up above the ionosphere at 10 eV. In additional trajectories that were calculated in this study, the polar wind outflow as measured directly by the Polar TIDE instrument taken near perigee is used as input for the trajectory modeling and the resultant ion trajectory and energization is compared with the same TIDE instrument data taken near apogee.

The timing marks along the trajectory are important. There are 10-min tic marks along the outward trajectory. It shows that from the time the ion leaves the ionosphere, out to the middle of the lobe at 40 R_E, takes 90 min, and for the next 20 min, it moves into the plasma sheet region, gets energized, and is moving earthward to become part of the ring current. This top panel views the magnetosphere from the duskside (XZ plane) and traces the motion of an ion that started at 10 eV and ends up with ring current energies. The middle panel looks down on the magnetosphere from the top (XY plane). Here, the ion starts on the dayside, goes over the polar cap into the dusk sector becoming the plasma sheet, and then moves earthward, to become the ring current. The small square panel on the lower left views the ion trajectory from the tail toward the Sun (YZ plane), and the panel on the lower right shows the changing energy of the ion with time. It starts with 10 eV, slightly above polar wind energy, and for that first hour and a half, it increases up to a few 10's of eV. When it goes into the plasma sheet region at 1.7 h, it gains a kilovolt of energy in about 10 min! That's, again, from the curvature drift in the cross-tail field that gives it a kilovolt, and then as it drifts earthward, it is further betatron accelerated until it reaches ring current energies of 10 kilovolts.

Now let's look at the timing. It is about an hour and a half to get from just above the ionosphere on the dayside out to the middle of the lobe at 50 R_E. The timing from the lobe into the plasma sheet region is only tens of minutes. If the lobe is full and if the Bz of the solar wind goes southward, these ions are going to move into the plasma sheet within 10–20 min. Later we will come back and look at how long it takes a solar wind particle to get into that region. In this example the same ion which begins as the polar wind, becomes the

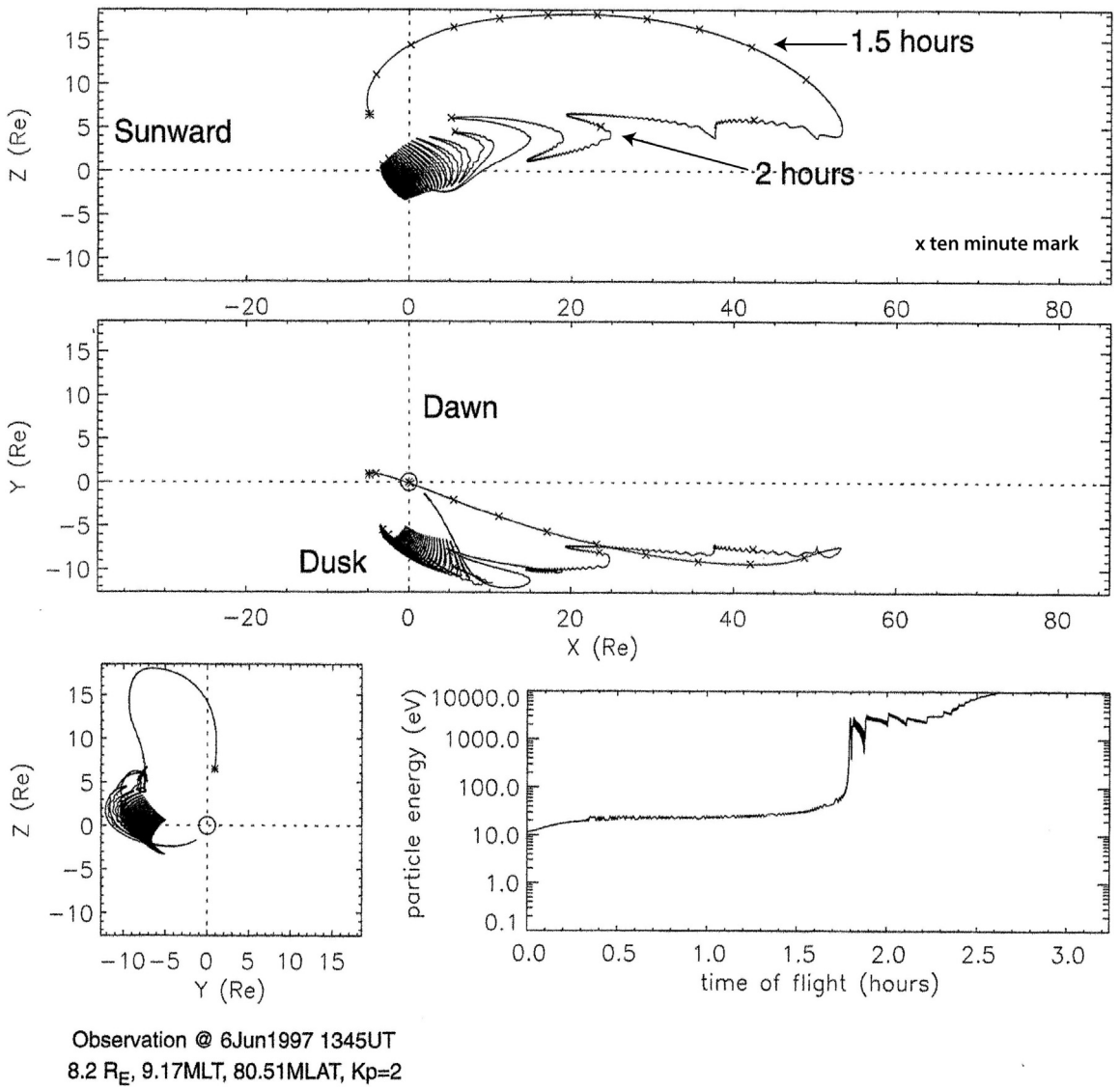

FIGURE 9 | An ion trajectory beginning above the ionosphere on the dayside and moving through the lobes and plasma sheet with its subsequent energization.

lobal wind, then the plasma sheet, and finally the ring current. It is the same ion moving through the magnetosphere, and of course, there are a very large number of ions doing this. For the polar wind, there are a few times 10^{26} ions/sec "threads in the magnetospheric tapestry."

In looking at the ion trajectory calculation approach, some colleagues have expressed hesitation about just using an isolated ion trajectory because they are concerned that the magnetosphere model is not self-consistent. The model does not let the currents flow and change the magnetic field configuration and strength self-consistently. In this case that is true, however we find that the ion trajectory is an excellent "pathway" to show us how the magnetospheric tapestry is woven. In addition, Alex Glocer has now developed a model that was published just this past year (Glocer et al., 2020) which is a merged ionosphere/magnetosphere, multi-fluid MHD model which has the self-consistent solutions.

The model presented in Glocer et al. (2020) generates the outflowing polar wind from the ionosphere and follows this plasma as it transverses the magnetosphere. It includes a plasmasphere, a ring current, a plasma sheet, and the model is multi-fluid. The model is able to use separate fluids for the ionospheric H^+ and the solar wind H^+ and thus tell us where these H^+ ions originate. This model can tell the difference in where these H^+ ions came from. Since H^+ is the dominant ion, the ability to separately track the ionospheric and solar wind H+ ions gives unique and very important new results. We will look at his model in more detail later in the paper.

Figure 10 from Glocer et al. (2020), addresses the concern about the utility of using single ion trajectories. This is the trajectory of an ion in the Glocer merged model in a situation similar to the Huddleston ion trajectory. The Sun is to the right in this figure. The color chart shows the ion thermal energy as it

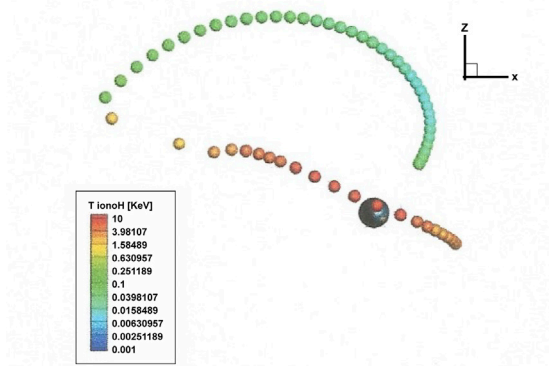

FIGURE 10 | An ion trajectory beginning above the dayside ionosphere and its movement through the polar cap and lobe to become energized upon entry into the plasma sheet and ring current (Glocer et al., 2020).

moves through the modeled trajectory. The ion flows out of the ionosphere at about 10 eV and then through the polar cap and lobe. By the time it gets across the polar cap and through the lobe and approaches the plasma sheet region it has about 100 eV of energy. Then note that the color of the trajectory changes to yellow, showing that the ion very quickly is energized to 1 keV, and then as it flows back in toward the earth, the color changes to red; it is 10 keV. The results of polar wind, lobal wind, plasma sheet and ring current is what the full merged ionosphere/magnetosphere MHD treatment is showing and it is conceptually very similar to the trajectory and energization given in the Huddleston et al., 2005 results. Although the fluid and particle pictures are conceptually similar, it is important to keep in mind that numerical resistivity drives heating near the x-line in the MHD simulation.

Now, in contrast to the ionospheric source timing of lobe/plasma sheet access and energization to 1 KeV in 20 min, we examine the solar wind source timing. **Figure 11** shows recent calculations regarding solar wind access to the magnetosphere by Sorathia et al. (2019). This paper looks at trajectory modeling of solar wind particle access during changing solar Bz. This paper calculates the trajectories of ions that start at the bow shock and then flow into the magnetosphere and the model results show where the solar wind particles go and how long it takes. This is with a northward Bz.

One of the things that is mentioned in the Sorathia et al., 2019 paper is that it is in northward Bz times in the solar wind that one expects Kelvin-Helmholtz instabilities to be stronger, giving more solar wind access through the flanks into the plasma sheet. This modeling also has reconnection included, but of course, with a northward Bz, it's not full reconnection but

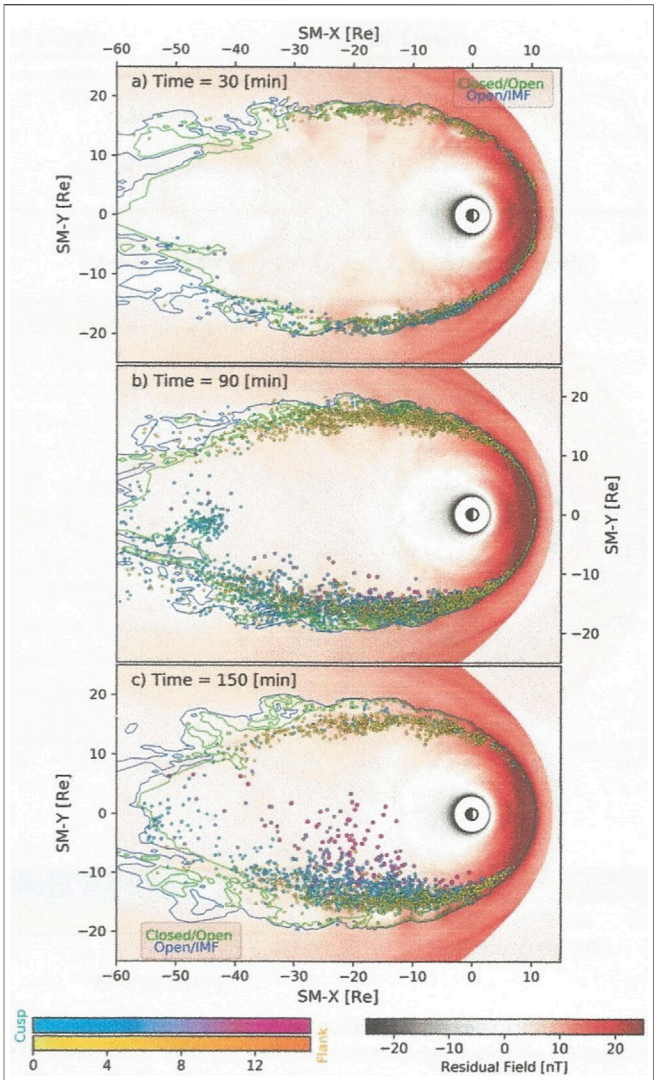

FIGURE 11 | A model (Sorathia et al., 2019) showing the flow and timing of solar wind H+ from the bow shock to the flanks of the magnetotail with subsequent diffusion toward the center of the tail.

partial just because of the magnetic field orientation in the solar wind.

The timing for access is shown in **Figure 11**. Panel a shows that for a particle to get from the bow shock to the flanks of the plasma sheet, not into it, but out on the flanks, takes 30 min. In Panel b it is an hour and a half before the solar wind ions begin to have penetration into the plasma sheet from the flanks. These are solar wind H^+ ions. In Panel c we see that it takes two and a half hours before these H^+ solar wind ions that started out at the bow shock begin to reach toward the center of the plasma sheet in the 20 to 30 R_E region. In contrast, the ionospheric ions that are flowing out through the lobes, because they are already in the center of the lobe and are very close, can get into the plasma sheet in 10–20 min. For ions that come from the solar wind, it can take 2 hours or more to reach the reconnection region at the center of the plasma sheet

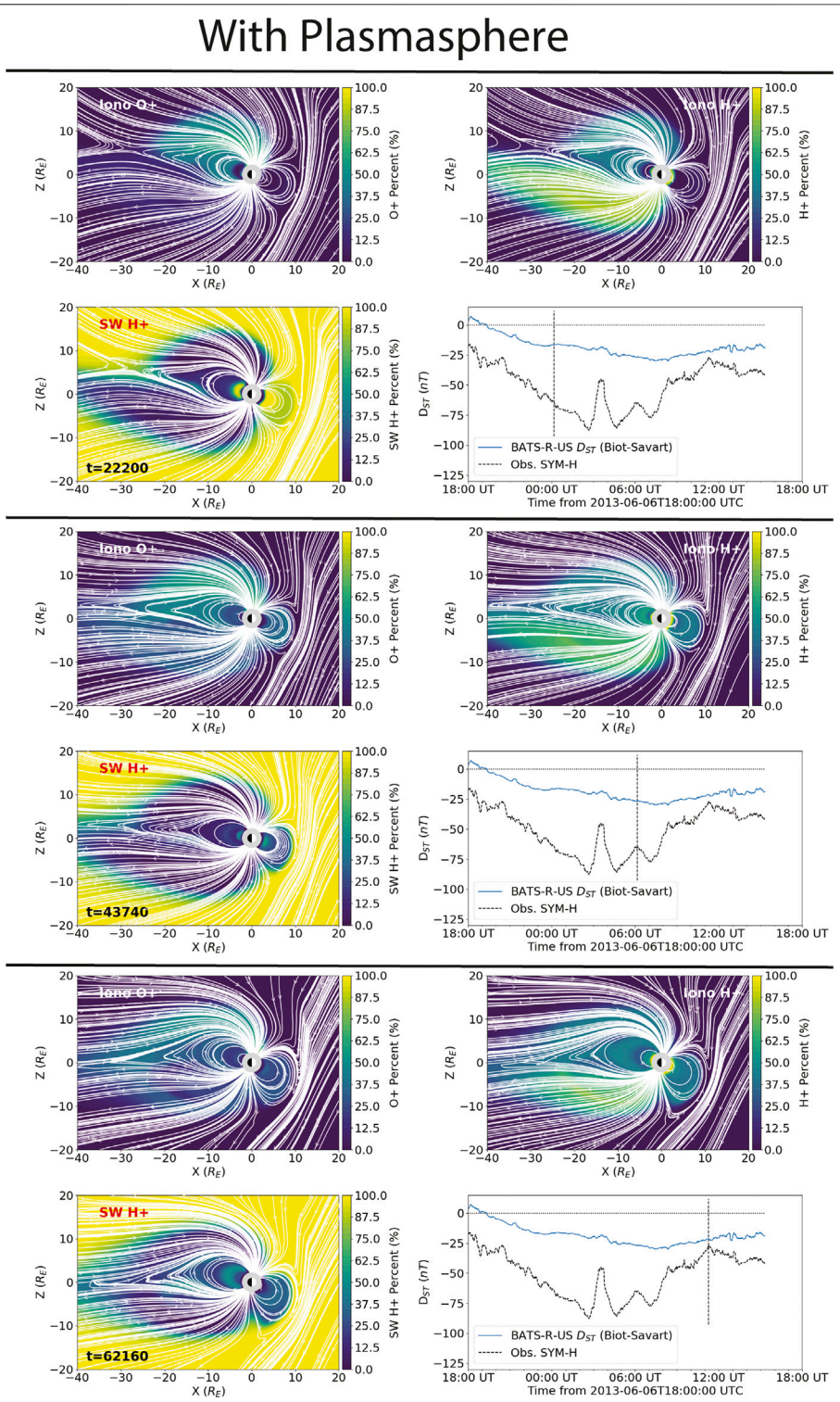

FIGURE 12 | Results of a merged multi-fluid model of a storm period showing the relative contributions of the ionosphere and solar wind to the magnetosphere.

even starting at the flanks. The ionosphere is in a very favorable position to supply plasma to the center of the tail because it has started inside the magnetosphere and because its continuous outflow is already in close proximity to the midnight sector of central plasma sheet just outside in the lobes.

Merged Models—Important New Insights on H^+ from the Ionosphere and Solar Wind

Modeling of the Earth's magnetosphere has been carried out over the years leading to important advances in our understanding of magnetospheric dynamics (Fok, 1999, Winglee, 2000, Moore et al., 2005, Glocer et al., 2009, Welling and Ridley, 2010, Brambles et al., 2010, Welling et al., 2011, Welling and Ridley, 2010. Recent multi-fluid models have brought an enhanced capability in understanding the role of different sources of plasma for the magnetosphere.

Figure 12 shows the Glocer et al. (2020) results for a case study which uses the merged ionosphere/magnetosphere multi-fluid MHD model that separates the ionospheric H^+ from the solar wind H^+. It also shows that outflow from different hemispheres makes an important difference. Both lobes aren't filled symmetrically, but there exists a strong seasonal effect associated with what portion of the ionosphere is illuminated. The solar zenith angle is an important element of the ion/electron production in the ionosphere.

Figure 12 from Glocer et al. (2020) shows three sets of four smaller panels which we summarize in the following discussion. The top set is in the main phase of a June 2013 storm as shown by the Dst small panel (lower right) of the larger panel and the location of the vertical line in this panel. The second set of panels is in the storm peak and the third set panels shows the early recovery phase. Within each large panel the upper right panel shows the ionospheric H^+ outflow (polar wind), the upper left panel shows the ionospheric O^+ outflow (polar cusp) and the lower left is the solar wind H^+ component. This case gives us an indication of the relative contribution of the ionospheric plasma as compared to the solar wind in the magnetosphere. The color bar on the right of each plot shows the % contribution. The yellow indicates that 100% of that area is filled by the species on that plot and blue indicates no contribution by that species in that area of the plot. The model has been run for an approximately 24 h period for this isolated storm.

In the top panel set of **Figure 12** the main phase, there is a relatively higher proportion of ionospheric H^+ (upper right) in the southern hemisphere; there is more in this lobe because it's favorably positioned with respect to solar illumination. There is ionospheric H^+ outflow coming out of both hemispheres, but it is dominant up to 100% in the southern lobe and is from the ionosphere. The upper left plot is the ionospheric O^+ outflow from the polar cusp and some from the auroral zone. The cusp is making about 50% of the outflow in the northern lobe. The solar wind presence is dominantly outside the magnetosphere with some penetration on the dayside with the plasma sheet region and lobes showing very little solar wind H^+ inside about 30 R_E with the southern lobe and plasma sheet being dominated by the outflowing ionospheric H^+.

The middle panel set shows the storm peak. At this time in the Glocer et al. (2020), study the ionospheric H^+ and O^+ fill more of the lobes and plasma sheet volumes with less H^+ from the solar wind in these regions. This model also includes the presence of the plasmasphere which results in the calculated cross-tail potential being smaller in magnitude than the simulation without the plasmasphere. The presence of the plasmasphere model appears to have an important influence on the polar cap potential and the Dst in the simulation. Note that the southern lobe of the magnetosphere continues to be dominated by the ionospheric H^+ throughout the storm as would be expected for the seasonal effect. The outflowing O^+ from the northern polar cusp also continues to dominate that hemisphere as well as the plasma sheet and ring current.

There is very little solar wind H^+ in the plasma sheet and ring current regions out to the 20–30 R_E equatorial region of the plasma sheet throughout this particular storm. At the storm peak, the solar wind H^+ is a very minor component in the equatorial plasma sheet out to 40 R_E.

The bottom panel set shows the early recovery phase of the storm, where there is solar wind H^+ penetration filling into the down tail regions of the plasma sheet at 30–40 R_E and displacing some of the ionospheric plasma prior dominance. The polar wind is still flowing out as seen in the upper right small panel, but it is starting to vent out the tail. The O^+ in the upper small panel is still there but diminishing, and the solar wind H^+ is beginning to penetrate. The Glocer et al. (2020) model shows that in the peak of this storm, the ring current content is dominated by the H^+ from the ionosphere plus O^+ from the ionosphere with some minor contribution in the ring current of the H^+ that comes from the solar wind.

In order to show the relative contributions of the ionosphere versus the solar wind more clearly, we have added the ionospheric polar wind H^+ outflow together with the ionospheric polar cusp O^+ outflow and compared this total ionospheric contribution with the solar wind H^+ contribution. **Figure 13** shows the three times indicating the main phase, storm peak phase and early recovery phase from this selected storm with the total ionospheric H^+ and O^+ shown in shades of blue and the solar wind H^+ shown in shades of red. The color scale is shown on the right-hand side of the three plots. In this figure, white areas show a 50/50 split between ionospheric and solar wind sources with the darker blue showing increasing ionospheric contribution up to 100%. Similarly, the darker red shows increasing solar wind contribution up to 100% and therefore 0% ionospheric contribution.

The solar wind parameters are shown in the left panel together with the timing of the simulation start followed by the main phase, storm peak and early recovery times in the simulation run shown by the four vertical lines in the solar wind drivers plot. The key Bz component of the solar wind is shown in the third panel down and this component of the solar wind turns southward at 1800 UT on June 6, 2013. This is the starting time of the previously discussed simulation with the ionospheric polar wind and polar cusp plasma flowing out of the ionosphere and through the lobes. In addition to the southward component of the solar wind Bz, the density of the solar wind had increased substantially during the day before the storm (panel 4)

The results are dramatic. The top panel of **Figure 13** shows the main phase of the storm. Because of the orientation of the Earth's spin axis and the dipole axis, the southern hemisphere and lobe are dominated by the polar wind outflow out to greater than 40 R_E

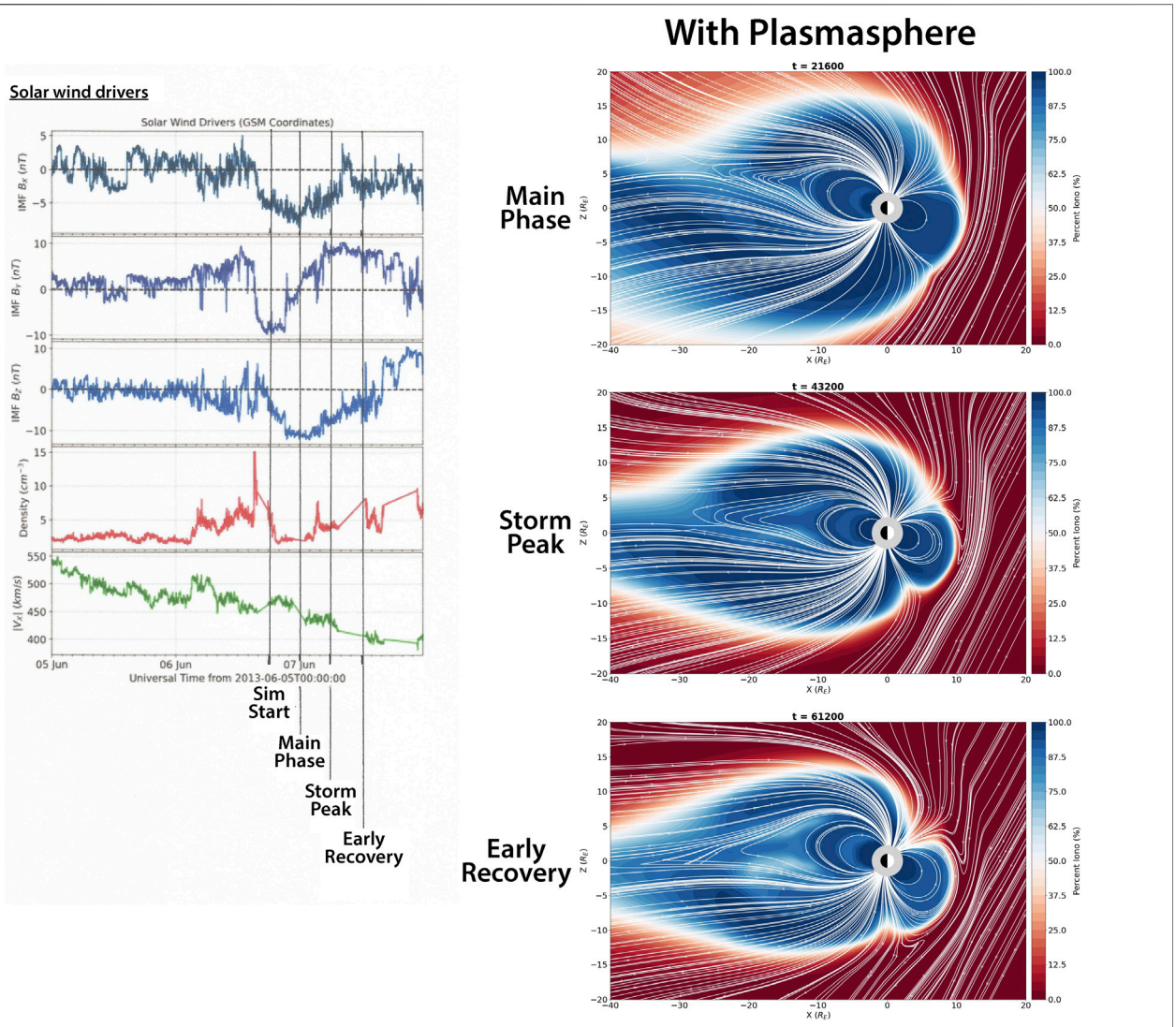

FIGURE 13 | Model results on the storm period shown in **Figure 12** combining the H^+ and O^+ contributions of the polar wind and polar cusp (blue) versus the solar wind H^+ (red).

and the northern hemisphere and lobe are dominated by the polar cusp outflow out to 20 R_E. The midplane of the tail has a dominant ionospheric H^+ and O^+ contribution out to 40 R_E and the lobes are full of outflowing ionospheric plasma which can continue to access the midplane in the 24 h while the Bz remains southward continuing to mass load the tail.

In the second panel, the storm peak phase is shown. The ionospheric plasma in the lobes has penetrated into the midplane giving an ionospheric contribution of H^+ and O^+ that dominates the solar wind in the mid-plane reconnection region of the tail out past 40 R_E with a thickness exceeding 10 R_E. It is during this time period that the ionospheric ions that were initially flowing in the lobes are energized to keV energies of the warm plasma cloak and plasma sheet reconnection region and subsequently to the 10's of keV ring current energies, causing the expansion phase of the storm.

In the third panel the recovery phase is shown. The southward Bz component of the solar wind is decreasing and the ionospheric plasma in the lobes is beginning to flow farther down the tail and will begin to exhaust out of the back of the tail as the Bz goes northward. The ionospheric contribution remains dominant throughout the tail region although the solar wind H^+ ions are beginning to show up in the inner plasma sheet region (white hazy regions). This ionospheric dominance has been discussed previously by Moore and Delcourt, 1995. It should be remembered that during these changing Bz periods, the ability of the ionospheric ions in the lobes of the tail to reach the midplane in the midnight sector is much faster (10's of min) than the solar wind ions which must diffuse from the flanks of the tail.

The Plasma Sheet Boundary Layer

A corollary thought regarding the entry of the low energy lobe plasma into the plasma sheet is the need to understand the processes that are taking place in what has been called the plasma sheet boundary layer. On the north and south outer

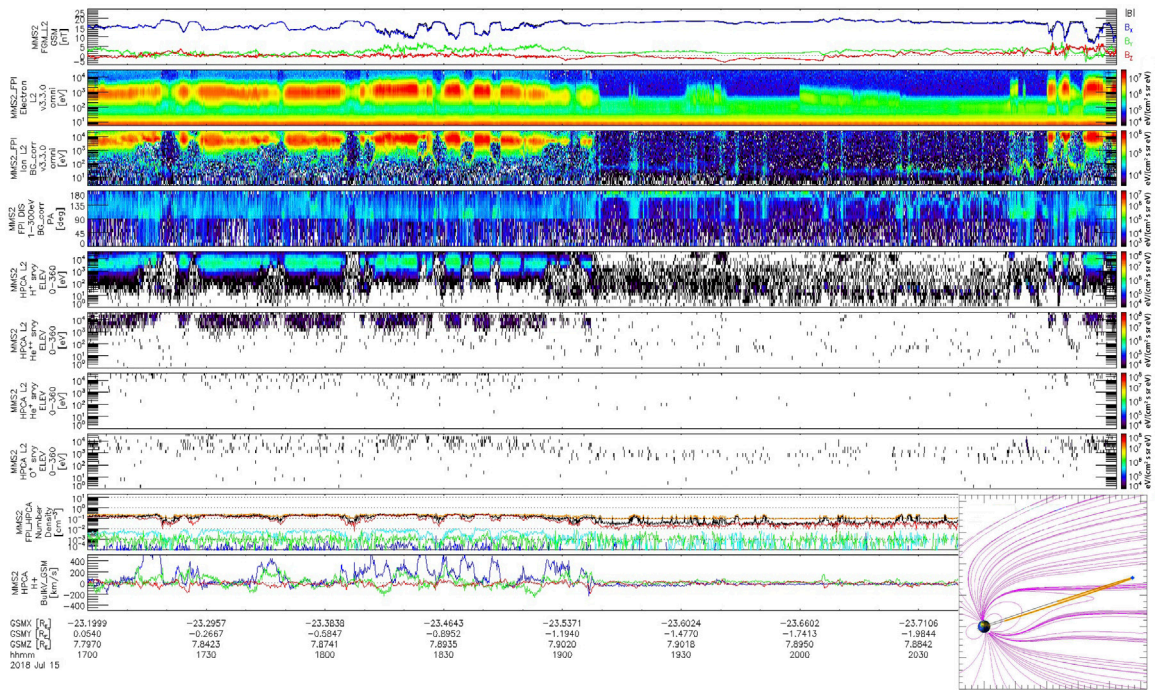

FIGURE 14 | A composite picture of MMS data on July 15, 2018 through the plasma sheet boundary layer at the interface of the lobe and plasma sheet.

layers of the plasma sheet, the characteristics of the plasma in the plasma sheet are different closer to the mid-plane than they are at the edges. Data from the MMS spacecraft offer interesting insights into how the transition from lobe plasma to plasma sheet plasma takes place. The energization of the ions as they enter the midplane has been discussed above in **Figure 5** and **Figure 9**. The orbits of the MMS spacecraft permit observations of this plasma sheet/lobe boundary interface.

In the past we have sought to explain this interface in terms of the different ways that the solar wind access can happen, but what may more likely be the case is that this plasma sheet boundary layer is showing us how the lower energy lobe plasma is energized to become the central plasma sheet. **Figure 14** shows an MMS orbit for July 15, 2018 in which the lobe/plasma sheet transitions happen several times during the pass. The lower right-hand corner inset figure shows the XZ plane of this MMS orbit which is crossing through the midnight sector at this time. The XZ plane of the orbit is projected on the calculated magnetospheric shape, and shows that the orbit is moving out of the plasma sheet region and into the lobe. When the plasma sheet thins and thickens because of the changing solar wind conditions during the time of passage, MMS can make multiple entries into and out of the lobe.

A look at the 24 h summary plot of MMS data for this orbit (not shown here) displays that there are significant lobe entries at 0100, 0600, 1900 and 2200 UT. We focus here on this expanded plot for the period from 1700 to 2200 UT where the plasma sheet thins, as seen by the dropout of keV electrons and ions at 1900 UT in the second and third panels of the stacked plots, This thinning is in response to an increased X component of the B field as shown by the blue line in the upper first panel. Throughout the time period of 1700–1900 UT as the spacecraft is approaching the northern edge of the plasma sheet from within, this repeated thinning puts the spacecraft alternately in the lobe and then back into the plasma sheet as the plasma sheet thins and then thickens again, multiple times.

These are places where the spacecraft is transitioning from plasma sheet to lobe to plasma sheet and this transition can give us information on the processes that take place at that interface. What can be seen here is that when the spacecraft goes into the lobe, the energy, as measured by the Fast Plasma Instrument in the third of the stacked plots, drops from 1 to 10 keV (plasma sheet) down to about 10–100 eV (lobal winds) and this energy change reverses when the plasma sheet thickens again (decreased X-component of B field).

Kitamura (2019) (GEM) has looked at this particular case in much more detail. The plasma sheet section ends at 1900 UT when the plasma sheet thins and the lobe is encountered by the spacecraft. Then the spacecraft goes back into the plasma sheet at 2100 UT when the plasma sheet thickens again. As was noted above, the first (top) of the stacked plots shows the three components of the magnetic field, the second plot is for the electrons from 10 eV to 10 keV, the third panel is the ions from less than 10 eV to 10 keV. The fourth plot displays the pitch angle distribution of the 1–300 eV ions. The stacked plots below that show the HPCA ion composition measurements integrated over all pitch angles beginning with H^+, then He^{++}, then He^+, then O^+ from 10 eV to 10 keV followed by the number density and the bulk flow velocity.

When the lobe is solidly encountered at 1900 UT, the energies of the ions measured by FPI drop from keV to less than 100 eV. The spacecraft has an ion emitter for potential control. The electrons in the second panel show a similar energy decrease at the lobe encounter. The fourth panel shows the pitch angle distribution for the 1–300 eV ions. In the lobe between 1900 and 2100 UT, these low energy ions are field-aligned at 180° pitch angle which indicates that they are flowing out of the northern ionosphere and flowing through the lobe into the plasma sheet. In the plasma sheet segments (1700–1900 UT) one can still see ions at low energy (panel 4). These are 0–300 eV, but they are now spread over pitch angles of 180 down to 90°. They are picking up perpendicular energy as they come into the plasma sheet region which is compatible with their curvature drift in the cross-tail potential as discussed above in **Figure 9**.

If we look at the HPCA data in stacked plots 5–8, we see that there is H^+ in both the plasma sheet and the lobes. There is He^{++}, which is in the plasma sheet but not in the lobes. The He^+ is mostly in the plasma sheet with some in the lobe and the O+ ions are found both in the plasma sheet and the lobe. Initial indication from the He^{++} is that there is solar wind entry into the plasma sheet. The H^+ measurements are ambiguous because of the possibility of both ionospheric and solar wind sources although their energies are much lower in the lobe, as expected for their polar wind source and they are energized in the plasma sheet region. There is O^+ in both the lobe and the plasma sheet that probably comes from the polar cusp through the lobes and possibly from the nightside auroral zone source. This single case suggests that very valuable information can be learned from MMS about the lobe/plasma sheet transition region which is found at the plasma sheet boundary layer and what it can show concerning the sources and processes that fill the plasma sheet.

The Role of the Ionosphere in Driving Substorms and Storms

In the previous sections we have shown how the ionosphere is capable of being the dominant source for the different plasma regions of the magnetosphere, based on observations of the outflowing plasma from the ionosphere and the processes that can move it and energize it to create the energetic plasma regions. The evidence for the ionosphere as a source is quite compelling based on both measurement and multi-fluid merged modeling.

We now examine how the outflowing ionospheric plasma can load the magnetosphere based on the changing Bz of the solar wind. We have shown the magnitude of the outflow and how it can move through the lobes of the tail to populate the plasma sheet, the principal region for reconnection in the magnetotail. We have also shown that the ionospheric outflow is affecting the magnetosphere from the inside-out and its omnipresence in the magnetotail lobes in the midnight sector gives it fast access (10's of min) to the plasma sheet region in contrast to the solar wind plasma entry which can take an hour or more to reach and begin to enter the flanks of the plasma sheet. The merged ionosphere/magnetosphere MHD modeling shown in **Figure 12** and **Figure 13** illustrates how the ionospheric outflow can load the magnetosphere sufficiently enough to create the plasma sheet and ring current in contrast to the solar wind.

The dynamics of the ionospheric source in combination with the changing solar wind Bz and with the different access and energization times for the ionosphere and solar wind plasma suggest a new or modified model for the initiation of substorms and storms in the magnetosphere. **Figure 15** illustrates the new model and serves as a basis by which we can examine how these dynamic magnetospheric processes might be triggered.

The timing considerations discussed above suggest that following the Bz southward turning of the solar wind magnetic field, the ionospheric source is poised to access the plasma sheet in tens of minutes and become energized in minutes, thus mass-loading the tail and distending the magnetic field lines in the neutral sheet. The entry and energization of the outflowing ionospheric plasma in the lobes establishes a changed environment in the plasma sheet that is very favorable for reconnection to begin, thus initiating substorms and storms. The availability and quick access of the ionospheric-origin plasma to the midnight sector neutral sheet in contrast to the access times required by the solar wind H^+ establishes the ionosphere together with the solar wind southward Bz as major components of the driving mechanism in the process of magnetospheric dynamics.

Figure 15 is a sketch which illustrates two time periods. In the upper panel the pre-storm northward Bz period is shown in which the solar wind is supplying plasma to the flanks of the tail as discussed above (Sorathia et al., 2019). In the lower panel the time period following the change of the solar wind Bz to southward is shown.

Beginning with the top panel, during a northward Bz, the solar wind plasma has been accessing the plasma sheet region with H^+ and He^{++} into the magnetotail on the flanks. The total solar wind access time from the bow shock in towards the center of the tail is about two and a half hours. The polar wind and polar cusp outflows move as shown by the blue lines through the lobes. There is no convection field, and a very small cross-tail potential if any, and the streaming ions flow almost entirely (90%) out of the tail of the magnetosphere (Haaland et al., 2012). These ionospheric polar wind and polar cusp low energy ions do not affect the plasma sheet significantly during northward Bz.

Then as illustrated in the lower panel, when the solar wind Bz turns southward, the H^+ and He^{++} solar wind ions that had entered the tail during the period of northward Bz remain there while the ions that are streaming outward in the lobes and down the tail have their trajectories dramatically altered by the increased convection electric field and are driven into the plasma sheet region quickly in 10's of min. These H^+, He^+ and O^+ ionospheric ions can enter quickly because they had flowed out to their positions in the tail during the previous northward Bz time period and only have to drift a short distance to reach the plasma sheet region. This begins to mass-load the neutral sheet field lines and distend/stretch them further. This increases their curvature and increases the energization of the entering lobe particles to keV energies through their curvature drift across the tail and the energization that comes from the cross-tail potential which has also been increased because of the southward turning solar wind Bz. These entering ions can gain their keV energies in about 10 min after they enter

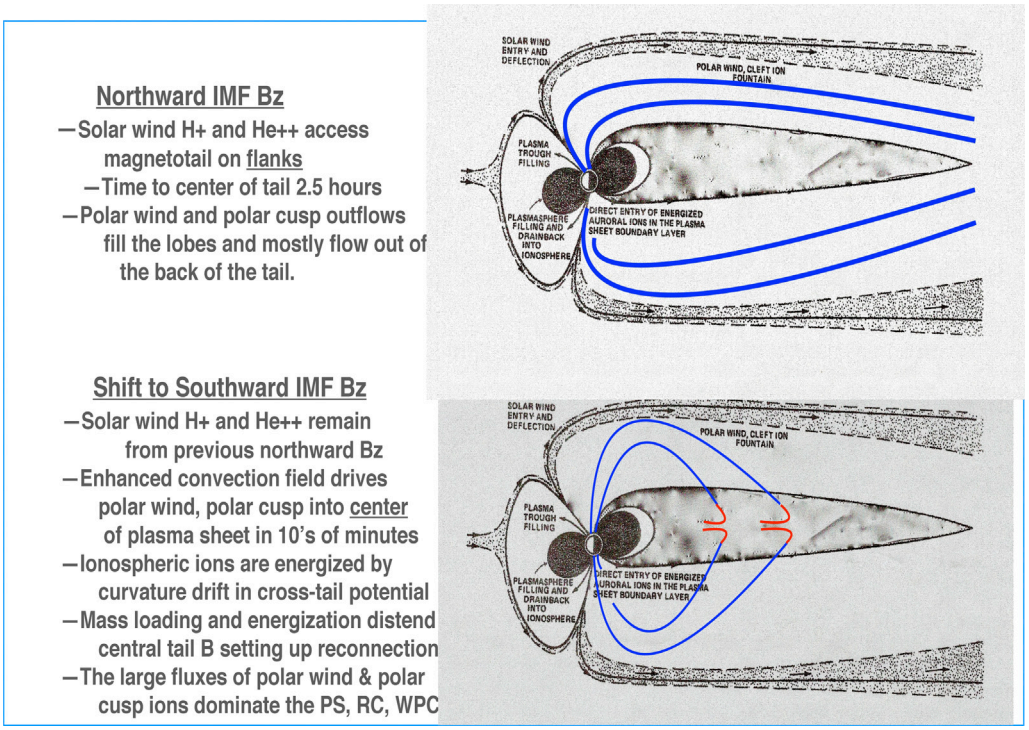

FIGURE 15 | Two sketches which give a schematic picture of the suggested process by which ionospheric and solar wind plasma access the magnetospheric tail and through which the ionosphere can be a dominant plasma source and a driver of magnetospheric storms and substorms.

the region of distended field lines (see **Figure 9**) improving the environment for reconnection to begin. With the southward Bz occurring, about 90% of these lobe ions will enter the plasma sheet region instead of flowing out of the back of the tail (Haaland et al., 2012). The stronger the southward Bz, the closer to the earth the lobe ions are pushed into the plasma sheet.

The large fluxes of polar wind and polar cusp ions, once energized, dominate the plasma sheet and flow earthward creating the ring current, and the warm plasma cloak. This is a very different way of thinking about a substorm or a storm. Solar wind Bz is still the trigger, but the particles are dominantly delivered by the ionosphere through the lobes.

It is important to note that the dynamics in the magnetotail may not only be due to steady convection and laminar flows, but can have a major contribution from turbulence and mesoscale structures. It was noted early on that injections from the magnetotail can contribute to ring current build up (Parks and Winckler, 1968). Indeed, recent numerical simulations suggest that the contribution of bursty flows in the plasma sheet can contribute much of the ring current build up (Yang et al., 2015). This picture is consistent with observations showing that bursty bulk flows (BBF's) can account for much of mass and energy transport in the plasma sheet (Angelopoulos et al., 1994). The potentially bursty nature of this transport can have important implications for the energization of particles in the tail, including ionospheric particles which reach the equatorial plane from the lobes. In particular, bursty transport means that some of the particle energization may be non-adiabatic. For O+ especially, which has a large gyroradius, there are indications in observations that non-adiabatic acceleration associated with fast flows can be important (Keika et al., 2010, 2013). Regardless of whether the transport is bursty or laminar in the tail, acceleration of particles of ionospheric origin reaching down tail will occur, albeit the details of the transport may change. Additionally, just as the transport in the magnetosphere can have important contributions from fast flows and mesoscale structures, the outflow itself can be significantly structured. For instance, Schunk et al., 2005 showed that one can have localized propagating patches of polar wind outflow. The contributions of such structure in the outflow in combination with the bursty nature of the transport are certainly worthy of continued study.

Here is the storm process in summary. Northward Bz has solar wind ions contributing to the plasma sheet and the ionospheric plasma, polar wind and polar cusp fills the lobes but is flowing out of the back of the tail. The growth phase occurs when Bz turns southward and the lobe outflows are convected into the mid-plane where they are energized in tens of minutes and stretch the tail. The distended tail increases the curvature drift and the cross-tail potential further energizes the formerly ionospheric ions. Then, when the tail is loaded, reconnection begins and makes the expansion phase. This is the area that is being studied extensively in detail for reconnection events by MMS spacecraft and the ionospheric source plays a significant role in creating this plasma reconnection region. The reconnection starts the aurora, which starts the ionospheric currents flowing, changes them, and gives the familiar magnetic signatures in the auroral zone.

Then the newly created and energized plasma sheet flows earthward and is further energized. The ring current strengthens so that the total of the polar wind H^+ and polar cusp O^+ are dominant in it over the solar wind H^+ (Glocer et al., 2020). A large storm can develop and continue as long as the southward solar wind Bz is there because the ionosphere is sending out polar wind and polar cusp ions continuously, and as long as the Bz delivers these ions to the mid-plane, the storm can continue. When Bz goes back northward again, the lobal wind begins to exhaust out the back of the tail and the storm ends.

SUMMARY CONCLUSIONS AND NEXT STEPS

What do we know? The ionospheric plasma plays a major role in populating the magnetosphere and affecting its dynamics. The initially cold (few eV) ionospheric plasma creates the polar wind, which fills the plasmasphere and the plasma trough, and creates the dense detached plasma and plumes that drift from the duskside plasmapause out to the magnetopause, which affects the reconnection rate there. At higher latitudes outside of the plasmasphere, the polar wind flows upward supersonically, dominated by cold H^+ and He^+ and together with the outflowing polar cusp plasma of H^+, He^+ and O^+ is convected across the polar cap to fill the lobes of the magnetotail continuously.

As the polar wind and polar cusp outflows move through the lobes, they can be convected into the mid-plane of the magnetotail to be a major contributor to the creation of the plasma sheet, the ring current and the warm plasma cloak. In addition, the lower latitude plasmasphere and plasma trough cold plasma drives wave-particle interactions that both create and determine the propagation of waves that are a dominant influence on the creation of the radiation belts.

Together with the solar wind IMF Bz, the ionospheric plasma is a major driver of substorms and major storms when the southward Bz convects the copius outflowing cold plasma in the lobes into the central plasma sheet region, mass-loading this region, distending the magnetospheric field lines in the neutral sheet, energizing the cold plasma to plasma sheet energies and setting up the reconnection process which results in substorms and storms.

Both the cold unaccelerated plasma of the plasmasphere and the accelerated outflowing ionospheric plasma of the warm plasma cloak influence the strength of the reconnection at the nose of the magnetosphere. In addition, both the unaccelerated polar wind outflow and the accelerated ionospheric lobal wind together with the accelerated ionospheric plasma sheet create a dominant element of the environment in which reconnection happens in the central plasma sheet of the magnetotail. The plasma sheet boundary layer is the transition layer where the cold outflowing lobe plasma is transformed into the hot plasma sheet plasma and warm plasma cloak regions.

Recently created merged ionosphere/magnetosphere multi-fluid MHD models are able to differentiate between the H^+ ions which come from the ionosphere in the polar wind and polar cusp from the H^+ ions that enter the magnetosphere from the solar wind. This otherwise unmeasurable difference has given invaluable new insight into the relative strength of these two magnetospheric plasma sources and their relative ability to drive substorms and storms.

What do we need to know? New measurements of the composition of the ionospheric outflow, and the resulting ion trajectories and energization of this outflow must be carried out together with the advancement of merged multi-fluid models of the ionosphere and magnetosphere that can clearly differentiate between ionospheric H^+ and solar wind H^+. These merged multi-fluid models will be our roadmap to track the pathways that cold ions and electrons follow as they move through the magnetosphere, are energized and create the distinctive magnetospheric plasma regions that we have observed for decades but have not fully understood—the magnetosphere tapestry.

The merged models together with ion trajectory models are needed in order to allow us to understand the observations in the lobe, plasma sheet boundary layer, central plasma sheet, ring current and warm plasma cloak. These new merged models should be expanded to include more multi-fluids in addition to the ionospheric and solar wind H^+. They should add particularly He^{++} and O^{6+} from the solar wind as well as O^+, He^+, N^+, O^{++}, and NO^+ from the ionosphere.

In summary, what are our next steps? We need to try to understand how the ions and electrons actually move through and are energized to make the principal regions of the magnetosphere and how changes in the solar wind Bz can cause a storm to occur there. The low energy electrons are even more difficult to measure accurately than the ions because of spacecraft charging and photoelectron emission from the spacecraft surface. We should continue to develop the multi-ion capabilities of the merged multi-fluid models that can separate the solar wind H^+ from the ionospheric H^+ in order to interpret the ion observations. There will be much significant new information that comes from running these multi-fluid models and comparing with the evolving ion trajectory observations.

We must also start again to fly missions that have specific separate instrumentation with large geometric factors that will give the sensitivity required to measure individual initially cold, few eV, ion phase space densities and how they are transformed as they move through the magnetosphere. These highly sensitive differential angle instruments which include composition must be accompanied by a successful plasma neutralizing device that can keep the spacecraft potential close to plasma potential without interfering with other measurements on the spacecraft.

Finally, new missions must be selected and flown which measure the composition, energy and angular distribution of all of the areas of outflow from the Earth's ionosphere, which become the very significant source of the distinctive regions of the magnetosphere. In addition, these missions should utilize the highly sensitive low to medium energy measurements to track the 100's of eV to 100 keV ion trajectories of the source ions and electrons as they are energized to populate the magnetosphere hot plasma regions and drive the substorms and storms.

We will be able to use the merged multifluid models as a roadmap to help understand what we are observing in the particles. The merged models using those additional ions and

the particle tracing will help us determine the ion pathways and unravel the origin of the particle measurements. They will also allow us to understand how the environment for reconnection is created in the plasma sheet and at the magnetopause.

AUTHOR CONTRIBUTIONS

All authors listed have made a substantial, direct, and intellectual contribution to the work and approved it for publication

ACKNOWLEDGMENTS

This paper is dedicated to Don Carpenter at Stanford University and Ed Shelley at the Lockheed Palo Alto Research Laboratory. One of us (CRC) had the privilege of working with Don and Ed when he went to Lockheed in Palo Alto. Don showed us the presence of ionospheric plasma in the magnetosphere, the plasmasphere, Carpenter's knee. Ed showed us that one can see O^+ in the magnetosphere that has keV energies that obviously came from the Earth's ionosphere and subsequently got energized. Our community has been, to a certain degree, not completely following through on what Ed showed us because we know that O^+ is from the ionosphere but we have tended to overlook the fact that the ionosphere is also putting copius amounts of H^+ into the magnetosphere; we have just never been able to tell it apart from the solar wind H^+ which we now can and certainly should do. One of us (CRC) would also like to thank his thesis advisor, Brian O'Brien, who has left his scientific imprints in the Earth's magnetosphere and on the moon and Martin Walt, who is the scientist leader who enabled him to come to Lockheed as a green PhD and gave him the opportunity to do work in these many different fascinating areas of magnetospheric physics. Rick was also able to meet Andy Nagy, Peter Banks and Bill Hanson and began learning about the ionosphere from them. Many thanks go to Stan Fields, David Reasoner, Bill Lewter and Bill Baker at MSFC for building the RIMS instrument for Dynamics Explorer satellite together with the University of Michigan and the University of Texas at Dallas and later to Thom Moore, Stan Fields and Nobie Stone at NASA/Marshall Space Flight Center as well as Jean-Jacques Berthelier at CNRS and Dave Young at SwRI, to build the TIDE instrument for the Polar satellite. Thanks also go to all of the members of the magnetospheric branch at the NASA/Marshall Space Flight Center for their important and essential contributions to the analysis of the RIMS and TIDE data. This research was supported by the National Aeronautics and Space Administration, Magnetospheric Multiscale Mission (MMS) in association with NASA contract NNG04EB99C.

REFERENCES

Abe, T., Watanabe, S., Whalen, B. A., Yau, A. W., and Sagawa, E. (1996). Observations of Polar Wind and thermal Ion Outflow by Akebono/SMS. *J. Geomagn. Geoelec* 48, 319–325. doi:10.5636/jgg.48.319

André, M., and Cully, C. M. (2012). Low-Energy Ions: A Previously Hidden Solar System Particle Population. *Geophys. Res. Lett.* 39, L03101. doi:10.1029/2011gl050242

André, M., and Yau, A. (1997). Theories and Observations of Ion Energization and Outflow in the High Latitude Magnetosphere. *Space Sci. Rev.* 80 (27), 27–48. doi:10.1007/978-94-009-0045-5_2

Angelopoulos, V., Kennel, C. F., Coroniti, F. V., Pellat, R., Kivelson, M. G., Walker, R. J., et al. (1994). Statistical Characteristics of Bursty Bulk Flow Events. *J. Geophys. Res.* 99 (21), 21257. doi:10.1029/94ja01263

Banks, P. M., and Holzer, T. E. (1968). The Polar Wind. *J. Geophys. Res.* 73, 6846–6854. doi:10.1029/ja073i021p06846

Banks, P. M., Nagy, A. F., and Axford, W. I. (1971). Dynamical Behavior of Thermal Protons in the Mid-latitude Ionosphere and Magnetosphere. *Planet. Space Sci.* 19 (9), 1053–1067. doi:10.1016/0032-0633(71)90104-8

Barakat, A. R., and Schunk, R. W. (2006). A Three-Dimensional Model of the Generalized Polar Wind. *J. Geophys. Res.* 111 (A12), 1978. doi:10.1029/2006ja011662

Brambles, O. J., Lotko, W., Damiano, P. A., Zhang, B., Wiltberger, M., and Lyon, J. (2010). Effects of Causally Driven Cusp O+ Outflow on the Storm Time Magnetosphere-Ionosphere System Using a Multifluid Global Simulation. *J. Geophys. Res.* 115, n/a. doi:10.1029/2010ja015469

Carpenter, D. L. (1963). Whistler Evidence of a "Knee" in the Magnetospheric Ionization Density Profile. *J. Geophys. Res.* 68, 1675. doi:10.1029/jz068i006p01675

Chandler, M. O., Moore, T. E., and Waite, J. H. (1991). Observations of Polar Ion Outflows. *J. Geophys. Res.* 96, 1412. doi:10.1029/90ja02180

Chappell, C. R., Fields, S. A., Baugher, C. R., Hoffman, J. H., Hanson, W. B., Wright, W. W., et al. (1981). The Retarding Ion Mass Spectrometer on Dynamics Explorer-A. *Space Sci. Instrum.* 5, 477.

Chappell, C. R., Giles, B. L., Moore, T. E., Delcourt, D. C., Craven, P. D., and Chandler, M. O. (2000). The Adequacy of the Ionospheric Source in Supplying Magnetospheric Plasma. *J. Atmosph.Solar-Terrestr. Phys.* 62, 421. doi:10.1016/s1364-6826(00)00021-3

Chappell, C. R., Huddleston, M. M., Moore, T. E., Gilse, B. L., and Delcourt, D. C. (2008). Observations of the Warm Plasma Cloak and an Explanation of its Formation in the Magnetosphere. *J. Geophys. Res.* 113, A09206. doi:10.1029/2007ja012945

Chappell, C. R., Moore, T. E., and Waite, J. H., Jr. (1987). The Ionosphere as a Fully Adequate Source of Plasma for the Earth's Magnetosphere. *J. Geophysic. Res.* 92, 5896. doi:10.1029/ja092ia06p05896

Chappell, C. R. (1972). Recent Satellite Measurements of the Morphology and Dynamics of the Plasmasphere. *Rev. Geophys. Space Phys.* 10 (4), 951. doi:10.1029/rg010i004p00951

Cladis, J. B. (2000). Obserations of Centrifugal Acceleration during Compression of Magnetosphere. *Geophys. Res. Lett.* 27, 915. doi:10.1029/1999gl010737

Cladis, J. B. (1986). Parallel Acceleration and Transport of Ions from Polar Ionosphere to Plasma Sheet. *Geophys. Res. Lett.* 13, 893. doi:10.1029/gl013i009p00893

Cully, C. M., Donovan, E. F., Yau, A. W., and Arkos, G. G. (2003a). Akebono/Suprathermal Mass Spectrometer Observations of Low-Energy Ion Outflow: Dependence on Magnetic Activity and Solar Wind Conditions. *J. Geophys. Res.* 108, 1093. doi:10.1029/2001ja009200

Cully, C. M., Donovan, E. F., Yau, A. W., and Opgenoorth, H. J. (2003b). Supply of Thermal Ionospheric Ions to the Central Plasma Sheet. *J. Geophys. Res.* 108, 1092. doi:10.1029/2002ja009457

Delcourt, D. C., Moore, T. E., and Chappell, C. R. (1994). Contribution of Low-Energy Ionospheric Protons to the Plasma Sheet. *J. Geophys. Res.* 99 (A4), 5681. doi:10.1029/93ja02770

Delcourt, D. C., Sauvaud, J. A., and Moore, T. E. (1993). Polar Wind Ion Dynamics in the Magnetotail. *J. Geophys. Res.* 98, 9155. doi:10.1029/93ja00301

Engwall, E., Eriksson, A. I., Cully, C. M., Andre, M., Puhl-Quinn, P. A., Vaith, H., et al. (2009a). Survey of Cold Ionospheric Outflows I the Magnetotail. *Ann. Geophys.* 27, 3185. doi:10.5194/angeo-27-3185-2009

Engwall, E., Eriksson, A. I., Cully, C. M., Andre, M., Torbert, R., and Vaith, H. (2009b). Earth's Ionospheric Outflow Dominated by Hidden Cold Plasma. *Nat. Geosci* 2 (24), 24–27. doi:10.1038/ngeo387

Engwall, E., Eriksson, E. I., Andre, M., Dandouras, I., Paschmann, G., Quinn, J., et al. (2006). Low- Energy (Order 10 eV) Ion Flow in the Magnetotail Lobes Inferred from Spacecraft Wake Observations. *Geophys. Res. Lett.* 33, 6110. doi:10.1029/2005gl025179

Fok, M.-C. (1999). Storm Time Modeling of the Inner Plasma Sheet/Outer Ring Current. *J. Geophys. Res.* 104, 14557. doi:10.1029/1999ja900014

Fuselier, S. A., Mukherjee, J., Denton, M. H., Petrinec, S. M., Trattner, K. J., Toledo-Redondo, S., et al. (2019). High-Density O+ in Earth's Outer Magnetosphere and its Effect on Dayside Magnetopause Magnetic Reconnection. *JGR Space Phys.* 124, 10257–10269. doi:10.1029/2019JA027396

Giles, B. L., Chappell, C. R., Moore, T. E., Comfort, R. H., and Waite, J. H., Jr. (1994). Statistical Survey of Pitch Angle Distributions in Core (0-50 eV) Ions from Dynamics Explorer 1: Outflow in the Auroral Zone, Polar Cap, and Cusp. *J. Geophys. Res.* 99 (17), 483. doi:10.1029/94JA00864

Glocer, A., Tóth, G., Gombosi, T., and Welling, D. (2009). Modeling Ionospheric Outflows and Their Impact on the Magnetosphere: Initial Results. *J. Geophys. Res.* 114, A05216. doi:10.1029/2009ja014053

Gringauz, K. I. (1963). The Structure of the Ionized Gas Envelope of Earth from Direct Measurements in the USSR of Local Charged Particle Concentrations. *Planet. Space Sci.* 11, 281. doi:10.1016/0032-0633(63)90030-8

Gurgiolo, C., and Burch, J. L. (1982). DE-1 Observations of the Polar Wind—A Heated and an Unheated Component. *Geophys. Res. Lett.* 9, 945. doi:10.1029/gl009i009p00945

Haaland, S., Eriksson, A., Engwall, E., Lybekk, B., Nilsson, H., Pedersen, A., et al. (2012). Estimating the Capture and Loss of Cold Plasma from Ionospheric Outflow. *J. Geophys. Res.* 117, A07311. doi:10.1029/2012ja017679

Harris, K. K., and Sharp, G. W. (1969). Ogo 5 Ion Spectrometer. *Trans. IEEE Geosci. Electron.* 7 (2), 93. doi:10.1109/tge.1969.271328

Hoffman, J. H. (1970). Studies of the Composition of the Ionosphere with a Magnetic Deflection Mass Spectrometer. *Int. J. Mass. Spectrom. Ion Phys.* 4, 315–322. doi:10.1016/0020-7381(70)85047-1

Horwitz, J. L., Ho, C. W., Scarbro, H. D., Wilson, G. R., and Moore, T. E. (1994). Centrifugal Acceleration of the Polar Wind. *J. Geophys. Res.* 99 (15), 051. doi:10.1029/94JA00924

Huddleston, M. M., Chappell, C. R., Delcourt, D. C., Moore, T. E., Giles, B. L., and Chandler, M. O. (2005). An Examination of the Process and Magnitude of Ionospheric Plasma Supply to the Magnetosphere. *J. Geophys. Res.* 110 (12), 202. doi:10.1029/2004ja010401

Keika, K., Brandt, P. C., Ohtani, S., Mitchell, D. G., Min, K., Nose, M., et al. (2010). Mass-Independent Evolution of Energetic Neutral Atoms Energy Spectra During Storm Time Substorms: Implication for O+ Nonadiabatic Acceleration. *J. Geophys.Res: Space Phys.* 115, A00I12. doi:10.1029/2010ja015889

Keika, K., Kistler, L. M., and Brandt, P. C. (2013). Energization of O+ Ions in the Earth's Inner Magnetosphere and the Effects on Ring Current Buildup: A Review of Previous Observations and Possible Mechanisms. *J. Geophys. Res: space Phys.* 118, 4441. doi:10.1002/jgra.50371

Kistler, L. M., Mouikis, C. G., Klecker, B., and Dandouras, I. (2010). Cusp as a Source for Oxygen in the Plasma Sheet during Geomagnetic Storms. *J. Geophys. Res.* 115, A03209. doi:10.1029/2009ja014838

Kitamura, N. (2019). *Cold Ion Observations by MMS at the Lobe and Near PSBL*. Santa Fe, NM: GEM Meeting.

Liao, J., Kistler, L. M., Mouikis, C. G., Klecker, B., Dandouras, I., and Zhang, J.-C. (2010). Statistical Study of O+ Transport from the Cusp to the Lobes with Cluster CODIF Data. *J. Geophys. Res.* 115, A00J15. doi:10.1029/2010ja015613

Liemohn, M. W., Moore, T. E., Craven, P. D., Maddox, W., Nagy, A. F., and Kozyra, J. U. (2005). Occurrence Statistics of Cold, Streaming Ions in the Near-Earth Magnetotail: Survey of Polar-TIDE Observations. *J. Geophys. Res.* 110, A07211. doi:10.1029/2004ja010801

Lockwood, M., Waite, J. H., Jr., Moore, T. E., Johnson, J. F. E., and Chappell, C. R. (1985). A New Source of Suprathermal O+ Ions Near the Dayside Polar Cap Boundary. *J. Geophys. Res.* 90, 4099. doi:10.1029/ja090ia05p04099

Moore, T. E., Chappell, C. R., Chandler, M. O., Craven, P. D., Giles, B. L., Pollock, C. J., et al. (1997). High Altitude Observations of the Polar Wind. *Science* 277, 349. doi:10.1126/science.277.5324.349

Moore, T. E., Chappell, C. R., Chandler, M. O., Fields, S. A., Pollock, C. J., Reasoner, D. L., et al. (1995). The Thermal Ion Dynamics Experiment and Plasma Source Instrument. *Space Sci. Revs* 71, 409. doi:10.1007/bf00751337

Moore, T. E., and Delcourt, D. C. (1995). The Geopause. *Rev. Geophys.* 33 (2). doi:10.1029/95RG00872

Moore, T. E., Fok, M.-C., Chandler, M. O., Chappell, C. R., Christon, S. P., Delcourt, D. C., et al. (2005). Plasma Sheet and (Nonstorm) Ring Current Formation from Solar and Polar Wind Sources. *J. Geophys. Res.* 110, A02210. doi:10.1029/2004ja010563

Mouikis, C. G., Kistler, L. M., Liu, Y. H., Klecker, B., Korth, A., and Dandouras, I. (2010). H+ and O+ Content of the Plasma Sheet at 15-19 Re as a Function of Geomagnetic and Solar Activity. *J. Geophys. Res.* 115, A00J16. doi:10.1029/2010ja015978

Nagai, T., Waite, J. H., Jr., Green, J. L., Chappell, C. R., Olsen, R. C., and Comfort, R. H. (1984). First Measurements of Supersonic Polar Wind in the Polar Magnetosphere. *Geophys. Res. Lett.* 11, 669. doi:10.1029/gl011i007p00669

Parks, G. K., and Winckler, J. R. (1968). Acceleration of Energetic Electrons Observed at the Synchronous Altitude during Magnetospheric Substorms. *J. Geophys. Res.* 73, 5786. doi:10.1029/ja073i017p05786

Schunk, R. W., Demars, H. G., and Soijka, J. J. (2005). Propagating Polar Wind Jets. *JASTP* 67, 357–364. doi:10.1016/j.jastp.2004.09.005

Schunk, R. W., and Sojka, J. J. (1997). Global Ionosphere-Polar Wind System during Changing Magnetic Activity. *J. Geophys. Res.* 102 (11), 62. doi:10.1029/97ja00292

Shelley, E. G., Johnson, R. G., and Sharp, R. D. (1972). Satellite Observations of Energetic Heavy Ions during a Geomagnetic Storm. *J. Geophys. Res.* 77, 6104. doi:10.1029/ja077i031p06104

Shelley, E. G., Peterson, W. K., Ghielmetti, A. G., and Geiss, J. (1982). The Polar Ionosphere as a Source of Energetic Magnetospheric Plasma. *Geophys. Res. Ltrs.* 9 (9), 941–944. doi:10.1029/gl009i009p00941

Sorathia, K. A., Merkin, V. G., Ukhorskiy, A. Y., Allen, R. C., Nykyri, K., and Wing, S. (2019). Solar Wind Ion Entry into the Magnetosphere during Northward IMF. *J. Geophys. Res.* 124, 5461–5481. doi:10.1029/2019JA026728

Strangeway, R. J., Ergun, E. R., Su, Y.-J., Carlson, C. W., and Elphic, R. C. (2005). Factors Controlling Ionospheric Outflows as Observed at Intermediate Altitudes. *J. Geophys. Res.* 110, A03221. doi:10.1029/2004JA010829

Su, Y. J., Horwitz, J. L., Moore, T. E., Giles, B. L., Chandler, M. O., Craven, P. D., et al. (1998). Polar Wind Survey with the Thermal Ion Dynamics Experiment/Plasma Source Instrument Suite Aboard POLAR. *J. Geophys. Res.* 103 (29), 29305–29337. doi:10.1029/98ja02662

Toledo-Redondo, S., André, M., Aunai, N., Chappell, C. R., Dargent, J., Fuselier, S. A., et al. (2021). Impacts of Ionospheric Ions on Magnetic Reconnection and Earth's Magnetosphere Dynamics. *Rev. Geophys.* 59, e2020RG000707. doi:10.1029/2020RG000707

Tsyganenko, N. A. (1989). A Magnetospheric Magnetic Field Model with a Warped Tail Current Sheet, Planet. *Space Sci.* 37, 5.

Welling, D. T., and Ridley, A. J. (2010). Exploring Sources of Magnetospheric Plasma Using Multispecies MHD. *J. Geophys. Res.* 115, A04201. doi:10.1029/2009ja014596

Welling, D. T., Jordanova, V. K., Zaharia, S. G., Glocer, A., and Toth, G. (2011). The Effects of Dynamic Ionospheric Outflow on the Ring Current. *J. Geophys. Res.* 116, n/a. doi:10.1029/2010ja015642

Winglee, R. M. (2000). Mapping of Ionospheric Outflows into the Magnetosphere for Varying IMF Conditions. *J. Atmos. Terr. Phys.* 62, 527. doi:10.1016/s1364-6826(00)00015-8

Yau, A. W., and Andre, M. (1997). Sources of Ion Outflow in the High Latitude Ionosphere. *Space Sci. Rev.* 80 (1), 1–25. doi:10.1007/978-94-009-0045-5_1

Yau, A. W., Shelley, E. G., Peterson, W. K., and Lenchyshyn, L. (1985). Energetic Auroral and Polar Ion Outflow at DE 1 Altitudes: Magnitude, Composititon, Magnetic Activity Dependence, and Long-Term Variations. *J. Geophys. Res.* 90, 8417. doi:10.1029/ja090ia09p08417

Conflict of Interest: The authors declare that the research was conducted in the absence of any commercial or financial relationships that could be construed as a potential conflict of interest.

frontiers in Astronomy and Space Sciences

ORIGINAL RESEARCH
published: 29 October 2021
doi: 10.3389/fspas.2021.745264

Quantification of Cold-Ion Beams in a Magnetic Reconnection Jet

Yu-Xuan Li[1], Wen-Ya Li[2], Bin-Bin Tang[2]*, C. Norgren[3], Jian-Sen He[1], Chi Wang[2], Qiu-Gang Zong[1], S. Toledo-Redondo[4,5], M. André[6], C. Chappell[7], J. Dargent[8], S. A. Fuselier[9,10], A. Glocer[11], D. B. Graham[6], S. Haaland[12,13,14], L. Kistler[15], B. Lavraud[5,16], T. E. Moore[10], P. Tenfjord[3], S. K. Vines[17] and J. Burch[9]*

[1]Institute of Space Physics and Applied Technology, Peking University, Beijing, China, [2]State Key Laboratory of Space Weather, National Space Science Center, Chinese Academy of Sciences, Beijing, China, [3]Space Plasma Physics Group, Department of Physics and Technology, University of Bergen, Bergen, Norway, [4]Department of Electromagnetism and Electronics, University of Murcia, Murcia, Spain, [5]Institut de Recherche en Astrophysique et Planétologie, Université de Toulouse, CNRS, UPS, CNES, Toulouse, France, [6]Swedish Institute of Space Physics, Uppsala, Sweden, [7]Physics and Astronomy Department, Vanderbilt University, Nashville, TN, United States, [8]Physics Department E. Fermi, University of Pisa, Pisa, Italy, [9]Southwest Research Institute, San Antonio, TX, United States, [10]Department of Physics and Astronomy, University of Texas at San Antonio, San Antonio, TX, United States, [11]NASA Goddard Space Flight Center, Greenbelt, MD, United States, [12]Max-Planck Institute for Solar Systems Research, Göttingen, Germany, [13]Birkeland Center for Space Science, University of Bergen, Bergen, Norway, [14]The University Centre in Svalbard, Longyearbyen, Svalbard, [15]Institute for the Study of Earth Oceans and Space, University of New Hampshire, Durham, NH, United States, [16]Laboratoire d'Astrophysique de Bordeaux, Univ. Bordeaux, Pessac, France, [17]Applied Physics Laboratory, Johns Hopkins University, Laurel, MD, United States

OPEN ACCESS

Edited by:
Olga V. Khabarova, Institute of Terrestrial Magnetism Ionosphere and Radio Wave Propagation (RAS), Russia

Reviewed by:
Elena E. Grigorenko, Space Research Institute (RAS), Russia
Tieyan Wang, Rutherford Appleton Laboratory, United Kingdom

***Correspondence:**
Wen-Ya Li
wyli@spaceweather.ac.cn
Bin-Bin Tang
bbtang@spaceweather.ac.cn

Specialty section:
This article was submitted to Space Physics, a section of the journal Frontiers in Astronomy and Space Sciences

Received: *21 July 2021*
Accepted: *11 October 2021*
Published: *29 October 2021*

Citation:
Li Y-X, Li W-Y, Tang B-B, Norgren C, He J-S, Wang C, Zong Q-G, Toledo-Redondo S, André M, Chappell C, Dargent J, Fuselier SA, Glocer A, Graham DB, Haaland S, Kistler L, Lavraud B, Moore TE, Tenfjord P, Vines SK and Burch J (2021) Quantification of Cold-Ion Beams in a Magnetic Reconnection Jet. Front. Astron. Space Sci. 8:745264. doi: 10.3389/fspas.2021.745264

Cold (few eV) ions of ionospheric origin are widely observed in the lobe region of Earth's magnetotail and can enter the ion jet region after magnetic reconnection is triggered in the magnetotail. Here, we investigate a magnetotail crossing with cold ions in one tailward and two earthward ion jets observed by the Magnetospheric Multiscale (MMS) constellation of spacecraft. Cold ions co-existing with hot plasma-sheet ions form types of ion velocity distribution functions (VDFs) in the three jets. In one earthward jet, MMS observe cold-ion beams with large velocities parallel to the magnetic fields, and we perform quantitative analysis on the ion VDFs in this jet. The cold ions, together with the hot ions, are reconnection outflow ions and are a minor population in terms of number density inside this jet. The average bulk speed of the cold-ion beams is approximately 38% larger than that of the hot plasma-sheet ions. The cold-ion beams inside the explored jet are about one order of magnitude colder than the hot plasma-sheet ions. These cold-ion beams could be accelerated by the Hall electric field in the cold ion diffusion region and the shrinking magnetic field lines through the Fermi effect.

Keywords: cold ions, plasma moments, acceleration, magnetic reconnection, Earth's magnetotail

1 INTRODUCTION

Cold (few eV) ions of ionospheric origin are widely present in the Earth's magnetosphere (Chappell et al., 1980; Moore et al., 1997; Cully et al., 2003). In the lobes of the magnetosphere, spacecraft can be positively charged to several tens of volts due to photoelectron emissions. The positive potential prevents cold ions from reaching onboard ion instrument. With large-scale convective motion, for example, magnetopause fluctuation or plasma-sheet flapping, cold ions can be accelerated via the **E**×**B** drift to overcome the positive spacecraft potential (Sauvaud et al., 2004), and be detected by an ion instrument. Besides direct measurement with particle instruments, cold ions can also be inferred

by a technique based on the wake signal of a charged spacecraft in a supersonic ion flow (Engwall et al., 2009; Li et al., 2013; André et al., 2015). Observational statistics show that cold ions dominate the plasma density in large regions of the nightside magnetosphere (e.g., lobe region) and polar regions (André and Cully, 2012). At times, the cold ions can also dominate in the dayside magnetosphere. Cold ions can play an important role in the solar wind-magnetosphere-ionosphere coupling system, including the terrestrial plasma escape and circulation and the magnetotail dynamics (Welling et al., 2015; Kistler and Mouikis, 2016; Yamauchi, 2019).

Magnetic reconnection is a fundamental and universal process to convert energy stored in the magnetic field into kinetic and thermal energies of charged particles (Priest and Forbes, 2007; Yamada et al., 2010). Magnetic reconnection is the major transport mechanism of mass, energy, and magnetic flux in the solar wind-magnetosphere coupling system, and is the predominant cause of the geomagnetic activity. In the past decade, the effects of cold ions on magnetic reconnection at the dayside magnetopause and in the magnetotail have been extensively analyzed via using *in-situ* measurements from multiple spacecraft missions (Wang et al., 2014; Toledo-Redondo et al., 2015; André et al., 2016; Li et al., 2017; Toledo-Redondo et al., 2021) and types of numerical simulation models (Aunai et al., 2011; Divin et al., 2016; Tenfjord et al., 2019; Dargent et al., 2019, 2020). At the dayside magnetopause, magnetic reconnection is typically asymmetric due to the large differences in plasma and magnetic field conditions between the magnetosheath and the magnetosphere. The gyroradii and the inertial lengths of the magnetosheath plasmas usually determine the two kinetic scales of the diffusion region, namely, ion and electron diffusion regions (Yamada et al., 2010). With the presence of cold-ion inflow from the magnetospheric side, cold ions bring a new diffusion region between the usual ion and electron diffusion regions (Toledo-Redondo et al., 2016a; Divin et al., 2016), and can push the reconnection jet towards the magnetosheath side (Cassak and Shay, 2007; Walsh et al., 2014). Li et al. (2017) present the first observation of the cold-ion outflows throughout the entire reconnection region via investigating the three-dimensional (3D) ion velocity distribution functions (VDFs). Cold-ion jets with high parallel velocities are formed on the magnetosheath side of the reconnection exhaust, and those cold ions remain relatively cold compared with the magnetosheath ions. Li et al. (2017) suggest that those fast cold-ion jets originate from the cold-ion inflow close to the X line, while the acceleration mechanism lacks detailed analysis.

In the magnetotail, the magnetic fields are oppositely directed on each side of the plasma sheet, and the plasma-sheet plasmas are hot with ion temperature of several to tens of keV. Magnetic reconnection is symmetric with homogeneous hot ion inflows from both sides. The plasma sheet boundary layer (PSBL) and lobe region always contain a certain amount of cold ions of ionospheric origin, which can affect the reconnection process in the magnetotail. One prominent feature is that cold ions create highly structured ion VDFs far from the Maxwellian shape. Among these distributions, counter-streaming cold-ion beams along the direction normal to the current sheet are frequently observed in the ion diffusion region both in observations and simulations (Fujimoto et al., 1996; Hoshino et al., 1998; Nagai et al., 1998; Shay et al., 1998; Wygant et al., 2005; Divin et al., 2016; Dai et al., 2021). The counter-streaming cold-ion beams are suggested to be accelerated by the Hall electric field along the normal direction at the separatrix, which is mostly along **Z** direction of Geocentric Solar Ecliptic (GSE) coordinates. The electric potential well across the separatrix is $B_X^2/2q_eN_0\mu_0$, where B_X and N_0 are the reconnection magnetic field and plasma number density in the inflow, q_e is the unit of charge and μ_0 is the magnetic permeability of free space (Wygant et al., 2005; Divin et al., 2016; Zaitsev et al., 2021). This electric potential can accelerate cold ions to the inflow Alfvén speed $V_A = B_X/\sqrt{\mu_0 m_i N_0}$, when the width of the separatrix is comparable to the cold-ion gyroradius. Using a hybrid simulation model, Aunai et al. (2011) show that the angular aperture of the potential well and the bouncing motion between the separatries make the cold ions transfer the kinetic energy gained from the V_Z component to V_X.

Besides the acceleration by the Hall electric field in the ion diffusion region, the Fermi mechanism (slingshot effect) and the reconnection electric field can also be important for cold-ion acceleration in the reconnection exhaust. Several studies report counter-streaming cold-ion beams observed in bursty bulk flows (BBFs) and analyze acceleration mechanisms and ion anisotropic instabilities associated with these beams (Eastwood et al., 2015; Hietala et al., 2015; Birn et al., 2017; Runov et al., 2017; Xu et al., 2019). BBFs are widely interpreted as magnetic reconnection jets (Angelopoulos et al., 1992; Nagai et al., 1998; Birn et al., 2011) and can transport significant amount of magnetic fluxes and plasmas towards Earth (Baumjohann et al., 1990; Angelopoulos et al., 1992, 1994). Eastwood et al. (2015) find that counter-streaming beams are sourced from the thermal population in the preexisting plasma sheet and are accelerated by the reconnection electric field. Birn et al. (2017) show that the beam ions are from the low-energy lobe regions. These beams are firstly accelerated by the **E**×**B** drift motion and then by the slingshot effect of the earthward convecting BBF. A similar process is also described by Xu et al. (2019). In the previous studies, the counter-streaming cold-ion beams are mostly observed near the front edge of the reconnection jet, and quantitative studies analyzing the acceleration are primarily via numerical simulations. The existence and dynamics of the cold ions in an entire reconnection jet still lack quantitative analysis using *in-situ* observations. In this study, we perform a more comprehensive survey of ion VDFs in a magnetotail crossing by the Magnetospheric Multiscale (MMS) spacecraft. Various types of ion VDFs with cold-ion beams are observed inside a magnetic reconnection jet, and plasma partial moments of the cold ions are computed to investigate their dynamics through the reconnection process.

2 OBSERVATIONS

In-situ observations from NASA's MMS mission (Burch et al., 2016) are utilized for this study. MMS was launched on March 13,

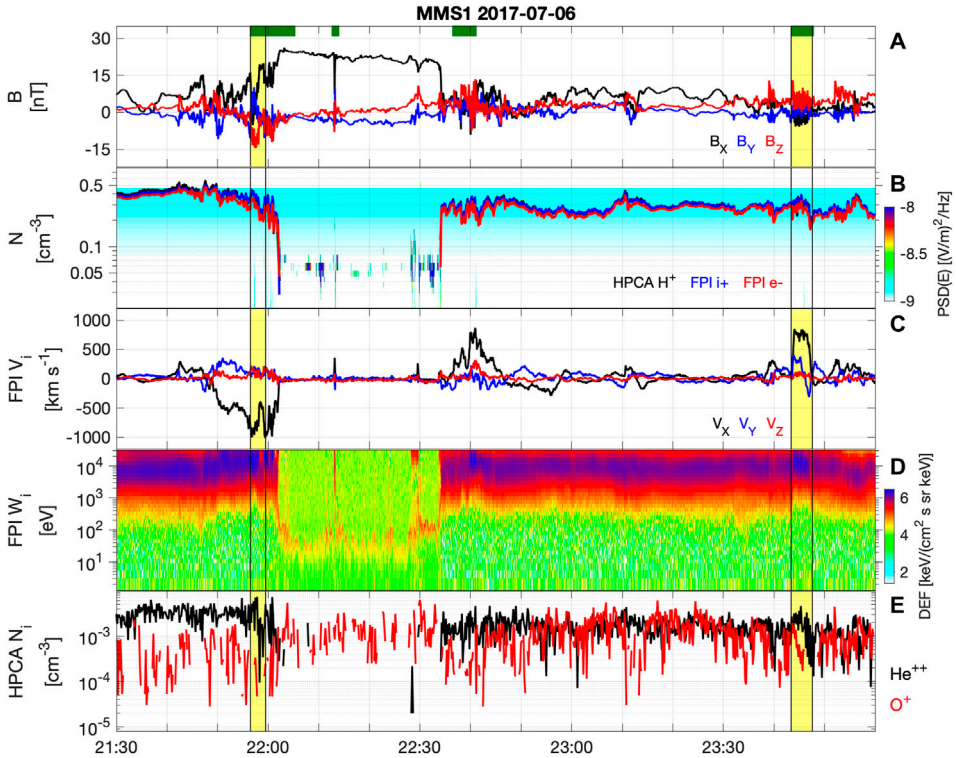

FIGURE 1 | MMS observation of the Earth's magnetotail on July 06, 2017. MMS1 data of **(A)** magnetic field **B**, **(B)** number densities of hydrogen (H^+, black) from HPCA, all ions (blue) and electrons (red) from FPI and electron number density derived from the Langmuir waves observed by EDP, **(C)** ion bulk velocity $\mathbf{V}_i$ from FPI, **(D)** FPI ion omnidirectional differential energy flux, **(E)** number densities of He^{++} (black) and O^+ (red) ions from HPCA. All vectors are presented in GSE coordinates, which are close to Geocentric Solar Magnetospheric (GSM) coordinates in this event. The horizontal green bars in the top of **(A)** denote the burst-mode time intervals, and detailed analysis of the ion VDFs in the two yellow-shaded intervals are presented in the following figures.

2015 and consists of four identical spacecraft designed to study the kinetic-scale physics of magnetic reconnection in the Earth's magnetosphere. In this study, we use magnetic field data from the FluxGate Magnetometer (FGM) (Russell et al., 2016) and electric field data from the Electric Double Probe (EDP) (Ergun et al., 2016; Lindqvist et al., 2016). The ion data are from the Fast Plasma Investigation (FPI) (Pollock et al., 2016) sampled at 4.5 s for the fast mode and 0.15 s for the burst mode, and also, from the mass-resolved instrument Hot Plasma Composition Analyzer (HPCA) (Young et al., 2016) at 10 s resolution.

We investigate an MMS magnetotail crossing from 21:30:00 to 24:00:00 UT on July 06, 2017. The four spacecraft moved from [−24.6, −0.8, 5.2] R_E (Earth radii) to [−24.5, −1.4, 5.4] R_E (GSE) during this time interval. Owing to a small spacecraft separation (~15 km), observations from the four spacecraft are nearly identical, and thus, we show results primarily from MMS1. An overview of the MMS1 observations is presented in **Figure 1**, and the data are in fast mode. The panels from top to bottom show 1) magnetic field **B**, 2) number densities of ions and electrons, 3) ion bulk velocities from FPI, 4) FPI ion omnidirectional differential energy flux, and 5) number densities of He^{++} and O^+ ions from HPCA. In **Figure 1B**, the number densities of H^+ from HPCA, all ions from FPI and electrons from FPI are shown in black, blue and red, respectively. The three curves almost overlap with each other, indicating reliable number density results. The MMS fleet is initially located in the plasma sheet, characterized by weak magnetic field (**Figure 1A**) and high-density (~0.5 cm^{-3}) and hot (~4,500 eV) ions. From 21:49:00 to 22:02:00 UT, MMS1 observes a strong tailward ion flow, with a peak V_X reaching -1,000 km s^{-1}. Such a strong ion flow indicates ongoing reconnection and that the spacecraft are located tailward of the reconnection X line. In this tailward ion jet, the B_X component is mostly positive, indicating that MMS cross the northern part of the ion jet.

At 22:02:00 UT, we identify a separatrix of the reconnection exhaust, where B increases, plasma number density decreases, ion bulk velocity decreases, and energetic particles vanish (see **Supplementary Figure S1** in **Supplementary Material** for more details). Then, MMS1 enters the lobe region until 22:34:00 UT. As shown by the ion energy flux in **Figure 1D**, cold ions of ionospheric origin, with ~10 eV thermal energy, are present in the lobe region, while their total energy can reach 100 eV due to the **E**×**B** drift motion. In the lobe, the penetrating radiation leads to a nearly constant background from the lowest to the highest energy channels in the FPI ion measurement unit (Gershman et al., 2019), as seen by the green fluxes in **Figure 1D**. Thus, the FPI ion number density from the integral over the whole energy range is overestimated. Besides, the FPI electron measurement unit cannot provide reliable electron moment data in the lobe because of the low thermal energy and the photoelectron contamination (Gershman et al., 2019). So, we take the

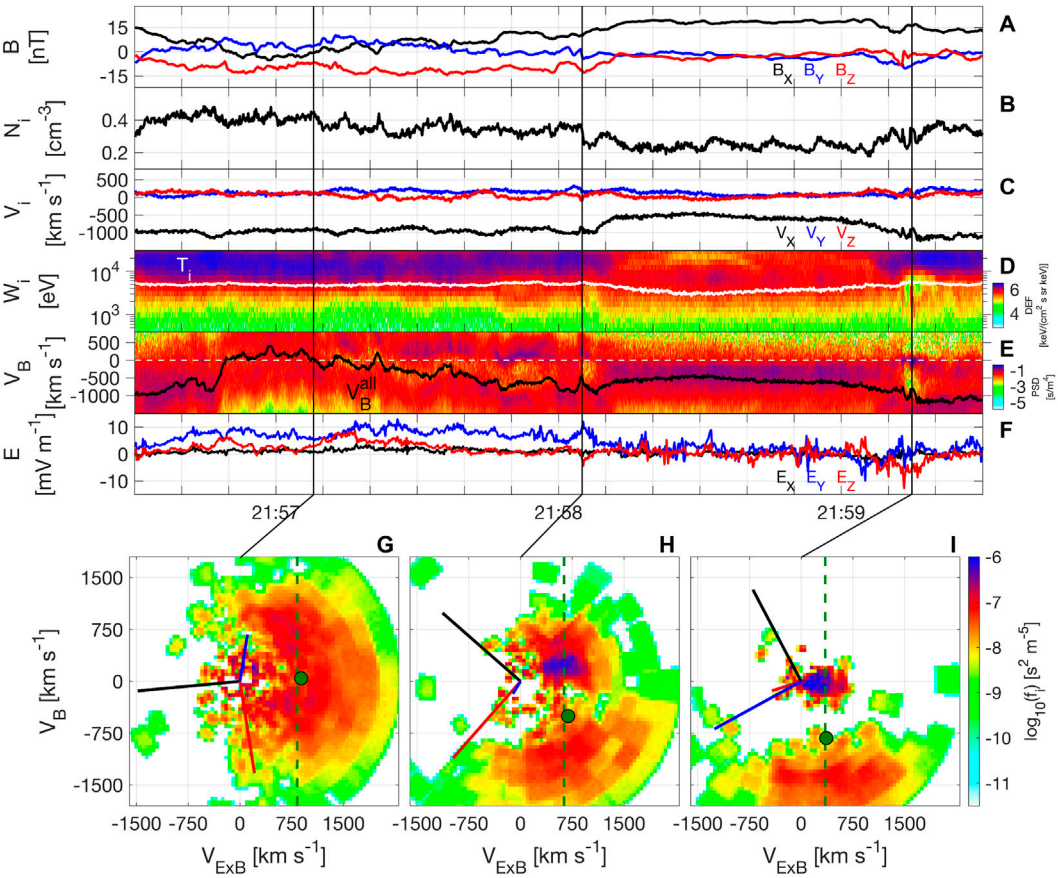

FIGURE 2 | Cold ions inside the tailward ion jet. **(A) B**. **(B)** N_i. **(C)** $\mathbf{V}_i$. **(D)** FPI ion omnidirectional differential energy flux with ion temperature (white curve). **(E)** Reduced ion VDF integrated over the directions perpendicular to the magnetic field. The black solid curve shows the parallel ion bulk speed V_B^{all} of all ions, and the white dashed line denotes $V_B = 0$. **(F)** Electric field **E**. **(G)–(I)** Two-dimensional (2D) reduced ion VDFs in the $\mathbf{V}_{ExB}$-$\mathbf{V}_B$ plane at times indicated by the three vertical lines in **(A)–(F)**. In **(G)–(I)**, the green dots represent the ion bulk velocities, and the vertical green dashed lines show the electric-field drift speeds ($|\mathbf{E}\times\mathbf{B}/B^2|$). The GSE-X (black), Y (blue) and Z (red) directions normalized by 1,500 km s^{-1} are projected in **(G)–(I)**.

number density (0.03–0.05 cm^{-3}) estimated from the waves at the electron plasma frequencies, as illustrated by the color-coded spectrum in **Figure 1B**. In the lobe, oxygen ions measured by HPCA have number densities about 0.0005–0.002 cm^{-3} (**Figure 1E**), and hydrogen is thus the primary ion species in terms of number density. From 22:13:04 to 22:13:15 UT, MMS cross a separatrix of the reconnection exhaust back and forth quickly (see **Supplementary Figure S2** in **Supplementary Material** for details). Based on the observations during this time interval, Alm et al. (2018) analyzed the role of cold ions in the separatrix layer. They find that the cold ions account for ~ 30% of the total ion number density and can significantly influence the Hall physics of reconnection. After 22:34:00 UT, MMS1 crosses back to the plasma sheet and sees two strong earthward ion jets, with aV_X peak reaching 860 km s^{-1}. O^+ ions, as tracers of cold ionospheric ions, are continuously observed inside the plasma sheet shown in **Figure 1**, and have similar number densities with those in the lobe. Meanwhile, He^{++} ions can be used as tracers of solar wind ions, and are also continuously observed in the plasma sheet. Thus, both the ionospheric and solar-wind ions are the ion sources of the plasma sheet in our event, even through the two sources are indistinguishable from the FPI ion energy flux panel (**Figure 1D**). We explore the 3D ion VDFs in the tailward and earthward reconnection jets and characterize different types of ion VDFs with cold-ion beams. In the following, we present results from the two time intervals indicated by the yellow-shaded bars in **Figure 1**.

Figures 2A–F present an overview of the tailward ion jet in the time interval indicated by the left yellow-shaded bar in **Figure 1**. Here, burst-mode data are used. In this jet, V_X varies between −1,240 km s^{-1} and −430 km s^{-1}, and ions with distinct energy fluxes are all above 500 eV in the spacecraft frame (**Figure 2D**). **Figure 2E** shows the phase space density of the reduced ion VDF projected on to the magnetic field directions, and the black curve represents the parallel bulk velocity $\mathbf{V}_B^{all}$ of all ions. One can clearly see complicated structures in this reduced ion VDF panel. To categorize the ions in this tailward jet, we perform a systematic survey of all the ion VDFs in the time interval of **Figure 2** and find three types of ion VDFs inside. **Figures 2G–I** show 2D reduced ion VDF examples in the $\mathbf{V}_{E\times B}$-$\mathbf{V}_B$ plane, as they clearly show the overall structures in the distribution functions. At times like 21:57:08 UT, $\mathbf{V}_B^{all}$ is close to the ion VDF peaks, denoting that there exists only a single energetic ion

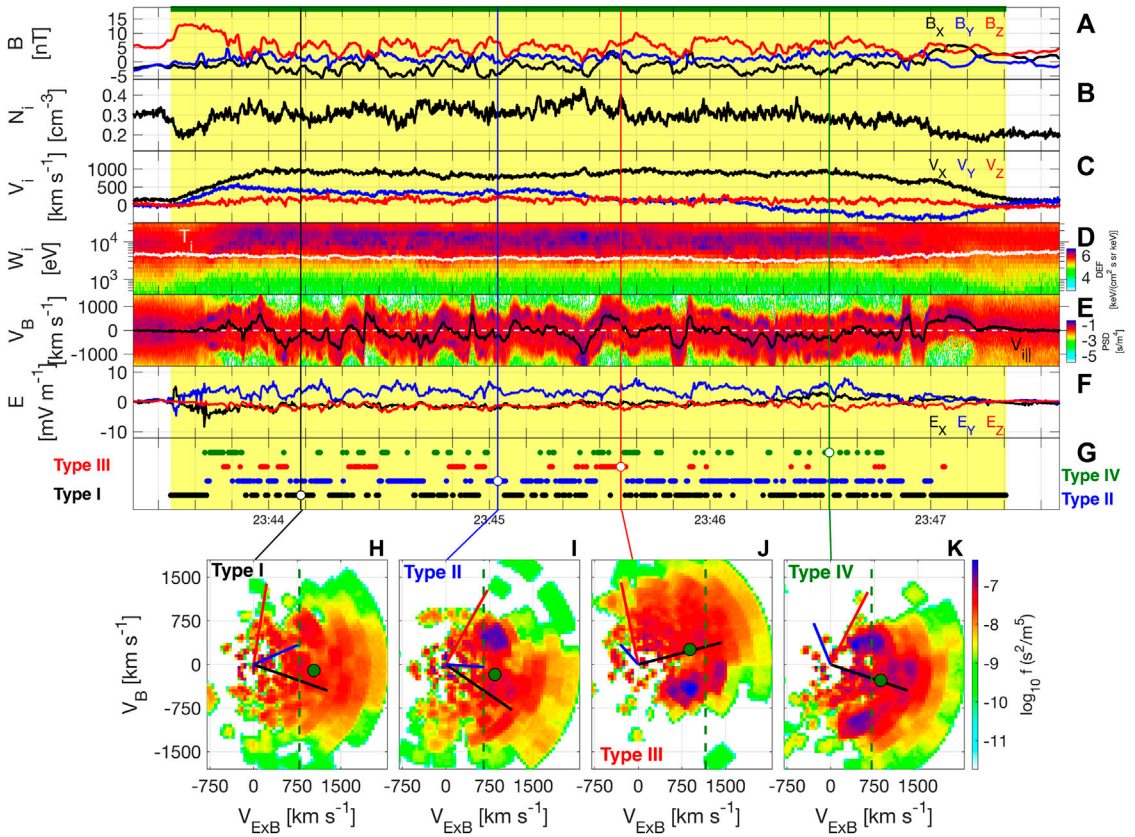

FIGURE 3 | Four types of ion velocity distribution functions (VDFs) in the earthward ion jet. **(A) B**. The green horizontal bar denotes the ion jet interval. **(B)** N_i. **(C)** $\mathbf{V}_i$. **(D)** FPI ion omnidirectional differential energy flux with ion temperature (white curve). **(E)** Reduced ion VDF integrated over the directions perpendicular to the magnetic field. The black solid curve shows the parallel ion bulk speed $V_{i\|}$, and the white dashed line denotes $V_{i\|} = 0$. **(F)** Electric field **E**. **(G)** Ion VDF types inside the ion jet. **(H)–(K)** Examples of the four-type ion VDFs at times indicated by the four vertical lines in **(A)–(G)**. **(H)–(K)** are in the same format with **Figures 2G–I**.

population of plasma-sheet origin (see **Figure 2G**). The hot population in **Figure 2G** has a temperature of 4.6 keV and follows **E**×**B** drift motion (green vertical dashed line), with negligible $\mathbf{V}_B$. In GSE coordinates, it moves predominantly along -**X** direction. From 21:59:12 to 21:59:19 UT, MMS1 observes two distinct ion populations in the FPI ion energy flux plot (**Figure 2D**). One energetic population has energy above 8 keV and originates from the plasma sheet. The other population has energies below 5 keV. An example of the ion VDFs within this interval is presented in **Figure 2I**. At this time, the magnetic field is mostly along the +**X** direction (**Figure 2A**), and its magnitude is close to that in the lobe (see **Figure 1**). The electric field is dominated by the -**Z** component, indicating Hall electric field in the northern separatrix layer of the magnetotail reconnection in the magnetotail (Wygant et al., 2005; Eastwood et al., 2007). The two ion populations have the same **E**×**B** drift velocity. The hot population has a large negative $\mathbf{V}_B$, and its bulk velocity is predominantly along the -**X** direction in GSE coordinates. The cold population has negligible $\mathbf{V}_B$ and moves along the -**Y** direction. Those cold ions can modify the balance of the Hall electric field at the separatrix, which has been extensively analyzed by previous studies using *in-situ* data (Toledo-Redondo et al., 2015; André et al., 2016; Alm et al., 2018) and numerical simulation models (Dargent et al., 2017; Toledo-Redondo et al., 2018).

From 21:57:12 UT to 21:58:10 UT, MMS1 also observes two distinct populations in the reduced ion VDFs shown in **Figure 2E**, even though the two populations are not distinguishable from the FPI ion energy flux (**Figure 2D**). **Figure 2H** displays an example of the ion VDFs in this time interval. The properties of the hot population are similar to those shown in **Figure 2I**. The cold population follows **E**×**B** drift (~630 km s^{-1}) motion and has a small (~200 km s^{-1}) positive $\mathbf{V}_B$. Its bulk velocity is predominantly along the -**Z** direction in GSE. These cold-ion beams may originate from the northern lobe. A small bulk speed (~660 km s^{-1}) of this cold population suggests that those beams may be not from the cold-ion inflow close to the X line. They may experience an acceleration process as discussed previously by Birn et al. (2017). The cold ions are probably accelerated by the **E**×**B** drift motion when crossing a distant separatrix, and are further accelerated by the Fermi mechanism as the cold ions convect together with the shrinking magnetic field lines. Another prominent feature between the cold populations shown in **Figures 2H,I** is that the cold population in **Figure 2H** is clearly thermalized, and we discuss that in the following section. In the earthward ion jet between 22:36:00 UT and 22:47:00 UT,

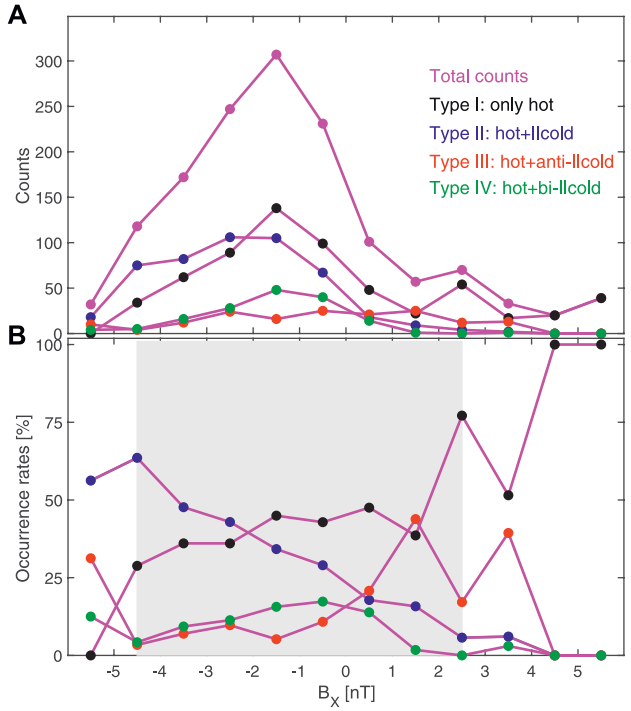

FIGURE 4 | Statistics of the four types of ion VDFs along B_X. **(A)** Counts profiles along B_X. The magenta curve shows the total counts, and the rest of the curves show the four types of VDFs. **(B)** Occurrence rates. The gray shadow highlights the interval with total counts over 50.

MMS observe similar features of the ion VDFs as those presented in **Figure 2**.

MMS see much more complicated features of cold-ion beams in the earthward ion jet between 23:43:23 UT and 23:47:53 UT (denoted by the right yellow-shaded bar in **Figure 1**). **Figures 3A–F** display a detailed overview of this ion jet using burst-mode data. MMS are originally located in the stagnant plasma sheet. When a dipolarization front (Nakamura et al., 2002; Runov et al., 2009; Fu et al., 2013) arrives at MMS at ~23:43:34 UT, the plasma density drops from 0.31 cm^{-3} to 0.20 cm^{-3} and the magnetic field B_Z component increases from 5 to 13 nT. The earthward flow speed subsequently increases to its maximum values, with aV_X peak reaching 1,040 km s^{-1}. This kind of fast ion flow is frequently interpreted as an earthward bursty bulk flow (BBF) driven by magnetic reconnection with an X line located tailward of the spacecraft. In **Figure 3**, we use a yellow-shaded bar to highlight the BBF or the jet interval. The average N_i of the jet is approximately 0.29 cm^{-3}, which is similar to that of the nearby plasma sheet. The average T_i is 3.8 keV, with a small temperature anisotropy ($T_{i\|}/T_{i\perp}$ ~0.92). After a detailed survey of all the ion VDFs, we find four types of ion VDFs inside the jet shown in **Figure 3**: Type I consists of only a single hot plasma-sheet population (see an example shown by **Figure 3H**), Type II consists of a hot population and a cold population with a positive $\mathbf{V}_B$ (see **Figure 3I**), Type III consists of a hot population and a cold population with a negative $\mathbf{V}_B$ (see **Figure 3J**), and Type IV consists of a hot population with counter-streaming cold populations (see **Figure 3K**). We categorize all the ion VDFs of this earthward ion jet, and the results are presented by colored dots in **Figure 3G**. In **Figures 3H–K**, the green dots denote the projected ion bulk velocities in the $V_{E\times B}$-V_B plane, and the green vertical dashed lines represent the **E**×**B** drift speeds. The small discrepancy between the two speeds is likely from the errors (0.5–1.0 mV m^{-1}) in electric field (Lindqvist et al., 2016) or could be caused by weak demagnetization of the ions. In GSE coordinates, all ions propagate earthward (illustrated by the black lines in **Figures 3H–K**). The large positive and negative V_B components of the cold ions correspond to the large positive and negative V_Z components (**Figures 3I–K**), respectively.

Previous studies like Eastwood et al. (2015) and Xu et al. (2019) explored the kinetic behavior of counter-streaming cold ions at the leading edges of the reconnection jets, with particular focus on the vicinity of dipolarization front. The cold-ion beams investigated in their works may originate from ions in the preexisting plasma sheet or the ionosphere and are swept up directly by a dipolarization front. In our study, we do not find the existence of isolated cold-ion beams in the region close to the dipolarization front, which could be due to the phase-space mixing by cold-ion thermalization. We find four types of ion VDFs widely distributed over the entire observed part of the jet. The cold-ion beams have total energies all above ~3 keV and mix together with the plasma-sheet hot ions in the spectrogram of the differential energy flux (**Figure 3D**), and one can only distinguish cold ions in three-dimensional VDFs. This is different from the cold ions reported in Eastwood et al. (2015) and Xu et al. (2019), where the total energies of cold ions are lower than those of hot ions and one can easily see them in the spectrograms of the differential energy fluxes.

In the magnetotail, the B_X component can be used as a guide to determine the normal distance to the plasma-sheet neutral line (B_X = 0). **Figure 4A** shows the count profiles of the four types of ion VDFs along B_X. MMS spend most of the time in the southern exhaust, and most of the counts are therefore in the negative B_X region, where Type I and Type II VDFs clearly dominate. **Figure 4B** presents the occurrence rates of the four-type ion VDFs, and the gray shadow highlights the results with total counts over 50. Despite the large variation due to relatively low counts, one can conclude that the occurrence rate of Type I is nearly constant. The occurrence rate of Type II decreases gradually along B_X or from the southern to the northern sides of the neutral line. Conversely, the occurrence rate of Type III increases gradually along B_X. The occurrence rate of Type IV peaks at the neutral line. Therefore, the antiparallel beams are predominantly observed in the northern side of the neutral sheet, and the parallel beams are predominantly observed on the southern side. The majority of cold-ion beams were found to be approaching the neutral sheet, with a smaller subset of VDFs also showing cold ion populations moving away from the neutral sheet. This indicates that there is some mechanism that either prevents cold ions from crossing far into the opposite exhaust, that the cold-ion populations are no longer cold after the neutral sheet crossing (heating), or that they can not be distinguished from the hotter background.

The distribution of VDFs shown in **Figure 4B** may be generated by several processes. First, MMS observe the

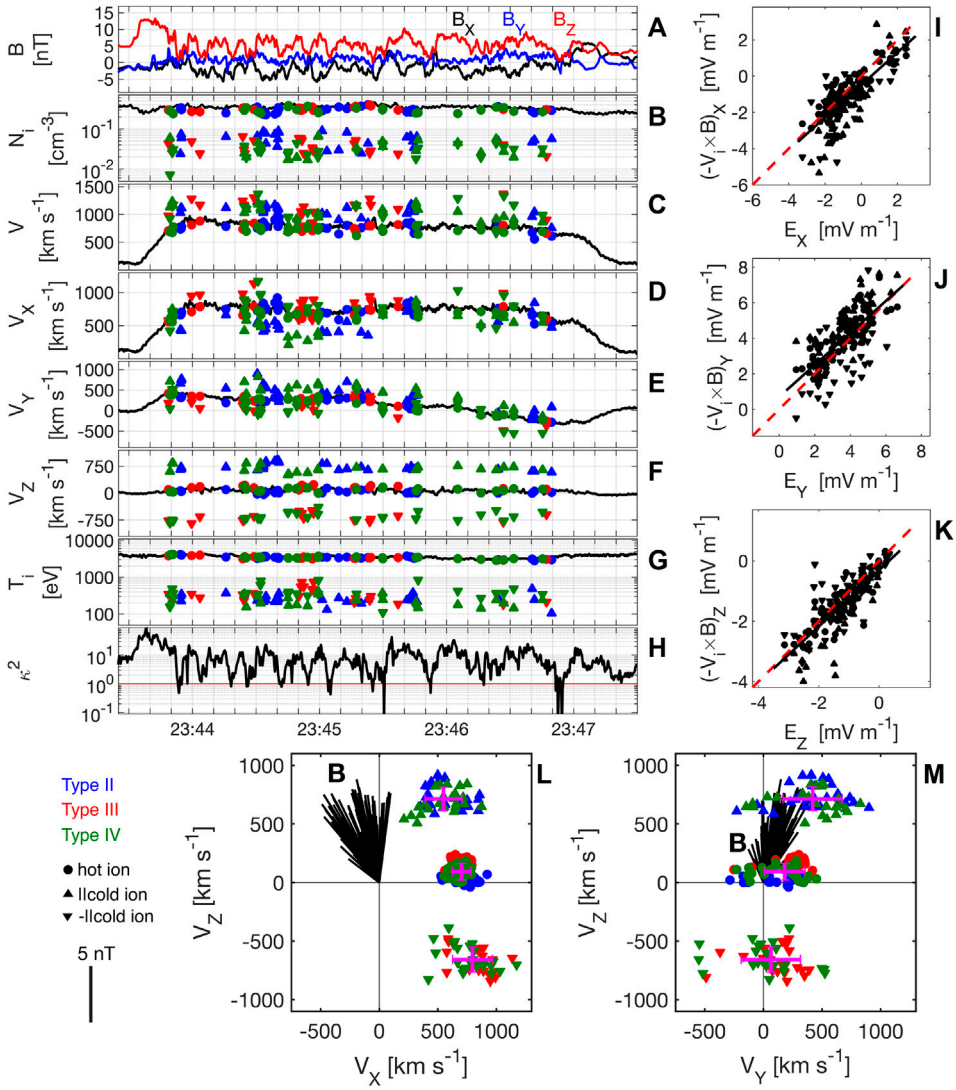

FIGURE 5 | Partial moments of the cold-ion beams and the hot ions inside the earthward ion jet. Those ions are from the three types (Types II, III and IV) with cold ions. Types II, III and IV are colored in blue, red and green, respectively. The partial-moment results of the hot, parallel cold and anti-parallel cold ions are marked by circles, upward-pointing triangles and downward-pointing triangles, respectively. **(A) B**. **(B)** N_i of all ions (black curve) and cold and hot ions from partial moments. **(C)** Ion bulk speed V. **(D)–(F)** Three components of the ion bulk velocities V_i. The black curves are the average bulk velocities. **(G)** T_i. **(H)** Adiabatic parameter defined by $\kappa^2 = \frac{R_B}{\rho_{ci}}$ (Büchner and Zelenyi, 1989), where R_B is magnetic field curvature radius and ρ_{ci} is the gyroradius of the 320 eV cold ions. **(I)–(K)** Scatter plots of the measured **E** from EDP and the convection electric field **(-V$_i$×B)** of hot and cold ions from selected data points. The black dashed lines denote slope = 1, and the red dashed lines are the linear fits of the partial-moment results. **(L)–(M)** Scatter plots of the ion bulk velocity of the selected points. The crosses present the averages and the standard deviations, and the black lines show the normalized magnetic fields.

northern (see **Figure 1**) and southern lobes on July 6,2,017 and see cold ions in both lobes. As an example shown in **Figure 1D**, the energy fluxes of the cold ions in the lobe are intermittent, indicating that the cold ions inflowing into the reconnection region could be patchy. Secondly, when cold ions enter the separatrices close to the X line (e.g., the cold-ion diffusion region), numerical simulations (Aunai et al., 2011; Divin et al., 2016) show that the cold ions bounce within an electrostatic potential well between the separatrices. The distribution feature in **Figure 4B** could be a statistical result of the bouncing motions of the cold ions inflowing from both lobes. Finally, as shown in **Figure 3A**, MMS see large-amplitude fluctuations in magnetic field, which may be convected from the upstream exhaust region or be driven by the ion temperature anisotropy associated with cold-ion beams (Hietala et al., 2015). Besides, the minimum curvature radii of the magnetic field lines in this event are comparable to the gyroradii of the cold ions (as shown by **Figure 5H**). Plasma waves and the curved magnetic field lines with small curvature radii can scatter and thermalize the cold ions when moving from one side of the neutral line to the other side, and thus, can mix them with the plasma-sheet hot ions. The distributions in **Figure 4B** could be combinational results of those three effects.

TABLE 1 | Average partial moments of the hot and cold ions of the selected data points shown in **Figure 5**

	Hot ion	Parallel cold ion	Anti-parallel cold ion
N_i [cm^{-3}]	0.30 ± 0.04	0.05 ± 0.02	0.03 ± 0.01
T_i [eV]	3,430 ± 290	250 ± 80	390 ± 180
V_i [km s^{-1}]	757 ± 71	1,034 ± 124	1,069 ± 175
$V_{E\times B}$ [km s^{-1}]	664 ± 118	688 ± 118	645 ± 135
V_X [km s^{-1}]	704 ± 79	548 ± 157	796 ± 170
V_Y [km s^{-1}]	182 ± 173	420 ± 254	63 ± 253
V_Z [km s^{-1}]	93 ± 72	713 ± 100	-657 ± 108

3 QUANTIFICATION OF COLD-ION BEAMS IN THE EARTHWARD JET

In order to study the dynamics of the cold-ion beams inside the jet, we utilize the same technique as used in Li et al. (2017) (see supporting information of that paper and **Supplementary Figure S3** in **Supplementary Material** for more details) to compute partial moments of the hot and cold populations. First, we select data points of the three types of ion VDFs with cold ions with most coverage of the variant magnetic field conditions. Then, we separate the cold and hot populations for each ion VDF in three-dimensional velocity space and compute their partial moments, including number density, bulk velocity and ion temperature. The results are presented in **Figure 5**, and the average results with standard deviations are listed in **Table 1**. In **Figures 5B–G, L,M**, the partial-moment results of the three-type VDFs (Types II, III and IV) with cold ions are labeled in blue, red and green, respectively. The hot ions from all three types are marked by circles. The parallel cold-ion beams from Types II and IV VDFs are marked by the upward-pointing triangles, while the anti-parallel beams from Types III and IV are marked by the downward-pointing triangles. The black lines in **Figures 5L,M** denote the magnetic fields of the selected data points for the partial-moment calculations. **Figures 5I–K** show the comparison between the measured electric field from EDP and the convection electric field ($-\mathbf{V}_i\times\mathbf{B}$) of the hot and cold ions from our partial-moment calculations. A good consistency of the three components means that the ions in the investigated jet are mainly frozen-in with the magnetic field lines. Also, it demonstrates a relatively good reliability of our partial-moment calculation via separating multiple populations from one VDF.

As presented in **Table 1**, the average number density (~0.04 cm^{-3}) of the cold-ion beams is comparable to that of the cold ions in the lobe and approximately 13% of that of the hot ions inside the jet. Even though the cold ions have large peak VDFs in velocity space, they are still minor populations in this investigated event. As shown by the circles in **Figure 5C**, the bulk velocities of the hot ions from the partial-moment calculations are close to the average bulk velocities (black curve) of all ions. This is consistent with the partial-moment number density results. All of the hot ions convect earthward, and their speed V_i^H (~760 km s^{-1}) is close to the **E×B** drift speed. As shown in **Figures 5C–F**; **Table 1**, all the cold-ion beams move earthward, meaning that all those ions are outflow ions of reconnection. The parallel cold ions have large positive V_Z component (~710 km s^{-1}), and the anti-parallel ones have large negative V_Z component (~-660 km s^{-1}). The bulk speed (~1,050 km s^{-1}) of the cold-ion beams is approximately 38% larger than that of the hot ions, which is predominantly contributed by the V_Z or parallel component.

It is difficult to know the acceleration process from the observational aspect. Here, we find a similarity between the velocity patterns in **Figures 5L,M** and previous numerical results (Aunai et al., 2011; Divin et al., 2016) and suggest that the cold ions inside this investigated jet may come from the region close to the X line. Cold ions are demagnetized while crossing the separatrices close to the X line (Toledo-Redondo et al., 2016a; Divin et al., 2016), and are accelerated primarily by the Hall electric field, while the beams can remain relatively cold. The cold-ion beams may bounce for several times within the Hall electrostatic potential well, and get significant V_Z and V_X components. Then, the accelerated cold-ion beams could be further accelerated by the shrinking magnetic field lines due to the Fermi effect. One can find a characteristic example of such acceleration process from **Figure 5** of Divin et al. (2016). This process could be responsible for the 38% extra speed at the MMS observation location.

Using Cluster data, Toledo-Redondo et al. (2016b) showed that cold ions can be heated by the large electric field gradient when crossing a separatrix boundary. Graham et al. (2017) analyzed a magnetopause reconnection event with cold ions and found lower-hybrid waves at the separatrix driven by the ion-ion streaming instability between the cold ions and the magnetosheath ions. The lower-hybrid waves can contribute to the cold-ion heating. Norgren et al. (2021) showed that the cold ions can be heated through a combination of thermalization at the separatrices and pitch angle scattering in the curved magnetic field around the neutral plane. Here, we calculate the temperature (~320 eV) of the cold-ion beams inside the reconnection jet, which corresponds to about 6% of the total energy in the spacecraft frame. The cold-ion beams are approximately one order of magnitude colder than the hot ions, while the cold-ion beams are thermalized compared to the cold ions (~10 eV) in the lobe. The large electric-field gradient at the separatrix and the scattering effect by the kinetic waves (see **Supplementary Figure S4** in **Supplementary Material** for more details) and small magnetic-field curvature radii (**Figure 5H**) may all contribute to the heating of the observed cold ions from the lobe into the ion jet. However, one should note that the temperature results have a large uncertainty from our partial-moment calculation. As shown in **Figures 3**; **Supplementary Figures S3**, the thermal parts of the hot and cold populations usually overlap with each other. We cut major parts of the cold-ion VDFs empirically by eye. The results of the number density and bulk velocity are relatively reliable, but the ambient treatment of the VDF boundaries brings large errors to the temperature. The temperature results can be improved by fitting the cold-ion VDFs in the three-dimensional velocity space, which will be tried in our future works.

4 CONCLUSION

We investigated an MMS magnetotail crossing from 21:30:00 UT to 24:00:00 UT on July 06, 2017 with cold ions and ongoing

magnetic reconnection and present quantitative analysis of the cold ions inside a reconnection ion jet. In this event, MMS cross one tailward and two earthward ion jets, and we explored the three-dimensional ion VDFs and find types of ion VDFs with cold-ion beams. MMS observe hot ions of plasma-sheet origin throughout the tailward jet and the first earthward ion jet, and cold ions with small $\mathbf{V}_B$ show up in part of the jet crossing. At the separatrix, MMS observe $\mathbf{E}\times\mathbf{B}$ drifting cold ions with negligible $\mathbf{V}_B$. The second earthward ion jet is lead by a dipolarization front, and we find four types of ion VDFs inside: Type I consists of only a single hot plasma-sheet population, Type II consists of a hot population and a cold population with a positive $\mathbf{V}_B$, Type III consists of a hot population and a cold population with a negative $\mathbf{V}_B$, and Type IV consists of a hot population with counter-streaming cold populations. Our analysis focuses on those VDFs with cold-ion beams. The occurrence rate of Type II VDFs decreases gradually from the southern to the northern sides of the neutral line. Conversely, the occurrence rate of Type III VDFs increase gradually from south to the north. The occurrence rate of Type IV peaks at the neutral line. This distribution of VDFs could be formed by the patchy cold-ion inflow, the bouncing motions within the divergent Hall electrostatic potential well, and the scattering effect due to plasma waves and the curved magnetic field lines with small curvature radii.

We adopted the same technique as used in Li et al. (2017) to compute the partial moments of the hot and cold populations of Types II, III and IV VDFs. The average number density of the cold-ion beams is approximately 13% of that of the hot ions, meaning that the cold ions are a minor population in this investigated event. All the hot and cold ions are outflow ions towards Earth. The average bulk speed of the cold-ion beams is approximately 38% larger than that of the hot plasma-sheet ions. This extra speed is predominantly along the magnetic field direction. Those cold-ion beams could come from the cold-ion diffusion region and be initially accelerated by the Hall electric field. Then, the accelerated cold-ion beams could be further accelerated by the shrinking field lines through the Fermi effect. The cold-ion beams are still one order of magnitude colder than the hot ions, while the electric field with large gradient at the separatrix and the scattering effect by the waves and highly curved magnetic field lines may thermalize those cold ions from the lobe into the ion jet.

DATA AVAILABILITY STATEMENT

All data used in this work are available at the MMS Data Center (https://lasp.colorado.edu/mms/sdc/public/). Data analysis was performed using the IRFU-MATLAB package (https://github.com/irfu/irfu-matlab).

AUTHOR CONTRIBUTIONS

WL, YL, and BT carried out the data analysis and interpretation. YL wrote the first-version article, and WL revised it. CN, JH, CW, and QZ contributed to the data interpretation and article preparation. JB led the design and operation of the MMS mission. The remaining co-authors contributed to the data analysis under the framework of an ISSI international team.

FUNDING

This work was supported by NNSFC Grant No. 41731070, 41974170, and 41974196, the Chinese Academy of Sciences (QYZDJSSW-JSC028, XDA15052500, XDA17010301 and XDB41000000), and the Specialized Research Fund for State Key Laboratories of China. WYL was also supported by the Youth Innovation Promotion Association (2018177), and the Young Elite Scientists Sponsorship Program by CAST and the Open Research Program of Key Laboratory of Geospace Environment CAS. CN received support from the Research Council of Norway under contract 300865.

ACKNOWLEDGMENTS

We thank the MMS team and instrument principal investigators for data access and support. We acknowledge support from the International Space Science Institute (ISSI) international team *Cold plasma of ionospheric origin in the Earth's magnetosphere*.

SUPPLEMENTARY MATERIAL

The Supplementary Material for this article can be found online at: https://www.frontiersin.org/articles/10.3389/fspas.2021.745264/full#supplementary-material

REFERENCES

Alm, L., André, M., Vaivads, A., Khotyaintsev, Y. V., Torbert, R. B., Burch, J. L., et al. (2018). Magnetotail hall physics in the presence of cold ions. *Geophys. Res. Lett.* 45 (10941–10), 950. doi:10.1029/2018GL079857

André, M., and Cully, C. M. (2012). Low-energy ions: A previously hidden solar system particle population. *Geophys. Res. Lett.* 39, L03101. doi:10.1029/2011GL05024210.1029/2011gl050242

André, M., Li, K., and Eriksson, A. I. (2015). Outflow of low-energy ions and the solar cycle. *J. Geophys. Res. Space Phys.* 120, 1072–1085. doi:10.1002/2014JA02071410.1002/2014ja020714

André, M., Li, W., Toledo-Redondo, S., Khotyaintsev, Y. V., Vaivads, A., Graham, D. B., et al. (2016). Magnetic reconnection and modification of the hall physics due to cold ions at the magnetopause. *Geophys. Res. Lett.* 43, 6705–6712. doi:10.1002/2016GL069665

Angelopoulos, V., Baumjohann, W., Kennel, C. F., Coroniti, F. V., Kivelson, M. G., Pellat, R., et al. (1992). Bursty bulk flows in the inner central plasma sheet. *J. Geophys. Res.* 97, 4027–4039. doi:10.1029/91ja02701

Angelopoulos, V., Kennel, C. F., Coroniti, F. V., Pellat, R., Kivelson, M. G., Walker, R. J., et al. (1994). Statistical characteristics of bursty bulk flow events. *J. Geophys. Res.* 99, 21257–21280. doi:10.1029/94ja01263

Aunai, N., Belmont, G., and Smets, R. (2011). Proton acceleration in antiparallel collisionless magnetic reconnection: Kinetic mechanisms behind the fluid dynamics. *J. Geophys. Res.* 116, a–n. doi:10.1029/2011ja016688

Baumjohann, W., Paschmann, G., and Lühr, H. (1990). Characteristics of high-speed ion flows in the plasma sheet. *J. Geophys. Res.* 95, 3801–3809. doi:10.1029/JA095iA04p03801

Birn, J., Nakamura, R., Panov, E. V., and Hesse, M. (2011). Bursty bulk flows and dipolarization in mhd simulations of magnetotail reconnection. *J. Geophys. Res.* 116, a–n. doi:10.1029/2010ja016083

Birn, J., Runov, A., and Zhou, X. Z. (2017). Ion velocity distributions in dipolarization events: Distributions in the central plasma sheet. *J. Geophys. Res. Space Phys.* 122, 8014–8025. doi:10.1002/2017ja024230

Büchner, J., and Zelenyi, L. M. (1989). Regular and chaotic charged particle motion in magnetotaillike field reversals: 1. basic theory of trapped motion. *J. Geophys. Res.* 94, 11821–11842. doi:10.1029/JA094iA09p11821

Burch, J. L., Moore, T. E., Torbert, R. B., and Giles, B. L. (2016). Magnetospheric Multiscale overview and science objectives. *Space Sci. Rev.* 199, 5–21. doi:10.1007/s11214-015-0164-910.1007/s11214-015-0164-9

Cassak, P. A., and Shay, M. A. (2007). Scaling of asymmetric magnetic reconnection: General theory and collisional simulations. *Phys. Plasmas* 14, 102114. doi:10.1063/1.279563010.1063/1.2795630

Chappell, C. R., Baugher, C. R., and Horwitz, J. L. (1980). New advances in thermal plasma research. *Rev. Geophys.* 18, 853–861. doi:10.1029/RG018i004p00853

Cully, C. M., Donovan, E. F., Yau, A. W., and Arkos, G. G. (2003). Akebono/Suprathermal mass spectrometer observations of low-energy ion outflow: Dependence on magnetic activity and solar wind conditions. *J. Geophys. Res.* 108, 1093. doi:10.1029/2001JA009200

Dai, L., Wang, C., and Lavraud, B. (2021). Kinetic imprints of ion acceleration in collisionless magnetic reconnection. *ApJ* 919, 15. doi:10.3847/1538-4357/ac0fde10.3847/1538-4357/ac0fde

Dargent, J., Aunai, N., Lavraud, B., Toledo-Redondo, S., and Califano, F. (2019). Signatures of cold ions in a kinetic simulation of the reconnecting magnetopause. *J. Geophys. Res. Space Phys.* 124, 2497–2514. doi:10.1029/2018JA026343

Dargent, J., Aunai, N., Lavraud, B., Toledo-Redondo, S., and Califano, F. (2020). Simulation of plasmaspheric plume impact on dayside magnetic reconnection. *Geophys. Res. Lett.* 47, e2019GL086546. doi:10.1029/2019gl086546

Dargent, J., Aunai, N., Lavraud, B., Toledo-Redondo, S., Shay, M. A., Cassak, P. A., et al. (2017). Kinetic simulation of asymmetric magnetic reconnection with cold ions. *J. Geophys. Res. Space Phys.* 122, 5290–5306. doi:10.1002/2016JA023831

Divin, A., Khotyaintsev, Y. V., Vaivads, A., André, M., Toledo-Redondo, S., Markidis, S., et al. (2016). Three-scale structure of diffusion region in the presence of cold ions. *J. Geophys. Res. Space Phys.* 121, 12001–12013. doi:10.1002/2016JA02360610.1002/2016ja023606

Eastwood, J. P., Goldman, M. V., Hietala, H., Newman, D. L., Mistry, R., and Lapenta, G. (2015). Ion reflection and acceleration near magnetotail dipolarization fronts associated with magnetic reconnection. *J. Geophys. Res. Space Phys.* 120, 511–525. doi:10.1002/2014ja020516

Eastwood, J. P., Phan, T.-D., Mozer, F. S., Shay, M. A., Fujimoto, M., Retinò, A., et al. (2007). Multi-point observations of the hall electromagnetic field and secondary island formation during magnetic reconnection. *J. Geophys. Res.* 112, a–n. doi:10.1029/2006ja012158

Engwall, E., Eriksson, A. I., Cully, C. M., André, M., Torbert, R., and Vaith, H. (2009). Earth's ionospheric outflow dominated by hidden cold plasma. *Nat. Geosci* 2, 24–27. doi:10.1038/ngeo387

Ergun, R. E., Tucker, S., Westfall, J., Goodrich, K. A., Malaspina, D. M., Summers, D., et al. (2016). The axial double probe and fields signal processing for the MMS mission. *Space Sci. Rev.* 199, 167–188. doi:10.1007/s11214-014-0115-x

Fu, H. S., Cao, J. B., Khotyaintsev, Y. V., Sitnov, M. I., Runov, A., Fu, S. Y., et al. (2013). Dipolarization fronts as a consequence of transient reconnection: *In situ* evidence. *Geophys. Res. Lett.* 40, 6023–6027. doi:10.1002/2013GL058620

Fujimoto, M., Nakamura, M. S., Nagai, T., Mukai, T., Yamamoto, T., and Kokubun, S. (1996). New kinetic evidence for the near-earth reconnection. *Geophys. Res. Lett.* 23, 2533–2536. doi:10.1029/96GL02429

Gershman, D. J., Dorelli, J. C., Avanov, L. A., Gliese, U., Barrie, A., Schiff, C., et al. (2019). Systematic Uncertainties in Plasma Parameters Reported by the Fast Plasma Investigation on NASA's Magnetospheric Multiscale Mission. *J. Geophys. Res. Space Phys.* 124, 10345–10359. doi:10.1029/2019JA026980

Graham, D. B., Khotyaintsev, Y. V., Norgren, C., Vaivads, A., André, M., Toledo-Redondo, S., et al. (2017). Lower hybrid waves in the ion diffusion and magnetospheric inflow regions. *J. Geophys. Res. Space Phys.* 122, 517–533. doi:10.1002/2016JA02357210.1002/2016ja023572

Hietala, H., Drake, J. F., Phan, T. D., Eastwood, J. P., and McFadden, J. P. (2015). Ion temperature anisotropy across a magnetotail reconnection jet. *Geophys. Res. Lett.* 42, 7239–7247. doi:10.1002/2015gl065168

Hoshino, M., Mukai, T., Yamamoto, T., and Kokubun, S. (1998). Ion dynamics in magnetic reconnection: Comparison between numerical simulation and geotail observations. *J. Geophys. Res.* 103, 4509–4530. doi:10.1029/97ja01785

Kistler, L. M., and Mouikis, C. G. (2016). The inner magnetosphere ion composition and local time distribution over a solar cycle. *J. Geophys. Res. Space Phys.* 121, 2009–2032. doi:10.1002/2015JA021883

Li, K., Haaland, S., Eriksson, A., André, M., Engwall, E., Wei, Y., et al. (2013). Transport of cold ions from the polar ionosphere to the plasma sheet. *J. Geophys. Res. Space Phys.* 118, 5467–5477. doi:10.1002/jgra.50518

Li, W. Y., André, M., Khotyaintsev, Y. V., Vaivads, A., Fuselier, S. A., Graham, D. B., et al. (2017). Cold ionospheric ions in the magnetic reconnection outflow region. *J. Geophys. Res. Space Phys.* 122 (10), 10194–10202. doi:10.1002/2017ja024287

Lindqvist, P.-A., Olsson, G., Torbert, R. B., King, B., Granoff, M., Rau, D., et al. (2016). The spin-plane double probe electric field instrument for MMS. *Space Sci. Rev.* 199, 137–165. doi:10.1007/s11214-014-0116-9

Moore, T. E., Chappell, C. R., Chandler, M. O., Craven, P. D., Giles, B. L., Pollock, C. J., et al. (1997). High-altitude observations of the polar wind. *Science* 277, 349–351. doi:10.1126/science.277.5324.349

Nagai, T., Fujimoto, M., Saito, Y., Machida, S., Terasawa, T., Nakamura, R., et al. (1998). Structure and dynamics of magnetic reconnection for substorm onsets with geotail observations. *J. Geophys. Res.* 103, 4419–4440. doi:10.1029/97ja0219010.1029/97ja02190

Nakamura, R., Baumjohann, W., Klecker, B., Bogdanova, Y., Balogh, A., Rème, H., et al. (2002). Motion of the dipolarization front during a flow burst event observed by cluster. *Geophys. Res. Lett.* 29, 3–1. –3–4. doi:10.1029/2002GL015763

Norgren, C., Tenfjord, P., Hesse, M., Toledo-Redondo, S., Li, W.-Y., Xu, Y., et al. (2021). On the presence and thermalization of cold ions in the exhaust of antiparallel symmetric reconnection. *Front. Astron. Space Sci.* 8, 149. doi:10.3389/fspas.2021.730061

Pollock, C., Moore, T., Jacques, A., Burch, J., Gliese, U., Saito, Y., et al. (2016). Fast Plasma Investigation for Magnetospheric Multiscale. *Space Sci. Rev.* 199, 331–406. doi:10.1007/s11214-016-0245-4

Priest, E., and Forbes, T. (2007). *Magnetic reconnection.* Magnetic Reconnection. Cambridge, UK: Cambridge University Press.

Runov, A., Angelopoulos, V., Artemyev, A., Birn, J., Pritchett, P. L., and Zhou, X. Z. (2017). Characteristics of ion distribution functions in dipolarizing flux bundles: Event studies. *J. Geophys. Res. Space Phys.* 122, 5965–5978. doi:10.1002/2017ja02401010.1002/2017ja024010

Runov, A., Angelopoulos, V., Sitnov, M. I., Sergeev, V. A., Bonnell, J., McFadden, J. P., et al. (2009). Themis observations of an earthward-propagating dipolarization front. *Geophys. Res. Lett.* 36. doi:10.1029/2009GL038980

Russell, C. T., Anderson, B. J., Baumjohann, W., Bromund, K. R., Dearborn, D., Fischer, D., et al. (2016). The Magnetospheric Multiscale Magnetometers. *Space Sci. Rev.* 199, 189–256. doi:10.1007/s11214-014-0057-310.1007/978-94-024-0861-4_8

Sauvaud, J.-A., Louarn, P., Fruit, G., Stenuit, H., Vallat, C., Dandouras, J., et al. (2004). Case studies of the dynamics of ionospheric ions in the Earth's magnetotail. *J. Geophys. Res.* 109. doi:10.1029/2003JA009996

Shay, M. A., Drake, J. F., Denton, R. E., and Biskamp, D. (1998). Structure of the dissipation region during collisionless magnetic reconnection. *J. Geophys. Res.* 103, 9165–9176. doi:10.1029/97ja03528

Tenfjord, P., Hesse, M., Norgren, C., Spinnangr, S. F., and Kolstø, H. (2019). The impact of oxygen on the reconnection rate. *Geophys. Res. Lett.* 46, 6195–6203. doi:10.1029/2019gl082175

Toledo-Redondo, S., André, M., Vaivads, A., Khotyaintsev, Y. V., Lavraud, B., Graham, D. B., et al. (2016b). Cold ion heating at the dayside magnetopause during magnetic reconnection. *Geophys. Res. Lett.* 43, 58–66. doi:10.1002/2015GL067187

Toledo-Redondo, S., André, M., Aunai, N., Chappell, C. R., Dargent, J., Fuselier, S. A., et al. (2021). Impacts of ionospheric ions on magnetic reconnection and earth's magnetosphere dynamics. *Rev. Geophys. n/a*, e2020RG000707. doi:10.1029/2020RG000707

Toledo-Redondo, S., André, M., Khotyaintsev, Y. V., Vaivads, A., Walsh, A., Li, W., et al. (2016a). Cold ion demagnetization near the x-line of magnetic reconnection. *Geophys. Res. Lett.* 43, 6759–6767. doi:10.1002/2016GL069877

Toledo-Redondo, S., Dargent, J., Aunai, N., Lavraud, B., André, M., Li, W., et al. (2018). Perpendicular current reduction caused by cold ions of ionospheric origin in magnetic reconnection at the magnetopause: Particle-in-cell simulations and spacecraft observations. *Geophys. Res. Lett.* 45, 10,033–10,042. doi:10.1029/2018GL079051

Toledo-Redondo, S., Vaivads, A., André, M., and Khotyaintsev, Y. V. (2015). Modification of the Hall physics in magnetic reconnection due to cold ions at the Earth's magnetopause. *Geophys. Res. Lett.* 42, 6146–6154. doi:10.1002/2015GL06512910.1002/2015gl065129

Walsh, B. M., Phan, T. D., Sibeck, D. G., and Souza, V. M. (2014). The plasmaspheric plume and magnetopause reconnection. *Geophys. Res. Lett.* 41, 223–228. doi:10.1002/2013GL058802

Wang, S., Kistler, L. M., Mouikis, C. G., Liu, Y., and Genestreti, K. J. (2014). Hot magnetospheric O + and cold ion behavior in magnetopause reconnection: Cluster observations. *J. Geophys. Res. Space Phys.* 119, 9601–9623. doi:10.1002/2014JA02040210.1002/2014ja020402

Welling, D. T., André, M., Dandouras, I., Delcourt, D., Fazakerley, A., Fontaine, D., et al. (2015). The earth: Plasma sources, losses, and transport processes. *Space Sci. Rev.* 192, 145–208. doi:10.1007/s11214-015-0187-2

Wygant, J. R., Cattell, C. A., Lysak, R., Song, Y., Dombeck, J., McFadden, J., et al. (2005). Cluster observations of an intense normal component of the electric field at a thin reconnecting current sheet in the tail and its role in the shock-like acceleration of the ion fluid into the separatrix region. *J. Geophys. Res.* 110. doi:10.1029/2004ja010708

Xu, Y., Fu, H. S., Norgren, C., Toledo-Redondo, S., Liu, C. M., and Dong, X. C. (2019). Ionospheric cold ions detected by mms behind dipolarization fronts. *Geophys. Res. Lett.* 46, 7883–7892. doi:10.1029/2019gl083885

Yamada, M., Kulsrud, R., and Ji, H. (2010). Magnetic reconnection. *Rev. Mod. Phys.* 82, 603–664. doi:10.1103/RevModPhys.82.603

Yamauchi, M. (2019). Terrestrial ion escape and relevant circulation in space. *Ann. Geophys.* 37, 1197–1222. doi:10.5194/angeo-37-1197-2019

Young, D. T., Burch, J. L., Gomez, R. G., De Los Santos, A., Miller, G. P., Wilson, P., et al. (2016). Hot plasma composition analyzer for the magnetospheric multiscale mission. *Space Sci. Rev.* 199, 407–470. doi:10.1007/s11214-014-0119-6

Zaitsev, I., Divin, A., Semenov, V., Kubyshkin, I., Korovinskiy, D., Deca, J., et al. (2021). Cold ion energization at separatrices during magnetic reconnection. *Phys. Plasmas* 28, 032104. doi:10.1063/5.0008118

Conflict of Interest: The authors declare that the research was conducted in the absence of any commercial or financial relationships that could be construed as a potential conflict of interest.

Publisher's Note: All claims expressed in this article are solely those of the authors and do not necessarily represent those of their affiliated organizations, or those of the publisher, the editors, and the reviewers. Any product that may be evaluated in this article, or claim that may be made by its manufacturer, is not guaranteed or endorsed by the publisher.

frontiers in Astronomy and Space Sciences

REVIEW
published: 09 December 2021
doi: 10.3389/fspas.2021.792653

Potential Association Between the Low-Energy Plasma Structure and the Patchy Pulsating Aurora

Jun Liang[1]*, *Y. Nishimura*[2], *E. Donovan*[1], *B. Yang*[1] and *V. Angelopoulos*[3]

[1]Department of Physics and Astronomy, University of Calgary, Calgary, AB, Canada, [2]Department of Electrical and Computer Engineering and Center for Space Sciences, Boston University, Boston, MA, United States, [3]Institute of Geophysics and Planetary Physics, University of California, Los Angeles, Los Angeles, CA, United States

While the pulsating auroral phenomena have been recognized and studied for decades, our understating of their generation mechanisms remains incomplete to date. In one main class of pulsating auroras which is termed "patchy pulsating auroras" (PPA), the auroral patches are found to basically maintain their shape and size over many pulsation cycles. Also, PPAs are repeatedly found to essentially co-move with the ExB convection drift. The above properties led many researchers to hypothesize that PPA might connect to a structure of enhanced cold plasma in the magnetosphere. In this study, we review the existing evidence, and provide new perspective and support, of the low-energy plasma structure potentially associated with PPA. Based on observations from both the magnetosphere and the topside ionosphere, we suggest that ionospheric auroral outflows might constitute one possible source mechanism of the flux tubes with enhanced low-energy plasma that connect to the PPA. We also review the existing theories of pulsating auroras, with particular focus on the role of low-energy plasma in these theories. To date, none of the existing theories are complete and mature enough to offer a quantitatively satisfactory explanation of pulsating auroras. At last, we suggest a few future research directions to advance our understanding of pulsating auroras: a) more accurate measurements of the cold plasma density, b) more developed theories of the underlying mechanisms of ELF/VLF wave modulation, and c) auxiliary processes in the topside ionosphere or near-Earth region accompanying pulsating auroras.

Keywords: pulsating aurora, low-energy plasma, auroral patch, wave-particle interaction, ionospheric outflows

OPEN ACCESS

Edited by:
Elena Kronberg,
Ludwig Maximilian University of Munich, Germany

Reviewed by:
Michael Henderson,
Los Alamos National Laboratory (DOE), United States
Nickolay Ivchenko,
Royal Institute of Technology, Sweden

***Correspondence:**
Jun Liang
liangj@ucalgary.ca

Specialty section:
This article was submitted to Space Physics, a section of the journal Frontiers in Astronomy and Space Sciences

Received: *10 October 2021*
Accepted: *17 November 2021*
Published: *09 December 2021*

Citation:
Liang J, Nishimura Y, Donovan E, Yang B and Angelopoulos V (2021) Potential Association Between the Low-Energy Plasma Structure and the Patchy Pulsating Aurora. Front. Astron. Space Sci. 8:792653. doi: 10.3389/fspas.2021.792653

1 INTRODUCTION

Pulsating aurora is an auroral form that undergoes quasi-periodic fluctuations in intensity (Johnstone, 1978). The period typically ranges from few seconds to tens of seconds (Royrvik and Davis, 1977; Yamamoto, 1988). Pulsating auroras are often observed in the equatorward portion of the auroral oval, and mainly occur in postmidnight-morning sectors and during late substorm expansion and recovery phases, but can persist for longer than individual substorm (e.g., Jones et al., 2011; 2013). Pulsating aurora is often organized in "patches," the size of which typically lies in the range of a few tens up to ~100 km in extent when mapped to ionospheric altitudes. The ultimate source of pulsating aurora is thought to be magnetospheric electrons with energies of a few keV to several tens of keV (Sandahl et al., 1980; McEwen et al., 1981; Miyoshi et al., 2010; Samara et al., 2010, 2015; Jaynes et al., 2013), though in some events the precipitation may also involve a portion of

electrons with energies as low as <1 keV (Liang et al., 2016) or as high as the relativistic energy range (Miyoshi et al., 2015). While there are other proposals of the driving mechanism of pulsating auroras (e.g., Sato et al., 2015; Mozer et al., 2017), the wave-particle interaction and its resulting pitch-angle scattering of energetic electrons in the equatorial magnetosphere remain to be the top candidate and most recognized mechanism underlying pulsating auroral precipitation. The lower-band whistler-mode chorus is usually the dominant wave mode at play in many cases (Miyoshi et al., 2010, 2015; Nishimura et al., 2010, 2011a, 2011b; Ozaki et al., 2015, 2018; Kasahara et al., 2018; Hosokawa et al., 2020), while the upper-band chorus (Nishiyama et al., 2011) and electron-cyclotron-harmonic (ECH) waves (Liang et al., 2010; Fukizawa et al., 2018) may also contribute in some events. For comprehensive reviews of pulsating auroras, see Lessard (2012) and most recently Nishimura et al. (2020).

Pulsating auroral features exhibit diverse characteristics, varying in terms of shape, size, brightness, altitude, spatial stability, modulation, lifespan, and velocity. In recent years, based on ground-based all-sky-imager (ASI) data the pulsating auroras are categorized into patchy pulsating auroras (PPA), patchy diffuse auroras (PDA), and amorphous pulsating auroras (APA), according to their morphology (Grono et al., 2017; Grono and Donovan, 2018, 2019, 2020; Yang et al., 2019). PPA is the classical type of pulsating auroras; it represents a highly structured patch that can persist for many minutes and pulsate over much of its area. PDA is similar to PPA but does not oscillate in brightness. While PDA is not "pulsating," it closely resembles PPA in terms of its spatial characteristics and occurrence distribution (Grono and Donovan, 2020). In some events, the same spatial structure is found to switch from pulsating to non-pulsating auroras (or vice versa). One such example is given in **Supplementary Material**, from which one can see that the auroral patch shifts from pronouncedly pulsating to virtually non-pulsating, yet basically maintains its structural shape. Their morphology in the ionosphere suggests that these two auroral types might be similar in generation mechanisms except for the presence/absence of modulation in precipitation. On the other hand, APA is a more dynamic pulsating auroral type with rapidly changing shapes and locations, yet lacking repeatable patch structures between successive images captured at a 3-sec cadence of THEMIS ASI. The motion of APA is more dynamic than PPA and seems unrelated to E × B drift. There is a possibility that APA could arise from time-aliasing of rapidly-propagating pulsating aurora with "streaming" behavior and pulsations faster than 3-sec, the sampling rate of THEMIS ASI (Nishimura et al., 2020). Statistically, the occurrence distributions of PPA and APA tend to map to different regions in the equatorial magnetosphere (Grono and Donovan, 2020), and there is evidence that the PPA and APA are likely associated with different energy ranges of electron precipitation (Yang et al., 2019; Tesema et al., 2020). It is thus reasonable to speculate that their generation mechanisms may be different. Most importantly, based upon phenomenological evidence there is no concrete rationale to conceive a link between the APA and enhanced cold plasma in the magnetosphere. In this paper, we shall mainly focus on the PPA type and explore the possible mechanism underlying its resilient spatial shape. For this research purpose, we examine all the studies to be referred to in this review, as long as the optical data are involved and available, to check whether their investigated pulsating auroral events are PPA or APA, based on established techniques and criteria in distinguishing the two types (Grono et al., 2017; Grono and Donovan, 2018; Yang et al., 2019) according to the cadence rate of available optical instruments.

One striking characteristic of PPA is that it can basically maintain its size shape through many cycles of pulsations (Scourfield et al., 1972; Johnstone, 1978; Humberset et al., 2018). Furthermore, it has often been noted that the motion of the overall PPA essentially conforms to the E × B convection drift (Davis, 1971; Nakamura and Oguti, 1987; Royrvik and Davis, 1977; Scourfield et al., 1983; Yang et al., 2014; 2017; Takahashi et al., 2019). The above two key features of PPA will be further elucidated with the most recent observations in **Section 2**. In a mathematical form, the spatiotemporal behaviors of a PPA can be approximately written as (e.g., Kangas and Cao, 1995):

$$P(\boldsymbol{r}, t) = f(t) \cdot g(\boldsymbol{r} - \boldsymbol{v}_E t) \tag{1}$$

in which f (t) depicts the temporal modulation, and g (r) depicts the spatial shape of the PPA. V_E denotes the E × B drift speed. The relation between the patch motion and E × B drift invalidates the scenario that the PPA shape maps to an energetic electron structure at the magnetic equator, whose gradient/curvature drift speed would usually by itself exceed the E × B drift in the near-Earth magnetosphere, and whose energy dispersion led by the gradient/curvature drift would tend to quickly deform the patch (Yang, 2017).

The above salient features of PPA has led many researchers to hypothesize that PPA might connect to a structure of enhanced "cold" plasma in the magnetosphere (Johnstone, 1978; Oguti, 1976; Davidson and Chiu, 1987; Davidson, 1990, Demekhov and Trakhtengerts, 1994; Tagirov et al., 1999; Liang et al., 2015; Nishimura et al., 2015). A brief discussion of the existing theories of pulsating auroras with be given in **Section 4**. In a nutshell, the classical theoretical view of pulsating auroras is that each luminous patch in the ionosphere represents the magnetic mapping of a region of enhanced cold plasma density near the equatorial plane. The gradient/curvature drift of energetic electrons brings fresh precipitation material into the regions of enhanced plasma density. The interaction between the drifting energetic electrons, the ambient cold plasma, and the ELF/VLF waves—though the details of such an interaction differ from theory to theory—lead to modulated scattering of energetic electrons into the loss cone within the area of each enhanced-density zone, resulting in an oscillatory precipitating flux having the outline of the plasma blob. In plasma physics, the definition of "cold" or "hot" particles is contingent upon the research objective and especially the reference plasma population they are compared to. In the context of pulsating auroral studies, a particle population is characterized as cold when: a) its energy is much lower than that of the thermal electron/ion population in the central plasma sheet (CPS) region; b) its energy range is lower

than the minimum resonant energy of the wave-particle interaction at play, and c) its gradient/curvature drift speed is distinctly smaller than the ambient E × B velocity. In the inner CPS, electrons with energy <~100 eV and ions with energy <1 keV would usually satisfy the above criteria and can be deemed "cold." Under such a definition the so-called "warm plasma cloak" (Chappell et al., 2008), which is warmer compared to the plasmaspheric population, would also be considered as "cold" population here. In the near-Earth CPS, such cold electron/ions are often distinctly separated from the thermal and suprathermal plasma sheet populations in terms of energy range, pitch-angle distribution, drift speed and trajectory, and source mechanisms [e.g., Wang et al. (2012); Delzanno et al. (2021)]. In this paper, we shall use the term "low-energy plasma" to denote the cold electrons and ions in the above-depicted sense. Such a low-energy plasma would not directly resonate with the waves by itself, but could form an ambient structure that can significantly affect the excitation/propagation of the waves within it (Cuperman and Landau, 1974; Li et al., 2011b; Wu et al., 2013; Katoh, 2014; Hanzelka and Santolik, 2019; Ke et al., 2021). We should also note that, while the notion that PPA is associated with a density enhancement structure was more often suggested, it is also possible that the PPA might be associated with a density depletion structure, since the density depletion structure may also affect the amplification/propagation of the whistler-mode chorus inside it [e.g., Wu et al. (2013); Li et al. (2011b); Katoh (2014)].

Of course, while **Eq. 1** offers an approximate depiction of the general characteristics of PPAs, a number of complications/exceptions may exist. First, the patch size is certainly not rigorously fixed over time (Humberset et al., 2016; 2018; Bolmgren, 2017; Partamies et al., 2019). Secondly, the PPA may have intra-patch sub-structures and fine-scale variations. For example, some of the patches may feature a "streaming/expansion" behavior, namely that the entire patch is not switched on/off simultaneously; instead, it grows from a portion and rapidly expands to its full extent during the on-time, followed by a retraction in the area as the pulsation switches off (Royrvik and Davis, 1977; Yamamoto, 1988; Tagirov et al., 1999). Using high-resolution imagers Nishiyama et al. (2016) investigated the sub-structures within a pulsating auroral patch. They found that the sub-structures smaller than ~20 km feature rapid back and forth fluctuations relative to the larger patch whose drift is much slower and steady. These rapid, intra-patch variations of pulsating auroras are almost certainly led by physical processes other than cold plasma [e.g., Fukuda et al. (2016)]. With the above complications in mind, and realizing that cold plasma is certainly not the only factor in controlling the spatiotemporal variations of pulsating auroras, in this paper we shall nevertheless focus on the role of low energy plasma in producing the overall patch shape, and leave the intra-patch fine structures, the fast motion of patches (e.g., streaming) and the subtleties in ionospheric electrodynamics for separate studies.

One other area of important new findings of pulsating auroras in the last decade, thanks to the deployment of high-time-resolution imagers, is the details of rapid modulation embedded in each on-time, and the subtleties and high variabilities in the on- and off-time durations, of pulsating auroras [e.g., Samara et al. (2010); Nishiyama et al. (2014; 2016); Humberset et al. (2016); Dahlgren et al. (2017)]. Though those fine-scale temporal characteristics are not of the core interest of this review, some of the results may also shed light on the possible role of low-energy plasma in pulsating auroras. For example, based on the observation that the on-off pulsation periods showed no significant correlations with auroral brightness, Nishiyama et al. (2014) suggested that variations in the cold plasma density play a dominant role in controlling the conditions of wave-particle interactions that have temporal scales of the on-off pulsation periods. On the other hand, Humberset et al. (2016) claimed that there is no clear candidate of the suggested mechanisms and drivers to explain the observational constraints set by the PPAs in a satisfactory manner, based on their observed temporal characteristics and energy deposition of PPAs.

While the speculation regarding PPA-associated cold plasma structure has existed for decades, it is fair to state that, the speculation still needs further investigation and validation to date. This is mainly due to two reasons: 1) the experimental difficulty in reliable measurements of cold plasma density as well as the shape and motion of the cold plasma in the magnetosphere; 2) the difficulty in establishing conjugacy between the magnetospheric *in-situ* probes and an individual PPA. That being said, certain progress has been achieved, thanks to the global deployment and technological advances of both ground-based and *in-situ* instruments/missions in the past couple of decades. Furthermore, a number of recent findings of pulsating auroras, though by themselves not directly observing low-energy plasma, may impose certain useful implications and constraints on the characteristics of the low-energy plasma associated with pulsating auroras. In this paper, we shall review existing observational evidence and theoretical consideration of the potential association between the low-energy plasma and the PPA. The rest of the paper is arranged as follows. In **Section 2** we shall first review some most recent reports on the shape persistence and overall motion speed of PPA. We shall then review existing *in-situ* observational evidence of low-energy plasma in potential association with PPA in **Section 3**. In **Section 4** we shall review some existing theories of pulsating auroras, with particular focus and comments on the role of low-energy plasma in these theories. **Section 5** concludes this paper, in which we also suggest a few future tasks to advance our understanding of pulsating auroras.

2 PATCHY PULSATING AURORA: RESILIENT PATCH SHAPE AND E × B DRIFT SPEED

As mentioned above, historically, the hypothesis that PPA might map to an enhanced cold plasma region stemmed from the long-standing observations that PPA features a resilient patch shape over many pulsations, and that the overall apparent motion of the patch is consistent with the E × B convective drift. In this section, we shall review some of the recent observations in the above regard, to prepare the context for a subsequent review of the *in-*

situ evidence of low-energy plasma potentially associated with PPA.

2.1 Persistence and Subtle Change of Patch Size

While the persistence in patch shape has long been known to be a key feature of PPA, in many previous works the above notion was qualitatively inferred from a visual browse of PPA over many pulsations by researchers. In recent years, quantitative and objective algorithms have been developed to discern repetitive PPA events (Grono et al., 2017), and to examine the persistence as well as gradual changes of the patch shape and size (Humberset et al., 2016, 2018; Bolmgren, 2017; Partamies et al., 2019). Individual patch sizes typically range from several hundred to a few thousand km^2, as inferred from existing studies and our experience with PPA. Using ASI data at Poker Flat Research Range, Alaska, Humberset et al. (2018) carefully examined the extent to which pulsating auroral patches maintain their morphology and fluctuate in a coherent fashion. They found that, for the PPA events they investigated the patch shape can be considered remarkably persistent with 85–100% of the patch being repeated for 4.5–8.5 min, while the total lifetime that the patch structure is discernible in the ASI FOV is ~7–11 min. While Humberset et al. (2018) did not explicitly calculate the change rate of the patch area, it can be inferred from their presented results (e.g., their **Figure 9**) that: a) Patch 1 appears to show a trend of slightly increasing size, largely due to a slight broadening in east-west extension. b) The other three patches generally show a trend of decreasing patch size, but the average decay rate is estimated to be no more than a few tens of km^2/min, as compared to the ~1,000–4,800 km^2 patch area in their events. Bolmgren (2017) and Partamies et al. (2019) investigated the patch size evolution based on a large dataset of pulsating aurora events from the MIRACLE network in northern Fennoscandia. Their technique did not track individual patches. Instead, they studied the average time-dependent trend of the total patch size, defined as the total area of all discernible patches within the ASI FoV, and the average patch size per frame image, defined as the total patch area divided by the number of patches. Bolmgren (2017)'s study focused more on the frame-averaged patch size. They found that most events show a stable or decreasing patch size, yet a small percentage of events show a trend of slightly increasing size. The patch decay rate typically ranges from a few km^2/min up to few tens of km^2/min. Partamies et al. (2019) also noticed that there are more events showing a decreasing patch size than events showing an increasing patch size. Based on a selected subset of events that show a consistently decreasing trend of patch size, Partamies et al. (2019) found the event-averaged decay rate of the total patch area is mostly within ~10–40 km^2/min. Given the fact the total patch area defined in Partamies et al. (2019) may often contain multiple patches (see their examples) which are uncorrelated with each other, the above decay rate of the total patch area can be considered as the upper limit of the decay rate of an individual patch. To summarize from the above studies: 1) the PPA patch shape and size can be resilient over many minutes, yet slowly changes with time; 2) there are more events showing a stable or overall decreasing patch size than events showing an increasing patch size; 3) the patch decay rate is most likely in the range between a few km^2/min and a few tens of km^2/min. The slow change of patch shape/size may allude to the time evolution of the low-energy plasma structure in the magnetosphere, e.g., led by the energy dispersion (Yang, 2017).

2.2 Patch Drift Speed

Ever since the recognition of pulsating auroral phenomena, it has been suggested that the motion of the pulsating auroral patch could be caused by convection drift in the magnetosphere (Johnstone, 1978). Akasofu et al. (1966) first noticed that auroral patches drift eastward in the morning sector at typical speeds of a few 100 m/s. Nakamura and Oguti (1987) found that the overall drift pattern of auroral structures derived from all-sky TV observations was very similar to the ionospheric convection pattern measured by radars and satellites, but the comparison was not based upon the data during the same time intervals. Using observations from Scandinavian Twin Auroral Radar Experiment and simultaneous sequences of auroral images in one event, Scourfield et al. (1983) noticed that motion of pulsating aurora patches is basically consistent with E × B drift velocity.

A more systematic and definitive comparison study between the motion of PPA patches and the local E × B drift velocities was done by Yang et al. (2014). Five PPA patches were identified in data obtained from the THEMIS ASI at Gillam, while the collocated E × B convection velocities were inferred from the Super Dual Auroral Radar Network (SuperDARN) data. Yang et al. (2014) found that azimuthal velocities of five patches derived from THEMIS ASI data were consistent with the local convection velocities obtained from SuperDARN. Yang et al. (2014) also compared the PPA velocity with the Swarm satellite observations of ion drifts (Knudsen et al., 2017) in the upper F-region ionosphere. Notwithstanding the uncertainty in both measurements, the east-west patch velocities were found to be within ~20% difference from the cross-track ion drifts measured by the Swarm satellite. In particular, the trend of the latitudinal variations of ion drifts is reproduced in changes of the motion velocities of the patches at different latitudes. Based upon an extensive database obtained from THEMIS ASI over 7 years, Yang et al. (2017) made a statistical survey on the east-west motion of PPA patches. Their results showed that PPA patches mainly drift eastward after midnight and drift westward before midnight, compatible with the general pattern of global convection, and that the patch velocities are in the range of convection velocities expected from empirical convection models given the magnetic latitude. This result also indirectly supports the idea that the patch motion is convection.

However, Humberset et al. (2018) found that in some cases the patch motion differed from the E × B drift locally measured in the ionosphere by SuperDARN. We note that the velocity level (~50–100 m/s) in their events is below average for PPAs (Yang et al., 2017), and is relatively difficult to be accurately measured by SuperDARN. Humberset et al. (2018) admitted the possible uncertainty in the SuperDARN velocities, and allowed for the possibility that the patches might indeed move with E × B drift. One other possible reason for the discrepancy might be that the

local electric field is modified by the ionospheric electrodynamics (e.g., polarization electric field) associated with the pulsating auroral precipitation (Hosokawa et al., 2008, 2010; Takahashi et al., 2019), and thus differs from the magnetospheric flux tube convection.

Takahashi et al. (2019) investigated the motion of PPA patches in an experiment using the European incoherent scatter (EISCAT) radars, Kilpisjärvi Atmospheric Imaging Receiver Array (KAIRA), and an all-sky imager simultaneously. One notable advantage of Takahashi et al. (2019) study over the above-mentioned studies using SuperDARN radar lies in that, Takahashi et al. (2019)'s multi-instrumental measurements offered height information of ion velocities. Their results showed that the electric field estimated from the drift speed of auroral patches approximately corresponded with the convective electric field derived from EISCAT and KAIRA, indicating that the motion of these auroral patches was overall governed by the magnetospheric convection, though height-dependent subtle variations due to the polarization electric field generated within the patch exist.

3 EXISTING OBSERVATIONS OF LOW-ENERGY PLASMA ASSOCIATED WITH PPA

In this section, we shall review existing reports of the *in-situ* observations of low-energy plasma potentially associated with pulsating auroral activities. Some new perspectives and datasets complementary to the existing studies will be introduced. It should be noted that in some of the studies, such as Li et al. (2011b) and Nishimura et al. (2015), their research focus is on the modulation of whistler-mode chorus waves based on *in-situ* measurements, yet without conjugate optical observations. However, given the notion that the pulsating auroras could be the direct consequence of the quasi-periodic modulation of the whistler-mode chorus, their studies are still deemed relevant to our research objective, though it is impossible to check whether the hypothesized pulsating auroras are of PPA or APA types.

3.1 Low-Energy Electron Observations From *In-Situ* Particle Measurements

Nemzek et al. (1995) compared the ground optical observations of pulsating auroras and the *in-situ* measurements of high-energy electrons and low-energy plasma obtained from Los Alamos National Laboratory (LANL) geosynchronous satellites, and then examined the observations against the existing theoretical models of pulsating auroras proposed by Davidson and Chiu (1987) and Demekhov and Trakhtengerts (1994). Nemzek et al. (1995) found that, for most events, the upper limit of the plasma density was $\leq$1–2 cm^{-3}, and they could not identify any clear dependence between the *in-situ* plasma density and the pulsating auroras. They however admitted that contaminations from high-energy penetrating particles in their dataset hindered a more reliable evaluation of the local plasma density in many of their events. It should also be noted that, Nemzek et al. (1995) did not examine exact conjugacy between the geosynchronous probe and individual auroral patches. Their conjugacy condition and measurements were relevant to extended intervals of overall pulsating auroral activities that presumably contained many individual patches stochastically passing over the satellite footprint in the ionosphere. Nemzek et al. (1995) did notice that there are some small and rapid increases in density which had apparent spatial scales (a few tens to hundreds of km when mapped to the ionosphere) similar to those of individual pulsating auroral patches. However, the relative density enhancement over the background was found to be on the order of ~10% only. Nemzek et al. (1995) thus suggested that plasma density enhancement (inside-outside enhancement ratio $\geq$1) required by Demekhov and Trakhtengerts (1994)'s flow-cyclotron-maser model might not be realistic, yet the minimum change in plasma density as proposed in the Davidson and Chiu (1987) relaxation oscillator model seems to be supported. Due to the lack of their optical data source, we cannot check whether their investigated pulsating auroras events belonged to PPA or APA type.

Nishimura et al. (2015) noticed the existence of low-energy (<20 eV) field-aligned electrons in their chorus modulation events, together with the low-energy (~100 eV) field-aligned ions (to be discussed in detail later in **Section 3.4**). However, the observable part of the field-aligned electrons reported in Nishimura et al. (2015) was found to be barely above the spacecraft potential, making it very difficult to directly infer the electron density contained in such field-aligned electron beams—their authors actually resorted to low-energy ions to estimate the cold plasma density, as we shall highlight later in this section.

Samara et al. (2015) investigated both the high-energy (>1 keV) and low-energy (<1 keV) electron features associated with pulsating auroras based on low-Earth-orbit (LEO) observations from the Defense Meteorological Satellite Program (DMSP) satellites and the Reimei satellite. The downgoing low-energy electrons in their observations were interpreted as the interhemispherically transported secondary electrons [e.g., Khazanov et al. (2014)] produced by the primary pulsating auroral precipitation. Upon examining their events, we note that their Event three to six appear to be most pertinent to the PPA type. Samara et al. (2015) found a trend of the reduction of low-energy electron precipitation corresponding to the pulsating aurora, and interpreted that such a reduction of low-energy electrons is consistent with the strongly temporally varying pulsating aurora being associated with upward field-aligned currents and hence parallel potential drops of up to ~1 kV, which blocks the secondary electrons from escaping the ionosphere. Under such a notion, Samara et al. (2015)'s results might allude to a possible depletion of low-energy electron density in the pulsating auroral flux tubes. However, the reduction of low-energy electron precipitation did not occur in every PPA event; it is not evident, for example, in their Event 5. Also, it should be noted that the instrumental limitation prevents their authors to examine the electron features at energies lower than a few tens of eV.

3.2 Plasma Density Measurement From Other Techniques

Li et al. (2011b; 2013) investigated the modulation of whistler-mode chorus intensity by cold electron density variations inferred from spacecraft potentials of THEMIS satellites at the equatorial magnetosphere (Angelopoulos, 2008). They found that the chorus intensity modulation is frequently strongly correlated with electron density variations, either a density enhancement or a density depletion. In terms of their occurrence distribution, the density depletion events mostly occur in the midnight-postmidnight sector, and may also be occasionally seen in the premidnight sector. In comparison, the density enhancement events mostly occur in the postmidnight-dawn sector and also in the dayside. The density depletion events extend to higher L-shells than the density enhancement events. There were no conjugate optical observations in their study. However, under the notion that the pulsating auroras could be the direct consequence of the quasi-periodic modulation of chorus waves, it is instructive to compare the equatorial occurrence distribution of PPA/APA (Grono and Donovan, 2020) with that of the density enhancement/depletion events in Li et al. (2011b). PPA tends to be closer to dawn, and limited to lower L-shells, than APA. It appears that the APA occurrence distribution mostly overlaps with that of the density depletion events, while the PPA occurrence contains a mixture of density enhancement and depletion events. Upon comparing with the Electrostatic Analyzer (ESA) measurements onboard THEMIS, Li et al. (2011b) noticed that electron fluxes at low energies (<a few 100 eV) and with field-aligned anisotropy increase correspondingly in density enhancement events, but no corresponding electron flux variation is identified for density decreases events in the measurable energy channels of ESA. There are two possibilities. 1) The changes in the electron population in the density depletion events likely occur at energy lower than the instrumental limit (~10 eV for THEMIS ESA). 2) The satellite potential from which Li et al. (2011b) inferred the electron density might contain an artificial effect because of photoelectron escaping due to intense chorus electric fields (Malaspina et al., 2014). With the possible artifact in density depletion events in mind, and by noting the similarity between the density enhancement events and PPAs in terms of their occurrence distribution, the density enhancement in Li et al. (2011b) appears to constitute a slightly more credible (i.e., with measurable and corroborative particle counterparts) source for some PPAs, though the existence of density-depletion events and their potential role in some pulsating auroras (including APA) cannot be excluded.

Nishiyama et al. (2011) adopted an indirect yet creative approach to estimate the cold plasma density in the equatorial source region of pulsating auroras. Their technique is based on Reimei satellite observations and a time-of-flight analysis of the energy dispersion of precipitating electrons (Miyoshi et al., 2010). They found that the equatorial cold plasma density ranges from 0.2 to 21.7 cm^{-3} in their events and tends to increase as the source region moved toward the Earth. Nishiyama et al. (2011) did not provide the full event list of their study, but their presented event examples appear to be PPA. Since their technique is applicable only during the on-time of an active pulsating aurora, it is difficult to evaluate whether their inferred cold plasma density represents an enhancement or depletion compared to the ambient plasma density. Nevertheless, the inferred plasma density was found to be generally compatible with the results of empirical models [e.g., Carpenter and Anderson (1992); Sheeley et al. (2001)], implying that a strong enhancement of cold plasma density in the pulsating auroral flux tube required by the Demekhov and Trakhtengerts (1994) model might not be achievable, consistent with Nemzek et al. (1995)'s conclusion.

3.3 Low-Energy Ions From LEO Satellite Observations

The difficulty in reliably measuring cold electrons from *in-situ* particle data impelled some researchers to look into the low-energy ion structures. Liang et al. (2015) investigated 28 event intervals and 54 pulsating auroral patches that were crossed by LEO satellites. Their event selection criteria, such as that the pulsating aurora patch must be repetitively active in 2-min surrounding the passage of the LEO satellite, implies that the pulsating auroral events studied in Liang et al. (2015) were predominantly the PPA type. We have carefully re-examined all the events in Liang et al. (2015). Using the discrimination criteria in Grono et al. (2017) and Yang et al. (2019), we confirm that 47 pulsating auroral events in Liang et al. (2015) are indeed PPAs, while the rest seven events may be questionable or better categorized as APA. In 33 out of the 47 PPA events, the PPA is found to be co-located with a particle structure with enhanced low-energy ion fluxes. These low-energy ion structures are usually energy-band limited, with core energy ranging from several tens of eV up to a few hundred eV. Their pitch-angle distribution is more or less isotropic in precipitating directions within the loss cone, yet tends to peak at oblique and/or quasi-perpendicular pitch angles. On the other hand, the distribution consistently shows a sharp cut-off beyond 90° pitch angle, indicating a small upgoing flux in all events. Therefore, those low-energy ion structures must come from higher altitudes above the LEO satellite. Those PPA-associated low-energy ion structures are located equatorward of the precipitation boundary of CPS thermal ions, conformal to the normal geometry of PPA with respect to the CPS ion precipitation boundary (Viereck and Stenbaek-Nielsen, 1985; Grono and Donovan, 2019). Based upon the above observations, Liang et al. (2015) suggested that the observed low-energy ion structure might owe its origin to the ion outflows from the ionosphere. The outflows from the ionospheres in both hemispheres may populate the magnetospheric flux tubes with the low-energy plasma, particularly during disturbed intervals. The flux tubes filled with enhanced low-energy plasma of ionospheric origin define the PPA region, when the other prerequisites of PPA are also met, i.e., energetic electron fluxes and ELF/VLF waves.

Not all the pulsating auroral events investigated in Liang et al. (2015) are accompanied by discernible low-energy ion structures in LEO satellite measurements. There are a few possible explanations. 1) As we shall discuss in **Section 5**, there is a

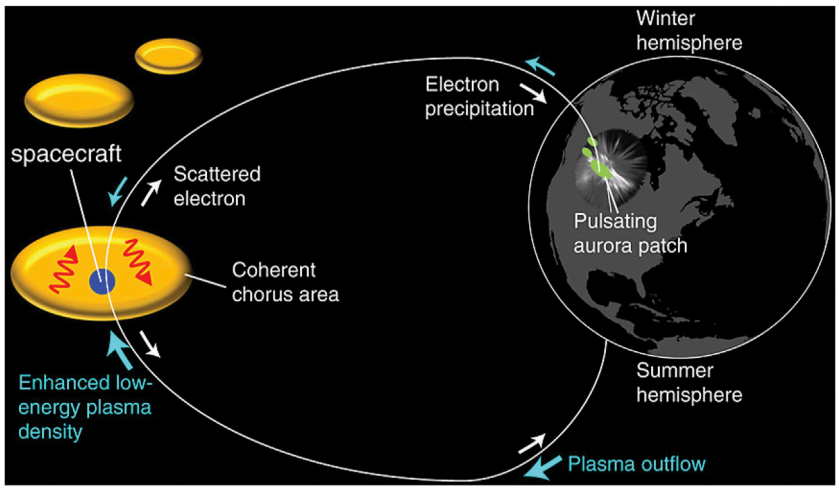

FIGURE 1 | Schematic illustration of the formation of cold plasma flux tubes from ionospheric outflows and its connection to PPA. Copied from Nishimura et al. (2015).

likely mixture of different types of pulsating auroras with different underlying generation/modulation mechanisms, and it is not surprising that some types of pulsating auroras are not necessarily related to a low-energy plasma structure. 2) A low-energy ion structure corresponding to the PPA may indeed exist in the magnetosphere, but does not extend to the topside ionosphere and thus cannot reach the LEO satellite. For example, the possible existence of parallel electric fields above the satellite in some events may hinder the low-energy ions from reaching the satellite. Also, contingent upon the source mechanisms of the low-energy ions and their transport history in the magnetosphere, in some events the low-energy ions could become entirely trapped in the magnetosphere and mirror at altitudes above the satellite. At last, it is also possible that in some cases the low-energy ion structure already reached the equatorial magnetosphere where the high-energy electron precipitation (and thus PPA) is produced, but has not reached the ionosphere by the time of satellite traversal, since high-energy electrons travel much faster than the low-energy ions.

3.4 Low-Energy Ions From Magnetospheric *In-Situ* Observations

Based on THEMIS observations Nishimura et al. (2015) identified in some events that low-energy ions of ~100 eV apparently modulate the whistler-mode chorus intensity. Those low-energy ions exist as a field-aligned structure, with noticeable oscillations superimposed. Such oscillations of the low-energy ion densities are found to correlate with the chorus intensity variations. Nishimura et al. (2015) also noticed the existence of low-energy (<20 eV) field-aligned electron structure together with the field-aligned ion structure, but it is difficult to reliably derive the low-energy electron density due to constraints imposed by the spacecraft potential and ESA energy range limit. The low-energy ion beam structure is however well above the spacecraft potential and its density is relatively easy to measure. Nishimura et al. (2015) then performed a theoretical calculation of the chorus wave growth rate. Assuming charge neutrality, the low-energy ions were used to represent cold plasma density in wave growth rate calculations, and the enhancements of the low-energy plasma density were found to contribute most effectively to chorus linear growth rates. The results in Nishimura et al. (2015) demonstrated that the low-energy plasma may directly modulate the whistler-mode chorus intensity in the equatorial magnetosphere. In line with Liang et al. (2015), Nishimura et al. (2015) also proposed that ionospheric outflows are the source of the field-aligned ion structures in their observations, and that they form the flux tubes with enhanced cold plasma, which connect to the PPA.

The proposed scenario based upon the results in Liang et al. (2015) and Nishimura et al. (2015) is sketched in **Figure 1** [copied from Nishimura et al. (2015)]. The PPA mechanism involves high-energy electrons of magnetospheric origin, the low-energy plasma of ionospheric origin, and certain ELF/VLF waves (chorus waves for example in **Figure 1**). In an overlapping region of energetic electrons and low-energy plasma flux tubes filled by outflows, ELF/VLF waves can be enhanced/modulated via an interaction with the low-energy plasma and energetic electrons. Such modulated ELF/VLE waves drive the scattering and precipitation of energetic electrons and result in the PPA. Since the plasma outflows are contingent upon the ionospheric condition in the specific hemisphere (e.g., winter or summer), it is certainly possible that the density distribution of low-energy plasma could be asymmetric in the northern and southern hemispherical segments of the outflow flux tubes. This may also affect the preferential direction of wave growth and its duct-propagation inside the flux tubes. Therefore, the shape and occurrence of PPAs, when observed simultaneously in two hemispheres, may be different and non-conjugate (Sato et al., 1998; Watanabe et al., 2007).

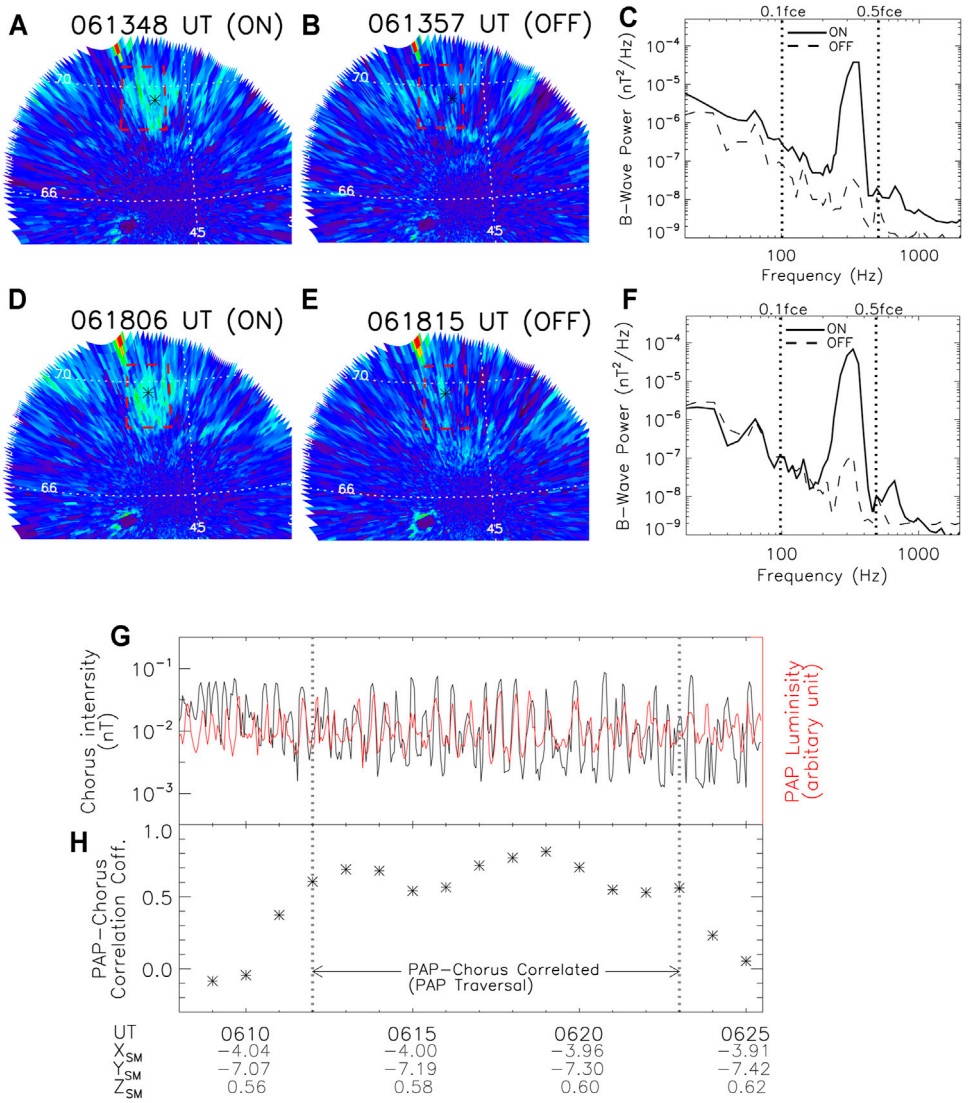

FIGURE 2 | (A,B) show the THEMIS ASI images exemplifying the on-off variation of the PPA; the ionospheric footprints of TH-E are shown as asterisk. **(C)** TH-E magnetic field wave spectra sampled at the same time epochs as in **(A,B)**; two vertical lines denote 0.1 and 0.5 f_{ce}, respectively. **(D–F)** are in the same formats as in **(A–C)**, but at different time epochs. **(G)** Temporal variations of the PPA luminosity (red) and the chorus wave intensity (black); see text for detailed procedures. **(H)** Correlation coefficients between the PPA luminosity and chorus intensity using a sliding-window technique: each data point represents the correlation coefficient calculated in a 2-min window centered at the time of the data point. SM coordinates of TH-E are labeled under the plot.

3.5 Conjugate Magnetosphere-LEO Satellite Observations of Low-Energy Ions

One key obstacle in efforts to link magnetospheric particle features to a PPA lies in the uncertainty of magnetosphere-ionosphere mapping. It is often difficult to determine whether the *in-situ* probe is situated in magnetospheric flux tubes connecting to the PPA. To date, the most reliable technique to infer conjugacy between a magnetospheric satellite and a pulsating aurora structure in the ionosphere is via the correlation between the temporal variation of the whistler-mode chorus intensity observed by the satellite and that of the optical auroral luminosity of pulsating auroras recorded by ground ASIs (Nishimura et al., 2010; 2011a; 2011b). In the following we shall re-investigate one of the events studied in Nishimura et al. (2011b), with new datasets and a focus on the low-energy plasma signatures associated with the PPA.

The event occurred on January 6, 2010. **Figures 2A,B,D,E** exemplify two on-off variations of the PPA of interest around 06: 13:50 and 06:18:10 UT, respectively. To relieve the moonlit contamination in this event we have performed a background subtraction procedure; the “darkest” pixel frame used for subtraction is determined according to the minimum brightness within 2 min surrounding the displayed image epoch. The ionospheric footprint of TH-E based upon the mapping scheme in Nishimura et al. (2011b) is shown as an

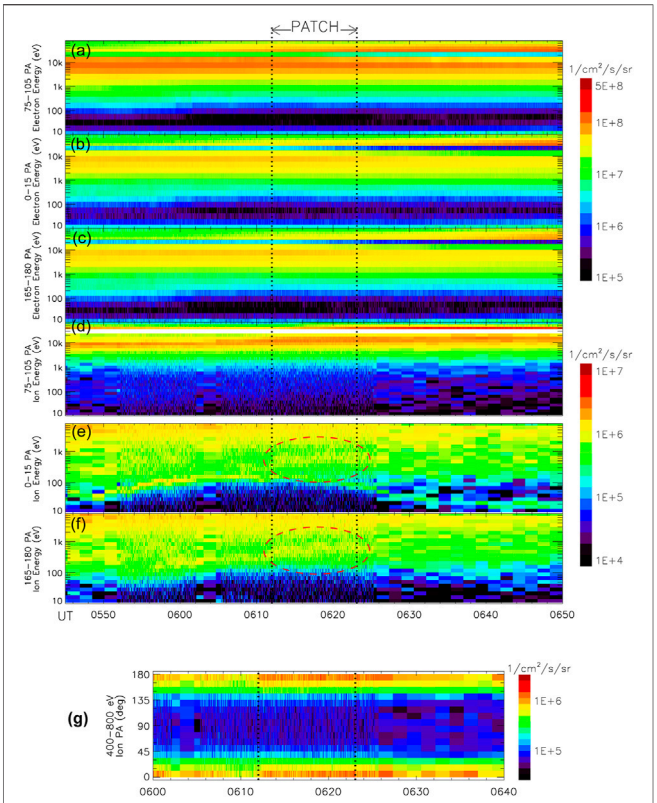

FIGURE 3 | Panels **(A–C)** show the electron energy flux spectrograms in perpendicular, parallel, and anti-parallel directions, respectively, observed by THEMIS-E. In each panel we have combined the ESA and SST data (the SST flux is multiplied by 40 for better vision). Panels **(D–F)** show the ion energy flux spectrograms in perpendicular, parallel, and anti-parallel directions, respectively. The energy range in panels **(E)** and **(F)** is adjusted to better focus on the low-energy ions of interest. Panel **(G)** shows the pitch-angle spectrogram of 400–800 eV ions.

asterisk. **Figures 2C,F** show the FFT wave spectra of the THEMIS-E magnetic field (Roux et al., 2008) sampled at the same time epochs as in **Figures 2A,B,D,E**, respectively. The variation of the lower-band chorus wave, characterized by a distinct power peak within the frequency range 0.1–0.5 f_{ce} (electron gyrofrequency), is in concert with the on-off pulsation of the PPA, revealing an inherent link between them. To examine the presence/absence of such a PPA-chorus correlation over an extended interval, we first calculate the PPA luminosity in each ASI frame by averaging the raw counts within a box region encompassing the PPA region of interest (see red boxes in the plot); such a box region may be slightly shifted every 2 min to accommodate the slow motion of the patch during the event interval. We then calculate the chorus intensities on THEMIS-E by integrating the magnetic wave spectra over the frequency range 0.1–0.5 f_{ce}, and resample them at ASI frame epochs. The temporal variations of the PPA luminosity and the chorus intensity resulting from the above procedures are shown in **Figure 2G**. We then compute the correlation coefficients (**Figure 2H**) between them in a sliding time window with 2-min in windows length and 1-min as sliding step. Both the PPA and the chorus waves persist over extended time intervals, but the PPA-chorus correlation is poor before ~0612 and after ~0623 UT, yet reasonably good between 0612 and 0623 UT. In line with Nishimura et al. (2011a; 2011b), we interpret the presence/absence of PPA-chorus correlation as indicative of whether THEMIS-E is situated inside/outside the PPA-associated flux tubes. According to the above observations and arguments, we evaluate that the TH-E traverses the PPA-associated flux tubes during ~0612–0623 UT.

Figure 3 displays the THEMIS-E particle observations (McFadden et al., 2008). Panels **Figures 3A–C** show the electron energy flux spectrograms in the perpendicular (75–105° pitch angle), parallel (0–15° pitch angle), and anti-parallel (165–180° pitch angle) directions, respectively. In each panel we have combined the ESA data in 5–25 keV energy range and the SST data in >28 keV energy range. There is a gradual rise of ≥30 keV electron fluxes with perpendicular fluxes distinctly higher than parallel/antiparallel fluxes after ~6 UT. It is reasonable to conceive that the enhanced flux and anisotropy of high-energy electrons may provide a free energy source for the growth of whistler-mode chorus, as well as contribute to a main part of the precipitation flux spectra when they are scattered by chorus waves. However, the rise of the energetic electron fluxes is gradual, and no high-energy electron structure can be specifically associated with the patch.

Figure 3D shows the ion energy flux spectrogram in the perpendicular direction. Except for the CPS thermal population, ion perpendicular fluxes at energies below 1 keV are very weak. **Figures 3E,F** offer the most important aspect of THEMIS observations of our interest in this paper. As one can see, the parallel and antiparallel fluxes are prevalent below 1 keV, and contain a number of energy-band-limited structures. We particularly highlight that the patch crossing interval is accompanied by a bi-directional low-energy field-aligned ion structures with energy band ~400–800 eV. The bottom panel of **Figure 4** shows the pitch-angle spectrogram of these 400–800 eV ions; they feature a field-aligned beam-like structure, and exist near-symmetrically in both parallel and anti-parallel directions.

In this event, a Polar Operational Environmental Satellite (POES), NOAA18, also traversed the PPA of interest at ~850 km altitude. To aid readers we shall first briefly introduce the instruments onboard NOAA18. The Total Electron Detector (TED) instrument measures the particle precipitation fluxes in two energy ranges, one between 1 and 20 keV, and the other between 50 and 1,000 eV. TED has two sensors: a 0°-sensor mounted to view roughly along the radial vector of the probe, and a 30°-sensor mounted to view in a direction 30° of the zenith. At auroral latitudes both sensors are well within the loss cone, and a total precipitation flux is evaluated from the directional fluxes in these two sensors. TED also records the particular energy band in the full range 50–20,000 eV that contains the maximum differential energy flux for the two sensors. TED has a limited capability of measuring differential energy fluxes in up to five energy bands, one from the max-flux energy band and others from four fixed energy bands in a low

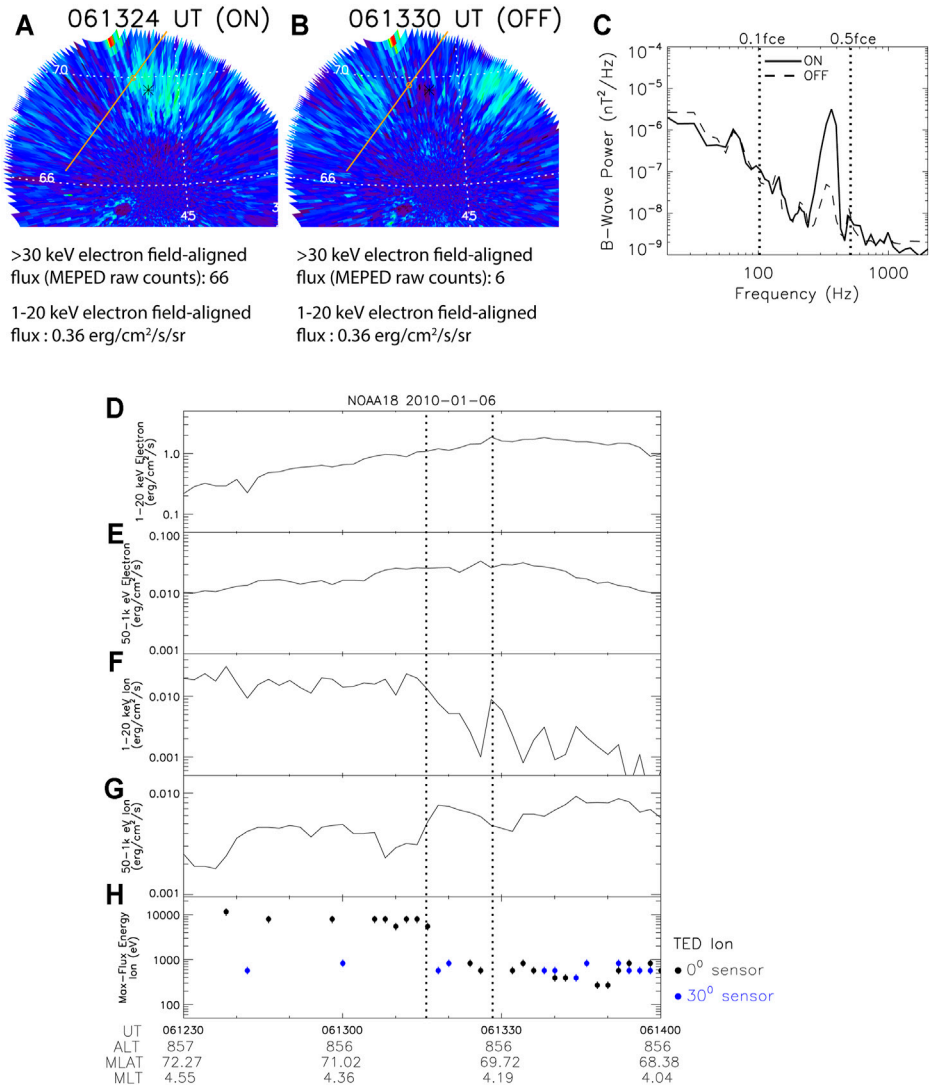

FIGURE 4 | (A,B) show the on-off variation of the PPA during the NOAA18 passage. The trajectory of NOAA18 is plotted as an orange line, and an open circle indicates the NOAA18 footprint at the current ASI frame epoch. THEMIS-E footprint is shown as asterisk. **(C)** THEMIS-E magnetic field wave spectra sampled at the same time epochs as in **(A,B)**. **(D–H)** show NOAA18 observations. **(D)** Electron precipitation fluxes in 1–20 keV energy range; **(E)** Electron precipitation fluxes in 50–1,000 eV energy range; **(F)** Ion precipitation fluxes in 1–20 keV energy range; **(G)** Ion precipitation fluxes in 50–1,000 eV energy range; **(H)** Ion max-flux energy band. Two vertical dotted lines mark the PPA crossing interval of NOAA18.

duty cycle. For more technical details and data processing procedures of POES data, see Liang et al. (2015).

Figures 4A,B display two auroral images at 06:13:24 and 06:13:30 UT, showing the on-off variation of the PPA surrounding the passage of NOAA18, and the THEMIS-E wave spectra sampled at the two time epochs. Though in the following we shall focus more on the ion signatures associated with the PPA, we have also checked the electron flux data on NOAA18 and noticed that, the >30 keV electron field-aligned flux, obtained from the 0^0-sensor of the Medium Energy Proton and Electron Detector (MEPED), drops by an order of magnitude over the on-off transition of the PPA, yet the 1–20 keV electron flux observed by the TED is much less changed (see **Figure 4D**). The above observations suggest that high-energy (>20 keV) electrons might contribute to a main portion of the modulated precipitation fluxes corresponding to the PPA in this event.

Figures 4D–H shows the NOAA18 TED observation. According to the patch dimension defined at its on-time, e.g., 06:13:24 UT, we estimate the interval when NOAA18 crossed the PPA, and mark it by vertical lines. The TED electron fluxes (**Figures 4D,E**) do not show appreciable variations across the patch in both 1–20 keV and 50–1,000 eV energy ranges. The ion flux variations are much more pronounced: the PPA occurs at a downslope of 1–20 keV ion precipitation fluxes (**Figure 4F**), yet is collocated with a peak of 50–1,000 eV ion precipitation fluxes (**Figure 4G**). Upon entering the PPA, the ion characteristic energy where the differential energy flux maximizes (**Figure 4H**) drops abruptly from ~10 keV (the CPS thermal

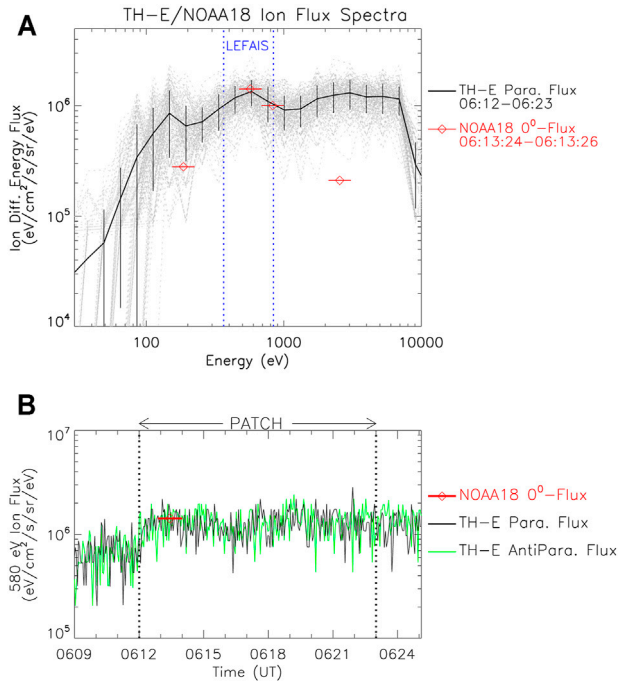

FIGURE 5 | (A) Ion parallel flux spectra sampled on NOAA18 and THEMIS-E during their respective PPA traversal intervals. For NOAA18 data, the red diamond marks the center energy, while the horizontal bar denotes the energy band. For THEMIS-E data, the energy flux spectra observed within the interval 0612–0623 UT are plotted as gray curves and superimposed; a thick dark curve and vertical bars denote the mean trend and standard deviations of THEMIS-E flux spectra averaged over the above interval. Two blue vertical dotted lines mark the energy band of the low-energy field-aligned ion structure (LEFAIS) seen on THEMIS-E. **(B)** Black and green curves denote the parallel and antiparallel fluxes of 580 eV ions observed by THEMIS-E; a red dashed line shows the 0°-flux of 580 eV ions observed by NOAA18 at 06:13:26 UT.

ions) to ~500–800 eV. The above features are consistent with those of the low-energy ion structure observed in Liang et al. (2015) as addressed in the previous subsection. Some lower-energy ions exist further equatorward over a broader MLAT width, possibly owing to some larger-scale warm cloak ions, but the high-energy electron fluxes (inferred from MEPED) become very weak there and thus no corresponding PPA is found.

We have shown that the low-energy ion structures associated with the PPA are identified in both the magnetosphere and the topside ionosphere in this event, which implies that the PPA-associated flux tubes are populated by such low-energy ion structures. According to Liouville's theorem, the field-aligned flux of the low-energy ion structure should be roughly conserved along the flux tube. To verify this, we collect the ion directional flux data from the 0°-sensor onboard NOAA18 as a proxy of the parallel flux. For THEMIS ESA measurements, we use the directional flux from the angular bin closest to the ambient magnetic field direction to approximate the parallel flux. **Figure 5** shows: a) superimposed THEMIS-E parallel flux spectra sampled during the patch crossing interval 0612–0623 UT, as well as their averaged trend; b) the temporal variations of ~580 eV ion parallel/antiparallel fluxes seen by THEMIS-E. The NOAA-18 parallel flux spectra and ~580 eV parallel flux level at its patch traversal epoch are overplotted. On average, the low-energy field-aligned ion structure measured by THEMIS-E matches well with that seen on NOAA18, in terms of both the max-flux energy (~580 eV) and the flux intensity at this energy. There is also close proximity between the ~850 eV ion flux seen on THEMIS-E and that on NOAA18, but the ion fluxes at ~3 keV and ~190 eV seen on NOAA18 are much lower than those measured on THEMIS-E. These observations indicate the presence of an energy-band-limited (~400–800 eV) low-energy ions flowing along the flux tubes threading the patch, which provides direct observational support to the scenario that the PPA connects to flux tubes filled with a low-energy plasma structure.

3.6 Possible Origin of the Field-Aligned Low-Energy Ion Structure

Liang et al. (2015) and Nishimura et al. (2015) both proposed that the ionospheric outflows are the likely source of low-energy ion structures in their observations, and that the outflows form the flux tubes with enhanced low-energy plasma that connect to the PPA. The ionospheric outflows would become a field-aligned beam structure in the magnetosphere due to the change of the magnetic field, though their pitch-angle distribution might be broadened by some processes, e.g., interaction with Alfven waves or other ULF waves (Li et al., 1997), leading the outflows to become partially trapped in the magnetosphere [see e.g., Welling et al. (2015)]. A bi-directional field-aligned distribution was found to be a common feature for ions with energies below several hundred eV in the near-Earth CPS (Wang et al., 2012). In a general sense, those field-aligned low-energy ions can be broadly categorized as "warm cloak plasma" in a classification of the cold plasma populations in the Earth's magnetosphere (Chappell, et al., 2008; Borovsky and Valdivia, 2018; Delzanno et al., 2021). In a nutshell, the warm plasma cloak consists of ions with energies of a few eV to greater than several hundred eV which display a characteristic bidirectional field-aligned pitch angle distribution. It is now well established that the ions in the warm plasma cloak owe their sources in the ionosphere, e.g., polar winds and auroral ion outflows. The occurrence distribution of warm cloak ions in the nightside (L~5–10 in the postmidnight-morning sector) overlaps with that of the PPAs (Chappell et al., 2008; Grono and Donovan, 2020).

That being said, we argue that the observed PPA-associated field-aligned low-energy ion structures may be different from the ambient warm plasma cloak ions, the latter of which owe their primary source from polar winds and are formed through stepwise energization processes in the polar cap and magnetotail (Chappell, et al., 2008). Instead, we speculate that the main source of the ~100 eV low-energy ion structures observed in Liang et al. (2015) and Nishimura et al. (2015) is likely auroral suprathermal ion outflows. Pulsating auroras usually occur during the later expansion phase and/or the recovery phase of a substorm (Jones et al., 2011; Partamies et al., 2017). Since auroral ion outflows often tend to be more structured and much more energetic than polar wind [e.g.,

Huddleston et al. (2005); Peterson et al. (2006); Welling et al. (2015)], the auroral ion outflows associated with the substorm intensification would add to the ambient warm cloak ions originating from the polar wind, and produce smaller-scale structures with above-par density and energy range over the ambient warm plasma cloak.

3.7 Indirect Clues of the Possible Existence of Low-Energy Electrons Associated With PPA

As addressed in the previous subsections, reliable detection of low-energy electrons and proper evaluation of their density remain to be challenging issues in practical *in-situ* observations to date. That said, there is indirect observational evidence that may allude to the possible existence of low-energy electrons associated with PPA. Liang et al. (2017; 2018) investigated the electron temperature (T_e) enhancement in the upper/topside ionosphere associated with PPAs. Based upon Swarm satellite measurements (Liang et al., 2017) and Poker Flat Incoherent Scatter Radar (PFISR) measurements (Liang et al., 2018), a strong T_e enhancement in the region of PPAs is found. The pulsating auroral precipitation itself that produces the optical luminosity usually consists of ~10 keV or even higher-energy electrons, which is ineffective in heating electrons in the upper/topside ionosphere. Instead, via model simulations Liang et al. (2017) reached a conclusion that, to account for realistic T_e observations in PPA events, the pulsating aurora is likely accompanied by a magnetospheric heat flux input distinctly higher than the typical ambient level of heat fluxes in the midnight-postmidnight ionosphere. It is reasonable to speculate that the heat flux leading to the observed T_e enhancement might be pertinent to certain specific mechanism of pulsating auroras. The heat flux is known to be led by the collisions between low-energy electrons (≤~10 eV) from the magnetosphere and the thermal electrons in the topside ionosphere. [e.g., Rees and Roble (1975)]. Under such a notion, the extra heat flux that results in the T_e enhancement related to PPA may allude to the potential existence of enhanced low-energy electron population extending from the magnetosphere to the upper boundary of the ionosphere in the PPA flux tubes.

4 DISCUSSION AND EXISTING THEORIES

While the phenomena of pulsating auroras have been known and extensively studied for decades, their generation mechanisms remain unclear and controversial to date. As correctly pointed out by Humberset et al. (2016), one problem that has confounded the exploration of the pulsating auroral mechanisms lies in that, there are probably many different types of auroral phenomena that have been mixed under the broad name of "pulsating auroras". Historically, pulsating auroras were subcategorized by Royrvik and Davis (1977) into patches, arcs, and arc segments, but modern literature generally only refers to "pulsating aurora" and "pulsating auroral patches" and would not consider the "streaming arc" of Royrvik and Davis (1977) to be a type of pulsating aurora. On the other hand, omega bands have been observed to be accompanied by pulsating aurora (Partamies et al., 2017; Sato et al., 2015; 2017). Such omega-band pulsating auroras are less frequent than normal pulsating auroras embedded in ambient diffuse auroras, and it is not clear that the former share the same generation mechanism as the latter—Sato et al. (2015; 2017) proposed that DC electric field variation and low-frequency electrostatic waves, instead of the whistler-mode chorus, may play important roles in the driving mechanism of omega band pulsating auroras. However, their satellite measurements were far from the equator and thus the equatorial wave activity was unknown. The recent differentiation of pulsating auroras into APA and PPA alludes to possible differences in their generation mechanisms. Most importantly, the APA appears not to be necessarily related to enhanced cold plasma structure in the magnetosphere. In this review, we focus our interest on classical PPAs that are embedded in ambient diffuse auroras and characterized by their persistent shape over the order of ~10 min, and their motion velocity approximately conformal to E × B convection. In passing, we note that many of the following discussions about PPA would also be applicable to the non-pulsating PDA. According to current understandings (Grono and Donovan, 2020), PDA likely shares the same precipitation mechanism as PPA and is also hypothesized to map to a low-energy plasma structure in the magnetosphere, but differs from PPA only in the lack of the modulation of electron precipitation.

The generation mechanisms of PPA contains three separate yet inter-related modules: 1) the precipitation mechanism, namely what process drives the energetic electrons into the loss cone, which then precipitate into the Earth's atmosphere; 2) the patch shaping mechanism, namely what process defines the patch shape and size; 3) the modulation mechanism, namely what process modulates the precipitation mechanism within the patch. The pulsating aurora is usually classified as diffuse aurora (Nishimura et al., 2020). It is generally conceived to result from the pitch-angle scattering of energetic electrons into the loss cone by certain ELF/VLF waves. In the following discussions, we shall follow this standard notion. This does not mean that we deem the ELF/VLF wave scattering as the only viable precipitation mechanism for pulsating auroras, and we do realize the existence of counter-arguments/counter-examples and other suggested precipitation mechanisms [e.g., Sato et al. (2004; 2015); Nishiyama et al. (2012); Mozer et al. (2017)]. Nevertheless, it is fair to state that the ELF/VLF wave scattering scenario remains to be the top candidate mechanism to date (Nishimura et al., 2018) and has been experimentally supported by various reports based upon good correlations between the auroral pulsations and the temporal oscillations of magnetospheric chorus waves or ECH waves (Nishimura et al., 2010, 2011b; Ozaki et al., 2015; Fukizawa et al., 2018; Kasahara et al., 2018; Hosokawa et al., 2020). Another practical reason for us to focus our attention on the ELF/VLF wave scattering mechanism is to help us thread our following discussions to avoid being too much diversified. Known ELF/VLF wave modes that are linked to diffuse auroral

precipitation are the whistler-mode chorus (both lower-band and upper-band) and the ECH wave (Throne et al., 2010; Zhang et al., 2015; Ni et al., 2016). We shall use the whistler-mode chorus, the more prevalent one at play in pulsating auroras, in most of our subsequent discussion, and note that many of the following arguments would be equally applicable to ECH waves. For some arguments specific to ECH waves, we shall explicitly annotate.

The process(es) that control and determine the spatial dimension and size of PPA is not entirely clear to date, yet some reasonable inferences can be deducted from available observations and knowledge on the wave-particle interaction process. Given the notion that the pulsating aurora precipitation results from pitch-angle scattering of CPS energetic electrons into the loss cone by chorus waves, the question then becomes what parameters/processes cause the loss-cone flux of energetic electrons in one specific area to be higher than that in its ambient surrounding. The loss-cone flux is dependent upon the trapped energetic electron fluxes and the pitch-angle scattering rate. The salient patch properties such as its persistence in shape and overall E × B drift generally invalidate the possibility that the patch size is defined by an energetic electron structure. The cold electron density then naturally arises as one topmost candidate of what defines the patch structure. The cold electron density is known to be capable of influencing almost all the properties of the generated waves: frequency, growth rate, and saturation amplitude [e.g., see a review in Delzanno et al. (2021)]. Contingent upon the other plasma/wave parameters, a density enhancement or a density depletion may cause either an increase or a decrease of the wave growth rate. Furthermore, when the density enhancement/depletion is not confined to the equator but distributed along the flux tube, which is often the case for cold plasma in the inner magnetosphere, the flux tube with enhanced/depleted plasma density would act as a duct for whistler-mode wave propagation [e.g., Katoh, (2014)]. Ke et al. (2021) numerically investigated the whistler-mode wave trapped by a field-aligned density enhancement duct, and found that the duct-trapped whistler-mode waves may remain quasi-parallel and usually get much larger amplitudes than those unducted whistler waves during propagation away from the magnetic equator. The equatorial cold plasma density is also known to affect the growth of ECH waves [e.g., Liu et al. (2018)], though a field-aligned ducted propagation scenario may not apply to ECH since ECH waves are more confined to the equator (Meredith et al., 2009; Ni et al., 2011; Zhang et al., 2015).

While the role of cold electrons in the growth/propagation of chorus waves is theoretically well recognized, it remains a challenging issue to reliably measure the density of cold electrons on *in-situ* particle detectors. In many cases, the energy range of such cold electrons may be close to even below the satellite potential and/or the low-energy bound of *in-situ* particle instruments. For a comprehensive review on the current difficulties in measuring the cold plasma density and serval existing attempts to overcome the difficulties, see Delzanno et al. (2021). That being stated, a few progresses have been made in examining the hypothesis of PPA connecting to a low-energy plasma structure in realistic observations. In this paper we have reviewed some existing reports in the above regard. At the time being, it seems that there is more supporting evidence that PPA is connected to a density-enhancement structure, consistent with the theoretical expectation under the circumstance that the low-energy plasma density is smaller than the hot plasma density (Cuperman and Landau, 1974; Wu et al., 2013; Nishimura et al., 2015), though the scenario of density-depletion PPA structure cannot be excluded. While the "warm plasma cloak" is known to be a common and large-scale feature in the postmidnight CPS (Chappell et al., 2008), the question is what extra sources/processes make the low-energy plasma have a structural dimension similar to that of PPAs. Liang et al. (2015) and Nishimura et al. (2015) both proposed that ionospheric auroral outflows may constitute one plausible formation mechanism of the flux tubes with enhanced cold plasma structure. There are of course other possible sources of the low-energy plasma structure in the magnetosphere. For example, the plasmaspheric plume, which is originally a plasmaspheric population, has known to be an important supplier of cold plasma in the outer magnetosphere (Chappell et al., 1970; Borovsky and Denton, 2008; Borovsky et al., 2013). The plume ions tend to have a perpendicular pitch-angle distribution, different from the field-aligned distribution of ionospheric outflows. However, in the postmidnight-dawn sector (>~3 MLT) auroral latitudes where PPAs are often found (Grono and Donovan, 2020), the occurrence probability of plasmaspheric plumes is fairly low (Moldwin et al., 2004; Darrouzet et al., 2008), leaving it a less likely candidate mechanism, as compared to auroral outflows, of the low-energy plasma structures shaping the PPA. At last, Liang et al. (2010) proposed that, in some cases magnetospheric ULF waves may spatially modulate the ambient low-energy plasma and generate density enhancement/depletion structures with spatial scales similar to the PPA dimension mapped to the magnetosphere.

We are then confronted with the central yet most puzzling question of pulsating auroras: what process(es) modulate the pulsating auroral precipitation. As pointed out by Humberset et al. (2016), there is so far a lack of satisfactory theories that can explain the nature of pulsating auroral modulation. Early in pulsating auroral studies, Coroniti and Kennel (1970) postulated that variations in the equatorial magnetic field, which in turn affected the strength of the ELF/VLF waves at play, are the cause of pulsating auroras. However, later observations in general invalidated such a hydromagnetic wave theory (Oguti et al., 1986; Li et al., 2011b; Nishimura et al., 2011; 2015). In many reported cases, when quasi-periodic modulation of chorus wave intensity at typical pulsating auroral periods (a few to a few tens of seconds) is observed, the oscillations of co-located electric/magnetic fields are found to be either trivial only or uncorrelated with the chorus wave modulation. This is in contrast to the observation that, modulation of whistler-mode chorus is often found in good correlation with longer-period (Pc4/Pc5) ULF waves (Li et al., 2011a; Jaynes et al., 2015).

The relaxation oscillator theory put forth by Davidson and Chiu (1987) and Davidson (1990) resorts to the nonlinear

feedback interaction between the pitch-angle anisotropy and the ELF/VLF wave growth. The picture is this: a particle distribution with a loss cone exists near the equator. Its pitch angle anisotropy favors a plasma instability that results in the generation of certain ELF/VLF waves which act to pitch-angle-scatter the electrons into the loss cone. Removal of the anisotropy reduces the growth of the waves. The loss cone is ultimately re-established when the electrons precipitate and are lost in the Earth's atmosphere, allowing the cycle to repeat. The nonlinearities inherent in the mechanism mean that in certain parameter regimes the interaction can act as a relaxation oscillator and yield quasi-periodic solutions, i.e., the auroral pulsation. The concept of the above theory seems to fit particularly well to ECH waves whose growth rate is controlled by the loss-cone distribution (Horne and Thorne, 2000; Zhang et al., 2015; Liu et al., 2018). Using their model Davidson and Chiu (1987) found that a small increase of as little as ~1% in cold plasma density can change the nonlinear system into a quasi-periodic regime. Unfortunately, the existing version of the relaxation oscillator theory remained heuristic to date. The intent of the theory was to describe a complicated physical system by a set of simple nonlinear equations, without becoming involved in the microphysics of the precise interaction mechanism. The appropriate physical parameters remained rather vaguely defined in the existing version of the theory.

Demekhov and Trakhtengerts (1994) proposed a theory which they dubbed the "flow cyclotron maser." Their theory suggested that a flux tube with enhanced cold plasma density can act as a resonance cavity for whistler-mode waves. The pulsating aurora is driven by a spike-like regime of whistler cyclotron instability (WCI) and in turn impulsive precipitation of energetic electrons in the duct with enhanced cold plasma density. Conceptually similar to the relaxation oscillator theory, the spike-like regime of WCI results from a nonlinear feedback interaction between the wave-driven pitch-angle diffusion and the growth rate of WCI (Trakhtengerts et al., 1986). Conditions for WCI to develop in a plasma duct depend strongly on the effective reflection coefficient at the edge of duct, and thus require a substantial difference between the plasma density inside of, and outside of, the PPA flux tube [$N_{inside} \geq 2N_{outside}$ as pointed out in Nemzek et al. (1995)]. Compared to the Davidson relaxation oscillator theory, the flow cyclotron maser theory dealt explicitly with the details of the wave-particle interactions, making the latter easier in some ways to compare with realistic observations. However, existing reports have directly indicated (Nemzek et al., 1995) or indirectly implied (Nishiyama et al., 2014; Nishimura et al., 2015) that the plasma density enhancement required by the flow cyclotron maser theory might not be satisfied in the realistic observations. Furthermore, Humberset et al. (2016) also found that Demekhov and Trakhtengerts (1994) model prediction of the on- and off-timescale may not fit the realistic observations.

Both the relaxation oscillator theory and the flow cyclotron maser theory postulate nonlinear dynamics as the cause of the modulation of ELF/VLF waves. They do not necessarily require time-oscillating cold plasma density for the wave modulation, though a region of enhanced cold plasma density is deemed as the necessary condition for those nonlinear dynamics to operate and produce solutions characteristic of PPA. On the other hand, Li et al. (2011b) and Nishimura et al. (2015) both noticed that the modulation of whistler-mode chorus with repetitive periods similar to that of pulsating auroras appears to be correlated with the concurrent low-energy plasma density variations. A theory is thus proposed that the low-energy plasma density may directly modulate the growth rate of the chorus. In contrast, no evident correlation is found between such chorus modulation and the variations of the CPS thermal plasma density and the local electric/magnetic fields. The low-energy electron/ion structures corresponding to those density enhancement variations were found to feature a field-aligned anisotropy (Li et al., 2011b; Nishimura et al., 2015). Nishiyama et al. (2014) also suggested that the temporal variation in cold plasma density is the most plausible process behind the on-off auroral pulsations. Under the notion that the overall patch corresponds to a spatial structure of density enhancement/depletion, if it is the case that the low-energy plasma density variations directly modulate the chorus intensity, such temporal variations are likely superimposed on the overall spatial density structure. This is evidenced by the observations in Nishimura et al. (2015) that, the density variations that modulate the chorus intensity appear as fine-scale fluctuations superimposed on a field-aligned ion beam structure.

One shortcoming of the existing theoretical studies regarding the modulation of chorus waves by density variations (Li et al., 2011b; Nishimura et al., 2015) lies in that, the wave growth rate was evaluated locally at the equator only. For a field-aligned plasma structure, its density tends to be minimum at the magnetic equator. Consequently, the low-energy plasma density inferred from the equatorial magnetospheric observations is often small, so is its modulation on the local growth rate of chorus waves [e.g., Nishimura et al. (2015)]. It is not clear that the small variations of the local chorus growth rate as shown in Nishimura et al. (2015) would produce pronounced on-off auroral pulsations. The other question is the origin of such lower-energy plasma density fluctuations. The field-aligned anisotropy of the corresponding electron/ion structures, and the lack of apparently correlated fluctuations in other local parameters (CPS thermal plasma density and the local electric/magnetic fields) in the chorus modulation region, imply that the low-energy plasma modulation presumably originates from some nonlocal processes. Unfortunately, the exploration of the origin of such density variations requires multi-point observations in the magnetosphere, which is so far pending. The lack of definite knowledge of the low-energy density profile along the flux tubes is also the major difficulty hindering Nishimura et al. (2015) from performing a full wave growth calculation along the ray paths.

While the above discussion is based upon the notion that the PPA is mainly caused by pitch-angle scattering of energetic electrons by ELF/VLF waves, which primarily occurs in the equatorial magnetosphere, we certainly do not write off the potential existence of one or more ionospheric or near-Earth processes that may act as a secondary control mechanism on the pulsating aurora. The possible role of ionospheric or near-Earth processes in pulsating auroras was addressed by a number of researchers (Stenbaek-Nielsen, 1980; Tagirov et al., 1999; Sato et al., 2004; Nishimura et al., 2015; Humberset et al., 2016; 2018).

For example, Tagirov et al. (1999) considered the effect of ionospheric feedback on the flow cyclotron maser model (Demekhov and Trakhtengerts, 1994). They suggested that, the enhanced ionospheric electron density led by the on-time pulsating auroral precipitation would increase the absorption of whistler-mode waves at the ionospheric end and thus decrease the wave reflection, therefore reducing the total wave energy in the plasma duct. This acts as a feedback quenching process and results in the off-time of the pulsating aurora. As the electron density decreases due to recombination, it allows waves to begin to grow once again. On the other hand, a number of existing studies suggested the possible existence of parallel electric fields on top of the ionosphere over the pulsating auroral region (Sato et al., 2004; Williams et al., 2006; Samara et al., 2015). Given the moderate FAC intensity associated with pulsating auroras (no more than a few $\mu A/m^2$, see Gillies et al. (2015); Liang et al. (2017)), the corresponding $E_{//}$, if existing, is presumably not strong enough to significantly affect the precipitation fluxes of high-energy electrons (≥~10 keV) typical of pulsating auroras, but might considerably influence the plasma outflows from the ionosphere. Under such a notion, the $E_{//}$associated pulsating auroras might affect the cold electron density and in turn the ELF/VLF wave growth in the magnetosphere. Admittedly, the above proposals all remain speculative at the time being. Operative near-Earth processes in pulsating auroras remain vague to date, and there is so far a lack of quantitative theories/models taking into account the role of the near-Earth processes in the generation/modulation of pulsating auroras in the existing literature.

5 CONCLUSION AND FUTURE DIRECTIONS

Despite decades of pulsating auroral studies, it remains unclear what processes define the shape/size of a PPA, though a hypothesis that PPA might be connected to a structure of enhanced cold plasma in the magnetosphere has long been one of the classical cornerstones of existing PPA theories. In this paper, we review the up-to-date observational reports, either direct or indirect, on the potential association between the low-energy plasma structure and the PPA. Based on existing evidence, we tentatively suggest that ionospheric auroral outflows might constitute one possible formation mechanism for the long-hypothesized flux tubes with enhanced cold plasma that connect to the PPA. At last, we review existing theories of pulsating auroras, with particular focus and comments on the role of low-energy plasma in these theories. To date, it is fair to state that none of the existing theories are complete and mature enough to offer a quantitatively satisfactory explanation of the observed PPA characteristics. To proceed with the pursuing of the pulsating auroras mechanisms, we would suggest the following tasks and research directions in the future.

1. Advance in an accurate measurement of the cold plasma density. Reliable measurements of the cold ion and cold electron populations and their interpretation are notoriously difficult. At a workshop on Unsolved Problems of Magnetospheric Physics in 2015, the lack of direct measurements of low-energy electrons and ions was listed as one of about a dozen unsolved problems of magnetospheric physics (Denton et al., 2016). Given the importance of cold electrons in magnetospheric dynamics, new methods that can reliably suppress photoemission or that can robustly distinguish photoelectrons from the cold-electron fluxes need to be developed. This would be key to the approval or disapproval of the long-pending hypothesis that PPA is connected to flux tubes filled with enhanced cold plasma. Besides, multi-point observations at different latitudes in the magnetosphere are also desirable to deduce the origin of the cold plasma structure and its temporal variations.
2. Advance in theories of the underlying mechanisms of oscillating ELF/VLF waves in the magnetosphere. The oscillation may come from either a nonlinear mechanism or a quasi-linear modulation by external parameter(s). A nonlinear mechanism is typically built upon a nonlinear feedback interaction between the pitch-angle anisotropy of energetic electrons and the growth of ELF/VLF waves. However, two major nonlinear theories of pulsating auroras to date, the relaxation oscillator theory (Davidson and Chiu, 1987; Davidson, 1990) and the flow cyclotron maser theory (Demekhov and Trakhtengerts, 1994), are both incomplete and/or unsatisfactory to a certain degree. New efforts must be made to renew the nonlinear theories to incorporate the updated understanding of waves and plasma parameters in the pulsating auroral region based on recent observations and simulations. It is desirable that the new nonlinear theory would explicitly contain microphysics of the wave-particle interaction and make falsifiable predictions of the wave evolution details. Nonlinear wave-particle interaction is widely accepted as the key component of the growth of ELF/VLF waves in the magnetosphere, and our understanding of such nonlinearities has greatly advanced in recent decades [see e.g., a review in Tao et al. (2020)]. Meanwhile, current observation techniques have enabled a high-resolution analysis of both ELF/VLF wave elements and pulsating auroras [e.g., Ozaki et al. (2019)].

For the quasi-linear modulation mechanism, the oscillation of ELF/VLF wave intensity is deemed to be modulated by the cold plasma density variation (Li et al., 2011b; Nishimura et al., 2015). However, in existing theoretical investigations along such a direction, the wave growth rate was evaluated locally at the equator only. For future theoretical development, convective growths along wave ray paths, taking into account the ducted propagation, should be calculated to examine whether the density structure can give significant wave amplification. To achieve this, profiles of enhanced densities along magnetic field lines must be properly modeled based upon the realistic context of the lower-energy plasma structure, e.g., originating from auroral outflows.

3. Certain auxiliary processes in the topside ionosphere or near-Earth region. As afore-addressed, while the main generation

mechanism of pulsating auroras likely resides in the equatorial magnetosphere, certain ionospheric or near-Earth processes may well act as a secondary control mechanism on the pulsating auroras. For example, certain near-Earth processes might affect the auroral outflows and their density distribution extending into the magnetosphere, and in turn affect the propagation/amplification of whistler-mode waves in the pulsating auroral flux tubes. That stated, no clear candidate of such ionospheric or near-Earth processes is well established to date, and consideration of their roles in the pulsating auroral mechanisms remains to be lacking or quantitative at best in the existing theories. More definitive observations of operative near-Earth processes in pulsating auroral events, as well as quantitative models/theories addressing the roles of these near-Earth processes in the modulation of ELF/VLF waves in the magnetosphere, are desirable research directions in the future.

AUTHOR CONTRIBUTIONS

JL and YN contributed to conception and design of the study. JL conducted the most data analyses and wrote the first draft of the manuscript. YN contributed to the contents and offered useful suggestions. BY aided in the data analyses. ED supervised this study and offered useful suggestions. VA is the PI of the THEMIS mission that is mostly used in this study. All authors contributed to manuscript revision, read, and approved the submitted version.

ACKNOWLEDGMENTS

The THEMIS mission is supported by NASA. Funding for the THEMIS ASI operation was provided by the Canadian Space Agency. We thank the entire THEMIS operation team for this important mission for pulsating auroral research. POES is launched and supported by NOAA. We thank for useful discussions with many colleagues, to name a few, Dr. Wen Li, Dr. Keisuke Hosokawa, Dr. Binbin Ni., and Dr. Sarah Jones, etc. We thank Dr. Joseph Borovsky for inviting us to write this review paper.

SUPPLEMENTARY MATERIAL

The Supplementary Material for this article can be found online at: https://www.frontiersin.org/articles/10.3389/fspas.2021.792653/full#supplementary-material

Supplementary Video 1 | Auroral movie recorded by THEMIS all-sky imager at Gillam, Canada, on 2012-10-23.

REFERENCES

Akasofu, S.-I., Meng, C.-I., and Kimball, D. S. (1966). Dynamics of the aurora-VI. *J. Atmos. Terrestrial Phys.* 28 (5), 505–511. doi:10.1016/0021-9169(66)90060-2

Angelopoulos, V. (2008). The THEMIS Mission. *Space Sci. Rev.* 141 (1-4), 5–34. doi:10.1007/s11214-008-9336-1

Bolmgren, K. (2017). *Time Dependence of Average Structure Size and Precipitation Energy in Pulsating aurora (Dissertation)*. Sweden: KTH Royal Institute of Technology. Available at: http://urn.kb.se/resolve?urn=urn:nbn:se:kth:diva-211561.

Borovsky, J. E., and Denton, M. H. (2008). A Statistical Look at Plasmaspheric Drainage Plumes. *J. Geophys. Res.* 113 (A9), a–n. doi:10.1029/2007JA012994

Borovsky, J. E., Denton, M. H., Denton, R. E., Jordanova, V. K., and Krall, J. (2013). Estimating the Effects of Ionospheric Plasma on Solar Wind/magnetosphere Coupling via Mass Loading of Dayside Reconnection: Ion-Plasma-Sheet Oxygen, Plasmaspheric Drainage Plumes, and the Plasma Cloak. *J. Geophys. Res. Space Phys.* 118 (9), 5695–5719. doi:10.1002/jgra.50527

Borovsky, J. E., and Valdivia, J. A. (2018). The Earth's Magnetosphere: A Systems Science Overview and Assessment. *Surv. Geophys.* 39 (5), 817–859. doi:10.1007/s10712-018-9487-x

Carpenter, D. L., and Anderson, R. R. (1992). An ISEE/Whistler Model of Equatorial Electron Density in the Magnetosphere. *J. Geophys. Res.* 97, 1097–1108. doi:10.1029/91JA01548

Chappell, C. R., Harris, K. K., and Sharp, G. W. (1970). The Morphology of the Bulge Region of the Plasmasphere. *J. Geophys. Res.* 75 (19), 3848–3861. doi:10.1029/JA075i019p03848

Chappell, C. R., Huddleston, M. M., Moore, T. E., Giles, B. L., and Delcourt, D. C. (2008). Observations of the Warm Plasma Cloak and an Explanation of its Formation in the Magnetosphere. *J. Geophys. Res.* 113 (A9), a–n. doi:10.1029/2007JA012945

Coroniti, F. V., and Kennel, C. F. (1970). Auroral Micropulsation Instability. *J. Geophys. Res.* 75 (10), 1863–1878. doi:10.1029/JA075i010p01863

Cuperman, S., and Landau, R. W. (1974). On the Enhancement of the Whistler Mode Instability in the Magnetosphere by Cold Plasma Injection. *J. Geophys. Res.* 79 (1), 128–134. doi:10.1029/ja079i001p00128

Dahlgren, H., Lanchester, B. S., Ivchenko, N., and Whiter, D. K. (2017). Variations in Energy, Flux, and Brightness of Pulsating aurora Measured at High Time Resolution. *Ann. Geophys.* 35, 493–503. doi:10.5194/angeo-35-493-2017

Darrouzet, F., De Keyser, J., Décréau, P. M. E., El Lemdani-Mazouz, F., and Vallières, X. (2008). Statistical Analysis of Plasmaspheric Plumes with Cluster/WHISPER Observations. *Ann. Geophys.* 26 (8), 2403–2417. doi:10.5194/angeo-26-2403-2008

Davidson, G. T., and Chiu, Y. T. (1987). A Nonlinear Model of Wave-Particle Interactions in the Trapped Radiation Belts: Auroral Pulsation Solutions. *Geophys. Res. Lett.* 14 (11), 1166–1169. doi:10.1029/gl014i011p01166

Davidson, G. (1990). The Supernatural Poems. *Space Sci. Rev.* 53 (1-2), 45–87. doi:10.1007/978-1-349-20497-7_4

Davis, T. N. (1971). Magnetospheric Convection Pattern Inferred from Magnetic Disturbance and Auroral Motions. *J. Geophys. Res.* 76, 5978–5984. doi:10.1029/ja076i025p05978

Delzanno, G. L., Borovsky, J. E., Henderson, M. G., Resendiz Lira, P. A., Roytershteyn, V., Welling, D. T., et al. (2021). The Impact of Cold Electrons and Cold Ions in Magnetospheric Physics. *J. Atmos. Solar-Terrestrial Phys.* 220, 105599. doi:10.1016/j.jastp.2021.105599

Demekhov, A. G., and Trakhtengerts, V. Y. (1994). A Mechanism of Formation of Pulsating Aurorae. *J. Geophys. Res.* 99 (A4), 5831–5841. doi:10.1029/93JA01804

Denton, M. H., Borovsky, J. E., Stepanova, M., and Valdivia, J. A. (2016). Preface: Unsolved Problems of Magnetospheric Physics. *J. Geophys. Res. Space Phys.* 121 (10), 783. doi:10.1002/2016JA023362

Fukizawa, M., Sakanoi, T., Miyoshi, Y., Hosokawa, K., Shiokawa, K., Katoh, Y., et al. (2018). Electrostatic Electron Cyclotron Harmonic Waves as a Candidate to Cause Pulsating Auroras. *Geophys. Res. Lett.* 45 (12), 668. doi:10.1029/2018GL080145

Fukuda, Y., Kataoka, R., Miyoshi, Y., Katoh, Y., Nishiyama, T., Shiokawa, K., et al. (2016). Quasi-periodic Rapid Motion of Pulsating Auroras. *Polar Sci.* 10, 183–191. doi:10.1016/j.polar.2016.03.005

Gillies, D. M., Knudsen, D., Spanswick, E., Donovan, E., Burchill, J., and Patrick, M. (2015). Swarm Observations of Field-aligned Currents Associated with Pulsating Auroral Patches. *J. Geophys. Res. Space Phys.* 120, 9484–9499. doi:10.1002/2015JA021416

Grono, E., and Donovan, E. (2019). Constraining the Source Regions of Pulsating Auroras. *Geophys. Res. Lett.* 46, 10267–10273. doi:10.1029/2019GL084611

Grono, E., and Donovan, E. (2018). Differentiating Diffuse Auroras Based on Phenomenology. *Ann. Geophys.* 36 (3), 891–898. doi:10.5194/angeo-36-891-2018

Grono, E., Donovan, E., and Murphy, K. R. (2017). Tracking Patchy Pulsating aurora through All-Sky Images. *Ann. Geophys.* 35 (4), 777–784. doi:10.5194/angeo-35-777-2017

Grono, E., and Donovan, E. (2020). Surveying Pulsating Auroras. *Ann. Geophys.* 38, 1–8. doi:10.5194/angeo-38-1-2020

Hanzelka, M., and Santolík, O. (2019). Effects of Ducting on Whistler Mode Chorus or Exohiss in the Outer Radiation belt. *Geophys. Res. Lett.* 46 (11), 5735–5745. doi:10.1029/2019gl083115

Horne, R. B., and Thorne, R. M. (2000). Electron Pitch Angle Diffusion by Electrostatic Electron Cyclotron Harmonic Waves: The Origin of Pancake Distributions. *J. Geophys. Res.* 105 (A3), 5391–5402. doi:10.1029/1999ja900447

Hosokawa, K., Miyoshi, Y., Ozaki, M., Oyama, S.-I., Ogawa, Y., Kurita, S., et al. (2020). Multiple Time-Scale Beats in aurora: Precise Orchestration via Magnetospheric Chorus Waves. *Sci. Rep.* 10, 3380. doi:10.1038/s41598-020-59642-8

Hosokawa, K., Ogawa, Y., Kadokura, A., Miyaoka, H., and Sato, N. (2010). Modulation of Ionospheric Conductance and Electric Field Associated with Pulsating aurora. *J. Geophys. Res.* 115 (A3), a–n. doi:10.1029/2009JA014683

Hosokawa, K., Sato, A., Bjornsson, N., SatoMilan, S. E., Lester, M., Bjornsson, G., et al. (2008). Electric Field Modulation behind Pulsating aurora. *J. Geophys. Res.* 113, a–n. doi:10.1029/2008JA013601

Huddleston, M. M., Chappell, C. R., Delcourt, D. C., Moore, T. E., Giles, B. L., and Chandler, M. O. (2005). An Examination of the Process and Magnitude of Ionospheric Plasma Supply to the Magnetosphere. *J. Geophys. Res.* 110 (A12), A12202. doi:10.1029/2004JA010401

Humberset, B. K., Gjerloev, J. W., Mann, I. R., Michell, R. G., and Samara, M. (2018). On the Persistent Shape and Coherence of Pulsating Auroral Patches. *J. Geophys. Res. Space Phys.* 123, 4272–4289. doi:10.1029/2017JA024405

Humberset, B. K., Gjerloev, J. W., Samara, M., Michell, R. G., and Mann, I. R. (2016). Temporal Characteristics and Energy Deposition of Pulsating Auroral Patches. *J. Geophys. Res. Space Phys.* 121, 7087–7107. doi:10.1002/2016JA022921

Jaynes, A. N., Lessard, M. R., Rodriguez, J. V., Donovan, E., Loto'aniu, T. M., and Rychert, K. (2013). Pulsating Auroral Electron Flux Modulations in the Equatorial Magnetosphere. *J. Geophys. Res. Space Phys.* 118, 4884–4894. doi:10.1002/jgra.50434

Jaynes, A. N., Lessard, M. R., Takahashi, K., Ali, A. F., Malaspina, D. M., Michell, R. G., et al. (2015). Correlated Pc4-5 ULF Waves, Whistler-mode Chorus, and Pulsating aurora Observed by the Van Allen Probes and Ground-based Systems. *J. Geophys. Res. Space Phys.* 120, 8749–8761. doi:10.1002/2015JA021380

Johnstone, A. D. (1978). Pulsating aurora. *Nature* 274, 119–126. doi:10.1038/274119a0

Jones, S. L., Lessard, M. R., Rychert, K., Spanswick, E., Donovan, E., and Jaynes, A. N. (2013). Persistent, Widespread Pulsating aurora: A Case Study. *J. Geophys. Res. Space Phys.* 118, 2998–3006. doi:10.1002/jgra.50301

Jones, S. L., Lessard, M. R., Rychert, K., Spanswick, E., and Donovan, E. (2011). Large-scale Aspects and Temporal Evolution of Pulsating aurora. *J. Geophys. Res.* 116, A03214. doi:10.1029/2010ja015840

Kangas, J., and Cao, C. (1995). Pulsating aurora --- a Review. *Chin. J. Polar Res.* 6, 39–50.

Kasahara, S., Miyoshi, Y., Yokota, S., Mitani, T., Kasahara, Y., Matsuda, S., et al. (2018). Pulsating aurora from Electron Scattering by Chorus Waves. *Nature* 554 (7692), 337–340. doi:10.1038/nature25505

Katoh, Y. (2014). A Simulation Study of the Propagation of Whistler-Mode Chorus in the Earth's Inner Magnetosphere. *Earth Planet. Sp* 66, 6. doi:10.1186/1880-5981-66-6

Ke, Y., Chen, L., Gao, X., Lu, Q., Wang, X., Chen, R., et al. (2021). Whistler-Mode Waves Trapped by Density Irregularities in the Earth's Magnetosphere. *Geophys. Res. Lett.* 48, e2020GL092305. doi:10.1029/2020GL092305

Khazanov, G. V., Glocer, A., and Himwich, E. W. (2014). Magnetosphere-ionosphere Energy Interchange in the Electron Diffuse aurora. *J. Geophys. Res. Space Phys.* 119, 171–184. doi:10.1002/2013JA019325

Knudsen, D. J., Burchill, J. K., Buchert, S. C., Eriksson, A. I., Gill, R., Wahlund, J. E., et al. (2017). Thermal Ion Imagers and Langmuir Probes in the Swarm Electric Field Instruments. *J. Geophys. Res. Space Phys.* 122, 2655–2673. doi:10.1002/2016JA022571

Lessard, M. R. (2012). "A Review of Pulsating Aurora," in *Auroral Phenomenology and Magnetospheric Processes: Earth and Other Planets*. Editors A. Keiling, E. Donovan, F. Bagenal, and T. Karlsson (Washington, D. C: American Geophysical Union). doi:10.1029/2011GM001187

Li, Y., Yoon, P. H., Wu, C. S., WeatherwaxIon, A. T., Chao, J. K., and Wu, B. H. (1997). Ion Pitch-Angle Scattering by Alfvén Waves. *Phys. Plasmas* 4, 4103–4117. doi:10.1063/1.872530

Li, W., Bortnik, J., Thorne, R. M., Nishimura, Y., Angelopoulos, V., and Chen, L. (2011b). Modulation of Whistler Mode Chorus Waves: 2. Role of Density Variations. *J. Geophys. Res.* 116, a–n. doi:10.1029/2010JA016313

Li, W., Thorne, R. M., Bortnik, J., Nishimura, Y., and Angelopoulos, V. (2011a). Modulation of Whistler Mode Chorus Waves: 1. Role of Compressional Pc4-5 Pulsations. *J. Geophys. Res.* 116 (A6), a–n. doi:10.1029/2010JA016312

Liang, J., Donovan, E., Jackel, B., Spanswick, E., and Gillies, M. (2016). On the 630 Nm Red-line Pulsating aurora: Red-line Emission Geospace Observatory Observations and Model Simulations. *J. Geophys. Res. Space Phys.* 121 (8), 7988–8012. doi:10.1002/2016JA022901

Liang, J., Donovan, E., Nishimura, Y., Yang, B., Spanswick, E., Asamura, K., et al. (2015). Low-energy Ion Precipitation Structures Associated with Pulsating Auroral Patches. *J. Geophys. Res. Space Phys.* 120, 5408–5431. doi:10.1002/2015JA021094

Liang, J., Donovan, E., Reimer, A., Hampton, D., Zou, S., and Varney, R. (2018). Ionospheric Electron Heating Associated with Pulsating Auroras: Joint Optical and PFISR Observations. *J. Geophys. Res. Space Phys.* 123, 4430–4456. doi:10.1029/2017JA025138

Liang, J., Uritsky, V., Donovan, E., Ni, B., Spanswick, E., Trondsen, T., et al. (2010). THEMIS Observations of Electron Cyclotron Harmonic Emissions, ULF Waves, and Pulsating Auroras. *J. Geophys. Res.* 115, a–n. doi:10.1029/2009JA015148

Liang, J., Yang, B., Donovan, E., Burchill, J., and Knudsen, D. (2017). Ionospheric Electron Heating Associated with Pulsating Auroras: A Swarm Survey and Model Simulation. *J. Geophys. Res. Space Phys.* 122, 8781–8807. doi:10.1002/2017JA024127

Liu, X., Chen, L., Gu, W., and Zhang, X. J. (2018). Electron Cyclotron Harmonic Wave Instability by Loss Cone Distribution. *J. Geophys. Res. Space Phys.* 123, 9035–9044. doi:10.1029/2018ja025925

Malaspina, D. M., Ergun, R. E., Sturner, A., Wygant, J. R., Bonnell, J. W., Breneman, A., et al. (2014). Chorus Waves and Spacecraft Potential Fluctuations: Evidence for Wave-Enhanced Photoelectron Escape. *Geophys. Res. Lett.* 41, 236–243. doi:10.1002/2013GL058769

McEwen, D. J., Yee, E., Whalen, B. A., and Yau, A. W. (1981). Electron Energy Measurements in Pulsating Auroras. *Can. J. Phys.* 59 (8), 1106–1115. doi:10.1139/p81-146

McFadden, J. P., Carlson, C. W., Larson, D., Ludlam, M., Abiad, R., Elliott, B., et al. (2008). The THEMIS ESA Plasma Instrument and In-Flight Calibration. *Space Sci. Rev.* 141, 277–302. doi:10.1007/s11214-008-9440-2

Meredith, N. P., Horne, R. B., Thorne, R. M., and Anderson, R. R. (2009). Survey of Upper Band Chorus and ECH Waves: Implications for the Diffuse aurora. *J. Geophys. Res.* 114, a–n. doi:10.1029/2009JA014230

Miyoshi, Y., Katoh, Y., Nishiyama, T., Sakanoi, T., Asamura, K., and Hirahara, M. (2010). Time of Flight Analysis of Pulsating aurora Electrons, Considering Wave-Particle Interactions with Propagating Whistler Mode Waves. *J. Geophys. Res.* 115, a–n. doi:10.1029/2009JA015127

Miyoshi, Y., Oyama, S., Saito, S., Kurita, S., Fujiwara, H., Kataoka, R., et al. (2015). Energetic Electron Precipitation Associated with Pulsating aurora: EISCAT and Van Allen Probe Observations. *J. Geophys. Res. Space Phys.* 120, 2754–2766. doi:10.1002/2014JA020690

Moldwin, M. B., Howard, J., Sanny, J., Bocchicchio, J. D., Rassoul, H. K., and Anderson, R. R. (2004). Plasmaspheric Plumes: CRRES Observations of Enhanced Density beyond the Plasmapause. *J. Geophys. Res.* 109, A05202. doi:10.1029/2003JA010320

Mozer, F. S., Agapitov, O. V., Hull, A., Lejosne, S., and Vasko, I. Y. (2017). Pulsating Auroras Produced by Interactions of Electrons and Time Domain Structures. *J. Geophys. Res. Space Phys.* 122, 8604–8616. doi:10.1002/2017JA024223

Nakamura, R., and Oguti, T. (1987). Drifts of Auroral Structures and Magnetospheric Electric fields. *J. Geophys. Res.* 92 (A10), 11241–11247. doi:10.1029/JA092iA10p11241

Nemzek, R. J., Nakamura, R., Baker, D. N., Belian, R. D., McComas, D. J., Thomsen, M. F., et al. (1995). The Relationship between Pulsating Auroras Observed from the Ground and Energetic Electrons and Plasma Density Measured at Geosynchronous Orbit. *J. Geophys. Res.* 100 (A12), 23935–23944. doi:10.1029/95JA01756

Ni, B., Thorne, R., Liang, J., Angelopoulos, V., Cully, C., Li, W., et al. (2011). Global Distribution of Electrostatic Electron Cyclotron Harmonic Waves Observed on THEMIS. *Geophys. Res. Lett.* 38, a–n. doi:10.1029/2011GL048793

Ni, B., Thorne, R. M., Zhang, X., Bortnik, J., Pu, Z., Xie, L., et al. (2016). Origins of the Earth's Diffuse Auroral Precipitation. *Space Sci. Rev.* 200, 205–259. doi:10.1007/s11214-016-0234-7

Nishimura, Y., Bortnik, J., Li, W., Angelopoulos, V., Donovan, E. F., and Spanswick, E. L. (2018). Comment on "pulsating auroras produced by interactions of electrons and time domain structures" by Mozer et al. *J. Geophys. Res. Space Phys.* 123, 2064–2070. doi:10.1002/2017JA024844

Nishimura, Y., Bortnik, J., Li, W., Liang, J., Thorne, R. M., Angelopoulos, V., et al. (2015). Chorus Intensity Modulation Driven by Time-varying Field-aligned Low-energy Plasma. *J. Geophys. Res. Space Phys.* 120, 7433–7446. doi:10.1002/2015JA021330

Nishimura, Y., Bortnik, J., Li, W., Thorne, R. M., Chen, L., Lyons, L. R., et al. (2011b). Multievent Study of the Correlation between Pulsating aurora and Whistler Mode Chorus Emissions. *J. Geophys. Res.* 116, a–n. doi:10.1029/2011JA016876

Nishimura, Y., Bortnik, J., Li, W., Thorne, R. M., Lyons, L. R., Angelopoulos, V., et al. (2011a). Estimation of Magnetic Field Mapping Accuracy Using the Pulsating aurora-chorus Connection. *Geophys. Res. Lett.* 38, a–n. doi:10.1029/2011GL048281

Nishimura, Y., Bortnik, J., Li, W., Thorne, R. M., Lyons, L. R., Angelopoulos, V., et al. (2010). Identifying the Driver of Pulsating Aurora. *Science* 330, 81–84. doi:10.1126/science.1193186

Nishimura, Y., Lessard, M. R., Katoh, Y., Miyoshi, Y., Grono, E., Partamies, N., et al. (2020). Diffuse and Pulsating Aurora. *Space Sci. Rev.* 216, 4. doi:10.1007/s11214-019-0629-3

Nishiyama, T., Miyoshi, Y., Katoh, Y., Sakanoi, T., Kataoka, R., and Okano, S. (2016). Substructures with Luminosity Modulation and Horizontal Oscillation in Pulsating Patch: Principal Component Analysis Application to Pulsating aurora. *J. Geophys. Res. Space Phys.* 121 (3), 2360–2373. doi:10.1002/2015ja022288

Nishiyama, T., Sakanoi, T., Miyoshi, Y., Hampton, D. L., Katoh, Y., Kataoka, R., et al. (2014). Multiscale Temporal Variations of Pulsating Auroras: On-Off Pulsation and a Few Hz Modulation. *J. Geophys. Res. Space Phys.* 119 (5), 3514–3527. doi:10.1002/2014JA019818

Nishiyama, T., Sakanoi, T., Miyoshi, Y., Kataoka, R., Hampton, D., Katoh, Y., et al. (2012). Fine Scale Structures of Pulsating Auroras in the Early Recovery Phase of Substorm Using Ground-Based EMCCD Camera. *J. Geophys. Res.* 117 (A10), a–n. doi:10.1029/2012JA017921

Nishiyama, T., Sakanoi, T., Miyoshi, Y., Katoh, Y., Asamura, K., Okano, S., et al. (2011). The Source Region and its Characteristic of Pulsating aurora Based on the Reimei Observations. *J. Geophys. Res.* 116, A03226. doi:10.1029/2010JA015507

Peterson, W. K., Collin, H. L., Lennartsson, O. W., and Yau, A. W. (2006). Quiet Time Solar Illumination Effects on the Fluxes and Characteristic Energies of Ionospheric Outflow. *J. Geophys. Res.* 111, A11S05. doi:10.1029/2005JA011596

Oguti, T., Hayashi, K., Yamamoto, T., Ishida, J., Higuchi, T., and Nishitani, N. (1986). Absence of Hydromagnetic Waves in the Magnetospheric Equatorial Region Conjugate with Pulsating Auroras. *J. Geophys. Res.* 91, 13711–13715. doi:10.1029/ja091ia12p13711

Oguti, T. (1976). Recurrent Auroral Patterns. *J. Geophys. Res.* 81 (10), 1782–1786. doi:10.1029/ja081i010p01782

Ozaki, M., Miyoshi, Y., Shiokawa, K., Hosokawa, K., Oyama, S.-i., Kataoka, R., et al. (2019). Visualization of Rapid Electron Precipitation via Chorus Element Wave-Particle Interactions. *Nat. Commun.* 10, 257. doi:10.1038/s41467-018-07996-z

Ozaki, M., Shiokawa, K., Miyoshi, Y., Hosokawa, K., Oyama, S., Yagitani, S., et al. (2018). Microscopic Observations of Pulsating Aurora Associated with Chorus Element Structures: Coordinated Arase Satellite-PWING Observations. *Geophys. Res. Lett.* 45 (22), 125–134. doi:10.1029/2018GL079812

Ozaki, M., Yagitani, S., Sawai, K., Shiokawa, K., Miyoshi, Y., Kataoka, R., et al. (2015). A Direct Link between Chorus Emissions and Pulsating aurora on Timescales from Milliseconds to Minutes: a Case Study at Subauroral Latitudes. *J. Geophys. Res. Space Phys.* 120, 9617–9631. doi:10.1002/2015JA021381

Partamies, N., Bolmgren, K., Heino, E., Ivchenko, N., Borovsky, J. E., and Sundberg, H. (2019). Patch Size Evolution during Pulsating aurora. *J. Geophys. Res. Space Phys.* 124, 4725–4738. doi:10.1029/2018JA026423

Partamies, N., Whiter, D., Kadokura, A., Kauristie, K., Nesse Tyssøy, H., Massetti, S., et al. (2017). Occurrence and Average Behavior of Pulsating aurora. *J. Geophys. Res. Space Phys.* 122, 5606–5618. doi:10.1002/2017JA024039

Rees, M. H., and Roble, R. G. (1975). Observations and Theory of the Formation of Stable Auroral Red Arcs. *Rev. Geophys.* 13 (1), 201–242. doi:10.1029/RG013i001p00201

Roux, A., Le Contel, O., Coillot, C., Bouabdellah, A., de la Porte, B., Alison, D., et al. (2008). The Search Coil Magnetometer for THEMIS. *Space Sci. Rev.* 141, 265–275. doi:10.1007/s11214-008-9455-8

Royrvik, O., and Davis, T. N. (1977). Pulsating Aurora: Local and Global Morphology. *J. Geophys. Res.* 82 (29), 4720–4740. doi:10.1029/ja082i029p04720

Samara, M., Michell, R. G., Asamura, K., Hirahara, M., Hampton, D. L., and Stenbaek-Nielsen, H. C. (2010). Ground-based Observations of Diffuse Auroral Structures in Conjunction with Reimei Measurements. *Ann. Geophys.* 28 (3), 873–881. doi:10.5194/angeo-28-873-2010

Samara, M., Michell, R. G., and Redmon, R. J. (2015). Low-altitude Satellite Measurements of Pulsating Auroral Electrons. *J. Geophys. Res. Space Phys.* 120, 8111–8124. doi:10.1002/2015JA021292

Sandahl, I., Eliasson, L., and Lundin, R. (1980). Rocket Observations of Precipitating Electrons over a Pulsating aurora. *Geophys. Res. Lett.* 7, 309–312. doi:10.1029/GL007i005p00309

Sato, N., Kadokura, A., Tanaka, Y., Nishiyama, T., Hori, T., and Yukimatu, A. S. (2015). Omega Band Pulsating Auroras Observed Onboard THEMIS Spacecraft and on the Ground. *J. Geophys. Res. Space Phys.* 120, 5524–5544. doi:10.1002/2015JA021382

Sato, N., Morooka, M., Minatoya, K., and Saemundsson, T. (1998). Nonconjugacy of Pulsating Auroral Patches Near L=6. *Geophys. Res. Lett.* 25, 3755–3758. doi:10.1029/1998gl900002

Sato, N., Wright, D. M., Carlson, C. W., Ebihara, Y., Sato, M., Saemundsson, T., et al. (2004). Generation Region of Pulsating aurora Obtained Simultaneously by the FAST Satellite and a Syowa-Iceland Conjugate Pair of Observatories. *J. Geophys. Res.* 109, A10201. doi:10.1029/2004JA010419

Sato, N., Yukimatu, A. S., Tanaka, Y., and Hori, T. (2017). Morphologies of omega Band Auroras. *Earth Planets Space* 69, 103. doi:10.1186/s40623-017-0688-1

Scourfield, M. W. J., Innes, W. F., and Parsons, N. R. (1972). Spatial Coherency in Pulsating aurora. *Planet. Space Sci.* 20, 1843–1848. doi:10.1016/0032-0633(72)90117-1

Scourfield, M. W. J., Keys, J. G., Nielsen, E., Goertz, C. K., and Collin, H. (1983). Evidence for theE×Bdrift of Pulsating Auroras. *J. Geophys. Res.* 88, 7983–7988. doi:10.1029/ja088ia10p07983

Sheeley, B. W., Moldwin, M. B., Rassoul, H. K., and Anderson, R. R. (2001). An Empirical Plasmasphere and Trough Density Model: CRRES Observations. *J. Geophys. Res.* 106, 25631–25641. doi:10.1029/2000JA000286

Stenbaek-Nielsen, H. C. (1980). Pulsating aurora: The Importance of the Ionosphere. *Geophys. Res. Lett.* 7, 353–356. doi:10.1029/GL007i005p00353

Tagirov, V. R., Ismagilov, V. S., Titova, E. E., Arinin, V. A., Perlikov, A. M., Manninen, J., et al. (1999). Auroral Pulsations and Accompanying VLF Emissions. *Ann. Geophys.* 17, 66–78. doi:10.1007/s00585-999-0066-9

Takahashi, T., Virtanen, I. I., Hosokawa, K., Ogawa, Y., Aikio, A., Miyaoka, H., et al. (2019). Polarization Electric Field inside Auroral Patches: Simultaneous experiment of EISCAT Radars and KAIRA. *J. Geophys. Res. Space Phys.* 124, 3543–3557. doi:10.1029/2018JA026254

Tao, X., Zonca, F., Chen, L., and Wu, Y. (2020). Theoretical and Numerical Studies of Chorus Waves: A Review. *Sci. China Earth Sci.* 63, 78–92. doi:10.1007/s11430-019-9384-6

Tesema, F., Partamies, N., Nesse Tyssøy, H., and McKay, D. (2020). Observations of Precipitation Energies during Different Types of Pulsating aurora. *Ann. Geophys.* 38, 1191–1202. doi:10.5194/angeo-38-1191-2020

Throne, R. M., Ni, B., Tao, X., Horne, R. B., and Meredith, N. P. (2010). Scattering by Chorus Waves as the Dominant Cause of Diffuse Auroral Precipitation. *Nature* 467, 943–946. doi:10.1038/nature09467

Trakhtengerts, V. Y., Tagirov, V. R., and Chernous, S. A. (1986). Flow Cyclotron Maser and Impulsive VLF Emissions. *Geomagn. Aeron.* 26 (1), 99–106.

Viereck, R. A., and Stenbaek-Nielsen, H. C. (1985). Pulsating Aurora and Hydrogen Emissions. *J. Geophys. Res.* 90 (11), 035. doi:10.1029/ja090ia11p11035

Wang, C.-P., Zaharia, S. G., Lyons, L. R., and Angelopoulos, V. (2013). Spatial Distributions of Ion Pitch Angle Anisotropy in the Near-Earth Magnetosphere and Tail Plasma Sheet. *J. Geophys. Res. Space Phys.* 118, 244–255. doi:10.1029/2012JA018275

Watanabe, M., Kadokura, A., Sato, N., and Saemundsson, T. (2007). Absence of Geomagnetic Conjugacy in Pulsating Auroras. *Geophys. Res. Lett.* 34, L15107. doi:10.1029/2007gl030469

Welling, D. T., André, M., Dandouras, I., Delcourt, D., Fazakerley, A., Fontaine, D., et al. (2015). The Earth: Plasma Sources, Losses, and Transport Processes. *Space Sci. Rev.* 192 (1), 145–208. doi:10.1007/s11214-015-0187-2

Williams, J. D., Macdonald, E., Mccarthy, M., Peticolas, L., and Parks, G. K. (2006). Parallel Electric fields Inferred during a Pulsating aurora. *Ann. Geophys.* 24, 1829–1837. doi:10.5194/angeo-24-1829-2006

Wu, S., Denton, R. E., and Li, W. (2013). Effects of Cold Electron Density on the Whistler Anisotropy Instability. *J. Geophys. Res. Space Phys.* 118, 765–773. doi:10.1029/2012ja018402

Yamamoto, T. (1988). On the Temporal Fluctuations of Pulsating Auroral Luminosity. *J. Geophys. Res.* 93, 897–911. doi:10.1029/ja093ia02p00897

Yang, B., Donovan, E., Liang, J., Knudsen, D., Burchill, J., Kouznetsov, A., et al. (2014). Coordinated Swarm *In-Situ* and THEMIS All Sky Imager Observations of the Motion of Patchy Pulsating aurora. *Eos. Trans. AGU Fall Meeting, Suppl. Gp44a-03.*

Yang, B., Donovan, E., Liang, J., and Spanswick, E. (2017). A Statistical Study of the Motion of Pulsating aurora Patches: Using the THEMIS All-Sky Imager. *Ann. Geophys.* 35, 217–225. doi:10.5194/angeo-35-217-2017

Yang, B., Spanswick, E., Liang, J., Grono, E., and Donovan, E. (2019). Responses of Different Types of Pulsating aurora in Cosmic Noise Absorption. *Geophys. Res. Lett.* 46, 5717–5724. doi:10.1029/2019gl083289

Yang, B. (2017). *Using the Motion of Patchy Pulsating Aurora to Remote Sense Magnetospheric Convection (Unpublished Doctoral Thesis)*. Calgary, AB: University of Calgary. doi:10.11575/PRISM/28621

Zhang, X.-J., Angelopoulos, V., Ni, B., and Thorne, R. M. (2015). Predominance of ECH Wave Contribution to Diffuse aurora in Earth's Outer Magnetosphere. *J. Geophys. Res. Space Phys.* 120, 295–309. doi:10.1002/2014JA020455

Conflict of Interest: The authors declare that the research was conducted in the absence of any commercial or financial relationships that could be construed as a potential conflict of interest.

Publisher's Note: All claims expressed in this article are solely those of the authors and do not necessarily represent those of their affiliated organizations, or those of the publisher, the editors and the reviewers. Any product that may be evaluated in this article, or claim that may be made by its manufacturer, is not guaranteed or endorsed by the publisher.

frontiers in Astronomy and Space Sciences

REVIEW
published: 04 January 2022
doi: 10.3389/fspas.2021.745357

A Review of Observations of Molecular Ions in the Earth's Magnetosphere-Ionosphere System

Mei-Yun Lin and Raluca Ilie*

Department of Electrical and Computer Engineering, University of Illinois at Urbana-Champaign, Urbana, IL, United States

Ionospheric molecular ions, such as NO^+, N_2^+ and O_2^+, are gravitationally bound, and are expected to undergo recombination to form a pair of neutral atoms, due to short dissociative recombination lifetime. Therefore, they are expected to be relatively cold in the Earth's atmosphere, compared with light ions such as H^+ and He^+, or even heavier ions such as N^+ or O^+. However, several spacecraft missions observed their presence in the high-altitude ionosphere and the magnetosphere, predominantly during the geomagnetically active times. This hints to the possibility that molecular ions have the ability to acquire sufficient energy in a very short time, and can be used as tracers of mass differentiated vertical transport to understand the mechanisms responsible for "fast ionospheric outflow." In this letter, we review the observational data sets that reported on the abundances of molecular ions in the Earth's magnetosphere-ionosphere system, starting from their first observations by the Sputnik III mission, to the current Arase (ERG) satellite and Enhanced Polar Outflow Probe (e-POP) missions. The available data suggests that molecular ions are quite abundant in the lower atmosphere at all times, but are only seen in the high-altitude ionosphere and magnetosphere during the times of increased geomagnetic activity.

Keywords: ionospheric outflow, molecular ions, cold plasma, heavy ions, polar wind

OPEN ACCESS

Edited by:
Gian Luca Delzanno,
Los Alamos National Laboratory (DOE), United States

Reviewed by:
Katherine Garcia-Sage,
National Aeronautics and Space Administration, United States
Roger Varney,
SRI International, United States

****Correspondence:***
Mei-Yun Lin
mylin2@illinois.edu

Specialty section:
This article was submitted to Space Physics, a section of the journal Frontiers in Astronomy and Space Sciences

Received: *21 July 2021*
Accepted: *22 November 2021*
Published: *04 January 2022*

Citation:
Lin M-Y and Ilie R (2022) A Review of Observations of Molecular Ions in the Earth's Magnetosphere-Ionosphere System. Front. Astron. Space Sci. 8:745357. doi: 10.3389/fspas.2021.745357

1 INTRODUCTION

Singly charged heavy ions observed in the magnetosphere, such as atomic N^+ and O^+, and molecular N_2^+, NO^+, and O_2^+ ions, are sourced from the Earth's ionosphere, and transported outward through the process of ionospheric escape. One of the main pathways of ionospheric loss is the polar wind, an ambipolar flow of plasma from the high-latitude ionosphere to the low pressure magnetosphere. This outflow (Axford and Hines, 1961; Shelley et al., 1972; Yau et al., 1991; Maggiolo et al., 2006; Schunk and Nagy, 2009; Kronberg et al., 2014; Ilie and Liemohn, 2016; Glocer et al., 2018; Lin et al., 2020) provides a pathway for atmospheric migration and escape at a rate that generally depends on solar extreme ultraviolet (EUV) photon flux striking the upper atmosphere, as well the electromagnetic driving from the solar wind. Therefore, heavy ions of ionospheric origin can be directed and further circulated into different regions of the magnetosphere: either on closed magnetic field lines (plasma sheet) where ions can potentially be returned to the ionosphere, or on open magnetic field lines (lobe region) directly connected to the interplanetary magnetic field where ions are lost to space (Christon et al., 1994; Haaland et al., 2012a; Haaland et al., 2012b; Ilie et al., 2013; Yamauchi, 2019). **Figure 1** shows an illustration of polar wind ion species, which could be created by the photoionization with the neutral atmosphere (and other ion-neutral-electron chemical reactions) and accelerated along magnetic field lines.

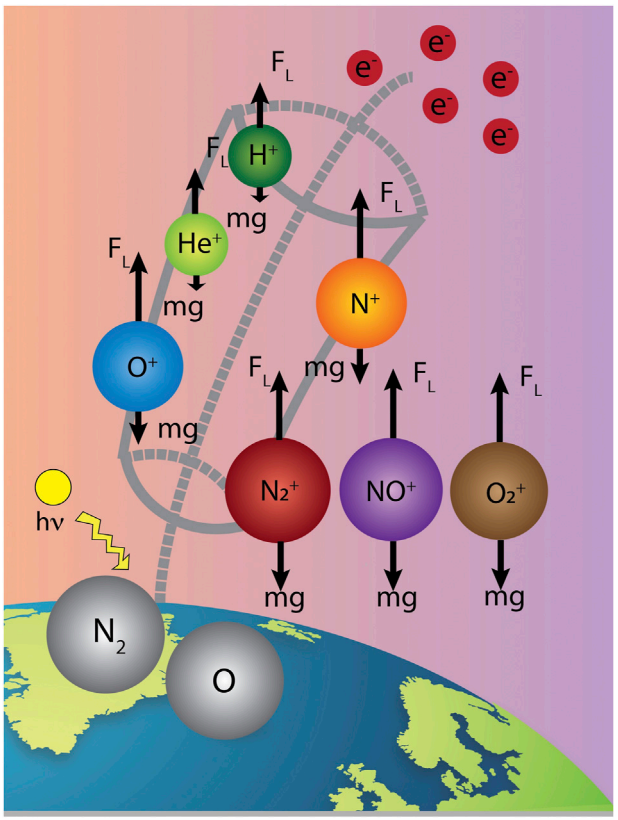

FIGURE 1 | Diagram of relevant ionospheric species (H^+, He^+,O^+, N^+, N_2^+, NO^+ and O_2^+) and electrons (e^-), with the forces they experience through the vertical transport: gravity (mg) and electromagnetic force (F_L). Following the open magnetic field line (grey dashed line), the polar wind plasma transports along the magnetic flux tube (grey cone around the dashed grey line). This illustration shows only O and N_2 species only, although the neutral composition at low altitudes includes additional species (as discussed in **Section 4**).

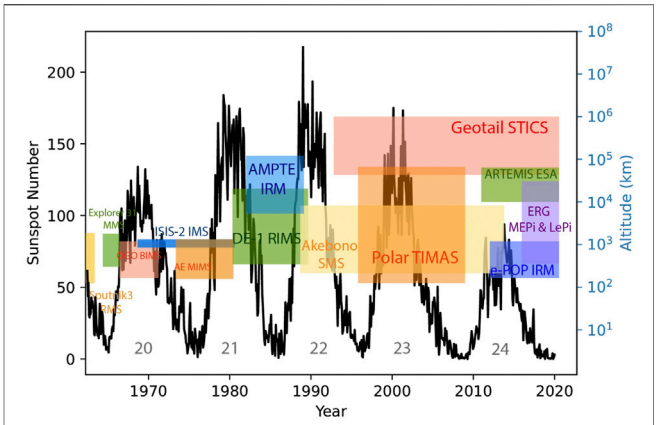

FIGURE 2 | Sunspot number from 1958 to 2021 (black lines) indicative of solar cycles 19 through 24 (numbers in grey). Over-plotted are the missions that reported on observations of molecular ions and their corresponding operating region in space, along with the timeframe of operation. Note that in most cases the actual data availability covers a time window less than the mission lifetime.

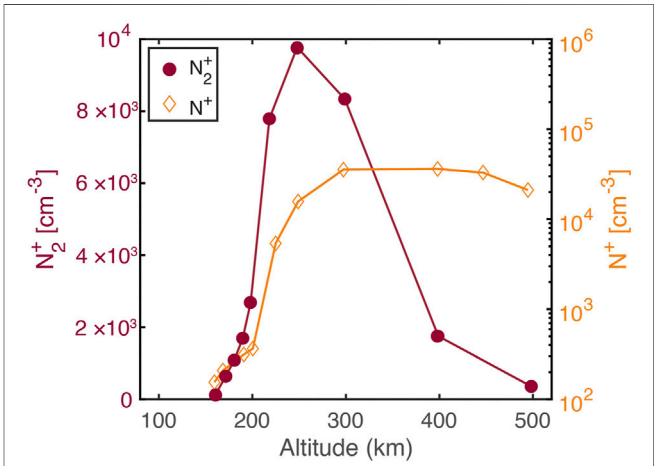

FIGURE 3 | First direct ions densities measurements by the Soviet Sputnik III satellite with the altitude profile (*x*-axis) for molecular N_2^+ (magenta line) and atomic N^+ ions (orange line) in the upper atmosphere. Noted that the left y-axis (N_2^+ ions density) and right y-axis (N^+ ions density) are on different scales. Figure digitized and adapted from (Istomin, 1966).

The dynamics leading to the ionospheric outflow of O^+ ions, and the impact on the evolution of the Earth's magnetosphere-ionosphere system have been the subject of numerous studies (e.g., Schunk and Raitt, 1980; Mukai et al., 1994; Schunk and Sojka, 1997; Seki et al., 1998; Daglis et al., 1999; Moore et al., 1999; Winglee et al., 2002; Nosé et al., 2005; Barakat and Schunk, 2006; Yau et al., 2007; Glocer et al., 2009; Garcia et al., 2010; Glocer et al., 2012; Ilie et al., 2013; Ilie et al., 2015; Lin et al., 2020). In contrast, the transport and energization of molecular ions, in addition to that of N^+ and O^+ ions, have received less attention, most likely due to the scarcity of measurements.

It is known that N_2^+, NO^+, and O_2^+ ions are the major ion populations in the ionospheric E and F layers, and primarily created through photoionization and ion-neutral-electron chemical reactions. These molecular ions maintain low energies due to their large masses and short dissociative recombination lifetimes with electrons, as they quickly form a pair of neutral atoms. In the F layer, the reaction rates of dissociative recombination of O_2^+ and NO^+ are approximately 10^{-7} cm^{-3} s^{-1}, while those of the charge exchange reactions to remove O^+ are approximately 10^{-11} cm^{-3} s^{-1}. Despite the fact that the abundance of molecular ions decreases significantly in the F2 layer, multiple missions reported their presence throughout the magnetosphere-ionosphere system (Taylor, 1974; Grebowsky et al., 1983; Craven et al., 1985; Klecker et al., 1986; Yau et al., 1993; Christon et al., 1994; Wilson and Craven, 1999; Lennartsson et al., 2000; Seki et al., 2019; Christon et al., 2020).

Figure 2 shows space missions that reported observations of molecular ions, starting from the early Sputnik III spacecraft to the Arase (ERG) mission, spanning from few hundreds km altitude to hundreds of Earth radii across several solar cycles. In this letter, we review the observational record of molecular ions from the Earth's terrestrial high latitude ionosphere to the magnetosphere. These observations provide context to understand the energization of

molecular ions, as well as to help interpret plasma observations from current and past space missions.

2 OBSERVATIONS OF MOLECULAR IONS IN THE IONOSPHERE

Molecular N_2^+ ions were first observed in the topside ionosphere by the Bennett-type radio frequency (RF) quadrupole mass spectrometer on board of the Soviet Sputnik III satellite (Nauk and Doklady, 1961). Launched on May 15, 1958, Sputnik III satellite aimed to observe the ionic compositions in the topside ionosphere, and its altitude range covered from 217 to 1864 km with 65.18° orbital inclination. **Figure 3** presents the first *in situ* observations of N^+ and N_2^+ densities as a function of altitude. These measurements from Sputnik III show that the density of N_2^+ is higher than that of N^+ at altitudes below 300 km, reaching a peak density of 9.8×10^3 cm^{-3} around 250 km altitude (Istomin, 1966). The reason for the fast decrease in N_2^+ density at higher altitudes is that in the F2 layer, N_2^+ undergoes fast recombination reactions with electrons to form a pair of neutral atoms, and charge exchanges quickly with most of the other neutral species. Thus, the concentration of N_2^+ rapidly decreases above 300 km altitude. On the other hand, N^+ is produced via N_2^+ dissociation and its concentration increases rapidly by 2–3 orders of magnitude as the altitude increases.

Previous observational data sets (Taylor et al., 1968; Johnson and Gerardo, 1972; Taylor, 1973) indicated that the abundances of molecular ions rapidly decreased due to short dissociative recombination lifetime, and therefore molecular ions were only occasionally observed. Thus, it has been concluded that the density of molecular ions in the topsides ionosphere is negligible. However, the Polar Orbiting Geophysical Observatory (OGO 6) mission launched on June 5, 1969, one of the first U.S. led large observatory to study the dynamics of high-altitude atmospheric parameters (Jackson and Vette, 1975), was the first to report observations of the high latitude trough (HLT), a prominent feature associated with the presence of molecular ions in the topside ionosphere (600–1,000 km). This HLT is a narrow (6°–10° latitude) region where the concentration of atomic H^+, He^+, O^+ and N^+ were observed to decrease by a factor of 3 or more, while molecular N_2^+, NO^+, and O_2^+ ion densities presented abrupt enhancements.

Although the inclination of the OGO 6 orbit was 82° north, due to the tilt of the dipole axis, OGO 6 covered a wide range of latitudes (Taylor, 1971), and the data coverage ranges from ~ 413 km to ~ 1077 km altitude. These unexpectedly abrupt and pronounced distributions of molecular ions were measured by the Bennett-type radio frequency ion mass spectrometer (Taylor, 1973) onboard OGO 6, showing enhancements in the density of NO^+ that reached 10^3 cm^{-3} at 1,000 km altitude near 70°–80° latitude, both in the northern and southern hemisphere, during the modest storm of June 20, 1970 (Max Kp = 4; Min Dst = −54 nT).

These large gradients in the abundances of molecular ions observed in the HLTs were later explained by the enhancement of soft electron precipitation associated with the polar cap region and the rapid loss of O^+ due to the strong electric

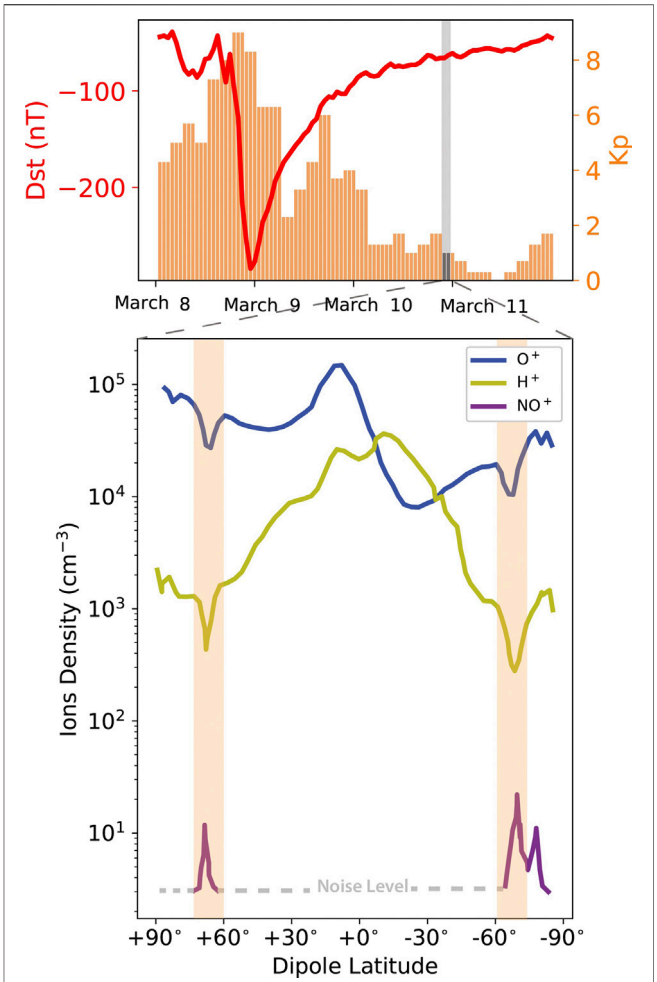

FIGURE 4 | Bottom panel shows the observed ion compositions of O^+ (blue), H^+ (light green) and NO^+ (purple) from OGO 6 satellite versus the latitudes, extracted during the recovery phase of March 8, 1970 geomagnetic storm. Note that the light orange blocks highlighted the HLTs with abrupt enhancements of NO^+ densities and decreases of atomic O^+ and H^+ ions densities. The Kp (orange bars) and Dst (red) indices during this storm are provided for reference. Figure digitized and adapted from (Taylor et al., 1975), and dipole latitudes in the *x*-axis are also identified as geomagnetic latitudes.

convection field (Taylor et al., 1975; Grebowsky et al., 1976; Grebowsky et al., 1983). On March 10, 1970, 1 day after the intense geomagnetic storm of March 8, 1970 (Max Kp = 9; Min Dst = -285 nT), the HLT was observed at altitudes between 700–800 km, and ~ 65.8° latitude in the northern hemisphere and ~ -65.2° latitude in the southern hemisphere. **Figure 4** shows the measurements of O^+, H^+ and NO^+ densities from OGO 6 satellite versus latitudes, extracted during the recovery phase of March 8, 1970 geomagnetic storm. It can be seen that in both HLT regions (with ~ 5° latitude range, highlighted as light orange), ~ 50% of both O^+ and H^+ densities are depleted at a time when NO^+ ions density increased about a factor of 8, while the peak value of NO^+ concentration was up to 20 cm^{-3} at ~ 700 km altitude. These observations suggest that the rapid loss of O^+ in the HLTs could contribute to the source of NO^+

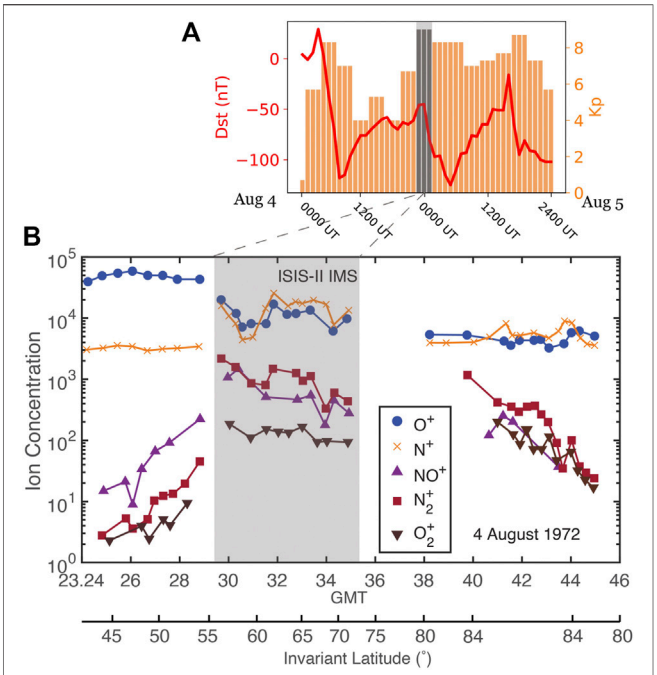

FIGURE 5 | High latitude ISIS 2 measurements showing the ion compositions of O^+ (blue), N^+ (orange), NO^+ (purple), N_2^+ (magenta) and O_2^+ (black), at 1,400 km altitude **(B)** during the storm of August 4, 1972. The measurements were observed along the ISIS 2 satellite trajectory, which is shown here as the combination of Greenwich Mean Time (GMT) and invariant latitudes. The Kp (orange bars) and Dst (red line) indices during this storm are shown for reference **(A)**; greyed out area on top panel corresponds to the time interval when the measurements present in bottom panel are extracted. Figure digitized and adapted from (Hoffman et al., 1974).

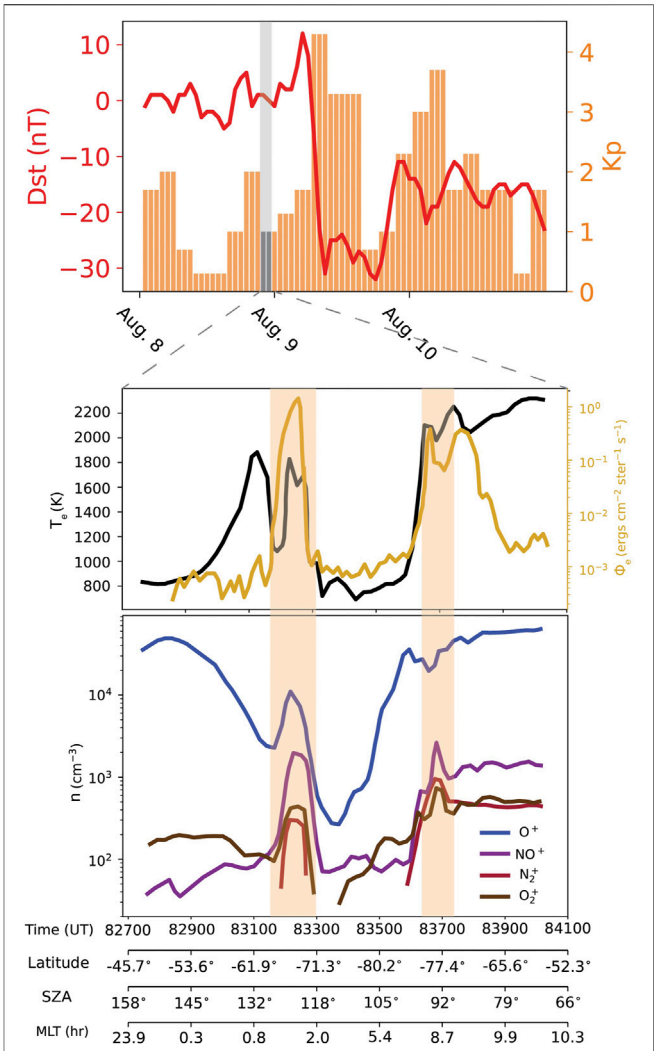

FIGURE 6 | AE-C measurement during the winter solar minimum at high southern latitude F layer. The bottom panel shows the ion compositions (n) of O^+ (blue line), NO^+ (purple line), N_2^+ (magenta line) and O_2^+ (black line) when the AE-C passed the orbit of 14 182 (versus UT, latitude and MLT). The center panel is electron temperature (T_e, black line), and energetic electron flux (Φ_e, gold line) measured at the same time and location as the bottom panel. The HLTs were highlighted as light orange blocks here, where the abrupt enhancements of molecular ions densities were observed. The Kp (orange bars) and Dst (red line) indices during this time of orbit 14 182 are shown for reference **(top panel)**; greyed out area on top panel corresponds to the time interval when the measurements present in bottom panel are extracted. Figure digitized and adapted from (Brinton et al., 1978).

ions through the reactions of O^+ ions with the neutral atmosphere, $O^+ + N_2 \rightarrow N + NO^+$ and possibly $O^+ + O_2 \rightarrow O_2^+ + O$. Note that the OGO 6 also had ability to distinguish the increasing ion densities of N_2^+ and O_2^+, but were not shown here due to clarity of the figure (Taylor et al., 1975). Grebowsky et al. (1983) further examined the average invariant latitude-magnetic local time (MLT) distribution of HLTs based on the OGO 6 data from 1969–1970 and found that the location of HLTs was aligned with the polar cap boundary, associated with the maximum electric convection field, as well as enhancements of soft electron fluxes.

The presence of molecular ions in the terrestrial ionosphere was also confirmed by measurements from the Ion Mass Spectrometer (IMS) on board NASA International Satellite for ionospheric Studies (ISIS 2) (Hoffman, 1970). Deployed on April 1, 1971, ISIS 2 operated in an orbit with an apogee of 1,440 km, a perigee of 1,360 km, and an inclination of 88.1°. The IMS onboard the ISIS 2 was designed to measure the ionic compositions of the ionosphere in the mass range of 1–64 amu. **Figure 5** shows such observations during the August 4, 1972 geomagnetic storm (Max Kp = 9, Min Dst = -125 nT) (Hoffman et al., 1974). These measurements indicated that during times of increased geomagnetic activity (Kp = 9), O^+ and N^+ have comparable concentrations from 55° latitude to 85° at 1,400 km altitude, while the concentration of NO^+ and N_2^+ reached more than 10^3 cm^{-3} and that of O_2^+ was ~ 10^3 cm^{-2} from 55° latitude to 70°. The ion densities ratio of NO^+/N^+ was ~ 0.015–0.35 during this event. When the spacecraft passed through above 55° latitude region, the molecular ions densities increase from 2×10^2 to 10^3 cm^{-3} and the densities of O^+ decreased from 3×10^4 to 10^4 cm^{-3}. There are several reasons that could explain the abundance of molecular ions during this time. First, based on the OGO 6 measurements from the neutral mass spectrometer in a similar event, the

densities of N_2 at high altitudes increased significantly, and this could provide a potential source of molecular N_2^+ ions (Hedin and Reber, 1972). Second, these unexpected enhancements of molecular ion densities had similar locations as those of HLTs observed by OGO 6 satellite (Taylor et al., 1975; Grebowsky et al., 1976; Grebowsky et al., 1983) and thus, the enhancement of soft electron precipitation and rapid loss of O^+ ions at a time associated with strong electric convection fields could provide an additional source of molecular ions in the topside ionosphere.

The concomitant observations of enhancements in molecular ion densities and HLTs were noted not only during solar maximum by OGO 6, but also during the solar minimum by instruments onboard the Atmosphere Explorer (AE-C) mission. Launched in December 1973, AE-C aimed to study the structure of thermosphere, especially how the photochemical processes govern the region (Richards and Voglozin, 2011). During the first year of operation, the perigee moved from about 68° latitude north down to about 60° south, and the orbit became circular at approximately 390 km altitude (Richards and Voglozin, 2011). The ion mass spectrometers on board the AE-C were a Bennett-type radio frequency ion mass spectrometer (Brinton et al., 1973) and a magnetic ion mass spectrometer (Hoffman et al., 1973), and were employed to measure ion densities.

HLTs were observed during June 1976 at 70° latitude and 300 km altitude in the southern hemisphere during quiet winter time conditions (Brinton et al., 1978). **Figure 6** shows the ion densities (bottom panel), electron temperature and energy fluxes (center panel), and the Dst and Kp indices (top; shown for context). It can be seen that at this time the density of NO^+ reached 2.5×10^3 cm^{-3}, and the density N_2^+ and O_2^+ were 9.5×10^2 and 5×10^2 cm^{-3}. Unlike the depletion of O^+ in the HLT observed by OGO 6, the observed O^+ density by AE-C didn't decrease as the molecular ion densities increased. By examining the electron temperature as well as the energetic particle flux near the HLTs, the increase of electron temperature suggests that the existence of a locally acting heating mechanism responsible for the enhancement in the energetic particle flux. This could possibly have provided the additional energy to molecular ions, leading the formation of HLTs in the high latitude ionosphere (Brinton et al., 1978). Furthermore, O^+ ions were the dominant heavy ion species above 50° latitude ionosphere and the dominant molecular ions species were either NO^+ or O_2^+. The NO^+ ions was likely to dominate the molecular ions species of the sunlit F region as well as 60°–90° latitude in the nightside region, while O_2^+ was likely to dominate the nightside region from 50°–60° latitude. Note that N_2^+ was never the dominant ion species during solar minimum conditions, but it could be the second most abundant molecular ions species where NO^+ was the major molecular ion. The highest observed density of O_2^+ and NO^+ were ~10^4 cm^{-3} near the cusp region, and ~10^3 cm^{-3} around the nightside auroral zone (Brinton et al., 1978).

The upflowing molecular ions at several thousand kilometers altitude were first observed by Suprathermal Ion Mass Spectrometer (SMS) carried on the Akebono (EXOS-D) spacecraft. Launched on February 21, 1989, the Akebono (EXOS-D) spacecraft was a Japan-led satellite mission designed to investigate processes leading to particle acceleration above the auroral region (Tsuruda and Oya, 1991). The Akebono spacecraft operated in an elliptical polar orbit, with an apogee of 2.65 R_E (~ 10,500 km) altitude, a perigee of 275 km, and inclination of 75°. The SMS on board the Akebono spacecraft was designed to measure mass-per-charge (m/q) and energy-per-charge (E/q) with the range of 1–67 amu/q and 0.1–4,000 eV/q by sampling the two dimensional thermal (0–25.5 eV) and suprathermal (55 eV/q–4.1 keV/q) ion energy distributions in the satellite spin plane (Whalen et al., 1990).

Table 1 summarizes the observations of molecular ions from Akebono spacecraft based on four storm events in 1990 [adapted from Yau et al. (1993)]. Molecular ions were a minor component of the upflowing ionospheric ion population, for which NO^+ and N_2^+ were the dominant molecular ion species, and the density of O_2^+ was one order of magnitude lower. Molecular ions could be observed during the storm main and recovery phases at altitudes between 7,000–10,000 km near 70° latitude. The abundance of molecular ions was correlated with the density ratio of N^+/O^+ (Yau et al., 1993), that is, the maximum flux of molecular ions was accompanied by the unity ratio of N^+/O^+, and the molecular ions flux could be at most 15% of the total ionospheric outflow fluxes during storm time. The increase in molecular ions densities can be explained by the increase in neutrals densities and their collisional ionization in the 500–1,000 km altitude range. For instance, the density of N_2 in this region, as predicted by the Mass-Spectrometer-Incoherent-Scatter (MSIS-86) model (Hedin, 1987), increases by a factor of ~ 80 from quiet time (Ap Index = 4) to storm time conditions (Ap Index = 60). Moreover, heavy ions produced in the 500–1,000 km altitude region are required to attain ~ 1 km/s velocities in order to reach the high altitude region. Based on the Akebono spacecraft observational data, the lifetimes of molecular ions between 300 and 1,000 km were estimated ~ tens of minutes. This implies that transverse heating commonly occurring between 400 and 1,000 km altitude during the active auroral conditions could be sufficient to energize them.

Previous observations indicated that molecular ions were likely to be present in the topside ionosphere, during and after strong geomagnetic storms, for which the minimum Dst was smaller than -100 nT. However, recent observations from the CASSIOPE Enhanced Polar Outflow Probe (e-POP) mission indicated that molecular ions were observed frequently even during modest geomagnetic storm at all e-POP altitudes, spanning between 325–1,500 km (Yau et al., 2006; Yau and Howarth, 2016). Based on the e-POP data collected during 2013–2018 time period, most observations of molecular ions occurred in the pre-midnight sector above 50° latitude ionosphere, while the lowest count rate events were located in the 8–10 MLT range, which coincided with the peak region of energetic precipitating electrons (Foss and Yau, 2019).

3 OBSERVATIONS OF MOLECULAR IONS IN THE MAGNETOSPHERE

Until the flight of the Dynamic Explorer (DE-1), instruments on board magnetospheric missions were not capable of fully resolving all heavy ion species, molecular ions in particular.

TABLE 1 | Observations of molecular ions from Akebono during four storm events in 1990, including the time and location of the observation as well as the ion fluxes of N^+ to O^+, molecular ions to O^+, and between molecular ions (NO^+:N_2^+:O_2^+). Data collected and summarized based on the Yau et al. (1993) study.

Storm event	Jan 21–23, 1990	Mar 11–13, 1990	Mar 17–19, 1990	May 25–27, 1990
Storm phase	Recovery phase	Main phase	Main phase	Recovery phase
Observed Latitude	near 70° Nightside	65°–76° Dayside	near 70° Dayside	near 70° Dayside
Observed Altitude (km)	8,700–9,950	6,100–8,160	9000–10,000	6,500–7,800
Flux of N^+/O^+	~ 0.08	~ 1	~ 0.6	~ 1
(Molecular ions)/O^+	~ 0.05	0.14	~ 0.05	0.1
Flux of NO^+:N_2^+:O_2^+	0.3: 1: 0.01	1: 0.9: 0.05	1: 0.9: 0.08	1: 1: 0.1
Min. Dst (nT) during Storm phase/Storm Event	–32/–45	–159/–162	–43/-67	–68/–87
Kp/Max Kp	4/4	7/7	6/6	6/7

TABLE 2 | AMPTE observations of molecular ions during three storm events in 1984, including the observed time intervals and spatial locations, ions energy densities, and the total molecular ions to O^+ flux ratios, with the corresponding Dst and Kp. Data collected and summarized based on the Klecker et al. (1986) study.

	Sep 4, 1984	Oct 19, 1984	Nov 17, 1984
Observed time	Onset phase	Recovery phase	Late recovery phase
Total energy density (keV/cm^3)	32	6	5.1
O^+ energy density (of total)	21%	12%	8.5%
(NO^++O_2^+)/O^+ flux (160 keV)	0.031 ± 0.004	0.018 ± 0.004	< 0.038
L	6.6–8.3	8.0–9.4	7.7–9.5
Dst/Minimum Dst (nT)	–58/–162	–60/–86	–60/–133
Kp/Max Kp	8/8	5/7	4/8

Explorer 45, launched on November 15, 1971, reported on the presence of an unexpected heavier ion species (M/Q ≥ 9) with energies in the range of tens of MeVs, observed in the radiation belt region during the geomagnetic storm of August 4, 1972 (Max Kp = 9, Min Dst = -125 nT). Because the heavy ion detector telescope on the Explorer 45 didn't have capability to accurately determine the mass of the observed ion species, Spjeldvik and Fritz (1981) identified these energetic ion species either as the magnesium, or silicon and iron ions.

Molecular N_2^+, NO^+, and O_2^+ ions were first observed in the magnetosphere by the Retarded Ion Mass Spectrometer (RIMS) (Chappell et al., 1982) on board the Dynamic Explorer (DE-1) (Craven et al., 1985). Launched on August 3, 1981, the DE-1 covered the altitude range between 500 km and ~ 3.6 Earth radii, and aimed to investigate in the interactive processes in the Earth's ionosphere, plasmasphere, and magnetosphere. RIMS was designed to measure ions with mass between 1 and 32 amu, and with energies ranging from 0 to 50 eV. To resolve molecular ions species and their corresponding kinetic energies, RIMS was designed with the mass voltage steps closer together for mass range between 28 and 32. During the storm of September 6, 1982 (Max Kp = 9, Min Dst = ~ -300 nT), DE-1 measurements show that the maximum flux of molecular ions was as high as ~ 10^6 cm^{-2} s^{-1} around 70° latitude at 1–3 R_E, and NO^+ and N_2^+ were the dominant molecular ions species with similar fluxes. Furthermore, the velocity distribution of molecular ions followed a Maxwellian distribution in the ionosphere, and transferred to the field-aligned velocity distribution at several Earth radii altitude (Craven et al., 1985). In the region between 1–3 R_E, the velocities of molecular ions were observed to be around 5–10 km/s, and their kinetic energies were at least 20 eV at 2.5 R_E geocentric distance. The DE-1 observational dataset suggests that molecular ions are likely to be produced in the polar cusp region and convected to the nightside cusp and polar cap region by the influence of crossed electric and magnetic fields ($\mathbf{E} \times \mathbf{B}$).

Energetic molecular ions with energies higher than 100 keV/e were first detected in the outer ring current region (L ~ 7) by Suprathermal Energy ionic Charge Analyzer (SULEICA) onboard the Active Magnetospheric Particle Tracer Explorers (AMPTE) Ion release Module (IRM) spacecraft. Launched on August 16, 1984, the AMPTE/IRM operated in an elliptical orbit with inclination of 28.8° with an apogee of 18.7 R_E (Mobius et al., 1985). The SULEICA instrument was a curved plate electrostatic energy-per-charge analyzer that measured ion energies between 5–270 keV/q (Hausler et al., 1985). While no observations of molecular ion were reported during quiet time periods by the AMPTE/IRM spacecraft, molecular ions in the outer ring current were observed during multiple storm events (Klecker et al., 1986). **Table 2** presents a synthesis of measured (NO^++O_2^+)/O^+ fluxes, and the relevant information regarding each storm interval (Dst, Kp, and observation time interval), as well as the ratio of O^+ energy flux to the total observed energy flux for these events. The observational record indicates that both O_2^+ and NO^+ were the dominant molecular ions species in this region. The average molecular ions flux was observed to be around 3–4% of O^+ flux in the energy range 80–230 keV during active times. **Figure 7** shows the change in energy flux with particle energy during the

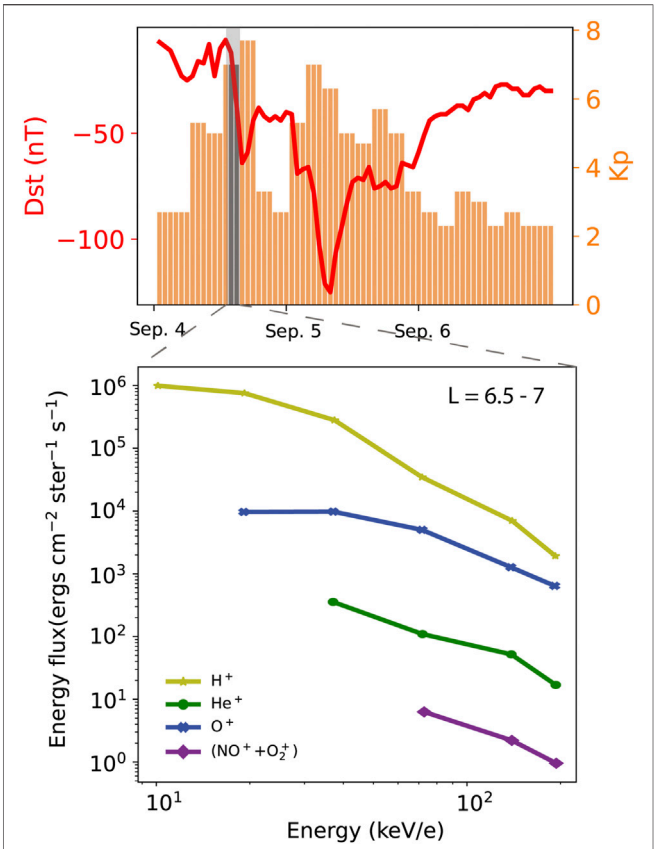

FIGURE 7 | Measurements from the SULEICA instrument on board the AMPTE/IRM spacecraft showing the energy spectra of H^+ (light green), He^+ (dark green), O^+ (blue), and molecular ions (purple) with energy range 10–230 keV/e **(bottom panel)**. The Kp (orange bars) and Dst (red line) indices from the September 4, 1984 storm are shown for reference **(top panel);** greyed out area on top panel corresponds to the time interval when the measurements presented in bottom panel are extracted. Figure digitized and adapted from (Klecker et al., 1986).

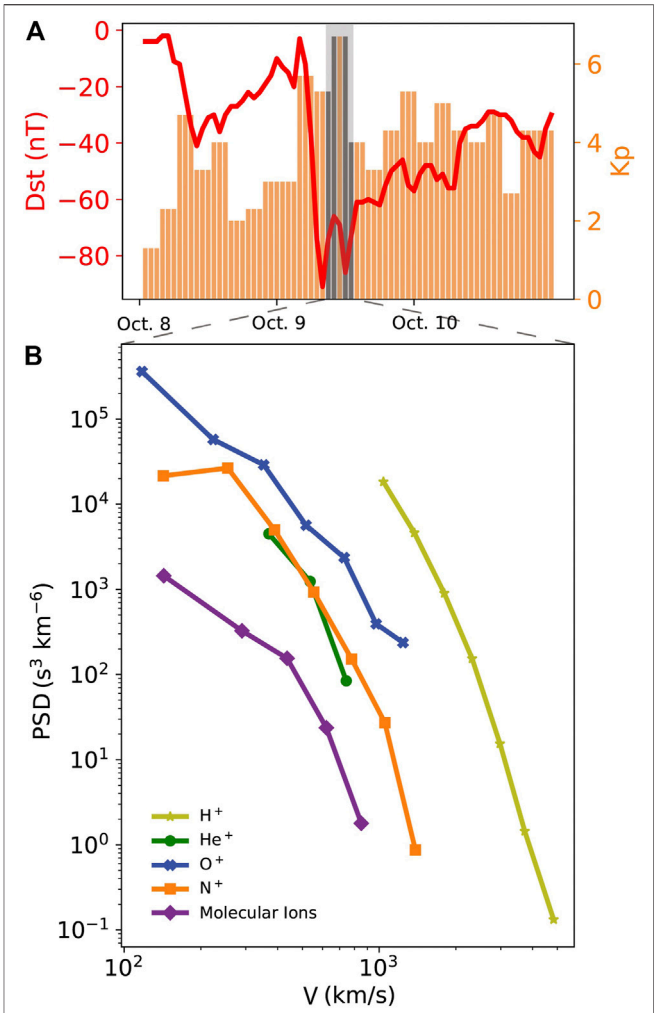

FIGURE 8 | Phase space densities (PSD) of N^+ (orange line), O^+ (blue line), and molecular ions (purple line) in the rest frame speed (v) for the interval 0958–018 and 1252–1330 UT during the storm of October 9, 1993, measured by the Geotail spacecraft **(B)**. The Kp (orange bars) and Dst (red line) indices during this storm are shown for reference **(A)**; greyed out area on top panel corresponds to the time interval when the measurements in bottom panel are extracted. Figure digitized and adapted from (Christon et al., 1994).

early main phase of the September 4, 1984 storm, based on SULEICA measurements (Klecker et al., 1986). Molecular NO^+ and O_2^+ ions (purple) were observed at L ~ 6.5–7, having energies of the order of 100 keV/e, contributing ~ 0.5% of the total energy of 32 keV/cm^{-3} in the energy range 20–230 keV/e. These observations of energetic molecular ions suggest that either the mass selection energization mechanisms or the density profile of the thermosphere during the storm time played a significant role in the efficient heating of the molecular ions as they were transported from the ionosphere to the magnetosphere.

Observations of molecular ions at hundreds of Earth radii downtail were first recorded by instruments onboard the Geotail mission (Nishida, 1994). The Suprathermal Ion Composition Spectrometer (STICS) of Geotail/EPIC (Energetic Particles and Ion Composition) instrument and the Low Energy Particle Energy Analyzer (LEP-EA) had the capability to measure ions in the energy range of 9.4–210 keV/e and 0.03–40 keV/e (Christon et al., 1994; Williams et al., 1994). Total kinetic energy, energy-per-charge, and time-of-flight measurements of individual ions are combined with various telescope parameters to generate pulse height analysis (PHAs) events and the count rates of PHAs were related to the abundances of ions in the observed region. Singly charged heavy ions, including atomic N^+ and O^+, and molecular N_2^+, NO^+, and O_2^+ ions, were observed in Earth's magnetotail at distances X ~ -146 R_E during geomagnetically active times (maximum Kp value was ~7, minimum Dst was only -40 nT). **Figure 8** shows the rest frame phase space ion densities vs. ion velocities based on Geotail observational data. It can be seen that the atomic N^+ and O^+ as well as molecular ions had relatively high velocities ~ 200–900 km/s in the rest frame of the tailward bulk plasma flow, where N^+/O^+ = ~ 25–30% and $(N_2^+ + NO^+ + O_2^+)/O^+$ = ~ 1–2%. In addition, the molecular ions observed at magnetosphere had similar velocity distribution as the atomic N^+ and O^+ in the

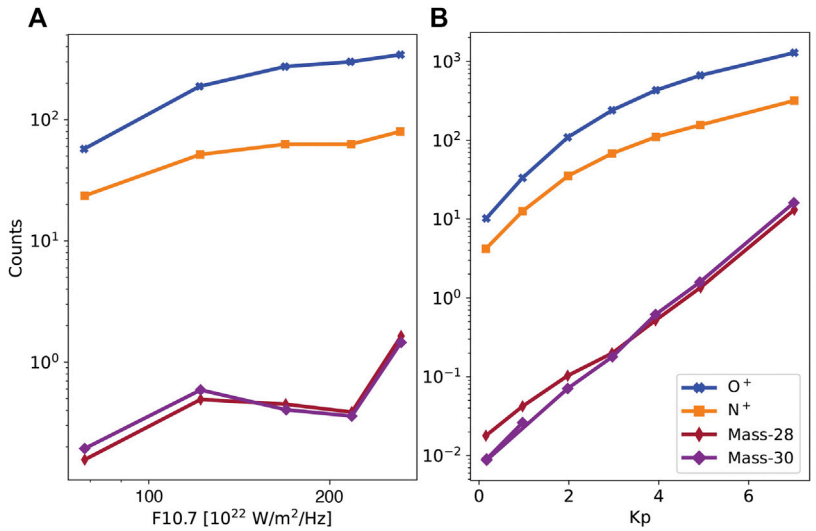

FIGURE 9 | Geotail measurements of suprathermal (~87–212 keV/e) N^+ (orange line), O^+ (blue line), and molecular ions (magenta and purple lines). Data shows average phase count rates over 3 h vs. Kp **(A)** and vs. F10.7 **(B)** indices covering observations made between 1995 and 2015. Figure digitized and adapted from (Christon et al., 2020).

outer magnetosphere (X ~ -146 R_E), but their densities were around two orders of magnitude lower.

Statistical studies based on 20 years of Geotail/STICS data (1995-2015) indicated that the relative abundance of molecular ions in the Earth's magnetosphere is ~43% N_2^+, ~47% NO^+ and ~ 10% O_2^+ (Christon et al., 2020). **Figure 9**, adapted from Christon et al. (2020), shows the variation in N^+ (orange line), O^+ (blue line) and molecular ions with mass 28 amu (magenta line) and mass 30 amu (purple line) count rates with F10.7 (left panel) and Kp (right panel) indices. These data show that the count rates of magnetospheric molecular ions are the most sensitive to geomagnetic activity, and increase faster with larger values of Kp. Moreover, the count rates of molecular ions and atomic N^+ and O^+ ions seem to indicate a different response to the F10.7 index; while the count rates of atomic N^+ and O^+ ions proportionally increased with F10.7, that of the molecular ions showed a decline for F10.7 ~ 120×10^{22} – 220×10^{22} W/m^2/Hz, and increased significantly at the highest F10.7.

Molecular ions have also been observed by the Toroidal Imaging Mass-Angle Spectrograph (TIMAS) on board the Polar satellite. Launched on February 24, 1996, the Polar spacecraft measured plasma properties in the polar ionosphere and magnetosphere, aiming to develop an understanding of the deposition of particle energy in the ionosphere and upper atmosphere (Shelley et al., 1995). The Polar spacecraft entered the orbit with an apogee of 9.0 R_E, a perigee of 1.8 R_E, and the inclination of 86°. The Polar/TIMAS instrument aimed to measure particles with energy between 15 eV/e–33 keV/e (Shelley et al., 1995). The mass spectra from TIMAS have been analysed with the help of color-coded count rates versus time and mass step at all energy channels, which allowed the separation of molecular ions from atomic O^+ and N^+ ions. However, due to the detection limit of the instrument, for particles with energies below 5 keV/e, the N_2^+, NO^+, and O_2^+ ions were not successfully distinguished (Lennartsson et al., 2000). A statistical study based on the first 22 months of data from TIMAS showed that the energy distribution of molecular ions were identical with O^+ ions, with the typical energy between 15–110 eV. However, the differential fluxes of molecular ions, ~ 10^5 cm^{-2}s^{-1}, were two orders of magnitude lower than that of O^+ ions. Furthermore, the detection frequency of molecular ions was determined to be more sensitive with the enhanced geomagnetic activity, than the O^+ detection. Therefore, the pathway and energization mechanisms of molecular ions were different from those of O^+, as they seem to be more specifically associated with enhanced geomagnetic activity (Lennartsson et al., 2000).

Surprisingly, molecular ions had been observed by the Acceleration, Reconnection, Turbulence, and Electrodynamics of the Moon's Interaction with the Sun (ARTEMIS) spacecraft, whose orbit is centered around the Moon, with periselene between 10–1,000 km and aposelene of 20,000 km (10 lunar radii) (Angelopoulos, 2010). Based on measurements from the electrostatic analyzer (ESA), Poppe et al. (2016) analyzed the ion composition data around 60 R_E away from the Earth during the storm of October 1, 2012 (Max Kp = 7, Min Dst = −122 nT) and storm of February 16, 2014 (Max Kp = 6, Min Dst = −119 nT). This study revealed that the fluxes of molecular ions were on the order of 10^5–10^6 cm^{-2} s^{-1}, while the proton fluxes were found to yield ~ 10^6–10^8 cm^{-2} s^{-1}, suggesting that molecular ions might have comparable velocities with those of protons. These observations of energetic molecular ions from ARTEMIS hint to the connection between Earth's ionospheric outflow and the composition of lunar exosphere, since the Earth could possibly deliver the nitrogen and oxygen components to the lunar volatile inventory (Poppe et al., 2016).

Recent observations based on the data from the Arase (Exploration of energization and Radiation in Geospace, ERG) satellite reveal frequent presence of molecular ions in the inner

magnetosphere during storm times. Launched on December 20, 2016, the Arase (ERG) satellite was designed to directly observe high energy particles in the magnetosphere (Miyoshi et al., 2018). The low-energy particle experiments-ion mass analyzer (LEPi) (Asamura et al., 2018) and medium-energy particle experiments-ion mass analyzer (MEPi) (Yokota et al., 2017) on board the Arase (ERG) satellite were capable of measuring the three-dimensional velocity distribution of ions in the energy range of 0.01–25 keV/q as well as 10–180 keV/q with ions species discrimination, including N^{++}/O^{++}, N^{+}/O^{+}, and $N_2^+/NO^+/O_2^+$. Based on the molecular ions measurements by LEPi and MEPi from March to December 2017, including 11 geomagnetic storms, molecular ions were frequently observed at L = 2.5–6.6 with energies above ~ 12 keV during most magnetic storms, and the average energy density ratio of the molecular ions to O^+ was found to be ~ 3% (Seki et al., 2019). The high occurrence rate of molecular ions in the inner magnetosphere indicates that fast ion outflows occur more frequently than expected during the storm time, while previous studies assumed the molecular ions were only observed during intense storms (the minimum Dst ≤ -100 nT).

The convection and energization mechanisms of molecular ions are likely to be different between the high-altitude ionosphere and magnetosphere. The molecular ions were observed to follow the similar energy distribution to O^+ by the Polar/TIMAS instrument (Lennartsson et al., 2000), but had similar velocity distribution to O^+ as observed by the Geotail/EPIC instrument and the ARTEMIS spacecraft (Christon et al., 1994; Poppe et al., 2016). In the high-altitude ionosphere, both O^+ and molecular ions with the escape energy (≥10 eV) can overcome the gravitational bound and flow out the Earth's ionosphere. Therefore, the energy distribution of these outflowing O^+ and molecular ions will be likely similar. On the other hand, O^+ and molecular ions in the magnetotail are possibly energized by the earthward $\mathbf{E} \times \mathbf{B}$ transport, which are charge and mass independent. Thus, O^+ and molecular ions can likely follow a similar velocity distribution in the magnetotail region.

Instrument limitations on board these spacecrafts brought some difficulties to the study of the cold plasma and the behavior of minor ion species in the ionosphere-magnetosphere system. For example, the minimum detection densities of ions for OGO and AE spacecrafts were 10 cm^{-3} and thus, the region with the molecular ions densities ≤10 cm^{-3} couldn't be detected. In addition, measurements of cold molecular ions in the magnetosphere are particularly difficult due to spacecraft surface charging, as the ions energy ≤10 eV had the difficulty to be fully resolved by the instruments. Nevertheless, multiple studies report on their occurrence both in the ionosphere and the magnetosphere, spanning a large energy range and radial distances.

4 DISCUSSION

Although several observations reveal that molecular ions are frequently observed in the high-latitude ionosphere and the magnetosphere, having energies of the order of eV to keV, the source and energization mechanisms leading to the outflow of these molecular ions in response to various geomagnetic conditions, are not yet fully understood. In this section, we will further explore the source and energization of outflowing molecular ions in the Earth's ionosphere-magnetosphere system.

4.1 Source of Molecular Ions

Molecular ions outflowing from the polar wind are mainly produced in the ionosphere F2 layer through the Suprathermal Electron (SE) production, including photoionization and secondary electron impact, and ion-neutral-electron chemical reactions. In this section, we provide the altitude profile of production and loss processes for all relevant polar wind molecular ions from 200–1,000 km altitude. The profiles are obtained using the Seven Ion Polar Wind Outflow Model (7iPWOM) (Lin et al., 2020) with the chemical reactions rates provided by Richards and Voglozin (2011).

The 7iPWOM expanded the chemical reactions of ionospheric N^+ ions in the ionosphere F2 layer, and SE production for all seven ion species, including O^+, N^+ and three molecular ion species, based on the GLobal airglOW (GLOW) model (Solomon et al., 1988; Glocer et al., 2012) and the cross-sectional area of the neutral-electron collision provided by (Gronoff et al., 2012b,a). The neutrals number density are obtained from NRLMSISE-00 empirical model. However, the 7iPWOM included neutral NO, $NO(^2D)$, $N(^2D)$ and $N(^4S)$ density based on the neutral density of the simulation results from the Global ionosphere Thermosphere Model (GITM) (Ridley et al., 2006).

The chemistry scheme of the 7iPWOM includes all relevant reactions with the chemical reactions rates provided by Richards and Voglozin (2011). Since the charge exchange between $O^+(^2D)$ and N_2 is the main source to produce N_2^+ in the ionosphere above 200 km altitude (Torr and Orsini, 1978), the 7iPWOM calculates this charge exchange reaction rate by deriving $O^+(^2D)$ from the Global ionosphere Thermosphere Model (GITM). In order to illustrate the influence of solar conditions to the molecular ions chemistry, we present here the production and loss rate of the molecular ions based on the steady state of the 7iPWOM quiet time solution during the Solar Maximum ($F10.7 = 180 \times 10^{-22}$ WHz/m^2) and Minimum ($F10.7 = 80 \times 10^{-22}$ WHz/m^2) summer noon, shown in **Figure 10**. The steady state of summer noon conditions are represented by the solution of a single field line, for which the foot point is located in 80° latitude and 12 MLT, initialized for 24 h to achieve steady state. Since molecular ions became the minor ion species above 1,000 km, and their detection in the polar wind during the quiet times at this altitude was reported to be challenging (Craven et al., 1985; Christon et al., 1994), here we only present the altitude profiles for molecular ions production and loss at 200–1,000 km altitudes.

The right-hand side of **Figure 10** shows the various chemical reactions contributing to the production and loss of N_2^+ (top row), NO^+ (center row), and O_2^+ (bottom row). Each column represents the simulation results of 7iPWOM during Solar Maximum and Solar Minimum from left to right. The production of molecular N_2^+ (dark red line), NO^+ (purple line), O_2^+ (brown line) ions takes place via photoionization, secondary electron impact, and various ion-neutral-electron chemical reactions, while the losses of molecular ions (grey lines) occur either via dissociative

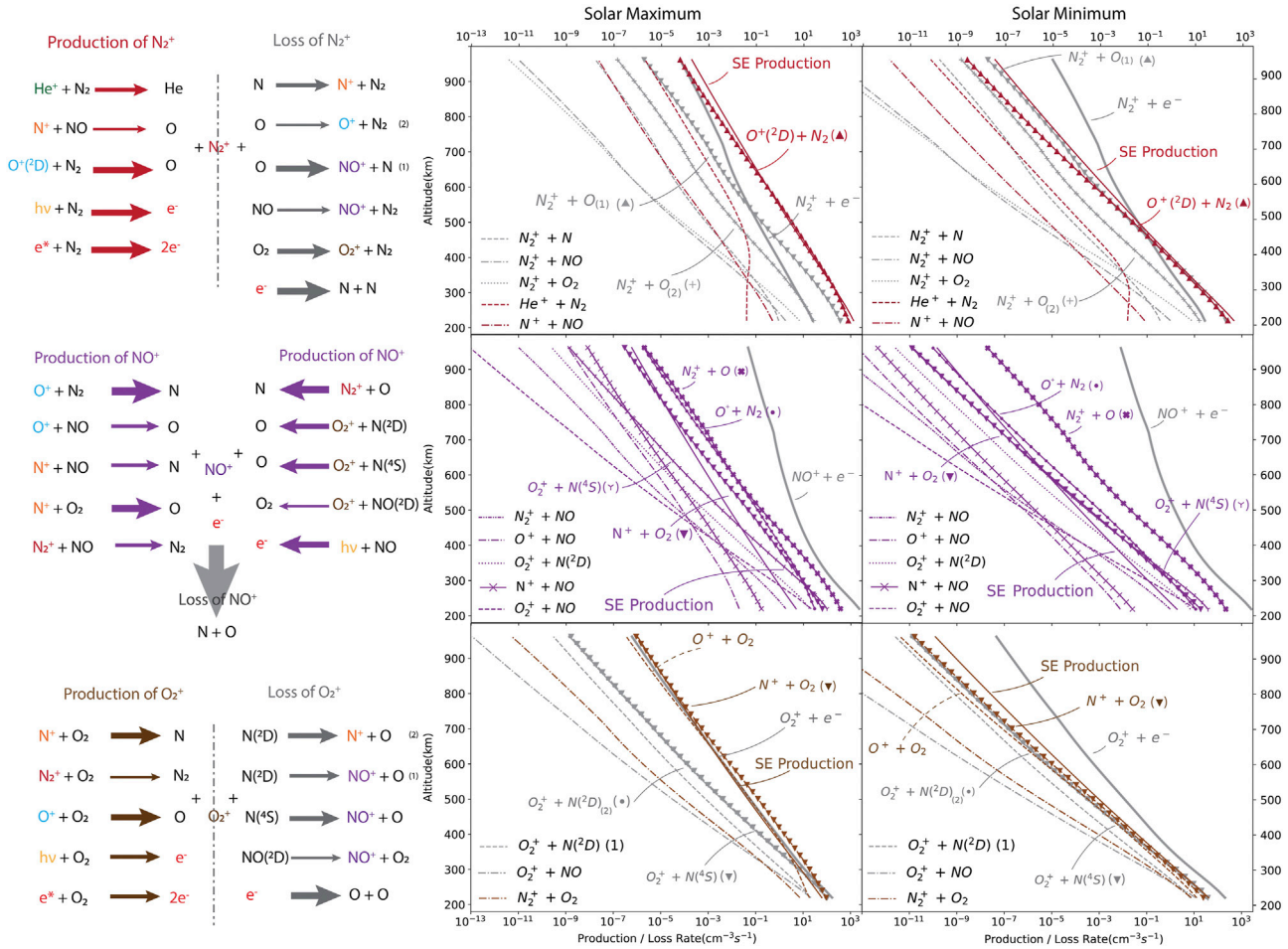

FIGURE 10 | Comparison of ion production (colored lines) and loss (grey lines) reactions between 200 and 1,000 km altitude range, based on the 7iPWOM simulation results during solar maximum **(left column)** and minimum **(right column)** summer noon. The diagram on the left-hand side shows various chemical reactions of productions and losses of molecular ions and the thickness of the arrows represents the magnitude of reactions rates ($cm^{-3}s^{-1}$).

recombination with e^- to form the neutral species or via various ion-neutral-electron chemical reactions. The diagrams on the left-hand side of **Figure 10** list the relevant ionospheric chemistry related to molecular N_2^+ (dark red), NO^+ (purple), O_2^+ (brown) ions. The participating ion species are marked by colored text, including O^+ (blue), N^+ (orange), He^+ (dark green) and e^- (red). The colored arrows represents the chemical production of molecular ions, while the grey arrows show their losses via chemical reactions. The thickness of these arrows indicates the efficiency of said reaction rates based on the quiet time simulation results of the 7iPWOM (right-hand side of **Figure 10**). Below, we will further explore the ionospheric chemistry of each molecular ion species.

4.1.1 The Ionospheric Chemistry of N_2^+

During Solar Maximum conditions, the main contributors to the production of N_2^+ ions in the altitude range of 200–1,000 km are the SE production (dark red solid line) and the charge exchange between $O^+(^2D)$ and N_2 (dark red triangle line). N_2^+ are mostly lost due to dissociative recombination with electrons and charge exchange between N_2^+ and neutral O species, reactions that are leading to the production of N, and N_2 neutral species, and NO^+ and O_2^+ ions. During Solar Maximum condition, the production and loss rates of N_2^+ varied more than from Solar Minimum case. Therefore, during Solar Minimum, the N_2^+ production rates via SE production and the charge exchange between $O^+(^2D)$ and N_2 could impede the losses of N_2^+ from dissociative recombination (grey dashed line) during the Solar Maximum, while these two production rates of N_2^+ were only larger than dissociative losses of N_2^+ below 500 km during Solar Minimum.

4.1.2 The Ionospheric Chemistry of NO^+

NO^+ is produced through a multitude of chemical reactions, with rates largely affected by the solar activity. The production rates of NO^+ due to charge exchange between N_2^+ and O (purple cross marker line) and charge exchange between O^+ and N_2 (purple dotted line) were comparable during Solar Maximum; however, the reaction rate of charge exchange between N_2^+ and O was at least one order of magnitude than other reactions during Solar Minimum. The SE production of NO^+ is not very important both

during the solar maximum and minimum as it is only the third or fourth important reactions, which followed the same conclusion of NO^+ ionospheric chemistry by the study of Richards and Voglozin (2011). Moreover, dissociative recombination rates of NO^+ (grey solid lines) was the only reaction to remove NO^+ from the ionosphere F2 layer. Since the dissociative recombination rate of NO^+ was generally one order of magnitude larger at the low altitude and five orders of magnitude larger at 1,000 km altitude, the NO^+ ions densities decreased substantially from 200 to 1,000 km altitude.

4.1.3 The Ionospheric Chemistry of O_2^+

The loss of O_2^+ ions in the ionosphere F2 layer is due to the dissociative recombination with electrons (grey solid line), and the loss of O_2^+ produces the neutral O species and molecular NO^+ ions, with minor N^+ ions species. Similar to the case of N_2^+ ions, solar activity also alters the ionospheric chemistry of O_2^+ ions. During Solar Maximum condition, the O_2^+ production rates due to the SE production (brown solid line) and the charge exchange of O^+ or N^+ ions with the neutral O_2 (brown dashed and triangle lines), could impede the O_2^+ losses of dissociative recombination. However, during Solar Minimum, the dissociative recombination can be at least one order of magnitude larger than the production rates of O_2^+.

The above analysis of the productions and losses of molecular NO^+, N_2^+ and O_2^+ ions between 200–1,000 km altitude range with the observations results in **Sections 2**, **3**, we can conclude that:

- The SE productions of molecular N_2^+, NO^+, O_2^+ are not the dominant chemical reactions for the production of NO^+ and O_2^+ in the ionosphere F2 layer, consistent with previous findings (Richards and Voglozin, 2011).
- The chemical reactions leading to the loss of O^+ are also leading to the production of NO^+ and therefore, the presence of NO^+ leads to the increasing ratio of N^+/O^+ in the ionosphere, as observed by Hoffman et al. (1974); Yau et al. (1993); Wilson and Craven (1999).
- The chemical reactions leading to the loss of N_2^+ are also leading to the production of NO^+ and neutral N_2 species, causing an increase in the neutral N_2 density in the low-altitude ionosphere, as reported in DE-2 measurements (Wilson and Craven, 1999).

4.2 Possible Energization Mechanisms

Molecular ions are required to be energized in a very short time once produced either by the SE production or reactions with neutral species, in order to impede with their fast dissociative recombination with electrons in the ionosphere F2 layer. Ionospheric observations of molecular ions by OGO and AE spacecraft missions showed that the abrupt enhancements of molecular ions densities in the region of HLTs were often accompanied by the decrease of O^+ ion densities, and an increase in the electron temperature and energetic particle flux. Therefore, fast molecular ions outflow were produced by the rapid losses of O^+ due to strong electric field and energized by the enhancement of soft electron precipitation associated with the polar cap region in the ionosphere (Taylor et al., 1975; Grebowsky et al., 1976; Brinton et al., 1978; Grebowsky et al., 1983).

Several studies have focused on the effect of ion frictional heating (ion-neutral collisions) due to strong electric convection field (Schunk et al., 1975; Wilson and Craven, 1999; Schunk and Nagy, 2009; Zettergren et al., 2010; Zettergren et al., 2011). As ions are convected through the slower moving neutral gas with $\mathbf{E} \times \mathbf{B}$ drift, they are heated through the ion-neutral collision, which leads to an increase in the ion temperatures. This in turn facilitates an increase in the chemical reactions rates in the ionosphere, and therefore also facilitates the production of molecular ions. As the convection electric field ($E_\perp$) approaches $50\,mV\,m^{-1}$, the ion temperature substantially increases, leading to the enhancement of $O^+ + N_2 \rightarrow N + NO^+$ reaction rate. Numerical simulations suggest that when $E_\perp$ approaches to $200\,mV\,m^{-1}$, the loss of O^+ causes rapid enhancement of NO^+ ion density. Therefore, NO^+ ions could become the dominant ion species in the high-latitude ionosphere up to 600 km altitude (Schunk et al., 1975).

The ion frictional heating of molecular ions outflow due to strong convection electric field was also investigated with the near-conjunction measurement of the DE-1 and DE-2 spacecraft missions (Wilson and Craven, 1999). By selecting the events when both spacecrafts passed through similar latitudes and longitudes, measurements of neutral species composition and temperature from the low-altitude DE-2 mission (335–746 km altitude range) were analyzed in conjunction with measurements of N^+, O^+ and molecular ions densities in the high altitude region observed by the DE-1 (1,000–4,000 km altitude range). The results showed that the increased molecular ions densities observed in the high altitude region by DE-1 were always accompanied by the enhancements of ions temperatures and strong electric fields in the low altitude region by DE-2. This points out the molecular ions outflow could be sourced and energized by the strong cusp associated plasma convection, which also modified the composition of the ionosphere and thermosphere.

Studies using the European Incoherent Scatter (EISCAT) data of ion velocity and temperature also suggest that ion frictional heating plays an important role in the molecular ions upflow. Based on the frequent observations of molecular ions in the innermagnetosphere by the Arase satellite during multiple storm times (Seki et al., 2019), Takada et al. (2021) further determined the energization supplied to ionospheric molecular ions with the ion velocity and temperature data from the EISCAT Ultra High Frequency (UHF) radar (933 MHz) at Tromsø (located at ~ 70° latitude). The measurement of temperature and velocity of ions were more than 2000 K and ~ 50–150 m/s at 250–350 km altitude, and the flux of molecular ions at 350 km altitude was two orders of magnitude higher than during nominal conditions, at which time the convection electric field increased a factor of 2. By examining the momentum equation of ions, the ion and electron pressure gradients were balanced with the gravitational force and thus, the ion frictional heating could be a possible energization mechanism of low-altitude molecular ions upflow.

Molecular ions observed at 300–1,000 km altitudes were also energized by ion resonance heating, enhancement of soft electron precipitation occurring in the cusp region, or the plasma instabilities and the role of various energization mechanisms

TABLE 3 | Mission details, including the information of orbit, launch and decay date, as well as the observed density ratio of $(NO^+ + O_2^+ + N_2^+)/O^+$ during the storm time only (if not specified). ARTEMIS is currently centered at the Moon and thus, the perigee and apogee are refereed as periselene and aposelene. Cross marker, x, in a cell indicates that the data are unavailable or not relevant.

Mission	Lifetime	Orbit				Energy range	Molecular ions/O^+	References
		Perigee	Apogee	Inclination	Period			
Sputnik 3	Launch Date: May 15, 1958 Decay Date: April 6, 1960	217 km	1864 km	65.18°	105.9 min	Bennett-type radio frequency quadrupole mass spectrometer	x	Nauk and Doklady (1961); Istomin (1966)
OGO 6	Launch Date: Jun 5, 1969 Decay Date: Oct 12, 1979	413 km	1,077 km	82°	99.7 min	Bennett-type Ion Mass spectrometer	0.01–0.1	Taylor (1971); Jackson and Vette (1975); Taylor (1974); Taylor et al. (1975); Grebowsky et al. (1976, 1983)
ISIS 2	Launch Date: Apr 1, 1971 Decay Date: Oct 1, 1979	1,360 km	1,440 km	88.1°	113.6 min	Ion Mass Spectrometer	10^{-4}–0.1	Hoffman (1970); Hoffman et al. (1974)
AE-C	Launch Date: Dec 16, 1973 Decay Date: Dec 12, 1978	149 km	4,294 km	68.1°	132.3 min	Bennett Ion Mass spectrometer or Magnetic Ion Mass spectrometer	10^{-3}–0.1	Brinton et al. (1973); Hoffman et al. (1973); Brinton et al. (1978)
DE-1	Launch Date: Aug 3, 1981 Decay Date: Feb 28, 1991	488 km	23,289 km	89.9°	409 min	Retarding Ion Mass Spectrometer (RIMS) 0–45 eV	x	Chappell et al. (1982); Craven et al. (1985); Wilson and Craven (1999)
AMPTE/IRM	Launch Date: Aug 16, 1984 Decay Date: Aug 14, 1986	6,944.89 km	119,965.93 km	28.6°	2,658 min	Suprathermal Energy ionic Charge Analyzer (SULEICA) 5–270 keV/e	≤0.03	Hausler et al. (1985); Mobius et al. (1985); Klecker et al. (1986)
Akebono	Launch Date: Feb 21, 1989 Decay Date: Apr 23, 2015	275 km	10,500 km	75°	211 min	Suprathermal Ion Mass Spectrometer (SMS) 0–25.5 eV; 55 eV/q–4.1 keV/q	≤0.1	Tsuruda and Oya (1991); Whalen et al. (1990); Yau et al. (1993); Peterson et al. (1994)
Geotail	Launch Date: July 24, 1992	51,328 km	190,664 km	10.51°	7,539.86 min	Suprathermal Ion Composition Spectrometer (STICS) 9.4–210 keV/e	Energy Flux ≤10^{-3}	Nishida (1994); Christon et al. (1994); Williams et al. (1994); Christon et al. (2020)
Polar	Launch date: Feb 24, 1996 Deactivated Date: Apr 28, 2008	185 km	50,551 km	85.9°	938.1 min	Toroidal Imaging Mass-Angle Spectrograph (TIMAS) 0–40 KeV/e	≤10^{-2}	Shelley et al. (1995); Lennartsson et al. (2000)
ARTEMIS (THEMIS B and C) (centered at Moon)	Launch date: Feb 17, 2007	~ 10–1,000 km	~ 20,000 km	x	1,650 min	Electrostatic Analyzer (ESA) 5 eV–25 keV	x	Angelopoulos (2010); Poppe et al. (2016)
e-POP	Launch Date: Sept 29, 2013	325 km	1,500 km	81°	103 min	Imaging and Rapid-Scanning Ion Mass Spectrometer (IRM); measures the composition and 3-dimensional velocity distributions of low-energy (1–90 eV/e) ions in the mass-per-charge (M/q) range of 1–40 AMU/e	x	Yau et al. (2006); Yau and Howarth (2016); Foss and Yau (2019)

(Continued on following page)

TABLE 3 | (*Continued*) Mission details, including the information of orbit, launch and decay date, as well as the observed density ratio of $(NO^+ + O_2^+ + N_2^+)/O^+$ during the storm time only (if not specified). ARTEMIS is currently centered at the Moon and thus, the perigee and apogee are refereed as periselene and aposelene. Cross marker, x, in a cell indicates that the data are unavailable or not relevant.

Mission	Lifetime	Orbit				Energy range	Molecular ions/O^+	References
		Perigee	Apogee	Inclination	Period			
Arase (ERG)	Launch Date: Dec 20, 2016	460 km	32,110 km	31°	565 min	Medium-energy particle ion mass analyzer (MEPi) 7–87 keV and low-energy particle experiments-ion mass analyzer (LEPi) 0.01–25 keV/q	Energy Density ≤0.03	Miyoshi et al. (2018); Asamura et al. (2018); Seki et al. (2019)

acting on the molecular ion populations in the 300–500 km altitude during multiple storm times were examined by Peterson et al. (1994). This study estimated that in this region, the lifetime of molecular ions due to recombination reactions is about few minutes, but the time needed to acquire sufficient escape energy (~ 10 eV) at the 400 km, solely by the ion frictional heating or resonance heating, was at least one order of magnitude more than the lifetime of molecular ions. Therefore, we currently lack a robust understanding of the possible mechanisms responsible to the acceleration of these heavy ions species.

4.2.1 Unresolved Issues of Energization Mechanisms of Fast Molecular Ions Outflow

The observed outflow of molecular ions implies the existence of energization mechanisms that can provide the additional escape energy (of at least ~10 eV) at comparable timescales with losses of molecular ions, and it is likely that these potential energization mechanisms are acting concomitantly, even though they might take place at different altitudes. However, the relative contributions of these energization mechanisms responsible for the molecular ions outflow are still difficult to assess due to the scarceness of observations, also linked to instrument limitations. For example, observations of particle precipitation with energies up to 1 keV by the Low Altitude Plasma Instrument (LAPI) on board the DE-2 were concurrent with the observation of molecular ions in the high altitude ionosphere (Wilson and Craven, 1999). Moreover, it has been suggested that the ionospheric plasma instabilities driven by magnetospheric electron precipitation could possibly energize molecular ions in the ionosphere (Peterson et al., 1994). However, due to the small scales of particle precipitation as well as low frequency waves, the instruments on board the DE-2 and Akebono couldn't resolve the spectrum with such high resolution.

There is also a need for additional observations of molecular ions in the magnetosphere, in order to understand the mechanisms responsible for their energization from eVs to keVs. Observations of molecular ions indicate that they could achieve ~ 5 eV at 4,000 km altitude, but their escape energies are typically between 10–20 eV. This indicates that outflowing molecular ions need to acquire additional 5 eV above 4,000 km altitude (Wilson and Craven, 1999). Moreover, the molecular ion energies could be observed up to 100 eV in the high-altitude ionosphere (Lennartsson et al., 2000) and 100 keV in the outer magnetosphere (Christon et al., 1994). This suggests that the further energization mechanisms of molecular ions takes place in the magnetosphere as well. Furthermore, the observed molecular ions in the high-latitude ionosphere had similar energy distributions to that of O^+ ions (Lennartsson et al., 2000). This indicates that outflowing molecular ions in the ionosphere are required to obtain more energy than outflowing O^+ ions, most likely by the mass selection mechanisms that heat the heavier ions preferentially.

One possible mass selection mechanisms to energize the molecular ions preferentially above 1,000 km is the resonant wave-particle interaction (WPI), which is considered to be a major pathway of ion heating and acceleration, both in the cusp and auroral region (Andre and Yau, 1997). The energization of ion outflow via WPI is caused by the electric field perturbation, perpendicular to the magnetic field, which leads to an increase in the ion perpendicular velocity in a very short time. Therefore, these energized particles move upward along the field lines and form ion conics, due to the acceleration by magnetic mirror force. The gyro-frequency of ions, inversely proportional to the mass, is resonant with the low frequency wave, meaning that molecular ions are preferentially heated via WPI. Although the efficacy of WPI in the energization of molecular ion species remains largely unknown, several studies addressed the energization of O^+ ions via WPI. For example, multiple observations from the Akebono, Interball-2 and Cluster satellites report on the abrupt energization of O^+ from 10 eV to 10 keV at 4.3 R_E in 10 min (Bouhram et al., 2004). Quasi-linear theory supports the hypothesis that the abrupt enhancements of O^+ energy along the magnetic field lines are due to WPI (Crew et al., 1990). Since the diffusion coefficient is inversely proportional to the mass of ions, molecular ions are expected to be preferentially energized by the resonant WPI.

5 CONCLUSION

Table 3 summarizes the existing observational data sets of molecular ions from past and currently operating spacecraft missions, covering altitudes from few hundred kilometers to hundreds of Earth radii. These observations of molecular ions in the ionosphere-magnetosphere system suggest that:

1. The densities of molecular ions in the polar ionosphere at altitudes between 200–1,000 km were reported to be 0.1–1% of O^+ densities; however, during geomagnetically active times, the abrupt enhancement of molecular ions densities in the high latitude troughs (whose latitudes were aligned with auroral activity) could reach about 10% of O^+ ion densities.
2. The possibility of detecting molecular ions in the magnetosphere was nearly zero during the quiet times; however, during geomagnetically active times they were frequently detected both in the inner and outer magnetosphere. The molecular ions fluxes were generally less than two orders of magnitude than that of O^+.
3. The increase in molecular ions densities or fluxes were often accompanied by a high ratio of N^+/O^+ in the ionosphere-magnetosphere system. This indicates that the presence of molecular ions could impact the abundances of N^+ and O^+ ions, and can act as a reference to investigate the energization of heavy ions in the polar wind.

Magnetospheric molecular ions were only observed during the storm times, and thus, the observations of molecular ions in the high altitude region are very scarce. This leads to very little knowledge on the convection and energization of molecular ions, causing lack of understanding of their behavior and dynamics both at low and high altitudes. There seems to be an increase in the molecular ions observations in the past 10 years, probably linked to improved mass resolution on instruments flying on current space missions. However, these observational data all occurred at the solar cycle 24, and couldn't fully represent the molecular ions dynamics in the Earth's magnetosphere-ionosphere system. Therefore, a dedicated geospace mission that would measure various plasma properties and provide detailed composition in the geospace, at all altitudes, is required in order to understand the relative contributions and the various energization mechanisms of these molecular ions throughout geospace.

Additionally, understanding the sources, energization mechanisms, and the overall dynamics of molecular ions in the magnetosphere-ionosphere system could possibly help understand the impact of the minor heavy ion species in the magnetosphere. Cluster (Haaland et al., 2021) and Geotail (Christon et al., 2017) missions have reported the observations of metal ions in the magnetosphere, but the sources and the transport mechanisms of these metal ions are still largely unknown. This review paper is intended to help inform and guide future ionosphere and magnetosphere studies, and provides context for the available observations of molecular ions. Knowledge of the different behaviors and paths of energization of heavy ions such as N^+, O^+, and molecular ions will play a crucial role in the interpretations and analysis of data from many current space missions.

AUTHOR CONTRIBUTIONS

All authors listed have made a substantial, direct, and intellectual contribution to the work and approved it for publication.

FUNDING

Work at University of Illinois at Urbana-Champaign was performed with financial support from AFOSR YIP award no. AF FA 9550-18-1-0195, and the NASA grants N99066ZO, 80NSSC20K1231, 80NSSC21K1425, and 3004631577. The PWOM model has been included in the Space Weather Modeling Framework, which is available for download (at http://csem.engin.umich.edu/tools/swmf/downloads.php). The simulation results of the GITM model has been available in the Community Coordinated Modeling Center (CCMC) webpage (at https://ccmc.gsfc.nasa.gov/models/modelinfo.php?model=GITM).

ACKNOWLEDGMENTS

The authors would like to thank the reviewers for their valuable comments and suggestions to improve the quality of the paper. The authors also thank HeRA team member Hsinju Chen for helpful suggestions and discussions on the paper.

REFERENCES

André, M., and Yau, A. (1997). Theories and Observations of Ion Energization and Outflow in the High Latitude Magnetosphere. *Space Sci. Rev.* 80, 27–48. doi:10.1007/978-94-009-0045-5_2

Angelopoulos, V. (2010). The Artemis mission. *Space Sci. Rev.* 165, 3–25. doi:10.1007/s11214-010-9687-2

Asamura, K., Kazama, Y., Yokota, S., Kasahara, S., and Miyoshi, Y. (2018). Low-energy Particle Experiments-Ion Mass Analyzer (LEPi) Onboard the ERG (Arase) Satellite. *Earth Planets Space* 70, 70. doi:10.1186/s40623-018-0846-0

Axford, W. I., and Hines, C. O. (1961). A Unifying Theory of High-Latitude Geophysical Phenomena and Geomagnetic Storms. *Can. J. Phys.* 39, 1433–1464. doi:10.1139/p61-172

Barakat, A. R., and Schunk, R. W. (2006). A Three-Dimensional Model of the Generalized Polar Wind. *J. Geophys. Res.* 111, A12314. doi:10.1029/2006ja011662

Bouhram, M., Klecker, B., Miyake, W., Rème, H., Sauvaud, J.-A., Malingre, M., et al. (2004). On the Altitude Dependence of Transversely Heated O+ Distributions in the Cusp/cleft. *Ann. Geophys.* 22, 1787–1798. doi:10.5194/angeo-22-1787-2004

Brinton, H. C., Grebowsky, J. M., and Brace, L. H. (1978). The High-Latitude WinterFRegion at 300 Km: Thermal Plasma Observations from AE-C. *J. Geophys. Res.* 83, 4767–4776. doi:10.1029/ja083ia10p04767

Brinton, H. C., Scott, L. R., Pharo, M. W., III, and Coulson, J. T. (1973). The bennett Ion-Mass Spectrometer on Atmosphere Explorer-C and -e. *Radio Sci.* 8, 323–332. doi:10.1029/RS008i004p00323

Chappell, C. R., Olsen, R. C., Green, J. L., Johnson, J. F. E., and Waite, J. H. (1982). The Discovery of Nitrogen Ions in the Earth's Magnetosphere. *Geophys. Res. Lett.* 9, 937–940. doi:10.1029/gl009i009p00937

Christon, S. P., Gloeckler, G., Williams, D. J., Mukai, T., McEntire, R. W., Jacquey, C., et al. (1994). Energetic Atomic and Molecular Ions of Ionospheric Origin Observed in Distant Magnetotail Flow-Reversal Events. *Geophys. Res. Lett.* 21, 3023–3026. doi:10.1029/94GL02095

Christon, S. P., Hamilton, D. C., Mitchell, D. G., Plane, J. M. C., and Nylund, S. R. (2020). Suprathermal Magnetospheric Atomic and Molecular Heavy Ions at and Near Earth, Jupiter, and Saturn: Observations and Identification. *J. Geophys. Res. Space Phys.* 125, e27271. doi:10.1029/2019ja027271

Christon, S. P., Hamilton, D. C., Plane, J. M. C., Mitchell, D. G., Grebowsky, J. M., Spjeldvik, W. N., et al. (2017). Discovery of Suprathermal Ionospheric Origin Fe+ in and Near Earth's Magnetosphere. *J. Geophys. Res. Space Phys.* 122, 175–200. doi:10.1002/2017JA024414

Craven, P. D., Olsen, R. C., Chappell, C. R., and Kakani, L. (1985). Observations of Molecular Ions in the Earth's Magnetosphere. *J. Geophys. Res.* 90, 7599–7605. doi:10.1029/JA090iA08p07599

Crew, G. B., Chang, T., Retterer, J. M., Peterson, W. K., Gurnett, D. A., and Huff, R. L. (1990). Ion Cyclotron Resonance Heated Conics: Theory and Observations. *J. Geophys. Res.* 95, 3959–3985. doi:10.1029/JA095iA04p03959

Daglis, I. A., Thorne, R. M., Baumjohann, W., and Orsini, S. (1999). The Terrestrial Ring Current: Origin, Formation, and Decay. *Rev. Geophys.* 37, 407–438. doi:10.1029/1999RG900009

Foss, V., and Yau, A. (2019). *Molecular Ions in Ion Upflows and Their Effect on Hot Atomic Oxygen Production*. Calgary, AB: University of Calgary. PhD Thesis.

Garcia, K. S., Merkin, V. G., and Hughes, W. J. (2010). Effects of Nightside O+outflow on Magnetospheric Dynamics: Results of Multifluid MHD Modeling. *J. Geophys. Res.* 115, a–n. doi:10.1029/2010JA015730

Glocer, A., Kitamura, N., Toth, G., and Gombosi, T. (2012). Modeling Solar Zenith Angle Effects on the Polar Wind. *J. Geophys. Res.* 117, a–n. doi:10.1029/2011JA017136

Glocer, A., Toth, G., and Fok, M.-C. (2018). Including Kinetic Ion Effects in the Coupled Global Ionospheric Outflow Solution. *J. Geophys. Res. Space Phys.* 123, 2851–2871. doi:10.1002/2018ja025241

Glocer, A., Tóth, G., Gombosi, T., and Welling, D. (2009). Modeling Ionospheric Outflows and Their Impact on the Magnetosphere, Initial Results. *J. Geophys. Res.* 114, a–n. doi:10.1029/2009JA014053

[Dataset] Grebowsky, J. M., Taylor, H. A., and Lindsay, J. M. (1983). *Location and Source of Ionospheric High Latitude Troughs*. Planetary and Space Science. doi:10.1016/0032–0633(83)90034-X

Grebowsky, J. M., Chen, A. J., and Taylor, H. A. (1976). High-latitude Troughs and the Polar Cap Boundary. *J. Geophys. Res.* 81, 690–694. doi:10.1029/ja081i004p00690

Gronoff, G., Simon Wedlund, C., Mertens, C. J., Barthélemy, M., Lillis, R. J., and Witasse, O. (2012a). Computing Uncertainties in Ionosphere-Airglow Models: Ii. The Martian Airglow. *J. Geophys. Res.* 117, a–n. doi:10.1029/2011JA017308

Gronoff, G., Simon Wedlund, C., Mertens, C. J., and Lillis, R. J. (2012b). Computing Uncertainties in Ionosphere-Airglow Models: I. Electron Flux and Species Production Uncertainties for mars. *J. Geophys. Res.* 117, a–n. doi:10.1029/2011JA016930

Haaland, S., Li, K., Eriksson, A., André, M., Engwall, E., FöRster, M., et al. (2012b). *Cold Ion Outflow as a Source of Plasma for the Magnetosphere*. American Geophysical Union, 341–354. doi:10.1029/2012GM001317

Haaland, S., Daly, P. W., and Vilenius, E. (2021). Heavy metal and rock in space: Cluster rapid observations of fe and si. Available at; http://resolver.sub.uni-goettingen.de/purl?gldocs-11858/8681.

Haaland, S., Eriksson, A., Engwall, E., Lybekk, B., Nilsson, H., Pedersen, A., et al. (2012a). Estimating the Capture and Loss of Cold Plasma from Ionospheric Outflow. *J. Geophys. Res. Space Phys.* 117, a–n. doi:10.1029/2012JA017679

Hausler, B., Melzner, F., Stocker, J., Valenzuela, A., Bauer, O., Parigger, P., et al. (1985). The Ampte Irm Spacecraft. *IEEE Trans. Geosci. Remote Sensing* GE-23, 192–201. doi:10.1109/TGRS.1985.289513

Hedin, A. E. (1987). MSIS-86 Thermospheric Model. *J. Geophys. Res.* 92, 4649–4662. doi:10.1029/JA092iA05p04649

Hedin, A. E., and Reber, C. A. (1972). Longitudinal Variations of Thermospheric Composition Indicating Magnetic Control of Polar Heat Input. *J. Geophys. Res.* (1896-1977) (77), 2871–2879. doi:10.1029/JA077i016p02871

Hoffman, J. H., Dodson, W. H., Lippincott, C. R., and Hammack, H. D. (1974). Initial Ion Composition Results from the Isis 2 Satellite. *J. Geophys. Res.* 79, 4246–4251. doi:10.1029/ja079i028p04246

Hoffman, J. H., Hanson, W. B., Lippincott, C. R., and Ferguson, E. E. (1973). The Magnetic Ion-Mass Spectrometer on Atmosphere Explorer. *Radio Sci.* 8, 315–322. doi:10.1029/RS008i004p00315

Hoffman, J. H. (1970). Studies of the Composition of the Ionosphere with a Magnetic Deflection Mass Spectrometer. *Int. J. Mass Spectrom. Ion Phys.* 4, 315–322. doi:10.1016/0020-7381(70)85047-1

Ilie, R., and Liemohn, M. W. (2016). The Outflow of Ionospheric Nitrogen Ions: A Possible Tracer for the Altitude-dependent Transport and Energization Processes of Ionospheric Plasma. *J. Geophys. Res. Space Phys.* 121, 9250–9255. doi:10.1002/2015ja022162

Ilie, R., Liemohn, M. W., Toth, G., Yu Ganushkina, N., and Daldorff, L. K. S. (2015). Assessing the Role of Oxygen on Ring Current Formation and Evolution through Numerical Experiments. *J. Geophys. Res. Space Phys.* 120, 4656–4668. doi:10.1002/2015JA021157.2015JA021157

Ilie, R., Skoug, R. M., Valek, P., Funsten, H. O., and Glocer, A. (2013). Global View of Inner Magnetosphere Composition during Storm Time. *J. Geophys. Res. Space Phys.* 118, 7074–7084. doi:10.1002/2012ja018468

Istomin, V. G. (1966). Observational Results on Atmospheric Ions in Region of Outer Ionosphere. *Ann. De Geophysique* 22, 255.

Jackson, J. E., and Vette, J. I. (1975). *The Orbiting Geophysical Observatories*. Washington, DC: NASA Special Publication, 7601.

Johnson, A. W., and Gerardo, J. B. (1972). Recombination and Ionization in a Molecular-Ion-Dominated Helium Afterglow. *Phys. Rev. A.* 5, 1410–1418. doi:10.1103/PhysRevA.5.1410

Klecker, B., Möbius, E., Hovestadt, D., Scholer, M., Gloeckler, G., and Ipavich, F. M. (1986). Discovery of Energetic Molecular Ions (NO+and O2+) in the Storm Time Ring Current. *Geophys. Res. Lett.* 13, 632–635. doi:10.1029/GL013i007p00632

Kronberg, E. A., Ashour-Abdalla, M., Dandouras, I., Delcourt, D. C., Grigorenko, E. E., Kistler, L. M., et al. (2014). Circulation of Heavy Ions and Their Dynamical Effects in the Magnetosphere: Recent Observations and Models. *Space Sci. Rev.* 184, 173–235. doi:10.1007/s11214-014-0104-0

Lennartsson, O. W., Collin, H. L., Peterson, W. K., and Shelley, E. G. (2000). Polar/timas Statistical Results on the Outflow of Molecular Ions from Earth at Solar Minimum. *Adv. Space Res.* 25, 2417–2420. doi:10.1016/S0273-1177(99)00531-1

Lin, M.-Y., Ilie, R., and Glocer, A. (2020). The Contribution of N+ Ions to Earth's Polar Wind. *Geophys. Res. Lett.* 47, 18. doi:10.1029/2020GL089321

Maggiolo, R., Sauvaud, J. A., Fontaine, D., Teste, A., Grigorenko, E., Balogh, A., et al. (2006). A Multi-Satellite Study of Accelerated Ionospheric Ion Beams above the Polar Cap. *Ann. Geophys.* 24, 1665–1684. doi:10.5194/angeo-24-1665-2006

Miyoshi, Y., Shinohara, I., Takashima, T., Asamura, K., Higashio, N., Mitani, T., et al. (2018). Geospace Exploration Project ERG. *Earth Planets Space* 70, 101. doi:10.1186/s40623-018-0862-0

Mobius, E., Gloeckler, G., Hovestadt, D., Ipavich, F. M., Klecker, B., Scholer, M., et al. (1985). The Time-Of-Flight Spectrometer Suleica for Ions of the Energy Range 5-270 Kev/charge on Ampte Irm. *IEEE Trans. Geosci. Remote Sensing* GE-23, 274–279. doi:10.1109/TGRS.1985.289527

Moore, T. E., Peterson, W. K., Russell, C. T., Chandler, M. O., Collier, M. R., Collin, H. L., et al. (1999). Ionospheric Mass Ejection in Response to a CME. *Geophys. Res. Lett.* 26, 2339–2342. doi:10.1029/1999gl900456

Mukai, T., Hirahara, M., Machida, S., Saito, Y., Terasawa, T., and Nishida, A. (1994). Geotail Observation of Cold Ion Streams in the Medium Distance Magnetotail Lobe in the Course of a Substorm. *Geophys. Res. Lett.* 21, 1023–1026. doi:10.1029/93gl02424

Nauk, V. I., and Doklady, A. (1961). Nitrogen Ions in the Upper Atmosphere and the Ionization of the Region at Night. *Dokl. Akad. Nauk SSSR* 137:5 (1961), 1102–1105.

Nishida, A. (1994). The Geotail mission. *Geophys. Res. Lett.* 21, 2871–2873. doi:10.1029/94GL01223

Nosé, M., Taguchi, S., Hosokawa, K., Christon, S. P., McEntire, R. W., Moore, T. E., et al. (2005). Overwhelming O+ Contribution to the Plasma Sheet Energy Density during the October 2003 Superstorm: Geotail/EPIC and IMAGE/LENA Observations. *J. Geophys. Res. Space Phys.* 110, 1.

Peterson, W. K., Abe, T., Fukunishi, H., Greffen, M. J., Hayakawa, H., Kasahara, Y., et al. (1994). On the Sources of Energization of Molecular Ions at Ionospheric Altitudes. *J. Geophys. Res.* 99, 23257–23274. doi:10.1029/94JA01738

Poppe, A. R., Fillingim, M. O., Halekas, J. S., Raeder, J., and Angelopoulos, V. (2016). Artemis Observations of Terrestrial Ionospheric Molecular Ion Outflow at the Moon. *Geophys. Res. Lett.* 43, 6749–6758. doi:10.1002/2016GL069715

Richards, P. G., and Voglozin, D. (2011). Reexamination of Ionospheric Photochemistry. *J. Geophys. Res. Space Phys.* 116, 47. doi:10.1029/2011JA016613

Ridley, A. J., Deng, Y., and Tóth, G. (2006). The Global Ionosphere-Thermosphere Model. *J. Atmos. Solar-Terrestrial Phys.* 68, 839–864. doi:10.1016/j.jastp.2006.01.008

Schunk, R., and Nagy, A. (2009). *Ionospheres*. second edn. Cambridge University Press. Cambridge Books Online.

Schunk, R. W., and Raitt, W. J. (1980). Atomic Nitrogen and Oxygen Ions in the Daytime High-Latitude F Region. *J. Geophys. Res.* 85, 1255–1272. doi:10.1029/ja085ia03p01255

Schunk, R. W., Raitt, W. J., and Banks, P. M. (1975). Effect of electric fields on the daytime high-latitude e and f regions. *J. Geophys. Res.* (1896-1977) (80), 3121–3130. doi:10.1029/JA080i022p03121

Schunk, R. W., and Sojka, J. J. (1997). Global Ionosphere-Polar Wind System during Changing Magnetic Activity. *J. Geophys. Res.* 102, 11625–11651. doi:10.1029/97ja00292

Seki, K., Keika, K., Kasahara, S., Yokota, S., Hori, T., Asamura, K., et al. (2019). Statistical Properties of Molecular Ions in the Ring Current Observed by the Arase (Erg) Satellite. *Geophys. Res. Lett.* 46, 8643–8651. doi:10.1029/2019gl084163

Seki, K., Terasawa, T., Hirahara, M., and Mukai, T. (1998). Quantification of Tailward Cold O+beams in the Lobe/mantle Regions with Geotail Data: Constraints on Polar O+outflows. *J. Geophys. Res.* 103, 29371–29381. doi:10.1029/98ja02463

Shelley, E. G., Ghielmetti, A. G., Balsiger, H., Black, R. K., Bowles, J. A., Bowman, R. P., et al. (1995). The Toroidal Imaging Mass-Angle Spectrograph (Timas) for the Polar mission. *Space Sci. Rev.* 71, 497–530. doi:10.1007/bf00751339

Shelley, E. G., Johnson, R. G., and Sharp, R. D. (1972). Satellite Observations of Energetic Heavy Ions during a Geomagnetic Storm. *J. Geophys. Res.* 77, 6104–6110. doi:10.1029/JA077i031p06104

Solomon, S. C., Hays, P. B., and Abreu, V. J. (1988). The Auroral 6300 Å Emission: Observations and Modeling. *J. Geophys. Res.* 93, 9867–9882. doi:10.1029/JA093iA09p09867

Spjeldvik, W. N., and Fritz, T. A. (1981). Observations of Ions with Nuclear charge$Z \geqq 9$ in the Inner Magnetosphere. *J. Geophys. Res.* 86, 7749–7754. doi:10.1029/JA086iA09p07749

Takada, M., Seki, K., Ogawa, Y., Keika, K., Kasahara, S., Yokota, S., et al. (2021). Low-altitude Ion Upflow Observed by Eiscat and its Effects on Supply of Molecular Ions in the Ring Current Detected by Arase (Erg). *J. Geophys. Res. Space Phys.* 126, e2020JA028951. doi:10.1029/2020JA028951

Taylor, H. A., Jr. (1971). Observed Solar Geomagnetic Control of the Ionosphere-Implications for Reference Ionospheres. *Space Res.* 12, 1275–1290.

Taylor, H. A., Brinton, H. C., Pharo, M. W., and Rahman, N. K. (1968). Thermal Ions in the Exosphere; Evidence of Solar and Geomagnetic Control. *J. Geophys. Res.* 73, 5521–5533. doi:10.1029/ja073i017p05521

Taylor, H. A., Grebowsky, J. M., and Chen, A. J. (1975). Ion Composition Irregularities and Ionosphere-Plasmasphere Coupling: Observations of a High Latitude Ion Trough. *J. Atmos. Terrestrial Phys.* 37, 613–623. doi:10.1016/0021-9169(75)90056-2

Taylor, H. A. (1974). High Latitude Minor Ion Enhancements: A Clue for Studies of Magnetosphere-Atmosphere Coupling. *J. Atmos. Terrestrial Phys.* 36, 1815–1823. doi:10.1016/0021-9169(74)90168-8

Taylor, H. A., Jr. (1973). Parametric Description of Thermospheric Ion Composition Results. *J. Geophys. Res.* 78, 315–319. doi:10.1029/JA078i001p00315

Torr, D. G., and Orsini, N. (1978). The Effect of N2+recombination on the Aeronomic Determination of the Charge Exchange Rate Coefficient of O+(^{2}D) with N2d) with N2. *Geophys. Res. Lett.* 5, 657–659. doi:10.1029/GL005i008p00657

Tsuruda, K., and Oya, H. (1991). Introduction to the Exos-D (Akebono) Project. *Geophys. Res. Lett.* 18, 293–295. doi:10.1029/91GL00039

Whalen, B. A., Burrows, J. R., Yau, A. W., Budzinski, E. E., Pilon, A. M., Iwamoto, I., et al. (1990). The Suprathermal Ion Mass Spectrometer(SMS) Onboard the Agebono (EXOS-D) Satellite. *J. Geomagn. Geoelec* 42, 511–536. doi:10.5636/jgg.42.511

Williams, D. J., Lui, A. T. Y., McEntire, R. W., Angelopoulos, V., Jacquey, C., Christon, S. P., et al. (1994). Magnetopause Encounters in the Magnetotail at Distances of ~80 Re 80 Re. *Geophys. Res. Lett.* 21, 3007–3010. doi:10.1029/94gl01298

Wilson, G. R., and Craven, P. (1999). Molecular Ion Upflow in the Cleft Ion fountain - Wilson - 1999-Journal of Geophysical Research: Space Physics - Wiley Online Library. *J. Geophys. Res.* 104, 4437–4446. doi:10.1029/1998JA900070

Winglee, R. M., Chua, D., Brittnacher, M., Parks, G. K., and Lu, G. (2002). Global Impact of Ionospheric Outflows on the Dynamics of the Magnetosphere and Cross-Polar Cap Potential. *J. Geophys. Res.* 107, 1237. doi:10.1029/2001JA000214

Yamauchi, M. (2019). Terrestrial Ion Escape and Relevant Circulation in Space. *Ann. Geophys.* 37, 1197–1222. doi:10.5194/angeo-37-1197-2019

Yau, A. W., Abe, T., and Peterson, W. K. (2007). The Polar Wind: Recent Observations. *J. Atmos. Solar-Terrestrial Phys.* 69, 1936–1983. doi:10.1016/j.jastp.2007.08.010

Yau, A. W., and Howarth, A. (2016). Imaging thermal Plasma Mass and Velocity Analyzer. *J. Geophys. Res. Space Phys.* 121, 7326–7333. doi:10.1002/2016JA022699

Yau, A. W., James, H. G., and Liu, W. (2006). The canadian Enhanced Polar Outflow Probe (E-pop) mission in ilwsMagnetospheric Dynamics and the International Living with a star Program. *Adv. Space Res.* 38, 1870–1877. doi:10.1016/j.asr.2005.01.058

Yau, A. W., Whalen, B. A., Goodenough, C., Sagawa, E., and Mukai, T. (1993). EXOS D (Akebono) Observations of Molecular NO(+) and N2(+) Upflowing Ions in the High-Altitude Auroral Ionosphere. *J. Geophys. Res.* 98, 11205–11224. doi:10.1029/92ja02019

Yau, A. W., Whalen, B. A., and Sagawa, E. (1991). Minor Ion Composition in the Polar Ionosphere. *Geophys. Res. Lett.* 18, 345–348. doi:10.1029/91gl00034

Yokota, S., Kasahara, S., Mitani, T., Asamura, K., Hirahara, M., Takashima, T., et al. (2017). Medium-energy Particle Experiments-Ion Mass Analyzer (MEP-I) Onboard ERG (Arase). *Earth Planets Space* 69, 69. doi:10.1186/s40623-017-0754-8

Zettergren, M., Semeter, J., Burnett, B., Oliver, W., Heinselman, C., Blelly, P.-L., et al. (2010). Dynamic Variability in F-Region Ionospheric Composition at Auroral Arc Boundaries. *Ann. Geophys.* 28, 651–664. doi:10.5194/angeo-28-651-2010

Zettergren, M., Semeter, J., Heinselman, C., and Diaz, M. (2011). Incoherent Scatter Radar Estimation of F Region Ionospheric Composition during Frictional Heating Events. *J. Geophys. Res. Space Phys.* 116, 1. doi:10.1029/2010JA016035

Conflict of Interest: The authors declare that the research was conducted in the absence of any commercial or financial relationships that could be construed as a potential conflict of interest.

Publisher's Note: All claims expressed in this article are solely those of the authors and do not necessarily represent those of their affiliated organizations, or those of the publisher, the editors, and the reviewers. Any product that may be evaluated in this article, or claim that may be made by its manufacturer, is not guaranteed or endorsed by the publisher.

frontiers in Astronomy and Space Sciences

ORIGINAL RESEARCH
published: 04 January 2022
doi: 10.3389/fspas.2021.785305

Charge-Exchange Byproduct Cold Protons in the Earth's Magnetosphere

Joseph E. Borovsky[1]*, *Jianghuai Liu*[2], *Raluca Ilie*[2] and *Michael W. Liemohn*[3]

[1]Center for Space Plasma Physics, Space Science Institute, Boulder, CO, United States, [2]Department of Electrical and Computer Engineering, University of Illinois at Urbana-Champaign, Urbana, IL, United States, [3]Department of Climate and Space Sciences and Engineering, University of Michigan, Ann Arbor, MI, United States

Owing to the spatial overlap of the ion plasma sheet (ring current) with the Earth's neutral-hydrogen geocorona, there is a significant rate of occurrence of charge-exchange collisions in the dipolar portion of the Earth's magnetosphere. During a charge-exchange collision between an energetic proton and a low-energy hydrogen atom, a low-energy proton is produced. These "byproduct" cold protons are trapped in the Earth's magnetic field where they advect via E×B drift. In this report, the number density and behavior of this cold-proton population are assessed. Estimates of the rate of production of byproduct cold protons from charge exchange are in the vicinity of 1.14 cm^{-3} per day at geosynchronous orbit or about 5 tons per day for the entire dipolar magnetosphere. The production rate of cold protons owing to electron-impact ionization of the geocorona by the electron plasma sheet at geosynchronous orbit is about 12% of the charge-exchange production rate, but the production rate by solar photoionization of the neutral geocorona is comparable or larger than the charge-exchange production rate. The byproduct-ion production rates are smaller than observed early time refilling rates for the outer plasmasphere. Numerical simulations of the production and transport of cold charge-exchange byproduct protons find that they have very low densities on the nightside of geosynchronous orbit, and they can have densities of 0.2–0.3 cm^{-3} at geosynchronous orbit on the dayside. These dayside byproduct-proton densities might play a role in shortening the early phase of plasmaspheric refilling.

Keywords: magnetosphere, charge exchange, ring current, cold ions, hydrogen geocorona

OPEN ACCESS

Edited by:
Chi Wang,
National Space Science Center (CAS), China

Reviewed by:
Tianran Sun,
National Space Science Center (CAS), China
Nickolay Ivchenko,
Royal Institute of Technology, Sweden

***Correspondence:**
Joseph E. Borovsky
jborovsky@spacescience.org

Specialty section:
This article was submitted to Space Physics, a section of the journal Frontiers in Astronomy and Space Sciences

Received: *29 September 2021*
Accepted: *17 November 2021*
Published: *04 January 2022*

Citation:
Borovsky JE, Liu J, Ilie R and Liemohn MW (2022) Charge-Exchange Byproduct Cold Protons in the Earth's Magnetosphere. Front. Astron. Space Sci. 8:785305. doi: 10.3389/fspas.2021.785305

1 INTRODUCTION

In the dipolar portions of the Earth's magnetosphere, ring current ions charge exchange with the neutral hydrogen exosphere of the Earth, which is known as the hydrogen geocorona (Carruthers et al., 1976; Rairden et al., 1986). For an energetic proton $H^+_{energetic}$ (expression (1a)), an energetic nitrogen ion $N^+_{energetic}$ (expression (1b)), or an energetic oxygen ion $O^+_{energetic}$ (expression (1c)), the charge-exchange reaction can be expressed as

$$H^+_{energetic} + H^0_{low-energy} \rightarrow H^0_{energetic} + H^+_{low-energy}, \quad (1a)$$

$$N^+_{energetic} + H^0_{low-energy} \rightarrow N^0_{energetic} + H^+_{low-energy}, \quad (1b)$$

$$O^+_{energetic} + H^0_{low-energy} \rightarrow O^0_{energetic} + H^+_{low-energy}, \quad (1c)$$

$$He^+_{energetic} + H^0_{low-energy} \rightarrow He^0_{energetic} + H^+_{low-energy}, \quad (1d)$$

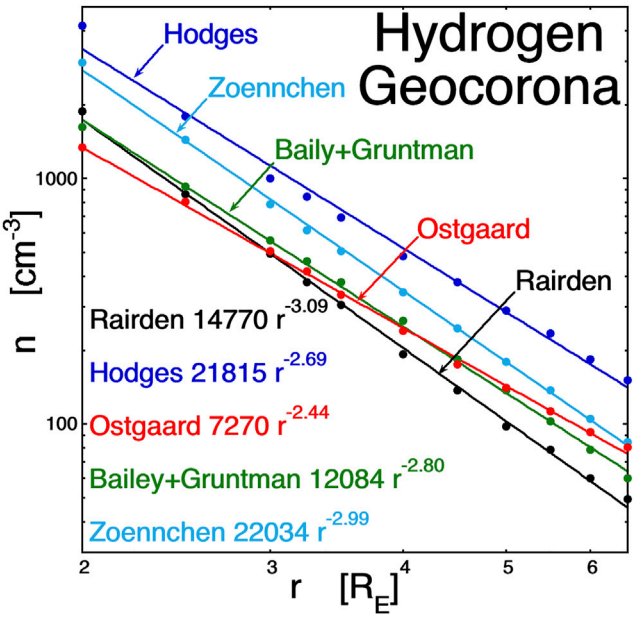

FIGURE 1 | Number density of the hydrogen geocorona as a function of the distance from the Earth's center along the Sun–Earth line in the nightside (local midnight). The plotted curves are from five different models of the geocorona. Power-law fits to the curves are displayed in the figure (after Ilie et al., 2013)).

where an energetic (~10's of keV) ion passes near a low-energy (less than an eV) hydrogen atom, and the result of the reaction is an energetic hydrogen atom or an energetic nitrogen atom or an energetic oxygen atom and, in all three cases, a low-energy proton. Charge exchange with the geocorona is an important process for the decay of the ring current (Smith and Bewtra, 1978; Kistler et al., 1989; Liemohn et al., 1999; Ilie et al., 2013; Ilie and Liemohn, 2016) and for the creation of unstable hot-ion distribution functions in the dipolar magnetosphere (Cornwall, 1977; Thomsen et al., 2011, Thomsen et al., 2017). In recent years, the space-physics community has become interested in this charge-exchange process because remote detection of the energetic atoms can allow the imaging of the ring current/geocorona overlap (e.g., Gruntman, 1997; Perez et al., 2016). In this report, the cold byproduct protons from the charge-exchange reactions are of great interest.

Charge-exchange byproduct protons are discussed briefly in Delzanno et al. (2021). At the 1998 GEM Summer Workshop, Pat Reiff posed a question after a presentation as to whether charge exchange could be an important source for the refilling of the plasmasphere (Borovsky et al., 1998a). This work is an outgrowth from that question.

This article is organized as follows: In **Section 2**, the expected properties of charge-exchange byproduct protons in the magnetosphere are described. In **Section 3**, two methods are used to estimate the rate of production of cold charge-exchange protons in the dipolar magnetosphere. In **Section 4**, computer simulations are performed to look at the global population of cold charge-exchange byproduct protons in the magnetosphere under varying levels of geomagnetic activity. In **Section 5**, the role of cold charge-exchange byproduct protons in the transition from early stage to late stage plasmaspheric refilling is assessed In **Section 6**, the results are summarized, and a new work is called for that will refine the conclusions of this report.

2 PROPERTIES OF CHARGE-EXCHANGE BYPRODUCT PROTONS

As ion-plasma-sheet (ring current) ions are convected into the dipolar magnetosphere from the near-Earth portions of the magnetotail, they encounter the neutral hydrogen geocorona of the Earth. The density of the geocorona falls off with the distance from the Earth. In **Figure 1** (cf. Fig. 1 of Ilie et al., 2013), the neutral-hydrogen number density is plotted at the equator at local midnight as a function of the distance from the Earth: here, power-law fits to five geocorona models are plotted in the five different colors. The models from Rairden et al. (1986) are in black, Hodges (1994) in blue, Ostgaard et al. (2003) in red, Bailey and Gruntman (2011) in green, and Zoennchen et al. (2011) in light blue. The power-law fits to the number density (in units of cm^{-3}) are displayed in the figure. As can be seen, the density of neutral hydrogen increases strongly approaching the Earth, and so the probability of charge exchange increases greatly as an ion approaches the Earth.

Because of this strong radial dependence, the cold byproduct protons of charge-exchange origin are predominantly born at high latitudes. The ion plasma sheet is relatively isotropic (at geosynchronous orbit, $T_{perp}/T_{||}$ values are typically in the 1 to 1.3 range for the <40-eV portion of the ion plasma sheet (Denton et al., 2005)), so there are significant numbers of ions that mirror at high latitudes in the dipolar magnetosphere. As the ions bounce in the magnetic flux tubes, they approach the Earth at high latitudes and spend more time there, where the geocoronal density is higher and so where the probability for charge exchange is higher. Assuming that the hot-ion distribution is isotropic at the equator, Liouville's theorem indicates that the hot-ion distribution will be isotropic everywhere away from the equator and that its number density will be everywhere the same as it is at the equator (cf. Borovsky and Cayton, 2011; Sect. 4.4 of Roederer and Zhang, 2014). For an isotropic hot-ion population at geosynchronous orbit (L = 6.6), this constant density is exploited to obtain the effective flux-tube–averaged number density of the geocorona, which is found to be 2.09 times the equatorial number density if $n_{geoc} \propto r^{-3.09}$ (e.g., the black curve in **Figure 1**), and the flux-tube–averaged number density of the geocorona is 1.64 times the equatorial number density if $n_{geoc} \propto r^{-2.44}$ (e.g., the red curve in **Figure 1**) (See Jordanova et al. (1996) or Liemohn and Kozyra (2003) for bounce averaging when the hot-ion distribution is not isotropic). At 6.5 R_E, the average value of the geocoronal number density n_{geoc} of the five curves in **Figure 1** is 82 cm^{-3}. So, if the boost in density given by flux-tube–averaging is 1.85 times (the average of the five power laws in **Figure 1**) the equatorial value, then the geosynchronous midnight flux tube has an effective geocorona density n_{geoc} of about 152 cm^{-3}.

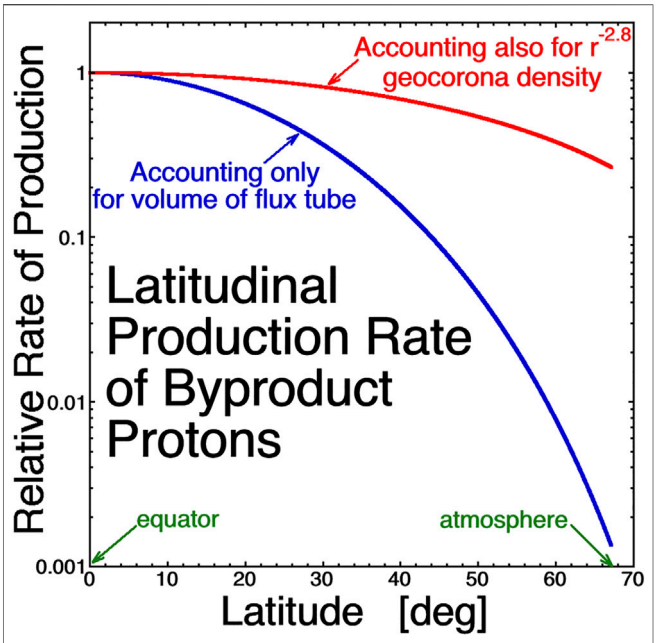

FIGURE 2 | In a dipole flux tube at geosynchronous orbit, the latitudinal distribution of the rate of production of charge-exchange byproduct protons is plotted for an isotropic distribution of energetic ions in the flux tube. The blue curve would be the case if the geocoronal density did not vary with the distance from the Earth, and the red curve is the case for a geocoronal density that varies as $r^{-2.8}$.

Figure 2 examines the production of charge-exchange byproduct protons in a flux tube as a function of latitude assuming the hot-ion distribution is isotropic at the equator. In that case, the number density of hot ions is independent of latitude, and the relative rate of production of charge-exchange byproduct protons depends only on the cross section of the flux tube as a function of latitude. For a dipole geosynchronous flux tube, the figure plots the rate of production of byproduct protons in the flux tube relative to the rate of production at the equator. The blue curve accounts only for the decreasing volume of the flux tube with increasing latitude: this would be the relative production curve, if the number density of the neutral hydrogen geocorona was uniform and did not vary with the distance from the Earth. The red curve in **Figure 2** is the relative rate of production as a function of latitude accounting for both the reduced volume of the dipolar flux tube with increasing latitude and the increasing number density of the geocorona with closeness to the Earth (A $n_{geoc} \propto r^{-2.8}$ case was taken for the red curve, with 2.8 being the mean value of the five exponents in **Figure 1**.). As can be seen comparing the red curve to the blue curve, the $n_{geoc} \propto r^{-2.8}$ geocorona greatly increases the byproduct-proton production at high latitudes. The median value of the blue distribution is at 14.0°, and the median value of the red distribution is at 25.5°. For the red curve, half of the byproduct cold protons produced in the flux tube are produced at a latitude higher than 25.5°, and half of the byproduct protons are produced at a latitude lower than 25.5°.

Since the byproduct protons from charge exchange are born predominantly away from the equator, the population of cold byproduct protons will be somewhat field-aligned at the equator owing to the enhanced birth rate of byproduct protons at portions of the flux tube away from the equator (essentially, the cold ions produced at each latitude in the flux tube will produce a sort of "inverse loss cone" population at the equator). If the hot-ion population in a flux tube is isotropic at the equator, it will be isotropic everywhere in the flux tube. If the hot-ion population is isotropic, then the cold byproduct protons will be produced with isotropic velocity vectors. The excess byproduct protons produced off the equator will show up at the equator as an excess of field-aligned protons.

The byproduct protons are born with low kinetic energies and are probably born with isotropic velocity distributions. The kinetic energies of the gravitationally bound geocoronal hydrogen atoms can be estimated with the use of the virial theorem, which states that for a circular orbit, the orbital kinetic energy ε_{kin} is one-half of the gravitational potential energy ε_{pot}. Thus,

$$\varepsilon_{kin} = G\,M\,m\,/\,2r, \tag{2}$$

where $G = 6.67 \times 10^{-8}$ cm^{-3} gm^{-1} s^{-2} is the gravitational constant, $M = 5.97 \times 10^{27}$ gm is the mass of the Earth, $m = 1.67 \times 10^{-24}$ gm is the mass of a hydrogen atom, and r is the distance from the center of the Earth. At geocentric-orbit distances ($r = 6.6\ R_E = 4.2 \times 10^9$ cm), the kinetic energy of a geocoronal hydrogen atom is $\varepsilon_{kin} \sim 7.9 \times 10^{-14}$ erg = 0.05 eV.

By kinematically analyzing the laboratory measurements of the deflection angles of fast protons that have undergone charge exchange with hydrogen atoms, it can be determined that the cold byproduct protons from charge exchange are born with very little kinetic energy. In a charge-exchange collision with a cold atom (assuming a spherically symmetric scatter potential), the fast proton with velocity $v_{energetic}$ and kinetic energy $\varepsilon_{energetic} = m v_{energetic}^2/2$ will be deflected by an angle θ_{defl} and will transfer a kinetic energy $\varepsilon_{collision}$ to the cold atom, with the cold atom becoming a cold proton. Using conservation of energy and momentum and assuming that the particle masses are identical, one finds that the kinetic energy received by the cold atom converted into a proton is

$$\varepsilon_{collision} = \varepsilon_{energetic} \sin^2(\theta_{defl}) / (1 + \sin^2(\theta_{defl})). \tag{3}$$

For a wide range of incident-proton energies, **Table 1** shows measured values of the maximum deflection angle of the fast proton as a function of its incident energy. The majority of charge-exchange events will occur at deflection angles below these quoted maximum deflection angles, which were qualitatively obtained from the published differential cross sections (Chen et al., 1973; Toshima et al., 1989; Gaussorgues et al., 1975; Schinke and Kruger, 1976; Martin et al., 1981). Using these values, the maximum energy imparted to the byproduct protons is calculated from expression (2), and these values are collected into **Table 1**. As can be seen from the table, the energies of the charge-exchange byproduct protons will be less than 0.6 eV for incident proton energies in the range from 500–125 keV,

TABLE 1 | Estimates of byproduct-proton kinetic energies from kinematic analysis of measured primary deflection angles.

Kinetic energy of primary H^+ ion	Maximum angle of deflection θ_{defl}	Byproduct-proton kinetic energy ε_{coll}	Reference
500 eV	<2°	<0.6 eV	Fig. 2b of Gaussorgues et al., 1975
1 keV	<1.5°	<0.6 eV	Fig. 6b of Chen et al., 1973
2 keV	<1°	<0.6 eV	Fig. 1c of Schinke and Kruger, (1976)
25 keV	<0.1°	<0.08 eV	Fig. 1 of Martin et al., 1981
125 keV	<0.03°	<0.04 eV	Fig. 2 of Toshima et al., 1989

which covers the ion plasma sheet. This small energy transfer makes sense since charge exchange is a tunneling process that can occur at larger distances than scattering between a proton and a neutral hydrogen atom. Consistent with this, it will be seen in **Section 3** that the charge-exchange cross section for a 1-keV hydrogen atom is ~20 times the cross-sectional area of the hydrogen atom. Note that the momentum transferred to the byproduct proton in the charge-exchange collision is in a direction that is nearly orthogonal to the initial trajectory of the fast ion. Since the velocity kick received by the byproduct proton during the charge-exchange collision is nearly transverse to the path of the fast proton, for an isotropic distribution of fast protons the byproduct protons are born with an isotropic velocity distribution.

If a byproduct proton is born in the corotational electric field, the cold byproduct proton will pick up a gyrational energy ε_{pickup} that is comparable to the corotational kinetic energy where it is born. If a proton is born at a distance ρ from the rotational axis of the Earth, this energy gain is

$$\varepsilon_{pickup} = 1.1 \times 10^{-3}\ \mathrm{eV}\left(\rho/1\ R_E\right)^2. \quad (4)$$

Even if $\rho = 10\ R_E$, this energy is considerably less than 1 eV. Outside the corotational region, **E**×**B** convection can be faster. But even if the convection speed is 10 km/s (5.7 R_E/h), the pickup kinetic energy ε_{pickup} will only be 0.52 eV.

It is possible that the byproduct protons can pick up parallel kinetic energies owing to parallel electrostatic potential differences that may exist in the dipolar magnetosphere. Substantial potential drops between the ionosphere and the magnetosphere are common in the auroral zone, as indicated by the inverted-V in low-altitude electron spectrograms (which map to the electron plasma sheet (Feldstein and Galperin, 1993)) and as also seen in downward-current regions (Lynch et al., 2002). The auroral zone can extend to L-shells lower than geosynchronous orbit on the nightside (Mauk and Meng, 1991; Motoba et al., 2015; Ozaki et al., 2015), particularly when the geomagnetic activity is high. Another source of field-aligned potential drops is the ambipolar electric field driven by the emission of photoelectrons from the upper atmosphere (Khazanov et al., 1997; Glocer et al., 2017). The photoelectron-driven potential drops are a few volts, so byproduct protons born at high latitudes could pick up a few eV of parallel kinetic energy. Ambipolar field-aligned potentials can also be set up, if the hot ions and hot electrons of the magnetosphere have different degrees of anisotropy (Persson, 1963; Lennartsson, 1976; Chiu and Schulz, 1978; Stern, 1981). This property is exploited to produce electrostatic ion confinement in laboratory mirror machines (e.g., Hershkowitz et al., 1982). One can imagine that the magnetospheric hot ions have an effective anisotropy that changes with time as the hot-ion population decays owing to charge exchange. These anisotropy-driven ambipolar potentials can be a fraction of the hot-particle temperatures (Whipple, 1977), so a parallel potential of at least a few volts driven by multi-keV ions and electrons is almost probable. Should the byproduct protons gain parallel kinetic energy owing to any of these parallel potential differences in the magnetosphere, they will appear as a cold, field-aligned proton beam in the equatorial magnetosphere.

A candidate population of cold ions that may be the byproduct protons produced by hot-ion charge exchange with the geocorona is seen in the equatorial magnetosphere at geosynchronous orbit by the Magnetospheric Plasma Analyzer (MPA) (Bame et al., 1993). An example of this ion population can be seen in the energy-time ion spectrogram as shown in **Figure 3**. Here, 3.8 h of ion measurements are shown from the spacecraft LANL-02A on September 23, 2003. The spacecraft was crossing the nightside in geosynchronous orbit at the equator. The vertical axis of the spectrogram is the logarithm of the ion energy going from 1 eV at the bottom to 40 keV at the top. The color is the intensity of the ion energy flux at that energy. On the horizontal axis, UT is plotted with the local time of the spacecraft indicated in parentheses: in the plot, the spacecraft travels from about 22.7 LT to about 2.5 LT. The vertical black lines in **Figure 3** denote the time interval when the spacecraft was in eclipse. The feature in the spectrogram to focus on is the narrow "ion line" that has darkness below it. In the hot electron plasma sheet, the MPA spacecraft charges to large negative potentials with respect to the ambient magnetospheric plasma (Thomsen et al., 2013): any low-energy ions in the magnetospheric plasma are accelerated across this potential to produce this narrow-energy (cold) line in the energy-time spectrogram. The energy of the ion line is used as a direct measure of the spacecraft potential with respect to infinity (Borovsky et al., 1998b). The vertical width of the ion line is narrow, indicating that the energy spread of the ions is small compared with the potential that the ions fell through. At around 21 UT in **Figure 3**, the potential of the ion line is about 30 V, and the line is still narrow. There are 40 evenly spaced energy channels in the spectrogram, so at 21 UT the energy spread in the ion-line population is much less than 30 eV. The density in the ambient magnetospheric plasma of these cold ions is difficult to determine owing to the sheath focusing by the large-radius and large-voltage spacecraft sheath (for example, at 19 UT in **Figure 3**, the hot-electron density is 0.51 cm^{-3} and the hot-electron temperature is 4.2 keV yielding a Debye length for the spacecraft of $\lambda_{De} = 0.68$ km). Preliminary calculations based on

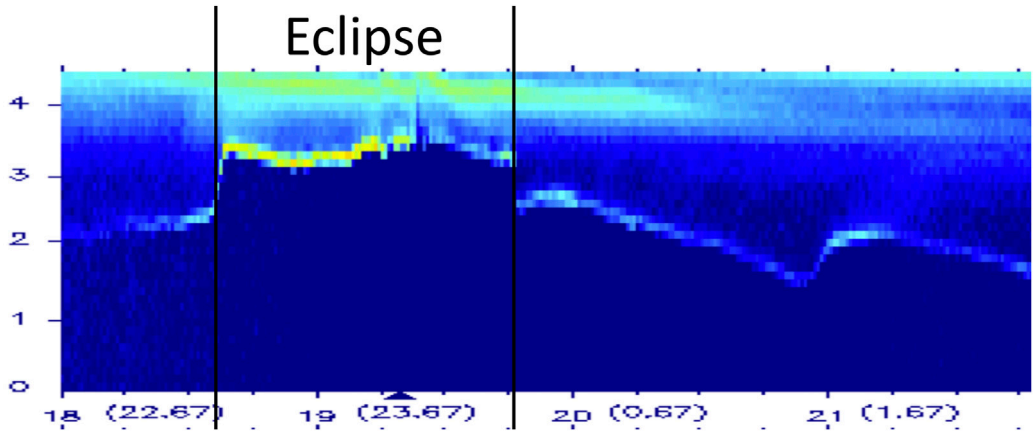

FIGURE 3 | 3.8-h long energy-time ion spectrogram taken from the MPA instrument on September 23, 2003, onboard the spacecraft LANL-02A at geosynchronous orbit crossing the nightside. The energy resolution of the spectrogram is 40 vertical channels logarithmically spaced. The time resolution is 86 s.

TABLE 2 | Estimates of the number of byproduct cold protons produced.

Method	Production rate
Examining loss of plasma-sheet ions	5 tons per day in dipole
Calculating local charge-exchange rate	1.14 cm^{-3} day^{-1} at L = 6.6
Calculating electron-impact ionization rate	0.14 cm^{-3} day^{-1} at L = 6.6
Calculating geocorona photoinization rate	1.2–2.6 cm^{-3} day^{-1} at L = 6.6

orbit-limited ion collection indicate that the densities of the cold ambient protons that produce the ion lines at high voltages are on the order of 10^{-2} cm^{-3}. It is believed that the ion-line ions with their low-ambient fluxes are only detectable because the spacecraft charges to high-negative potentials so that its sheath collecting area is much greater than its surface area (e.g., Chen, 1965; Hershkowitz, 1989).

3 PRODUCTION ESTIMATES FOR BYPRODUCT PROTONS

In this section, the rate of production of cold protons owing to the charge exchange of ion-plasma-sheet (ring current) ions with geocoronal hydrogen atoms is estimated in two different ways. In the first method, the total number of plasma-sheet protons passing into the dipolar region per day is considered, and then the fraction lost owing to charge exchange is applied to these to obtain the total number of charge-exchange collisions in the dipolar region of the magnetosphere per day. The second method involves examining the number density and temperature of the ion plasma sheet at geosynchronous orbit, estimating the density of the geocorona there, and applying measured charge-exchange cross sections to these numbers to obtain the rate of charge-exchange collisions at geosynchronous orbit. Then, similar calculations will be carried out to determine the rate of production of cold protons by electron-impact ionization of the geocorona hydrogen atoms by electron-plasma-sheet electrons and the rate of production of cold protons by photoionization of the geocorona hydrogen atoms. The values are collected in **Table 2**.

The first calculation proceeds as follows: The proton mass of the earthward-convecting portion of the ion plasma sheet M_{ps} on the nightside of the Earth is about 1,150 kg (Table 4 of Borovsky et al.(1998c)), assuming that all of the plasma-sheet ions are protons. This material convects from the near-Earth magnetotail, into the dipolar region of the magnetosphere, past the Earth's terminators, to the dayside magnetopause where it is lost. The convection time τ_{conv} (replacement time) for the nightside plasma sheet is estimated to be about 2.1 h (Table 4 of Borovsky et al.(1998c)). This gives a mass flow rate of $M_{ps}/\tau_{conv} \sim 1.3 \times 10^4$ kg/day of hot protons into the dipole from the magnetotail, which is about 13 metric tons per day. By comparing the number density of the ion plasma sheet on the dayside of the dipolar region at geosynchronous orbit with its number density on the nightside of the dipolar region, a rough estimate of the fraction of ion-plasma-sheet ions that undergo charge exchange can be obtained. At geosynchronous orbit, the ion-plasma-sheet number density on the nightside is typically $n_{night} \sim 0.7$ cm^{-3}, and the density on the dayside is $n_{day} \sim 0.4$ cm^{-3} (e.g., Korth et al., 1999). This represents a ~40% loss in the ions in passing the dipole from the nightside to the dayside (the loss is probably slightly higher since the flux-tube volume is larger on the nightside of geosynchronous orbit than it is on the dayside; the equatorial field strength being typically ~30% less on the nightside than it is on the dayside (Rufenach et al., 1992; Borovsky and Denton, 2010)). Assuming that the density reduction is solely due to charge-exchange loss (ignoring loss of hot protons to the atmosphere), the ~40% of 1.3×10^4 kg/day represents a $\sim 5 \times 10^3$ kg/day loss of hot protons owing to charge exchange. For every hot proton lost to charge exchange, one cold byproduct proton is produced. Hence, $\sim 5 \times 10^3$ kg/day, or ~5 metric tons per day, of cold protons are produced in the dipolar magnetosphere as byproducts of charge exchange. This value is entered into **Table 2**. This number should be taken as an order-of-magnitude estimate, since the mass of the plasma sheet is difficult to discern, and the estimated convection time for the plasma sheet differs depending on whether ionospheric or magnetospheric flows are analyzed. The number density of the plasma sheet also varies

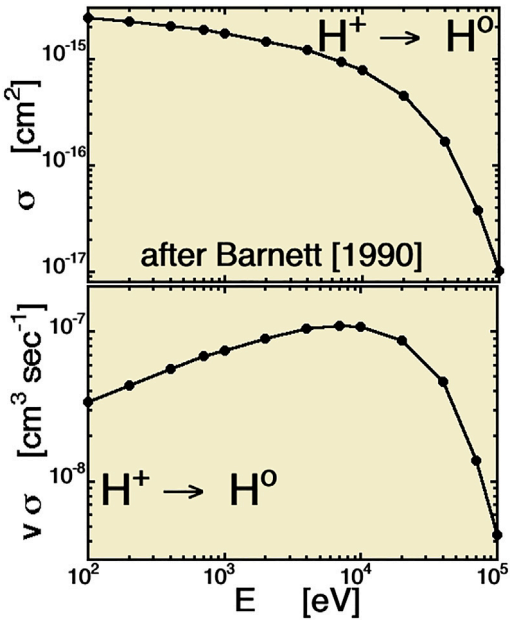

FIGURE 4 | In the top panel, the charge-exchange cross section σ of a hydrogen atom to a proton is plotted as a function of the proton kinetic energy E (after Barnett (1990)). In the bottom panel, the product vσ is plotted as a function of E, where v is the proton velocity.

considerably from day-to-day depending on solar-wind conditions (Borovsky et al., 1998d). As a comparison to the five tons per day of byproduct protons, the mass of the protons in the outer filled plasmasphere (the region that tends to drain and refill) is on the order of 34 tons (Borovsky and Steinberg, 2006).

The second calculation, which estimates the rate of occurrence R of charge-exchange collisions at geosynchronous orbit, proceeds as follows: the rate of production of byproduct protons (number per unit time per unit volume) is

$$R = n_{energetic}\, f, \tag{5}$$

where $n_{energetic}$ is the number density of hot (energetic) ions, and f is the frequency that one of these energetic ions undergoes charge-changing collisions. For the number density and temperature of the hot protons at geosynchronous orbit at local midnight, the values $n_{energetic} = 0.88\ cm^{-3}$ and $T_{energetic} = 8.9$ keV are taken from the upper-right geosynchronous-orbit point in Fig. 2 of Borovsky et al., (1998c). The frequency f of charge-exchange collisions for a proton in the hydrogen geocorona is

$$f = n_{geoc}\, v_{energetic} \sigma, \tag{6}$$

where n_{geoc} is the number density of hydrogen atoms in the geocorona, $v_{energetic}$ is the velocity of the energetic proton, and σ is the charge-exchange cross section for a proton on a hydrogen atom. For $v_{energetic}$, the velocity of a proton with a kinetic energy of 8.9 keV is taken, which is $v_{energetic} = 1.3 \times 10^8$ cm/s. For n_{geoc}, the mean value of the five curves in **Figure 1** at r = 6.5 R_E is 82 cm^{-3}, and an effective flux-tube average value (for an isotropic hot-ion distribution at the equator) is about 1.85 times that of the equatorial density, yielding $n_{geoc} = 152\ cm^{-3}$ for the "bounce-averaged" geocorona number density (cf. **Section 2**). The measured charge-exchange cross section σ for a proton is plotted in the top panel of **Figure 4** as a function of the proton kinetic energy, taken from the data in Table A-22 of Barnett (1990), which is a compilation of a number of laboratory experiments. Note, in the top panel, the large size of this cross section at 1 keV is $\sigma = 1.7 \times 10^{-15}\ cm^2$, which is 19.4 times than that of the cross-sectional area of a hydrogen atom $\pi a_o^2 = 8.8 \times 10^{-17}\ cm^2$, where $a_o = 5.29 \times 10^{-9}$ cm is the Bohr radius and the radius of a hydrogen atom (cf. Table 1 of Ghosh and Biswas (2002)). A 1-keV proton coming within 4.4 atomic radii of a hydrogen atom can undergo charge exchange, hence the very weak kinetic energy transfer $\varepsilon_{collision}$ to the byproduct proton during the exchange (cf. **Section 2** and **Table 1**). At 8.9 keV, the charge-exchange cross section is $\sigma = 8.3 \times 10^{-16}\ cm^2$. In the bottom panel of **Figure 4**, $v_{energetic}\sigma$ is plotted. Ideally, to utilize expression (5) for a distribution of hot ions, one should average $v_{energetic}\sigma$ over the distribution of ions (this is complicated because the distribution functions of plasma sheet ions at geosynchronous orbit are non-Maxwellian; e.g., see Fig. 9 of Birn et al.(1997)). Fortunately, in the energy range of the ions of the ion plasma sheet, the quantity $v_{energetic}\sigma$ does not vary very much; as can be seen in the bottom panel of **Figure 4**, in the kinetic energy range from 100 eV to 50 keV, $v_{energetic}\sigma$ varies by less than a factor of 4. For a distribution of protons with a temperature of about 8.9 keV, a value of $v_{energetic}\sigma \approx 1 \times 10^{-7}\ cm^{-3}\ s^{-1}$ will be used. Using these values in expression (6) with $n_{geoc} \approx 152\ cm^{-3}$ yields a frequency of charge exchange of $f \approx 1.3 \times 10^{-5}\ s^{-1}$ (this represents a half-life to charge exchange of about 15 h for a hot proton at geosynchronous orbit). Using this value of f in expression (5) along with $n_{energetic} \approx 0.88\ cm^{-3}$ yields a production rate of cold byproduct protons of $R \approx 1.3 \times 10^{-5}\ cm^{-3}\ s^{-1}$, which is $1.14\ cm^{-3}day^{-1}$. This value is entered into **Table 2**.

For comparison with the rate of production of cold protons by charge exchange, the rate of production of cold protons by electron-impact ionization of geocoronal hydrogen by the electron plasma sheet is estimated. Similar to the aforementioned calculation of charge-exchange production, the electron-impact ionization rate R will be

$$R = n_{elec}\, n_{geoc}\, v_{elec}\, \sigma_{ioniz}, \tag{7}$$

where n_{elec} is the number density of hot electrons, v_{elec} is the velocity of a hot electron, σ_{ioniz} is the impact-ionization cross section for the hot electron on a hydrogen atom, and n_{geoc} is the density of hydrogen atoms. The number density of the hot electrons is taken to be $n_{elec} = 0.88\ cm^{-3}$, and the electron-plasma-sheet temperature is taken to be $T_{elec} = 2$ keV (cf. Fig. 2 of Denton et al.(2005)). The velocity of an electron with an energy of 2 keV is $v_{elec} = 1.9 \times 10^9$ cm/s. The electron-impact ionization cross section for a hydrogen atom to 2 keV electrons is $\sigma_{ioniz} \approx 6.3 \times 10^{-18}\ cm^{-3}$ (e.g., Fig. 7 of Shah et al.(1987) or Fig. 5 of Tawara and Kato (1987)). Again, the bounce-averaged density

of the hydrogen geocorona as seen by an isotropic population of electrons at L = 6.6 is n_{geoc} = 152 cm^{-3}. Using these values in expression (7) yields a rate of ionization of R ~ 1.6 × 10^{-6} cm^{-3} s^{-1}, which is R ~ 0.14 cm^{-3} day^{-1} at geosynchronous orbit. This value is entered into **Table 2**. For electron energies E_{elec} in the range from 400 eV to 4 keV, the quantity $v_{elec}\sigma_{ioniz}$ varies with electron energy approximately as $v_{elec}\sigma_{ioniz} \propto E_{elec}^{-0.35}$; hence, averaging over a thermal distribution of electrons does not greatly vary the value of $v_{elec}\sigma_{ioniz}$ and R, and the value of R ~ 0.14 cm^{-3} day^{-1} is relatively insensitive to the temperature of the electrons of the electron plasma sheet (however, the rate R is sensitive to the number density of the hot electrons, which varies with time). This is the rate of production of cold protons by electron-impact ionization by the electron plasma sheet. This R ~ 0.14 cm^{-3} day^{-1} rate is about 12% of the 1.14 cm^{-3} day^{-1} rate of production by charge exchange of the ion plasma sheet.

For another comparison, the rate of production of cold protons from solar photoionization of the neutral hydrogen geocorona is estimated. At 1 AU from the sun, the photoinization rate of a hydrogen atom is about 1 × 10^{-7} s^{-7} to 2 × 10^{-7} s^{-1} (Gruntman, 1990; Ogawa et al., 1995), i.e., the lifetime of a hydrogen atom to photoionization is about 57–115 days. If the effective number density of the geocorona for a midnight geosynchronous-orbit flux tube is n_{geoc} = 152 cm^{-3}, then the production rate from photoionization is on the order of 1.5 × 10^{-5} cm^{-3}/s to 3 × 10^{-5} cm^{-3}/s or 1.3–2.6 $cm^{-3}day^{-1}$, which is comparable to the production rate from charge exchange. This value is entered into **Table 2**.

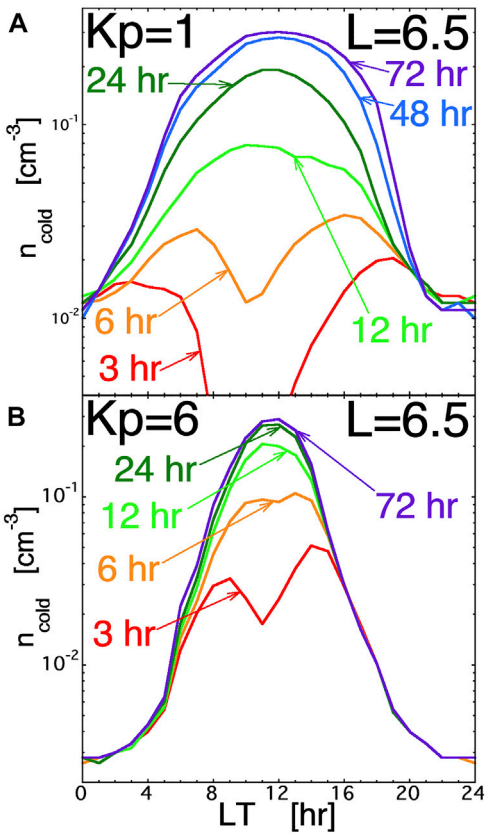

FIGURE 5 | From two HEIDI simulations, the number density of cold charge-exchange byproduct protons is plotted in the equatorial plane at L = 6.5 as functions of local time. Panel **(A)** is for a Kp = 1 run with the nightside ion plasma sheet having n = 0.93 cm^{-3} and T = 5 keV, and panel **(B)** is for a Kp = 6 run with the nightside ion plasma sheet having n = 1.45 cm^{-3} and T = 11.6 keV.

4 MAGNETOSPHERIC SIMULATIONS OF BYPRODUCT-PROTON PRODUCTION AND TRANSPORT

To explore the rudimentary behavior of the population of cold byproduct protons, numerical simulations are utilized. The HEIDI (Hot Electron Ion Drift Integrator) simulation code (Liemohn and Jazowski, 2008; Ilie et al., 2012) is used to look at the production and transport of the cold charge-exchange protons for two cases of steady geomagnetic activity. The HEIDI code simulates the evolution of the hot ring-current (ion-plasma-sheet) ion population by calculating the velocity moments of the ion phase–space distribution function through the dipolar magnetosphere, whose evolution is under the action of the **E**×**B** drift and gradient and curvature drifts. HEIDI includes hot-ion loss via charge exchange with the geocorona and loss to precipitation into the atmosphere. The outer boundary of the simulation is at L = 6.5 (approximately geosynchronous orbit), and a boundary condition for the simulations is that the number density and temperature of the hot ion plasma sheet (ring current) is specified at L = 6.5 on the nightside. In the two simulations, the Volland–Stern electric-field model (Volland, 1973; Stern, 1975) was used, parameterized by Kp. For the magnetic field, a non-tilted dipole was used. The HEIDI code incorporates a variety of neutral hydrogen geocorona models (Ilie et al., 2013); the Rairden et al.(1986) model for the neutral hydrogen geocorona is used for the two simulations.

The cold charge-exchange byproduct protons are advected via **E**×**B** in the simulations. The small losses of the cold protons 1) via scattering into the loss cone and 2) via charge exchange with the hydrogen geocorona are ignored in the simulations. The loss timescale for a 1-eV proton scattering into the atmosphere is estimated to be 89 h at L = 3 and 87 days at L = 6.6. The loss timescale for a 1-eV proton to charge exchange with the Hodges (1994) geocorona (the highest-density model in **Figure 1**) is 55 h at L = 3 and 370 h at L = 6.6. But, note that if a cold proton is lost to charge exchange, it is replaced by another cold proton.

For the two simulations, **Figure 5** plots the number density of cold charge-exchange protons at near-geosynchronous orbit (L = 6.5) as a function of local time. **Figure 5A** is for a low-activity simulation in which Kp = 1, and the nightside number density of the ion plasma sheet was 0.93 cm^{-3} and the temperature was 5 keV; **Figure 5B** is for a very high-activity simulation in which Kp = 6, and the nightside number density of the ion plasma sheet was 1.45 cm^{-3} and the temperature was 11.6 keV. In both simulations, the ionic composition of the plasma sheet on the

nightside was taken to be 100% H^+, and so only cold protons produced by energetic protons charge exchanging with atomic hydrogen (expression (1a)) are calculated in the simulations. Each simulation was run for 72 h with a time-independent level of magnetospheric convection (parameterized by the steady level of Kp) and with a time-independent number density and temperature of the ion plasma sheet at L = 6.5 on the nightside. In the plots of **Figure 5**, the number density of cold charge-exchange protons is artificially low on the nightside at L = 6.5: the number density at L = 6.5 on the nightside is only related to the combination of production in the first outer cell of the code and advection out of that cell. In reality, there is production of cold protons beyond L = 6.5 on the nightside followed by advection through the L = 6.5 region; that production beyond L = 6.5 does not appear in the simulation since the outer boundary of the simulation domain is at L = 6.5. At local midnight in the simulations at 72 h, a comparison of the number density of cold byproduct protons at L = 6.5 and at L = 6.25 finds the density in the Kp = 1 simulation goes from 1.1×10^{-2} at 6.6 to 4.6×10^{-2} cm^{-3} at 6.25, and in the Kp = 6 simulation the density goes from 2.8×10^{-3} to 6.8×10^{-3} cm^{-3}. This is a factor of ~3 increase from L = 6.6 to L = 6.0, so if the production of byproduct cold protons beyond L = 6.5 was accounted for in the simulations, the number-density values at L = 6.5 on the nightside could easily triple. Note in **Figure 5** that the cold-ion number density at local midnight is much less for the Kp = 6 case than it is for the Kp = 1 case: this is dominantly a function of the plasma advection strength where cold ions are more rapidly convected away in the Kp = 6 case but can build up in number density in the Kp = 1 case.

The major production of charge-exchange cold protons is in the inner dipolar region where the neutral hydrogen geocorona is denser. The cold protons produced in the inner dipolar regions advect sunward, and so the number density of cold charge-exchange byproduct protons is relatively larger where they cross geosynchronous orbit on the dayside. In **Figure 5**, both simulations yield number densities of cold byproduct protons of 0.2–0.3 cm^{-3} at local noon at L = 6.5 (unfortunately, the ion-line analysis performed for the MPA spacecraft on the nightside, where there is strong charging, does not work on the dayside, where there is an absence of strong charging). Note, however, that the local-time width of the higher-density cold protons is narrow in the high-activity simulation (**Figure 5B**) and wide in the low-activity simulation (**Figure 5A**).

The number densities of charge-exchange byproduct protons are proportional to the number density of the ion plasma sheet flowing into the dipolar region on the nightside. It will also depend on the ion composition of the plasma sheet. Further, the (Rairden et al., 1986) geocorona model was used in the simulations of **Figure 5**: if another geocorona model were to be used (cf. **Figure 1**), the number density of cold byproduct protons would be higher.

At L = 6.5, the number density of cold charge-exchange byproduct protons is less than the number density of the ion plasma sheet. The peak cold-proton number densities of 0.2–0.3 are about half of the typical dayside ion-plasma-sheet densities $n_{day} \sim 0.4\,cm^{-3}$ (e.g., Korth et al., 1999). For cold-ion measurements in the dayside magnetosphere, these byproduct cold-proton densities may be lost in the population of plasmaspheric-refilling outflows, which can result in number density buildups of $50\,cm^{-3}$/day at geosynchronous orbit (Sojka and Wrenn, 1985; Lawrence et al., 1999; Su et al., 2001; Denton and Borovsky, 2014). In the following section, an assessment is made of the role that the cold charge-exchange byproduct proton distribution plays in the early time refilling of the plasmasphere in the dayside magnetosphere: it is found that the number densities of the byproduct protons are probably not sufficient to eliminate the early phase of refilling, but the byproduct population probably contributes to the shortening of the early phase, helping to bring on the transition to the rapid late phase refilling.

A study is in progress on the behavior of the cold charge-exchange byproduct proton population at all L-shells in simulations of the magnetospheric under time-dependent geomagnetic activity.

5 COLD BYPRODUCT PROTONS AND EARLY TIME PLASMASPHERIC REFILLING

On the dayside, the sunlit ionosphere has cold-proton outflows that can build up to refill the outer plasmasphere in the dipolar magnetosphere. It is argued that there are two different timescales for the refilling (Wilson et al., 1992; Lawrence et al., 1999; Su et al., 2001; Gallagher et al., 2021): a slow refilling at early times and a faster refilling at late times. (But see Denton and Borovsky (2014) for evidence against a two-timescale picture.)

Early refilling is slow because the protons coming out of one ionosphere ballistically traverse the length of the magnetospheric flux tube and end up lost in the conjugate atmosphere. It is argued that until there is sufficient cold plasma in the flux tube to sufficiently Coulomb scatter a transiting proton, that proton is likely to be lost in the conjugate atmosphere. Sufficient Coulomb scatter means enough angular scattering to knock the transiting proton out of the loss cone during its transit. To get to this stage where a transition to faster late-time refilling occurs, the amount of angular scattering per transit should be greater than or equal to the atmospheric loss cone as seen at the equator.

Equation (6.4.11) of Krall and Trivelpiece (1973) expresses the timescale τ for a thermal proton in a hydrogen plasma of density n and temperature T to be scattered through a total angle of 1 radian by multiple Coulomb scattering events. The timescale to scatter through the small loss-cone angle θ_{loss} is θ_{loss}^2 times this timescale, where θ_{loss} is expressed in radians. This gives

$$\tau = \theta_{loss}^2 \left\{ \left(m_p^{1/2} (k_B T)^{3/2} \right) / \left(2^{1/2} \pi\, n\, e^4 \log_e(\Lambda) \right) \right\} [0.843 + 0.415]^{-1} \tag{A1}$$

where $\log_e(\Lambda)$ is the Coulomb logarithm, 0.843 is a factor for the scattering of the proton by the electrons of the plasma, and 0.415 is a factor for the scattering of the proton by the protons of the plasma (Note that the square-bracket final factor $[]^{-1}$ in expression (A1) is written incorrectly as $[]^{+1}$ in eq. (6.4.11) of

Krall and Trivelpiece (1973)). We are interested in the number density n that will produce a scattering by θ_{loss} in a time $\tau = d/v_o$, where d is the transit pathlength through the plasma and v_o is the speed of the transiting proton. Using $\tau = d/v_o$ in expression (A1) and solving for n yields, we get

$$n = \theta_{loss}^{\ 2}\left\{\left(m_p^{1/2}\,(k_B T)^{3/2} v_o\right)/\left(2^{1/2}\pi\, d\, e^4\, \log_e(\Lambda)\right)\right\}[0.843 + 0.415]^{-1} \quad \text{(A2)}$$

At the geosynchronous-orbit equator for a 100-nT field, the loss cone angle is $\theta_{loss} = 2.5^\circ = 4.5 \times 10^{-2}$ radian. As the proton transits from one ionosphere to the other, any angular scattering that occurs at high latitude is not effective at moving the proton out of the loss cone; hence, for d, we will take a transit length at lower latitude in the dipolar flux tube. For L = 6.6, this length is taken to be $d = 6.6\ R_E = 4.2 \times 10^4$ km. Taking the transiting proton to have an energy of 1 eV and the building-up proton–electron plasma in the magnetosphere to have that same 1-eV temperature, this gives T = 1 eV and $v_o = 14$ km/s. The Coulomb logarithm for a plasma with a temperature of 1 eV and a density of about 1 cm^{-3} is $\log_e(\Lambda) = 23$. Using these values in expression (A2) yields the critical number density of a 1-eV proton–electron plasma to be n = 0.26 cm^{-3}.

The number densities of charge-exchange byproduct protons can be non-negligible compared with this number density n = 0.26 cm^{-3} (cf. **Figure 5**). That 0.26 cm^{-3} number density was calculated for a $T_i = T_e = 1$-eV plasma. However, the cold charge-exchange byproduct protons are produced by removing hot protons (or hot O^+ ions or hot N^+ ions) from the magnetosphere and not altering the hot electrons, and so there is no 1-eV population of electrons accompanying the cold byproduct protons to help with the Coulomb scattering of a transiting proton (the hot ions and hot electrons in the flux tube are not effective at Coulomb scattering of a cold proton). Hence the factor $[0.843 + 0.415]^{-1}$ in expression (A2) becomes $[0 + 0.415]^{-1}$ for cold charge-exchange protons without accompanying cold electrons. This increases the calculated critical number density 0.26 cm^{-3} by a factor of 3.0, yielding a critical number density of byproduct protons of n = 0.79 cm^{-3} to cause a transition from slow early time refilling to fast late-time refilling. However, a number density of 0.2–0.3 cm^{-3} (cf. **Figure 5**) will do some angular scattering to shorten the time that early time refilling needs to go on before the transition density can be reached.

Also in the magnetospheric flux tube, there are the two "refilling" beams of protons from the ionospheric outflow that have non-zero number densities, and each beam contributes to the Coulomb scattering of the other beam. For these two beams to be able to account for the late-stage refilling rate of the plasmasphere R_{late}, each beam must have a number density n_{beam} at the equator of

$$n_{beam} = (2/2) R_{late} \tau_{transit}, \quad \text{(A3)}$$

where $\tau_{transit}$ is the transit time from the ionosphere to the equator, the factor of 2 in the denominator accounts for the fact that two beams give rise to the refilling rate R_{late} so that each beam takes half the density, and the factor of 2 in the numerator accounts for the fact that the refilling is only on for about 12 h out of 24 h because the refilling only occurs from the sunlit ionosphere so the dayside refilling rate is twice the daily rate. The transit time in the dipole flux tube at geosynchronous orbit from the ionosphere to the equator is $\tau_{transit} = (1.3)\ (6.6)\ (1\ R_E)/v_{beam} = 5.4 \times 10^4$ km/v_{beam}. The measured late-stage refilling rate at geosynchronous orbit is 25–50 cm^{-3}/day (Sojka and Wrenn, 1985; Lawrence et al., 1999; Su et al., 2001; Denton and Borovsky, 2014). For a 1-eV outflow beam of protons (with $v_{beam} = 14$ km/s), the transit time is $\tau_{transit} = 1.1$ h, and the equatorial number density of each beam given by expression (A3) is $n_{beam} = 1.1$–2.2 cm^{-3}. This is a substantially higher number density than the 0.2–0.3 cm^{-3} number densities of the cold charge-exchange byproduct proton population found at geosynchronous orbit in the HEIDI simulations (although the HEIDI simulations yielded densities that are lower bounds, owing to the use of the (Rairden et al., 1986) geocorona and the absence of charge exchange beyond L = 6.5 on the nightside). However, the effectiveness of proton–proton Coulomb scattering is very sensitive to the relative velocities of the colliding protons, and the protons of one beam pass the protons of the other beam with a relative speed v_o of 28 km/s whereas the protons of each beam pass through the byproduct protons with a relative speed v_o of about 14 km/s. To obtain the same angular-scattering effect, one needs a critical density n_{crit} that increases as $n_{crit} \propto v_o^4$ (cf. expression (6.2.4) or (6.2.6) of Krall and Trivelpiece (1973)), so the density of a beam is not as effective as at scattering by a factor of about 4 as is the density of the byproduct protons are. Based on observations, the temperature of the outer plasmasphere may be higher when the plasmaspheric density is low, and the temperature is lower when the density is high (e.g., Comfort et al., 1985; Moldwin et al., 1995). There is some argument that the outflow energy of protons from the ionosphere is greater during early stage refilling than it is during late-stage refilling (cf. Wilson et al., 1992; Su et al., 1998). If the proton outflow energy is 3 eV (with $v_{beam} = 24$ km/s), then expression (A3) yields the equatorial number density of each beam to be $n_{beam} = 0.65$–1.3 cm^{-3}, and if the proton outflow energy is 10 eV (with $v_{beam} = 44$ km/s), then expression (A3) yields the equatorial number density of each beam to be $n_{beam} = 0.36$–0.71 cm^{-3}.

Note that in the dayside magnetosphere, there is also the oxygen-rich warm plasma cloak (Chappell et al., 2008). The ions of the cloak have been explored (Horwitz and Chappell, 1979; Borovsky et al., 2013; Lee and Angelopoulos, 2014; Takahashi et al., 2014; Jahn et al., 2017; Delzanno et al., 2021), but the electrons of the cloak are mostly a mystery (Li et al., 2011; Nishimura et al., 2013; Mozer et al., 2017; Walsh et al., 2020). The dayside cloak can have ion densities of a fraction of 1 cm^{-3} (cf. Fig. 9 of Jahn et al., 2017) or even higher than 1 cm^{-3} during storm times (cf. Fig. 20 of Borovsky et al., 2013). For a calculation, we take n = 0.2 cm^{-3} for the O^+ of the cloak at geosynchronous orbit on the dayside (cf. Fig. 9 of Jahn et al., 2017). The temperature of the cloak varies (as does its number density), but for the sake of calculation we take the O^+ temperature to be 20 eV. For Coulomb scattering, it is the relative velocity of the colliding particles that controls the strength of the scatter; 20-eV

O^+ ions have a velocity distribution very similar to that of 1-eV H^+ ions. Note, however, that heavy O^+ ions are more effective at angular scattering a transiting proton since an O^+ ion recoils less than an H^+ ion does during a collision, and so the transiting proton deflects more off of O^+ than it does off of H^+. Hence, 0.2 cm^{-3} of 20-eV cloak oxygen is probably a more important factor in ending the early time refilling phase than is 0.2–0.3 cm^{-3} of byproduct protons.

The densities of all of the populations (byproduct and cloak) vary with time, so at times the byproduct protons may play an important role in bringing about the transition from slow early time plasmasphere refilling to rapid late-time plasmasphere refilling.

6 SUMMARY

In this report, the production of cold protons from charge-exchange collisions between the protons of the ion plasma sheet (ring current) and the neutral hydrogen geocorona was investigated, and the properties of these byproduct protons were ascertained.

The properties of the byproduct protons are as follows (see also **Section 2**): Each charge-exchange collision produces one byproduct proton. The byproduct protons are born primarily off equatorial in the dipolar portions of the magnetosphere, owing to the intersection of the quasi-isotropic ions of the ion plasma sheet and the radially decreasing density of hydrogen atoms in the Earth's geocorona. When they are born, the byproduct protons are trapped in the magnetosphere by mirror geometry of the dipole magnetic field of the Earth. Since they are born primarily away from the equator, the distribution of cold protons will tend to be field aligned. The protons are born with very little kinetic energy (<0.6 eV) from the charge-exchange collisions, and they pick up very little energy (<1 eV) owing to the corotational and convectional electric field in which they are suddenly born. If there are field-aligned electrostatic potentials residing in the dipolar magnetosphere (driven perhaps by photoelectrons off the atmosphere, by anisotropies in the ion- and electron-plasma-sheet populations, by contact of the hot magnetospheric electrons with the ionosphere, or by field-aligned currents), then the byproduct protons may pick up a parallel-to-$\underline{\mathbf{B}}$ kinetic energy.

A population of ions that are seen at the equator in geosynchronous orbit was identified as a candidate for being these byproduct protons produced by charge-exchange collisions (see **Section 2**). The population of ions is known as the "ion line" in energy-time ion spectrograms. The ion line is formed by ambient ions (with thermal energies less than a few 10's of eV) that are accelerated across the spacecraft sheath from the ambient magnetospheric plasma to the negatively charged satellite. The ion line is typically seen in the midnight-to-dawn region of local time at geosynchronous orbit where satellites encounter the electron plasma sheet. At the equator, the cold ions of the ion line tend to be field aligned. The ambient densities of the cold ions that make up the line are estimated to be about $\sim 10^{-2}$ cm^{-3} in the nightside magnetosphere at geosynchronous orbit. Without strong spacecraft charging (which occurs in the electron plasma sheet) and the associated strong sheath focusing of ion orbits onto the satellite, these ions would be difficult to detect with standard ion instruments.

The rates of production of byproduct protons from charge exchange were estimated by two different ways (see **Section 3**). By combining an estimate of the total flow of ion-plasma-sheet protons into the nightside of the dipolar region and an estimate of the fraction of those ion-plasma-sheet ions that are lost to charge exchange as they pass the dipole from the nightside to the dayside, the total number of charge-exchange collisions in the dipolar region was estimated: the estimate yields about 5 tons per day of cold byproduct protons in the magnetosphere. By examining the temperature and density of the ion plasma sheet at geosynchronous orbit (L = 6.6) and using a model of the neutral hydrogen geocorona, the rate of charge-exchange collisions was estimated: about 1.14 cm^{-3} per day of byproduct protons is produced in geosynchronous-orbit flux tubes on a typical day.

The rate of production of cold protons owing to electron-impact ionization of geocoronal hydrogen atoms by the electrons of the electron plasma sheet was estimated (see **Section 3**). About 0.14 cm^{-3} per day of cold protons is produced this way at geosynchronous orbit, predominantly on the nightside and dawnside. The production rate of cold protons by electron-impact ionization is a factor of 10 less than the production rate by charge exchange.

The rate of production of cold protons owing to solar photoionization of geocoronal hydrogen atoms was estimated (see **Section 3**). About 1.3–2.6 cm^{-3} per day of cold protons is produced this way at geosynchronous orbit. The production rate of cold protons by photoionization is comparable to or greater than the production rate by charge exchange.

The production and transport of cold byproduct protons was investigated with the HEIDI simulation code. Two steady-state convection runs were investigated (Kp = 1 and Kp = 6), and the number density at L = 6.5 in the equatorial plane was examined. Both simulations yielded byproduct-proton number densities that peaked on the dayside, with maximum number densities of 0.2–0.3 cm^{-3} near local noon (note that these number densities would be higher, perhaps by a factor of 2, if a geocorona model other than the Rairden et al., 1986 model would have been used in the simulations; further, the number densities are lowered by the fact that the charge-exchange production of protons beyond L = 6.5 on the nightside is not included). These number densities are small compared with expected number densities of plasmaspheric-refilling proton outflows from the ionosphere and are also small compared with dayside cloak-ion number densities. An assessment at geosynchronous orbit of the population of cold charge-exchange byproduct protons in the dayside magnetosphere finds that they likely contribute to the shortening of any "early phase" of plasmaspheric refilling by Coulomb scattering ionospheric-outflow protons out of the atmospheric loss cone, yielding a trapping of the outflows and a buildup of the magnetospheric plasmaspheric density.

To test whether or not the ions making the ion line are the predicted byproduct protons from charge exchange, the statistics of the observed properties of the "ion-line" population versus ion-plasma-sheet densities, magnetospheric convection rates, etc., are called for. If the ion-line ions are cold byproduct protons from charge-exchange collisions on the nightside of the dipolar region, then there should be a positive correlation between the density of the ion-line ions and the density of the ion plasma sheet,

particularly when the convection age of the flux tube is accounted for. If there are factors that cause the density of the neutral hydrogen geocorona to vary (e.g., Banks and Kockarts, 1973; Bzowski and Fahr, 1996; Kuwabara et al., 2017), then the density of the ion line should also be affected by these factors, which can be tested observationally.

DATA AVAILABILITY STATEMENT

The original contributions presented in the study are included in the article/Supplementary Material; further inquiries can be directed to the corresponding author.

AUTHOR CONTRIBUTIONS

JB initiated this project, performed some of the analysis, and wrote the first draft of the manuscript. JL performed and analyzed the simulations under the supervision of RI. ML helped to write an earlier version of the manuscript. JL, RI, and ML helped to write the final version of the manuscript.

FUNDING

This work was supported at the Space Science Institute by the NSF GEM Program via grant AGS-2027569, by the NASA Heliophysics LWS program via award NNX16AB75G, by the NSF SHINE program via grant AGS-1723416, and by the NASA Heliophysics Guest Investigator Program via award NNX17AB71G. The work at the University of Michigan was supported by the NASA grants 80NSSC17K0015, NNX17AB87G, and 80NSSC19K0077.

ACKNOWLEDGMENTS

The authors thank Gian Luca Delzanno, Pedro Resendiz, and Michelle Thomsen for helpful conversations.

REFERENCES

Bailey, J., and Gruntman, M. (2011). Experimental Study of Exospheric Hydrogen Atom Distributions by Lyman-alpha Detectors on the TWINS mission. *J. Geophys. Res.* 116, A09302. doi:10.1029/2011ja016531

Bame, S. J., McComas, D. J., Thomsen, M. F., Barraclough, B. L., Elphic, R. C., Glore, J. P., et al. (1993). Magnetospheric Plasma Analyzer for Spacecraft with Constrained Resources. *Rev. Scientific Instr.* 64, 1026–1033. doi:10.1063/1.1144173

Banks, P. M., and Kockarts, G. (1973). *Aeronomy, Part B*. ch. 16. New York: Academic Press.

Barnett, C. F. (1990). *Atomic Data for Fusion Volume 1. Collisions of H, H_2, He and Li Atom and Ions with Atoms and Molecules, Table A-22, Oak Ridge National Laboratory Report ORNL-6086/V1, Controlled Fusion Atomic Data Center*. Oak Ridge, Tennessee.

Birn, J., Thomsen, M. F., Borovsky, J. E., Reeves, G. D., McComas, D. J., and Belian, R. D. (1997). Characteristic Plasma Properties during Dispersionless Substorm Injections at Geosynchronous Orbit. *J. Geophys. Res.* 102, 2309–2324. doi:10.1029/96ja02870

Borovsky, J. E., and Cayton, T. E. (2011). Entropy Mapping of the Outer Electron Radiation belt between the Magnetotail and Geosynchronous Orbit. *J. Geophys. Res.* 116, A06216. doi:10.1029/2011ja016470

Borovsky, J. E., Denton, M. H., Denton, R. E., Jordanova, V. K., and Krall, J. (2013). Estimating the Effects of Ionospheric Plasma on Solar Wind/magnetosphere Coupling via Mass Loading of Dayside Reconnection: Ion-Plasma-Sheet Oxygen, Plasmaspheric Drainage Plumes, and the Plasma Cloak. *J. Geophys. Res. Space Phys.* 118, 5695–5719. doi:10.1002/jgra.50527

Borovsky, J. E., and Denton, M. H. (2010). The Magnetic Field at Geosynchronous Orbit during High-Speed-Stream-Driven Storms: Connections to the Solar Wind, the Plasma Sheet, and the Outer Electron Radiation belt. *J. Geophys. Res.* 115, A08217. doi:10.1029/2009ja015116

Borovsky, J. E., Funsten, H. O., Thomsen, M. F., and Reiff, P. H. (1998a). Byproduct Cool Protons from Ring-Current Charge Exchange: A Source and a Catalyst for the Plasmasphere. *EOS Trans. Amer. Geophys. Union* 79 (45), F766.

Borovsky, J. E., and Steinberg, J. T. (2006). The "calm before the Storm" in CIR/magnetosphere Interactions: Occurrence Statistics, Solar Wind Statistics, and Magnetospheric Preconditioning. *J. Geophys. Res.* 111, A07S10. doi:10.1029/2005ja011397

Borovsky, J. E., Thomsen, M. F., Elphic, R. C., Cayton, T. E., and McComas, D. J. (1998c). The Transport of Plasma Sheet Material from the Distant Tail to Geosynchronous Orbit. *J. Geophys. Res.* 103, 20297–20331. doi:10.1029/97ja03144

Borovsky, J. E., Thomsen, M. F., and Elphic, R. C. (1998d). The Driving of the Plasma Sheet by the Solar Wind. *J. Geophys. Res.* 103, 17617–17639. doi:10.1029/97ja02986

Borovsky, J. E., Thomsen, M. F., McComas, D. J., Cayton, T. E., and Knipp, D. J. (1998b). Magnetospheric Dynamics and Mass Flow during the November 1993 Storm. *J. Geophys. Res.* 103, 26373–26394. doi:10.1029/97ja03051

Bzowski, M., Fahr, H. J., and Ruciński, D. (1996). Interplanetary Neutral Particle Fluxes Influencing the Earth's Atmosphere and the Terrestrial Environment. *Icarus* 124, 209–219. doi:10.1006/icar.1996.0199

Carruthers, G. R., Page, T., and Meier, R. R. (1976). Apollo 16 Lyman Alpha Imagery of the Hydrogen Geocorona. *J. Geophys. Res.* 81, 1664–1672. doi:10.1029/ja081i010p01664

Chappell, C. R., Huddleston, M. M., Moore, T. E., Giles, B. L., and Delcourt, D. C. (2008). Observations of the Warm Plasma Cloak and an Explanation of its Formation in the Magnetosphere. *J. Geophys. Res.* 113, A09206. doi:10.1029/2007ja012945

Chen, F. F. (1965). "Electric Probes," in *Plasma Diagnostic Techniques*. Editors R. H. Huddlestone and S. L. Leonard (New York: Academic Press), 113.

Chen, J. C. Y., Ishihara, T., Ponce, V. H., and Watson, K. M. (1973). Electronic Transitions in Slow Collisions of Atoms and Molecules. V. Multichannel Eikonal Approximation for the Differential (P+, H) Excitation and Rearrangement Collisions. *Phys. Rev. A.* 8, 1334–1344. doi:10.1103/physreva.8.1334

Chiu, Y. T., and Schulz, M. (1978). Self-consistent Particle and Parallel Electrostatic Field Distributions in the Magnetospheric-Ionospheric Auroral Region. *J. Geophys. Res.* 83, 629. doi:10.1029/ja083ia02p00629

Comfort, R. H., Waite, J. H., and Chappell, C. R. (1985). Thermal Ion Temperatures from the Retarding Ion Mass Spectrometer on DE 1. *J. Geophys. Res.* 90, 3475. doi:10.1029/ja090ia04p03475

Cornwall, J. M. (1977). On the Role of Charge Exchange in Generating Unstable Waves in the Ring Current. *J. Geophys. Res.* 82, 1188–1196. doi:10.1029/ja082i007p01188

Delzanno, G. L., Borovsky, J. E., Henderson, M. G., Resendiz Lira, P. A., Roytershteyn, V., and Welling, D. T. (2021). The Impact of Cold Electrons and Cold Ions in Magnetospheric Physics. *J. Atmos. Solar-Terrestrial Phys.* 220, 105599. doi:10.1016/j.jastp.2021.105599

Denton, M. H., and Borovsky, J. E. (2014). Observations and Modeling of Magnetic Flux Tube Refilling of the Plasmasphere at Geosynchronous Orbit. *J. Geophys. Res. Space Phys.* 119, 9246–9255. doi:10.1002/2014ja020491

Denton, M. H., Thomsen, M. F., Korth, H., Lynch, S., Zhang, J. C., and Liemohn, M. W. (2005). Bulk Plasma Properties at Geosynchronous Orbit. *J. Geophys. Res.* 110, A07223. doi:10.1029/2004ja010861

Feldstein, Y. I., and Galperin, Y. I. (1993). An Alternative Interpretation of Auroral Precipitation and Luminosity Observations from the DE, DMSP, AUREOL, and Viking Satellites in Terms of Their Mapping to the Nightside Magnetosphere. *J. Atmos. Terrestrial Phys.* 55, 105–121. doi:10.1016/0021-9169(93)90160-z

Gallagher, D. L., Comfort, R. H., Katus, R. M., Sandel, B. R., Fung, S. F., and Adrian, M. L. (2021). The Breathing Plasmasphere: Erosion and Refilling. *J. Geophys. Res.* 126, e2020JA028727. doi:10.1029/2020ja028727

Gaussorgues, C., Sech, C. L., Masnou-Seeuws, F., McCarroll, R., and Riera, A. (1975). Common Trajectory Methods for the Calculation of Differential Cross Sections for Inelastic Transitions in Atom(ion)-Atom Collisions. II. Application to Proton-Hydrogen Scattering. *J. Phys. B: Mol. Phys.* 8, 253–264. doi:10.1088/0022-3700/8/2/015

Ghosh, D., and Biswas, R. (2002). Theoretical Calculation of Absolute Radii of Atoms and Ions. Part 1. The Atomic Radii. *Ijms* 3, 87–113. doi:10.3390/i3020087

Glocer, A., Khazanov, G., and Liemohn, M. (2017). Photoelectrons in the Quiet Polar Wind. *J. Geophys. Res. Space Phys.* 122, 6708–6726. doi:10.1002/2017ja024177

Gruntman, M. A. (1990). Two-step Photoionization of Hydrogen Atoms in Interplanetary Space. *Planet. Space ScienceSpace Sci* 38, 1225–1230. doi:10.1016/0032-0633(90)90127-c

Gruntman, M. (1997). Energetic Neutral Atom Imaging of Space Plasmas. *Rev. Scientific Instr.* 68, 3617–3656. doi:10.1063/1.1148389

Hershkowitz, N., Breun, R. A., Callen, J. D., Chan, C., Ferron, J., Golovato, S. N., et al. (1982). Dynamic Electrostatic Confinement in an Rf-Sustained Tandem Mirror. *Phys. Rev. Lett.* 49, 1489–1492. doi:10.1103/physrevlett.49.1489

Hershkowitz, N. (1989). "How Langmuir Probes Work," in *Plasma Diagnostics Volume 1*. Editors O. Auciello and D. L. Flamm (New York: Academic Press), 113. doi:10.1016/b978-0-12-067635-4.50008-9

Hodges, R. R. (1994). Monte Carlo Simulation of the Terrestrial Hydrogen Exosphere. *J. Geophys. Res.* 99, 23229. doi:10.1029/94ja02183

Horwitz, J. L., and Chappell, C. R. (1979). Observations of Warm Plasma in the Dayside Plasma Trough at Geosynchronous Orbit. *J. Geophys. Res.* 84, 7075–7090. doi:10.1029/ja084ia12p07075

Ilie, R., and Liemohn, M. W. (2016). The Outflow of Ionospheric Nitrogen Ions: A Possible Tracer for the Altitude-dependent Transport and Energization Processes of Ionospheric Plasma. *J. Geophys. Res. Space Phys.* 121, 9250–9255. doi:10.1002/2015ja022162

Ilie, R., Liemohn, M. W., Toth, G., and Skoug, R. M. (2012). Kinetic Model of the Inner Magnetosphere with Arbitrary Magnetic Field. *J. Geophys. Res.* 117, A04208. doi:10.1029/2011ja017189

Ilie, R., Skoug, R. M., Funsten, H. O., Liemohn, M. W., Bailey, J. J., and Gruntman, M. (2013). The Impact of Geocoronal Density on Ring Current Development. *J. Atmos. Solar-Terrestrial Phys.* 99, 92–103. doi:10.1016/j.jastp.2012.03.010

Jahn, J.-M., Goldstein, J., Reeves, G. D., Fernandes, P. A., Skoug, R. M., Larsen, B. A., et al. (2017). The Warm Plasma Composition in the Inner Magnetosphere during 2012-2015. *J. Geophys. Res.* 122, 11018. doi:10.1002/2017ja024183

Jordanova, V. K., Kistler, L. M., Kozyra, J. U., Khazanov, G. V., and Nagy, A. F. (1996). Collisional Losses of Ring Current Ions. *J. Geophys. Res.* 101, 111–126. doi:10.1029/95ja02000

Khazanov, G. V., Liemohn, M. W., and Moore, T. E. (1997). Photoelectron Effects on the Self-Consistent Potential in the Collisionless Polar Wind. *J. Geophys. Res.* 102, 7509–7521. doi:10.1029/96ja03343

Kistler, L. M., Ipavich, F. M., Hamilton, D. C., Gloeckler, G., Wilken, B., Kremser, G., et al. (1989). Energy Spectra of the Major Ion Species in the Ring Current during Geomagnetic Storms. *J. Geophys. Res.* 94, 3579–3599. doi:10.1029/ja094ia04p03579

Korth, H., Thomsen, M. F., Borovsky, J. E., and McComas, D. J. (1999). Plasma Sheet Access to Geosynchronous Orbit. *J. Geophys. Res.* 104, 25047–25061. doi:10.1029/1999ja900292

Krall, N. A., and Trivelpiece, A. W. (1973). *Principles of Plasma Physics*. New York: McGraw-Hill.

Kuwabara, M., Yoshioka, K., Murakami, G., Tsuchiya, F., Kimura, T., Yamazaki, A., et al. (2017). The Geocoronal Responses to the Geomagnetic Disturbances. *J. Geophys. Res. Space Phys.* 122, 1269–1276. doi:10.1002/2016ja023247

Lawrence, D. J., Thomsen, M. F., Borovsky, J. E., and McComas, D. J. (1999). Measurements of Early and Late Time Plasmasphere Refilling as Observed from Geosynchronous Orbit. *J. Geophys. Res.* 104, 14691–14704. doi:10.1029/1998ja900087

Lee, J. H., and Angelopoulos, V. (2014). On the Presence and Properties of Cold Ions Near Earth's Equatorial Magnetosphere. *J. Geophys. Res. Space Phys.* 119, 1749–1770. doi:10.1002/2013ja019305

Lennartsson, W. (1976). On the Magnetic Mirroring as the Basic Cause of Parallel Electric fields. *J. Geophys. Res.* 81, 5583–5586. doi:10.1029/ja081i031p05583

Li, W., Bortnik, J., Thorne, R. M., Nishimura, Y., Angelopoulos, V., and Chen, L. (2011). Modulation of Whistler Mode Chorus Waves: 2. Role of Density Variations. *J. Geophys. Res.* 116, A06206. doi:10.1029/2010ja016313

Liemohn, M. W., and Jazowski, M. (2008). Ring Current Simulations of the 90 Intense Storms Durng Solar Cycle 23. *J. Geophys. Res.* 113, A00A17. doi:10.1029/2008ja013466

Liemohn, M. W., Kozyra, J. U., Jordanova, V. K., Khazanov, G. V., Thomsen, M. F., and Cayton, T. E. (1999). Analysis of Early Phase Ring Current Recovery Mechanisms during Geomagnetic Storms. *Geophys. Res. Lett.* 26, 2845–2848. doi:10.1029/1999gl900611

Liemohn, M. W., and Kozyra, J. U. (2003). Lognormal Form of the Ring Current Energy Content. *J. Atmos. Solar-Terrestrial Phys.* 65, 871–886. doi:10.1016/s1364-6826(03)00088-9

Lynch, K. A., Bonnell, J. W., Carlson, C. W., and Peria, W. J. (2002). Return Current Region aurora:E‖,jz, Particle Energization, and Broadband ELF Wave Activity. *J. Geophys. Res.* 107, 1115. doi:10.1029/2001ja900134

Martin, P. J., Blankenship, D. M., Kvale, T. J., Redd, E., Peacher, J. L., and Park, J. T. (1981). Electron Capture at Very Small Scattering Angles from Atomic Hydrogen by 25-125-keV Protons. *Phys. Rev. A.* 23, 3357–3360. doi:10.1103/physreva.23.3357

Mauk, B. H., and Meng, C.-I. (1991). "The aurora and Middle Magnetospheric Processes," in *Auroral Physics*. Editors C.-I. Meng, M. J. Rycroft, and L. A. Frank (Cambridge: Cambridge Press), 223.

Moldwin, M. B., Thomsen, M. F., Bame, S. J., and McComas, D. J. (1995). The fine-scale Structure of the Outer Plasmasphere, J. Geophys. Res., 100, 8021Self-Consistent Simulation of the Photoelectron-Driven Polar Wind from 120 Km to 9 R_E. *J. Geophys. Res.* 103, 2279.

Motoba, T., Ohtani, S., Anderson, B. J., Korth, H., Mitchell, D., Lanzerotti, L. J., et al. (2015). On the Formation and Origin of Substorm Growth Phase/onset Auroral Arcs Inferred from Conjugate Space-ground Observations. *J. Geophys. Res. Space Phys.* 120, 8707–8722. doi:10.1002/2015ja021676

Mozer, F. S., Agapitov, O. A., Angelopoulos, V., Hull, A., Larson, D., Lejosne, S., et al. (2017). Extremely Field-Aligned Cool Electrons in the Dayside Outer Magnetosphere. *Geophys. Res. Lett.* 44, 44–51. doi:10.1002/2016gl072054

Nishimura, Y., Bortnik, J., Li, W., Thorne, R. M., Ni, B., Lyons, L. R., et al. (2013). Structures of Dayside Whistler-Mode Waves Deduced from Conjugate Diffuse aurora. *J. Geophys. Res. Space Phys.* 118, 664–673. doi:10.1029/2012ja018242

Ogawa, H. S., Wu, C. Y. R., Gangopadhyay, P., and Judge, D. L. (1995). Solar Photoionization as a Loss Mechanism of Neutral Interstellar Hydrogen in Interplanetary Space. *J. Geophys. Res.* 100, 3455–3462. doi:10.1029/94ja03234

Østgaard, N., Mende, S. B., Frey, H. U., Gladstone, G. R., and Lauche, H. (2003). Neutral Hydrogen Density Profiles Derived from Geocoronal Imaging. *J. Geophys. Res.* 108, 1300. doi:10.1029/2002ja009749

Ozaki, M., Yagitani, S., Sawai, K., Shiokawa, K., Miyoshi, Y., Kataoka, R., et al. (2015). A Direct Link between Chorus Emissions and Pulsating aurora on Timescales from Milliseconds to Minutes: A Case Study at Subauroral Latitudes. *J. Geophys. Res. Space Phys.* 120, 9617–9631. doi:10.1002/2015ja021381

Perez, J. D., Goldstein, J., McComas, D. J., Valek, P., Fok, M.-C., and Hwang, K.-J. (2016). Global Images of Trapped Ring Current Ions during Main Phase of 17 March 2015 Geomagnetic Storm as Observed by TWINS. *J. Geophys. Res. Space Phys.* 121, 6509–6525. doi:10.1002/2016ja022375

Persson, H. (1963). Electric Field along a Magnetic Line of Force in a Low-Density Plasma. *Phys. Fluids* 6, 1756. doi:10.1063/1.1711018

Rairden, R. L., Frank, L. A., and Craven, J. D. (1986). Geocoronal Imaging with Dynamics Explorer. *J. Geophys. Res.* 91, 3613. doi:10.1029/ja091ia12p13613

Roederer, J. G., and Zhang, H. (2014). *Dynamics of Magnetically Trapped Particles*. Second Edition. Heidlberg: Springer. doi:10.1007/978-3-642-41530-2

Rufenach, C. L., McPherron, R. L., and Schaper, J. (1992). The Quiet Geomagnetic Field at Geosynchronous Orbit and its Dependence on Solar Wind Dynamic Pressure. *J. Geophys. Res.* 97, 25. doi:10.1029/91ja02135

Schinke, R., and Kruger, H. (1976). Differential and Integral Cross Sections for Proton-Hydrogen Scattering. *J. Phys. B: Mol. Phys.* 9, 2469–2478. doi:10.1088/0022-3700/9/14/016

Shah, M. B., Elliott, D. S., and Gilbody, H. B. (1987). Pulsed Crossed-Beam Study of the Ionisation of Atomic Hydrogen by Electron Impact. *J. Phys. B: Mol. Phys.* 20, 3501–3514. doi:10.1088/0022-3700/20/14/022

Smith, P. H., and Bewtra, N. K. (1978). Charge Exchange Lifetimes for Ring Current Ions. *Space Sci. Rev.* 22, 301. doi:10.1007/bf00239804

Sojka, J. J., and Wrenn, G. L. (1985). Refilling of Geosynchronous Flux Tubes as Observed at the Equator by GEOS 2. *J. Geophys. Res.* 90, 6379. doi:10.1029/ja090ia07p06379

Stern, D. P. (1981). One-dimensional Models of Quasi-Neutral Parallel Electric fields. *J. Geophys. Res.* 86, 5839. doi:10.1029/ja086ia07p05839

Stern, D. P. (1975). The Motion of a Proton in the Equatorial Magnetosphere. *J. Geophys. Res.* 80, 595–599. doi:10.1029/ja080i004p00595

Su, Y.-J., Horwitz, J. L., Wilson, G. R., Richards, P. G., Brown, D. G., and Ho, C. W. (1998). Self-consistent Simulation of the Photoelectron-Driven Polar Wind from 120 Km to 9REaltitude. *J. Geophys. Res.* 103, 2279–2296. doi:10.1029/97ja03085

Su, Y.-J., Thomsen, M. F., Borovsky, J. E., and Lawrence, D. J. (2001). A Comprehensive Survey of Plasmasphere Refilling at Geosynchronous Orbit. *J. Geophys. Res.* 106, 25615–25629. doi:10.1029/2000ja000441

Takahashi, K., Denton, R. E., Hirahara, M., Min, K., Ohtani, S.-i., and Sanchez, E. (2014). Solar Cycle Variation of Plasma Mass Density in the Outer Magnetosphere: Magnetoseismic Analysis of Toroidal Standing Alfvén Waves Detected by Geotail. *J. Geophys. Res. Space Phys.* 119, 8338–8356. doi:10.1002/2014ja020274

Tawara, H., and Kato, T. (1987). Total and Partial Ionization Cross Sections of Atoms and Ions by Electron Impact. *At. Data Nucl. Data Tables* 36, 167–353. doi:10.1016/0092-640x(87)90014-3

Thomsen, M. F., Denton, M. H., Gary, S. P., iu, K., and Min, K. (2017). Ring/shell Ion Distributions at Geosynchronous Orbit. *J. Geophys. Res.* 122, 12055. doi:10.1002/2017ja024612

Thomsen, M. F., Denton, M. H., Jordanova, V. K., Chen, L., and Thorne, R. M. (2011). Free Energy to Drive Equatorial Magnetosonic Wave Instability at Geosynchronous Orbit. *J. Geophys. Res.* 116, A08220. doi:10.1029/2011ja016644

Thomsen, M. F., Henderson, M. G., and Jordanova, V. K. (2013). Statistical Properties of the Surface-Charging Environment at Geosynchronous Orbit. *Space Weather* 11, 237–244. doi:10.1002/swe.20049

Toshima, N., Ishihara, T., Ohsaki, A., and Watanabe, T. (1989). Impact-parameter Treatment of Classical Trajectory Monte Carlo Calculations for Ion-Atom Collisions. *Phys. Rev. A.* 40, 2192–2194. doi:10.1103/physreva.40.2192

Volland, H. (1973). A Semiempirical Model of Large-Scale Magnetospheric Electric fields. *J. Geophys. Res.* 78, 171–180. doi:10.1029/ja078i001p00171

Walsh, B. M., Hull, A. J., Agapitov, O., Mozer, F. S., and Li, H. (2020). A Census of Magnetospheric Electrons from Several eV to 30 keV. *J. Geophys. Res.* 125, e2019JA027577. doi:10.1029/2019ja027577

Whipple, E. C. (1977). The Signature of Parallel Electric fields in a Collisionless Plasma. *J. Geophys. Res.* 82, 1525–1531. doi:10.1029/ja082i010p01525

Wilson, G. R., Horwitz, J. L., and Lin, J. (1992). A Semikinetic Model for Early Stage Plasmasphere Refilling: 1, Effects of Coulomb Collisions. *J. Geophys. Res.* 97, 1109–1119. doi:10.1029/91ja01459

Zoennchen, J. H., Bailey, J. J., Nass, U., Gruntman, M., Fahr, H. J., and Goldstein, J. (2011). The TWINS Exospheric Neutral H-Density Distribution under Solar Minimum Conditions. *Ann. Geophys.* 29, 2211–2217. doi:10.5194/angeo-29-2211-2011

Conflict of Interest: The authors declare that the research was conducted in the absence of any commercial or financial relationships that could be construed as a potential conflict of interest.

Publisher's Note: All claims expressed in this article are solely those of the authors and do not necessarily represent those of their affiliated organizations, or those of the publisher, the editors, and the reviewers. Any product that may be evaluated in this article, or claim that may be made by its manufacturer, is not guaranteed or endorsed by the publisher.

frontiers | Frontiers in Astronomy and Space Sciences

TYPE Review
PUBLISHED 12 January 2023
DOI 10.3389/fspas.2022.1005845

OPEN ACCESS

EDITED BY
Philip J. Erickson,
Massachusetts Institute of Technology,
United States

REVIEWED BY
Scott Alan Thaller,
Atmospheric and Space Technology
Research Associates, United States
John Bonnell,
University of California, Berkeley,
United States

*CORRESPONDENCE
Carlos A. Maldonado,
cmaldonado@lanl.gov

SPECIALTY SECTION
This article was submitted to Space
Physics,
a section of the journal
Frontiers in Astronomy and Space
Sciences

RECEIVED 28 July 2022
ACCEPTED 21 December 2022
PUBLISHED 12 January 2023

CITATION
Maldonado CA, Resendiz Lira PA,
Delzanno GL, Larsen BA, Reisenfeld DB
and Coffey V (2023), A review of
instrument techniques to measure
magnetospheric cold electrons and ions.
Front. Astron. Space Sci. 9:1005845.
doi: 10.3389/fspas.2022.1005845

A review of instrument techniques to measure magnetospheric cold electrons and ions

Carlos A. Maldonado[1]*, Pedro A. Resendiz Lira[2], Gian L. Delzanno[2], Brian A. Larsen[1], Daniel B. Reisenfeld[1] and Victoria Coffey[3]

[1]Intelligence and Space Research Division, Los Alamos National Laboratory, Los Alamos, NM, United States, [2]Theoretical Division, Los Alamos National Laboratory, Los Alamos, NM, United States, [3]Marshall Space Flight Center, Huntsville, AL, United States

A review of the instruments and techniques to directly measure the full distributions of the cold-ion and cold-electron populations in the magnetosphere is presented. Relatively few studies have focused on the cold plasma populations of the magnetosphere due to difficulties associated with obtaining measurements. The cold particle populations are defined here as those with total energy approximately <100 eV which is an energy range for which measurements are difficult (regardless of species), but which often make up the bulk of the plasma density. These populations have known and suspected impacts on the structure and dynamics of the magnetosphere but to date have not yet been measured adequately. The lack of accurate measurements cold ion and electron populations through the magnetosphere makes closure of these science questions extremely difficult if not impossible. Reaching closure will require innovations in plasma spectrometers and associated techniques required to obtain high-fidelity measurements of the cold ion and electron populations in the magnetosphere. This paper seeks to review the instruments and techniques that have been used to date and present possible options for future missions.

KEYWORDS

cold plasma, magnetosphere, ions, electrons, magnetic reconnection

1 Introduction

Relatively few studies have focused on the cold electron and cold ion populations of the magnetosphere due to difficulties associated with obtaining measurements using instruments mounted on charged spacecraft. The cold particle populations are defined as those with total energy approximately <100 eV which is an energy range for which measurements are difficult (regardless of species), but which often make up the bulk of the plasma density. These populations have a number of known impacts on the structure and dynamics of the magnetosphere (Delzanno et al., 2021) but to date have not yet been measured extensively. In sunlight, spacecraft in the magnetosphere typically float from a few volts positive to several tens of volts positive (Thomsen, et al., 2007), preventing the bulk of the cold ion spectrum from reaching spacecraft instruments (Genestreti, et al., 2017). This effectively limits the energy measurement range to just the ion population with energy above the spacecraft potential. Simultaneously, sunlit spacecraft surfaces emit a constant flux of low-energy electrons (DeForest 1972) which contaminate or completely mask instrument measurements of ambient, low-energy magnetospheric electrons (Scime et al., 1994; Gershman, et al., 2017). These difficulties and subsequent scarcity of measurements have been well described in the literature (Andre and Cully 2012; Lee and Angelopoulos 2014; Haaland, et al., 2015; Delzanno, et al., 2021) leading to the colloquial term for low-energy magnetospheric ions as the "hidden

populations" (Olsen 1982). This paper seeks to describe the instruments and techniques that have been used to date and present options for future missions.

There have been many theories, studies, and debates regarding the processes of magnetosphere-ionosphere coupling (MIC), currently focused on the location and driving conditions for magnetic reconnection and how the ionosphere regulates reconnection and convection (Lotko 2007; Welling, et al., 2015). An improved understanding of the complex plasma dynamics is needed to answer these long-standing mysteries and requires appropriate instrumentation for obtaining *in-situ* observations. Low-energy ions originating from the ionosphere dominate the magnetosphere 50%–70% of the time (Andre and Cully 2012). To accurately model the impact of various plasma sources on magnetospheric composition, distributed *in-situ* measurements of cold ion and cold electron populations are needed from the outflow regions through the magnetosphere. As described in detail by Delzanno et al. (2021), the primary sources of plasma in the Earth's magnetosphere are attributed to ion and electron outflow at the low and high latitude ionosphere in addition to contributions from the solar wind. The outflow populations can get strongly energized as they journey through the magnetosphere and contribute to the warm plasma cloak, ring current and plasma sheet (C. R. Chappell 1982; Chappell et al., 2008).

Since the initial observations of heavy ions in the magnetosphere by Shelley et al. (1972), the dynamics leading to the ionospheric outflow of O^+ ions and their impact on the evolution of the magnetosphere-ionosphere system have been the subject of numerous studies. At low latitudes, charged particles travel along closed field lines and create the cold (<eV) protons and electrons that make up the plasmasphere (Carpenter 1962; Lemaire, et al., 1998; Kotova 2007). Magnetospheric cold electron sources include outflow of low-energy photoelectrons from the sunlit upper atmosphere (Kitamura, et al., 2012). This creates a spatial separation between the light electrons and heavier ions resulting in the ambipolar electric field which aids in the acceleration of ions upwards in the polar wind (Khazanov et al., 1997; Haaland, et al., 2015; Glocer et al., 2017). The high latitude auroral outflow is composed of hydrogen and other heavy ions (O^+, He^+, N^+, N_2^+, and NO^+) which flow from the high-latitude ionosphere along or near open magnetic field lines and into the low-pressure magnetosphere (Moore et al., 2005a; Ilie and Liehohn 2016). Outflow is commonly observed at high latitudes (Moore, et al., 1999a; Andre 2015) and is generally divided into three categories: 1) cold-temperature ion flows with energies of a few eV in which all ions acquire a bulk flow velocity such as the polar wind and auroral bulk O^+ up-flow from the topside auroral and polar-cap ionosphere; 2) ions with suprathermal energies above the ionosphere (Eliasson, et al., 1994) or with higher energies at higher altitude (Möbius, et al., 1998) and 3) heated ion outflows in the cusp and auroral zone in which a fraction of the ions have been energized to much greater energies including transversely accelerated ions, upwelling ions, ion conics, and ion beams (Yau and Andre 1997; Welling, et al., 2015). The low-energy outflowing ions provide cold plasma filling to the plasmasphere (Welling, et al., 2015) and cold supersonic outflow to the inner magnetosphere and magnetotail such as from the polar wind (Su, et al., 1998; Engwall, et al., 2006a; Engwall, et al., 2009). A depiction of the ion outflow process as a function of ion energy category and destination as described by Yamauchi (2019) is shown in Figure 1. Consequently, the outflow flux of ions and electrons are highly dynamic and vary with the solar magnetospheric activity, including solar extreme ultra-violet (EUV) radiation, interplanetary magnetic fields, solar wind pressure, geomagnetic indices, precipitating electron fluxes and Poynting fluxes into the ionosphere (Yau, Shelley, et al., 1985; Barghouthi et al., 1998; Tam et al., 1998; Moore et al., 1999b; Barakat and Schunk 2001; Cully, et al., 2003; Strangeway, et al., 2005; Kitamura et al., 2011; Delzanno, et al., 2021).

The solar wind is composed of predominantly hydrogen, alpha particles, and high charge-state heavy ions (Bame, Hundhausen, et al., 1968; Geiss et al., 1995; Zurbuchen et al., 2002). While not traditionally considered a source of cold ions or cold electrons, the solar wind does contribute significantly to the overall magnetospheric plasma populations. The solar wind protons and electrons travel outward at ~400 km/s with temperature on the order of 10 eV (Feldman, et al., 1974; McComas et al., 1998). Upon crossing the bow shock the solar wind temperature in the magnetosheath increases to ~20–60 eV for electrons and ~100 eV–1 keV for ions on the dayside (Wang, et al., 2012; Delzanno, et al., 2021). As the magnetosheath plasma moves to the nightside the temperature decreases to ~10–30 eV for electrons and ~30–300 eV for ions (Wang, et al., 2012; Dimmock and Nykyri 2013). This results in a total energy of the magnetosheath ~1 keV for ions while the electrons remain relatively cold (Delzanno, et al., 2021).

As a result of the ionospheric outflow and incident solar wind, the magnetospheric environment consists of multiple ion and electron populations with a broad range of energies, from sub-eV particles of the ionosphere to the relativistic energies of the radiation belts (Singh and Horowitz 1992; Zhao, et al., 2015; Genestreti, et al., 2017). Traditional ion mass spectrometer instruments are designed to detect the hot tenuous magnetospheric ion species and are typically not as effective at measuring cold, low energy (<100 eV) plasmas. This is due to the trade-off in the instrument design's objective between having a large dynamic energy range from a few eV to tens of keV, *versus* focusing on low-energy sensitivity.

The amount of coupling of the solar wind to the Earth's magnetosphere-ionosphere system is controlled by magnetic field-line reconnection between the solar wind and the magnetosphere, which is a function of local plasma parameters at the reconnection site (Cassak and Shay 2007; Borovsky et al., 2008; Borovsky et al., 2008). The magnetic field strength and mass density of the magnetospheric and magnetopause plasma populations at the magnetopause determine the reconnection rate between the solar wind and the magnetosphere. Ionospheric outflows, which can control the magnetospheric mass density, can have a direct role in controlling the dayside reconnection rate; therefore ionospheric outflows potentially have a significant role in controlling solar wind/magnetosphere coupling through mass loading (Borovsky et al., 2013; Fuselier et al., 2019a; Toledo-Redondo et al., 2021). Plasmaspheric plumes and the warm plasma cloak (whose energy spectrum partially overlaps with our definition of cold plasma) also affect solar wind/magnetospheric coupling during geomagnetically active times. Mass loading could also operate in the magnetotail although to what extent particles remains cold as they cross the tail remains an open question [see the discussion in Delzanno et al. (2021)].

The diverse magnetospheric particle populations are co-located and interact by means of plasma waves. For instance, acceleration and loss of radiation belt electrons is thought to be due to wave-particle interactions, with the relevant waves modulated by lower energy plasma particles (Summers et al., 2007; Reeves et al., 2009). In addition to mass loading and dayside magnetopause reconnection, the cold magnetospheric plasma impact the generation of whistler and electromagnetic ion cyclotron (EMIC) waves by the cyclotron instability (de Soria-Santacruz et al., 2013) and their subsequent

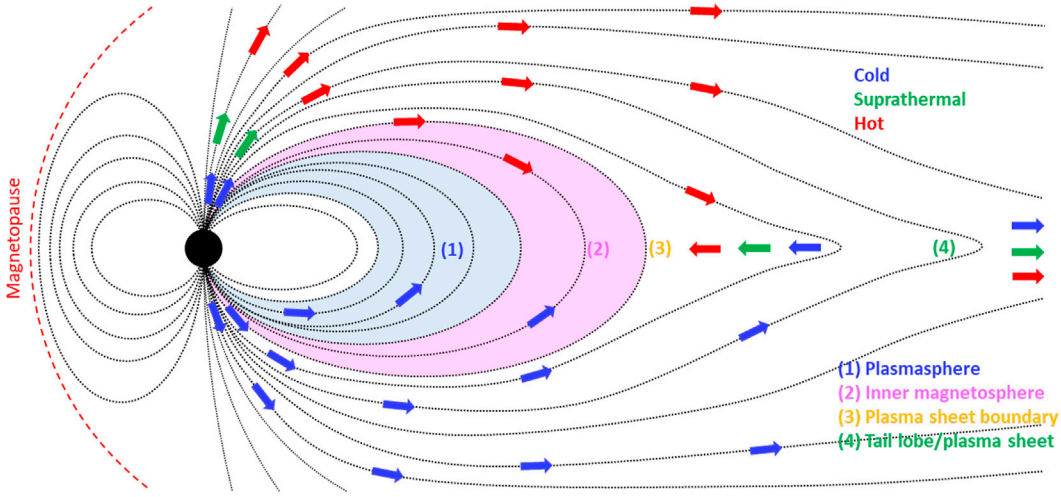

FIGURE 1
Schematic of the outflowing ions classified by energy and destination, recreated from Yamauchi (2019).

propagation in the inhomogeneous magnetospheric plasma. The cold particle populations affect the frequencies and amplitudes of ultra-low-frequency (ULF) waves (Fraser, et al., 2005), whistler waves (Thorne 2010), whistler-mode hiss waves (Dunckel and Helliwell 1969; Russell et al., 1969; Bortnik et al., 2008; Hartley, et al., 2018), and EMIC waves (Blum et al., 2009; Chen et al., 2011; Blum and Breneman 2019), which control scattering and energization rates of the higher-energy populations, impacting the dynamics of the plasma sheet, ring current and radiation belts. Note also that accurate knowledge of the ion composition of the cold plasma in the magnetosphere is critical to determine the properties of EMIC waves. The mass density of cold ions also affects the magnetopause stability to Kelvin-Helmholtz waves and the transport of solar wind into the magnetosphere (Melander and Parks 1981; Hasegawa, et al., 2004).

To date, the majority of cold plasma research efforts have focused on the cold ion populations leaving a considerable gap in the understanding of cold electron populations in the magnetosphere. Cold electrons are considered to play an important role in wave-particle interactions such as chorus and hiss waves. Recent work by Roytershteyn and Delzanno (2021) suggests that the presence of cold electron population introduces coupling of the whistler modes to short-wavelength, oblique, electrostatic instabilities. This can subsequently lead to cold-electron heating and damping of the primary whistler waves. EMIC waves can also interact with cold electrons resulting in cold-electron heating (Zhou, et al., 2013; Yuan, et al., 2014). This mechanism is thought to be responsible for stable auroral arcs (Chandra et al., 1971; Chandra et al., 1972) through the enhancement of ionospheric electron temperature. A proposed mechanism for the subauroral heating is energy transfer from the ring current to magnetospheric electrons and the downward heat conduction into the ionosphere (Brace et al., 1967, Kozyra, et al., 1986, Khazanov et al., 1992).

The lack of accurate measurements of low-energy or “cold” ion and electron populations through the magnetosphere makes closure of these science questions extremely difficult if not impossible. Therefore, to significantly advance our understanding of magnetospheric plasma physics, the full phase-space densities of the cold plasma population must be thoroughly measured. This will require innovations in plasma spectrometers and associated techniques required to obtain high-fidelity measurements of the cold ion and electron populations in the magnetosphere.

2 Challenges related to magnetospheric cold ion and cold electron measurements

One of the primary challenges related to making cold ion and cold electron measurements in the magnetosphere is due to spacecraft charging. In sunlight, the spacecraft floating potential is typically a few volts or less in the plasmasphere and can be tens of volts or more in the tenuous outer magnetosphere (Thomsen, et al., 2007; Ferguson et al., 2015; Sarno-Smith, et al., 2016). The potential difference between the charged spacecraft and the ambient plasma will result in either an increase or decrease to the particle energy and total density measured by electrostatic analyzers depending on the charge of the incident particle. For example, ions impinging on negatively charged spacecraft surfaces will be accelerated and experience an increase in measured energy, while electrons will experience a decrease in measured energy. When the polarity of the spacecraft potential and the particle charge are the same, the resulting electrostatic repulsion results in truncation of the energy distributions at low energies and the resulting loss in density. A number of studies have examined the deleterious effects of spacecraft charging on charged particle measurements when comparing particle trajectories measured at the spacecraft with the actual particle distributions in the ambient plasma (Sojka et al., 1984, W. C; Knudsen 1966; Parker and Whipple 1970; Toledo-Redondo et al., 2019).

Measurements of low-energy electrons present additional challenges due to a combination of spacecraft charging effects and the presence of photoelectrons continuously emitted from sunlit spacecraft surfaces (DeForest 1972). The photoelectron population is emitted at ~ eV energy and can contaminate the low-energy

channels of instruments measuring ionospheric and magnetospheric electrons (Mozer, et al., 2017). Secondary electrons emitted by impact of high energy ambient electrons and ions create similar problems. Spacecraft with positive potentials accelerate both ambient low-energy electrons and photoelectrons alike into detector apertures resulting in an indiscernible measured distribution. The difficulty associated with deconvolving the two electron distributions has led to a lack of observations and understanding of the cold-electron impact in the magnetosphere (Gershman, et al., 2017).

2.1 Spacecraft charging

Any object immersed in a plasma builds up a charge by collecting ambient particles (electrons and ions) and by emitting photoelectrons and secondary electrons. The accumulated charge generates an electric potential with respect to the ambient plasma. Then, the generated electric field alters the dynamics of the particles in the spacecraft vicinity, creating all sort of challenging problems for the interpretation of *in-situ* measurements.

As described by Purvis et al. (1984); Garrett and Whittlesey (2012), the total current to the spacecraft, I_T, can be determined from

$$I_T(\Phi_{SC}) = I_e(\Phi_{SC}) + I_i(\Phi_{SC}) + I_{se}(\Phi_{SC}) + I_{si}(\Phi_{SC}) + I_{ph}(\Phi_{SC}), \quad (1)$$

where Φ_{SC} is the surface potential relative to space, I_e is the current due to incident electrons, I_i is the incident ion current, I_{se} and I_{si} are the secondary emitted electron currents due to incident electrons and ions, and I_{ph} is the photoelectron current. At equilibrium, the total current absorbed by the spacecraft is zero ($I_T(\Phi_{SC}) = 0$, floating condition). The voltage with respect to the ambient plasma (infinity) at which the current is balanced is known as the spacecraft floating potential Φ_{SC}. Depending on the ambient plasma conditions and material parameters, spacecraft can float positively or negatively with respect to infinity.

For simplicity, the spacecraft charging dependence with ambient plasma conditions and material parameters can be illustrated with the Orbital-Motion-Limited (OML) theory (Mott-Smith and Langmuir 1926), by approximating the spacecraft as a conducting sphere of radius r_{sc}. Assuming Maxwellian distributions for the particle populations, the electron current collected by a sphere is given by

$$I_e = -e4\pi r_{SC}^2 n_e \sqrt{\frac{eT_e}{2\pi m_e}} exp\left(\frac{e\Phi_{SC}}{k_B T_e}\right), \ \Phi_{SC} < 0, \quad (2)$$

and

$$I_e = -e4\pi r_{SC}^2 n_e \sqrt{\frac{eT_e}{2\pi m_e}}\left(1 + \frac{e\Phi_{SC}}{k_B T_e}\right), \ \Phi_{SC} \geq 0. \quad (3)$$

For the ion current,

$$I_i = e4\pi r_{SC}^2 n_i \sqrt{\frac{eT_i}{2\pi m_i}}\left(1 - \frac{e\Phi_{SC}}{k_B T_i}\right), \ \Phi_{SC} \leq 0, \quad (4)$$

and

$$I_i = e4\pi r_{SC}^2 n_i \sqrt{\frac{eT_i}{2\pi m_i}} exp\left(-\frac{e\Phi_{SC}}{k_B T_i}\right), \ \Phi_{SC} > 0. \quad (5)$$

OML theory is an appropriate approximation when the electron Debye length (λ_{De}) is larger than the radius of the spacecraft (thick sheath approximation), which is typically the case for magnetospheric plasma conditions. Typical values of λ_{De} range from meters to kilometers while typical spacecraft dimensions are a few meters. Moreover, the effect of the Earth's magnetic field in the current collection is not accounted for in this approximation justified by assuming that the gyroradius is larger than the spacecraft dimensions which is typically the case in the Earth's magnetosphere. We note that if any of these two approximations are not satisfied, the use of the unmagnetized OML theory presented here is not appropriate to estimate the current collected by the spacecraft. Alternatively, the thin sheath approximation (Conde 2011) and/or alternative analytic models that accounts for magnetic field effects in the particle collection (Laframboise 1976) can be used depending on the specific plasma conditions.

The photoelectron current is given by

$$I_{ph} = \mathcal{A}4\pi r_{SC}^2 J_{ph}, \ \Phi_{SC} < 0, \quad (6)$$

and

$$I_{ph} = \mathcal{A}4\pi r_{SC}^2 J_{ph}\left(1 + \frac{e\Phi_{SC}}{k_B T_{ph}}\right) exp\left(-\frac{e\Phi_{SC}}{k_B T_{ph}}\right), \ \Phi_{SC} > 0. \quad (7)$$

In Eq. 7 the point source approximation is used along with a single Maxwellian distribution to describe photoemission (Grard 1973). Note that the source point approximation is better suited to characterize photoemission when the size of the body is smaller than photoelectron Debye length. On the other hand, photoemission is better described with the planar source approximation [also given in Grard (1973)] when the size of the body is larger than shielding distance for the photoelectrons as shown in Nakagawa et al. (2000). For completeness, the current due to the secondary electron (Shukla and Mamun 2015) emission is given by

$$I_{se} = e\frac{8\pi^2 r_{sc}^2}{m_e^2}\int_0^\infty E\delta_{se}(E) f_{se}(E - e\Phi_{SC})dE, \Phi_{SC} < 0 \quad (8)$$

and

$$I_{se} = e\frac{8\pi^2 r_{sc}^2}{m_e^2} exp\left(-\frac{e\Phi_{SC}}{k_B T_{se}}\right) \times \left(1 + \frac{e\Phi_{SC}}{k_B T_{se}}\right)\int_0^\infty E\delta_{se}(E) f_{se}(E - e\Phi_{SC})dE, \Phi_{SC} > 0 \quad (9)$$

Where the secondary emission yield δ_{se}, characterized by the maximum yield δ_m and energy at maximum yield E_m, is given by the Sternglass formula (Bruining 2016)

$$\delta_{se}(E) = \frac{7.4\delta_m E}{E_m} exp\left(-2\sqrt{\frac{E}{E_m}}\right) \quad (10)$$

while

$$f_{se}(E - e\Phi_{SC}) = n_e\left(\frac{m_e}{2\pi k_B T_e}\right)^{3/2} exp\left(-\frac{E - e\Phi_{SC}}{k_B T_e}\right) \quad (11)$$

is the distribution function of the incident electrons. Note that different functional forms of the secondary emission yield δ_{se} can be found in the literature (see for example Whipple, 1981) given the different experimental setups and assumptions taken in the derivation of these theoretical models.

Here, e is the elementary charge, k_B is the Boltzmann constant, m_α, n_α, T_α are the mass, density and temperature of the plasma species,

respectively. For photoelectron emission, T_{ph} and J_{ph} are the temperature and current density of the photoelectrons, respectively, while $\mathcal{A}$ is the fraction of the spacecraft illuminated area relative to the total surface area. T_{se} is the temperature of the secondary electron emitted while E is the kinetic energy.

The current balance which determines the floating potential of a spacecraft immersed in a plasma is given by the environmental plasma conditions and the spacecraft material parameters. The OML equations above can be used to illustrate two different charging regimes in the Earth space environment: dayside ionosphere and dayside magnetosphere. Plasma densities in the ionosphere range between 1×10^5 cm^{-3} and 1×10^6 cm^{-3} on the dayside and 1×10^3 cm^{-3} and 1×10^4 cm^{-3} on the nightside. The plasma temperature is of the order of a fraction of eV while the predominant ion species is Oxygen. For example, let us consider a perfectly conducting spherical spacecraft of 1 m radius, immersed in the dayside ionospheric singly ionized plasma with $m_\alpha = 16$ amu, $n_\alpha = 1 \times 10^5$ cm^{-3}, $T_\alpha = 0.5$ eV, and with material parameters given by $T_{ph} = 2$ eV, $J_{ph} = 40$ μA/m^2 and $\mathcal{A} = 0.3$. The spacecraft charges negatively to −3 V with respect to the ambient plasma. On the other hand, in the Earth's magnetosphere, the plasma density is several orders of magnitude lower than in the ionosphere, while Hydrogen dominates the ion plasma composition. Under dayside magnetospheric plasma conditions given by $m_\alpha = 1$ amu, $n_\alpha = 1$ 3.5 cm^{-3}, $T_\alpha = 0.5$ eV, and considering the same material parameters as in the previous example, $T_{ph} = 2$ eV, $J_{ph} = 40$ μA/m^2 and $\mathcal{A} = 0.3$, the spherical spacecraft charges positively to 4.2 V with respect to the ambient plasma.

If the spacecraft is negatively charged, ions are attracted by the spacecraft and tend to reach the particle detector and be measured. This is the case for instance for the LANL MPA detectors mounted on the LANL-GEO spacecraft (Bame et al., 1993; Denton, et al., 2015). In this scenario, the energy resolution of the instrument becomes important, as well as correcting for the acceleration of the particles due to the electric field generated around the spacecraft (Lavraud et al., 2006). In a positively-charged spacecraft, however, incoming cold ions with energies below the spacecraft potential are repelled by the electric field near the spacecraft. As a result, the full distribution of the cold ions can not be measured (Olsen 1982). Panel A in Figure 3 (Olsen, 1982) illustrate the problem of cold ion measurements perfectly. The SCATHA data show that when the spacecraft potential is ~10 V cold ions cannot reach the particle detector. However, when the spacecraft potential drops to ~1–2 V (~6 UT), part of the cold ion distribution is measured. This has been known for decades and has led to the term "hidden magnetosphere" as a reference to the elusive cold ions with energies below the spacecraft potential. The tail of the partially measured ion distribution can be extrapolated to estimate moments of the distribution (Genestreti, et al., 2017). The downside of using this approach, however, is that plasma parameter estimates may come with significant uncertainties when the spacecraft potential is much larger than the mean energy of the cold ions. This situation is similar for negatively-charged spacecraft and cold electrons. Indeed, this is why spacecraft charging is one of the main obstacles for cold-plasma measurements.

2.2 Photoelectron contamination

Cold electron measurements in the Earth's magnetosphere are more difficult than cold ion measurements. A negatively charged spacecraft repels cold electrons and, depending on the mean cold electron energy compared to the spacecraft potential, the cold electron distribution may be measured only partially or, in the case of a strongly negatively charged spacecraft, not at all. In cases where the mean cold electron energy and the spacecraft potential are comparable, the extrapolation from the tail of the distribution can be used, similarly to what has been done for ions (Genestreti, et al., 2017). When the spacecraft is charged positively, which usually occurs for satellites in sunlight and in low density plasma conditions, cold electron measurements should in principle be possible, in the sense that ambient cold electrons can reach the particle detectors. In practice, however, spacecraft-generated photoelectrons are attracted back to the spacecraft and their flux can overwhelm the flux of the ambient cold electrons. Figure 2B shows an example of photoelectron contamination from a spectrogram for SCATHA data from 19 October 1979 (Olsen, 1982). Between 21 and 22 UTC (local midnight), a high flux of the low-energy photoelectrons is observed by the particle detector completely masking any signal of an ambient cold electron population.

To further illustrate the issue of photoelectron contamination, Figure 4 shows kinetic simulation results of the response of a particle detector in magnetospheric plasma conditions modeled with the Curvilinear Particle-in-Cell code (CPIC) (Meierbachtol, et al., 2017). Specifically, the ambient plasma consists of electrons and protons modeled by a Maxwellian distribution function with density equal to 13.50 cm^{-3} and electron (ion) temperature equal to 0.5 (0.35) eV. The spacecraft mimics the geometry of the Van Allen Probes spacecraft (Figure 3 right). The photoemission current density is $J_{ph} = 100$ μA/m^2 while the photoelectron temperature is 2 eV. Only the top part of the spacecraft is illuminated by UV sunlight and emits photoelectrons. In this example, the detector is mounted on the sun-illuminated, top part of the spacecraft, as can be seen in the right panel in Figure 4. Under these conditions, the spacecraft and the particle detector are floating at 4.7 V with respect to the ambient plasma. For a positively charged spacecraft, the full distribution of the cold electrons can indeed be measured by a particle detector as shown in the bottom left panel in Figure 3 (blue histogram), where the contribution of the photoelectrons and ambient electrons can be easily distinguished in the simulations. However, the problem of characterizing the ambient electrons from the photoelectrons reaching the particle detector at the same time becomes evident. Because the energy of the spacecraft-emitted electrons is comparable to that of the ambient cold electrons (generally a few ~ eV, 2 eV in this case), it can be very difficult to distinguish between the two species in the detector signal, as can be seen in the top left panel of Figure 3, where the total signal is plotted and the photoelectron flux is overwhelming the ambient electron flux. In fact, in low density ambient plasma conditions (less than ~10 cm^{-3}), the particle detector signal is typically dominated by photoelectrons since materials used for space applications have photoelectron current densities of the order of 10–40 μA/m^2 (measured in the lab, (Grard 1973), and <100 μA/m^2 when estimated from spacecraft data (Nakagawa, et al., 2000; Scudder et al., 2000). As such, near the particle detector the photoelectron density can be two or three orders of magnitude larger than that of the ambient cold-electrons, as illustrated in the bottom right panel of Figure 3 (orange histogram). Additionally, the studies by Nakagawa et al. (2000); Scudder et al. (2000); Thiebault et al. (2006) suggest that the emission of low energy electrons by spacecraft materials in real space conditions is more complicated than what has been reported in laboratory studies, where photoemission is typically characterized by a single Maxwellian energy distribution. These studies report higher values for the current density compared to those estimated in the lab, <~100 μA/m^2, as well as materials emitting

10.3389/fspas.2022.1005845

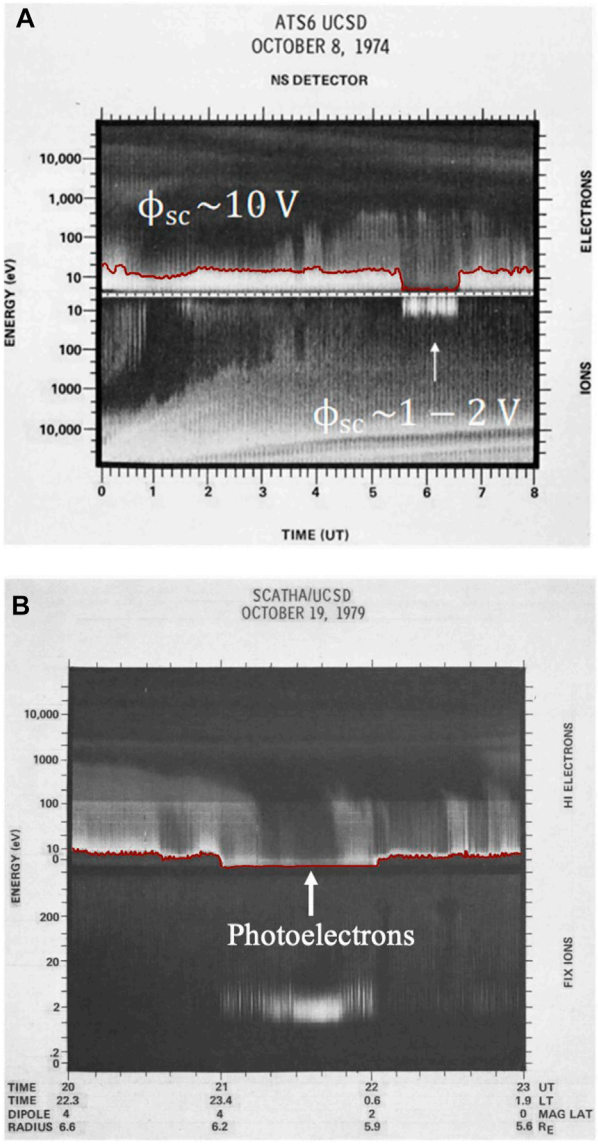

FIGURE 2
From (Olsen 1982) **(A)** ATS six measurements in the plasma sheet in eclipse, **(B)** SCATHA Hi electron data where photoelectron fluxes are detected.

photoelectrons with more complex spectra that can be characterized by multiple Maxwellians with different temperatures. As such, the tendency of photoelectrons to "blind" the particle measurements and the complexity of photoelectron spectra make it extremely hard to extract accurate information on the ambient cold electrons from particle measurements in nominal sunlight conditions. To date, this problem remains unsolved and it is the major reason why we know very little about cold electrons in the Earth magnetosphere.

3 *In-situ* ion measurements

Multiple instruments have made partial measurements of the cold ion populations in the magnetosphere with the difficulties discussed in Section 2. Traditional ion mass spectrometer instruments are designed to detect the hot tenuous magnetospheric ion species and are typically not as effective at measuring cold low-energy (<100 eV) plasmas. This is due to the trade-off in instrument design between having a large dynamic energy range from a few eV to tens of keV, *versus* focusing on low-energy sensitivity. Traditionally, space plasma instruments have focused on measuring large dynamic ranges due to limited spacecraft resources and mission opportunities.

An overview of ion mass spectrometers is captured (see Table 1) by briefly reviewing ion composition studies of the terrestrial magnetosphere by the Hot Plasma Composition Analyzers (HPCA) (Young, Burch, et al., 2016), the Helium, Oxygen, Proton, and Electron (HOPE) (Funsten, et al., 2013) mass spectrometer, the Cluster Ion Spectrometry (CIS) Experiment (Reme, et al., 1997), and the Retarding Ion Mass Spectrometer (RIMS) (Chappell, et al., 1981). These ion composition instruments and subsequent observations have provided the steppingstone for some of the most exciting magnetospheric science discoveries of the modern space science era. For example, the data from these instruments have been used to characterize the equatorial plasma environment and ion composition (Fernandes, et al., 2017; Yue, et al., 2018), evolution of the ring current during geomagnetic storms (Zhao, et al., 2015), initial observations of the "oxygen plasma torus" (Chappell 1982), magnetospheric ion influence on magnetic reconnection at the duskside and dayside magnetopause (Fuselier et al., 2016; Fuselier et al., 2019b), and the confirmation that wave-particle interactions can play a key role in acceleration within the radiation belts (Thorne 2010; Turner, et al., 2014; Baker 2021). These examples are a very limited sampling of the literature and by no means an exhaustive discussion of the total scientific advancements enabled by these instruments. For context, the Cluster mission alone has generated more than 2,587 refereed publications and 142 PhD/thesis (Escoubet, et al., 2020). However, while the HOPE, CIS/CODIF, and HCPA ion mass spectrometers have provided invaluable insights into the plasma source and transport within the terrestrial magnetosphere, these instruments have only made limited observations of the cold ions which often constitute the bulk of the magnetospheric plasma density.

The difficulties associated with measuring low-energy magnetospheric ions have been addressed with limited success, i.e., measurements of partial distributions and limited time-series data sets, by earlier missions through the use of active spacecraft control (Riedler, et al., 1997; Torkar, et al., 2016) and electrostatic biasing of entrance apertures (Chappell, et al., 1981) or the entire instrument (Knudsen, et al., 2015). These active spacecraft potential controls reduced the spacecraft potential, but did not reduce the potential to zero for all measurements, resulting in portions of the distributions unmeasured.

The RIMS instrument on-board the Dynamics Explorer 1 (DE-1) mission has provided some of the earliest and most robust observations of the cold ion populations in the magnetosphere to date. The sensor design utilized a front aperture capable of being commanded to any of four values as a bias for a non-zero spacecraft potential (Chappell, et al., 1981). This bias created an electrostatic potential to steer low-energy ions through the spacecraft potential sheath to the detector aperture. The sensor had the ability to resolve H^+, He^+, O^+, and O^{++} within a narrow energy range of 0–50 eV. This allowed for the initial observations of the O^+ torus, warm plasma cloak, thermal composition of the plasmapause, and the ionospheric outflow or polar wind (Chappell, et al., 1981, C. R; Chappell 1982, C. R; Chappell 1988, Chappell et al., 2008). However, due to a lack of

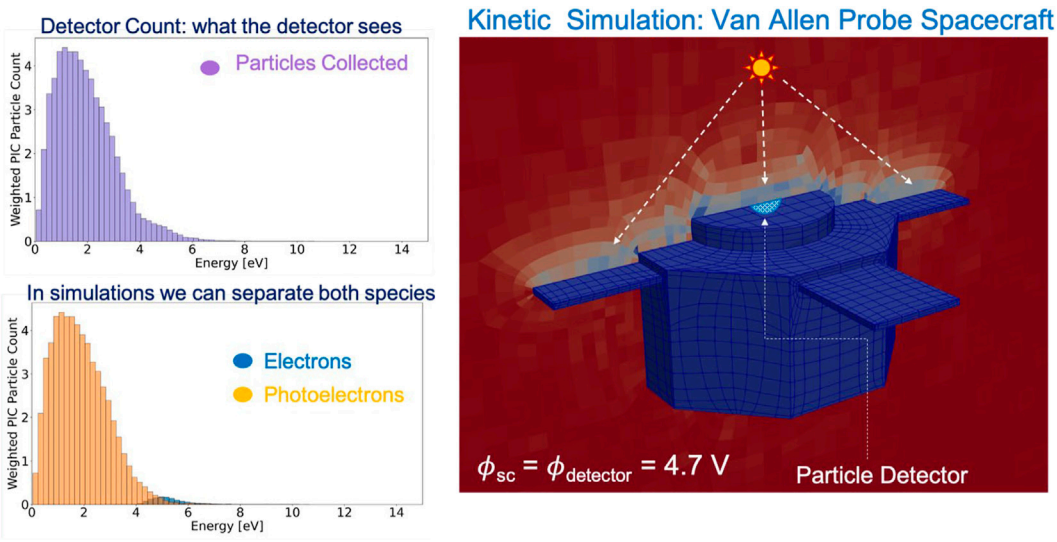

FIGURE 3
Kinetic simulation result: photoelectron blinding the signal of a particle detector mounted on a Van Allen Probe type spacecraft. Plasma parameters used in the simulation: n = 13.5 cm^{-3}, T_e = **0.5 eV** T_i = 0.35 eV, T_{ph} = 2 eV and J_{ph} = 100 μA/m^2.

spacecraft potential measurements the ion densities derived from the RIMS observations have considerable uncertainties. Initial density values were arrived at through an iterative method involving estimating the spacecraft potential as a function of geocentric distance and the electron density profile (Persoon et al., 1983), applying the spacecraft potential estimates to an empirical relation (Comfort et al., 1988), comparing to modeled total density (Ho and Horwitz 1993), and iterating until the spacecraft potential and density converged (Ho and Horwitz 1994). The temperatures obtained from the instrument measurements consist of a high degree of uncertainty due to the energy spacing of the RPA steps being larger than the thermal energies (Ho and Horwitz 1994). The temperature is also derived using a thin sheath approximation for the spacecraft potential sheath (Comfort et al., 1985) which has been shown to introduce significant error (W. C. Knudsen 1966; Parker and Whipple 1970; Sojka et al., 1984; Marchand et al., 2010; Lavraud and Larson 2016). Lastly, the radial retarding potential analyzer (RPA) head of the RIMS failed, limiting the DE-1 data set (Ho and Horwitz 1994). Although there are some limitations of the RIMS instrument, it has provided a wealth of data and contributed to our understanding of the ionosphere-magnetosphere system and provided a crucial steppingstone for cold ion and cold electron observations in the magnetosphere.

A statistical study of the spacecraft potential on Van Allen Probes demonstrated that the satellites charged to between 0 and 10 V for much of the mission (Sarno-Smith, et al., 2016; Denton, et al., 2017). Consequently, the low-energy portion of the magnetospheric cold ion population has not been measured by the HOPE instrument due to the positive spacecraft potential. The CIS/CODIF instrument demonstrated the ability to measure ~0–25 eV ions (O^+, H^+, He^+) while emitting indium ions to control the spacecraft potential (Reme, et al., 1997; Riedler, et al., 1997). However, while the active spacecraft control used for Cluster and the Magnetospheric Multiscale (MMS) missions (Burch, et al., 2016) does reduce the spacecraft potential it does not eliminate it. The potential is reduced to ~1–2 V, thus leaving a portion of the cold ion energy distribution unobserved. ~1 The Thermal Ion Dynamics Experiment (TIDE) on POLAR was designed to measure the low-energy polar winds at very high altitudes. The TIDE ion mass spectrometer was used in combination with the Plasma Source Instrument (PSI) to measure to overcome the effects of spacecraft potential on low-energy ion measurements (Moore et al., 1997). The PSI could actively control the spacecraft potential using emitted xenon ions to reduce the spacecraft potential to 1.8–2.2 V (Su, et al., 1998), resulting in a portion of the cold ion population remaining unmeasured. Unfortunately, TIDE lost its mass resolution capability in 1996, then returning total ion results. A critical distinction must also be made regarding the capabilities of the instruments listed in Table 1. The HOPE sensor is the only instrument that was designed to be insensitive to energetic particle contamination background counts as a result of penetrating radiation and capable of making measurements throughout the inner magnetosphere. The HOPE data were also used to estimate the temperature of plasmaspheric ions using novel techniques required to extract the low-energy values while correcting for charged spacecraft moving through the ambient plasma (Genestreti, et al., 2017).

While these methods have allowed for limited measurements of low-energy ions, there were also impacts to the measured distributions as a result of the non-uniform sheath near the spacecraft (Scime et al., 1994; Marchand et al., 2010). These effects can be mitigated by operating the plasma instrument outside of the spacecraft sheath, at least for conditions when the local plasma Debye length is not too large, thus minimizing ion trajectory distortions due to asymmetric spacecraft potential sheaths. As has been done for ionospheric missions, this requires either a low-resource instrument or an engineering solution to mount a larger instrument to a boom. Several thermal ion and electron instruments have been successfully developed as low-resource payloads for sounding rocket missions (Frederick-Frost, et al., 2007; Fernandes et al., 2016; Fraunberger, et al., 2020) even utilizing aperture biasing techniques to accelerate target populations in the presence of spacecraft potential (Cohen, et al., 2016). As opposed to driving the spacecraft potential to near 0 V relative to the plasma potential,

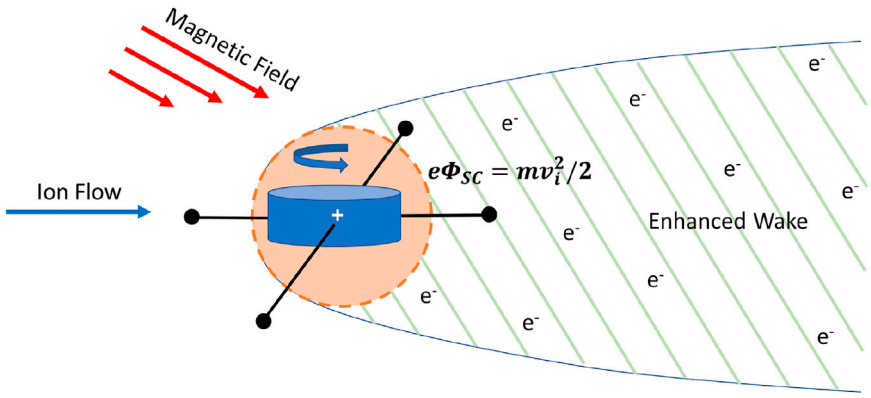

FIGURE 4
Schematic of the enhanced wake behind a positively charged spacecraft. The dashed circle illustrates the equipotential of the spacecraft electrostatic field where $e\Phi_{SC} = mv_i^2/2$.

TABLE 1 Performance specifications for representative state-of-the-art mass spectrometers.

Instrument	Type	FOV	Energy range	ΔE/E	Mass range (amu)	M/ΔM	Geometric factor	Mass (kg)	Power (W)	Volume (cm^3)	References
HOPE	TOF	180° FW × 4.5 FWHM° 5 pixels over 144°	1 eV-50 keV	16% @ 1 eV 12% @ 50 keV	1–20	≥2	1.25×10^{-3} cm^2 sr @ 1 eV 1.3×10^{-3} cm^2 sr @ 50 keV	18.06	18.2 (BOL), 23.0 (EOL)	12,869	Funsten et al. (2013)
HPCA	TOF	11.25° × 360°	100eV-30 keV	20%	1–16	>4	2×10^{-4} cm^2 sr @ 1 eV	8.91	14.48	1,018[a]	Young, Burch et al. (2016)
CIS/CODIF	TOF	360° × 8°	1eV-40 keV	16%	1–32	~4–7	2×10^{-3} cm^2 sr	8.3	7.28	~8,000	Reme et al. (1997)
TIDE	TOF	11.25° × 22.5° × 7 sectors; spinning SC 96% of 4π sr	0.1–500 eV	5%–100% commandable	1–40	4	<0.03 cm^2 sr × 7 sectors	17.1	9.1	-	Moore Chappell, et al. (1995)
RIMS	magnetic	±55° conical 3 sensor heads	0–52.5 eV	—	1–32	—	—	—	—	—	Chappell et al. (1981)

as done with ion beams or plasma contactors (Torkar et al., 2016), an alternate method of making these low-energy measurements would be to actively bias the spacecraft potential to focus on either cold ions or cold electrons. A sufficient negative potential will enable transport of low-energy ions to detector apertures and thus be observed. This is the case of the LANL-GEO spacecraft, which tend to charge negatively (Thomsen et al., 2013). Conversely, a large positive potential will enable low-energy electrons to be distinguishable from contaminating photoelectrons as discussed in Section 5.

More recently, the Swarm (Friis-Christensen, et al., 2008) and Magnetospheric Multiscale (Burch, et al., 2016) missions have utilized computational methods to assess spacecraft charging effects with to analyze and develop correction relations for instrument data interpretation (Marchand et al., 2010; Barrie, et al., 2019). Importantly, these studies have demonstrated that thicker plasma sheaths tend to induce more distortions in particle trajectories. Therefore, spacecraft sheath effects are most pronounced in the low density, high temperature plasmas of the magnetosphere and are less pronounced in the high density, low temperature plasmas of the ionosphere (Marchand et al., 2010). Additionally, both Marchand et al. (2010) and Barrie et al. (2019) observed that spacecraft geometry, most notably spacecraft booms, produce asymmetrical spacecraft sheaths which cause additional trajectory perturbations. These previous studies have demonstrated the clear need for spacecraft charging corrections for all low-energy particle measurements intended for operation in the ionosphere to magnetosphere.

It is well established that our understanding of the terrestrial magnetosphere can be significantly advanced by flying suitable ion mass spectrometers. Ion mass spectrometers need to be designed for the appropriate energy range, be able to mitigate the effects of penetrating radiation, and have sufficient mass resolution to resolve at a minimum (O^+, H^+, He^+, N^+). If not operated in conjunction with active spacecraft potential control, it would be beneficial for the instrument to be mounted on a biasable panel or of such low-

TABLE 2 Performance specifications for representative state-of-the-art electron spectrometers.

Instrument	FOV	Energy range	ΔE/E	Geometric factor	Mass (kg)	Power W)	References
HOPE [ESA-TOF]	18° FW × 4.5 FWHM°	15 eV-50 keV	16% @ 1 eV	1.25 × 10^{-3} cm^2 sr @ 1 eV	18.06	18.2 (BOL), 23.0 (EOL)	Funsten, et al. (2013)
	5 pixels over 144°		12% @ 50 keV	1.3 × 10^{-3} cm^2 sr @ 50 keV			
LANL/MPA [ESA]	18° FW × 4.5 FWHM°	1 eV-40 keV	40%	5.74 × 10^{-4} cm^2 sr	3.6	3.5	Bame, (1993)
	5 pixels over 144°						
PEACE [ESA]	Polar 179.4°	0.7 eV-26 keV	12.7%	1.6 × 10^{-4} cm^2 sr	5.49	3.299	Johnstone, et al. (1997)
	Azimuthal 2.79°						
SWEPAM-E [ESA]	Polar 10°–170°	1.6 eV–1.35 keV	12%	2–7 × 10^{-4} cm^2 sr	2.5	2.7 (average)	McComas, Bame and Barker, et al. (1998)
	Azimuthal 9°–28°, spinning SC					2.9 (peak)	
THEMIS ESA [ESA]	i: 22.5°×22.5°, 4π str	i: 1.6 eV–25 keV	i: ~19%	i: 8.75 × 10^{-4} cm^2 sr keV/keV	2.96	1.7	Angelopoulos (2008); McFadden, et al., 2008
	e: 22.5° × 11.25.5°, 4π str	e: 2 eV–32 keV	e: ~17%	e: 3.13 × 10^{-4} cm^2 sr keV/keV			
DES-FPI [ESA]	Polar 180° Azimuth ±17°	i: 0.01–30 keV	i: 11%–15%	i: 1–2 × 10^{-4} cm^2 sr keV/keV	i: 6.21	i: 5.2	Pollock, et al., 2016
		e: 0.01–30 keV	e: 14%–20%	e: 1–7 × 10^{-4} cm^2 sr eV/eV	e: 5.87	e: 5.5	

resource constraints as to enable mounting on a boom outside of the spacecraft sheath. While the instruments described here and listed in Table 1 are advanced in both design and capability at the time of their build, the measurement sensitivity comes at a high cost that precludes them from missions operating under ever increasing fiscal constraints or for implementation as science payloads of large constellations required for ubiquitous multi-point space plasma measurements. Specifically, the ion mass spectrometers listed in Table 1 come with such high monetary costs that they cannot be used in large constellations without incurring an exorbitant mission cost.

3.1 Wake measurements

Engwall et al. (2009) have developed and validated a novel method to measure some properties of the cold ion populations using two different electric field measurements. This was demonstrated using the Electric Fields and Waves (EFW) (Gustafsson, et al., 1997) and the Electron Drift Instrument (EDI) (Paschmann, et al., 1997) payloads on-board the Cluster satellites. Positively charged spacecraft traveling through the magnetosphere develop an electron-rich environment in their wake due to the surrounding potential structure (Andre and Cully 2012). An enhanced wake forms if the bulk ion flow energy $mv_i^2/2$ exceeds the thermal energy KT_i but remains lower than the spacecraft potential, as shown below

$$KT_i < \frac{mv_i^2}{2} < e\Phi_{SC}. \tag{12}$$

As the wake becomes broader and increases in length, i.e., enhanced due to the positive spacecraft potential, the electron-rich volume develops a local wake field between the spacecraft and ambient plasma environment that can be measured by the EFW (Engwall et al., 2006b; Eriksson, et al., 2006). The EDI payloads measure the drift of artificial high-energy (keV) electrons that gyrate back to the spacecraft along the geophysical magnetic field. Since these electrons have gyroradii, on the order of kilometers, and the enhanced wake length scale is on the order of 100 km, the EDI measurements are not significantly affected by the enhanced wake (Eriksson, et al., 2006; André, et al., 2021). The wake electric field is then given by

$$E^W = E^{EFW} - E^{EDI}, \tag{13}$$

from which the flow velocity of the cold ions in the enhanced wake could be obtained. The derivation of the ion flow velocity calculation is described in detail by Engwall et al. (2009). A schematic of the enhanced wake is shown in Figure 4. With this method, Andre and Cully (2012) demonstrated that the cold ions are present in the magnetosphere 50%–70% of the time but were not detectable by standard, body-mounted particle instruments due to the ions' very low energy. Limitations of the wake method include: 1) inability to distinguish between ion species and charge state, 2) measurement is not possible during active spacecraft potential control, since it removes the wake signature, 3) sufficiently strong magnetic fields must be present to enable EDI measurements, 4) the wake must not be completely perpendicular to the spin plane, 5) the technique does not work with cold ions coexisting with hot plasma, as the energetic ions will fill the wake and cancel the electric field, and 6) this technique provides bulk property observations and does not measure particle distributions (Engwall et al., 2009). Additionally, the wake technique is more sensitive to lighter ions which due to their higher mobility tend to dominate the ion density throughout the enhanced wake (Haaland, et al., 2015).

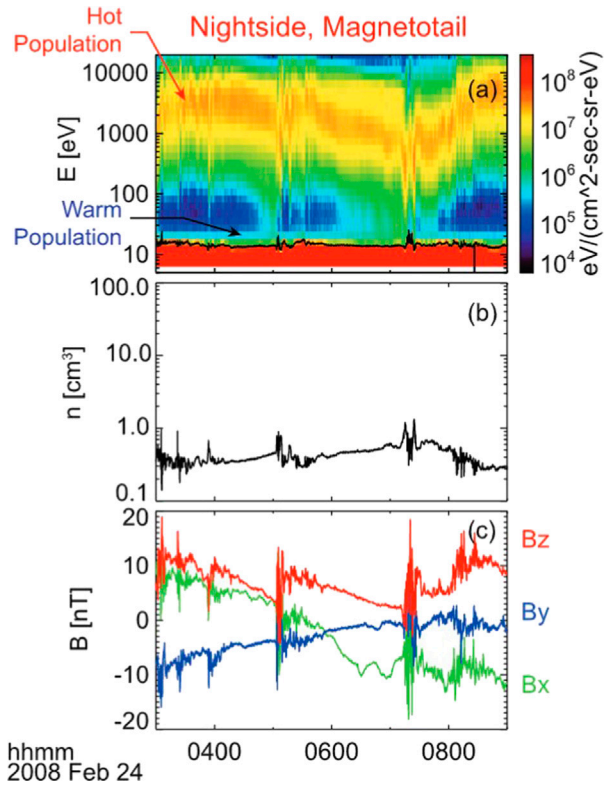

FIGURE 5
THEMIS D observations through the nightside magnetosphere of **(A)** electron energy spectra, **(B)** electron number density, and **(C)** magnetic field measurements in GSM coordinates. The spacecraft potential of ~10 V is indicated by the black line (Walsh, et al., 2020).

4 *In-situ* electron measurements

While the cold plasma populations of the magnetosphere have been termed a "hidden population", the cold electron populations have received even less attention when compared to the cold ion populations. This can largely be attributed to the challenges associated with the contaminating photoelectrons in combination with the effects of spacecraft charging. An overview of state-of-the-art plasma spectrometers for measuring electron populations in the magnetosphere is briefly presented in Table 2. These spectrometers are based on conventional spherical electrostatic analyzer (ESA) designs and have provided observations of electron energy spectra data in the magnetosphere to advance our understanding of Whistler anisotropy instabilities as the source of banded chorus (Fu, et al., 2014), the contribution of precipitating electrons to pulsating aurora (Miyosh, et al., 2015), and spacecraft charging effects (Thomsen et al., 2013; Sarno-Smith, et al., 2016). Again, these are but a few of the many scientific discoveries enabled by the electron spectrometers described in this section.

While the instruments in Table 2 have provided invaluable insights regarding the electron populations within the terrestrial magnetosphere, these instruments have made extremely limited observations of the cold electrons which often constitute the bulk of the magnetospheric plasma density. This is due in part to the effects of spacecraft potential but predominantly due to the difficulties associated with contamination of low-energy channels due to photoelectrons. The effects of spacecraft potential on the three-dimensional measurements of electron distributions in the solar wind were observed in the electron spectrometer data aboard the Ulysses spacecraft. It was observed that the electron distributions varied with the look angle of the instrument prompting the development of a correction factor to recover more gyrotropic distributions (Scime et al., 1994). The same effect is observed in the Solar Wind Electron Proton Alpha Monitor (SWEPAM) data which are subsequently corrected for spacecraft potential prior to dissemination to the broader space physics community (Koning, et al., 2006; Skoug, et al., 2006). It is important to note that the SWEPAM electron (SWEPAM-E) spectrometer is one of three nearly identical instruments flown, in chronological order, on the Ulysses (Bame et al., 1992), Advanced Composition Explorer (ACE) (McComas et al., 1998), and Genesis missions (Barraclough, et al., 2003). The initial observations of the Ulysses low-energy electron measurements near the spacecraft potential were identified as contaminated with photoelectrons (Bame et al., 1992) and subsequently the Genesis instrument avoided photoelectron contamination by setting the minimum measurable energy band at 61 eV (Barraclough, et al., 2003). The Los Alamos National Laboratory (LANL) Magnetospheric Plasma Analyzer (MPA) was also subject to background counts caused by photoelectrons believed to be created on nearby spacecraft surfaces within the instrument field-of-view (McComas et al., 1993). Further LANL/MPA observations concluded that the relatively high count rates at electron energies below 20 eV were caused by photoelectron contamination (McComas et al., 1993). The Plasma Electron And Current Experiment (PEACE) electron spectrometers (Johnstone, et al., 1997), on-board the Cluster satellites, also demonstrate that low-energy electron measurements (particularly below the spacecraft potential) are contaminated by photoelectrons and secondaries originating at the spacecraft (Chaston, et al., 2005). The Cluster satellites used active spacecraft potential control to reduce the potential to a few volts. However, the low-energy electron population below the controlled spacecraft potential could still not be differentiated from the contaminating background counts (Szita, et al., 2001).

More recent instruments include the HOPE on board the Van Allen Probes and the ESAs on board the Time History of Events and Macroscale Interactions during Substorms (THEMIS) and MMS satellites. The HOPE electron data go down to only 15 eV due to photoelectron contamination at the lowest energies (Goldstein et al., 2014). Note, the HOPE instrument is the only design capable of measuring the TOF of negatively charged particles, thus it can simultaneously measure electron and negative ion populations. During the in-flight calibration of the THEMIS ESA, the cold electron data with energies ~ $e\Phi_{SC}$ were avoided due to the difficulty associated with separating the photoelectron and cold electron populations (McFadden, et al., 2008). The THEMIS ESA data with spacecraft potential and contaminating photoelectron population are shown in Figure 5 (Walsh, et al., 2020). The Dual Electron Spectrometers (DES), designed for electron measurements to support the Fast Plasma Investigation (FPI) on-board the MMS satellites (C. Pollock, et al., 2016), have also been shown to be susceptible to photoelectron contamination. Therefore, the DES plasma moments are determined by excluding the electron energy ranges below the spacecraft potential (Gershman, et al., 2017).

In summary, cold electron measurements have been severely hindered by the inability to resolve ambient magnetospheric electrons from photoelectrons and this holds back our full understanding of the magnetosphere. Indeed, cold electrons play an important role in a variety of critical magnetospheric processes, including setting the ambipolar electric field and taking part in heating processes that drives some of the ionospheric outflow, controlling aspects of wave-particle interactions and magnetosphere-ionosphere

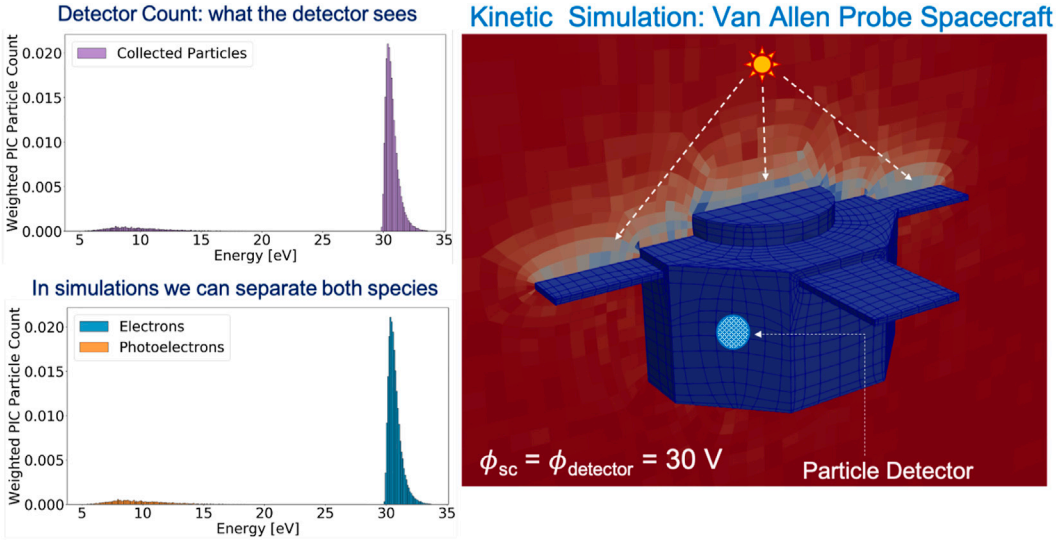

FIGURE 6
Kinetic simulation result: active spacecraft control enables cold-electron measurements. Cold-electron and photoelectron populations are clearly separated in detector signal as shown in the top-left panel and confirmed in the bottom-left panel. Simulation inputs: $\boldsymbol{n}$ = 13.5 cm^{-3}, $\boldsymbol{T_e}$ = **0.5 eV** $\boldsymbol{T_i}$ = 0.35 eV, $\boldsymbol{T_{ph}}$ = 2 eV and $\boldsymbol{J_{ph}}$ = 100 μA/m^2.

coupling (such as the structuring of the pulsating aurora) (Delzanno, et al., 2021). The following section will discuss viable techniques to allow for the measurement of the elusive cold electron population within the magnetosphere.

5 Techniques to measure cold plasmas in the magnetosphere

As discussed in Sections 3 and Section 4, there have been limited successes at measuring the cold ion populations but there are essentially no measurements of cold electrons. Outside of ionospheric sounding rocket missions and POLAR, there has yet to be a large magnetospheric spacecraft mission dedicated to measuring the source of both the low energy electron and ion particle populations robustly.

While there are challenges to making measurements of the cold magnetospheric ions and electrons, a number of viable techniques exist for cold ions that have been conducted for sounding rocket missions such as 1) mounting a low-resource (mass and volume) instrument on a boom (L. Brace 1998, C. J; Pollock, et al., 1996), and 2) biasing the electrostatic plasma spectrometer mounted to a boom or plate thus allowing for differential biasing of the instrument and/or spacecraft (Chappell, et al., 1981, C. J; Pollock, et al., 1996). Measuring cold ion bulk properties through the properties of the wake of the spacecraft (Engwall et al., 2009) has also been performed successfully, but this technique does not yield the full energy distributions.

5.1 Active spacecraft potential control for cold electron measurements

Based on the experience gained from past missions (Section 4) and assuming that the detector cannot be mounted on booms due to mass restrictions, a promising idea to enable robust cold-electron measurements by a particle detector, i.e. measuring the full distribution of the ambient low-energy electrons, is to use an electron beam to control the spacecraft potential. This concept of active spacecraft control is similar to the use of plasma contactors (Comfort, et al., 1998) used to make cold ion measurements. By using an electron beam, on the other hand, the spacecraft is biased positively with respect to the ambient plasma with the objective of mitigating/removing the photoelectron contamination in the detector signal to enable robust cold electron measurements. This concept idea has been demonstrated with kinetic simulations, shown in Figure 6, where the response of a particle detector mounted on a Van-Allen-Probes-type spacecraft (Mauk, et al., 2012) is again simulated using the first-principles model CPIC. The local plasma parameters and the spacecraft photoelectron properties are the same as those used for the results presented in Figure 3. In Figure 6, the whole spacecraft (including the detector) is biased to 30 V with respect to the ambient plasma. In this simulation the authors do not include an actual electron beam emitted by the spacecraft. Rather, we assume that the effects of the emission of a suitable electron beam are to charge the whole spacecraft to 30 V. By biasing the entire spacecraft to a sufficiently positive voltage, the cold ambient electrons are attracted and accelerated towards the particle detector. The photoelectrons generated at the spacecraft, on the other hand, are attracted back to the spacecraft due to the strong electric field near the spacecraft with the same energy at which these were born. In other words, in this configuration, photoelectrons do not experiment any acceleration due to the spacecraft potential control, only the cold background electrons do. This can be seen in the histograms in the top left panel and bottom left panel of Figure 6. Here, if the detector is in shade, as shown in the right panel of Figure 6, fewer photoelectrons will be able to reach it and the photoelectron particle count in the detector will be reduced drastically. Note that the few photoelectrons that reached the detector are some of those born with sufficient energy to overcome the spacecraft potential, or/and those that are born with oblique trajectories with

respect to the spacecraft surface at which these are generated. Nonetheless, by restoring the photoelectrons trajectories using active spacecraft control, and by positioning the particle detector away from the surfaces where photoelectron are generated, enables a robust way to clearly separate both species in the detector signal.

These results indicate that the full distribution of the magnetospheric cold particle populations, electrons and ions, can be measured using active spacecraft potential control and instrument biasing, respectively. However, by using these approaches, the effect of the electric field on the dynamics of the particles measured by the detector is enhanced drastically and are to be accounted for in the computation of the moments of the particle distributions. The parameters of the unperturbed plasma can be estimated using the Liouville theorem where the particle count measured by the detector (affected by the spacecraft electric field) is related to the distribution function of the unperturbed ambient plasma (Lavraud and Larson 2016). The caveat is that in this approximation, the sheath electric field depends on the geometry of the spacecraft, whether planar or spherical, and should be accounted for. Error estimation in the moments of the distribution due to dependence of the sheath electric field with spacecraft geometry is non-trivial. However, one way to estimate these is using kinetic simulations such as the ones presented in this paper. As for the uncertainties due to statistical errors, these can be computed as a covariance matrix using the approach presented in (Gershman, 2015). This approach is particularly useful for complex distribution functions and/or high order moments. For low-order moments, e. g, density, the uncertainty can simply scale as $\sim 1/\sqrt{\sum N}$ where N in the number of counts when a Maxwellian-Boltzmann distribution is assumed.

5.2 Low-resource instruments

Recent years have witnessed a tremendous growth in satellite constellations for scientific (Escoubet et al., 1997; Angelopoulos 2008; Burch, et al., 2016), commercial (Radtke et al., 2017; McDowell 2020), and government applications (Tournear 2020). Readily identifiable challenges with implementing a large or even mega-constellation of small satellites or CubeSats for scientific missions are: 1) the platforms need to be sophisticated enough that they can support quality sensors and subsystems while operating in the required space environments and 2) the sensors need to be reduced in size, weight, volume, and cost while still having the ability to make the appropriate measurements. The first topic includes the platform ability to support mission requirements such as power generation, pointing accuracy of attitude dynamics and control systems (ADCS), along with the ability to survive and operate in the natural space radiation environment. The survivability issue is a difficult task as the mass and volume constraints of these vehicles present considerable challenges in terms of supporting radiation shielding. However, engineering solutions such as appropriate electronics part selection, spot shielding, and software techniques to mitigate single-event-effects (SEUs) offer attractive engineering solutions for CubeSat missions targeting environments beyond low-Earth orbit (Klesh, et al., 2018; Blum et al., 2020; Maldonado et al., 2022).

As the space physics community has developed a growing interest in the benefits of CubeSat missions, with their ability to provide multiple spatial and temporal measurements at a reduced cost, there has been an increased focus on the development of miniaturized instruments. Historically, instrument design has been guided by the philosophy of "build to performance". However, the current fiscal environment of ever dwindling budgets coupled with expanding CubeSat opportunities has revitalized the demand for low-resource instruments that can yield relevant science return (Funsten and McComas 1998; Young 1998; MacDonald et al., 2009; Fernandes et al., 2019). This interest, combined with advances in microelectromechanical systems (MEMS) have enabled the rapid increase in the number of miniaturized plasma analyzers with flight heritage (Maldonado, et al., 2019; Maldonado, et al., 2020a). Examples include retarding potential analyzers (RPA) (Fanelli, et al., 2015), laminated electrostatic analyzers (Maldonado, et al., 2020b; Maldonado et al., 2020c), ion mass spectrometers (Nordholt, et al., 2003; Kepko, et al., 2017; Ogasawara, et al., 2020), and traditional spherical analyzers (MacDonald et al., 2006).

These low-resource instruments have the potential to be mounted to booms outside of the spacecraft potential sheath. As has been done on sounding rockets, it would be advantageous to use a low-resource ion mass spectrometer or plasma spectrometer to enable the instrument to be mounted to a boom and biased or swept, positive or negative depending on the target population of interest, thus mitigating the effects of spacecraft potential and enabling greatly improved cold magnetospheric plasma measurements. Alternatively, a low-resource or traditional plasma spectrometer can be mounted to a biasable plate which can be differentially biased with respect to the spacecraft potential. This bias can be set to a sufficiently large positive or negative voltage thus creating a pathway for cold ions through the spacecraft potential sheath to the detector aperture. Additionally, a large constellation of CubeSats equipped with plasma spectrometers have the potential to provide multi-point simultaneous *in-situ* low energy measurements of ionospheric outflow and cold magnetospheric plasma. These data would enable closure of important science questions regarding the source of magnetospheric plasma, magnetosphere-ionosphere coupling, mass loading of the magnetosphere, magnetic reconnection, and with wave-particle interactions (Zurbuchen and Gershman 2016). The challenge remains for low-resource instruments operating within the deep inner magnetosphere to mitigate the effects penetrating radiation which can potentially obscure observations of low-energy ions and electrons (Denton, et al., 2017).

5.3 Other techniques

Due to the inherent difficulties associated with direct measurement of the low-energy ion and electron populations, alternative methods have been implemented to aid in indirect measurements beyond the wake technique (Walsh, et al., 2020). These additional methods include using the spacecraft potential to derive electron density (Escoubet, et al., 1997b; Pedersen, et al., 2008; Andriopoulou, et al., 2016) and standing Alfvén waves (Chi and Russell 2005; Takahashi, et al., 2014) along with limiting observations to periods when the bulk flow exceeds the spacecraft velocity (Lee and Angelopoulos 2014). As an example of the latter, the low-energy ion observations made using the Orbiting Geophysical Observatory 5 (OGO 5) ion spectrometer relied on the spacecraft velocity to raise the relative energy of cold ions past the potential barrier (Harris et al., 1970; Serbu and Maier 1970).

Remote sensing techniques such as radio tomography and EUV imaging have the potential to advance our understanding of global and regional scale phenomena pertaining to ionospheric outflow, erosion and refilling of the plasmasphere, along with subsequent redistribution of mass through the magnetosphere (Malaspina, et al., 2022). The radio tomography technique utilizes space-based radio receivers and transmitters to measure total electron content along line of sight between receiver-transmitter pairs which can then be used to produce two-dimensional images of plasma density (Ergun, et al., 2000). The EUV imaging technique utilizes optical cameras to detect resonantly-scattered emissions to capture light and heavy ion population densities for observations of global and mesoscale refilling dynamics (Sandel, et al., 2000).

While bulk parameters or densities can be obtained using remote and indirect measurements or even spacecraft potential, the full distributions of the cold ion and cold electron populations are required to close science questions related to the microphysics of individual flux tubes such as ion trapping, heating, and transport (Goldstein et al., 2021).

6 Conclusion

In-situ cold ion and cold electron measurements are key to understand the dynamics of the Earth magnetosphere. There are two main challenges to overcome to achieve the measuring of the full particle distribution of the cold plasma populations in the magnetosphere: spacecraft potential and contamination of low-energy spacecraft-generated electrons in the particle detector.

Cold ion and electron measurements are both affected by the sheath electric field on and surrounding the spacecraft which alters the trajectories of the particle measured by a detector. Depending on the polarity at which the spacecraft charges with respect to the ambient plasma, which depends on the environment and spacecraft materials, some plasma species will be attracted and some other repelled. For the repelled species, depending on the mean energy compared to the spacecraft potential, the particle distribution will be partially measured. In this case the full distribution can be approximated by extrapolating from the measured, truncated distribution. This approach, however, could yield large uncertainties in the parameter estimation. As for the attracted species, the problem comes from accounting for the acceleration that measured particles experiment inside the spacecraft sheath. It is mandatory to correct for the spacecraft potential effect on the particle counts to accurately estimate the plasma moments that characterize the unperturbed magnetospheric cold plasma. Given the complex spacecraft geometries on which the structure of the sheath depends, this is a challenging task.

On the other hand, the contamination of low-energy spacecraft-generated electrons only affects the cold electron measurements. Because the cold electrons and the spacecraft-generated electrons can have similar energies (a few eV), it is very difficult to distinguish one species from the other in the detector particle count. Moreover, the density of the spacecraft-generated electrons can be orders of magnitude larger than the density of magnetospheric cold electrons resulting in a complete masking of the ambient electron signal. This is the main reason why cold electron measurements of the lowest energies have not been accomplished yet.

Fortunately, there are promising techniques to enable robust cold ion and cold electron measurements in the Earth's magnetosphere. Those discussed herein include, active spacecraft potential control, biasing of aperture surfaces, and low-resource instruments mounted to booms. Each of these methods have been demonstrated sparsely in space and some have been supported by numerical simulations. One possibility to measure the full ion distribution is to use differential biasing of the detector and mounting face to a sufficiently negative voltage with respect to the ambient plasma. This will eliminate any potential barrier due to the spacecraft sheath, giving free access for the cold ions to reach the detector. As for the cold electron measurements, this can be achieved by active spacecraft potential control realized by an electron beam. By biasing the entire spacecraft to sufficiently positive voltage, the spacecraft-generated electrons are clearly differentiated from the ambient cold electron signal in the detector count. Note that although these approaches (differential biasing for ions and active spacecraft potential control for electrons) enable robust measurement of the full particle distributions, the effect of the spacecraft sheath in the particle counts still needs to be corrected in order to compute accurate ambient plasma parameters.

In a complex system of interconnected parts like the Earth's magnetosphere, a lack of understanding of one part of the system (the cold electron and ion populations) is disabling. Hence, until cold electron and cold ion measurements are obtained robustly with every mission, the magnetospheric plasma environment cannot be completely understood.

Author contributions

All authors listed have made a substantial, direct, and intellectual contribution to the work and approved it for publication.

Funding

This work was funded through the Los Alamos National Laboratory (LANL) Laboratory Directed Research and Development–Exploratory Research (LDRD-ER) Project Number 20220453ER. LANL is operated by Triad National Security, LLC, for the National Nuclear Security Administration of U.S. Department of Energy (DOE) (Contract No. 89233218CNA000001).

Acknowledgments

The research conducted at Los Alamos National Laboratory was under the auspices of the Department of Energy.

Conflict of interest

The authors declare that the research was conducted in the absence of any commercial or financial relationships that could be construed as a potential conflict of interest.

Publisher's note

References

Andre, M. (2015). Previously hidden low-energy ions: A better map of near-earth space and the terrestrial mass balance. *Phys. Scr.* 90, 128005. doi:10.1088/0031-8949/90/12/128005

Andre, M., and Cully, C. M. (2012). Low-energy ions: A previously hidden solar system particle population. *Geophys. Res. Lett.* 39, L03101. doi:10.1029/2011GL050242

André, M., Eriksson, A. I., Khotyaintsev, Y. V., and Toledo-Redondo, S. (2021). The spacecraft wake: Interference with electric field observations and a possibility to detect cold ions. *J. Geophys. Res. Space Phys.* 126, e2021JA029493. doi:10.1029/2021JA029493

Andriopoulou, M., Nakamura, R., Torkar, K., Baumjohann, W., Torbert, R. B., Lindqvist, P.-A., et al. (2016). Study of the spacecraft potential under active control and plasma density estimates during the MMS commissioning phase. *Geophys. Res. Lett.* 43, 4858–4864. doi:10.1002/2016GL068529

Angelopoulos, V. (2008). The THEMIS mission. *Space Sci. Rev.* 141, 5–34. doi:10.1007/s11214-008-9336-1

Baker, D. N. (2021). Wave–particle interaction effects in the Van Allen belts. *Earth, Planets, Space* 73, 189. doi:10.1186/s40623-021-01508-y

Bame, S. J., Hundhausen, A. J., Asbridge, J. R., and Strong, I. B. (1968). Solar wind ion composition. *Phys. Rev. Lett.* 20 (8), 393–395. doi:10.1103/PhysRevLett.20.393

Bame, S. J., McComas, D. J., Barraclough, B. L., Phillips, J. L., Sofaly, K. J., Chavez, J. C., et al. (1992). The Ulysses solar wind plasma experiment. *Astronomy Astrophysics Suppl. Ser.* 92, 237–265.

Bame, S. J., McComas, D. J., Thomsen, M. F., Barraclough, B. L., Elphic, R. C., Glore, J. P., et al. (1993). Magnetospheric plasma analyzer for spacecraft with constrained resources. *Rev. Sci. Instrum.* 64, 1026–1033. doi:10.1063/1.1144173

Barakat, A., and Schunk, R. (2001). Effects of wave-particle interactions on the dynamic behavior of the generalized polar wind. *J. Atmos. Solar-Terrestrial Phys.* 63, 75–83. doi:10.1016/S1364-6826(00)00106-1

Barghouthi, I. A., Barakat, A. R., and Persoon, A. M. (1998). The effects of altitude-dependent wave particle interactions on the polar wind plasma. *Astrophysics Space Sci.* 259, 117–140. doi:10.1023/A:1001569207346

Barraclough, B. L., Dors, E. E., Abeyta, R. A., Alexander, J. F., Ameduri, F. P., Baldonado, J. R., et al. (2003). The plasma ion and electron instruments for the Genesis mission. *Space Sci. Rev.* 105, 627–660. doi:10.1023/A:1024426112422

Barrie, A. C., Cipriani, F., Escoubet, C. P., Toledo-Redondo, S., Nakamura, R., Torkar, K., et al. (2019). Characterizing spacecraft potential effects on measured particle trajectories. *Phys. Plasma* 26, 103504. doi:10.1063/1.5119344

Blum, L. W., and Breneman, A. W. (2019). "Observations of radiation belt losses due to cyclotron wave-particle interactions," in *The dynamic loss of earth's radiation belts*. Editors A. N. Jaynes and M. E. Usanova (Amsterdam, Netherlands: Elsevier), 49–98. doi:10.1016/B978-0-12-813371-2.00003-2

Blum, L. W., Kepko, L., Turner, D., Gabrielse, C., Jaynes, A., Kanekal, S., et al. (2020). "The GTOSat CubeSat: Scientific objectives and instrumentation proceedings volume 11389," in *Micro- and nanotechnology sensors, systems, and applications XII* (Washington, United States: SPIE).

Blum, L. W., MacDonald, E. A., Gary, S. P., Thomsen, M. F., and Spence, H. E. (2009). Ion observations from geosynchronous orbit as a proxy for ion cyclotron wave growth during storm times. *J. Geophys. Res. Space Phys.* 114, A10214. doi:10.1029/2009JA014396

Borovsky, J. E., Denton, M. H., Denton, R. E., Jordanova, V. K., and Krall, J. (2013). Estimating the effects of ionospheric plasma on solar wind/magnetosphere coupling via mass loading of dayside reconnection: Ion-plasma-sheet oxygen, plasmaspheric drainage plumes, and the plasma cloak. *J. Geophys. Res. Space Phys.* 118, 5695–5719. doi:10.1002/jgra.50527

Borovsky, J. E., Hesse, M., Birn, J., and Kuznetsova, M. M. (2008). What determines the reconnection rate at the dayside magnetosphere? *J. Geophys. Res.* 113, A07210. doi:10.1029/2007JA012645

Bortnik, J., Thorne, R. M., and Meredith, N. P. (2008). The unexpected origin of plasmaspheric hiss from discrete chorus emissions. *Nature* 452, 62–66. doi:10.1038/nature06741

Brace, L. H. (1998). Langmuir probe measurements in the ionosphere. *Geophys. Monograph-American Geophys. Union* 102, 23–26.

Brace, L. H., Reddy, B. M., and Mayr, H. G. (1967). Global behavior of the ionosphere at 1000-kilometer altitude. *J. Geophys. Res.* 72, 265–283. doi:10.1029/JZ072i001p00265

Bruining, H. (2016). *Physics and applications of secondary electron emission*. London: Pergamon Science Series: Electronics and Waves—a Series of Monographs.

Burch, J. L., Moore, T. E., Torbert, R. B., and Giles, B. L. (2016). Magnetospheric Multiscale overview and science objectives. *Space Sci. Rev.* 199, 5–21. doi:10.1007/s11214-015-0164-9

Carpenter, D. L. (1962). Electron-density variations in the magnetosphere deduced from whistler data. *J. Geophys. Res.* 67, 3345–3360. doi:10.1029/JZ067i009p03345

Cassak, P. A., and Shay, M. A. (2007). Scaling of asymmetric magnetic reconnection: General theory and collisional simulations. *Phys. Plasmas* 14, 102114. doi:10.1063/1.2795630

Chandra, S., Maier, E. J., and Stubbe, P. (1972). The upper atmosphere as aregulator of subauroral red arcs. *Planet. Space Sci.* 20 (4), 461–472. doi:10.1016/0032-0633(72)90078-5

Chandra, S., Maier, E. J., Troy, B. E., Jr., and Narasinga Rao, B. C. (1971). Subauroral red arcs and associated ionospheric phenomena. *J. Geophys. Res.* 76, 920–925. doi:10.1029/JA076i004p00920

Chappell, C. R., Fields, S., Baugher, C., Hoffman, J., Hanson, W., Wright, W., et al. (1981). *The retarding ion mass spectrometer on dynamics Explorer-A*. United States: Marshall Space Flight Center, 447. NASA-TM-82418.

Chappell, C. R., Huddleston, M. M., Moore, T. E., Giles, B. L., and Delcourt, D. C. (2008). Observations of the warm plasma cloak and an explanationof its formation in the magnetosphere. *J. Geophys. Res.* 113, A09206. doi:10.1029/2007ja012945

Chappell, C. R. (1982). Initial observations of thermal plasma composition and energetics from Dynamics Explorer-1. *Geophys. Res. Lett.* 9, 929–932. doi:10.1029/gl009i009p00929

Chappell, C. R. (1988). The terrestrial plasma source' A new perspective in solar-terrestrial processes from dynamics explorer. *Rev. Geophys.* 26, 229–248. doi:10.1029/RG026i002p00229

Chaston, C. C., Peticolas, L. M., Carlson, C. W., McFadden, J. P., Mozer, F., Wilber, M., et al. (2005). Energy deposition by Alfvén waves into the dayside auroral oval: Cluster and FAST observations. *J. Geophys. Res. Space Phys.* 110 (A2), A02211. doi:10.1029/2004JA010483

Chen, L., Thorne, R. M., and Bortnik, J. (2011). The controlling effect of ion temperature on EMIC wave excitation and scattering. *Geophys. Res. Lett.* 38, L16109. doi:10.1029/2011GL048653

Chi, P. J., and Russell, C. T. (2005). Travel-time magnetoseismology: Magnetospheric sounding by timing the tremors in space. *Geophys. Res. Lett.* 32, L18108. doi:10.1029/2005GL023441

Cohen, I. J., Widholm, M., Lessard, M. R., Riley, P., Heavisides, J., Moen, J. I., et al. (2016). Rocket-borne measurements of electron temperature and density with the Electron Retarding Potential Analyzer instrument. *J. Geophys. Res. Space Phys.* 121, 6774–6782. doi:10.1002/2016JA022562

Comfort, R. H., Craven, P. D., Gallagher, D. L., West, R. L., and Chappell, C. R. (1988). Spacecraft potential dependence on plasma density from GEOS-2 and DE-1 measurements. *Eos, Trans. Am. Geophys. Union* 69, 448.

Comfort, R. H., Moore, T. E., Craven, P. D., Pollock, C. J., Mozer, F. S., and Williamson, W. S. (1998). Spacecraft potential control by the plasma source instrument on the POLAR satellite. *J. Spacecr. Rockets* 35 (6), 845–849. doi:10.2514/2.7586

Comfort, R. H., Waite, J. H., and Chappell, C. R. (1985). Thermal ion temperatures from the retarding ion mass spectrometer on DE 1. *J. Geophys. Res.* 90 (A4), 3475–3486. doi:10.1029/JA090iA04p03475

Cully, C. M., Donovan, E. F., Yau, A. W., and Arkos, G. G. (2003). Akebono/Suprathermal Mass Spectrometer observations of low-energy ion outflow: Dependence on magnetic activity and solar wind conditions. *J. Geophys. Res. Space Phys.* 108, 1093. doi:10.1029/2001JA009200

de Soria-Santacruz, M., Spasojevic, M., and Chen, L. (2013). EMIC waves growth and guiding in the presence of cold plasma density irregularities. *Geophys. Res. Lett.* 40, 1940–1944. doi:10.1002/grl.50484

DeForest, S. E. (1972). Spacecraft charging at synchronous orbit. *J. Geophys. Res.* 77 (4), 651–659. doi:10.1029/JA077i004p00651

Delzanno, G. L., Henderson, M. G., Borovsky, J. E., Lira, P. A. R., Roytershteyn, V., and Welling, D. T. (2021). The impact of cold electrons and cold ions in magnetospheric physics. *J. Atmos. Solar-Terrestrial Phys.* 220, 105599. doi:10.1016/j.jastp.2021.105599

Denton, M. H., Reeves, G. D., Larsen, B. A., Friedel, R. H. W., Thomsen, M. F., Ffernandes, P. A., et al. (2017). On the origin of low-energyelectrons in the inner magnetosphere:Fluxes and pitch-angle distributions. *J. Geophys. Res. Space Phys.* 122, 1789–1802. doi:10.1002/2016JA023648

Denton, M. H., Thomsen, M. F., Jordanova, V. K., Henderson, M. G., Borovsky, J. E., Denton, J. S., et al. (2015). An empirical model of electron and ion fluxes derived from observations at geosynchronous orbit. *Space weather.* 13 (4), 233–249. doi:10.1002/2015sw001168

Dimmock, A. P., and Nykyri, K. (2013). The statistical mapping of magnetosheath plasma properties based on THEMIS measurements in the magnetosheath interplanetary medium reference frame. *J. Geophys. Res. Space Phys.* 118, 4963–4976. doi:10.1002/jgra.50465

Dunckel, N., and Helliwell, R. A. (1969). Whistler-mode emissions on the OGO 1 satellite. *J. Geophys. Res.* 74, 6371–6385. doi:10.1029/JA074i026p06371

Eliasson, L., Andre, M., Eriksson, A., Norqvist, P., Norberg, O., Lundin, R., et al. (1994). Freja observations of heating and precipitation of positive ions. *Geophys. Res. Lett.* 21, 1911–1914. doi:10.1029/94GL01067

Engwall, E., Eriksson, A. I., Andre, M., Dandouras, I., Paschmann, G., Quinn, J., et al. (2006a). Low-energy (order 10 eV) ion flow in the magnetotail lobes inferred from spacecraft wake observations. *Geophys. Res. Lett.* 33, L06110. doi:10.1029/2005GL025179

Engwall, E., Eriksson, A. I., Cully, C. M., Andre, M., Puhl-Quinn, P. A., Vaith, H., et al. (2009). Survey of cold ionospheric outflows in the magnetotail. *Ann. Geophys.* 27, 3185–3201. doi:10.5194/angeo-27-3185-2009

Engwall, E., Eriksson, A. I., and Forest, J. (2006b). Wake formation behind positively charged spacecraft in flowing tenuous plasmas. *Phys. Plasmas* 13, 062904. doi:10.1063/1.2199207

Ergun, R. E., Larson, D. E., Phan, T., Taylor, D., Bale, S., Carlson, C. W., et al. (2000). Feasibility of a multisatellite investigation of the Earth's magnetosphere with radio tomography. *J. Geophys. Res.* 105, 361–373. doi:10.1029/1999JA900170

Eriksson, A. I., Andre, M., Klecker, B., Laakso, H., Lindqvist, P.-A., Mozer, F., et al. (2006). Electric field measurements on cluster: Comparing the double-probe and electron drift techniques. *Ann. Geophys.* 24, 275–289. doi:10.5194/angeo-24-275-2006

Escoubet, C. P., Pedersen, A., Schmidt, R., and A Lindqvist, P. (1997b). Density in the magnetosphere inferred from ISEE 1 spacecraft potential. *J. Geophys. Res.* 102 (A8), 17595595609. doi:10.1029/97JA00290

Escoubet, C. P., Schmidt, R., and Goldstein, M. L. (1997). "Cluster - science and mission overview," in *The cluster and phoenix missions. Schmidt*. Editors C. P. Escoubet and C. T. Russell, (Dordrecht: Springer), 11–32. doi:10.1007/978-94-011-5666-0_1

Escoubet, P., Masson, A., Laakso, H., and Goldstein, M. L. (2020). "Cluster mission's recent highlights at dayside boundaries," in *Dayside magnetosphere interactions*. Editors Q. Zong, P. Escoubet, D. Sibeck, G. Le, and H. Zhang (Hoboken, NJ: AGU Monograph Series, John Wiley & Sons), 99–115. doi:10.1002/9781119509592.ch6

Fanelli, L., Noel, S., Earle, G. D., Fish, C., Davidson, R. L., Robertson, R. V., et al. (2015). A versatile retarding potential analyzer for nano-satellite platforms. *Rev. Sci. Instrum.* 86, 124501. doi:10.1063/1.4937622

Feldman, W. C., Asbridge, J. R., Bame, S. J., and Montgomery, M. D. (1974). Interpenetrating solar wind streams. *Rev. Geophys. Space Phys.* 12 (4), 715–723. doi:10.1029/rg012i004p00715

Ferguson, D. C., Hilmer, R. V., and Davis, V. A. (2015). Best geosynchronous Earth orbit daytime spacecraft charging index. *J. Spacecr. Rockets* 52 (2), 526–543. doi:10.2514/1.A32959

Fernandes, P. A., Funsten, H. O., E> Dors, E., Larsen, R. W., Harper, B. A., MacDonald, E. A., et al. (2019). Low-resource technique for measurement of H+ and O+ in the terrestrial magnetosphere. *J. Geophys. Res.:Space Phys.* 124, 9137–9153. doi:10.1029/2019JA027138

Fernandes, P. A., Larsen, B. A., Thomsen, M. F., Skoug, R. M., Reeves, G. D., Denton, M. H., et al. (2017). The plasma environment inside geostationary orbit: A van allen probes HOPE survey. *J. Geophys. Res.* 122, 9207–9227. doi:10.1002/2017JA024160

Fernandes, P. A., Lynch, K. A., Zettergren, M., Hampton, D. L., Bekkeng, T. A., Cohen, I. J., et al. (2016). Measuring the seeds of ion outflow: Auroral sounding rocket observations of low-altitude ion heating and circulation. *J. Geophys. Res. Space Phys.* 121, 1587–1607. doi:10.1002/2015JA021536

Fraser, B. J., Horwitz, J. L., Slavin, J. A., Dents, Z. C., and Mann, I. R. (2005). Heavy ion mass loading of the geomagnetic field near the plasmapause and ULF wave implications. *J. Gephys. Res.* 32, L04102. doi:10.1029/2004GL021315

Fraunberger, M., Lynch, K. A., Clayton, R., Roberts, T. M., Hysell, D., Lessard, M., et al. (2020). Auroral ionospheric plasma flow extraction using subsonic retarding potential analyzers. *Rev. Sci. Instrum.* 91, 094503. doi:10.1063/1.5144498

Frederick-Frost, K. M., Lynch, K. A., Jr., Kintner, P. M., Klatt, E., Lorentzen, D., Moen, J., et al. (2007). Sersio: Svalbard EISCAT rocket study of ion outflows. *J. Geophys. Res.* 112, A08307. doi:10.1029/2006JA011942

Friis-Christensen, E., Luhr, H., Knudsen, D., and Haagmans, R. (2008). Swarm - an Earth observation mission investigating geospace. *Adv. Space Res.* 41 (1), 210–216. doi:10.1016/j.asr.2006.10.008

Fu, X., Cowee, M. H., Reinhard, R. H., Friedel, H., Funsten, H. O., Peter Gary, S. P., et al. (2014). Whistler anisotropy instabilities as the source of banded chorus: Van Allen Probes observations and particle-in-cell simulations. *J. Geophys. Res. Space Phys.* 119 (10), 8288–8298. doi:10.1002/2014JA020364

Funsten, H. O., and McComas, D. J. (1998). "Limited resource plasma analyzers: Miniaturization concepts," in *Measurement techniques in space plasmas: Particles*. Editors R. F. Pfaff, J. E. Borovsky, and D. T. Young (Washington, DC: AGU Monograph Series), 157–167.

Funsten, H. O., Skoug, R. M., Guthrie, A. A., MacDonald, E. A., Baldonado, J. R., Harper, R. W., et al. (2013). Helium, oxygen, proton, and electron (HOPE) mass spectrometer for the radiation belt storm probes mission. *Space. Sci. Rev.* 179, 423–484. doi:10.1007/s11214-013-9968-7

Fuselier, S. A., Burch, J. L., Cassak, P. A., Goldstein, J., Gomez, R. G., Goodrich, K., et al. (2016). Magnetospheric ion influence on magnetic reconnection at the duskside magnetopause. *Geophys. Res. Lett.* 43, 1435–1442. doi:10.1002/2015GL067358

Fuselier, S. A., Mukherjee, J., Denton, M. H., Petrinec, S. M., Trattner, K. J., Toledo-Redondo, S., et al. (2019b). High-density O+in Earth's outer magnetosphere and its effect on dayside magnetopause magnetic reconnection. *J. Geophys. Res. Space Phys.* 124 (10), 10257–10269. doi:10.1029/2019JA027396

Fuselier, S. A., Trattner, K. J., Petrinec, S. M., Denton, M. H., Toledo-Redondo, S., André, M., et al. (2019a). Mass loading the Earth's dayside magnetopause boundary layer and its effect on magnetic reconnection. *Geophys. Res. Lett.* 46, 6204–6213. doi:10.1029/2019GL082384

Garrett, H. B., and Whittlesey, A. C. (2012). *Guide to mitigating spacecraft charging effects*. Hoboken, NJ: Wiley.

Geiss, J., Gloeckler, G., and von Steiger, R. (1995). Origin of the solar wind from composition data. *Space Sci. Rev.* 72, 49–60. doi:10.1007/BF00768753

Genestreti, K. J., Goldstein, J., Corley, G. D., Farner, W., Kistler, L. M., Larsen, B. A., et al. (2017). Temperature of the plasmasphere from van allen probes HOPE. *J. Geophys. Res. Space Phys.* 122, 310–323. doi:10.1002/2016JA023047

Gershman, D. J., Avanov, L. A., Boardsen, S. A., Dorelli, J. C., Gliese, U., Barrie, A. C., et al. (2017). Spacecraft and instrument photoelectrons measured by the dual electron spectrometers on MMS. *J. Geophys. Res. Space Phys.* 122, 11548–11558. doi:10.1002/2017JA024518

Glocer, A., Khazanov, G., and Liemohn, M. (2017). Photoelectrons in the quiet polar wind. *J. Geophys. Res.* 122, 6708–6726. doi:10.1002/2017JA024177

Goldstein, J., De Pascuale, S., Kletzing, C., Kurth, W., Genestri, K. J., Skoug, R. M., et al. (2014). Simulation of van allen probes plasmapause encounters. *J. Geophys. Res. Space Phys.* 119, 7464–7484. doi:10.1002/2014JA020252

Goldstein, J., Molymeux, D. L., and Reeves, G. (2021). *Core-plasma refilling and erosion: Science justification."* heliophysics 2050 white papers. NASA Heliophysics Division.

Grard, R. J. (1973). Properties of the satellite photoelectron sheath derived from photoemission laboratory measurements. *J. Geophys. Res.* 78 (16), 2885–2906. doi:10.1029/JA078i016p02885

Gustafsson, G., Bostrom, R., Holback, B., Holmgren, G., Lundgren, A., Stasiewicz, K., et al. (1997). The electric field and wave experiment for the cluster mission. *Space Sci. Rev.* 79, 137–156. doi:10.1023/A:1004975108657

Haaland, S., Eriksson, A., André, M., Maes, L., Baddeley, L., Barakat, A., et al. (2015). Estimation of cold plasma outflow during geomagnetic storms. *J. Geophys. Res. Space Phys.* 120, 639. doi:10.1002/2015JA021810

Harris, K., Sharp, G., and Chappell, C. R. (1970). Observations of the plasmapause from OGO 5. *J. Geophys. Res.* 116, 219–224. doi:10.1029/JA075i001p00219

Hartley, D. P., Kletzing, C. A., Santolík, O., Chen, L., and Horne, R. B. (2018). Statistical properties of plasmaspheric hiss from van allen probes observations. *J. Geophys. Res. Space Phys.* 123, 2605–2619. doi:10.1002/2017JA024593

Hasegawa, H., Fujimoto, M., Phan, T.-D., Reme, H., Balogh, A., Dunlop, M. W., et al. (2004). Transport of solar wind into Earth's magnetosphere through rolled-up Kelvin–Helmholtz vortices. *Nature* 430, 755–758. doi:10.1038/nature02799

Ho, C. W., Horwitz, J. L., and Moore, T. E. (1994). DE1 observations of polar O⁺stream bulk parameters and comparison with a model of the centrifugally-accelerated polar wind. *Geophys. Res. Lett.* 21 (23), 2459–2462. doi:10.1029/94GL02340

Ho, C. W., and Horwitz, J. L. (1993). Warm O+ polar wind and the DE-1 polar cap electron density profile. *Geophys. Res. Lett.* 20, 1715–1717. doi:10.1029/93GL01980

Ilie, R., and Liehohn, M. W. (2016). The outflow of ionospheric nitrogen ions: A possible tracer for the altitude-dependent transport and energization processes of ionospheric plasma. *J. Geophys. Res. Space Phys.* 121, 9250–9255. doi:10.1002/2015JA022162

Johnstone, A. D., Burge, S., Carter, P. J., Coates, A. J., Coker, A. J., Fazakerley, A. N., et al. (1997). "Peace: A plasma electron and current experiment,". Editors C. P. Escoubet, C. T. Russell, and R. Schmidt (Dordrecht: Springer), 79, 351–398. doi:10.1007/978-94-011-5666-0_13*Clust. Phoenix Missions*

Kepko, L., Clagett, C., Santos, L., Azimi, B., Berry, D., Chai, T., et al. (2017.Dellingr: NASA goddard space flight center's first 6U spacecraft, Proceedings of the 31st AIAA/USU Small Satellite Conference, Logan, UT, August 5–10: Utah State University .

Khazanov, G. V., Liemohn, M. W., and Moore, T. E. (1997). Photoelectron effects on the self-consistent potential in the collisionless polar wind. *J. Geophys. Res.* 102, 7509–7521. doi:10.1029/96JA03343

Khazanov, G. V., Nagy, A. F., Gombosi, T. I., Koen, M. A., and Cariglia, S. J. (1992). Analytic description of the electron temperature behavior in the upper ionosphere and plasmasphere. *Geophys. Res. Lett.* 19, 1915–1918. doi:10.1029/92GL01940

Kitamura, N., Ogawa, Y., Nishimura, Y., Terada, N., Ono, T., Shinbori, A., et al. (2011). Solar zenith angle dependence of plasma density and temperature in the polar cap

ionosphere and low altitude magnetosphere during geomagnetically quiet periods at solar maximum. *J. Geophys. Res. Space Phys.* 116, A08227. doi:10.1029/2011JA016631

Kitamura, N., Seki, K., Nishimura, Y., Terada, N., Ono, T., Hori, T., et al. (2012). Photoelectron flows in the polar wind during geomagnetically quiet periods. *J. Geophys. Res. Space Phys.* 117, A07214. doi:10.1029/2011JA017459

Klesh, A., Clement, B., Colley, C., Essmiller, J., Forgette, D., Krajewski, J., et al. (2018).MarCO: Early operations of the first CubeSats to mars. 32nd Annual AIAA/USU Conference on Small Satellites. 4th – 9th August 2018, Utah, USA (Logan, UT: AIAA/USU), 1–6 .

Knudsen, D. J., Burchill, J. K., Cameron, T. G., Enno, G. A., Howarth, A., and Yau, A. W. (2015). The CASSIOPE/e-POP suprathermal electron imager (SEI). *Space. Sci. Rev.* 189, 65–78. doi:10.1007/s11214-015-0151-1

Knudsen, W. C. (1966). Evaluation and demonstration of the use of retarding potential analyzers for measuring several ionospheric quantities. *J. Geophys. Res.* 71 (19), 4669–4678. doi:10.1029/JZ071i019p04669

Koning, C. A., Gosling, J. T., Skoug, R. M., and Steinberg, J. T. (2006). Widths of suprathermal pitch angle distributions during solar electron bursts: ACE observations. *J. Geophys. Res.* 111, A04101. doi:10.1029/2005ja011326

Kotova, G. A. (2007). The Earth's plasmasphere: State of studies (a review). *Geomagnetism Aeronomy* 47, 409–422. doi:10.1134/S0016793207040019

Kozyra, J. U., Brace, L. H., Cravens, T. E., and Nagy, A. F. (1986). A statistical study of the subauroral electron temperature enhancement using Dynamics Explorer 2 Langmuir probe observations. *J. Geophys. Res.* 91 (11), 11270280–11270311. doi:10.1029/JA091iA10p11270

Lavraud, B., and Larson, D. E. (2016). Correcting moments of *in situ* particle distribution functions for spacecraft electrostatic charging. *J. Geophys. Res. Space Phys.* 121 (9), 8462–8474. doi:10.1002/2016JA022591

Lavraud, B., Thomsen, M. F., Borovsky, J. E., Denton, M. H., and Pulkkinen, T. I. (2006). Magnetosphere preconditioning under northward IMF: Evidence from the study of coronal mass ejection and corotating interaction region geoeffectiveness. *J. Geophys. Res. Space Phys.* 111, A09208. doi:10.1029/2005JA011566

Lee, J. H., and Angelopoulos, V. (2014). On the presence and properties of cold ions near Earth's equatorial magnetosphere. *J. Geophys. Res. Space Phys.* 119, 1749–1770. doi:10.1002/2013JA019305

Lemaire, J. F., Gringauz, K. I., Carpenter, D. L., and Bassolo, V. (1998). The earth's plasmasphere. *The earth's plasmasphere*. Cambridge, United Kingdom: Cambridge University Press. doi:10.1017/CBO9780511600098

Lotko, W. (2007). The magnetosphere-ionosphere system from the perspective of plasma circulation: A tutorial. *J. Atmos. Sol.-Terr. Phys.* 69, 191–211. doi:10.1016/j.jastp.2006.08.011

MacDonald, E. A., Funsten, H. O., Dors, E. E., Thomsen, M. F., Janzen, P. H., Skoug, R. M., et al. (2009). AIP, 168–172. doi:10.1063/1.3169283New magnetospheric ion composition measurement techniques, Procedings of the AIP Conference Proceedings, 27–28 February 2021, Krishnagiri, India

MacDonald, E. A., Lynch, K. A., Widholm, M., Arnoldy, R., Kintner, P. M., Klatt, E. M., et al. (2006). *In situ* measurement of thermal electrons on the SIERRA nightside auroral sounding rocket. *J. Geophys. Res.* 111, A12310. doi:10.1029/2005JA011493

Malaspina, D., Ergun, R., Goldstein, J., Spittler, C., Andersson, L., Borovsky, J., et al. (2022). Plasma imaging, LOcal measurement, and tomographic experiment (pilot): A mission concept for transformational multi-scale observations of mass and energy flow dynamics in Earth's magnetosphere. *Front. Astron. Space Sci.* 9, 910730. doi:10.3389/fspas.2022.910730

Maldonado, C. A., Cress, R., Gresham, P., Armstrong, J. L., Wilson, G., Reisenfeld, D., et al. (2020c). *Space radiation dosimetry using the integrated Miniaturized Electrostatic Analyzer - reflight (iMESA-R)*. Space Weather.

Maldonado, C. A., Deming, J., Mosley, B. N., Morgan, K. S., McGlown, J., Nelson, A., et al. (2022). The experiment for space radiation analysis: A 12U CubeSat to explore the earth's radiation belts, Proceedings of the IEEE Aerospace Conference. 9-16 March 2002: Big SkyIEEE, 1–15.

Maldonado, C. A., Eyler, Z., Pierce, B., Matson, L., Neal, P., Richards, H., et al. (2020b). A laminated energetic electrostatic analyzer for 0-5 keV charged particles. *Rev. Sci. Instrum.* 91 (1), 013303. doi:10.1063/1.5123395

Maldonado, C. A., Reisenfeld, D., Fernandes, P., Larsen, B., Wilson, G., Balthazor, R. L., et al. (2020a). The effects of spacecraft potential on ionospheric ion measurements. *J. Spacecr. Rockets* 58, 1704–1713. (submitted). doi:10.2514/1.a34995

Maldonado, C., McHarg, M., Balthazor, R., and Osiander, R. (2019). "Undergraduate research and science mission opportunities with microtechnology enabled particle detectors," in *Micro- and nanotechnology sensors, systems, and applications XI* (Washington, United States: SPIE), 109820I. doi:10.1117/12.2519128

Marchand, R., Burchill, J. K., and Knudsen, D. J. (2010). Modelling electrostatic sheath effects on Swarm electric field instrument measurements. *Space Sci. Rev.* 156, 73–87. doi:10.1007/s11214-010-9735-y

Mauk, B. H., Fox, N. J., Kanekal, S. G., Kessel, R. L., Sibeck, D. G., and Ukhorskiy, A. (2012). Science objectives and rationale for the radiation belt storm probes mission. *Space Sci. Rev.* 179, 3–27. doi:10.1007/s11214-012-9908-y

McComas, D. J., Bame, S. J., Barker, P., Feldman, W. C., Phillips, J. L., Griffee, J. W., et al. (1998). Solar wind electron proton alpha monitor (SWEPAM) for the advanced composition explorer. *Space Sci. Rev.* 86, 563–612. doi:10.1023/a:1005040232597

McComas, D. J., Bame, S. J., Barraclough, B. L., Donart, J. R., Elphic, R. C., Gosling, J. T., et al. (1993). Magnetospheric plasma analyzer: Initial three-spacecraft observations from geosynchronous orbit. *J. Geophys. Res.* 98, 13453–13465. doi:10.1029/93JA00726

McDowell, J. C. (2020). The low Earth orbit satellite population and impacts of the SpaceX starlink constellation. *Astrohpysical J. Lett.* 892 (2), L36–L10. doi:10.3847/2041-8213/ab8016

McFadden, J. P., Carlson, C. W., Larson, D., Ludlam, M., Abiad, R., Elliot, B., et al. (2008). The THEMIS ESA plasma instrument and in-flight calibration. *Space Sci. Rev.* 141, 277–302. doi:10.1007/s11214-008-9440-2

Meierbachtol, C. S., Svyatskiy, D., Delzanno, G. L., Vernon, L. J., and Moulton, J. D. (2017). An electrostatic particle-in-cell code on multi-block structured meshes. *J. Comput. Phys.* 350, 796–823. doi:10.1016/j.jcp.2017.09.016

Melander, B. G., and Parks, G. K. (1981). The effects of cold plasma on the kelvin-helmholtz instability. *J. Geophys. Res.* 86 (A6), 4697–4707. doi:10.1029/JA086iA06p04697

Miyosh, Y., Oyama, S., Saito, S., Kurita, S., Fujiwara, H., Kataoka, R., et al. (2015). Energeticelectron precipitation associated withpulsating aurora: EISCAT and van AllenProbe observations. *J. Geophys. Res. Space Phys.* 120, 2754–2766. doi:10.1002/2014JA020690

Möbius, E., Tang, L., Kistler, L. M., Popecki, M., Lund, E. J., Klumpar, D., et al. (1998). Species dependent energies in upward directed ion beams over auroral arcs as observed with FAST TEAMS. *Geophys. Res. Lett.* 25, 2029–2032. doi:10.1029/98GL00381

Moore, T. E., Chappell, C. R., Chandler, M. O., Craven, P. D., Giles, B. L., Pollock, C. J., et al. (1997). High-altitude observations of the polar wind. *Science* 277, 349–351. doi:10.1126/science.277.5324.349

Moore, T. E., Chappell, C. R., Chandler, M. O., Fields, S. A., Pollock, C. J., Reasoner, D. L., et al. (1995). The thermal ion dynamics experiment and plasma source instrument. *Space Sci. Rev.* 71, 409–458. doi:10.1007/bf00751337

Moore, T. E., Fok, M.-C., Chandler, M. O., Chappell, C. R., Christon, S. P., Delcourt, D. C., et al. (2005). Plasma sheet and (nonstorm) ring current formation from solar and polar wind sources. *J. Geophys. Res.* 110. doi:10.1029/2004JA010563

Moore, T. E., Lundin, R., Alcayde, D., Andre, M., Ganguli, S. B., Temerin, M., et al. (1999b). Source processes in the high-latitute ionosphere. *Space Sci. Rev.* 88, 7–84. doi:10.1023/A:1005299616446

Moore, T. E., Peterson, W. K., Russell, C. T., Chandler, M. O., Collier, M. R., Collin, H. L., et al. (1999a). Ionospheric mass ejection in response to a CME. *Geophys. Res. Lett.* 26, 2339–2342. doi:10.1029/1999GL900456

Mott-Smith, H. M., and Langmuir, I. (1926). The theory of collectors in gaseous discharges. *Phys. Rev.* 28 (4), 727–763. doi:10.1103/PhysRev.28.727

Mozer, F. S., Agapitov, O. A., Angelopoulos, V., Hull, A., Larson, D., Lejosne, S., et al. (2017). Extremelyfield-aligned cool electrons inthe dayside outer magnetosphere. *Geophys. Res. Lett.* 44, 44–51. doi:10.1002/2016GL072054

Nakagawa, T., Ishii, T., Tsuruda, K., Hayakawa, H., and Mukai, T. (2000). Net current density of photoelectrons emitted from the surface of the GEOTAIL spacecraft. *Earth, planets space* 52 (4), 283–292. doi:10.1186/bf03351637

Nordholt, J. E., Reisenfeld, D. B., Wiens, R. C., Gary, S. P., Crary, F., Delapp, D. M., et al. (2003). Deep Space 1 encounter with Comet 19P/Borrelly: Ion compositionmeasurements by the PEPE mass spectrometer. *Geophys. Res. Lett.* 30 (9), 1465. doi:10.1029/2002GL016840

Ogasawara, K., George, D. E., Goldstein, J., Hwang, K.-J., Nishimura, Y., Ruggles, D. A., et al. (2020). 3DI: A novel ion composition and three-dimensional velocity analyzer for the topside ionosphere. *Sci. Rep.* 10 (1), 7967–8013. doi:10.1038/s41598-020-64407-4

Olsen, R. C. (1982). The hidden ion population of the magnetosphere. *J. Geophys. Res.* 87 (A5), 3481. doi:10.1029/JA087iA05p03481

Parker, L. W., and Whipple, E. C. (1970). Theory of spacecraft sheath structure, potential, and velocity effects on ion measurements by traps and mass spectrometers. *J. Geophys. Res.* 75 (25), 4720–4733. doi:10.1029/JA075i025p04720

Paschmann, G., Melzner, F., Frenzel, R., Vaith, H., Parigger, P., Pagel, U., et al. (1997). The electron drift instrument for cluster. *Space Sci. Rev.* 79, 233–269. doi:10.1023/A:1004917512774

Pedersen, A., Lybekk, B., André, M., Eriksson, A., Masson, A., Mozer, F. S., et al. (2008). Electron density estimations derived from spacecraft potential measurements on Cluster in tenuous plasma regions. *J. Geophys. Res.* 113, A07S33. doi:10.1029/2007JA012636

Persoon, A. M., Gurnett, D. A., and Shawhan, S. D. (1983). Polar cap electron densities from DE 1 plasma wave observations. *J. Geophys. Res.* 88, 10123–10136. doi:10.1029/ja088ia12p10123

Pollock, C. J., Moore, T. E., Adrian, M. L., Kintner, P. M., and Arnoldy, R. L. (1996). Scifer - cleft region thermal electron distribution functions. *Geophys. Res. Lett.* 23 (14), 1881–1884. doi:10.1029/96GL01486

Pollock, C., Moore, T., Jacques, A., Burch, J., Gliese, U., Saito, Y., et al. (2016). Fast plasma investigation for magnetospheric Multiscale. *Space Sci. Rev.* 199, 331–406. doi:10.1007/s11214-016-0245-4

Purvis, C. K., Garret, H. B., Whittlesey, A. C., and Stevens, N. J. (1984). *Design guidelines for assessing and controlling spacecraft charging effects*. United States: NASA. TP-2361.

Radtke, J., Kebschull, C., and Stoll, E. (2017). Interactions of the space debris environment with mega constellations—using the example of the OneWeb constellation. *Acta Astronaut.* 131, 55–68. doi:10.1016/j.actaastro.2016.11.021

Reeves, G. D., Chan, A. A., and Rodger, C. (2009). New directions for radiation belt research. *Space weather.* 7, S07004. doi:10.1029/2008sw000436

Reme, H., Bosqued, J. M., Sauvaud, J. A., Cros, A., Dandouras, J., Aoustin, C., et al. (1997). The cluster ion Spectrometry (CIS) experiment. *Space. Sci. Rev.* 79, 303–350. doi:10.1023/a:1004929816409

Riedler, W., Torkar, K., Rudenauer, F., Fehringer, M., Pedersen, A., Schmidt, R., et al. (1997). Active spacecraft potential control, in the cluster and phoenix missions. *Space. Sci. Rev.* 79, 271–302. doi:10.1023/A:1004921614592

Roytershteyn, V., and Delzanno, G. L. (2021). Nonlinear coupling of whistler waves to oblique electrostatic turbulence enabled by cold plasma. *Phys. Plasmas* 28, 042903. doi:10.1063/5.0041838

Russell, C. T., Holzer, R. E., and Smith, E. J. (1969). OGO 3 observations of ELF noise in the magnetosphere: 1. Spatial extent and frequency of occurrence. *J. Geophys. Res.* 74 (3), 755–777. doi:10.1029/JA074i003p00755

Sandel, B. R., Broadfoot, A. L., Curtis, C. C., King, R. A., Stone, T. C., Hill, R. H., et al. (2000). "The extreme ultraviolet imager investigation for the image mission," in *The image mission*. Editor J. L. Burch (Dordrecht: Springer), 197–242. doi:10.1007/978-94-011-4233-5_7

Sarno-Smith, L. K., Larsen, B. A., Skoug, R. M., Liemohn, M. W., Breneman, A., Wygant, J. R., et al. (2016). Spacecraft surface charging within geosynchronous orbit observed by the Van Allen Probes. *Space weather.* 14, 151–164. doi:10.1002/2015SW001345

Scime, E. E., Phillips, J. L., and Bame, S. J. (1994). Effects of spacecraft potential on three-dimensional electron measurements in the solar wind. *J. Geophys. Res.* 99, 14769–14814. doi:10.1029/94JA00489

Scudder, J. D., Cao, X., and Mozer, F. S. (2000). Photoemission current-spacecraft voltage relation: Key to routine, quantitative low-energy plasma measurements. *J. Geophys. Res. Space Phys.* 105 (A9), 21281–21294. doi:10.1029/1999ja900423

Serbu, G., and Maier, E. (1970). Observations from OGO 5 of the thermal ion density and temperature within the magnetosphere. *J. Geophys. Res.* 75 (31), 6102–6113. doi:10.1029/JA075i031p06102

Shelley, E. G., Johnson, R. G., and Sharp, R. D. (1972). Satellite observations of energetic heavy ions during a geomagnetic storm. *J. Geophys. Res.* 77, 6104–6110. doi:10.1029/JA077i031p06104

Shukla, P. K., and Mamun, A. A. (2015). *Introduction to dusty plasma physics*. Florida, United States: CRC Press. doi:10.1201/9781420034103

Singh, N., and Horowitz, J. L. (1992). Plasmasphere refilling: Recent observations and modeling. *J. Geophys. Res.* 97, 1049–1079. doi:10.1029/91JA02602

Skoug, R. M., Gosling, J. T., McComas, D. J., Smith, C. W., and Hu, Q. (2006). Suprathermal electron 90° pitch angle depletions at reverse shocks in the solar wind. *J. Geophys. Res.* 111, A01101. doi:10.1029/2005ja011316

Sojka, J. J., Wrenn, G. L., and Johnson, J. F. E. (1984). Pitch angle properties of magnetospheric thermal protons and satellite sheath interference in their observation. *J. Geophys. Res.* 89, 9801–9811. doi:10.1029/JA089iA11p09801

Strangeway, R. J., Ergun, R. E., Su, Y.-J., Carlson, C. W., and Elphic, R. C. (2005). Factors controlling ionospheric outflows as observed at intermediate altitudes. *J. Geophys. Res. Space Phys.* 110, A03221. doi:10.1029/2004JA010829

Su, Y. J., Horowitz, J. L., Moore, T. E., Giles, B. L., Chandler, M. O., Craven, P. D., et al. (1998). Polar wind survey with the thermal ion dynamics experiment/plasma source instrument suite aboard POLAR. *J. Geophys. Res.* 103, 29305–29337. doi:10.1029/98JA02662

Summers, D., Ni, B., and Meredith, N. P. (2007). Timescales for radiation belt electron acceleration and loss due to resonant wave-particle interactions: 2. Evaluation for VLF chorus, ELF hiss, and electromagnetic ion cyclotron waves. *J. Geophys. Res.* 112, A04207. doi:10.1029/2006JA011993

Szita, S., Fazakerley, A. N., Carter, P. J., James, A. M., Travnicek, P., Watson, G., et al. (2001). Cluster PEACE observations of electrons of spacecraft origin. *Ann. Geophys.* 19, 1721–1730. doi:10.5194/angeo-19-1721-2001

Takahashi, K., Denton, R. E., Hirahara, M., Min, K., Ohtani, S., and Sanchez, E. (2014). Solar cycle variation of plasma mass density in the outer magnetosphere: Magnetoseismic analysis of toroidal standing Alfvén waves detected by Geotail. *J. Geophys. Res. Space Phys.* 119, 8338–8356. doi:10.1002/2014JA020274

Tam, S. W. Y., Yasseen, F., and Chang, T. (1998). Further development in theory/data closure of the photoelectron-driven polar wind and day-night transition of the outflow. *Ann. Geophys.* 16, 948–968. doi:10.1007/s00585-998-0948-2

Thiebault, B., Hilgers, A., Masson, A., Escoubet, C. P., and Laakso, H. (2006). Simulation of the Cluster-spacecraft floating probe potential. *IEEE Trans. Plasma Sci.* 34 (5), 2078–2083. doi:10.1109/TPS.2006.883407

Thomsen, M. F., Denton, M. H., Lauvraud, B., and Bodeau, M. (2007). Statistics of plasma fluxes at geosynchronous orbit over more than a full solar cycle. *Space weather.* 5, S03004. doi:10.1029/2006SW000257

Thomsen, M. F., Henderson, M. G., and Jordanova, V. (2013). Statistical properties of the surface-charging environment at geosynchronous orbit. *Space weather.* 11, 237–244. doi:10.1002/swe.20049

Thorne, R. M. (2010). Radiation belt dynamics: The importance of wave-particle interactions. *Geophys. Res. Lett.* 37, L22107. doi:10.1029/2010GL044990

Toledo-Redondo, S., André, M., Aunai, N., Chappell, C. R., Dargent, J., Fuselier, S. A., et al. (2021). Impacts of ionospheric ions on magnetic reconnection and Earth's magnetosphere dynamics. *Rev. Geophys.* 59 (3). doi:10.1029/2020RG000707

Toledo-Redondo, S., Lavraud, B., Fuselier, S. A., André, M., Khotyaintsev, Y. V., Nakamura, N., et al. (2019). Electrostatic spacecraft potential structure and WakeFormation effects for characterization of cold IonBeams in the earth's magnetosphere. *J. Geophys. Space Phys.* 124 (10), 10048–10062. doi:10.1029/2019JA027145

Torkar, K., Nakamura, R., Tajmar, M., Scharlemann, C., Jeszenszky, H., Laky, G., et al. (2016). Active spacecraft potential control investigation. *Space. Sci. Rev.* 199, 515–544. doi:10.1007/s11214-014-0049-3

Tournear, D. (2020). "Future directions: Delivering capabilities," in Proceedings of the Small Satellite Conference, SSC20-IV-02, Logan, UT, August 5-10, 2023 (AIAA/USU), 1–13.

Turner, D. L., Angelopoulos, V., Li, W., Bortnik, J., Ni, B., Ma, Q., et al. (2014). Competingsource and loss mechanisms due to wave-particle interactions in Earth's outer radiation belt during the 30 September to 3 October 2012 geomagnetic storm. *J. Geophys. Res. Space Phys.* 119, 1960–1979. doi:10.1002/2014JA019770

Walsh, B. M., Hull, A. J., Agapitov, O., Mozer, F. S., and Li, H. (2020). A census of magnetospheric electrons from several eV to 30 keV. *J. Geophys. Res. Space Phys.* 125, e2019JA02757. doi:10.1029/2019JA027577

Wang, C.-P., Gkioulidou, M., Lyons, L. R., and Angelopoulos, V. (2012). Spatial distributions of the ion to electron temperature ratio in the magnetosheath and plasma sheet. *J. Geophys. Res. Space Phys.* 117, A08215. doi:10.1029/2012JA017658

Welling, D. T., Andre, M., Dandouras, I., Delcourt, D., Fazakerley, A., Fontaine, D., et al. (2015). The Earth: Plasma sources, losses, and transport processes. *Space Sci. Rev.* 192, 145–208. doi:10.1007/s11214-015-0187-2

Yamauchi, M. (2019). Terrestrial ion escape and relevant circulation in space. *Ann. Geophys.* 37, 1197–1222. doi:10.5194/angeo-37-1197-2019

Yau, A. W., and Andre, M. (1997). Sources of ion outflow in the high latitude ionosphere. *Space Sci. Rev.* 80, 1–25. doi:10.1023/A:1004947203046

Yau, A. W., Shelley, E. G., Peterson, W. K., and Lenchyshyn, L. (1985). Energetic auroral and polar ion outflow at DE 1 altitudes: Magnitude, composition, magnetic activity dependence, and long-term variations. *J. Geophys. Res. Space Phys.* 90, 8417–8432. doi:10.1029/JA090iA09p08417

Young, D. T., Burch, J. L., Gomez, R. G., De Los Santos, A., Miller, G. P., Wilson IV, P., et al. (2016). Hot plasma composition analyzer for the magnetospheric multiscale mission. *Space. Sci. Rev.* 199, 407–470. doi:10.1007/s11214-014-0119-6

Young, D. T. (1998). "Space plasma particle instrumentation and the new paradigm: Faster, cheaper, better," in *Measurement techniques in space plasmas: Particles*. Editors R. F. Pfaff, J. E. Borovsky, and D. T. Young (D.C., United States: American Geophysical Union), 102, 1–16.

Yuan, Z., Xiong, Y., Huang, S., Deng, X., Pang, Y., Zhou, M., et al. (2014). Cold electron heating by EMIC waves in the plasmaspheric plume with observations of the Cluster satellite. *Geophys. Res. Lett.* 41, 1830–1837. doi:10.1002/2014GL059241

Yue, C., Bortnik, J., LiMa, W. Q., Gkioulidou, M., Reeves, G. D., Wang, C.-P., et al. (2018). The composition of plasmainside geostationary orbit based on VanAllen Probes observations. *J. ofGeophysical Res. Space Phys.* 123, 6478–6493. doi:10.1029/2018JA025344

Zhao, H., Li, X., Baker, D. N., Fennell, J. F., Blake, J. B., Larsen, B. A., et al. (2015). The evolution of ring current ion energy density and energy content during geomagnetic storms based on Van Allen Probes measurements. *J. Geophys. Res. Space Phys.* 120, 7493–7511. doi:10.1002/2015JA021533

Zhou, Q., Xiao, F., Yang, C., He, Y., and Tang, L. (2013). Observation and modeling of magnetospheric cold electron heating by electromagnetic ion cyclotron waves. *J. Geophys. Res. Space Phys.* 118, 6907–6914. doi:10.1002/2013JA019263

Zurbuchen, T. H., Fisk, L. A., Gloeckler, G., and von Steiger, R. (2002). The solar wind composition throughout the solar cycle: A continuum of dynamic states. *Geophys. Res. Lett.* 29 (9), 66-1–66-4. doi:10.1029/2001GL013946

Zurbuchen, T. H., and Gershman, D. J. (2016). Innovations in plasma sensors. *J. Geophys. Res. Space Phys.* 121, 2891–2901. doi:10.1002/2016JA022493

frontiers | Frontiers in Astronomy and Space Sciences

TYPE Review
PUBLISHED 24 February 2023
DOI 10.3389/fspas.2023.1096595

OPEN ACCESS

EDITED BY
Larry Lyons,
Department of Atmospheric and Oceanic Sciences, College of Physical Sciences, University of California, Los Angeles, United States

REVIEWED BY
Jun Liang,
University of Calgary, Canada
Adolfo F. Vinas,
The Catholic University of America, United States

*CORRESPONDENCE
J.-F. Ripoll,
jean-francois.ripoll@cea.fr

SPECIALTY SECTION
This article was submitted to Space Physics, a section of the journal Frontiers in Astronomy and Space Sciences

RECEIVED 12 November 2022
ACCEPTED 06 February 2023
PUBLISHED 24 February 2023

CITATION
Ripoll J-F, Pierrard V, Cunningham GS, Chu X, Sorathia KA, Hartley DP, Thaller SA, Merkin VG, Delzanno GL, De Pascuale S and Ukhorskiy AY (2023), Modeling of the cold electron plasma density for radiation belt physics.
Front. Astron. Space Sci. 10:1096595.
doi: 10.3389/fspas.2023.1096595

Modeling of the cold electron plasma density for radiation belt physics

J.-F. Ripoll[1,2]*, V. Pierrard[3,4], G. S. Cunningham[5], X. Chu[6], K. A. Sorathia[7], D. P. Hartley[8], S. A. Thaller[9], V. G. Merkin[7], G. L. Delzanno[10], S. De Pascuale[11] and A. Y. Ukhorskiy[7]

[1]CEA, DAM, DIF, Bruyeres-leChatel, France, [2]UPS, CEA, LMCE, Bruyeres-leChatel, France, [3]Royal Belgian Institute for Space Aeronomy, STCE and Space Physics, Brussels, Belgium, [4]Université Catholique de Louvain (UCLouvain), Center for Space Radiations (CSR) and Georges Lemaître Centre for Earth and Climate Research (TECLIM), Earth and Life Institute (ELI), Louvain-La-Neuve, Belgium, [5]Space Science and Applications Group, Los Alamos National Laboratory, Los Alamos, NM, United States, [6]Laboratory for Atmospheric and Space Physics, University of Colorado, Boulder, CO, United States, [7]Applied Physics Laboratory, Johns Hopkins University, Laurel, MD, United States, [8]Department of Physics and Astronomy, University of Iowa, Iowa City, IA, United States, [9]Orion Space Solutions, Louisville, CO, United States, [10]Theoretical Division, Los Alamos National Laboratory, Los Alamos, NM, United States, [11]Oak Ridge National Laboratory, Oak Ridge, TN, United States

This review focusses strictly on existing plasma density models, including ionospheric source models, empirical density models, physics-based and machine-learning density models. This review is framed in the context of radiation belt physics and space weather codes. The review is limited to the most commonly used models or to models recently developed and promising. A great variety of conditions is considered such as the magnetic local time variation, geomagnetic conditions, ionospheric source regions, radial and latitudinal dependence, and collisional vs. collisionless conditions. These models can serve to complement satellite observations of the electron plasma density when data are lacking, are for most of them commonly used in radiation belt physics simulations, and can improve our understanding of the plasmasphere dynamics.

KEYWORDS

electron density, plasmasphere, plasmapause, empirical models, physical models, machine learning, radiation belts

1 Introduction

The Earth's plasmasphere is a region of cold (a few eV) plasma which originates from the ionosphere and forms a rotating torus that surrounds the Earth (Storey, 1953; Carpenter, 1963; Carpenter, 1966). Reviews of the plasmasphere can be found in Goldstein (2006), Kotova, 2007, Singh et al. (2011), Darrouzet and De Keyser (2013). For Earth's radiation belt codes computing the dynamics of energetic trapped electrons, accurate knowledge of the electron density over the entire plasmasphere is crucial for parameterizing the various diffusion coefficients (e.g., Glauert and Horne, 2005) used in modeling wave-particle interactions, either from a modeled density (e.g., Dahmen et al., 2022) or from local measurements (e.g., Ripoll et al., 2020b; Pierrard et al., 2021a). In addition, knowledge of the position of the outer edge of the plasmasphere is required for specifying a location to delineate between the high-density region where plasmaspheric hiss waves are present and the low-density region where chorus waves occur, with each wave causing different local loss

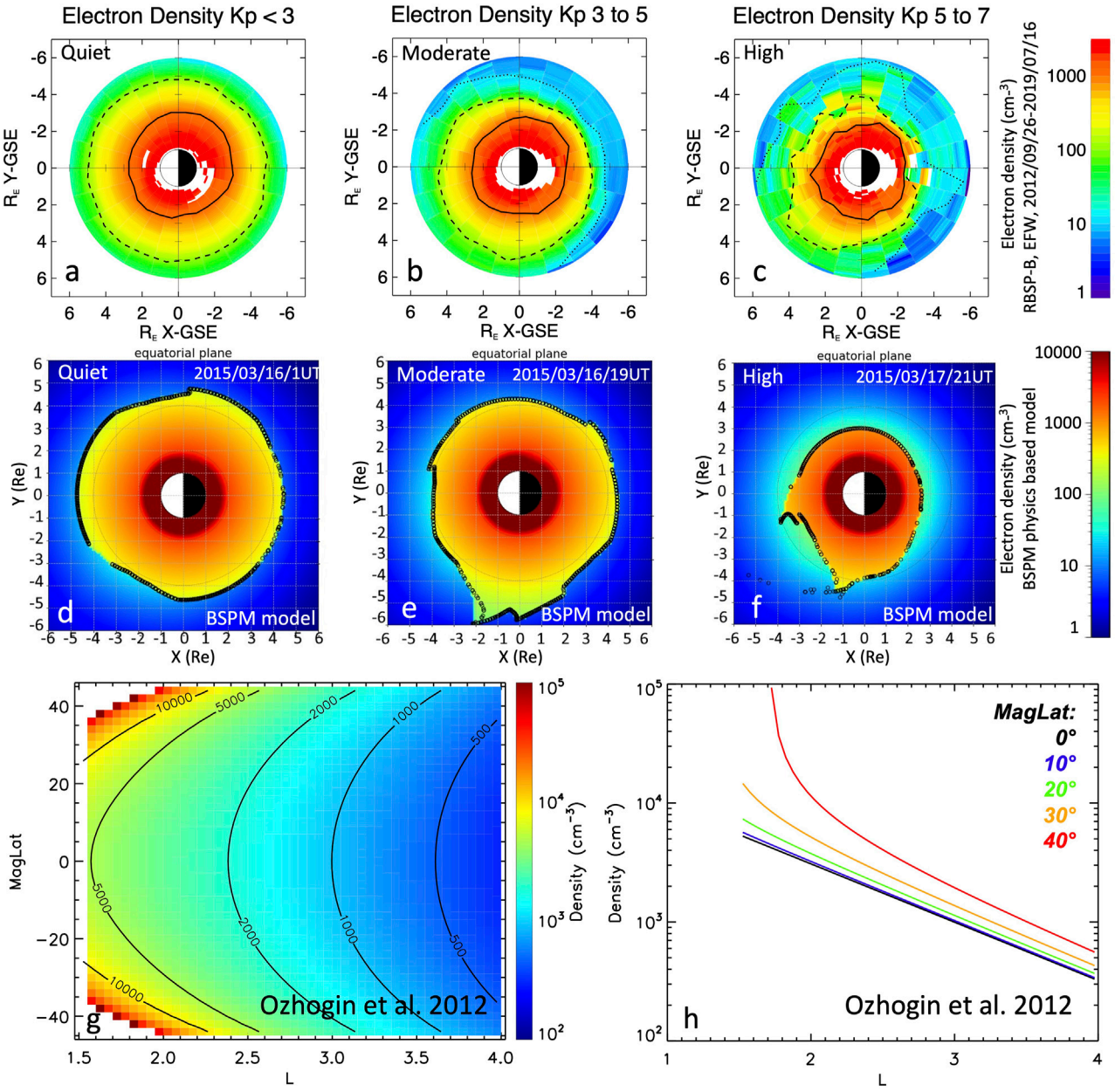

FIGURE 1
(A–C) Statistics of the electron plasma density (log_{10} of the density in units cm^{-3}) from EFW on Van Allen Probes B during the whole mission (09/2012-07/2019) for 3 Kp bins of geomagnetic activity (Ripoll et al., 2022a). **(D–E)** The physics-based Belgian SWIFF Plasmasphere Model (BSPM) model of (color scale) the electron density and (black circles) the plasmapause during times of **(D)** quiet, **(E)** substorm, and **(F)** storm activity (Pierrard et al., 2021b). The empirical Ozhogin et al. (2012) density model derived from the IMAGE Radio Plasma Imager (RPI) measurement plotted **(G)** *versus* L-shell (L) and magnetic latitudes and **(H)** *versus* L-shell extracted at a few magnetic latitudes.

and acceleration processes through wave-particle interactions (Thorne, 2010). The ion compositions are undoubtedly also very important in radiation belt dynamics, for example, regarding the wave-particle interactions with electromagnetic ion cyclotron (EMIC) waves but this topic is not covered in this review. Authors interested in this topic can read the recent extended review of the known impact of the cold-ion and cold-electron populations in the Earth's magnetosphere by Delzanno et al. (2021) with focus on the source of hot magnetospheric plasma, solar-wind/magnetosphere coupling, magnetotail reconnection and substorms, Kelvin–Helmholtz instabilities on the magnetopause, wave–particle interactions, aurora structuring and spacecraft charging.

Figures 1A–C show statistics of the electron plasma density taken from Ripoll et al. (2022a) in which density is inferred from the Electric Field and Waves (EFW) spacecraft potential (Wygant et al., 2013) from Van Allen Probes B during the whole mission (09/2012-07/2019) (see more details about the method and the accuracy of the

cold plasma density in section 3.3). This figure illustrates the state of the plasmasphere for 3 bins in Kp index spanning quiet to high levels of geomagnetic activity, a range of conditions that models intend to reproduce. During quiet times, the plasmasphere is approximately circular in shape around the Earth, expanding out up to L-shell (L) of ~5.5. With increasing activity, the plasmasphere evolves to become asymmetric in shape, with density structures forming in the morning and afternoon sectors. The increase of geomagnetic activity produces a general erosion of the plasmasphere on the dayside, an outward expansion of the plasma density in the dusk sector, and an increase of density in some of the night-morning sectors due to detached plasma regions rolling and wrapping around Earth.

In this article, we review existing plasma density models, including ionospheric source models, empirical density models, physics-based and machine-learning density models. A great variety of conditions is considered such as the magnetic local time (MLT) variation, geomagnetic conditions, ionospheric source regions, radial and latitudinal dependence, and collisional vs. collisionless conditions. This review is framed in the context of radiation belt physics (see review in Ripoll et al., 2020a) and space weather codes. This implies the models are usually derived to be applied on the large spatial scales and large temporal conditions. Models that will be referred to and discussed are limited to those most commonly used for radiation belt simulations. We also focus on the more recent progress made during the last decade and to the promising models or data, such as those from the National Aeronautics and Space Administration's (NASA) mission of the Van Allen Probes (Mauk et al., 2013). Models or data discussed in this review have gone through the calibration/correction analysis/process required to qualify the proper data to use (such as spacecraft potential correction, secondary electron effects, crosstalk effects correction in particle detectors, calibration corrections and modulation corrections on field detector antennae, etc.).

These models can be used to complement plasmaspheric densities inferred from satellite observations where or when data are lacking to fill data gaps, to be compared with these new data for evaluation, to be aggregated together or with observations to form more global models, or to analyze them for improving our understanding of the plasmasphere dynamics. Some of these models will serve as reference point or reference method from which we can improve and build a new generation of electron density models from the most recent observations, such as the NASA Van Allen Probes and the Japan Aerospace Exploration Agency (JAXA) Arase satellite missions (Miyoshi et al., 2018). The accuracy of the plasma density is essential for the computation of wave-particle interactions, which themselves determine the dynamics of the radiation belts.

2 The ionospheric source for the plasmasphere from the IRI model

The cold plasma in the plasmasphere has its origins in the ionosphere. Because the ionosphere is strongly driven by the Sun, the number density and temperature of the electrons, ions and neutrals in the ionosphere depend on solar activity, season, and local time, with a reset every day.

The earliest model of the topside ionosphere used only three bins in geomagnetic latitude and a linear dependence on F10.7 radio flux. In the 1990's, a diffusive equilibrium model was used to compute the density in the topside ionosphere. The diffusive equilibrium model is a first-principles model that specifies the plasma density along a flux tube given boundary conditions at the footpoints (Angerami and Thomas, 1964). The boundary conditions include the number density and temperature of electrons, ions and neutrals. A diffusive equilibrium model is applicable at low altitudes where collisions are frequent, but may have limited utility at higher altitudes where the plasma is collisionless.

The main empirical model of the ionosphere, the International Reference Ionosphere (IRI), uses trigonometric functions to fit both temporal (local, seasonal, and annual) and spatial variations in measurements of electron density coming from worldwide network of ionosondes, powerful incoherent scatter radars, topside sounders, and *in situ* instruments flown on many satellites and rockets, with the coefficients depending on solar activity. IRI has several altitude regions of interest: the D, E, F1, and F2 regions, and the topside ionosphere, which extends from the F2 peak to the maximum altitude in the model, 2000 km in IRI-2012 (Bilitza et al., 2014) (see also Bilitza et al., 2017; Biliitza, 2018). The IRI model is driven by several solar and ionospheric indices including the sunspot number R, the solar radio flux at 10.7 cm wavelength F10.7 (Tapping, 2013), and the ionosonde-based ionospheric global (IG) index (Bilitza, 2018). Last version is IRI 2020 on irimodel.org.

More specifically, the transition from highly collisional to collisionless in the topside ionosphere makes it a particularly difficult region to model. In IRI-2007, the topside ionosphere model from NeQuick (Coïsson et al., 2006) was included as the default option. This model has been constructed from ISIS-2 topside sounder data orbiting at 1,400 km (see also Gulyaeva, 2012). Further extension to higher altitudes includes the work of Gulyaeva et al. (2002) who took available topside sounder profiles up to 3,500 km and built a connection of IRI to the bottom of the plasmasphere (IRI-PLAS) (see also Gulyaeva, 2011; Gulyaeva et al., 2011). Reinisch et al. (2007) also made an attempt to connect the IMAGE/RPI density data (see section 3.2) with IRI 2001 topside using the vary-Chap approach (see also discussion in Bilitza and Reinisch, 2008). This model was further improved in Nsumei et al. (2012).

3 Empirical models

3.1 Empirical plasma density models

Early efforts to model the plasmaspheric electron density included effects due to solar activity and season, with the first models providing the density using simple empirical relations depending on the McIlwain parameter L in Earth radii. Carpenter and Anderson (1992) derived a "reference profile" of the plasmaspheric electron density, valid for $2.25 < L < 8$, to describe the saturated plasmasphere, $N(L) = 10^{(-0.3145L+3.0943)}$, with additional dependences to include perturbations due to season and phase of the solar cycle. This model uses the International Sun-Earth Explorer (ISEE) measurements and is limited to the local time interval of

0–15 MLT omitting plasma expansion on the dusk side, which these authors had aimed to treat separately (Carpenter and Anderson, 1992). Lyons and Thorne (1973) used a form $N(L) = 1000\,(4/L)^4$, that was consistent with Carpenter et al. (1964), to derive electron lifetimes that yielded equilibrium flux profiles for L = [1,5] using a Fokker-Planck radial diffusion code, even though the density model was not valid below L = 2. Albert (1999) used an exponential, $N(L) = 16400e^{-0.875L}$, instead of a power law in L. Sheeley et al. (2001) reported $N(L) = 1390\,(3/L)^{4.8} \pm 440\,(3/L)^{3.6}$ in the plasmasphere for $3 \le L \le 7$, where the authors show that the standard deviation captures differences between a newly filled and saturated plasmasphere. They did not find a magnetic local time (MLT) dependence for the plasmasphere, but did model the MLT-dependence of the plasma trough. A combination of Albert (1999) within the plasmasphere and Sheeley et al. (2001) within the plasma trough is used in the wave-particle interaction simulations of Ripoll et al. (2017) when satellite observations are lacking.

Gallagher et al. (2000) developed the Global Core Plasma Model (GCPM), a single unified model of the whole plasmasphere using an 'amalgam' of previously developed 'region-specific' models. GCPM addresses the density, temperature and composition of the plasmasphere, plasmapause, trough and polar cap. It depends on solar and geomagnetic indices, but is intended to be 'representative' of these conditions rather than used as a dynamic model. GCPM uses a modified version of the reference profile of Carpenter and Anderson (1992), $N(L) = 10^{-0.79L+5.3}$, added to the perturbations due to the solar cycle and season. It joins the topside ionosphere model of IRI to the equatorial plasma density model by first extrapolating the slope of the IRI model above the F2 peak using an exponential function and extrapolating the slope of the equatorial model downward in altitude with another exponential function, then blending the two functions with hyperbolic tangents. At higher latitudes, the shape of the exponential function is determined from IRI above the F2 peak, but the form is shifted by a constant so that the exponential decays to the equatorial value. The plasmapause location and width depend on local time. GCPM could be considered as the best compilation of all empirical density models. However, the GCPM model has not been directly coupled to radiation belt codes or wave particle interactions codes (to the knowledge of the authors) but it has been used for the validation of other plasma density models, themselves used in radiation belt codes (e.g., Ozhogin et al., 2012).

3.2 Latitudinal dependence

There have been recent efforts to model the variation of electron density with magnetic latitude. Denton et al. (2006) used satellite measurements from Polar and the Combined Release and Radiation Effects Satellite (CRRES) to model the latitudinal variations as a power law of the radial distance R to any point along the field line, $N(L,R) = N_{eq}(LR_E/R)^{\alpha}$, and fit α as a function of L and equatorial density for L > 2. Denton et al. (2006) fit this model to IMAGE RPI data and found that it did not perform well at high magnetic latitudes. Reinisch et al. (2004) and Huang et al. (2004) found that the following form fits data from IMAGE RPI well:

$$N(L,\lambda) = N_{eq}(L)\left[1 + \gamma\lambda/\lambda_{INV}\right]\left[\cos\left((\pi/2)(\alpha\lambda/\lambda_{INV})\right)\right]^{-\beta} \quad (1)$$

where λ is the magnetic latitude, λ_{INV} is the invariant magnetic latitude, and the fitting parameters are α, β, γ. Ozhogin et al. (2012) built on the earlier work of Reinisch et al. (2004) and fixed the values of the fitting parameters to

$$\alpha = 1.01 \pm 0.03, \beta = 0.75 \pm 0.08, \gamma = 0 \text{ and } N_{eq}(L) = 10^{-(0.4903\pm0.0315)L+(4.4693\pm0.0921)} \quad (2)$$

The Ozhogin et al. (2012) model is restricted to altitudes greater than 2000 km and L > 1.5, up to L = 4, and does not address dependence on MLT, season, solar activity, or differences in density between the Northern and Southern hemispheres. This model is plotted in Figures 1G, H to illustrate the increase of density with latitude. Models of Carpenter and Anderson (1992), Gallagher et al. (2000), Denton et al. (2006), Sheeley et al. (2001) and Ozhogin et al. (2012) are compared in Figure 8 of Ozhogin et al. (2012).

Empirical and first-principles models of the cold plasma density in the plasmasphere have been in development since the 1960's, but there is just one model (Ozhogin et al., 2012) that is valid below L = 2 and includes latitudinal dependence. To our knowledge, there was no valid empirical model below L = 1.5, nor one that includes variations due to solar activity, season, local time, and hemispheric differences, in addition to L, λ below L = 2. Recently, Hartley et al. (2023) combined Van Allen Probes data for latitudes below 20° with Arase data up to 40° for $1 < L \le 3$ and derived a new electron density model with both a latitudinal and MLT dependence. Comparison with the L dependence of the Ozhogin model shows good agreement above L = 1.5. Below L = 1.5, a fitting form similar to the Ozhogin model is adopted with new parameters defined as $\alpha = 1.03, \beta = 0.44$. An MLT dependence of the plasma density was identified, which is consistent with the diurnal variation of ionosphere. This variation is strongest at low L, but persists out to L = 3. All empirical electron density models discussed in this article are listed and succinctly synthetized in Table 1.

3.3 Empirical plasmapause models

There exist a variety of empirical plasmapause models currently used in radiation belt simulations. They generally provide the radial distance of the plasmapause in the equatorial plane as a simple function of the geomagnetic activity level. Tu et al. (2009) used, for instance, the CRRES data driven model of O'Brien and Moldwin (2003), whereas Tu et al. (2013) implemented the Carpenter and Anderson (1992) plasmapause model (noted CA92). The CA92 plasmapause model is the most commonly used model to our knowledge. It has been largely used for radiation belt studies over the last 10 years (Subbotin and Shprits, 2009; Kim et al., 2011; Shprits et al., 2013; Ripoll et al., 2016; Ripoll et al., 2019; Wang and Shprits, 2019; Cervantes et al., 2020a; Cervantes et al., 2020b; Malaspina et al., 2020; Saikin et al., 2021).

Recently, Ripoll et al. (2022a) derived both a plasmapause and a 100 #/cc density level models based on the entire Van Allen Probes mission (2012-2019) from both the Electric and Magnetic Field Instrument Suite and Integrated Science (EMFISIS) suite's (Kletzing et al., 2013) and the Electric Field and Waves (EFW) (Wygant et al.,

TABLE 1 Empirical electron density models discussed in this article.

Name/Reference	Modeled quantity	Data in use (or type of physics)	Model validity domain	Known limitation
Carpenter and Anderson (1992)	Plasmasphere and plasma trough density with MLT dependence. Plasmapause	ISEE	valid for 2.25 < L < 8	0 to 15 MLT. Underestimation of the plasmapause position shown in Ripoll et al. (2022a)
Lyons and Thorne (1973)	Density	Whistler measurements and OGO-5	L = [1,5]	Not valid below L = 2. Limited to within the plasmasphere
Albert (1999)	Density	ISEE	Based on Carpenter and Anderson (1992) averaged over MLT	Limited to within the plasmasphere
Sheeley et al. (2001)	Density with MLT dependence	CRRES	3 ≤ L ≤ 7	CRRES limitation in MLT and temporal coverage. Gap at high L shell between dawn and noon. No dependence on magnetic activity
Albert (1999) within the plasmasphere and Sheeley et al. (2001) within the plasma trough	Density	ISEE and CRRES	valid for 2.25 < L < 7	Limitations of Carpenter and Anderson (1992) and Sheeley et al. (2001)
GCPM Gallagher et al. (2000)	3D Density, temperature and composition of the plasmasphere, plasmapause, trough and polar cap	Compilation of all empirical density models	L in [1, 8]	Not a dynamic model and only representative of typical conditions
Denton et al. (2004)	Density with MLT dependence	Polar	L in [2, 8], ne < 1,500 #/cm-^{3}	Limited to March 1996 to September 1997
Denton et al. (2006)	Density with latitudinal dependence	Polar and CRRES	L in [2, 8]	Power law form to describe the field line distribution
Ozhogin et al. (2012)	Density with latitudinal dependence	IMAGE/RPI	altitudes greater than 2000 km and L > 1.5, up to L = 4	no MLT, season, solar activity, or differences between both hemispheres
Berube et al. (2005)	Equatorial density	IMAGE/RPI	L in 2–5	data between May 2000 and May 2001
Hartley et al. (2023)	Density with latitudinal and MLT dependences	Van Allen Probes data for latitudes below 20° with Arase data up to 40°	L in [1,3]. Continuous with Ozhogin et al. (2012) up to L = 4	Low L-shell model
Denton et al. (2012)	Long-term (>1 day) density refilling rates	IMAGE/RPI	L in [2, 9]	No MLT dependence of refilling rate. Kp < 1.5. 34 quiet periods of ~2 days between 2001 and the end of 2005

2013) data. The cold plasma densities are either determined by the upper hybrid resonance (UHR) method from EMFISIS measurements (Kurth et al., 2015) or by using the spacecraft floating potential (Escoubet et al., 2007; Torkar et al., 2016; Torkar et al., 2019) measured by the Electric Field and Waves (EFW) instrument (Wygant et al., 2013).

About the accuracy of these density measurements, we note the densities derived along with the corresponding spacecraft potentials are fit to a function with a non-linear least squares fit. The resulting fits typically have a Pearson (R^2) coefficient in the range of ~0.75–0.95 and an average percent error between the selected fit derived densities and the densities used to perform the fit of ~15%. Experiments with individual orbits show that fits of the functional form can capture the density voltage relation over a range of densities from ~few cm^{-3} up to 3,000 cm^{-3} with the lower densities still agreeing with the EMFISIS UHR densities to within 10%. However, using the same fit for a longer period (larger than an orbit) the EFW and EMFISIS densities may diverge by over factor of two at densities <10 cm^{-3}. The reason for this is the variability of the plasma environment outside the plasmasphere. For periods during which the upper hybrid resonance line is clearly resolved in the High Frequency Receiver (HFR) spectral data, the EMFISIS density product is generally more accurate than the EFW. However, during times in which there are high levels of wave activity that make identification of the upper hybrid line difficult or impossible, resulting in increased uncertainty in the EMFISIS densities, the EFW density fits still return densities by applying the relevant fit equation to the spacecraft potential. Regarding the semi-automated process for determining the EMFISIS density from the UHR (Kurth et al., 2015), there is a 8.7% mean percentage difference between the manual process and the semiautomatic process, which is less than the ~10% resolution available for an individual measurement. This difference is visible in Figure A2 of Goldstein et al. (2014a), where the average difference is often low (~7%), is less than 20% in general, but can be up to 100% for a very small number of data points. Another main source of error is the spectral resolution, due to the upper hybrid resonance that can only be defined at specific values dictated by the binned frequency spectrum. This translates to a density resolution of Δne/ne of about 10%. The uncertainty increases when the spectra become difficult to interpret,

TABLE 2 Empirical plasmapause models discussed in this article.

Name/ References	Modeled quantity	Data in use (or type of physics)	Model validity domain	Known limitation
O'Brien and Moldwin (2003)	Plasmapause with MLT dependence	CRRES	L in [2, 8]	CRRES limitation in MLT and temporal coverage. Gap at high L shell between dawn and noon
Ripoll et al. (2022a)	Plasmapause and 100 #/cc level line, with MLT dependence	Van Allen Probes	L in [1.5, 6]	Single index modeling
Kwon et al. (2015)	Plasmapause	THEMIS	Kp~1	Limited to quiet times
Bandić et al. (2016)	Plasmapause with MLT dependence	CRRES	L in [2, 8]	Sector (12–18 MLT) contains significantly less data than other sectors
Cho et al. (2015)	Plasmapause	THEMIS (2008–2012)	L in [2, 8]	Ascending phase of Solar Cycle 24. Sharper gradient than commonly used. No MLT dependence
Liu and Liu (2014)	Plasmapause with MLT dependence	THEMIS D (2010-2011)	L in [3, 6]	Generalized in Liu et al. (2015)
Liu et al. (2015)	Plasmapause with MLT dependence	THEMIS (2009–2013)	L in [2, 8]	Limited to plasmapause crossings with one sharp density gradient
Verbanac et al. (2015)	Plasmapause with MLT dependence	Cluster	L in [2.9, 8.8]	Limited to 311 plasmapause crossing
NSW-GDP Model He et al. (2017)	Plasmapause with MLT dependence	Multiple sources (18 satellites in 1977–2015). 48,899 plasmapause locations	L in [2, 8]	The maximum RMS error of 0.91 RE at 17 h MLT. Minimum RMSE of 0.57 RE at midnight. Diurnal plasmapause variations may be faded through 36 years data averagd in 1 h UT intervals

as discussed in Goldstein et al. (2014a). In most instances, the spectral resolution uncertainty is estimated to be between 10% and 20% (Hartley et al., 2016). The EMFISIS and EFW densities from ~10 cm^{-3} to 3,000 cm^{-3} are statistically compared in Jahn et al. (2020), who found that the EFW values predominantly fall in a range of 50%–200% of their corresponding EMFISIS measured value (e.g., 0.5 to 2 times the actual value), while most of the EFW to EMFISIS points used for comparison are ~100% (e.g., $n_{EFW} \sim n_{EMFISIS}$). Further comparisons of the 100 #/cc level are carried out in Ripoll et al. (2022a) in which Figures 1K, L confirm the good agreement between both methods, with the bulk of normalized differences below ±20%.

A comparison of the CA92 plasmapause model with Van Allen Probes measurements is performed in Ripoll et al. (2022a). These authors first recover the CA92 model using EMFISIS data and a gradient method to localize the plasmapause, showing the practical reliability of the CA92 model. However, direct comparisons of the 100 cm^{-3} level deduced from Van Allen Probes EFW measurements and the CA92 model show the dense plasmasphere expands farther out than predicted by the CA92 model. Departure of the CA92 model from the 100 cm^{-3} EFW data increases as the maximum value of the Kp index over the last 24 h (Kp) increases and L-shell decreases, and storm-induced erosions are less deep than predicted by the CA92 model (Ripoll et al., 2022a).

The model of O'Brien and Moldwin (2003) based on CRRES data is the first to show the MLT dependence as well as the relevance of parametrizing the plasmapause model with various indices, such as Kp, AE, and Dst (see also Moldwin et al. (2002)). Carpenter et al. (2000) states the experimental error in the CRRES density is associated with measuring the UHR or plasma frequencies on the SFR records. They estimated to be +/− 6% in spectral resolution (Δf/f), which corresponds to +/− 12% in density. Kwon et al. (2015) derived the median/mean plasmapause locations from the electron density inferred from the Time History of Events and Macroscale Interactions during Substorms (THEMIS) spacecraft potential under steady quiet conditions (Kp ≤ 1). The comparison of their plasmapause model with the estimated Lpp from models such as GCPM (Gallagher et al., 2000), Moldwin et al. (2002), and O'Brien and Moldwin (2003) with Kp = 1 shows the plasmapause is farther extended ~1–2 L from the Earth (i.e., GCPM and CRESS based-models models underestimate the extend of the plasmapause). Ripoll et al. (2022a) show the underestimation of the plasmapause position is caused by the gradient method that fails identifying gradients particularly during quiet times and on the dusk.

Other plasmapause models include Bandić et al. (2016) based on CRRES data, Cho et al. (2015), Liu and Liu (2014) and Liu et al. (2015) based on THEMIS data, and Larsen et al. (2007) based on IMAGE data. Verbanac et al. (2015) plasmapause model is based on CLUSTER data and analytical relationships obtained from geomagnetic and solar wind observations. Bandic et al. (2017) derived a plasmapause model from a large dataset including multiple sources. A comparison of these models is provided in Pierrard et al. (2021c) showing a great variability of mean plasmapause empirical models (see also Guo et al., 2021). All empirical plasmapause models discussed in this article are listed and succinctly synthetized in Table 2 (see also Table 1 in He et al. (2017) listing the model dependences).

The large variability of the measurements underlying the mean empirical plasmapause models (more generally mean plasma density empirical models) is one major limitation of this type of

models that calls for the use of either physic-based models or machine learning technics.

4 Physic-based models of the plasmasphere

4.1 Ionosphere-plasmasphere models

The 3D global ionosphere/plasmasphere fluid model SAMI3 (Huba and Krall, 2013; Krall and Huba, 2013) of the Naval Research Laboratory (NRL) solves the continuity and momentum fluid equations for seven ion species (H^+, He^+, N^+, O^+, N^+_2, NO^+ and O^+_2) and includes the thermospheric wind-driven dynamo electric field. It is based on SAMI2 (Huba et al., 2000). SAMI3 uses the partial donor cell method (Hain, 1987; Huba, 2003) and a newly implemented 4-order flux-corrected transport scheme for ExB transport perpendicular to the magnetic field (Huba and Liu, 2020). The temperature equation is solved for three atomic ion species and electrons. The model has a co-rotation potential, a neutral wind dynamo potential (with winds from HWM93 (Hedin, 1987)), and a time-dependent Volland-Stern-Maynard-Chen potential. In Huba and Krall (2013), SAMI3 density results are compared at the equator for 4 MLT sectors with the quiet time empirical electron density of Berube et al. (2005) defined as $n_{eq} = 10^{0.51L+4.56}$ for L in 2–5 from IMAGE RPI data between May 2000 and May 2001. They find the SAMI3 electron density is lower by a factor 2 attributed to a lower F10.7 index used in the simulation.

The SAMI3 model has been recently modified to support the NASA ICON mission and provide ionosphere and thermosphere properties during this mission (Huba et al., 2017). SAMI3 recently integrated an improved model of counterstreaming H^+ outflows from the two hemispheres during storm using a two fluid species for H+ (Krall and Huba, 2019) in order to avoid non-physical high-altitude 'top-down refilling' density peaks (Krall and Huba, 2021). SAMI3 is currently used to try to reproduce the formation of density ducts in the plasmasphere (e.g., Jacobson and Erickson, 1993; Loi et al., 2015) caused by the thermosphere composition and winds on plasmaspheric refilling outflows (Krall et al., 2018) as observed from the Murchison Widefield Array (MWA) interferometric radio telescope in Australia (Helmboldt and Hurley-Walker, 2020). SAMI3 recently coupled to the atmosphere/thermosphere code WACCM-X (Whole Atmosphere Community Climate Model with thermosphere and ionosphere extension) provided the first high-resolution global simulation using realistic thermospheric conditions of the formation and penetration of plasma bubbles into the topside *F* layer (Huba and Liu, 2020). These structures will further propagate to higher altitudes and introduce longitudinal and seasonal dependence structures into the plasmasphere. Further coupling of SAMI3 and applications are discussed in Huba (2023).

The Ionosphere-Plasmasphere-Electrodynamics (IPE) model is derived in Maruyama et al. (2016) to investigate the connection between terrestrial and space weather (e.g., Fuller-Rowell et al., 2008). IPE provides 3D thermal plasma densities for nine ion species, electron and ion temperatures, and parallel and perpendicular velocities of the ionosphere and plasmasphere. The parallel plasma transport is based on the Field Line Interhemispheric Plasma (FLIP) Model (Richards et al., 2010). There is a detailed model of the Earth's magnetic field using Apex coordinates (Richmond, 1995) and the International Geomagnetic Reference Field IGRF (as in SAMI3). The transport is computed with the same solver all the way from the equator to the pole on a global static grid with a semi-Lagrangian scheme that allows for the global plasma transport perpendicular to magnetic field lines. There is a self-consistent photoelectron calculation enabling more accurate studies of the longitudinal/UT dependence of the ionospheric mass loading process. IPE is generally defined from 90 km to approximately 10,000 km. The spatial resolution of the radial direction in the plasmasphere varies from 0.05 R_E (L = 1.5) to 0.46 R_E (L = 5). IPE has used to reproduce the Weddle Sea Anomaly (Sun et al., 2015) and for studying extreme plasmaspheric erosion as low as L~1.7 (Obana et al., 2019). Current applications of IPE include plasmaspheric drainage plumes, ionospheric storm enhanced density (SED) plumes, plasmaspheric refilling, and plasmaspheric composition. The Whole Atmosphere Model (WAM)(e.g., Akmaev and Juang, 2008) has been coupled with IPE (WAM-IPE) and provides today space weather forecast 24/7 at NOAA SWPC (https://www.swpc.noaa.gov/products/wam-ipe). WAM-IPE has recently be used to simulate ESF irregularities (Hysell et al., 2022).

The IRAP Plasmasphere Ionosphere Model (IPIM) uses a 16-moment approach for strong temperature anisotropy at high altitude and for accurately modeling the transition between collision dominated at low altitude and collisionless media at high altitude (Marchaudon and Blelly, 2015). IPIM solves the interhemispheric hydrodynamics convection and corotation of six ions and thermal electrons along flux tubes at different distances from Earth. IPIM has a kinetic model for suprathermal electrons and solves for the chemical reactions in the ionosphere. IPIM has been used to simulate the depletion of the ionospheric F_2 layer by a high-speed stream for short-term behavior on the scale of a few hours Simulations were found to be consistent with EISCAT radar and the ionosonde measurements (Marchaudon et al., 2018). For the long-term evolution of the plasmasphere-ionosphere system and during quiet conditions, IPIM simulations indicate that the plasmasphere in not stable in MLT and that no real dynamic equilibrium can be reached (Marchaudon and Blelly, 2020).

4.2 Plasmasphere models

Different plasmasphere models combining semi-empirical relations and physics-based backgrounds have been developed to reproduce the inner magnetosphere, the plasmapause, and even the plasma trough above the plasmasphere limit (see Pierrard et al., 2009 for a review of the plasmasphere models before 2009).

Pierrard and Stegen (2008) have developed the Belgian SWIFF Plasmasphere Model (BSPM), a 3D dynamic kinetic model of the plasmasphere. The BSPM model is based on physical mechanisms, including the interchange instability for the formation of the plasmapause (Pierrard and Lemaire, 2004), and provides the density and the temperature of the electrons, protons and other ions, both inside and outside the plasmasphere in the plasma trough. It has been coupled to the ionosphere (Pierrard and Voiculescu, 2011) using the IRI model as a boundary condition and is continuously improved by including other physical processes like

plasmapause thickness and plasmaspheric wind (Pierrard et al., 2021b). The input of the model is the date that determines the geomagnetic indices Kp and Dst. The plasmapause position does strongly correlate with the Bartels geomagnetic index, Kp index, which is retained as the main parameter used in the model to determine the plasmapause position. These indices may be predicted values when forecasting is required, or observed values when past events are simulated. They determine also the convection electric field. As BSPM uses the IRI model, it also depends on IRI parameters listed in Section 2. The BSPM model includes plasmapause erosion during geomagnetic storms as well as refilling, and is able to reproduce the plumes generated during storms and other structures like shoulders. It uses the kinetic approach that allows for the inclusion of non-Maxwellian distributions (Pierrard and Lemaire, 2001). The last version of the BSPM model is shown in Figures 1D–F for quiet, substorm, and storm activity. On 16 March 2015 1H (UT) with a quiet period with Kp~2 (and almost constant during several hours), the plasmasphere is quite extended and almost circular (to compare with Figure 1A). A few hours later after a substorm injection on 16 March 2015 19 h (UT) with Kp~4, there is formation of a plume in the dusk sector rotating with the Earth (to compare with Figure 1B). On 17 March 2015 21 h (UT) during an intense storm with Kp = 8$^-$, the model shows a strong erosion of the plasmasphere and formation of a long plume rotating with Earth (to relate with the statistics of Figure 1C).

The kinetic approach based on particle-in-cell simulations has also been combined with the fluid approach in Wang et al. (2015) to develop a dynamic fluid-kinetic model for plasma transport within the plasmasphere. A semi-kinetic model of plasmasphere refilling following geomagnetic storms has also been recently developed by Chatterjee and Schunk (2020b) and compared with hydrodynamic models to explore their differences. In hydrodynamic plasmasphere models, the non-linear inertial terms in the plasma transport equations are retained (Chatterjee, 2018; Chatterjee and Schunk, 2019; Chatterjee and Schunk, 2020a; Chatterjee and Schunk, 2020b). Limitations of such models are generally related to the difficulty to reproduce the mechanisms implicated in the formation of the plasmapause and the refilling process that is a key physics-based problem to solve to obtain a fully coupled plasmasphere-ionosphere model.

A two-dimensional physics-based plasmasphere model called Cold Plasma (CPL) (Jordanova et al., 2006; Jordanova et al., 2014) is used in a ring current-atmosphere interactions model of the source and loss processes of refilling and erosion driven by empirical inputs to simulate equatorial plasmaspheric electron densities. The performance of CPL has been evaluated against *in situ* measurements by the Van Allen Probes (Radiation Belt Storm Probes) for two events (De Pascuale et al., 2018). This study finds that severe erosion is best captured by an effective Kp-index for scaling the inner-magnetospheric potential governing E x B flows while refilling subsequent to moderate activity requires a solar wind parameterization of the quiet time background after the onset of a geomagnetic storm. Empirical models driving plasmasphere dynamics can be improved by capturing localized enhancements in electric field measurements and asymmetric profiles in electron density observations. More specific simulations were dedicated to comparisons with Van Allen Probes plasmapause observations (Goldstein et al., 2014a; Goldstein et al., 2016).

4.3 Plasmapause models

Physics-based models also provide the plasmapause location (e.g., Pierrard et al. (2021b)), with some models integrating Van Allen Probes measurements and plasma trough densities (e.g., Botek et al., 2021). Goldstein et al. (2003), Goldstein et al. (2005) developed a plasmapause test particle (PTP) dynamic model that represents the plasmaspheric boundary as an ensemble of E × B-drifting particles. The PTP model uses an electric field which is driven by the solar wind E field and Kp. The evolution of the plasmapause is modeled by the changing shape of the curve defined by the aggregate of the test particles evolving in a time-varying convection E-field. PTP simulation for the moderately disturbed interval 18–20 January 2000 shows a narrow drainage plume followed by significant plasmaspheric erosion, forming a second plume that coexists with the residue of the first plume (Goldstein et al., 2014b). Observations from three of the Los Alamos National Laboratory geostationary satellites are globally consistent with this PTP simulation in terms of the durations of plume sector transits while the MLT widths and timings of the simulated plumes do not precisely agree (Goldstein et al., 2014b). Goldstein et al. (2019) further generated a plasmapause statistical model from the simulations of 60 storms with $Dst_{,PEAK} \leq -60$nT based on Van Allen probes data yielding over 7 million model plasmapause locations. The epoch-binned PTP simulation results are combined in order to create an analytical plasmapause model for moderate storms (-120nT $\leq Dst_{,PEAK} \leq -60$nT) and strong storms ($Dst_{,PEAK} \leq -120$nT) that explicitly includes plumes. This model depends on the duskside plasmapause radius and two fitted coefficients, all three depend on epoch time (from −24 h to 36 h).

4.4 Global geospace model

A new promising approach is to couple a global geospace model of the magnetosphere with a physics-based density model. Figure 2 provides an example of the global geospace model, GAMERA (Zhang et al., 2017; Sorathia et al., 2020; Sorathia et al., 2021) coupled to RCM (Toffoletto et al., 2003). With a two-way coupling, these models are subparts of the Multiscale Atmosphere-Geospace Environment (MAGE) (e.g., Chen et al., 2021; Pham et al., 2021; Lin et al., 2022). The details of GAMERA's core MHD numerics and its verification are presented in Zhang et al. (2019). GAMERA uses high-order spatial reconstruction for the preservation of sharp structures. For typical MHD problems, Zhang et al. (2019) showed lower-order reconstruction (e.g., Second-order) requires four to eight times finer grid resolution (corresponding to a 250-4,000 factor increase of the cost resolution in 3D) as the higher-order (seventh- or eighth-order) reconstruction to reach the same accuracy. In addition to coupling the global MHD model to the inner magnetosphere model *via* ring current pressure ingestion (e.g., Pembroke et al., 2012), here the RCM is additionally evolving a cold fluid to model the evolution of the plasmaspheric density. In this coupling, the plasmasphere density is initialized using an empirical model (Gallagher et al., 2000) and refilling rate (Denton et al., 2012), and evolved using the same dynamically-calculated electrostatic potential as in the MHD simulation (e.g., Merkin and Lyon, 2010).

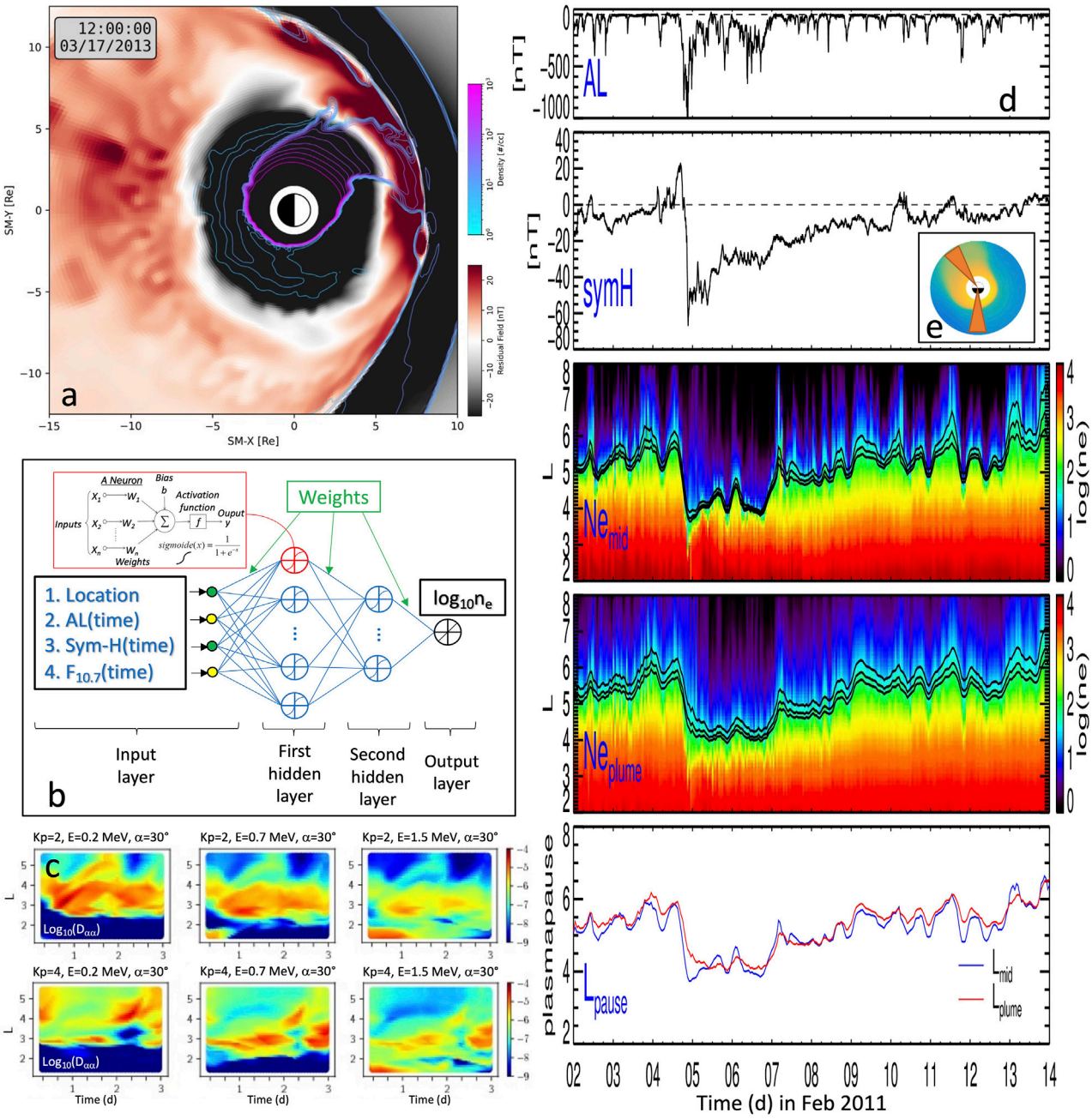

FIGURE 2
(A) Coupled GAMERA global geospace model and RCM simulation depicting localized nightside dipolarizations and dayside plasmaspheric plume. Shown is the non-dipolar component of the northward magnetic field (left color bar) and contours of constant density (right color bar) in the equatorial plane (Sorathia et al., 2018). **(B)** The neural network architecture of DEN2D in Chu et al. (2017a). **(C)** Predictions of diffusion coefficients for variable density and wave properties from the neural network model of Ripoll et al. (2022b) during (top) quiet (Kp = 2) and (bottom) moderate (Kp = 4) activity. A Kp-based model of plasma density and wave properties would find constant values in time. **(D)** Density and plasmapause location predicted by the DEN2D neural network at midnight (noted mid) and in the plume (noted plume) based on the AL and Sym-H indices in February 2011 during a refilling event showing dynamic rates of refilling (Chu et al., 2017b). **(E)** Equatorial density predicted by DEN2D and MLT sectors shown in **(D)**.

Note that RCM can further be coupled with SAMI3 as done by Huba et al. (2017b) to study the ionosphere-plasmasphere system response to the 17 March 2015 geomagnetic storm. The coupling occurs through the electrostatic potential equation (Huba et al., 2005; Huba and Sazykin, 2014) in which the conductance is defined by the sum of the conductance associated with solar activity computed by SAMI3 and the auroral enhanced conductance provided by RCM.

Figure 2A depicts localized dipolarizations on the nightside and the formation of a dayside plasmaspheric plume during the 17 March 2013 geomagnetic storm (Sorathia et al., 2018). There is a complex interacting mesoscale process with nightside flows,

TABLE 3 First-principles physics models discussed in this article.

Name/References	Modeled quantity	Physics principles	Model validity domain	Known limitation
Ionosphere-Plasmasphere-Electrodynamics (IPE) (Maruyama et al., 2016)	3D densities for nine ion species, electron and ion temperatures, and parallel and perpendicular velocities of the ionosphere and plasmasphere	Parallel plasma transport based on the Field Line Interhemispheric Plasma (FLIP) Model Richards et al. (2010). Detailed model of the Earth's magnetic field using Apex coordinates Richmond (1995) and IGRF.	from 90 km to approximately 10,000 km	Lack of kinetic processes
IPIM Marchaudon and Blelly (2015)	Ionosphere-plasmasphere model	2D interhemispheric fluid model for 6 ions coupled with a kinetic model for suprathermal electrons. Includes a chemistry solver	Defined for single L	Change of flux tube volume during a full rotation. Need an evolution of the chemistry in the D region
3DPM Pierrard and Stegen (2008)	Dynamic plasmapause, 3D Density	3D dynamic kinetic model	L = [2-8]	Sharp plasmapause
SPM (SWIFF Plasmaphere model) Pierrard and Voiculescu (2011)	Dynamic plasmapause, 3D Density	3D dynamic kinetic model, improved version by adding coupling with the ionosphere	from 60 km to L = 8	Limitations to reproduce the refilling process
BSPM (Belgian SWIFF Plasmasphere model) Pierrard et al. (2021b)	Dynamic plasmapause, 3D Density in plasmasphere and plasm trough	3D dynamic kinetic model coupled to the ionosphere, improved version by adding trough and refilling	from 60 km to L = 10	Plasmaspheric wind only on request
Wang et al. (2015)	Electron density along the magnetic field line	Dynamic fluid-kinetic model with an overlapped transition region (800 km–1,100 km in altitude)	Defined for single L	Limitations related to the difficulty to reproduce the mechanisms implicated in the formation of the plasmapause and the refilling process
Chatterjee and Schunk (2019), Chatterjee and Schunk (2020a)	1D hydrodynamic plasmasphere refilling model along magnetic flux tube	Fluid model. Three ions (H+, He+, and O+) and two neutrals (H and O)	Defined for single L	Discontinuities in the early to middle phases of refilling
Chatterjee and Schunk (2020b)	Density refilling: 1D spce and 1D velocity	Semi-kinetic model	Defined for single L	Do not include the effect of ion-neutral charge exchange mechanisms. 3D models needed for more detailed and thorough simulations
SAMI3 Huba and Krall (2013), Krall and Huba (2013)	3D Density, velocity, ion species	3D global ionosphere/plasmasphere fluid model. Use co-rotation potential, neutral wind dynamo potential, and a time-dependent Volland-Stern-Maynard-Chen potential. Use the partial donor cell method. 4-order flux-corrected transport scheme for E x B transport perpendicular to the magnetic field	Magnetic latitude range ± 88°. 90 km up to ~16 RE at the magnetic equator	Used in practice till L~8. Non-physical high-altitude 'top-down refilling' for single fluid
Cold Plasma (CPL) Jordanova et al. (2006), Jordanova et al. (2014)	Density with MLT dependence	2D fluid model	L in [1.75,6.6] (*via* continuity equation and prescribed empirical or self-consistent electric field)	Empirical refilling timescales determined from ionospheric measurements of Hedin (1987), and Bilitza (1986). Empirical saturated flux tube densities determined from ISEE observations of Carpenter and Anderson (1992)
RCM Toffoletto et al. (2003)	Density with MLT dependence	2D cold fluid to model the plasmaspheric density	L in [2,8]	No field-aligned density structure. Modeling plasmasphere refilling requires separate model, typically empirical refilling model like Denton et al. (2012)
Plasmapause test particle (PTP) dynamic model Goldstein et al. (2003), Goldstein et al. (2005)	Plasmapause with MLT dependence	Test-particle model	Validated at gobal scales (e.g., durations of plume sector transits)	Limited accuracy at meso-scales (e.g., MLT widths and timings of plumes)

(Continued on following page)

TABLE 3 (*Continued*) First-principles physics models discussed in this article.

Name/References	Modeled quantity	Physics principles	Model validity domain	Known limitation
Goldstein et al. (2019)	Plasmapause with MLT dependence	Statistical and analytical model based on PTP simulations	Dst < −60 nT	Defined for 2 types of storms: moderate (−120nT ≤ Dst≤−60nT) and strong (Dst≤−120nT)

boundary Kelvin-Helmholtz on the dayside and flanks, and rolling dense plasmaspheric plume and structures. The plume is shown at 12 UT, i.e., 6 h after the CME impacted the Earth, with a typical expansion in the dusk-day sector that reaches L~6 and has started to roll around Earth.

The Kelvin-Helmoltz instability we see forming on the magnetopause and rolling side way of the magnetosphere (Merkin et al., 2013) may contribute to transfer shear and turbulence to the plume as it expands and removes pockets of dense plume plasma. In this way, the plume may potentially inherit a complex shape that is here captured by the global MHD model. The dense plasmasphere has a circular aspect for levels above 1,000 #/cc and there are structured plasma pockets of low density from 1-10 #/cc on the nightside beyond the main plasmapause gradient at L~3. On the night side, the magnetic field (and similarly the electric field) has a fine scale structure (with finger-like regions of higher field value) that reach the L~6 region and imprint a fluctuating profile to the dense pockets down to the plasmapause layer. As simulation resolution increases, some aspects of these structures become finer and more torturous. However, understanding the full cascade of energies down to the smallest scales requires global kinetic modeling.

These kinds of mesoscale structures play a critical role in shaping both the global-scale and micro-scale processes of the magnetosphere. Localized injections are believed to be an important part of the transport of magnetic flux and energetic particles into the inner magnetosphere (e.g., Gkioulidou et al., 2014; Merkin et al., 2019), thus building the large-scale ring current and affecting global dipolarization of the inner magnetosphere, as well as resulting in density enhancements at the dayside magnetopause that will alter local reconnection rates (e.g., Zhang et al., 2017) with potentially global consequences. Additionally, these mesoscale processes shape the different wave populations of the inner magnetosphere: anisotropic ion injections provide free energy for the ElectroMagnetic Ion Cyclotron (EMIC) wave population and the evolving plasmapause boundary correlates with the relative distribution of hiss and chorus waves, with important consequence on flux enhancements of energetic trapped particles in the radiation belts. Physics-based models discussed in this article are listed and succinctly synthetized in Table 3.

5 Machine learning models

Machine learning (ML) techniques have advanced significantly over the past decade, especially during the past few years, mainly due to three factors: enormously increased volumes of data, significantly improved algorithms, and substantially more-powerful computation hardware (especially Graphics Processing Unit (GPU) computation that can accelerate the training by a factor of ~100) (Goodfellow et al., 2016). Although the applications of ML techniques are not entirely new in space physics, the unique combinations of the three aforementioned factors are leading to a new era where proper ML techniques could significantly enhance scientific progress, especially in understanding the non-linear nature of many physical processes. The combination of density data and models through machine learning techniques is one of the future and promising paths.

Taking advantage of the improvements in ML techniques and the extensive spatiotemporal coverage of NASA satellites, a series of ML-based models have been developed to study the cold plasma density for two purposes: 1) providing time- and history-dependent global distributions of total electron density in the Earth's magnetosphere, and 2) automatic detection of upper-hybrid-resonance frequency to calculate the total electron density.

A ML-based method was first proposed to reconstruct the global and time-varying distributions of any physical quantity Q that is sparsely sampled at various locations within the magnetosphere at any time (Bortnik et al., 2016). A feedforward neural network model was developed using point measurements of total electron density (i.e., cold plasma density) inferred from THEMIS spacecraft potential as an illustrative example. The model additionally takes the time series of the sym-H index as input and reconstructs global distributions of electron density at any time. Later, an optimized model of the electron density (DEN2D) near the equatorial plane was developed using THEMIS data (Chu et al., 2017a). The optimal input parameters of the DEN2D model are determined to be sym-H, AL, and F10.7 indices based on the neural network and neuron illustrated in Figure 2B. Time series of these indices are used as input so that the DEN2D model is both time- and history-dependent (i.e., dependent on a time sequence). The DEN2D model succeeds in reconstructing various plasmaspheric features during a geomagnetic storm, such as quiet time plasmasphere, erosion, and refilling of the plasmasphere and plume formation. Figures 2D, E shows the DEN2D density prediction extracted at both midnight and in the afternoon/day sector during plume expansion in February 2011. Analysis of these results demonstrated that refilling rates are dynamically changing (Chu et al., 2017b). The uncertainty of the DEN2D model can be estimated using a probabilistic model (Camporeale et al., 2019). Using global density profiles from the DEN2D model, it is shown that plasmaspheric hiss wave power is better parameterizing by plasma density rather than L shell, which should be adopted in current empirical models (Malaspina et al., 2018). A three-dimensional model of the electron density (DEN3D) was further developed using point measurements of the cold plasma density inferred from the upper hybrid resonance obtained from equatorial (ISEE and CRRES) and polar-orbiting satellites (POLAR and IMAGE). It has been verified using the additional measurements of density along the field line provided by IMAGE RPI (Chu et al., 2017b). The DEN2D and DEN3D models are shown

TABLE 4 Machine learning models of the electron density discussed in this article.

Name/References	Modeled quantity	Data in use (or type of physics)	Model validity domain	Known limitation
DEN2D Chu et al. (2017a)	Density with MLT dependence	THEMIS	L in [2, 8]	Same as DEN3D
DEN3D Chu et al. (2017b)	3D Density	ISEE, CRRES, POLAR, IMAGE	L in [1.5, 12]	Limited to the ranges of the training data, in spatial and activity coverage. Cannot usually make predictions during extreme geomagnetic storms
PINE Zhelavskaya et al. (2017)	Density with MLT dependence	Van Allen Probes	L in [1.75, 6.15]	Performance of neural networks limited by training data. No extreme geomagnetic storms in the PINE data
Neural network combined with physics-based model using Kalman filtering Zhelavskaya et al. (2021)	Density with MLT dependence	Neural network from Van Allen Probes (2012-2018) + Physics-based + Kalman filter	L in [1.75, 6.15]. Assimilation up to L = 10	Performance of neural networks limited by training data. No extreme geomagnetic storms in the PINE data. No MLT dependence of refilling rate. Too low density at low L-shell
Recurent neural network model (encoder-decoder model) Huang et al. (2022)	Density with MLT dependence	Recurent neural network model with encoder-decoder model with Long Short-Term Memory (LSTM) architecture. Van Allen Probes data	L in [1.75, 6.15]. Decoder of 270-min long. Encoder of 200-h long	Limited validation: model evaluated for only two plume events

to represent a large fraction of the observed variability in plasma density, with correlation coefficients on the order of 0.95, and a root-mean-square (rms) uncertainty about a factor of 2. There is room for improvement, since the model uncertainty is larger than the relative error of the underlying density measurements that are typically close to, or less than, 20% (Reinisch et al., 2004). For example, the confined density enhancements or depletions (ducts) may contribute to the model uncertainty since these localized structures may not be accurately predicted using geomagnetic indices. The DEN2D and DEN3D models can reconstruct the electron density with much smaller bias and error compared to previous empirical models (e.g., Global core plasma model (Gallagher et al., 2000; Sheeley et al., 2001; Denton et al., 2004; Denton et al., 2006), and the model of Ozhogin et al. (2012)), although the model of Ozhogin et al. (2012) has competitive performance inside the plasmasphere at the lowest L shells. DEN3D's predictive ability provides unprecedented opportunities to gain insight into the 3-D behavior of plasmaspheric features (e.g., plasmaspheric erosion and refilling, as well as plume formation). Using a recurrent neural network, Huang et al. (2022) shows that the model could predict the formation and evolution of stable and evident plume configuration.

An electron density model of equatorial electron densities (PINE) was developed using Van Allen Probes measurements (Zhelavskaya et al., 2017). The PINE model also successfully reproduced erosion of the plasmasphere on the nightside and plume formation and evolution. However, ML-based models in space physics usually suffer from the problem of imbalanced dataset, i.e., many days of quiet conditions and a few days of storms (Camporeale, 2019). To overcome this difficulty, a coupled model was developed by using data assimilation, which is a weighted average of the neural-network-based PINE model for quiet times and a physics-based plasmaspheric model for active times, to provide the plasma density during both quiet times and geomagnetic storms (Zhelavskaya et al., 2021). In addition to modeling electron density, a neural-network-based model was developed to reconstruct the time-varying plasmapause location near the equatorial plane, which outperformed previous empirical models within its database (Guo et al., 2021).

The application of ML density models in Fokker-Planck diffusion model has been performed in Ma et al. (2018) and Bortnik et al. (2018). Neural networks (and other ML techniques) can also be used to perform assimilation and interpolation/extrapolation of large datasets. Diffusion coefficients computed from variable density and wave properties are directly embedded in a machine learning model in Kluth et al. (2022). Predictions of this model for 3 days of quiet (Kp = 2) and moderate (Kp = 4) times following the storm are shown in Figure 2C (Ripoll et al., 2022b). Temporal variations are related to the simultaneous change of density and wave properties, calling for future models that will couple density and wave properties together. A Kp-based model of density and wave properties, as commonly used nowadays, would find constant values of the diffusion coefficients in time at fixed L-shell in Figure 2C while the ML model shows multiple variations with time.

The ML techniques can also be applied to labor-intensive tasks. For example, the electron densities can be inferred from plasma wave spectra, which can be both time-consuming and challenging (e.g., Kurth et al., 2015). A neural-network-based upper hybrid resonance (UHR) determination algorithm (NURD) was developed to automatically determine the electron density from plasma wave measurements using Van Allen Probes data (Zhelavskaya et al., 2016, 2018; 2020). NURD is applied to Van Allen Probes EMFISIS data in Allison et al. (2021) to show that the plasma density has a controlling effect over acceleration of radiation belt electrons to ultra-relativistic energies. ML-based methods for automatically determining the UHR frequency have also been applied to the Arase satellite using convolutional neural network (Hasegawa et al., 2019; Matsuda et al., 2020) and the CLUSTER mission using several automated pipelines based on neural network

methods (Gilet et al., 2021). Machine models of the electron density discussed in this article are listed and succinctly synthetized in Table 4.

6 Conclusion and perspectives

This review article strictly focuses on existing plasma density models, with an emphasis on those most commonly used (or most recent or promising) in radiation belt physics or space weather codes. Plasma density models describe the state of the plasmasphere in radiation belt simulations and are at the heart of the coupling between the ionosphere, which provides the plasma source, and the magnetosphere, wherein the intensity and variability of wave-particle interactions are conditioned by the plasma density (see Thaller et al., 2022 and references therein). All models discussed in this review article are listed in Tables 1, 2, 3, 4 with their main properties listed.

This review shows that most of the current empirical density or plasmapause models in use for the last decade are relatively simple in their geomagnetic activity dependence, often including a dependence on a single geomagnetic index, e.g., Kp (Carpenter and Anderson (1992)), and not including a magnetic local time dependence. Some of these models are incomplete, limited by either short temporal coverage, such as those extracted from CRRES measurements (e.g., O'brien and Moldwin, 2003), or omitting magnetic local time sectors (Carpenter and Anderson (1992)) or geomagnetic activity (Ozhogin et al. (2012). The variability of the electron plasma density is also very large when sorted with a single index, even if retaining magnetic local time dependence (see Figure 3 of Ripoll et al., 2022a). The spatial and temporal variations in plasma density depend on multiple parameters, such as the refilling rate, which is itself dependent on UV irradiance, the state of the thermosphere (neutral winds, composition, etc.), and the time history and level of convective processes due to geomagnetic activity, the coupling between the magnetosphere and ionosphere, particle precipitation, and other processes. For instance, the standard deviation of the 100 #/cc density level (assimilable to the plasmapause) varies from ~±0.5L for quiet times (Kp < 2, AE<300, Dst > −50) up to ~±1L for active times (Ripoll et al., 2022a). This variability can be explained from the multiple factors that influence the plasmaspheric density. For instance, Denton et al. (2006) retained in their plasma mass density model, the F10.7 EUV index, magnetic local time, the solar wind dynamic pressure Pdyn, the phase of the year, and the solar wind B_Z in GSM coordinates (parameters listed in order of decreasing importance). Chu et al. (2017a) found the optimal input parameters of the neural network DEN2D model are the sym-H, AL, and F10.7 indices. This highlights that new models should keep the main parameter dependences, including ionospheric and geomagnetic variability, and the MLT dependence.

Density variations are well observed between L~1.5 and L~6 at each pass of the Van Allen Probes (see Figure 2F in Ripoll et al., 2017), thus directly influencing the diffusion coefficients describing wave particle interactions in the radiation belts. Diffusion coefficients vary linearly with the electron plasma frequency, $f_{pe}(N)$, however changes in density further correlate with changes in the power of plasmaspheric hiss waves, which typically reside within the plasmasphere. Wave power is found to increase as density increases (Malaspina et al., 2016; Malaspina et al., 2018; Thomas et al., 2021). As a result, the simultaneous change in both density and hiss power leads to strong and complex variations of the diffusion coefficients (see Figure 5 in Ripoll et al., 2017). For instance, substorm activity causes short duration (within ± 4 h) reductions in density, and therefore a lowering of the amplitude of the whistler-mode waves within the plasmasphere. Variation in these parameters causes opposite effects in terms of pitch angle diffusion and, eventually, an overall decrease of pitch-angle diffusion during the main substorm activity (Ripoll et al., 2020b). Therefore, an accurate description of the plasma density, and its variation with geomagnetic activity, directly impacts the accuracy of modeling wave particle interactions.

The large number of parameters and mutually interdependent processes operating over different spatial and temporal scales, as just described, require models that include detailed physics or use machine learning methods in order to accurately capture or model these diverse plasma density features. Physics-based models have progressed well in the last decade, for instance, from 2D to 3D (e.g., Huba and Krall, 2013; Pierrard et al., 2021b) or by introducing new physical models or couplings, for instance, with detailed atmospheric sources (e.g., Huba and Liu, 2020). Physics-based models intrinsically simulate the geomagnetic activity and can retain various geomagnetic indices, whether these codes are limited to the atmosphere/ionosphere/plasmasphere system or are more global MHD codes, such as the MAGE-GAMERA project (e.g., Sorathia et al., 2021). It is only nowadays that physics-based models have started to be coupled with radiation belt codes (e.g., Dahmen et al., 2022), due to the overall complexity and multiplicity of the physical processes modeled in radiation belt codes (Ripoll et al., 2020a). An undeniable strength of physics-based models is that they can mitigate the inherent limitations of sparse spatial coverage of the data, in particular for active times (e.g., Zhelavskaya et al., 2021). Machine learning models also account intrinsically for multiple dependences (e.g., Chu et al., 2017a; Zhelavskaya et al., 2021), and are undoubtedly a promising approach to combine multiple satellite observations and produce the next-generation of global empirical plasma density models. A neural network-based density model has recently served to show that the plasma density has a controlling effect over acceleration of radiation belt electrons to ultra-relativistic energies (Allison et al., 2021). Contrary to empirical fits that do not allow trustable extrapolation, machine learning techniques, such as neural networks, are extremely promising in terms of predictive capability, which is a keystone for space weather codes. Progress in neural network technics are also expected in the coming years. For instance, the use of the recent physics-informed neural networks (e.g., Raissi et al., 2019), in which the neural network is constrained to respect any given physical law described by general non-linear partial differential equations, could be an hybrid way between physics-based models and machine learning technics, possibly well applying to plasma density modeling. Finally, the close relationship between plasmaspheric waves and plasmaspheric density also highlights the need for more coupling between them, whether that coupling is done when generating physical

models or embedded within macroscopic quantities such as diffusion coefficients (e.g., Kluth et al., 2022).

In any case, all models eventually aim to capture the effect caused by magnetic local time variations of the plasma density for various geomagnetic conditions. There is an undeniable need of new measurements to support model development and validation. However, most measurements of the electron density used to build and/or validate these models, are often single observation per time at a single location in space, leading to a reliance on statistics to capture the magnetic local time resolution. This reliance on statistics means that the dynamics at any given location are averaged over, resulting in the loss of some of the structures, their rate of change, and motion at any given spatial location. This limitation is difficult to overcome, even when combining observations from multiple satellites with machine learning techniques. Future missions should consider the use of multiple spacecraft/cubesats azimuthally separated across various magnetic local times in order to provide better coverage and resolution of plasma density dynamics coupled with simultaneous measurements of the ambient electromagnetic waves, which ultimately impact the models used in radiation belt and space weather codes.

Author contributions

J-FR conceptualized and led the study. J-FR wrote the manuscript with the contribution of VP(Section 4), GC (Section 2 and Section 3), XC (Section 5), KS, and VM (Section 4). J-FR created Tables 1, 2, 3, 4. ST treated the Van Allen Probes B EFW data presented in Figures 1A–C. VP ran the SPM code to generate Figures 1D–F. DH performed model computation in Figures 1G, H. KS performed Gamera runs to generate Figure 2A. J-FR generated Figures 2B, C. XC generated Figures 2D, E. All authors contributed to writing of the manuscript through reviews and edits.

Funding

NSF-GEM grant 2040708. NASA grant 80NSSC20K1324. Horizon 2020 PITHIA-NRF grant agreement No. 101007599. EURAMET's European Partnership on Metrology project 21GRD02 BIOSPHERE. US DOE DE-AC05-00OR22725. LANL project 20220453ER, ANR ASTRID project "PACTE-ESPACE".

Acknowledgments

The authors thank the EFW and EMFISIS teams of the Van Allen Probes mission for their support. This research was supported by the International Space Science Institute (ISSI) in Bern, through ISSI International Team project #477 (Radiation Belt Physics From Top To Bottom: Combining Multipoint Satellite Observations And Data Assimilative Models To Determine The Interplay Between Sources And Losses). The work of J-FR and GC was performed under the auspices of an agreement between CEA/DAM (Commissariat a l'Energie Atomique, Direction des Applications Militaires) and NNSA/DP (National Nuclear Security Administration, Defense Program) on cooperation on fundamental science. J-FR thank the Direction Générale de l'Armement (DGA) and the Agence pour l'Innovation de Défense (AID) for funding the ASTRID project "PACTE-ESPACE". DH, GC, and J-FR acknowledge NSF-GEM grant 2040708. DH acknowledges NASA grant 80NSSC20K1324. VP acknowledges the Horizon 2020 PITHIA-NRF grant agreement No. 101007599 and the EURAMET's European Partnership on Metrology project 21GRD02 BIOSPHERE. SD acknowledges support by the US DOE under contracts DE-AC05-00OR22725. GD was supported by the Laboratory Directed Research and Development program at Los Alamos National Laboratory (LANL) under project 20220453ER.

Conflict of interest

ST was employed by the company Orion Space Solutions.

The remaining authors declare that the research was conducted in the absence of any commercial or financial relationships that could be construed as a potential conflict of interest.

Publisher's note

References

Albert, J. M. (1999). Analysis of quasi-linear diffusion coefficients. *J. Geophys. Res.* 104, 2429–2441. doi:10.1029/1998JA900113

Allison, H. J., Shprits, Y. Y., Zhelavskaya, I. S., Wang, D., and Smirnov, A. G. (2021). Gyroresonant wave-particle interactions with chorus waves during extreme depletions of plasma density in the Van Allen radiation belts. *Sci. Adv.* 7, eabc0380. doi:10.1126/sciadv.abc0380

Angerami, J. J., and Thomas, J. O. (1964). Studies of planetary atmospheres: 1. The distribution of electrons and ions in the earth's exosphere. *J. Geophys. Res.* 69 (21), 4537–4560. doi:10.1029/JZ069i021p04537

Bandić, M., Verbanac, G., Moldwin, M. B., Pierrard, V., and Piredda, G. (2016). MLT dependence in the relationship between plasmapause, solar wind, and geomagnetic activity based on CRRES: 1990–1991. *J. Geophys. Res. Space Phys.* 121, 4397–4408. doi:10.1002/2015JA022278

Bandic, M., Verbanac, G., Pierrard, V., and Cho, J. (2017). Evidence of MLT propagation of the plasmapause inferred from THEMIS data. *J. Atmosph. Sol.-Terr. Phys.* 161, 55–63. doi:10.1016/j.jastp.2017.05.005

Berube, D., Moldwin, M. B., Fung, S. F., and Green, J. L. (2005). A plasmaspheric mass density model and constraints on its heavy ion concentration. *J. Geophys. Res.* 110, A04212. doi:10.1029/2004JA010684

Bilitza, D., and Reinisch, B. W. (2008). International reference ionosphere 2007: Improvements and new parameters. *Adv. Space Res.* 42 (4), 599–609. doi:10.1016/j.asr.2007.07.048

Bilitza, D., Altadill, D., Truhlik, V., Shubin, V., Galkin, I., Reinisch, B., et al. (2017). International Reference Ionosphere 2016: From ionospheric climate to real-time weather predictions. *Space weather.* 15, 418–429. doi:10.1002/2016sw001593

Bilitza, D., Altadill, D., Zhang, Y., Mertens, C., Truhlik, V., Richards, P., et al. (2014). The international reference ionosphere 2012 – A model of international collaboration. *J. Space Weather Space Clim.* 4, A07–A12. doi:10.1051/swsc/2014004

Bilitza, D. (1986). International reference ionosphere: Recent developments. *Radio Sci.* 21 (3), 343–346. doi:10.1029/RS021i003p00343

Bilitza, D. (2018). IRI the international standard for the ionosphere. *Adv. Radio Sci.* 16, 1–11. doi:10.5194/ars-16-1-2018

Bortnik, J., Chu, X., Ma, Q., Li, W., Zhang, X., Thorne, R. M., et al. (2018). "Artificial neural networks for determining magnetospheric conditions," in *Machine learning techniques for space weather*. Editors E. Camporeale, S. Wing, and J. R. Johnson (Netherlands: Elsevier), 279–300. doi:10.1016/b978-0-12-811788-0.00011-1

Bortnik, J., Li, W., Thorne, R. M., and Angelopoulos, V. (2016). A unified approach to inner magnetospheric state prediction. *J. Geophys. Res. Space Phys.* 121 (3), 2423–2430. doi:10.1002/2015ja021733

Botek, E., Pierrard, V., and Darrouzet, F. (2021). Assessment of the Earth's cold plasmatrough modeling by using Van Allen Probes/EMFISIS and Arase/PWE electron density data. *J. Geophys. Res. Space Res.* 126. doi:10.1029/2021JA029737

Camporeale, E., Chu, X., Agapitov, O. V., and Bortnik, J. (2019). On the generation of probabilistic forecasts from deterministic models. *Space weather*. 17, 455–475. doi:10.1029/2018SW002026

Camporeale, E. (2019). The challenge of machine learning in Space Weather: Nowcasting and forecasting. *Space weather*. 17, 1166–1207. doi:10.1029/2018SW002061

Carpenter, D. L., and Anderson, R. R. (1992). An ISEE/whistler model of equatorial electron density 740 in the magnetosphere. *J. Geophys. Res.* 97 (A2), 1097–1108. doi:10.1029/91JA01548

Carpenter, D. L., Anderson, R. R., Calvert, W., and Moldwin, M. B. (2000). CRRES observations of density cavities inside the plasmasphere. *J. Geophys. Res.* 105 (10), 23323–23338. doi:10.1029/2000JA000013

Carpenter, D. L., and Smith, R. L. (1964). Whistler measurements of electron density in the 738 magnetosphere. *Rev. Geophys. Space Phys.* 2, 415. doi:10.1029/91JA01548

Carpenter, D. L. (1963). Whistler evidence of a 'knee' in the magnetospheric ionization density profile. *J. Geophys. Res.* 68, 1675–1682. doi:10.1029/jz068i006p01675

Carpenter, D. L. (1966). Whistler studies of the plasmapause in the magnetosphere,1, Temporal variations in the position of the knee and some evidence on plasma motions near the knee. *J. Geophys. Res.* 71, 693–709. doi:10.1029/jz071i003p00693

Cervantes, S., Shprits, Y. Y., Aseev, N. A., and Allison, H. J. (2020a). Quantifying the effects of EMIC wave scattering and magnetopause shadowing in the outer electron radiation belt by means of data assimilation. *J. Geophys. Res. Space Phys.* 125, e2020JA028208. doi:10.1029/2020JA028208

Cervantes, S., Shprits, Y. Y., Aseev, N. A., Drozdov, A. Y., Castillo, A., and Stolle, C. (2020b). Identifying radiation belt electron source and loss processes by assimilating spacecraft data in a three-dimensional diffusion model. *J. Geophys. Res. Space Phys.* 125, e2019JA027514. doi:10.1029/2019JA027514

Chatterjee, K., and Schunk, R. W. (2019). A multiion, flux-corrected transport based hydrodynamic model for the plasmasphere refilling problem. *J. Geophys. Res. Space Phys.* 125 (1), 250. doi:10.1029/2019JA026834

Chatterjee, K., and Schunk, R. W. (2020b). A semikinetic model of plasmasphere refilling following geomagnetic storms and comparison with hydrodynamic results. *J. Geophys. Res. Space Phys.* 125, e2020JA028016. doi:10.1029/2020JA028016

Chatterjee, K., and Schunk, R. W. (2020a). The development and validation of a "flux-corrected transport" based solution methodology for the plasmasphere refilling problem following geomagnetic storms. *Earth, Planets Space* 72 (26), 26. doi:10.1186/s40623-020-01150-0

Chatterjee, K. (2018). The development of hydrodynamic and kinetic models for the Plasmasphere refilling problem following a geomagnetic storm. Available at: https://digitalcommons.usu.edu/etd/7364.

Chen, X., Dang, T., Zhang, B., Lotko, W., Pham, K., Wang, W., et al. (2021). Global effects of a polar solar eclipse on the coupled magnetosphere-ionosphere system. *Geophys. Res. Lett.* 48, e2021GL096471. doi:10.1029/2021GL096471

Cho, J., Lee, D.-Y., Kim, J.-H., Shin, D.-K., Kim, K.-C., and Turner, D. (2015). New model fit functions of the plasmapause location determined using THEMIS observations during the ascending phase of solar cycle 24. *J. Geophys. Res. Space Phys.* 120, 2877–2889. doi:10.1002/2015JA021030

Chu, X., Bortnik, J., Li, W., Ma, Q., Angelopoulos, V., and Thorne, R. M. (2017b). Erosion and refilling of the plasmasphere during a geomagnetic storm modeled by a neural network. *J. Geophys. Res. Space Phys.* 122 (7), 7118–7129. doi:10.1002/2017ja023948

Chu, X., Bortnik, J., Li, W., Ma, Q., Denton, R., Yue, C., et al. (2017a). A neural network model of three-dimensional dynamic electron density in the inner magnetosphere. *J. Geophys. Res. Space Phys.* 122 (9), 9183–9197. doi:10.1002/2017ja024464

Coïsson, P., Radicella, S. M., Leitinger, R., and Nava, B. (2006). Topside electron density in IRI and NeQuick: Features and limitations. *Adv. Space Res.* 37 (5), 937–942. doi:10.1016/j.asr.2005.09.015

Dahmen, N., Sicard, A., Brunet, A., Santolik, O., Pierrard, V., Botek, E., et al. (2022). Farwest: Efficient computation of wave-particle interactions for a dynamic description of the electron radiation belt diffusion. *J. Geophys. Res. Space Phys.* 127, e2022JA030518. doi:10.1029/2022JA030518

Darrouzet, F., and De Keyser, J. (2013). The dynamics of the plasmasphere: Recent results. *J. Atmos. Solar-Terrestrial Phys.* 99, 53–60. doi:10.1016/j.jastp.2012.07.004

De Pascuale, S., Jordanova, V. K., Goldstein, J., Kletzing, C. A., Kurth, W. S., Thaller, S. A., et al. (2018). Simulations of Van Allen Probes plasmaspheric electron density observations. *J. Geophys. Res. Space Phys.* 123, 9453–9475. doi:10.1029/2018JA025776

Delzanno, G. L., Borovsky, J. E., Henderson, M. G., Resendiz Lira, P. A., Roytershteyn, V., and Welling, D. T. (2021). The impact of cold electrons and cold ions in magnetospheric physics. *J. Atmos. Solar-Terrestrial Phys.* 220, 105599. doi:10.1016/j.jastp.2021.105599

Denton, R. E., Menietti, J. D., Goldstein, J., Young, S. L., and Anderson, R. R. (2004). Electron density in the magnetosphere. *J. Geophys. Res.* 109, A09215. doi:10.1029/2003JA010245

Denton, R. E., Takahashi, K., Galkin, I. A., Nsumei, P. A., Huang, X., Reinisch, B. W., et al. (2006). Distribution of density along magnetospheric field lines. *J. Geophys. Res.* 111, A04213. doi:10.1029/2005JA011414

Denton, R. E., Wang, Y., Webb, P. A., Tengdin, P. M., Goldstein, J., Redfern, J. A., et al. (2012). Magnetospheric electron density long-term (>1 day) refilling rates inferred from passive radio emissions measured by IMAGE RPI during geomagnetically quiet times. *J. Geophys. Res. Space Phys.* 117. doi:10.1029/2011ja017274

Escoubet, J., Song, P., Reinisch, B. W., and Green, J. L. (2007). Smooth electron density transition from plasmasphere to the subauroral region. *J. Geophys. Res.* 112, A05227. doi:10.1029/2007JA012298

Fuller-Rowell, T. J., Akmaev, R. A., Wu, F., Anghel, A., Maruyama, N., Anderson, D. N., et al. (2008). Impact of terrestrial weather on the upper atmosphere. *Geophys. Res. Lett.* 35, L09808. doi:10.1029/2007GL032911

Gallagher, D. L., Craven, P. D., and Comfort, R. H. (2000). Global core plasma model. *J. Geophys. Res. Space Phys.* 105, 18819–18833. doi:10.1029/1999JA000241

Gilet, N., De Leon, E., Gallé, R., Vallières, X., Rauch, J.-L., Jegou, K., et al. (2021). Automatic detection of the thermal electron density from the WHISPER experiment onboard CLUSTER-II mission with neural networks. *J. Geophys. Res. Space Phys.* 126, e2020JA028901. doi:10.1029/2020JA028901

Gkioulidou, M., Ukhorskiy, A. Y., Mitchell, D. G., Sotirelis, T., Mauk, B. H., and Lanzerotti, L. J. (2014). The role of small-scale ion injections in the buildup of Earth's ring current pressure: Van Allen Probes observations of the 17 March 2013 storm. *J. Geophys. Res. Space Phys.* 119, 7327–7342. doi:10.1002/2014ja020096

Glauert, S. A., and Horne, R. B. (2005). Calculation of pitch angle and energy diffusion coefficients with the PADIE code. *J. Geophys. Res.* 110, A04206. doi:10.1029/2004JA010851

Goldstein, J., Baker, D. N., Blake, J. B., De Pascuale, S., Funsten, H. O., Jaynes, A. N., et al. (2016). The relationship between the plasmapause and outer belt electrons. *J. Geophys. Res. Space Phys.* 121, 8392–8416. doi:10.1002/2016JA023046

Goldstein, J., Burch, J. L., and Sandel, B. R. (2005). Magnetospheric model of subauroral polarization stream. *J. Geophys. Res.* 110, A09222. doi:10.1029/2005JA011135

Goldstein, J., De Pascuale, S., Kletzing, C., Kurth, W., Genestreti, K. J., Skoug, R. M., et al. (2014a). Simulation of van allen probes plasmapause encounters. *J. Geophys. Res. Space Phys.* 119, 7464–7484. doi:10.1002/2014JA020252

Goldstein, J., Pascuale, S., and Kurth, W. S. (2019). Epoch-based model for stormtime plasmapause location. *J. Geophys. Res.* 124, 4462–4491. doi:10.1029/2018JA025996

Goldstein, J. (2006). Plasmasphere response: Tutorial and review of recent imaging results. *Space Sci. Rev.* 124, 203–216. doi:10.1007/s11214-006-9105-y

Goldstein, J., Sandel, B. R., Hairston, M. R., and Reiff, P. H. (2003). Control of plasmaspheric dynamics by both convection and sub-auroral polarization stream. *Geophys. Res. Lett.* 30 (24), 2243. doi:10.1029/2003GL018390

Goldstein, J., Thomsen, M. F., and DeJong, A. (2014b). *In situ* signatures of residual plasmaspheric plumes: Observations and simulation. *J. Geophys. Res. Space Phys.* 119, 4706–4722. doi:10.1002/2014JA019953

Goodfellow, I., Bengio, Y., Courville, A., and Bengio, Y. (2016). *Deep learning*. Cambridge: MIT press.

Gulyaeva, T. L., Arikan, F., and Stanislawska, I. (2011). Inter-hemispheric imaging of the ionosphere with the upgraded IRI-Plas model during the space weather storms. *Earth Planet Sp.* 63, 929–939. doi:10.5047/eps.2011.04.007

Gulyaeva, T. L. (2012). Empirical model of ionospheric storm effects on the F2 layer peak height associated with changes of peak electron density. *J. Geophys. Res.* 117, A02302. doi:10.1029/2011JA017158

Gulyaeva, T. L., Huang, X., and Reinisch, B. W. (2002). Plasmaspheric extension of topside electron density profiles. *Adv. Space Res.* 29 (6), 825–831. doi:10.1016/s0273-1177(02)00038-8

Gulyaeva, T. L. (2011). Storm time behavior of topside scale height inferred from the ionosphere-plasmasphere model driven by the F2 layer peak and GPS-TEC observations. *Adv. Space Res.* 47, 913–920. doi:10.1016/j.asr.2010.10.025

Guo, D., Fu, S., Xiang, Z., Ni, B., Guo, Y., Feng, M., et al. (2021). Prediction of dynamic plasmapause location using a neural network. *Space weather*. 19, e2020SW002622. doi:10.1029/2020SW002622

Hain, K. (1987). The partial donor cell method. *J. Comput. Phys.* 73, 131–147. doi:10.1016/0021-9991(87)90110-0

Hartley, D. P., Cunningham, G. S., Ripoll, J.-F., Malaspina, D. M., Kasahara, Y., Miyoshi, Y., et al. (2023). *Using van allen probes and Arase observations to develop an empirical plasma density model in the inner zone. J. Geophys. Res. Space Phys., in press.* doi:10.1029/2022JA031012

Hartley, D. P., Kletzing, C. A., Kurth, W. S., Bounds, S. R., Averkamp, T. F., Hospodarsky, G. B., et al. (2016). Using thecold plasma dispersion relation and whistler mode waves to

quantify the antenna sheath impedance of the Van Allen Probes EFW instrument. *J. Geophys. Res. SpacePhysics* 121, 4590–4606. doi:10.1002/2016JA022501

Hasegawa, T., Matsuda, S., Kumamoto, A., Tsuchiya, F., Kasahara, Y., Miyoshi, Y., et al. (2019). Automatic electron density determination by using a convolutional neural network. *IEEE Access* 7, 163384–163394. doi:10.1109/ACCESS.2019.2951916

He, F., Zhang, X.-X., Lin, R.-L., Fok, M.-C., Katus, R. M., Liemohn, M. W., et al. (2017). A new solar wind-driven global dynamic plasmapause model: 2. Model and validation. *J. Geophys. Res. Space Physics*. 122, 7172–7187. doi:10.1002/2017JA023913

Hedin, A. E. (1987). MSIS-86 thermospheric model. *J. Geophys. Res.* 92 (A5), 4649–4662. doi:10.1029/JA092iA05p04649

Helmboldt, J. F., and Hurley-Walker, N. (2020). Ionospheric irregularities observed during the GLEAM survey. *Radio Sci.* 55, e2020RS007106. doi:10.1029/2020RS007106

Huang, S., Li, W., Shen, X.-C., Ma, Q., Chu, X., Ma, D., et al. (2022). Application of recurrent neural network to modeling Earth's global electron density. *J. Geophys. Res. Space Phys.* 127, e2022JA030695. doi:10.1029/2022JA030695

Huang, X., Reinisch, B. W., Song, P., Green, J. L., and Gallagher, D. L. (2004). Developing an empirical density model of the plasmasphere using IMAGE/RPI observations. *Adv. Space Res.* 33, 829–832. doi:10.1016/j.asr.2003.07.007

Huba, J. D. (2023). Resolution of the equatorial spread F problem: Revisited. *Front. Astron. Space Sci.* 9, 1098083. doi:10.3389/fspas.2022.1098083

Huba, J. D. (2003). "A tutorial on Hall magnetohydrodynamics," in *Space simulations*. Editors M. Scholer, C. T. Dum, and J. Büchner (New York: Springer), 170.

Huba, J. D., Joyce, G., and Fedder, J. A. (2000). Sami2 (Sami2 is another model of the ionosphere): A new low-latitude ionosphere model. *J. Geophys. Res.* 105 (10), 53.

Huba, J. D., Joyce, G., Sazykin, S., Wolf, R., and Spiro, R. (2005). Simulation study of penetration electric field effects on the low-to mid-latitude ionosphere. *Geophys. Res. Lett.* 32, L23101. doi:10.1029/2005GL024162

Huba, J. D., and Krall, J. (2013). Modeling the plasmasphere with Sami3. *Geophys. Res. Lett.* 40, 6–10. doi:10.1029/2012GL054300

Huba, J. D., and Liu, H.-L. (2020). Global modeling of equatorial spread F with Sami3/WACCM-X. *Geophys. Res. Lett.* 47, e2020GL088258. doi:10.1029/2020GL088258

Huba, J. D., Maute, A., and Crowley, G. (2017). Sami3_ICON: Model of the ionosphere/plasmasphere system. *Space Sci. Rev.* 212, 731–742. doi:10.1007/s11214-017-0415-z

Huba, J. D., Sazykin, S., and Coster, A. (2017b). Sami3-RCM simulation of the 17 March 2015 geomagnetic storm. *J. Geophys. Res. Space Phys.* 122, 1246–1257. doi:10.1002/2016JA023341

Huba, J. D., and Sazykin, S. (2014). Storm time ionosphere and plasmasphere structuring: Sami3-RCM simulation of the 31 March 2001 geomagnetic storm. *Geophys. Res. Lett.* 41, 8208–8214. doi:10.1002/2014GL062110

Hysell, D. L., Fang, T. W., and Fuller-Rowell, T. J. (2022). Modeling equatorial F-region ionospheric instability using a regional ionospheric irregularity model and WAM-IPE. *J. Geophys. Res. Space Phys.* 127, e2022JA030513. doi:10.1029/2022JA030513

Jacobson, A. R., and Erickson, W. C. (1993). Observations of electron density irregularities in the plasmasphere using the VLA radio interferometer. *Ann. Geophys.* 11 (10), 869–888.

Jahn, J., Goldstein, J., Kurth, W., Thaller, S., De Pascuale, S., Wygant, J., et al. (2020). Determining plasmaspheric density from the upper hybrid resonance and from spacecraft potential: How do they compare? *J. Geophys. Res. Space Phys.* 125, 1–17.

Jordanova, V. K., Miyoshi, Y. S., Zaharia, S., Thomsen, M. F., Reeves, G. D., Evans, D. S., et al. (2006). Kinetic simulations of ring current evolution during the geospace environment modeling challenge events. *J. Geophys. Res.* 111, A11S10. doi:10.1029/2006JA011644

Jordanova, V. K., Yu, Y., Niehof, J. T., Skoug, R. M., Reeves, G. D., Kletzing, C. A., et al. (2014). Simulations of inner magnetosphere dynamics with an expanded RAM-SCB model and comparisons with Van Allen Probes observations. *Geophys. Res. Lett.* 41, 2687–2694. doi:10.1002/2014GL059533

Kim, K. C., Shprits, Y., Subbotin, D., and Ni, B. (2011). Understanding the dynamic evolution of the relativistic electron slot region including radial and pitch angle diffusion. *J. Geophys. Res.* 116, A10214. doi:10.1029/2011JA016684

Kletzing, C. A., Kurth, W. S., Acuna, M., MacDowall, R. J., Torbert, R. B., Averkamp, T., et al. (2013). The electric and magnetic field instrument suite and integrated science (EMFISIS) on RBSP. *Space Sci. Rev.* 179, 127–181. doi:10.1007/s11214-013-9993-6

Kluth, G., Ripoll, J.-F., Has, S., Fischer, A., and Mougeot, M. (2022). Machine learning methods applied to the global modeling of event-driven pitch angle diffusion coefficients during high-speed streams. *Front. Phys.* 10, 786639. doi:10.3389/fphy.2022.786639

Kotova, G. A. (2007). The Earth's plasmasphere: State of studies (a review). *Geomagnetism Aeronomy* 47 (4), 409–422. doi:10.1134/s0016793207040019

Krall, J., and Huba, J. D. (2021). Counterstreaming cold H+, He+, O+, and N+ outflows in the plasmasphere. *Front. Astron. Space Sci.* 8, 712611. doi:10.3389/fspas.2021.712611

Krall, J., Huba, J. D., and Borovsky, J. E. (2018). Sami3 simulations of a persistent plasmasphere plume. *Geophys. Res. Lett.* 45, 3374–3381. doi:10.1002/2017GL076448

Krall, J., and Huba, J. D. (2013). Sami3 simulation of plasmasphere refilling. *Geophys. Res. Lett.* 40, 2484–2488. doi:10.1002/grl.50458

Krall, J., and Huba, J. (2019). Simulation of counterstreaming H+ outflows during plasmasphere refilling. *Geophys. Res. Lett.* 46, 3052–3060. doi:10.1029/2019GL082130

Kurth, W. S., De Pascuale, S., Faden, J. B., Kletzing, C. A., Hospodarsky, G. B., Thaller, S., et al. (2015). Electron densities inferred from plasma wave spectra obtained by the Waves instrument on Van Allen Probes. *J. Geophys. Res. Space Phys.* 120, 904–914. doi:10.1002/2014JA020857

Kwon, H.-J., Kim, K.-H., Jee, G., Park, J.-S., Jin, H., and Nishimura, Y. (2015). Plasmapause location under quiet geomagnetic conditions ($K_p \leq 1$): THEMIS observations. *Res. Lett.* 42, 7303–7310. doi:10.1002/2015GL066090

Larsen, B. A., Klumpar, D. M., and Gurgiolo, C. (2007). Correlation between plasmapause position and solar wind parameters. *J. Atmos. Solar-Terrestrial Phys.* 69, 334–340. doi:10.1016/j.jastp.2006.06.017

Lin, D., Wang, W., Merkin, V. G., Huang, C., Oppenheim, M., Sorathia, K., et al. (2022). Origin of dawnside subauroral polarization streams during major geomagnetic storms. *AGU Adv.* 3, e2022AV000708. doi:10.1029/2022AV000708

Liu, X., and Liu, W. (2014). A new plasmapause location model based on THEMIS observations. *Sci. China Earth Sci.* 57, 2552–2557. doi:10.1007/s11430-014-4844-1

Liu, X., Liu, W., Cao, J. B., Fu, H. S., Yu, J., and Li, X. (2015). Dynamic plasmapause model based on THEMIS measurements. *J. Geophys. Res. Space Phys.* 120, 10543–10556. doi:10.1002/2015JA021801

Loi, S. T., Murphy, T., Cairns, I. H., Menk, F. W., Waters, C. L., Erickson, P. J., et al. (2015). Real-time imaging of density ducts between the plasmasphere and ionosphere. *Geophys. Res. Lett.* 42, 3707–3714. doi:10.1002/2015GL063699

Lyons, L. R., and Thorne, R. M. (1973). Equilibrium structure of radiation belt electrons. *J. Geophys. Res.* 78 (13), 2142–2149. doi:10.1029/JA078i013p02142

Ma, Q., Li, W., Bortnik, J., Thorne, R. M., Chu, X., Ozeke, L. G., et al. (2018). Quantitative evaluation of radial diffusion and local acceleration processes during GEM challenge events. *J. Geophys. Res. Space Phys.* 123, 1938–1952. doi:10.1002/2017JA025114

Malaspina, D. M., Jaynes, A. N., Boulé, C., Bortnik, J., Thaller, S. A., Ergun, R. E., et al. (2016). The distribution of plasmaspheric Hiss Wave Power with respect to plasmapause location. *Geophys. Res. Lett.* 43, 7878–7886. doi:10.1002/2016GL069982

Malaspina, D. M., Jaynes, A. N., Elkington, S., Chan, A., Hospodarsky, G., and Wygant, J. (2020). Testing the organization of lower-band whistler- mode chorus wave properties by plasmapause location. *J. Geophys. Res. Space Phys.* 126, e2020JA028458. doi:10.1029/2020JA028458

Malaspina, D. M., Ripoll, J.-F., Chu, X., Hospodarsky, G., and Wygant, J. (2018). Variation in plasmaspheric hiss wave power with plasma density. *Geophys. Res. Lett.* 45. doi:10.1029/2018GL078564

Marchaudon, A., and Blelly, P.-L. (2015). A new interhemispheric 16-moment model of the plasmasphere-ionosphere system: Ipim. *J. Geophys. Res. Space Phys.* 120, 5728–5745. doi:10.1002/2015JA021193

Marchaudon, A., Blelly, P.-L., Grandin, M., Aikio, A., Kozlovsky, A., and Virtanen, I. (2018). IPIM modeling of the ionospheric F2 layer depletion at high latitudes during a high-speed stream event. *Space Phys. Space Phys.* 123, 7051–7066. doi:10.1029/2018JA025744

Marchaudon, A., and Blelly, P.-L. (2020). Impact of the dipole tilt angle on the ionospheric plasma as modeled with IPIM. *IPIM. J. Geophys. Res. Space Phys.* 125, e2019JA027672. doi:10.1029/2019JA027672

Maruyama, N., Sun, Y.-Y., Richards, P. G., Middlecoff, J., Fang, T.-W., Fuller-Rowell, T. J., et al. (2016). A new source of the midlatitude ionospheric peak density structure revealed by a new ionosphere-plasmasphere model. *Geophys. Res. Lett.* 43, 2429–2435. doi:10.1002/2015GL067312

Matsuda, S., Hasegawa, T., Kumamoto, A., Tsuchiya, F., Kasahara, Y., Miyoshi, Y., et al. (2020). Detection of UHR frequencies by a convolutional neural network from Arase/PWE data. *J. Geophys. Res. SpacePhysics* 125, e2020JA028075. doi:10.1029/2020JA028075

Mauk, B. H., Fox, N. J., Kanekal, S. G., Kessel, R. L., Sibeck, D. G., and Ukhorskiy, A. (2013). Science objectives and rationale for the radiation belt storm probes mission. *Space Sci. Rev.* 179 (1–4), 3–27. doi:10.1007/s11214-012-9908-y

Merkin, V. G., Lyon, J. G., and Claudepierre, S. G. (2013). Kelvin-Helmholtz instability of the magnetospheric boundary in a three-dimensional global MHD simulation during northward IMF conditions. *J. Geophys. Res. Space Phys.* 118, 5478–5496. doi:10.1002/jgra.50520

Merkin, V. G., and Lyon, J. G. (2010). Effects of the low-latitude ionospheric boundary condition on the global magnetosphere. *J. Geophys. Res.* 115, A10202. doi:10.1029/2010ja015461

Merkin, V. G., Panov, E. V., Sorathia, K., and Ukhorskiy, A. Y. (2019). Contribution of bursty bulk flows to the global dipolarization of the magnetotail during an isolated substorm. *J. Geophys. Res. Space Phys.* 64, 8647–8668. doi:10.1029/2019ja026872

Miyoshi, Y., Shinohara, I., Takashima, T., Asamura, K., Higashio, N., Mitani, T., et al. (2018). Geospace exploration project ERG. *Earth Planets Space* 70, 101. doi:10.1186/s40623-018-0862-0

Moldwin, M. B., Downward, L., Rassoul, H. K., Amin, R., and Anderson, R. R. (2002). A new model of the location of the plasmapause: CRRES results. *J. Geophys. Res.* 107 (11), 1339. doi:10.1029/2001JA009211

Nsumei, P., Reinisch, B. W., Huang, X., and Bilitza, D. (2012). New Vary-Chap profile of the topside ionosphere electron density distribution for use with the IRI model and the GIRO real time data. *Radio Sci.* 47, RS0L16. doi:10.1029/2012RS004989

Obana, Y., Maruyama, N., Shinbori, A., Hashimoto, K. K., Fedrizzi, M., Nosé, M., et al. (2019). Response of the ionosphere-plasmasphere coupling to the September 2017 storm: What erodes the plasmasphere so severely? *Space weather*. 17, 861–876. doi:10.1029/2019SW002168

O'Brien, T. P., and Moldwin, M. B. (2003). Empirical plasmapause models from magnetic indices. *Geophys. Res. Lett.* 30 (4), 2002GL016007. doi:10.1029/2002GL016007

Ozhogin, P., Tu, J., Song, P., and Reinisch, B. W. (2012). Field-aligned distribution of the plasmaspheric electron density: An empirical model derived from the IMAGE RPI measurements. *J. Geophys. Res.* 117, A06225. doi:10.1029/2011JA017330

Pembroke, A., Toffoletto, F., Sazykin, S., Wiltberger, M., Lyon, J., Merkin, V., et al. (2012). Initial results from a dynamic coupled magnetosphere-ionosphere-ring current model. *J. Geophys. Res.* 117, A02211. doi:10.1029/2011JA016979

Pham, K., Zhang, B., Sorathia, K., Dang, T., Wang, W., Merkin, V., et al. (2021). Thermospheric density perturbations produced by traveling atmospheric disturbances during August 2005 Storm. *Earth Space Sci. Open Archive* 19, 10508477. doi:10.1002/essoar.10508477.1

Pierrard, V., Botek, E., and Darrouzet, F. (2021b). Improving predictions of the 3D dynamic model of the plasmasphere. *Front. Astron. Space Sci.* 88, 69681401. doi:10.3389/fspas.2021.681401

Pierrard, V., Botek, E., Ripoll, J.-F., Thaller, S. A., Moldwin, M. B., Ruohoniemi, M., et al. (2021c). Links of the plasmapause with other boundary layers of the magnetosphere: Ionospheric convection, radiation belt boundaries, auroral oval. *Auror. Oval. Front. Astron. Space Sci.* 8, 728531. doi:10.3389/fspas.2021.728531

Pierrard, V., Goldstein, J., André, N., Jordanova, V. K., Kotova, G. A., Lemaire, J. F., et al. (2009). Recent progress in physics-based models of the plasmasphere. *Space Sci. Rev.* 145, 193–229. doi:10.1007/s11214-008-9480-7

Pierrard, V., and Lemaire, J. (2004). Development of shoulders and plumes in the frame of the interchange instability mechanism for plasmapause formation. *Geophys. Res. Lett.* 31 (5), L05809–L05811. doi:10.1029/2003GL018919

Pierrard, V., and Lemaire, J. (2001). Exospheric model of the plasmasphere. *J. Atmos. Solar-Terrestrial Phys.* 63 (11), 1261–1265. doi:10.1016/s1364-6826(00)00227-3

Pierrard, V., Ripoll, J.-F., Cunningham, G., Botek, E., Santolik, O., Thaller, S., et al. (2021a). Observations and simulations of dropout events and flux enhancements in October 2013: Comparing MEO equatorial with LEO polar orbit. *J. Geophys. Res. Space Phys.* 126, e2020JA028850. doi:10.1029/2020JA028850

Pierrard, V., and Stegen, K. (2008). A three dimensional dynamic kinetic model of the plasmasphere. *J. Geophys. Res. Space Phys.* 113, A10209. doi:10.1029/2008ja013060

Pierrard, V., and Voiculescu, M. (2011). The 3D model of the plasmasphere coupled to the ionosphere. *Geophys. Res. Lett.* 38, L12104. doi:10.1029/2011GL047767

Raissi, M., Perdikaris, P., and Karniadakis, G. E. (2019). Physics-informed neural networks: A deep learning framework for solving forward and inverse problems involving nonlinear partial differential equations. *J. Comput. Phys.* 378, 686–707. doi:10.1016/j.jcp.2018.10.045

Reinisch, B. W., Huang, X., Song, P., Green, J. L., Fung, S. F., Vasyliunas, V. M., et al. (2004). Plasmaspheric mass loss and refilling as a result of a magnetic storm. *J. Geophys. Res.* 109, A01202. doi:10.1029/2003JA009948

Reinisch, B. W., Nsumei, P., Huang, X., and Bilitza, D. K. (2007). Modeling the F2 topside and plasmasphere for IRI using IMAGE/RPI, and ISIS data. *Adv. Space Res.* 39, 731–738. doi:10.1016/j.asr.2006.05.032

Richards, P. G., Meier, R. R., and Wilkinson, P. J. (2010). On the consistency of satellite measurements of thermospheric composition and solar EUV irradiance with Australian ionosonde electron density data. *J. Geophys. Res.* 115, A10309. doi:10.1029/2010JA015368

Richmond, A. D. (1995). Ionospheric electrodynamics using magnetic apex coordinates. *J. Geomagn. Geoelectr.* 47, 191–212. doi:10.5636/jgg.47.191

Ripoll, J.-F., Claudepierre, S. G., Ukhorskiy, A. Y., Colpitts, C., Li, X., Fennell, J., et al. (2020a). Particle dynamics in the Earth's radiation belts: Review of current research and open questions. *J. Geophys. Res. Space Phys.* 125, e2019JA026735. doi:10.1029/2019JA026735

Ripoll, J.-F., Denton, M. H., Hartley, D. P., Reeves, G. D., Malaspina, D., Cunningham, G. S., et al. (2020b). Scattering by whistler-mode waves during a quiet period perturbed by substorm activity. *J. Atmos. Solar-Terrestrial Phys.* 215, 105471. doi:10.1016/j.jastp.2020.105471

Ripoll, J.-F., Kluth, G., Has, S., Fischer, A., Mougeot, M., and Camporeale, E. (2022b). "Exploring pitch-angle diffusion during high speed streams with neural networks," in 2022 3rd URSI Atlantic and Asia Pacific Radio Science Meeting (AT-AP-RASC), Gran Canaria, Spain, 2022, 1–4. doi:10.23919/AT-APRASC54737.2022.9814235

Ripoll, J.-F., Loridan, V., Denton, M. H., Cunningham, G., Reeves, G., Santolík, O., et al. (2019). Observations and Fokker-Planck simulations of the L-shell, energy, and pitch angle structure of Earth's electron radiation belts during quiet times. *J. Geophys. Res. Space Phys.* 124, 1125–1142. doi:10.1029/2018ja026111

Ripoll, J.-F., Reeves, G. D., Cunningham, G. S., Loridan, V., Denton, M., Santolik, O., et al. (2016). Reproducing the observed energy dependent structure of Earth's electron radiation belts during storm recovery with an event-specific diffusion model. *Geophys. Res. Lett.* 43, 5616–5625. doi:10.1002/2016GL068869

Ripoll, J.-F., Santolík, O., Reeves, G. D., Kurth, W. S., Denton, M. H., Loridan, V., et al. (2017). Effects of whistler mode hiss waves in March 2013. *J. Geophys. Res. Space Phys.* 122, 7433–7462. doi:10.1002/2017JA024139

Ripoll, J.-F., Thaller, S. A., Hartley, D. P., Cunningham, G. S., Pierrard, V., Kurth, W. S., et al. (2022a). Statistics and empirical models of the plasmasphere boundaries from the van allen probes for radiation belt physics. *Geophys. Res. Lett.* 49, e2022GL101402. doi:10.1029/2022GL101402

Saikin, A. A., Shprits, Y. Y., Drozdov, A. Y., Landis, D. A., Zhelavskaya, I. S., and Cervantes, S. (2021). Reconstruction of the radiation belts for solar cycles 17–24 (1933–2017). *Space weather*. 19, e2020SW002524. doi:10.1029/2020SW002524

Sheeley, B. W., Moldwin, M. B., Rassoul, H. K., and Anderson, R. R. (2001). An empirical plasmasphere and trough density model: CRRES observations. *J. Geophys. Res.* 106 (11), 25631. doi:10.1029/2000JA000286

Shprits, Y., Subbotin, D., Drozdov, A., Usanova, M. E., Kellerman, A., Orlova, K., et al. (2013). Unusual stable trapping of the ultrarelativistic electrons in the Van Allen radiation belts. *Nat. Phys.* 9, 699–703. doi:10.1038/nphys2760

Singh, A. K., Singh, R. P., and Siingh, D. (2011). State studies of Earth's plasmasphere: A review. *Planet. Space Sci* 59, 810–834. doi:10.1016/j.pss.2011.03.013

Sorathia, K. A., Michael, A., Merkin, V., Ukhorskiy, A., Turner, D. L., Lyon, J., et al. (2021). The role of mesoscale plasma sheet dynamics in ring current formation. *Front. Astron. Space Sci.* 8, 761875. doi:10.3389/fspas.2021.761875

Sorathia, K. A., Merkin, V. G., Panov, E. V., Zhang, B., Lyon, J. G., Garretson, J., et al. (2020). Ballooning-interchange instability in the near-earth plasma sheet and auroral beads: Global magnetospheric modeling at the limit of the MHD approximation. *Geophys Res. Lett.* 47, e2020GL088227. doi:10.1029/2020gl088227

Sorathia, K., Ukhorskiy, A. Y., Merkin, V. G., Fennell, J. F., and Claudepierre, S. G. (2018). Modeling the depletion and recovery of the outer radiation belt during a geomagnetic storm: Combined MHD and test particle simulations. *J. Geophys. Res. Space Phys.* 123, 5590–5609. doi:10.1029/2018ja025506

Storey, L. R. O. (1953). An investigation of whistling atmospherics. *Math. Phys. Sci.* 246, 246113–246141. doi:10.1098/rsta.1953.0011

Subbotin, D. A., and Shprits, Y. Y. (2009). Three-dimensional modeling of the radiation belts using the Versatile Electron Radiation Belt (VERB) code. *Space weather*. 7, S10001. doi:10.1029/2008SW000452

Sun, Y.-Y., Matsuo, T., Maruyama, N., and Liu, J.-Y. (2015). Field-aligned neutral wind bias correction scheme for global ionospheric modeling at midlatitudes by assimilating FORMOSAT-3/COSMIC <scp> h _m F </scp> $_2$ data under geomagnetically quiet conditions. *J. Geophys. Res. Space Phys.* 120, 3130–3149. doi:10.1002/2014JA020768

Tapping, K. F. (2013). The 10.7 cm solar radio flux (F10.7). *Space weather*. 11, 394–406. doi:10.1002/swe.20064

Thaller, S., Ripoll, J-F., Nishimura, T., and Erickson, P. (2022). Editorial: Coupled feedback mechanisms in the magnetosphere-ionosphere system. *Front. Astron. Space Sci.* 9, 1011217. doi:10.3389/fspas.2022.1011217

Thomas, N., Shiokawa, K., Miyoshi, Y., Kasahara, Y., Shinohara, I., Kumamoto, A., et al. (2021). Investigation of small-scale electron density irregularities observed by the Arase and Van Allen Probes satellites inside and outside the plasmasphere. *J. Geophys. Res. Space Phys.* 126, e2020JA027917. doi:10.1029/2020JA027917

Thorne, R. M. (2010). Radiation belt dynamics: The importance of wave-particle interactions. *Geophys. Res. Lett.* 37, L22107. doi:10.1029/2010GL044990

Toffoletto, F., Sazykin, S., Spiro, R., and Wolf, R. (2003). Inner magnetospheric modeling with the rice convection model. *Space Sci. Rev.* 107, 175–196. doi:10.1023/a:1025532008047

Torkar, K., Nakamura, R., Wellenzohn, S., Jeszenszky, H., Torbert, R. B., Lindqvist, P. A., et al. (2019). Improved determination of plasma density based on spacecraft potential of the magnetospheric Multiscale mission under active potential control. *IEEE Trans. Plasma Sci.* 47 (8), 3636–3647. doi:10.1109/TPS.2019.2911425

Torkar, K., Nakamura, R., Tajmar, M., Scharlemann, C., Jeszenszky, H., Laky, G., et al. (2016). Active spacecraft potential control investigation. *Space Sci. Rev.* 199, 515–544. doi:10.1007/s11214-014-0049-3

Tu, W., Cunningham, G. S., Chen, Y., Henderson, M. G., Camporeale, E., and Reeves, G. D. (2013). Modeling radiation belt electron dynamics during GEM challenge intervals with the DREAM3D diffusion model. *J. Geophys. Res. Space Phys.* 118, 6197–6211. doi:10.1002/jgra.50560

Tu, W., Li, X., Chen, Y., Reeves, G. D., and Temerin, M. (2009). Storm-dependent radiation belt electron dynamics. *J. Geophys. Res.* 114 (2), A02217. doi:10.1029/2008JA013480

Verbanac, G., Pierrard, V., Bandić, M., Darrouzet, F., Rauch, J.-L., and Décréau, P. (2015). The relationship between plasmapause, solar wind and geomagnetic activity between 2007 and 2011. *Ann. Geophys.* 33, 1271–1283. doi:10.5194/angeo-33-1271-2015

Wang, D., and Shprits, Y. Y. (2019). On how high-latitude chorus waves tip the balance between acceleration and loss of relativistic electrons. *Geophys. Res. Lett.* 46, 7945–7954. doi:10.1029/2019GL082681

Wang, Y., Tu, J., and Song, P. (2015). A new dynamic fluid-kinetic model for plasma transport within the plasmasphere. *J. Geophys. Res.* 120, 8486–8502. doi:10.1002/2015ja021345

Wygant, J. R., Bonnell, J. W., Goetz, K., Ergun, R. E., Mozer, F. S., Bale, S. D., et al. (2013). The electric field and waves instruments on the radiation belt storm probes mission. *Space Sci. Rev.* 179 (1-4), 183–220. doi:10.1007/s11214-013-0013-7

Zhang, B., Brambles, O. J., Cassak, P. A., Ouellette, J. E., Wiltberger, M., Lotko, W., et al. (2017). Transition from global to local control of dayside reconnection from ionospheric-sourced mass loading. *J. Geophys Res. Space Phys.* 122, 9474–9488. doi:10.1002/2016ja023646

Zhang, B., Sorathia, K. A., Lyon, J. G., Merkin, V. G., Garretson, J. S., and Wiltberger, M. (2019). Gamera: A threedimensional finite-volume MHD solver for non-orthogonal curvilinear geometries. *Astrophys. J. Suppl. Ser.* 244 (1), 20.

Zhelavskaya, I. S., Aseev, N. A., and Shprits, Y. Y. (2021). A combined neural network- and physics-based approach for modeling plasmasphere dynamics. *J. Geophys. Res. Space Phys.* 126, e2020JA028077. doi:10.1029/2020JA028077

Zhelavskaya, I., Shprits, Y., Spasojevic, M., and Kurth, W. (2020). Electron density derived with the neural-network-based upper-hybrid resonance determination algorithm from the van allen probes EMFISIS measurements. *GFZ Data Serv.* 2020, 245. doi:10.5880/GFZ.2.8.2020.002

Zhelavskaya, I. S., Shprits, Y. Y., and Spasojevic, M. (2017). Empirical modeling of the plasmasphere dynamics using neural networks. *J. Geophys. Res. Space Phys.* 122, 11227–11244. doi:10.1002/2017JA024406

Zhelavskaya, I. S., Shprits, Y. Y., and Spasojevic, M. (2018). "Reconstruction of plasma electron density from satellite measurements via artificial neural networks," in *Machine learning techniques for space weather*. Editors E. Camporeale and S. J. R. WingJohnson (Netherlands: Elsevier), 301–327. doi:10.1016/B978-0-12-811788-0.00012-3

Zhelavskaya, I. S., Spasojevic, M., Shprits, Y. Y., and Kurth, W. S. (2016). Automated determination of electron density from electric field measurements on the Van Allen Probes spacecraft. *J. Geophys. Res. Space Phys.* 121, 4611–4625. doi:10.1002/2015JA022132

Advantages of publishing in Frontiers

OPEN ACCESS
Articles are free to read for greatest visibility and readership

FAST PUBLICATION
Around 90 days from submission to decision

HIGH QUALITY PEER-REVIEW
Rigorous, collaborative, and constructive peer-review

TRANSPARENT PEER-REVIEW
Editors and reviewers acknowledged by name on published articles

Frontiers
Avenue du Tribunal-Fédéral 34
1005 Lausanne | Switzerland

Visit us: www.frontiersin.org
Contact us: frontiersin.org/about/contact

REPRODUCIBILITY OF RESEARCH
Support open data and methods to enhance research reproducibility

DIGITAL PUBLISHING
Articles designed for optimal readership across devices

FOLLOW US
@frontiersin

IMPACT METRICS
Advanced article metrics track visibility across digital media

EXTENSIVE PROMOTION
Marketing and promotion of impactful research

LOOP RESEARCH NETWORK
Our network increases your article's readership